

Dissertation zur Erlangung des Doktorgrades
der Fakultät für Chemie und Pharmazie
der Ludwig-Maximilians-Universität München

**Translating Molecular Concepts to the Solid State:
Synthetic Modification, Dynamics and Diffusion
in Covalent Organic Frameworks**

Lars Grunenberg

aus
Bad Neuenahr-Ahrweiler, Deutschland

2023

Erklärung

Diese Dissertation wurde im Sinne von § 7 der Promotionsordnung vom 28. November 2011 von Frau Prof. Dr. Bettina V. Lotsch betreut.

Eidestattliche Versicherung

Diese Dissertation wurde eigenständig und ohne unerlaubte Hilfe erarbeitet.

München, den 31.08.2023

Lars Grunenberg

Dissertation eingereicht am: 31.08.2023
1. Gutachterin: Prof. Dr. Bettina V. Lotsch
2. Gutachter: Prof. Dr. Konstantin Karaghiosoff
Mündliche Prüfung am : 06.11.2023

“What I cannot create, I do not understand.”

Richard Feynman

Danksagung

Als Erstes bedanke ich mich herzlich bei Prof. Bettina V. Lotsch für die Möglichkeit, meine Arbeit in Ihrer Gruppe anzufertigen zu dürfen. Bettina, ich danke Dir für Dein Vertrauen, die Betreuung und Unterstützung, aber ganz besonders auch für Deine thematische Flexibilität und die gewährte wissenschaftliche Freiheit, mit der ich interessante Fragestellungen untersuchen durfte. Deine Offenheit gegenüber eigenen Ideen hat mich bereits in unseren ersten Gesprächen vor dem Beginn meiner Arbeit sehr überzeugt.

Außerdem danke ich Prof. Konstantin Karaghiosoff für die Anfertigung des Zweitgutachtens sowie Prof. Andreas Kornath, Prof. Oliver Trapp, Prof. Thomas M. Klapötke und Prof. Silvija Markic für die Bildung der Prüfungskommission, sowie Dr. Dieter Fischer als externen Ansprechpartner am Max-Planck-Institut für Festkörperforschung.

Für die tatkräftige Unterstützung danke ich meinem F-Praktikanten Vincent P. Ruf und den Bachelor-Studierenden Afonso Cima Bergesch und Sara G. M. Dieffenbach.

Ich danke meinen Kollaborationspartner*innen vom MPI Stuttgart und den Universitäten Groningen, Stuttgart und München. Besonders möchte ich Maxwell W. Terban, Gökcen Savasci, Cosima Stähler, Simon Krause, Christopher Keßler und Stefan Trenker hervorheben. Danke für inspirierende und kreative fachliche Diskussionen, für die tolle Zeit und die großartige Zusammenarbeit an gemeinsamen Projekten, die ohne euch nicht möglich gewesen wären! Mein Dank richtet sich außerdem an die Professoren Robert Dinnebier, Christian Ochsenfeld, Ben L. Feringa und Niels Hansen für die Förderung und Unterstützung der Zusammenarbeit.

Zusätzlich möchte ich mich bei denen bedanken, die mich auf meinem Weg bereits vor der Promotion begleitet und unterstützt haben. Allen voran danke ich meiner Familie, besonders meiner Mutter Marion, die meinen Experimentierdrang stets mit Toleranz, Wohlwollen und großem Vertrauen unterstützt hat. Ich danke Andreas Windscheif, dass ich im Rahmen meines Apotheken-Praktikums, meiner Facharbeit und auch darüber hinaus in seinem Labor experimentieren durfte. Ich danke meinem Lehrer Paul Goertz für seine Unterstützung beim Aufbau der heimischen Experimentiermöglichkeiten und der Betreuung des "Jugend forscht"-Projekts. Ich danke den ehemaligen Mitgliedern von versuchschemie.de für die Inspiration und die gebotene Vielfalt an hervorragenden und gleichzeitig öffentlich zugänglichen Versuchssprotokollen, die meine Faszination und meinen frühen Kontakt mit synthetischer Chemie maßgeblich beeinflusst haben. Dabei spielte auch das FFF-Programm der Universität Bonn eine Rolle, dessen Koordinator Dr. Thoralf Räsch und Förderern ich danken möchte.

Außerdem danke ich Nina Hartrampf für die Unterstützung während der Studienzeit. Liebe Nina, ich danke Dir nicht nur für Deine erstklassige Betreuung im Rahmen meiner

Bachelorarbeit, sondern auch für Deine Hilfe bei meinen Bewerbungen für Stipendien und der Masterarbeit. Ich bin dankbar für alles, was ich von Dir lernen durfte! Auch den Betreuer*innen der F-Praktika und der Masterarbeit, Nicolas Guimond, Anastasia Hager, Kerstin Gottschling, Frederik Haase und Fabio Lima möchte ich für die spannenden Projekte und die aufregende und abwechslungsreiche Zeit danken.

Ich möchte allen Kolleg*innen aus der Lotsch Gruppe in München und Stuttgart von Herzen danken. Ihr habt meine Zeit in der Gruppe zu einer wunderbaren Erfahrung gemacht. Lustige Retreats, anregende Diskussionen, gemütliche Kaffeerunden und gesellige Grillabende haben nicht nur unsere gemeinsame Zeit bereichert, sondern auch langanhaltende Erinnerungen geschaffen. Ein besonderer Dank geht an Alex, Andi, Charlie, Christian, Fabian, Johannes, Marie, Max, Sam und Sebastian für entspannte Labor- und Bürostunden, gelegentlich begleitet von Popcorn und erfrischenden Getränken, aber stets unter fluffiger Beschallung. Ebenso danke ich Albi, Anna, Claudia, Jakob, Katalin, Kerstin, Leo, Sascha und Stefan für die wundervolle Zeit während meines halben Jahres bei euch in München. Ein herzliches Dankeschön auch an Claudi, Vio und Sigrid für eure offenen Ohren bei organisatorischen und persönlichen Angelegenheiten.

Außerdem danke ich aus tiefstem Herzen meiner Partnerin Göta und unserem treuen Hund Elli. Ich bin dankbar für eure Liebe und seelische Unterstützung, die mich auch durch schwierige Phasen getragen hat. Ihr seid in meinem Leben unersetzlich, und ich freue mich auf weitere unvergessliche Momente mit euch.

Abstract

Covalent organic frameworks are a novel class of crystalline and porous framework materials composed of light elements linked by covalent bonds between their building units. Their unique combination of properties, including permanent porosity, chemical and structural stability, light absorption, and versatility in structural design and composition, has led to an ever-expanding range of applications, including energy storage and conversion, heterogeneous (photo)catalysis, gas adsorption, and sensing. Even though COFs are solid-state materials, their organic composition promises unparalleled possibilities for modifications in chemical structure with similar versatility and precision as known from small organic molecular compounds. This comparability is inspiring for transferring additional classical molecular concepts to this class of solid-state materials.

In this thesis we transfer typical molecular concepts, such as the *modification* of organic functional groups as part of the chemical structure, stimuli-responsive *dynamics* and *mobility*, to covalent organic frameworks – as solid-state materials.

We present novel topochemical *modification* methods for post-synthetic linkage conversion of imine linkages to convert imine COFs into secondary amine-linked and nitrone-linked frameworks. These methods allow for a fine-tuning of materials properties, such as the stabilization of their chemical connectivity, reactivity for further functionalization, and pore channel polarity. To follow the conversion of bonds, properties, and structure, we employ a diverse set of analytical techniques, including FT-IR and solid-state NMR spectroscopy, gas and vapor sorption experiments and X-ray powder diffraction coupled with pair-distribution function analysis.

With the aim to study stimuli-responsive *dynamics* in COFs, we synthesize the first covalent organic framework with light-driven molecular motors embedded as building blocks in its chemical structure. The dynamics of the rotors in the material are probed by *in situ* spectroscopic techniques including Raman, FT-IR and UV-Vis spectroscopy. Although the presented materials fulfill important characteristics such as permanent porosity and thus, void space for motor rotation, motor isomerization could not be visualized by available analysis techniques, but allowed to gain insights into experimental and design challenges for transferring this property to solid-state materials. These findings allow to extend the design principles for the construction of next-generation dynamic COFs with stimuli-triggered response.

Finally, we study *mobility* by means of self-diffusion of acetonitrile in an imine-linked covalent organic framework by pulsed field gradient NMR experimentation, complemented by computational simulation methods, i.e. molecular dynamics simulations.

Table of Contents

Danksagung.....	1
Abstract.....	3
Table of Contents.....	5
1 Introduction: Covalent Organic Frameworks.....	9
1.1 Design Principles of COFs	9
1.1.1 Geometry Matching of Building Blocks: Topologies in COFs	10
1.1.2 Reversibility of Bond Formation: Dynamic Covalent Chemistry.....	11
1.1.3 Linkage Types in COFs	12
1.1.4 (Un-)limited Structural Variety in COFs?	13
1.2 Structural Elements Define Properties.....	15
1.2.1 Topology-Guided Properties	16
1.2.2 Chemical Diversity of Building Blocks Creates Function	17
1.2.3 Linkages as Active Structural Elements	18
1.3 Bibliography	19
2 Post-Synthetic Modification of COFs.....	23
2.1 Introduction to Post-Synthetic Modification	24
2.1.1 Building Block Engineering vs. Post-Synthetic Modification	24
2.1.2 Types of Post-Synthetic Modification Reactions.....	25
2.1.3 Target Sites for Post-Synthetic Modification.....	26
2.2 Post-Synthetic Linkage Modification.....	27
2.2.1 Stability vs. Crystallinity – The Role of Linkages in COFs.....	28
2.2.2 Stability with Reversible Bonds? – Fundamental Influences in COFs	29
2.3 PSM of Imine-Linked Frameworks: A Literature Overview	31
2.3.1 Oxidative Linkage Transformation Reactions.....	33
2.3.2 Reductive Transformations of Imine Linkages	36
2.3.3 Oxidative and Reductive Cycloadditions with Imine Linkages	38
2.3.4 Conclusion	39
2.4 How to: Practical Aspects for Linkage Conversions.....	40
2.4.1 Step 1: Defining the Goal of the PSM Strategy	40
2.4.2 Step 2: Selection of the Framework	41
2.4.3 Step 3: Selection of a Modification Reaction.....	42
2.4.4 Step 4: Planning Workup and Analysis.....	44
2.4.5 Step 5: Starting Experiments: Variation of Reaction Conditions	50
2.5 Bibliography	52

3 Research Objective.....	55
4 Amine-Linked COFs: A Platform for Post-Synthetic Structure Interconversion and Modification.....	57
4.1 Introduction	59
4.2 Results	60
4.2.1 Previous Strategies and Drawbacks	60
4.2.2 Synthesis of Amine-Linked COFs	60
4.2.3 One-Pot Procedure: Reductive Crystallization	65
4.2.4 Reductive Formylation: Combined Reduction and Protection	65
4.2.5 Crystalline vs. Disordered	66
4.2.6 Hybrid Materials and Functionalization.....	68
4.3 Conclusion.....	70
4.4 Acknowledgements	71
4.5 Bibliography	71
5 Post-Synthetic Transformation of Imine- into Nitrone-linked COFs for Water Harvesting.....	75
5.1 Introduction	77
5.2 Results	79
5.2.1 Material Synthesis and Analysis.....	79
5.2.2 Water Adsorption Properties.....	82
5.3 Conclusion.....	86
5.4 Acknowledgements	86
5.5 Bibliography	86
6 Light-Driven Molecular Motors Embedded in Covalent Organic Frameworks	89
6.1 Introduction	91
6.2 Results	93
6.2.1 Synthesis and Characterization of the Building Blocks.....	95
6.2.2 Materials Synthesis	97
6.2.3 Irradiation of Solid-State Materials	102
6.3 Conclusion.....	105
6.4 Acknowledgements	106
6.5 Bibliography	106
7 Self-Diffusion of Acetonitrile in a Covalent Organic Framework: Simulation and Experiment.....	113
7.1 Introduction	114
7.2 Results	115
7.2.1 Synthesis and Characterization of COFs	115

7.2.2	Probing Diffusion Experimentally by PFG NMR.....	116
7.2.3	Computational Modelling.....	121
7.3	Conclusion.....	123
7.4	Acknowledgements	124
7.5	Bibliography	125
8	Summary and Conclusions.....	131
9	Appendix	135
9.1	Supporting Information to Chapter 4 Amine-Linked COFs: A Platform for Post-Synthetic Structure Interconversion and Modification.....	136
9.1.1	Methods and Equipment.....	136
9.1.2	Synthetic Procedures.....	139
9.1.3	FT-IR Spectroscopy	154
9.1.4	X-Ray Powder Diffraction	159
9.1.5	ssNMR Spectroscopy.....	167
9.1.6	Nitrogen Gas Adsorption Data	184
9.1.7	Scanning Electron Microscopy.....	200
9.1.8	Transmission Electron Microscopy	203
9.1.9	Stability Tests.....	206
9.1.10	Quantum-Chemical Calculations.....	208
9.1.11	Pair Distribution Function (PDF) Analysis	220
9.1.12	References.....	231
9.2	Supporting Information to Chapter 5 Post-Synthetic Transformation of Imine-into Nitrone-linked COFs for Water Harvesting	234
9.2.1	Methods and Equipment.....	234
9.2.2	Synthetic Procedures.....	236
9.2.3	FT-IR Spectra.....	239
9.2.4	XRPD Data and Structure Refinement.....	241
9.2.5	ssNMR Spectra	244
9.2.6	Nitrogen Gas Sorption Experiments.....	248
9.2.7	Water Vapor Sorption Experiments	255
9.2.8	CO ₂ Gas Sorption Experiments	259
9.2.9	Thermogravimetric Analysis	260
9.2.10	Quantum Chemical Calculations.....	263
9.2.11	<i>In-Situ</i> X-ray Powder Diffraction	265
9.2.12	References.....	269
9.3	Supporting Information to Chapter 6 Light-Driven Molecular Motors Embedded in Covalent Organic Frameworks	271
9.3.1	Methods and Equipment.....	271
9.3.2	Synthetic Procedures.....	274
9.3.3	UV-Vis Spectra	279
9.3.4	FT-IR Spectra.....	280

9.3.5	Raman Spectra	282
9.3.6	XRPD Data and Structure Modeling	283
9.3.7	Pair Distribution Function (PDF) Analysis.....	287
9.3.8	NMR Spectra.....	289
9.3.9	ssNMR Spectra	295
9.3.10	Nitrogen Gas Sorption Analysis.....	301
9.3.11	SEM/TEM Analysis	307
9.3.12	DFT Calculations	308
9.3.13	DIFFaX Simulations.....	317
9.3.14	References.....	318
9.4	Supporting Information to Chapter 7 Self-Diffusion of Acetonitrile in a Covalent Organic Framework: Simulation and Experiment	319
9.4.1	Materials and Methods.....	319
9.4.2	Experimental Procedures	323
9.4.3	Supporting Analytical Data	323
9.4.4	References.....	334
9.5	List of Figures.....	337
9.6	List of Publications	342

1 Introduction: Covalent Organic Frameworks

This chapter provides a general introduction to covalent organic frameworks (COFs). We detail the design principles of COFs as reticular materials and explain how reversible bond formation and the choice of linkage govern the crystallinity and stability of these porous frameworks. We also mention factors that pose a challenge to the seemingly infinite variety of COF structures. Finally, we outline how the individual structural elements can be used to generate functionality in these materials, making them attractive for a variety of applications.

1.1 Design Principles of COFs

Covalent organic networks are a new class of porous materials. Their structure brings together a unique combination of properties that make them attractive and adaptable to a wide range of applications.^[1] They are crystalline, porous, and consist of covalently linked organic molecules as building blocks, making them consist entirely of light elements and tremendously versatile in chemical composition and function. This distinguishes them from other porous materials, such as zeolites or MOFs, whose structural elements are metals.^[2, 3]

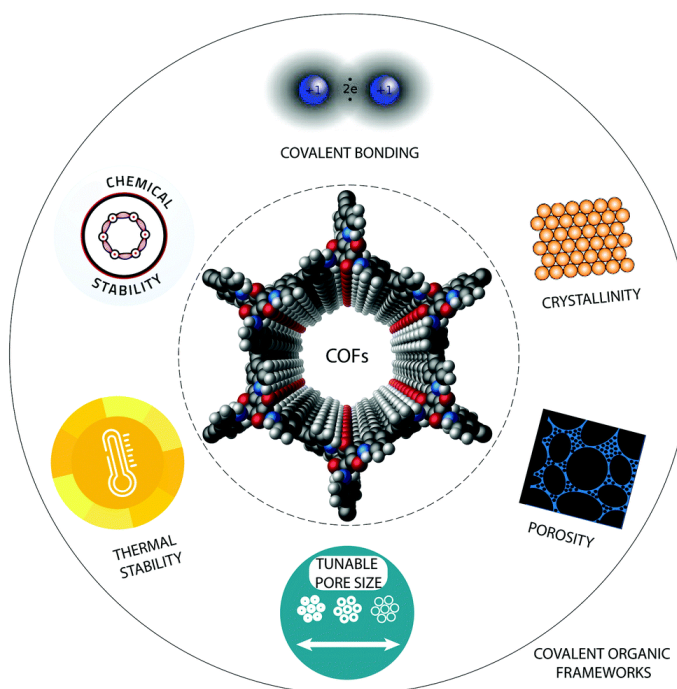


Figure 1-1: COFs provide a unique combination of properties, such as permanent porosity, chemical and thermal stability on a single crystalline platform, which is highly versatile and tunable by the tools of organic chemistry. Reproduced under the terms of CC-BY-NC 3.0 license.^[4] Copyright 2021 Royal Society of Chemistry.

1.1.1 Geometry Matching of Building Blocks: Topologies in COFs

The structure of COFs results from the covalent bonding of symmetrical organic molecules as building blocks. Unlike one-dimensional polymer chains, whose monomers are linked at two positions in the molecule, COFs regularly form two- or even three-dimensional networks as a structure, while extension and symmetry depend on the geometry and number of connectable binding sites of the building blocks as well as their combination.^[5] Thus, their structure may be precisely predesigned by rational choice of building blocks with different symmetries, representing vertices or edges of the framework. Depending on the selected combinations, a variety of network topologies are accessible as depicted in Figure 1-2.^[3]

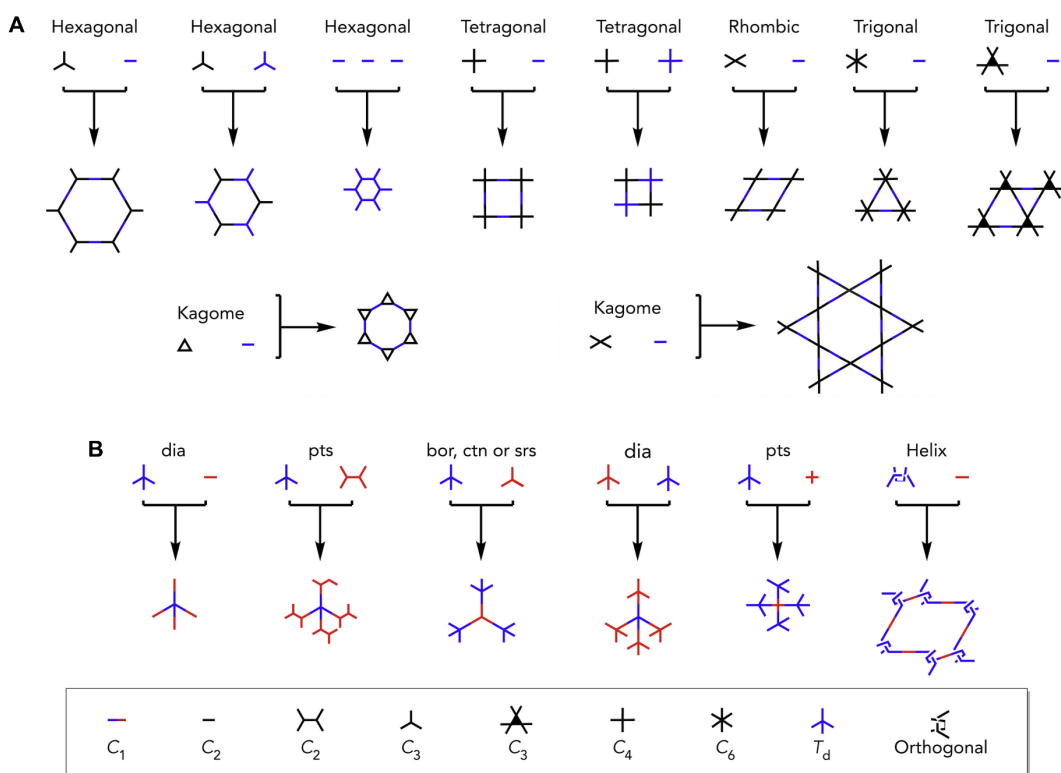


Figure 1-2: Different network topologies can be designed by the choice of building blocks. (A) Combinations of planar building blocks, creating two-dimensional COFs. (B) Selected topologies of 3D COFs. Adapted with permission.^[3] Copyright 2020 Elsevier.

For example, connecting planar building blocks as a $[C_3+C_3]$ knot or $[C_3+C_2]$ knot+linker combination form flat hexagonal nets, i.e. layers, with honeycomb meshes. Other combinations, of square-planar knots $[C_4+C_4]$ or even higher symmetry knots $[C_6+C_2]$ translate to tetragonal or trigonal network topologies, with square- or triangular shaped meshes. It becomes evident that the size of these building blocks and their symmetry combination dictate shapes and sizes of the created nets. While the mentioned examples solely focused on simple building block combinations leading to a single type of pore shape, the kagome lattice possesses both trigonal and hexagonal shapes in different sizes and may be created by combining linear linker and a tetratopic knot with C_2 symmetry. Analogous to

the planar monomers leading to two-dimensional layers, non-planar symmetrical building blocks, for example with tetragonal symmetry (T_d), can form three-dimensional networks and found the scaffolds of 3D COFs.^[2, 6-8] However, also two-dimensional net-like layers in 2D COFs are typically stacked into three-dimensional structures held together by non-covalent interactions, such as π - π interactions between aromatic building blocks of different layers. As a consequence of this assembly in 2D and 3D COFs, there is on the one hand a precise spatial arrangement of each building block in the framework and thus crystallinity, and on the other hand intrinsic porosity in the form of pore channels (2D COFs) or pore networks (3D COFs), the diameter of which is defined by the size, connectivity and symmetry of the building blocks.

1.1.2 Reversibility of Bond Formation: Dynamic Covalent Chemistry

Strong covalent bonds between the building blocks ensure that the spatial assembly, and thus the porosity, is permanently maintained and can withstand various chemical and physical influences.^[9-11] This persistence of porosity in COF scaffolds makes their intrinsically high surface area and variable pore space available for various applications, e.g. for the uptake of (gas) molecules,^[12] as a surface for catalysis^[13-16] or as a sensor,^[17, 18] among others.

While geometry matching of COF building blocks defines their skeletal constitution and important parameters of their pore environment, structural definition in these materials is only accessible by precisely linking their monomers under thermodynamic control. Unlike irreversible bond formation reactions, used for example for the synthesis of amorphous polymers, COF linkages make use of the principle of dynamic covalent chemistry.^[19] This concept relies on reversible bond formation reactions, allowing linkages between building blocks to break up and reform dynamically during synthesis. As a result, defects in the framework can heal and the structure of the product no longer remains kinetically trapped in the defect-rich state but approaches its structural thermodynamic minimum, characterized by crystalline order (Figure 1-3) as predicted by reticular design.^[20]

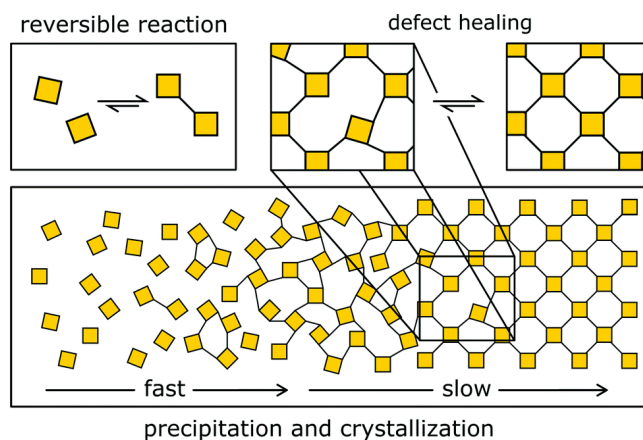


Figure 1-3: Reversible bond formation during COF synthesis allows to heal defects in the material. Reproduced under the terms of CC-BY-NC 3.0 license.^[11] Copyright 2020 Royal Society of Chemistry.

1.1.3 Linkage Types in COFs

The reversibility of bond formation is a critical requirement towards realizing crystalline COFs by bottom-up synthesis from organic precursors. In 2005, the first report of a covalent organic framework by Yaghi and co-workers demonstrated that (self-)condensation reaction of building blocks bearing boronic acids to boroxine-linkages (COF-1) and their condensation with catechols to boronic ester linkages (COF-5), fulfill the reversibility criterion to afford COFs.^[1] Synthesis of these materials was performed in a closed vessel to avoid eliminated water molecules to escape the reaction medium at elevated temperatures, and thus to maintain reversible conditions throughout the entire synthesis. Although boroxine and boronic ester linkages have been shown to provide an excellent basis for inducing long-range order in COFs, even affording single crystalline materials with crystal sizes in the μm range,^[21] these linkages are also prone to hydrolysis, drastically limiting their potential for applications. Ever since, the scope of bond formation reactions to synthesize COFs has been extended by a range of C-N and even C-C bonds aiming to improve stability of the obtained frameworks.

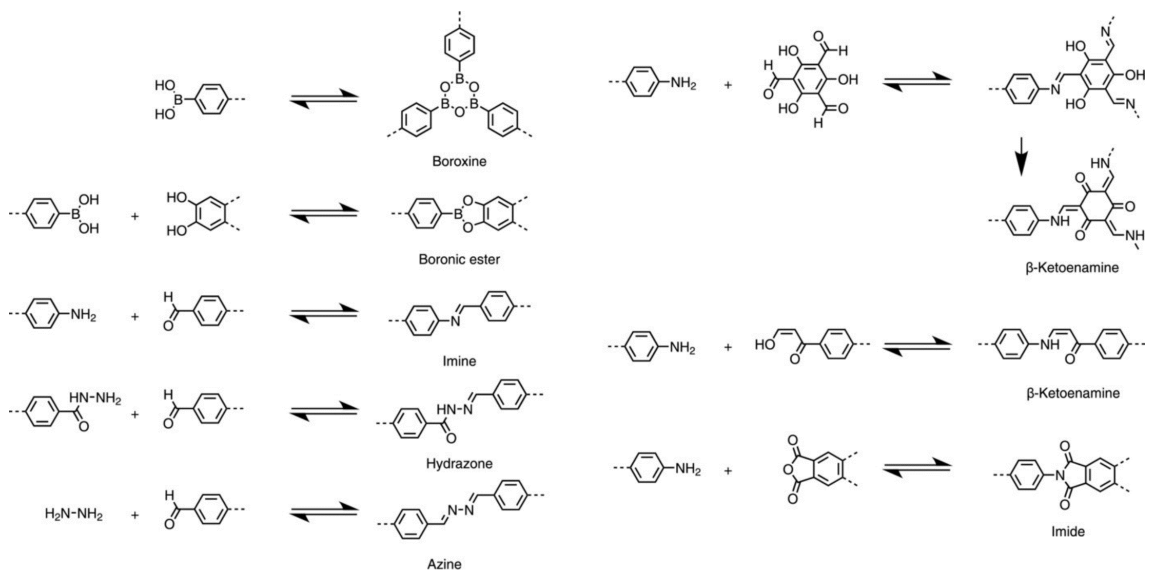


Figure 1-4: A selection of common condensation reactions to construct linkages in COFs. Reprinted with permission.^[2] Copyright 2018 John Wiley and Sons.

To date the collection of available linkages for de-novo synthesis of COFs include imine, hydrazone,^[13, 22] azine,^[23, 24] ketoenamine,^[25, 26] imide,^[27, 28] and olefin linkages,^[29, 30] among others. Despite the enormous variety of linkages,^[31] imine linked COFs constitute the largest class of COFs to date owing to their acceptable hydrolytic stability and reversibility of bond formation, structural rigidity, simple accessibility of precursor building blocks and their versatility for post-synthetic linkage modification towards tailored applications (see Chapter 2.2).^[11, 31]

1.1.4 (Un-)limited Structural Variety in COFs?

Already the presented selection of examples of COF linkage chemistries and varieties in building block topologies may seem to lead to an infinite of material matrix with different structures, stabilities and properties. Even though the space of possible combinations is fairly huge, there are also limitations rendering the practical accessibility of certain arbitrary materials still challenging.

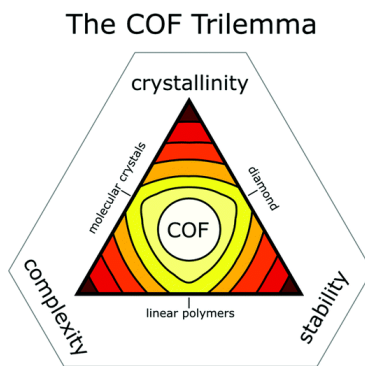


Figure 1-5: Obtaining complex COFs with high crystallinity and high stability remains a challenging task for COF researches, known as the COF trilemma. Adapted under the terms of CC-BY 4.0 license.^[11] Copyright 2020 Royal Society of Chemistry.

A prototypical example for these challenges is the dichotomy between crystallinity and stability in COFs constructed from reversible bonds. The fact that increased chemical stability of a linkage, at the same time reduces the reversibility of bond formation, often causes a less structurally defined material with decreased crystallinity, as defects in the material can only heal to limited extent (see Chapter 2.2.1).^[11] In turn, to compensate for reduced reversibility, harsh reaction conditions, such as strong acids as catalysts, or elevated temperatures may be used. However, this often leads to an incompatibility of functional groups in structurally more complex building blocks, which are often desired to create tailored COFs for demanding applications. This complex dependence of parameters in COF chemistry has been introduced as “the COF trilemma”.^[11] Although it still remains as a challenge for researches working with complex framework materials, a range of strategies to overcome the trilemma have been suggested, among which post-synthetic building block exchanges, or post-synthetic linkage modifications (see Chapters 2, 4, 5) have been shown to provide elegant solutions by decoupling the framework crystallization, as the order inducing step, from the stability and/or functionality providing post-synthetic modification step.^[32]

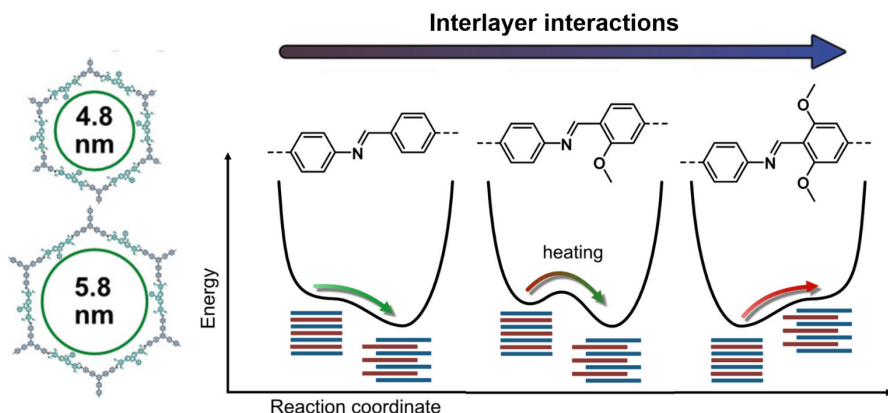


Figure 1-6: Methoxy group substituted building blocks increase interlayer interactions in large pore diameter COFs and stabilize the structure against thermally induced layer displacement. Adapted under the terms of CC-BY 4.0 license.^[33] Copyright 2021 American Chemical Society.

The simplistic approach of considering COFs solely from the perspective of reticular materials whose pore size can be varied simply by geometric extension of edges within the lattice neglects the substantial role of interlayer interactions in these materials. It has been observed that COFs with larger pore diameters (>3 nm) tend to exhibit thermal instability in their stacking order^[33] (Figure 1-6) as well as pore collapse under the influence of solvents evaporating from the pores.^[34] In detail, interlayer interactions based on π - π interactions of the aromatic building blocks only were insufficient to ensure structural stability of the network with larger pores. In contrast, by varying the chemical structure of the building blocks to add additional contributions of dipole interactions by introducing methoxy groups into the building block's chemical structure^[33] or, in another example, hydrogen bonding of amide functional groups as supporting interlayer interactions,^[34] record pore diameters up to 10 nm^[35] could be achieved, and the materials were less susceptible to pore collapse or thermal displacement of the layers (Figure 1-6).

Interestingly, however, interactions between layers or building blocks in other COF systems can also hinder the synthetic accessibility of seemingly analogous systems if topological relation is considered solely. As an example, the interpenetration of frameworks in 3D COFs can be mentioned in this context.^[36] Here, π -interactions of the building blocks lead to the growth of interpenetrated networks within the pore space of the targeted skeleton.^[6]

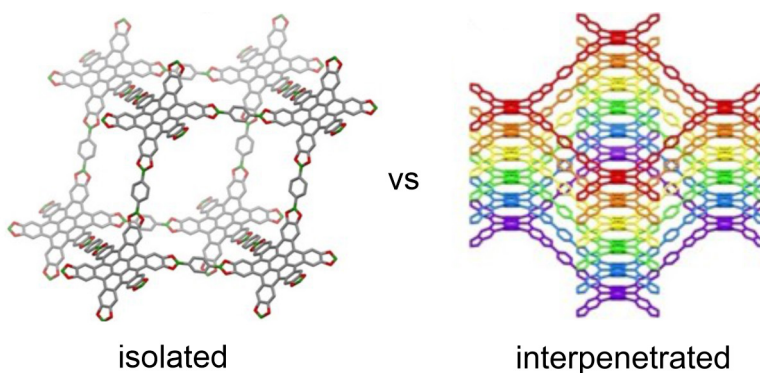


Figure 1-7: A comparison between a targeted isolated network and the experimentally obtained interpenetrated structure due to extensive π -stacking of building blocks. Adapted with permission.^[6] Copyright 2021 John Wiley and Sons.

As a result, an interpenetrated network is formed, which complicates the synthetic realization of high pore volume in the material, which in contrast would be expected from the idealized non-interpenetrated structure. Only in selected COFs^[37] the interpenetration was successfully suppressed by the inclusion of guest molecules and solvent during synthesis. Furthermore, the stability of the network after removal of guest molecules is usually compromised, which required additional stabilization by sterically demanding functional groups in the pore void space.^[37]

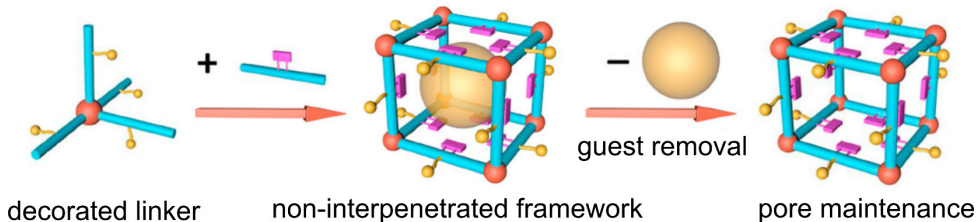


Figure 1-8: A steric stabilization strategy combined with guest molecule incorporation during synthesis allowed synthesis of a non-interpenetrated, yet structurally stable 3D COF. Reprinted with permission.^[37] Copyright 2020 American Chemical Society.

In summary, although simplified models are helpful to understand the general concepts of the structure of COFs, these models only lead to feasible structures when the entirety of building block properties, namely, geometry, chemical structure and interactions between them are considered collectively. On the basis of this consideration an almost infinite number of different materials of this class can still be achieved.

1.2 Structural Elements Define Properties

The structured assembly of COFs, starting from each individual structural element, offers possibilities for customizing the material and its properties. Systematic modification of the properties makes this class of materials not only diverse, but also methodically adaptable and designable for tailored applications with respect to possible applications.^[38] In the following

section, we will explain these structure-property relationships in the context of realized fields of application and their relation to structural elements, defined as network topology, chemical structure of building blocks and the linkages.

1.2.1 Topology-Guided Properties

As explained in the previous section, the symmetries of the combined building blocks generally determine the topology of the resulting network and define the shape and size of the resulting pores. Varying combinations of building blocks of different symmetry and size is therefore a direct and easily understood way to modulate material properties. Varying the pore size can alter the accessibility of the pore space to molecules of different sizes, thus creating selectivity for small molecules in microporous pore channels, for example, while excluding larger molecules.^[39] This size selectivity can thus be used not only for selective adsorption of gases^[40, 41] or vapors,^[42] but, extended to larger pore diameters, also for optimized product selectivity in catalysis.^[43] Here, it was shown that the selectivity for ring closure, i.e. cyclization, is increased in a ruthenium-catalyzed olefin metathesis reaction, while oligomerization is disfavored in the narrow pore channels.^[14]

A change in pore shape can also alter the interactions between sorbate and sorbent. Jiang and co-workers^[44] observed increased interaction of imine bonds as part of the pore wall with adsorbed water molecules in imine-linked microporous COFs with trigonal pore channels. This resulted in reduced hysteresis between water vapor uptake and release. At the same time, condensation of water vapor in the pores was achieved at reduced relative humidity, which was attributed to the facilitated formation of water clusters in these pore channels.^[44]

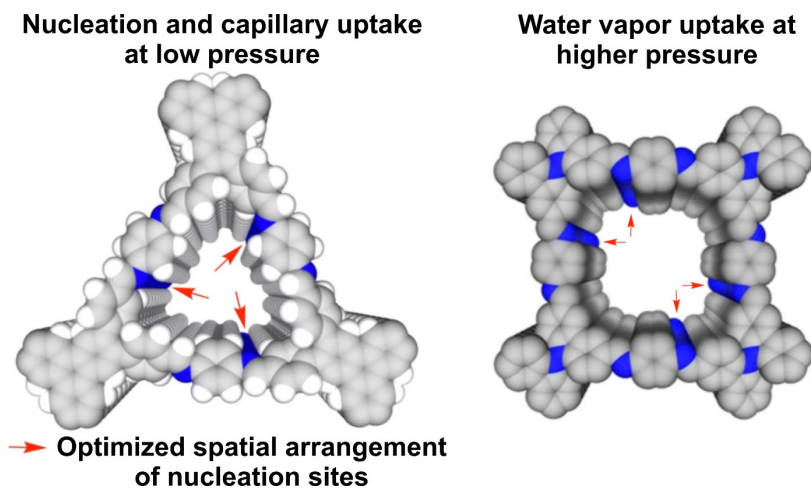


Figure 1-9: Trigonal pore channels feature an optimized spatial arrangement of nucleation sites in their pore channels, leading to optimized properties for water vapor adsorption, compared to COFs with different topologies. Adapted under the terms of CC-BY 4.0 license.^[44] Copyright 2021 Springer Nature.

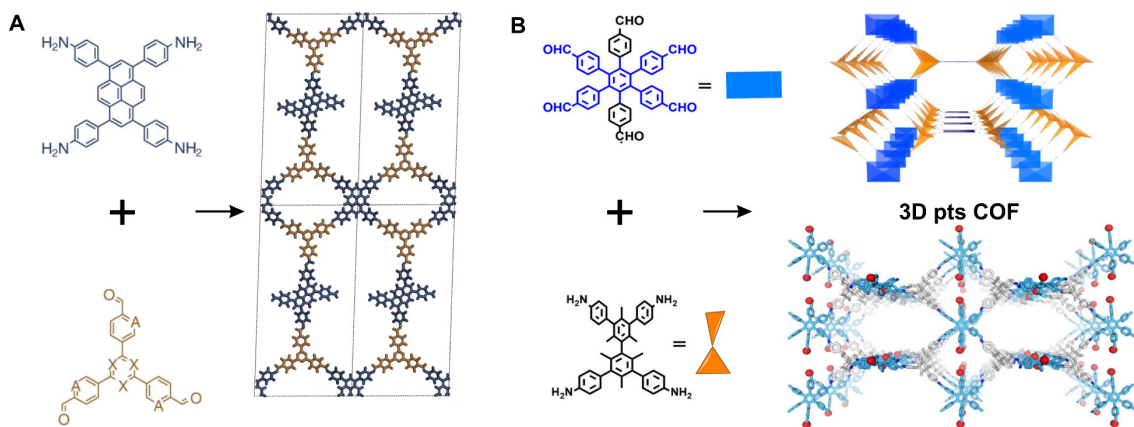


Figure 1-10: Substoichiometric designs for COFs in 2D (A) and 3D (B) structures. Adapted under the terms of CC-BY 4.0 license,^[45] and with permission.^[46] Copyright 2019 Springer Nature, and 2021 American Chemical Society, respectively.

As a basis for the choice of a network topology, in most COF systems it is assumed that the binding sites in the monomers are linked as completely as possible in order to reduce defects in the material and to obtain the desired network topology, which can usually be achieved with stoichiometric amounts of the required building blocks. In contrast, using non-stoichiometric or sub-stoichiometric amounts of one of the monomers, crystalline polymers with modified topologies can also be synthesized, which are additionally contain uncondensed binding sites (Figure 1-10). In this context, highly symmetric building blocks are considered as building blocks with a reduced symmetry and number of bonding sites, leading to substoichiometric two-^[45] or three-dimensional^[46] COFs depending on the chosen monomer combination. For example, C₄ building blocks with four binding sites can be used as an equivalent to linearly symmetric C₂ building blocks with two binding sites. The unreacted functional groups in these materials can modulate the polarity of the pores and thus the interaction with molecules, serve as binding sites for further post-synthetic modification, or even generate functionality as catalytically active sites in the materials.^[45, 46]

1.2.2 Chemical Diversity of Building Blocks Creates Function

Besides their function as purely structural components in the network, the variability of the chemical structure of the molecular building blocks offers perhaps the greatest diversity of customization possibilities in COFs. Analogous to the explained examples of unlinked functional groups in substoichiometric COFs, the chemical structure of the building blocks can change fundamental properties such as the polarity of the pore channels or optical properties of the COF, or provide binding sites for (post-synthetic) immobilization of molecules or metals and thus facilitate further complexity of the frameworks structure and functionality. As a selected illustrative example in which the chemical structure of the monomers provides an interesting function that directly translates to an application, we would like to limit this section to redox-active building blocks in COFs to outline the concept.

Engaging redox-active building blocks as linkers in COFs endows these with interesting properties such as electrical energy storage or conductivity.^[47, 48]

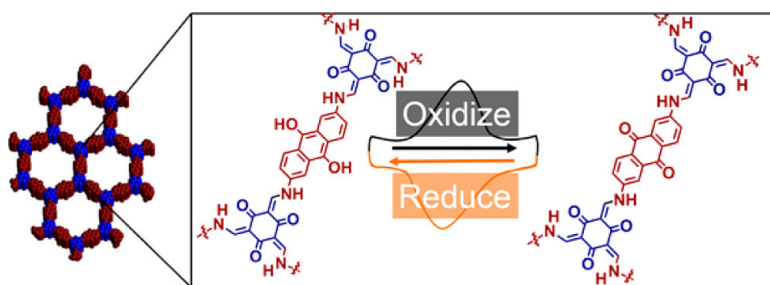


Figure 1-11: Redox-active 2,6-diaminoanthraquinone (DAAQ) moieties as building blocks enables energy storage. Reprinted with permission.^[49] Copyright 2013 American Chemical Society.

1.2.3 Linkages as Active Structural Elements

One design element that is often reduced only to its role in stabilizing the COF structure is the linkage between building blocks in COFs. Since the chemical structure is constructed to a much higher mass fraction by the monomers, which are very diverse and variable in their chemical structure, the bond often takes a background role as a nevertheless important neighbor along the pore channels.

However, with the development of post-synthetic modification reactions that specifically target the linkage of the material, this component of the COF structure is also moving back into focus as a basis for the modification of properties in addition to the stabilization of the network.^[50-53]

A rare but illustrative example of how pore polarity, and thus adsorption of water vapor in the pore channels, cannot be accomplished exclusively via a building block-based approach is shown by the partial post-synthetic oxidation of (hydr)azine bonds to hydrazides (Figure 1-12). Although complete bond conversion was not achieved (about 10%), the partially oxidized materials showed improved water vapor uptake at low relative pressures. This work highlights that even small changes in bonding can lead to a significant change in material properties and highlights the importance of the bond as an equal partner in fulfilling this role alongside the chemical structure of the building blocks.^[54]

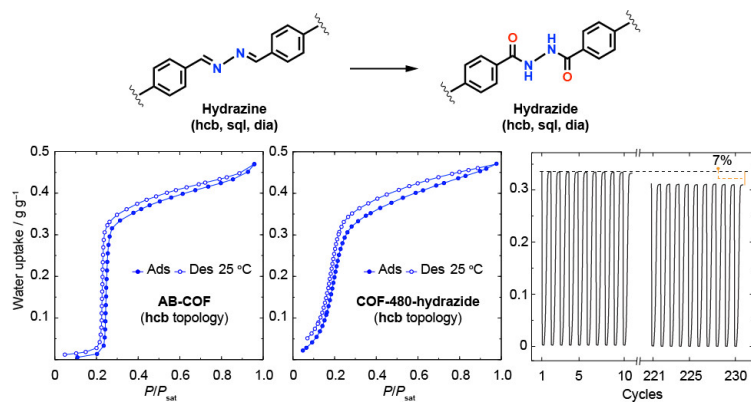


Figure 1-12: Pore surface engineering presented by post-synthetic linkage modification to fine-tune water vapor adsorption highlights the potential of the linkages as an active site, besides the building block, to modulate framework functions. Reprinted under the terms of CC-BY-NC-ND 4.0 license.^[54] Copyright 2022 American Chemical Society.

The distinctive role of bonds and new methods for their post-synthetic modification are also part of the research presented in this dissertation. A detailed introduction to post-synthetic bond modification is given in the following chapter (Chapter 2), while the methods and applications developed for this purpose are presented in Chapters 4 and 5, respectively.

1.3 Bibliography

1. Cote A. P. et al. Porous, Crystalline, Covalent Organic Frameworks. *Science* **310**, 1166-1170 (2005).
2. Lohse M. S., Bein T. Covalent Organic Frameworks: Structures, Synthesis, and Applications. *Adv. Funct. Mater.* **28** (2018).
3. Jiang D. Covalent Organic Frameworks: An Amazing Chemistry Platform for Designing Polymers. *Chem* **6**, 2461-2483 (2020).
4. Zhao X., Pachfule P., Thomas A. Covalent Organic Frameworks (Cofs) for Electrochemical Applications. *Chem. Soc. Rev.* **50**, 6871-6913 (2021).
5. Bisbey R. P., Dichtel W. R. Covalent Organic Frameworks as a Platform for Multidimensional Polymerization. *ACS Cent. Sci.* **3**, 533-543 (2017).
6. Martinez-Abadia M. et al. Pi-Interpenetrated 3d Covalent Organic Frameworks from Distorted Polycyclic Aromatic Hydrocarbons. *Angew Chem Int Ed Engl* **60**, 9941-9946 (2021).
7. Gao C. et al. Redox-Triggered Switching in Three-Dimensional Covalent Organic Frameworks. *Nat. Commun.* **11**, 4919 (2020).
8. Ma Y. et al. Three-Dimensional Chemically Stable Covalent Organic Frameworks through Hydrophobic Engineering. *Angew. Chem. Int. Ed.* **59**, 19633-19638 (2020).
9. Cusin L., Peng H., Ciesielski A., Samorì P. Chemical Conversion and Locking of the Imine Linkage: Enhancing the Functionality of Covalent Organic Frameworks. *Angew. Chem. Int. Ed.* **133**, 14356-14370 (2021).
10. Geng K. et al. Covalent Organic Frameworks: Design, Synthesis, and Functions. *Chem. Rev.* **120**, 8814-8933 (2020).

11. Haase F., Lotsch B. V. Solving the Cof Trilemma: Towards Crystalline, Stable and Functional Covalent Organic Frameworks. *Chem. Soc. Rev.* **49**, 8469-8500 (2020).
12. Krause S., Hosono N., Kitagawa S. Chemistry of Soft Porous Crystals: Structural Dynamics and Gas Adsorption Properties. *Angew. Chem. Int. Ed.* **59**, 15325-15341 (2020).
13. Stegbauer L., Schwinghammer K., Lotsch B. V. A Hydrazone-Based Covalent Organic Framework for Photocatalytic Hydrogen Production. *Chem. Sci.* **5**, 2789-2793 (2014).
14. Emmerling S. T. et al. Olefin Metathesis in Confinement: Towards Covalent Organic Framework Scaffolds for Increased Macrocyclization Selectivity. *Chemistry* **28**, e202104108 (2022).
15. Biswal B. P. et al. Sustained Solar H(2) Evolution from a Thiazolo[5,4-D]Thiazole-Bridged Covalent Organic Framework and Nickel-Thiolate Cluster in Water. *J. Am. Chem. Soc.* **141**, 11082-11092 (2019).
16. Alsudairy Z. et al. Covalent Organic Frameworks in Heterogeneous Catalysis: Recent Advances and Future Perspective. *Mater. Chem. Front.* **7**, 3298-3331 (2023).
17. Jiang S. et al. Dual-Functional Two-Dimensional Covalent Organic Frameworks for Water Sensing and Harvesting. *Mater. Chem. Front.* **5**, 4193-4201 (2021).
18. Gomes R., Bhaumik A. A New Triazine Functionalized Luminescent Covalent Organic Framework for Nitroaromatic Sensing and Co2 Storage. *RSC Adv.* **6**, 28047-28054 (2016).
19. Belowich M. E., Stoddart J. F. Dynamic Imine Chemistry. *Chem. Soc. Rev.* **41**, 2003-2024 (2012).
20. Haase F. et al. Topochemical Conversion of an Imine- into a Thiazole-Linked Covalent Organic Framework Enabling Real Structure Analysis. *Nat. Commun.* **9**, 2600 (2018).
21. Evans A. M. et al. Seeded Growth of Single-Crystal Two-Dimensional Covalent Organic Frameworks. *Science* **361**, 52-57 (2018).
22. Uribe-Romo F. J. et al. Crystalline Covalent Organic Frameworks with Hydrazone Linkages. *J. Am. Chem. Soc.* **133**, 11478-11481 (2011).
23. Stegbauer L. et al. Tunable Water and Co2 Sorption Properties in Isostructural Azine-Based Covalent Organic Frameworks through Polarity Engineering. *Chem. Mater.* **27**, 7874-7881 (2015).
24. Dalapati S. et al. An Azine-Linked Covalent Organic Framework. *J. Am. Chem. Soc.* **135**, 17310-17313 (2013).
25. Karak S. et al. Constructing Ultraporous Covalent Organic Frameworks in Seconds Via an Organic Terracotta Process. *J. Am. Chem. Soc.* **139**, 1856-1862 (2017).
26. Zhang W. et al. Reconstructed Covalent Organic Frameworks. *Nature* **604**, 72-79 (2022).
27. Maschita J., Banerjee T., Lotsch B. V. Direct and Linker-Exchange Alcohol-Assisted Hydrothermal Synthesis of Imide-Linked Covalent Organic Frameworks. *Chem. Mater.* **34**, 2249-2258 (2022).
28. Maschita J. et al. Ionothermal Synthesis of Imide-Linked Covalent Organic Frameworks. *Angew. Chem. Int. Ed. Engl.* **59**, 15750-15758 (2020).

29. Lyu H., Diercks C. S., Zhu C., Yaghi O. M. Porous Crystalline Olefin-Linked Covalent Organic Frameworks. *J. Am. Chem. Soc.* **141**, 6848-6852 (2019).
30. Yuan C. et al. Crystalline C-C and C=C Bond-Linked Chiral Covalent Organic Frameworks. *J. Am. Chem. Soc.* **143**, 369-381 (2021).
31. Li X. et al. Chemically Robust Covalent Organic Frameworks: Progress and Perspective. *Matter* **3**, 1507-1540 (2020).
32. Segura J. L., Royuela S., Mar Ramos M. Post-Synthetic Modification of Covalent Organic Frameworks. *Chem. Soc. Rev.* **48**, 3903-3945 (2019).
33. Emmerling S. T. et al. Interlayer Interactions as Design Tool for Large-Pore Cofs. *J. Am. Chem. Soc.* **143**, 15711-15722 (2021).
34. Diwakara S. D. et al. Supramolecular Reinforcement of a Large-Pore 2d Covalent Organic Framework. *J. Am. Chem. Soc.* **144**, 2468-2473 (2022).
35. Mu Z. et al. Covalent Organic Frameworks with Record Pore Apertures. *J. Am. Chem. Soc.* **144**, 5145-5154 (2022).
36. Ma T. et al. Observation of Interpenetration Isomerism in Covalent Organic Frameworks. *J. Am. Chem. Soc.* **140**, 6763-6766 (2018).
37. Wang Y. et al. Three-Dimensional Mesoporous Covalent Organic Frameworks through Steric Hindrance Engineering. *J. Am. Chem. Soc.* **142**, 3736-3741 (2020).
38. Liu R. et al. Covalent Organic Frameworks: An Ideal Platform for Designing Ordered Materials and Advanced Applications. *Chem. Soc. Rev.* **50**, 120-242 (2021).
39. Shinde D. B. et al. Crystalline 2d Covalent Organic Framework Membranes for High-Flux Organic Solvent Nanofiltration. *J. Am. Chem. Soc.* **140**, 14342-14349 (2018).
40. Zhu Y., Zhang W. Reversible Tuning of Pore Size and Co₂ Adsorption in Azobenzene Functionalized Porous Organic Polymers. *Chem. Sci.* **5**, 4957-4961 (2014).
41. Lyu H. et al. Covalent Organic Frameworks for Carbon Dioxide Capture from Air. *J. Am. Chem. Soc.* **144**, 12989-12995 (2022).
42. Byun Y., Je S. H., Talapaneni S. N., Coskun A. Advances in Porous Organic Polymers for Efficient Water Capture. *Chem. Eur. J.* **25**, 10262-10283 (2019).
43. Fang Q. et al. 3d Microporous Base-Functionalized Covalent Organic Frameworks for Size-Selective Catalysis. *Angew. Chem. Int. Ed.* **53**, 2878-2882 (2014).
44. Tan K. T., Tao S., Huang N., Jiang D. Water Cluster in Hydrophobic Crystalline Porous Covalent Organic Frameworks. *Nat. Commun.* **12**, 6747 (2021).
45. Banerjee T. et al. Sub-Stoichiometric 2d Covalent Organic Frameworks from Tri- and Tetratopic Linkers. *Nat. Commun.* **10**, 2689 (2019).
46. Chen L. et al. Substoichiometric 3d Covalent Organic Frameworks Based on Hexagonal Linkers. *J. Am. Chem. Soc.* **143**, 10243-10249 (2021).
47. Bian G., Yin J., Zhu J. Recent Advances on Conductive 2d Covalent Organic Frameworks. *Small* **17**, e2006043 (2021).
48. Zhang J. L. et al. Conductive Covalent Organic Frameworks with Conductivity- and Pre-Reduction-Enhanced Electrochemiluminescence for Ultrasensitive Biosensor Construction. *Anal. Chem.* **94**, 3685-3692 (2022).

49. DeBlase C. R. et al. Beta-Ketoenamine-Linked Covalent Organic Frameworks Capable of Pseudocapacitive Energy Storage. *J. Am. Chem. Soc.* **135**, 16821-16824 (2013).
50. Grunenberg L. et al. Amine-Linked Covalent Organic Frameworks as a Platform for Postsynthetic Structure Interconversion and Pore-Wall Modification. *J. Am. Chem. Soc.* **143**, 3430-3438 (2021).
51. Yan Q. et al. Post-Synthetic Modification of Imine Linkages of a Covalent Organic Framework for Its Catalysis Application. *RSC Adv.* **10**, 17396-17403 (2020).
52. Grunenberg L. et al. Postsynthetic Transformation of Imine- into Nitrone-Linked Covalent Organic Frameworks for Atmospheric Water Harvesting at Decreased Humidity. *J. Am. Chem. Soc.* **145**, 13241-13248 (2023).
53. Ding H., Mal A., Wang C. Tailored Covalent Organic Frameworks by Post-Synthetic Modification. *Mater. Chem. Front.* **4**, 113-127 (2020).
54. Nguyen H. L. et al. Hydrazine-Hydrazide-Linked Covalent Organic Frameworks for Water Harvesting. *ACS Cent. Sci.* **8**, 926-932 (2022).

2 Post-Synthetic Modification of COFs

The presented work of this chapter will be published as:

Chapter 7: Post-Synthetic Linkage Modification in Covalent Organic Frameworks

L. Grunenberg, F. Haase and B.V. Lotsch, in *Reticular Chemistry – A Practical Approach for Metal-Organic Frameworks and Covalent Organic Frameworks* (Eds.: M. Kalmutzki, C. Diercks and O.M. Yaghi), *in preparation*.

L.G. wrote the manuscript with input of F.H. and B.V.L.

This book will focus on the practical aspects of the chemistry of metal-organic and covalent organic frameworks useful to students in this field. It will provide insight into the design and synthesis of such materials (i.e. blueprints of a typical approach to new materials) including the refinement of synthetic conditions, as well as the thorough characterization of their structures and properties using various analytical methods. It will provide content that can be used to carry out laboratory courses, as well as for seminars accompanying these laboratory courses.

2.1 Introduction to Post-Synthetic Modification

This introductory section explains differences between post-synthetic modification and building block engineering to modify the properties of a covalent organic framework. In addition it illustrates possible target sites of both strategies and details how the porosity of COFs enables efficient post-synthetic modification with high conversion compared to dense polymers.

2.1.1 Building Block Engineering vs. Post-Synthetic Modification

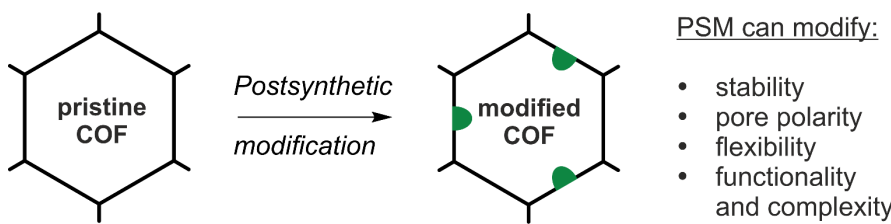


Figure 2-1: Post-synthetic modification of as synthesized COFs can change application-relevant properties of the porous framework, including its stability, among other factors.

As covalent organic frameworks are isoreticular materials constructed from molecular building blocks, the structure of these molecular precursors not only determines the framework topology but also dictates their physical and chemical properties. An adjustment of these properties, e.g. surface polarity, stability or functionality is often desired to meet the requirements for certain applications in gas sorption or heterogeneous catalysis. As an example, functional groups on the pore-wall surface can catalyze chemical reactions in the confined space of the pore channels or act as anchor points to attach molecular catalysts covalently.

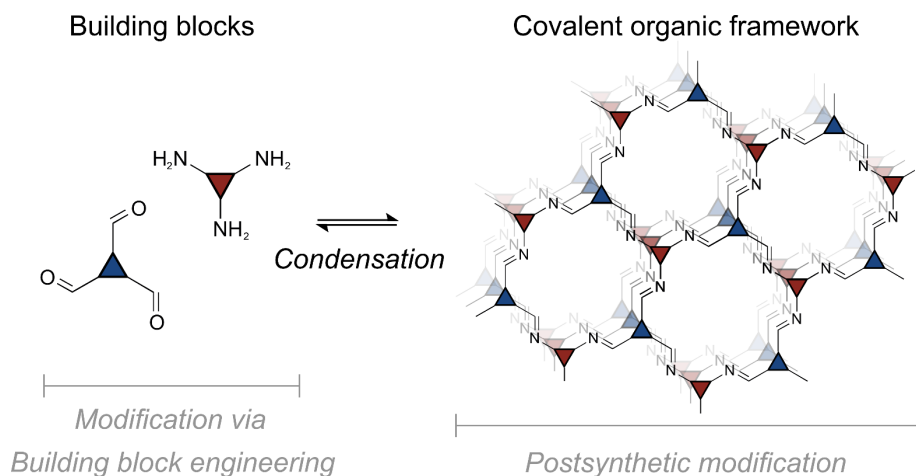


Figure 2-2: A comparison of modification strategies for an exemplary imine-linked COF is shown. In contrast to building block engineering, post-synthetic modification strategies make use of the condensed, crystalline, porous structure and circumvent incompatibilities that may occur during the synthesis of the framework.

An obvious way to address these needs is by designing the chemical structure of the building blocks – also known as *building block engineering*. Although a number of derivatives of the building blocks may be principally accessible with the tools of organic chemistry, minor changes in their chemical structure also cause changes in their respective physical properties, for example their solubility. This can also affect molecular interactions during the crystallization of the material with profound effects passing along to the structure of the synthesized framework. Consequently, a tedious optimization of synthesis conditions (solvent/temperature/catalyst) is often required. These changes may even entirely prevent the formation of a crystalline framework.

Additionally, certain functional groups cannot be installed easily by *building block engineering*. Either because they do not withstand the solvothermal synthesis conditions or because they compete with the framework crystallization, for example if amine or aldehyde functional groups are required on the pore channels. Apart from chemical incompatibility of functional groups, also geometric effects, e.g. steric shielding by bulky substituents, or their flexibility, can render certain functionalized building blocks incompatible for COF crystallization by preventing sufficient stacking interactions between the two-dimensional layers in the COF.

Due to the presence of pores, which allow the penetration of reagents into the materials, an elegant way to circumvent these incompatibilities is a *post-synthetic modification* (PSM) of the framework. Notably, access to the inner surface of the material down to the chemical bonds that constitute the framework is a prerequisite, which is usually not found in dense, non-porous polymers.

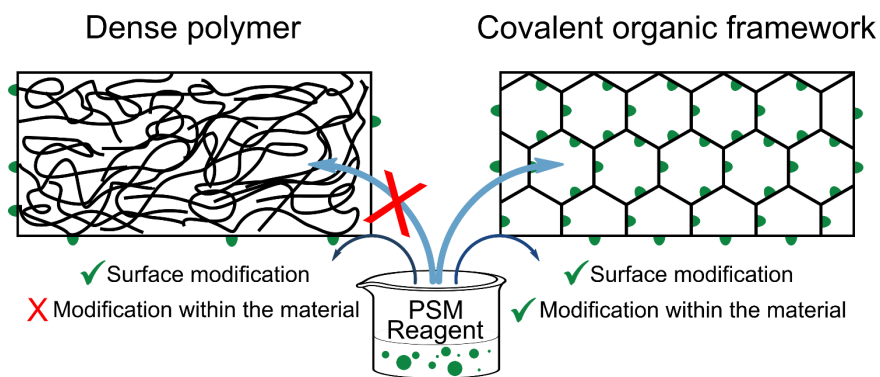


Figure 2-3: The porous and ordered structure of COFs, which enables the penetration of PSM reagents deep into the material, allows a precise modification of both outer and inner surfaces (pore channels). In contrast to porous polymers, traditional dense polymers only allow (outer) surface modification.

2.1.2 Types of Post-Synthetic Modification Reactions

The term “post-synthetic modification” includes a vast number of diverse reaction types and is used in differing contexts, whenever a change of chemical or physical properties of the framework is achieved by a reaction with a crystallized COF. Besides selective chemical modifications, it may also include unspecific modifications such as calcination/carbonization

of the framework by thermal decomposition, plasma treatments, or physisorption of metals/molecules.

Different strategies can be classified by their type of binding to the material upon post-synthetic modification: *non-covalent*, including trapping of molecules by physisorption or coordination of metals, as well as *covalent* modifications of the framework, such as reductions, oxidations or (cyclo-)addition reactions. A special case of a covalent modification, making use of the reversibility of the COF linkage, is a *building block exchange*, where building blocks embedded in the backbone of the COF are substituted by modified ones, having the same or similar geometry. This allows to incorporate building blocks with a modified chemical structure in the material, while the topology of the framework is preserved.^[1-3]

2.1.3 Target Sites for Post-Synthetic Modification

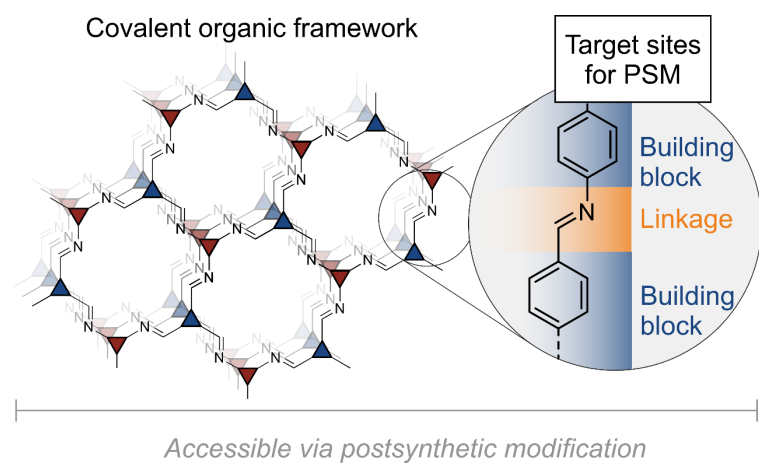


Figure 2-4: Post-synthetic modification reactions can target different sites in the framework, leading to changes at the linkage, the building block, or multiple sites in the material.

PSM strategies can also differ in the target site within the framework: post-synthetic transformations can not only aim to change the building block related moiety of the framework, but also the linkage of the network, expanding the level of control beyond the dedicated molecular units accessible for *building block engineering*. If the structure of the building block allows, both strategies can also be combined, as shown by the coordination of a metal in a salen-linked COF (Figure 2-5).^[4] In this example, the coordination of the metal cannot be pinned down to a single coordination site solely at the building block or the linkage, but instead combines both, highlighting that a strict classification may not always be applicable and should be understood as a guide to distinguish general strategies.

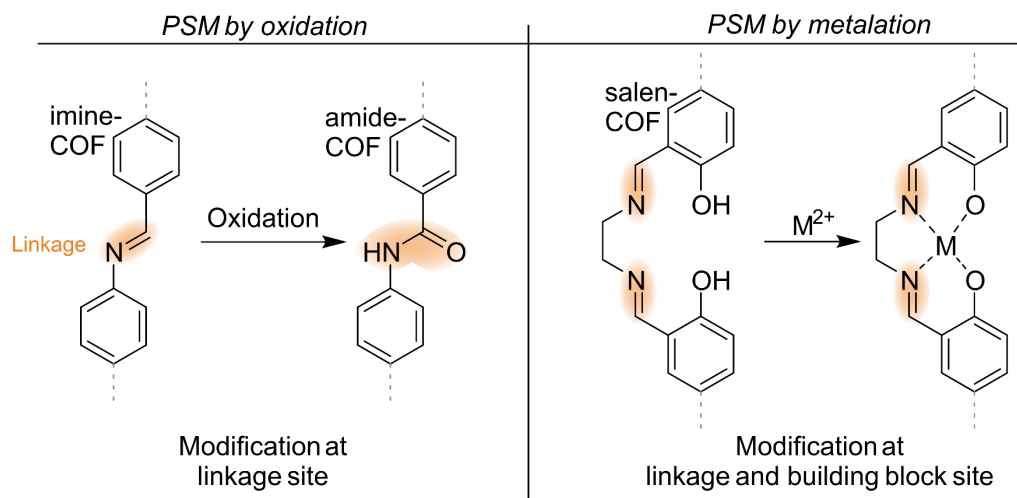


Figure 2-5: In contrast to an isolated modification of imine-linkages by oxidation, post-synthetic metallation of coordination sites in a salen-COF leads to a combined modification at linkage- and building block-related sites in the material.

Due to the vast number of different modification strategies, in the following we will focus on reactions aiming to modify specific sites in the framework *covalently* in a controlled fashion. The first part of the chapter will detail post-synthetic modification strategies involving the linkage, while the second discusses those aiming at the building block sites.

2.2 Post-Synthetic Linkage Modification

In the first section we will explain the role of the COF linkage as a key element for the material's stability. We will discuss how reversibility of linkage formation creates a dichotomy between framework stability and crystallinity, which paves the way for designing appropriate post-synthetic linkage modification strategies to overcome this limitation. The properties of COFs will be compared to those of structurally related small organic molecules to highlight important additional structural factors, besides the chemical structure of building blocks and linkages. These factors arise from condensing the molecular building blocks into a porous framework and will be important for understanding and successfully performing PSM of linkages.

The second part will highlight recently reported examples of PSM reactions of imine linkages in COFs. The goal of this section is to understand how different synthetic strategies are connected to intrinsic chemical properties of imine bonds and to highlight how property changes upon linkage PSM enable a range of diverse applications.

Inspired and motivated by these established strategies, we will follow to explain practical aspects of linkage modification reactions in the third part of this chapter. Introduced design strategies and stability/accessibility aspects presented in the previous parts will be revisited in the context of experimental design.

2.2.1 Stability vs. Crystallinity – The Role of Linkages in COFs

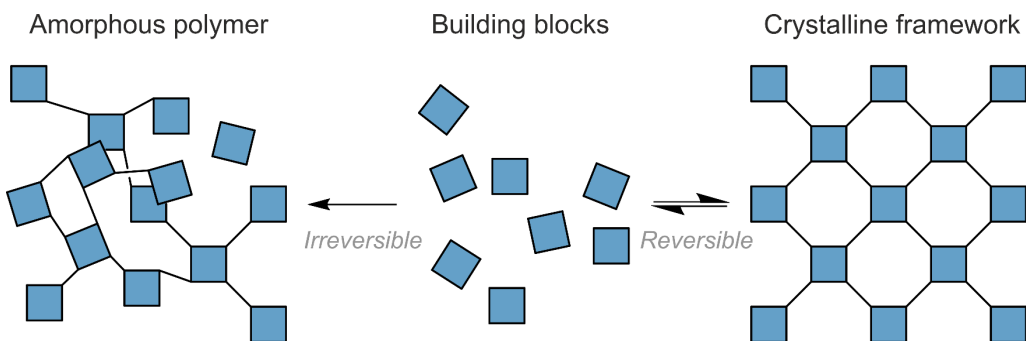


Figure 2-6: Irreversible polymerization reactions do not allow defect healing. Thus, irreversibility in bond-formation reactions leads to less crystalline, usually amorphous polymers. In contrast, reversibility of dynamic covalent reactions allow to obtain well-ordered frameworks, such as crystalline COFs.

A fundamental concept to achieve crystallinity in COFs is dynamic covalent chemistry. During synthesis, reversible bond formation and dissociation heals defects in the material and thus ensures a controlled assembly of the building blocks towards the crystalline thermodynamic-minimum assembly. Since the first report of boroxine and boronic ester linked COFs in 2005,^[5] this concept has been utilized for diverse COF forming reactions, such as Schiff base or Knoevenagel condensations among others, and enabled to establish an entire ensemble of COF linkages reported to date, based on the formation of C=N and C=C bonds.

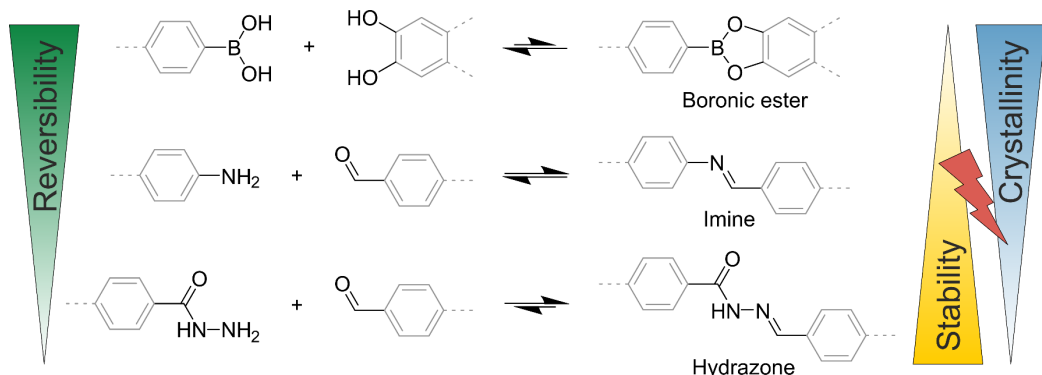


Figure 2-7: Selected linkage types reported for covalent organic frameworks. A dichotomy between stability and crystallinity occurs, since linkages formed by less reversible reactions suffer from limited error-correction governed by the reversibility of linkage formation. On the other hand, well-ordered materials usually suffer from limited stability.

In contrast to the prototypical boroxine linkage which readily hydrolyzes under aqueous conditions, these developments have allowed to obtain COFs with intrinsically higher chemical stability and paved the way for their use in advanced applications. Some of these materials usually benefit from less reversible, i.e. “stable”, linkages but harsh synthesis conditions, such as higher temperatures or addition of strong acids during synthesis to

compensate for the low reversibility of bond formation, necessary to facilitate error-correction.

Although the reversibility of the linkage has a beneficial contribution to the crystallinity of the framework, all linkages constructed by reversible bond formation reactions share the same fate: Their stability is intrinsically limited to certain conditions. Even if a material may be considered "stable", this term should not be understood as absolute, but rather as a relative, comparative term. The reversibility of bond formation during COF synthesis implies that the synthesis conditions define the intrinsic stability limit of the linkage. At these conditions the linkages break up, i.e. hydrolyze, and reassemble. This creates a competition between reversibility and crystallinity in COF synthesis, limiting the formation of stable, but well-defined crystalline COFs. An elegant way to overcome this problem is a subsequent post-synthetic stabilization, i.e. "locking", of the linkage after the framework crystallized. This strategy allows to decouple the order inducing crystallization step, while the stability is introduced post-synthetically into the crystalline framework, ensuring optimal reversibility for high crystallinity in the material combined with increased chemical, and thus structural, stability.

2.2.2 Stability with Reversible Bonds? – Fundamental Influences in COFs

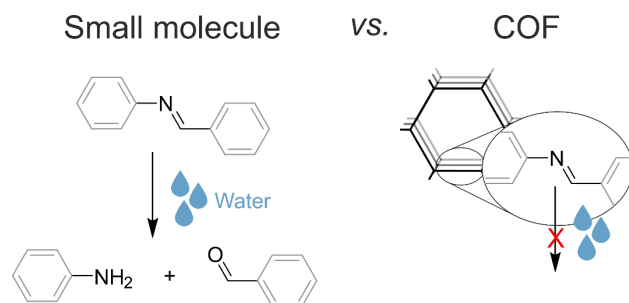


Figure 2-8: How can imine COFs withstand aqueous conditions, while small molecular imines hydrolyze?

Reading through recent literature about COFs, one will come across many examples demonstrating acceptable stabilities for as-synthesized materials, although the presented frameworks consist of building blocks linked by well reversible bonds, such as imine linkages in the presence of water. From a small molecule perspective, most imine-linked frameworks would be expected to show an entirely opposite behavior, as imine bonds in many small molecules may already hydrolyze readily in the presence of water (Figure 2-8). How can COFs based on these linkages withstand even aqueous acidic or basic conditions? This example shows that there are additional factors, which influence the stability of linkages in a COF besides the type of chemical bond connecting the building blocks.

2.2.2.1 Stacking Interactions in 2D COFs – Pore Accessibility and Steric Shielding of the Linkages

Additional factors can also have a drastic influence on the stability of the material. A major difference between COFs and small molecules are stabilizing interactions between the extended two-dimensional layers in 2D COFs or the building blocks in interpenetrated 3D systems, often generally referred to as *stacking interactions*. These are usually a combination of dispersion forces and attractive π -orbital interactions between nearest neighbor building units, i.e. the interlayer interactions in 2D COFs.^[6] Depending on the chemical structure of the building blocks and specifically their substitution patterns, these interactions can be complemented by interlayer hydrogen bonding or dipole interactions.^[7, 8] In consequence, these forces determine the three-dimensional structure of the framework by interconnecting the layers non-covalently, and the ability of the framework to withstand layer delamination. At the same time, they also define how the layers are stacked, i.e. whether they are assembled in an eclipsed or staggered fashion or stacked with an offset.^[9-11] These stacking modes influence important parameters such as the shape of the pore-channels, the effective pore size and pore size distribution, and, hence, the *accessibility* of the inner pore surface.^[12] In turn, the stacking structure affects the accessibility of the linkages, and thus the framework's stability, against solvents, reagents and other external chemical stimuli, with the linkages being located within the pore wall and sterically shielded by the neighboring layers. Due to this *steric shielding* the linkages are less exposed and only accessible from specific directions along the channels in the bulk material, even in an idealized eclipsed stacked, rigid framework with regular cylindrical pore channels and well-accessible pore-surface. In this regard, the environment of linkages in a condensed framework is substantially different to a small molecule in solution, even though the type of chemical bond may look the same in both cases. This causes bonds like aldimines to be comparably stable in a COF. Nevertheless, this situation can change with increased *defect concentration, disorder or flexibility* of the building blocks/layers, exposing the linkages to reagents and thereby facilitating reactions, such as hydrolysis in the presence of water.

2.2.2.2 Stability as a Function of Conditions – Solubility and Hydrophobicity of the Framework

The aforementioned factors focused mainly on the ability of a reagent to attack the linkage site of the framework, but the following steps after the linkage disassembly, e.g. dissolution and diffusion of the building blocks, are critical factors likewise, and determine if the framework breaks up entirely and dissolves under the respective conditions. Indeed this is mainly influenced by the *solubility of the building blocks* and varies depending on the composition of the surrounding solvent: While an imine-linked COF constructed from hydrophobic building blocks may be stable in purely aqueous basic conditions, the same COF may not survive if an aprotic, yet water-miscible solvent is added to the aqueous basic suspension.^[12]

In a purely aqueous environment, the local hydrolysis of a few accessible imine-bonds may not destroy the structure of a COF entirely, because the exposed building blocks remain at their position in the assembly due to their insolubility in the purely aqueous solvent and may even reform the previously broken bonds in a bond healing step. If their solubility, however, is increased with a second, organic, non-polar component in the solvent, the released building blocks dissolve and dissociate from the framework: the COF disassembles.^[13]

Apart from these factors, the hydrolytic stability of a framework can also be altered by hydrophobicity – or *wettability* – of the pore-wall surface or steric shielding by bulky substituents, protecting the linkage from attacking water molecules, similar to the discussed shielding caused by layer stacking (see section 2.2.2.1). In recent examples, non-polar alkyl- or perfluoro-alkyl groups have been incorporated into the building blocks to render the pore-surface hydrophobic, causing an increase in the framework's hydrolytic stability.^[14-17]

In summary, the presented examples highlight that the chemical identity of the COF linkage is a key element determining the stability of the material. Nevertheless, additional factors such as the chemical structure of the building blocks, as well as structural aspects of the macromolecular assembly in the framework have to be considered additionally to understand structure–reactivity relations in COFs. In the following section, we will give an overview of different established modification strategies of imine linked COFs.

2.3 PSM of Imine-Linked Frameworks: A Literature Overview

Among the different linkages utilized for building COFs, imines have become the most popular class of linkages and constitute the largest family of COFs to date. The crystallinity of these frameworks, synthesized from readily accessible amine and aldehyde building blocks, benefits from good reversibility of dynamic imine chemistry. To overcome the dilemma between crystallinity and stability, to increase their structural complexity or endow them with beneficial properties –known as the COF trilemma– (see section 1.1.4), prevalent frameworks became a target for linkage modification and will serve as a prototype to outline general synthetic strategies for post-synthetic linkage conversion in this section. Besides their advantageous reversibility in COF synthesis, imine-bonds are also a versatile functional group in organic synthesis. So-called Schiff bases are known as reagents or intermediates in famous name reactions, such as Leuckart-Wallach, Eschweiler-Clarke, Strecker, Mannich or Ugi reactions, among others. A closer look at the chemical structure of a prototypical imine bond helps to understand this versatility for derivatization in organic synthesis (Figure 2-9).

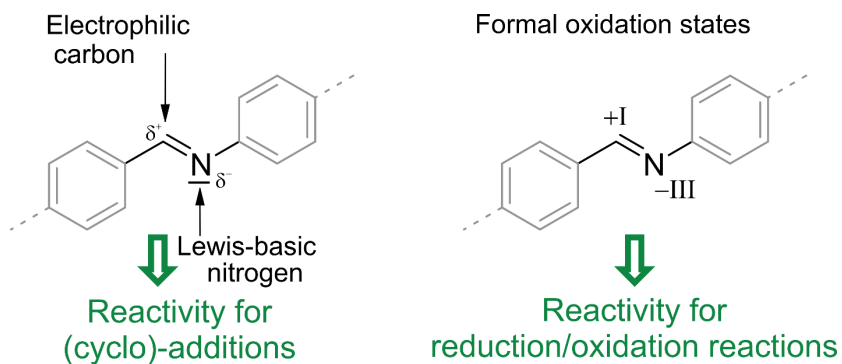


Figure 2-9: Imine bonds are reactive toward oxidation and reduction reactions. Due to polarization, the carbon center of the imine bond is susceptible for addition of nucleophiles, especially if promoted by the coordination of Lewis acids to the nitrogen. Likewise, the polarized imine bond can also engage in cycloaddition reactions.

Due to the electronegativity difference of carbon and nitrogen, imine bonds are polarized. Polarization results in an electron deficient, i.e. electrophilic, carbon center, which allows addition reactions with nucleophiles, such as cyanide anions used in the Strecker reaction, for example. On the other hand, the electron lone pair at the nitrogen center can bind to Lewis acids. Binding of a Lewis acid increases the polarization effect on the carbon. This enhances the reactivity of the imine bond even further and is used for example to engage imines in cyclization reactions, such as inverse electron-demand Diels-Alder reactions.

Besides this reactivity for (cyclo-)additions, imines can also undergo simple redox reactions. The imine carbon shows a formal oxidation state of +I. As carbon can occupy a range of oxidation states between +IV and - IV, we expect it to be susceptible to both reduction or oxidation reactions, forming amines (- I) or amides (+III), respectively. The imine nitrogen, on the other hand, is present in its most reduced state (-III), which promises that *N*-oxidations to nitrone or hydroxylamines (-I) may be possible to modulate its redox state.

The selected examples highlight that a rather simplistic visualization of the chemical structure of bonds can be an initial approach toward exploring bond modification reactions. Due to the fact that the presented assumptions of reactivity do not only apply for small molecules, but have also proven to be transferable to organic solid-state materials, such as COFs, underlines that the tools of organic small molecule chemistry can indeed be a blueprint for PSM of linkages. This versatile chemistry of imines is unique among COF linkages, rendering imines the most popular platform for linkage conversions in COFs. In the following part of the chapter, we discuss the reported strategies in detail.

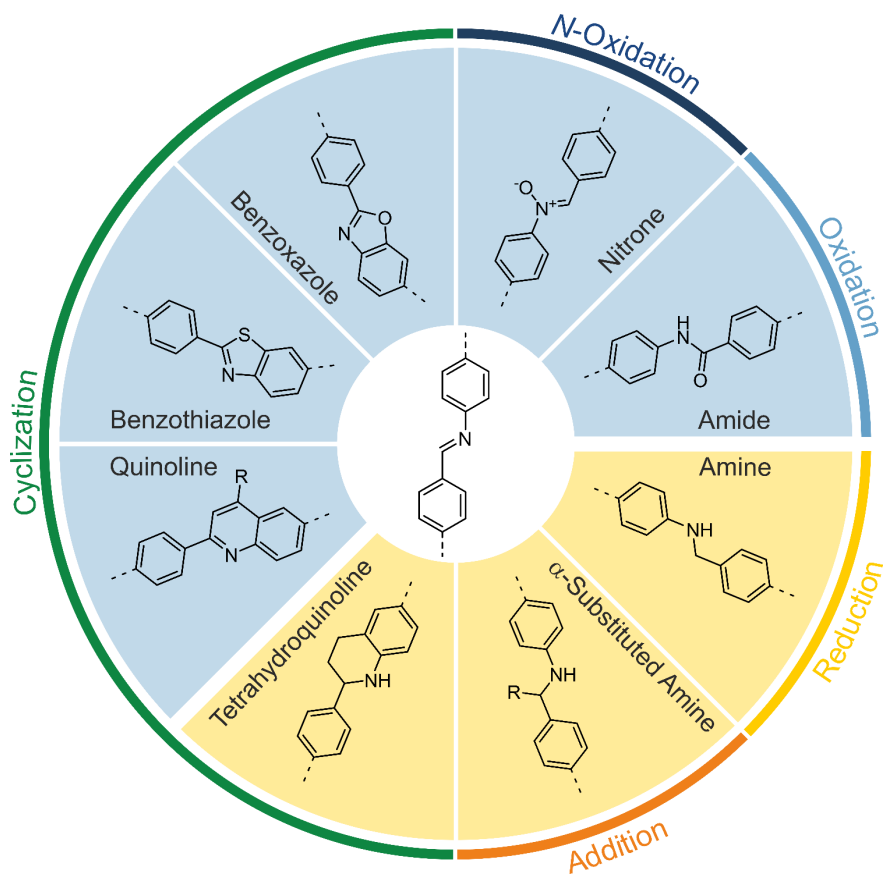


Figure 2-10: An overview of reported post-synthetic linkage conversions of imine linkages in COFs. The strategies are categorized by oxidative (light blue segments) and reductive transformations (yellow). Besides simple oxidations or reductions, also reductive additions, or oxidative/reductive cyclizations have been developed.

2.3.1 Oxidative Linkage Transformation Reactions

2.3.1.1 Linkage Modification by C-Oxidation or Oxidative Cyclization

The first reported linkage modification in imines, published in 2016, oxidizes imine linkages to more stable amides under Pinnick-Lindgren-like conditions with sodium chlorite as a strong oxidant.

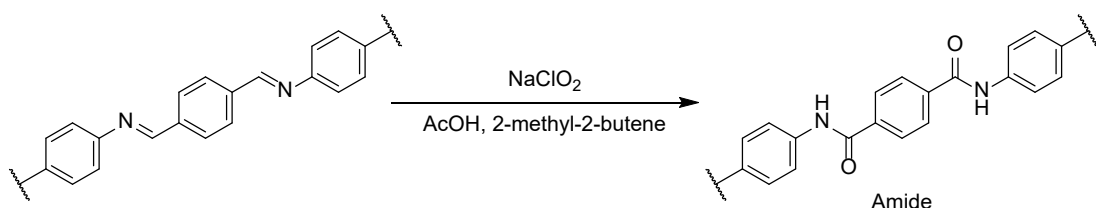


Figure 2-11: Oxidative linkage conversion of imine- to amide-linked COFs.

Due to the high oxidation potential of hypochlorite formed from sodium chlorite as a side product, which can result in unselective side reactions such as chlorination, 2-methyl-2-

butene was employed as an hypochloric acid scavenger to increase selectivity.^[18] The less electrophilic amide bonds and in turn the framework itself increased the hydrolytic stability of the frameworks under acidic and basic conditions, due to their irreversible character. At the same time, amide-COFs are very difficult to synthesize directly, as the limited reversibility of amide-bond formation cannot form well-ordered, i.e. crystalline, frameworks. In the following years, other oxidative transformations have been developed. These reactions, involving 2,3-dichloro-5,6-dicyano-1,4-benzoquinone (DDQ) or elemental sulfur as oxidants, led to oxazole or thiazole moieties, respectively.

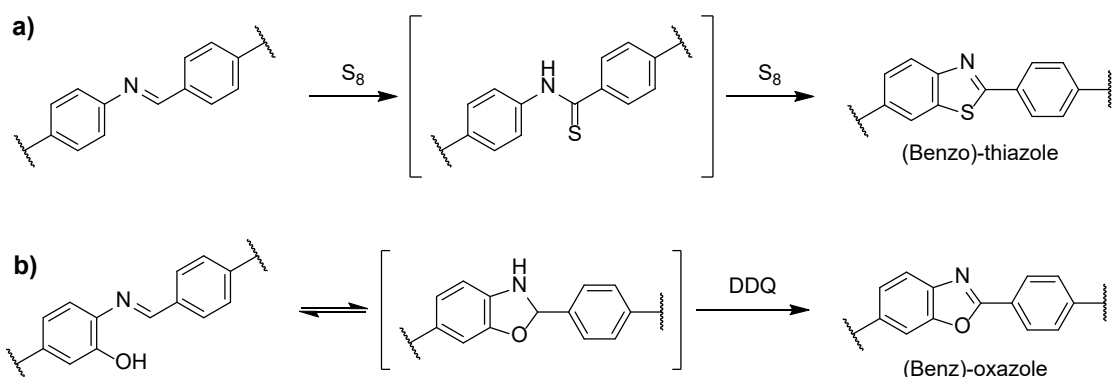


Figure 2-12: Oxidative cyclizations to benzothiazole (a) and benzoxazole (b) linkages in COFs, with respective benoxazolidine and thioamide intermediates.

These linkages combine the oxidation of the imine-carbon with a cyclization between the linkage and the building block moiety. The thiazole^[19, 20] and oxazole^[21, 22] heterocycles effectively prevent hydrolysis as well as the attack by strong reductants and nucleophiles, rendering these frameworks extraordinary robust. Besides their improved stability toward chemical stimuli, their stability to an electron beam enabled a real-structure analysis in thiazole-COFs by transmission electron microscopy (TEM) and visualized grain boundaries as defect sites in the material — a fingerprint for the COF condensation process.^[19] However, an improved chemical or thermal stability and modulated light absorption upon modification of the linkage can also manifest in superior performance of the material, for example as a catalyst. Benzoxazole-linked frameworks showed improved performance and recyclability in the visible light driven oxidative hydroxylation of arylboronic acids, surpassing their imine derivatives.^[22]

2.3.1.2 Ex-Situ vs. In-Situ Linkage Modification

In the previously mentioned reference, benzoxazole COFs were synthesized from amine (2,5-dihydroxy-*p*-phenylenediamine), aldehyde building blocks and benzimidazole as a base to promote dehydrogenation.^[22] Notably, this *in-situ* reaction consists of two discrete, successive steps involving the imine framework as an intermediate: The reversible crystallization step followed by an irreversible linkage conversion step (Figure 2-13). In

summary it composes the same elements as a typical *ex-situ* PSM sequence. Notably, the linkage conversion is still performed on the crystalline framework, i.e. post-synthetically, but the crystallization/linkage-conversion steps are not separated by an isolation or work-up.

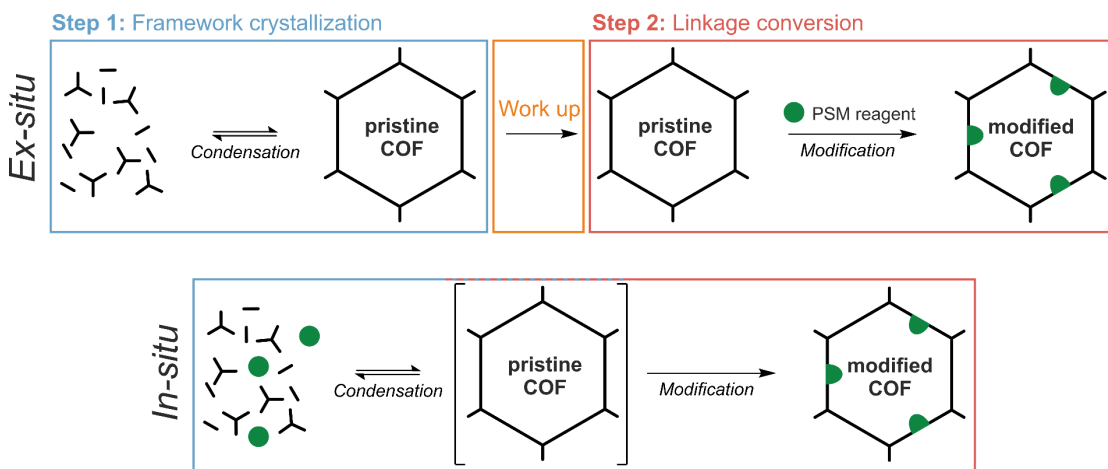


Figure 2-13: A comparison of synthetic steps associated with *ex-situ* PSM protocols and condensed *in-situ* PSM reactions, where the pristine COF occurs as an intermediate.

This condensed protocol offers an advantage over general *ex-situ* procedures, because the successive steps proceed in the same reaction medium and do not require a work up between the crystallization and (post-synthetic) modification that causes a loss of material and additional chemicals. Although other linkage conversion reactions of imines, to thiazoles^[20] for example, have been successfully adapted to *one-pot* in *in-situ* protocols, certain requirements to the kinetics of the crystallization and the reactivity of the building blocks have to be met to enable this simplification: In a typical *in-situ* procedure, the building blocks and the modification reagent are dissolved together in a suitable solvent and the reaction mixture is heated to speed up the (back-)reaction. Because these components are already combined during the initial phase of the synthesis at which the crystalline framework is not present (Figure 2-13), the building blocks and the modification reagent need to be chemically compatible. In an ideal case, the reagent is entirely unreactive towards aldehyde or amine building blocks and only reacts with imine bonds in the condensed framework, to prevent interference with the crystallization process. Unfortunately, this situation is sometimes difficult to find in reality, especially at elevated temperature typically used for COF synthesis. As an appropriate alternative, a slow reaction with the modification reagent may also be well tolerated if the condensation of the building blocks and crystallization of the framework is significantly faster, quickly providing a crystalline framework as the reaction partner before noteworthy consumption of the uncondensed building blocks occurs.^[12] However, if the reaction with the linkage proceeds too fast, limiting the error-correction during the condensation, only a disordered, yet (partially) modified, polymer with diminished porosity can be obtained. For a given combination of building blocks a variation of temperature, solvent or PSM reagents with reduced reactivity (or increased selectivity) may allow to

optimize the kinetic parameters of the crystallization-modification interplay to limited extent, rendering *in-situ* linkage modifications an elegant protocol albeit within a limited scope of linkage transformations and building block combinations.

2.3.1.3 Linkage Modification by *N*-Oxidation

Above mentioned oxidative linkage transformation reactions only increased the oxidation state of the imine carbon. Nevertheless, oxidations at the opposing end of the imine linkage can also be used to modify the framework.

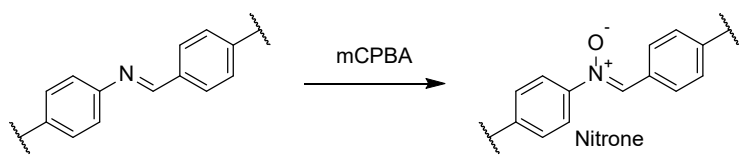


Figure 2-14: *N*-oxidation of imine linkages with an electrophilic oxidizing agent led to more polar nitrone linkages.

Selective oxidation of the nitrogen center of the linkages by the electrophilic oxidizing agent 3-chloro perbenzoic acid (mCPBA) converted imines into nitrone linkages (oxidation state of the nitrogen $-I$).^[23] Due to the concomitant increase in polarity of the pore channels, decorated with polar nitrone linkages, the obtained framework showed improved uptake of water vapor at lower humidity and higher carbon dioxide capacity, compared to the parent imine framework, rendering nitrone-linked frameworks promising material for atmospheric water harvesting. This example further highlights the diversity of applications for post-synthetically modified frameworks and underlines that a comparably simple modification of the linkages can modulate characteristic properties, such as the polarity of the pore channels, even though they represent only a small proportion of the involved atoms in the pore.

2.3.2 Reductive Transformations of Imine Linkages

Besides these oxidative transformations, the electrophilic character and oxidation state ($+I$) of the imine carbon also allows a reduction to a secondary amine linkage, as known for famous name reactions such as Eschweiler-Clarke (reductive methylation of amines) or Leuckart-Wallach (reductive amination of aldehydes).

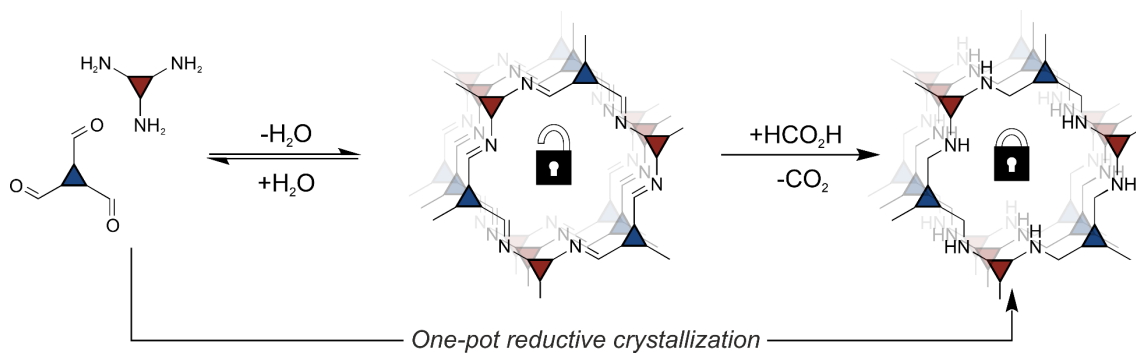


Figure 2-15: Reduction of imine to amine linked COFs with formic acid. The strategy “locks“ the linkage against hydrolysis and can be performed as an *in-situ*, i.e. one-pot reductive crystallization.

Secondary amine linked COFs have recently been prepared with different reagents including classical nucleophilic borohydride reagents, such as NaBH_4 ^[24] or NaCNBH_3 ,^[25] but also reductive acids such as formic acid^[12] or phosphonic acid,^[26] for example. Due to the acidic and reductive reactivity of formic and phosphonic acid, these acids can both catalyze the imine condensation and subsequently reduce imines to secondary amines *in-situ* in a one-pot reductive crystallization, in addition to the typically conducted *ex-situ* reaction protocol. While the hydrolytic stability of the material is enhanced, the basicity of the nitrogen sites is increased upon reduction, which caused varying success in maintaining the crystalline structure among the explored protocols: As the rotationally restricted imine double bond is reduced to a more flexible single carbon-nitrogen bond, protonation to the aminium ion creates a charged amine site and induces both intra- and interlayer structural rearrangements, which can cause amorphization of the reduced materials under acidic conditions.^[12] In contrast to other amorphization pathways, usually based on chemical decomposition of the material, the loss of crystallinity is due to layer corrugation and random, relative interlayer offsets, while the linkages are kept intact.^[12, 27] Interestingly, disordered frameworks could be transformed back to a crystalline material by simple re-oxidation to the imine linked progenitor or cyclization to carbamate linked frameworks in a multi-step reaction sequence, proving the close relation in intralayer chemical structure between these materials.^[12, 25]

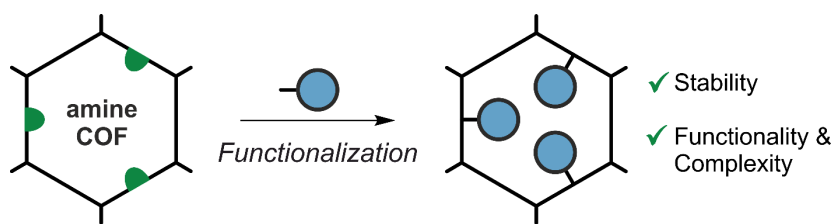


Figure 2-16: Besides their enhanced hydrolytic stability, the nucleophilic secondary amine centers in amine-linked COFs can serve as reactive centers for functionalization at the pore wall. This enables access to tailored functional and stable, yet crystalline frameworks.

In contrast to the afore mentioned oxidative linkage conversions of imines, which only create more robust linkages, a reduction to secondary amines also activates the pore-surface for

further covalent modification (Figure 2-16). This enables an additional pathway toward tailored structural complexity in COFs besides traditional building block engineering. As demonstrated in the synthesis of carbamate-linkages, these tools can be used to access new linkage types, or serve as reactive anchoring sites for further functionalization within the confined pore channels.^[12] This feature renders amine-linked COFs particularly suitable for applications in catalysis, where crystallinity, stability and structural complexity is required at the same time, and highlights how post-synthetic modification of the linkages can help to overcome this challenge in COF chemistry.^[28]

2.3.2.1 Addition Reactions to Imine Linkages

Due to the difference in electronegativity between carbon and nitrogen, the imine bond is polarized and renders the carbon an electrophilic center susceptible to addition reactions – the simplest example being a nucleophilic attack of water to form a hemiaminal species as an intermediate in the hydrolysis of an imine. The efficiency of the addition reaction usually depends on both the electronic structure of the imine as well as the nucleophilicity of the reagent attacking. Unfortunately, in a given framework with a specific nucleophilic reagent these parameters cannot be varied promiscuously, requiring an efficient activation of the imine bond supporting the reagent to add to the imine bond. Upon protonation of the nitrogen, or by coordination of even stronger Lewis acids, such as BF_3 , the electron density is withdrawn from the imine carbon, creating an even stronger electrophilic center.

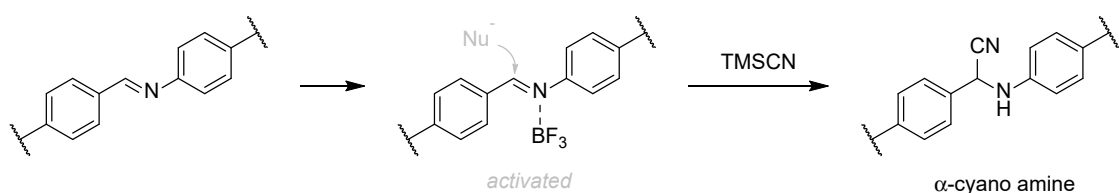


Figure 2-17: Coordination of a Lewis acid on the nitrogen center of the imine polarizes and thus activates the electrophilicity of the carbon center for an addition of a nucleophile, such as cyanide to yield cyano-substituted amine linkages.

Under these conditions, the addition of cyanide to imine linkages in COFs has been demonstrated, employing TMSCN as the cyanide source.^[29] Historically this addition is known as the Strecker reaction and provides synthetic access to amino acids from aldehydes, if the nitrile group is subsequently hydrolyzed to a carboxylic acid. Similar to its historic paragon, the reaction can also be performed as a multicomponent, i.e. *in-situ*, reaction, affording frameworks with α -cyano amine linkages under solvothermal conditions.^[29]

2.3.3 Oxidative and Reductive Cycloadditions with Imine Linkages

With a similar Lewis acid activation by a combination of scandium and ytterbium triflate, imine-linkages in COFs can also undergo cycloaddition reactions with electron-rich alkenes.

In this inverse electron-demand aza-Diels-Alder reaction, the Lewis acid activated aryl-imine acts as an electron-poor diene. Upon reaction, a tetrahydroquinoline linkage with exceptional stability under acidic and basic conditions is formed.^[30]

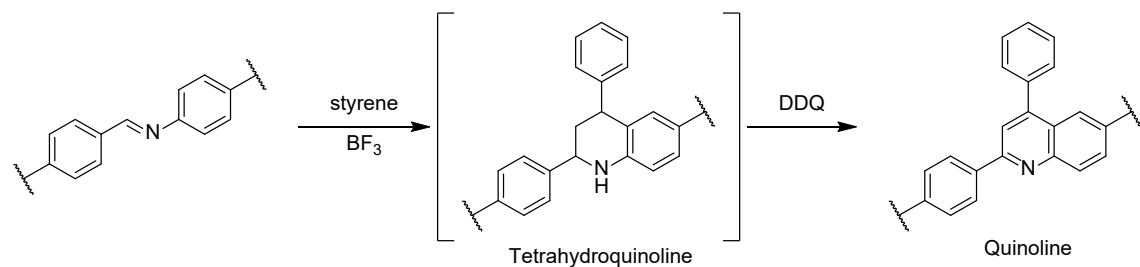


Figure 2-18: Lewis acid activation activates the imine linkage for cycloaddition reactions, affording tetrahydroquinoline-linked frameworks. Further oxidation leads to quinoline-linked COFs.

If an additional oxidizing agent such as 2,3-dichloro-5,6-dicyano-benzoquinone (DDQ), or chloranil, is employed with trifluoro borane as the Lewis acid and an alkyne, an oxidative cycloaddition occurs, creating stable, aromatic quinoline-linked frameworks.^[29, 31] This reaction, known as the Povarov reaction, can again also be performed as multi component protocol,^[29] or occur intramolecularly^[32] if alkyne substituted building blocks are embedded in the framework. This intramolecular cyclization is another example of a PSM strategy combining linkage and building block elements.

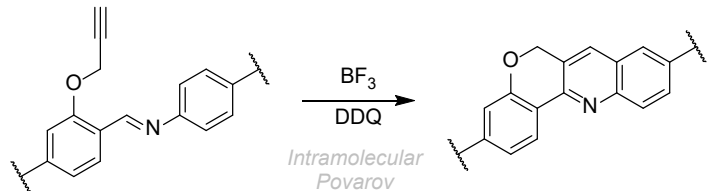


Figure 2-19: Oxidative cyclization with an alkyne may also occur intramolecularly – combining linkage modification strategies with building block engineering approaches.

2.3.4 Conclusion

In summary, the presented post-synthetic linkage modification reactions aim at modulating the framework's properties in terms of reversibility i.e. hydrolytic stability of the linkages, but can also affect the flexibility, pore channel polarity, or graft reactive sites for enhanced functional complexity into the skeleton. While reading these established protocols, linkage conversion in COFs may appear as easily performable as for small molecules. In fact, the protocols need to be adjusted to be applied successfully to porous materials. In the following section, we will focus on important practical aspects and design criteria for post-synthetic conversion of linkages in COFs.

2.4 How to: Practical Aspects for Linkage Conversions

After explaining different reactions and motivations for post-synthetic modification of linkages in COFs in the previous part, this section of the chapter deals with practical aspects of linkage modification. We address in detail criteria with to select suitable networks and PSM strategies and specify problems, and possible solutions, that may arise during the practical conduction of experiments. In addition, this part provides a practical guide for researchers aiming to perform linkage modification in COFs. We explain the advantages and disadvantages of common analytical techniques for evaluating experimental results and outline a decision tree that is useful for optimizing reaction conditions.

2.4.1 Step 1: Defining the Goal of the PSM Strategy

A successful PSM of the network is always preceded by careful planning. First of all, one must be aware of the objectives targeted by the bond modification. Is it a matter of pure **stabilization** of the bond, because the COF hydrolyzes under the specific conditions, for example? Or, is an increase in the complexity of the network by **functionalization** planned, for example via covalent-binding of functional groups, molecules, or catalysts? Based on these questions, suitable existing methods can be selected, or if these have not been described previously, new strategies may need to be developed. The combination of multiple of these properties is also possible, for example as described in the case of secondary amine COFs in the previous chapter. Here, the secondary amine linkage offers improved hydrolytic stability, compared to the imine-linked network, and at the same time the amines provide nucleophilic binding sites on the pore-wall surface for further functionalization.

Helpful hints for required attributes are also provided by considering the intended field of application. If the material is to be used in catalysis under protic conditions, a certain resistance to hydrolysis is obviously a prerequisite. On the other hand, oxidative conditions, high temperatures, or strong nucleophiles may also affect the integrity of the material. The first step in planning should therefore be the **definition of the field of application**. Then the important contributing factors under these conditions have to be identified and an orthogonal bond modification strategy can be selected.

If one comes to the conclusion that the primary goal is to increase the **complexity** of the structure by binding a functional unit, one should also ask for the necessary degree of functionalization in the material. This can be important from a pore accessibility point of view - requiring that the reactants should still be able to diffuse to the catalytic center, whereas anchored functional sites reduce the available pore volume. High functionalization degrees can also lead to altered (interlayer) interactions in the material, resulting in decreased structural order. In addition to these structural influences, low bond conversion can also have an unexpectedly strong impact on the properties. For example, Yaghi and co-workers were able to show, that already a conversion of barely 10% of azine linkages to hydrazides led to an enhanced water uptake in the pores of the COF.^[33] It is therefore not always

essential for the function of the material to achieve a quantitative conversion of linkages by PSM. In these cases, lower levels of functionalization in the material may not only be preferred, but necessary and sufficient to achieve the desired effect. In contrast, in the case of a gain in stability, a complete conversion of the bonds in the COF is usually sought by means of PSM. The examples show that it is useful to clearly **define the area of application** of the material and the goals of its modification.

2.4.2 Step 2: Selection of the Framework

The next step is to **find a suitable COF** for the PSM. This can be useful for several reasons. First of all, one has to be aware that the search for suitable synthesis conditions for the linkage modification usually requires several synthesis-analysis cycles until one can finish the optimization of the synthesis conditions and obtain a modified but at the same time crystalline product with intended porosity. Especially for tailored materials e.g. for complex catalytic systems that have building blocks with synthetically challenging chemical structures as a basis, these optimization steps can be expensive and substantially laborious. Also, and especially, when exploring new linkage chemistries that have not been described before, usually requiring even more optimization steps, it appears to be of little use to waste an expensive, complex starting material. In this case, it makes sense to use an already **well-known network**, possibly structurally related to the complex building block, as a substitute for **initial optimization**. After the reaction conditions for the PSM have been tuned, or the desired new bond is obtained, the method can be transferred to a more complex system. This limits the loss of expensive starting materials and, in a scientific context, also highlights the robustness and applicability of the developed PSM method if successfully transferred to additional and structurally more complex systems. Especially for the new development of PSM methods, where for applicability reasons there are no specific requirements for the starting COF, it is a good idea to start with literature-reported COFs. Ideally, the parent COF is easy to crystallize and is based on commercially or synthetically readily available building blocks in order to produce sufficient material amounts for the required screenings cheaply and easily. It is also helpful if the pore size of the material is not chosen too large (> 4 nm), as these COFs are usually more prone to disorder between layers unless they have optimized interlayer interactions.^[9] This manifests itself, for example, in the fact that larger pore COFs may lose their crystalline order when dried from a polar solvent by using vacuum.^[9, 27, 34] It is easy to imagine that structural changes in the bonding would then also lead to disorder in these systems, whereas more stable smaller-pore COFs would tolerate such conditions and remain crystalline during identical PSM conditions. On the other hand, the pore diameter should also not be chosen too small (< 1 nm), because the access of the reagents to the COF bonds must be guaranteed to be able to chemically modify them. Needless to say, that this accessibility prerequisite is only fulfilled the case in **COFs with high porosity**, evident from large pore volumes and surface area. In a non-porous material complete conversion of the bond will not be achievable. Practical COF systems therefore ideally have **good**

crystallizability, high porosity with pore diameters between approximately 1-4 nm and consist of easily **accessible building blocks**.

2.4.3 Step 3: Selection of a Modification Reaction

Once a suitable COF system has been identified and the goal of the PSM has been determined, a **suitable PSM reaction** that achieves the conversion of the linkages to the desired extent must be found. Successful strategies from small molecule reactions can serve as helpful blueprints for this purpose. Although some of the reaction types mentioned in the previous chapter may retrospectively seem obvious and directly transferable from small molecules, there are some pitfalls that must be considered when aiming to transfer these reactions to COFs in order to generate a robust and applicable method for linkage modification.

2.4.3.1 Small-Molecular Reactions vs. COF Linkage Modifications: A Comparison of Reaction Environments

In a typical homogeneous reaction, small molecules are dissolved in a solvent and reacted with a reagent. Here, the molecules exhibit a certain degree of flexibility defined by their chemical structure, adjacent substituents and the solvation in the reaction medium. Likewise, the reagents are also dissolved and can access the reactive centers in the molecule. Depending on the reaction type, the solvent not only solvates the reactants, but can also influence the reactivity, for example, by polarizing the reactants, stabilizing transition states or reaction intermediates.

If we compare the homogeneous reaction conditions in solution with the available environment of the linkages on the surface of the pore channels, clear differences become evident. In the solid state, the **flexibility of the linkages** is restricted by the connectivity and rigidity of the extended layers. Similarly, the accessibility of the linkages is no longer only determined by the local structure within the molecule, but additionally by the pore-diameter and the stacking order of the net-like layers. Disorder and defects in the stacking of the layers can lead to a strong change in the **accessibility of the pore surface**, and hence in the reaction ability of the bond.

The interaction with the solvent also changes between dissolved molecules and heterogeneous COFs. While a dissolved molecule is surrounded by a dynamic solvation sphere of solvent molecules, interlayer interactions continue to dominate in the COF, even if the pores are wetted with solvent, preventing complete solvation of the layers. The stacking of layers only allows the solvent to penetrate into the pores, with limited changes in the reaction environment compared to a solvated molecule. The linkages, as being part of the pore wall, remain in place being surrounded by other layers above and below them, which **sterically shield** the surroundings of the bond. Reactants dissolved in the solvent can

therefore not react with the bond from arbitrary directions, e.g. axially or equatorially to the bond as in the homogeneous case, but only attack the bond from parallel to the layers in the COF (i.e. equatorially). An attack perpendicular to the layer, on the other hand, is sterically hindered.^[23] It is clear, that these factors **alter the reactivity of the linkages**. At the same time, steric shielding and **limited flexibility** also make it difficult to realize complex, spatially challenging transition states that would provoke deformation of the layers. From the restricted flexibility and steric shielding, as well as the altered reaction environment due to the stacking of the layers, a modulation of the properties in the COF results: comparing similar functional groups found in small molecules with COFs, a modulated reactivity in the solid state appears, which has to be taken into account when planning post-synthetic modifications of the linkages.

2.4.3.2 Suitable Strategies for Linkage Modifications

The afore-mentioned differences in the reaction environment and the reactivity of the linkages require adjustments of reaction conditions to enable a successful transformation. Due to the embedded functionalities in the framework, typical purification of the desired species from a reaction mixture, e.g. by chromatographic techniques, is not achievable with the insoluble COF. Ideal reaction strategies thus involve reagents with a **high reactivity**, which only lead to a **single product**. Furthermore, due to the restricted space and accessibility of the linkages, **reagents should be small** enough to enter the pore-channels and **fully soluble** in the reaction solvent. Thus, biphasic reaction media or surface reactions on heterogeneous particles in the reaction mixture are mostly incompatible. Transition states and reaction intermediates should be sterically compatible – excluding large transition metal complexes with bulky ligands as reagents to perform PSM of linkages.

In addition to these circumstances, it is very helpful for the following reaction optimization to **familiarize with the influencing factors of the synthetic strategy**. Helpful information may be obtained from previous reports in the small-molecule literature or found in reports for comparable systems, e.g. post-synthetic modification of polymers or even MOFs. Important considerations may include: Role and type of solvent compatible with the reaction? How can the **reactivity** be increased, considering additives such as Lewis acids, temperature or solvent changes? Is the reagent **selective**, or might it also react with other functional groups in the framework, besides the linkages? Which (side) products are formed and how may they be removed from the framework? Especially the removal of starting materials and **side products** is an important concern, as the purification capabilities in the COF are limited, and molecules remaining trapped in the pore-channels will give rise to misleading analytical results and may hamper the performance of the material during the targeted application. Disadvantages of certain reagents can sometimes be circumvented by the use of **alternative reagents** accomplishing the same reaction strategy. The identified

factors regarding the reactivity and selectivity of reaction conditions and reagents may be summarized, and serve as a guide for reaction screenings (step 5).

2.4.4 Step 4: Planning Workup and Analysis

After having chosen a PSM strategy for the targeted field of application, a suitable COF system and selected a reaction type and procedure to accomplish this transformation, it is important to identify appropriate analytical techniques that allow to follow the course of the PSM reaction. These or additional techniques may be used to decide whether further optimization of the reaction conditions are needed or which reagent among the selected ones gives the highest **conversion** and affords a material with ideally unaltered porosity. Furthermore, a set of analyses may be defined, which allow to quantify the degree of converted linkages in the material. In the following we will briefly discuss common analytical techniques used to characterize COFs and their value to assess the results of a PSM reaction. Although these analyses are necessary, one should note that it is equally important to prepare the framework samples correctly prior to analysis in order to conclude meaningful results from the analysis. Therefore, we will first take a closer look at sample preparation after PSM.

2.4.4.1 A Best Practice Guide to the Workup

As mentioned in the previous part on PSM strategy planning, the removal of by-products and starting materials, as well as reagents from the pores of the material is essential. Molecules that remain in the pores of the COF can not only reduce its porosity, but also misleadingly influence the results of spectroscopic analyses. In the worst case, it is impossible to distinguish between trapped and covalently bound molecules due to overlapping signals in the spectrum. This can result in a falsified statement about the conversion of the linkages.

As part of the reaction workup of the PSM, a strategy to remove these impurities is thus recommended. A simple, yet useful way is a thorough and repeated extraction of the porous material with a sequence of selected solvents. The choice of solvent should be adapted to the solubility of impurities, and may include strong polar aprotic solvents, such as DMF or DMSO, followed by THF or polar protic solvents, like MeOH. To enable a simple drying of the remaining material under reduced pressure, the series is completed by washing with a volatile, low-boiling point solvent (DCM or even alkanes). In addition, this solvent is ideally less-, or even, non-polar to avoid drying induced collapse of the pores.

While this simple general workup procedure may be practically performed with very basic lab filtration equipment, it is time consuming and requires multiple washing cycles to ensure complete removal of trapped molecules. As a more solvent- and labor-economic solution, repetitive extraction cycles can also be performed automatically in a Soxhlet extractor. Here, the powdered material is loaded into a small filtration bag made of folded lab grade filter-paper and extracted for several hours with an appropriate solvent. As an additional advantage

of this solvent-economic procedure, the material is extracted at elevated temperature close to the boiling point of the solvent, which further increases the solubility. If required for hardly soluble impurities, the extraction process can be extended for multiple days or subsequent Soxhlet extraction steps with different solvents can be used.

Although researchers have shown that vacuum drying of the material may not lead to pore collapse if the material is dried from a low-polarity solvent, such as pentane, the gold standard to preserve porous features remains supercritical CO₂ drying.^[27, 34-36] Here, the last washing step must involve a liquid CO₂ miscible solvent, such as MeOH or acetone. During the drying process, the remaining solvent is exchanged multiple times with liquid CO₂. Then, the CO₂ soaked powder is heated under pressure above the critical point at which the liquid loses its surface tension, and the material is dried by a pressure release. This procedure is usually performed by specialized critical-point dryers and thus involves the availability of this equipment and liquid CO₂, but has been shown to be the least destructive to the materials.

2.4.4.2 Selecting Analytical Techniques

To fully characterize a COF in terms of its fundamental characteristics, a range of different analytical techniques have to be utilized. These include X-ray diffraction, to assess the crystalline order of the material, gas sorption experiments to determine the porosity of the material, electron microscopy to assess the morphology, and spectroscopic techniques such as FT-IR and ssNMR spectroscopy to gain information on the chemical structure in the material. Although these are equally important for fully characterizing a final material, it is not practical to perform all the analyses for every reaction tested in order to optimize the synthesis parameters because of the time and materials involved. Instead, a researcher should limit the initial attention to a significant selection of techniques that is sufficient to provide a rapid indication of the outcome of the reaction. Due to the time and material consumption for the individual techniques, they are differently suited to achieve this goal. A comparative overview about selected analytical techniques with regards to these factors is presented in Table 1:

Table 1: Comparative overview about selected analytical techniques for characterizing COFs

Technique	Information	Req. Amount	Quantitative information on linkage?
FT-IR	Chemical structure, good sensitivity for specific functional groups	< 1 mg	Semi-quantitative
ssNMR	Chemical structure	> 10 mg	Depends on experiment and use of standards or enrichment
Elemental analysis	Elemental composition	>1 mg	Rarely, since it is not selective for the linkage only
XRPD	Crystalline order	1-5 mg	N/A – not sensitive for linkage
Gas sorption	Porosity	≥ 10 mg	N/A – not sensitive
SEM/TEM	Morphology, localized crystallinity	< 1 mg	N/A – not sensitive
(SEM/TEM)- EDX	Heavy atoms, especially metals	< 1 mg	N/A – only surface sensitive

For the detection of a structural change of the linkage, analyses of the chemical structure are crucial. These allow the detection and, if necessary, selected ones also allow quantification of the linkage conversion. This is of highest priority for the identification of suitable reagents for the planned PSM. From the comparison of the different analysis techniques presented in Table 1 it is clear that not all of them are equally suitable for this purpose, because some of them do not give any information on the chemical connectivity, only probe the material surface, or require large amounts of material. Therefore, FT-IR and NMR techniques are used in particular to probe linkage transformations. We will briefly discuss the characteristics of these selected, most useful analytic techniques, for screening of PSM conditions, in the following. For more detailed information on these and other analyses, we would like to refer to detailed chapters on the analysis of COFs in this book. At this point, we only give focused ideas and outline possibilities for the analysis of PSMs.

2.4.4.2.1 Fourier Transform Infra-Red Spectroscopy (FT-IR)

Fourier transform infra-red (FT-IR) spectroscopy uses the excitation of molecular vibrations for structural elucidation, induced by absorption of infra-red irradiation. In the absorption spectrum, these excitation processes become visible as absorption bands, which can often be assigned to characteristic vibrations of functional groups in a range of 4000-1500 cm⁻¹. Provided that overlapping of other bands does not occur, a band in a characteristic region thus indicates the presence of a certain functional group. In COFs, this property is often used to screen the framework for residues of the starting materials, e.g. aldehyde or amine building block residues after the synthesis of imine COFs. Thus, provided that a characteristic vibration is produced by the targeted bond modification, this technique may be excellently used to analyze the material after the PSM reaction.

Modern IR spectrometers are usually equipped with an attenuated total reflection (ATR) unit, which completely bypasses a previously common, time-consuming preparation of the sample as KBr compacts. The washed and dried powdered sample of the corresponding material is simply applied directly to the ATR unit without further preparation and the measurement can be started. As FT-IR is a non-destructive method, the material can be recovered after the measurement. Due to the extremely low material input (<1mg), the use without special preparation of the sample and the very short measurement time (<1min), FT-IR spectroscopy is an excellent technique for time- and material-efficient analysis of PSM reactions in COFs during screening of synthesis parameters. Unfortunately, the evaluation of the intensity of the adsorption bands only allows a semi-quantitative evaluation, since the intensity changes with the chemical environment of the molecular vibration bands. Depending on the vibration, as well as the material composition and the occurrence of hydrogen bonds in the material, the intensity, as well as the absolute position of the band can differ. Thus, a quantification cannot be achieved by a straight-forward integration of the bands, unless a complex calibration with reference materials can be performed. Nevertheless, within a series of screenings with the same COF, a **semi-quantitative** statement about the conversion of bonds can be obtained if the spectra are normalized (e.g. to an intense band) and the relative intensity of the characteristic vibrational band is compared. For example, this can be useful when studying linkage conversion as a function of reaction time. Even if the conversion cannot be calculated exactly from the FT-IR spectra peak integral, a **steady state** is reached when the linkages are fully converted: even with longer reaction times, the intensity of the product vibrational band will not change any further, and the linkage vibration of the pristine material (e.g. imine vibration) is no longer visible. This type of semi-quantitative analysis allows estimation of conversion using a rapid, non-destructive technique, although FT-IR spectra in principle do not allow exact quantification without prior calibration.

2.4.4.2.2 Solid-State Nuclear Magnetic Resonance Spectroscopy (ssNMR)

Another helpful technique to characterize structural changes, including linkage transformations in COFs, is ssNMR spectroscopy. This technique utilizes the excitation of nuclear spins in a strong magnetic field by electromagnetic radiation. Although only certain nuclei are NMR active, i.e. possess a (non-zero) nuclear spin, organic molecules and thus COFs mainly consist of atoms with NMR-active isotopes such as ^1H , ^{13}C , ^{15}N . In contrast to FT-IR spectroscopy, with sensitivity for specific functional groups, NMR spectroscopy captures the probed nuclei as a function of its chemical environment and thus, under certain conditions, also allows a quantification of the conversion. Besides, multidimensional experiments such as ^1H - ^{13}C heteronuclear correlation (HETCOR) spectra, for example, give a detailed information on the neighboring atoms and thus an unparalleled, direct precision to the chemical structure of the materials. However, the indispensable information of this technique for a thorough characterization of the framework comes at the expense of longer

experimental measuring times of a few (^{13}C) to several hours (^{15}N), larger required sample amounts (>10 mg) and increased acquisition and maintenance costs for NMR equipment, compared to FT-IR spectroscopy. This renders ssNMR spectroscopy a valuable, non-destructive tool for in-depth analysis and especially for quantification of linkage and building block related transformations of the chemical structure, but limits its utility for a quick evaluation during reaction screenings.

2.4.4.2.2.1 Quantification of Linkage Conversion Reactions with ssNMR

Unlike solution-based NMR spectra which usually benefit from sharp peaks that may be integrated for quantification, signals in solid-state spectra are broadened due to anisotropic chemical shielding and dipolar and quadrupolar interactions between the nuclei. Although these effects are partly suppressed by the magic-angle spinning technique, many proton spectra of COFs in the solid state show very broad, overlapping signals, that do not allow simple integration to quantify. Since linkage modifications usually also modulate the chemical environment of carbon and nitrogen centers, spectra of these nuclei appear as promising alternatives for this purpose. The low abundance of ^{13}C (1.1%), and ^{15}N (0.4%) compared to ^1H (99.9%) however makes chemical shifts for these nuclei harder to detect. One way to increase the sensitivity for these atoms, which is widely used to measure these spectra, is known as the cross-polarization (CP) technique. CP NMR spectra make use of a polarization transfer from abundant nuclei, such as protons, which transfer their polarization to neighboring nuclei – such as ^{13}C or ^{15}N . Although this technique makes spectra of reasonably quality for these nuclei accessible without tedious isotope enriched synthesis, it comes at the expense of being essentially non-quantitative. For example proton substituted carbon or nitrogen atoms appear with high intensities, compared to an equal amount of quaternary atoms. Intensities thus become a function of polarization transfer rate in general CP spectra, and do no longer reflect the quantity of spins in a chemical environment. A strategy to circumvent this incompatibility can be quantitative direct-polarization experiments for ^{13}C , which obey the CP transfer and suffer from long experiment times with often diminished signal-to-noise ratio, unless combined with ^{13}C enriched samples, but preserve quantitative information.^[37] Another alternative for quantification in carbon and nitrogen spectra even employing the powerful CP technique are multiCP experiments, using a series of CP experiments at multiple contact times, essentially eliminating the polarization transfer rate dependence.^[38] This method has successfully been demonstrated for the quantification of a multi-step linkage conversion of imines to (thio-)carbamates by ^{15}N multiCP-MAS ssNMR experiments.^[25]

Using direct polarization ssNMR techniques, with increased number of scans or isotopically enriched samples to enhance signal-to-noise ratio, or by using multiCP experiments quantitative information on the linkage conversion reactions may be obtained. Integration of the non-modified linkage peak, or a reference that does not change during the linkage

conversion, i.e. an atom located in the building block moiety, and comparing it to the peak integration of the modified linkage will lead to a meaningful conversion ratio, if signal overlapping does not occur. In cases where only one of the above mentioned signals is clearly separated, quantitative information may still be accessible by diluting the framework with a controlled mass of an internal standard that shows a distinguishable signal in the respective NMR spectrum. Ideally this standard does not react with the sample material, and is a solid with reasonable solubility, in order to be able to remove it by simple solvent washing/filtration after the NMR experiment to recover the sample. On the other hand, the internal standard strategy may also serve as a handle to employ an orthogonal nucleus for quantification not present in the pristine framework, but is introduced upon linkage modification. As an example one may assume to employ 4-fluoro styrene instead of styrene in a Povarov reaction (see section 2.3.3) with imine linkages. In this case, abundant and NMR-sensitive ^{19}F nuclei are introduced by PSM. Diluting the modified samples with a known amount of a fluoride salt, such as NaF, after PSM reaction and workup, which must be capable of removing any 4-fluoro styrene precursors, signal integration of the ^{19}F ssNMR spectrum will deliver the fluorine content in the modified sample as a fingerprint for the conversion achieved during PSM.

2.4.4.2.3 Other Techniques and Conclusion

While FT-IR and selected ssNMR experiments deliver valuable information on the chemical structure, with ssNMR also allowing the possibility for quantification of the reached conversions, other common techniques for the characterization of COFs, such as SEM/TEM-EDX, are not meaningful to follow, and especially to optimize, linkage conversion reactions due to their sensitivity limited to the material's surface only.

Nevertheless, in order to optimize the synthesis conditions, the influence of the modification reaction on the crystallinity of the sample must also be taken into account. Differences can become visible here, especially due to the different selectivity of reagents, leading to a destruction of the material's structure or unwanted side reactions. X-ray powder diffraction (XRPD) is used as a fast, simple and direct method, but is unable to give any information about the chemical structure of the samples. Likewise, gas sorption analysis is also required to study the effect of the PSM on the porosity of the sample, at least at a later stage of condition optimization. Thus helpful information for developing robust PSM strategies cannot be given by only one of the presented analytical techniques, but instead a combination of spectroscopic and, at least, diffraction techniques is mandatory. Nevertheless, during reaction optimization only a limited set of fast techniques should be used for an initial assessment. Taking into account this, yet manageable number of techniques, the material and time required can be reduced to a minimum by a wise selection of fast techniques (e.g. FT-IR + XRPD), whereby the experimenter can already obtain the utmost important information from the screening.

2.4.5 Step 5: Starting Experiments: Variation of Reaction Conditions

After familiarizing with important practical influences during workup, and having selected appropriate techniques for reaction optimization, which can depict the targeted modification by a characteristic signal, it's now time to start the first experiments.

As with typical optimization screening, general experimental design practices also apply when performing PSM reaction optimization. Common parameters, such as reaction time, temperature, solvents and reagents, as well as specific influencing factors from the conditions used in literature reports (section 2.4.3.2) that were identified during the PSM reaction planning, can be variables for the screening reactions. These parameters should be varied independently to obtain meaningful cause-effect relationships as a basis for subsequent optimization cycles. As detailed in the previous sections, a robust, non-destructive and reproducible workup procedure and a selected set of analytical techniques provide the basis for interpreting the experimental outcomes and thus the influences of the addressed parameters in the tested reaction conditions. On this basis decisions for the following optimization steps have to be made. Figure 2-20 depicts a typical workflow for these reaction-analysis cycles and can serve as guide for decision making. One of the key elements in this decision tree is the hierarchical structuring of analytical techniques, arranging them with at different priority levels in the workflow.

The highest priority (Level 1) is assigned to detecting a noticeable conversion of the linkages during the initial set of experiments by FT-IR spectroscopy. At this stage it is not relevant if the analyzed materials are crystalline, or if they possess high pore volumes. If none of the tested conditions and reagents led to a noticeable conversion, the set of parameters has to be varied and another cycle of reactions is started. However, if some conversion is visible from FT-IR for a certain set of tested reactions one may move forward to evaluate crystallinity by XRPD (Level 2).

At this stage, conversion is principally achieved, however, another important factor for PSM strategies is, that they preserve the crystallinity of the frameworks. When deciding which parameters should be varied to allow conversion of the linkages with preservation of the crystallinity, one may also consider to review the work-up procedure. Because crystalline order in the materials can also be reduced during workup, besides during the PSM reaction. Analogous to varied conditions for achieving linkage conversion (Level 1) additional reactions are performed and analyzed. Once linkages have been transformed, and the procedures are optimized to certain extend at which crystallinity is still present in the samples, quantification of the achieved conversions by ssNMR may be the following step (Level 3).

During the initial planning steps, one may have chosen a certain target conversion yield required for the targeted property in the tailored material. At this level of optimization, conditions are further varied to achieve this goal. Increasing temperature, reaction times or concentration of PSM reagents may lead to improved conversion yield in your materials.

Finally, at Level 4 assessment of porosity by gas sorption analysis is used to do the remaining optimizations. This is the final step before scale-up and additional material characterization may be performed.

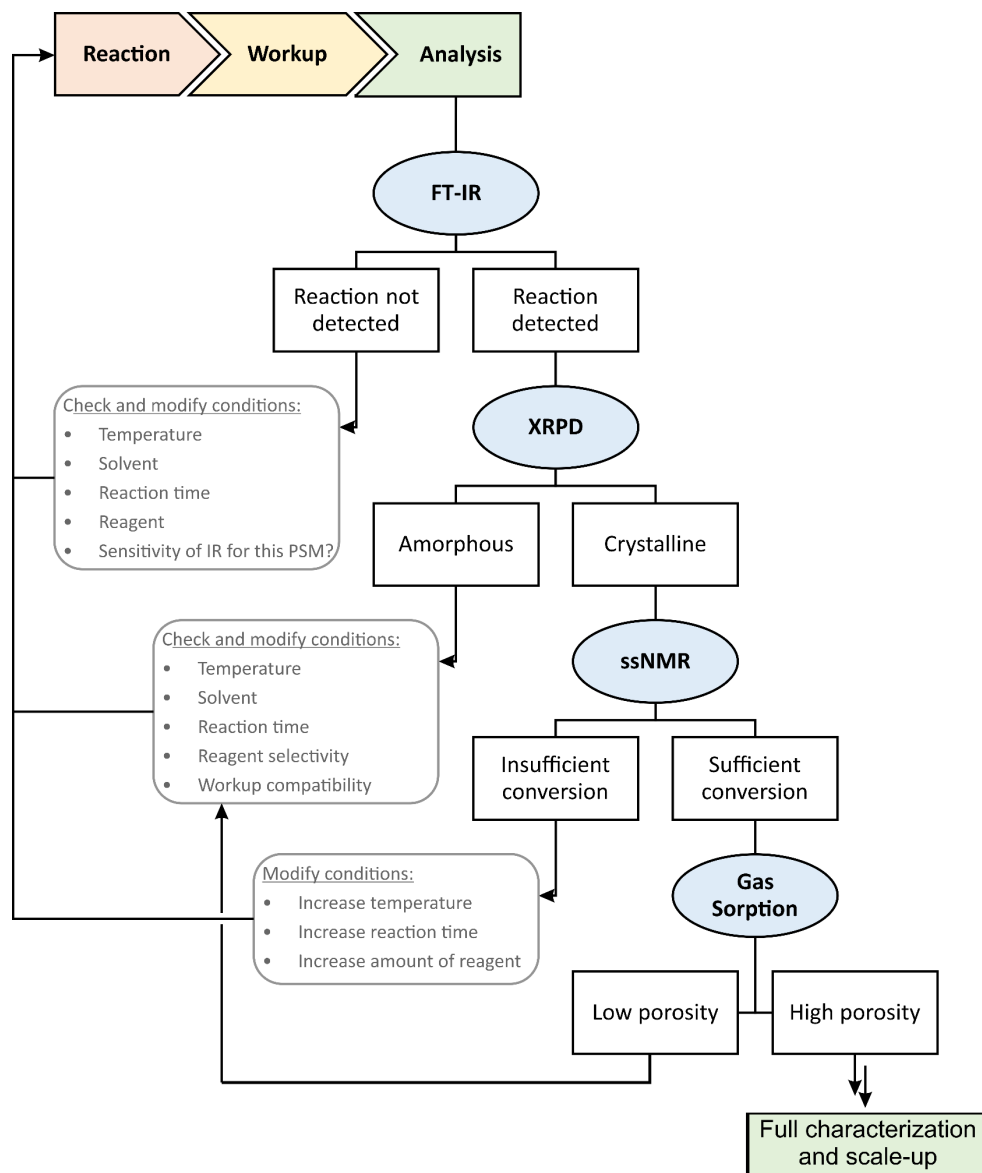


Figure 2-20: A guide for decision making in reaction optimization of PSM reactions in COFs.

While this structure may seem unnecessarily complicated at first glance, it is important to understand its benefits: (1) Prioritizing on fast, but meaningful analyses at the initial two optimization levels saves time. As reaction conditions approach their optimum with each cycle, the number of experiments required decreases with each level of optimization. As a result, only a small fraction of the already optimized screening samples are analyzed using time-consuming analytical techniques. (2) The hierarchical optimization steps allow to gain the most information, and thus value, from every test reaction – even from those that would be considered “unsuccessful”. As visible from the decision tree, the first level of optimization does not consider the crystallinity of the material after the reaction, but instead focusses only

on finding sufficient conditions for the approached PSM reaction. In turn, all conditions which afford amorphous materials after PSM, which may be considered a “failed experiment”, can still deliver valuable information on the reaction conditions.

In summary, these considerations for experimental design and the decision tree for conducting experiments will be supportive to obtain the desired materials within a short amount of time and reduced effort.

2.5 Bibliography

1. Waller P. J. et al. Conversion of Imine to Oxazole and Thiazole Linkages in Covalent Organic Frameworks. *J. Am. Chem. Soc.* **140**, 9099-9103 (2018).
2. Maschita J., Banerjee T., Lotsch B. V. Direct and Linker-Exchange Alcohol-Assisted Hydrothermal Synthesis of Imide-Linked Covalent Organic Frameworks. *Chem. Mater.* **34**, 2249-2258 (2022).
3. Zhang W. et al. Reconstructed Covalent Organic Frameworks. *Nature* **604**, 72-79 (2022).
4. Li L. H. et al. Salen-Based Covalent Organic Framework. *J. Am. Chem. Soc.* **139**, 6042-6045 (2017).
5. Cote A. P. et al. Porous, Crystalline, Covalent Organic Frameworks. *Science* **310**, 1166-1170 (2005).
6. Chen X. et al. Control of Crystallinity and Porosity of Covalent Organic Frameworks by Managing Interlayer Interactions Based on Self-Complementary Pi-Electronic Force. *J. Am. Chem. Soc.* **135**, 546-549 (2013).
7. Alahakoon S. B., Diwakara S. D., Thompson C. M., Smaldone R. A. Supramolecular Design in 2d Covalent Organic Frameworks. *Chem. Soc. Rev.* **49**, 1344-1356 (2020).
8. Alahakoon S. B. et al. 2d-Covalent Organic Frameworks with Interlayer Hydrogen Bonding Oriented through Designed Nonplanarity. *J. Am. Chem. Soc.* **142**, 12987-12994 (2020).
9. Emmerling S. T. et al. Interlayer Interactions as Design Tool for Large-Pore Cofs. *J. Am. Chem. Soc.* **143**, 15711-15722 (2021).
10. Pütz A. M. et al. Total Scattering Reveals the Hidden Stacking Disorder in a 2d Covalent Organic Framework. *Chem. Sci.* **11**, 12647-12654 (2020).
11. Koo B. T., Dichtel W. R., Clancy P. A Classification Scheme for the Stacking of Two-Dimensional Boronate Ester-Linked Covalent Organic Frameworks. *J. Mater. Chem. 22*, 17460-17469 (2012).
12. Grunenberg L. et al. Amine-Linked Covalent Organic Frameworks as a Platform for Postsynthetic Structure Interconversion and Pore-Wall Modification. *J. Am. Chem. Soc.* **143**, 3430-3438 (2021).
13. Chen L. et al. Substoichiometric 3d Covalent Organic Frameworks Based on Hexagonal Linkers. *J. Am. Chem. Soc.* **143**, 10243-10249 (2021).
14. Ma Y. et al. Three-Dimensional Chemically Stable Covalent Organic Frameworks through Hydrophobic Engineering. *Angew. Chem. Int. Ed.* **59**, 19633-19638 (2020).

15. Wu X. et al. Control Interlayer Stacking and Chemical Stability of Two-Dimensional Covalent Organic Frameworks Via Steric Tuning. *J. Am. Chem. Soc.* **140**, 16124-16133 (2018).
16. Lanni L. M., Tilford R. W., Bharathy M., Lavigne J. J. Enhanced Hydrolytic Stability of Self-Assembling Alkylated Two-Dimensional Covalent Organic Frameworks. *J. Am. Chem. Soc.* **133**, 13975-13983 (2011).
17. Wu X. et al. Perfluoroalkyl-Functionalized Covalent Organic Frameworks with Superhydrophobicity for Anhydrous Proton Conduction. *J. Am. Chem. Soc.* **142**, 14357-14364 (2020).
18. Waller P. J. et al. Chemical Conversion of Linkages in Covalent Organic Frameworks. *J. Am. Chem. Soc.* **138**, 15519-15522 (2016).
19. Haase F. et al. Topochemical Conversion of an Imine- into a Thiazole-Linked Covalent Organic Framework Enabling Real Structure Analysis. *Nat. Commun.* **9**, 2600 (2018).
20. Wang K. et al. Synthesis of Stable Thiazole-Linked Covalent Organic Frameworks Via a Multicomponent Reaction. *J. Am. Chem. Soc.* **142**, 11131-11138 (2020).
21. Seo J. M., Noh H. J., Jeong H. Y., Baek J. B. Converting Unstable Imine-Linked Network into Stable Aromatic Benzoxazole-Linked One Via Post-Oxidative Cyclization. *J. Am. Chem. Soc.* **141**, 11786-11790 (2019).
22. Wei P. F. et al. Benzoxazole-Linked Ultrastable Covalent Organic Frameworks for Photocatalysis. *J. Am. Chem. Soc.* **140**, 4623-4631 (2018).
23. Grunenberg L. et al. Postsynthetic Transformation of Imine- into Nitrone-Linked Covalent Organic Frameworks for Atmospheric Water Harvesting at Decreased Humidity. *J. Am. Chem. Soc.* **145**, 13241-13248 (2023).
24. Liu H. et al. Covalent Organic Frameworks Linked by Amine Bonding for Concerted Electrochemical Reduction of Co₂. *Chem* **4**, 1696-1709 (2018).
25. Lyle S. J. et al. Multistep Solid-State Organic Synthesis of Carbamate-Linked Covalent Organic Frameworks. *J. Am. Chem. Soc.* **141**, 11253-11258 (2019).
26. Hu J. et al. Catalyst-Enabled in Situ Linkage Reduction in Imine Covalent Organic Frameworks. *ACS Appl. Mater. Interfaces* **13**, 21740-21747 (2021).
27. Sick T. et al. Switching on and Off Interlayer Correlations and Porosity in 2d Covalent Organic Frameworks. *J. Am. Chem. Soc.* **141**, 12570-12581 (2019).
28. Haase F., Lotsch B. V. Solving the Cof Trilemma: Towards Crystalline, Stable and Functional Covalent Organic Frameworks. *Chem. Soc. Rev.* **49**, 8469-8500 (2020).
29. Li X. T. et al. Construction of Covalent Organic Frameworks Via Three-Component One-Pot Strecker and Povarov Reactions. *J. Am. Chem. Soc.* **142**, 6521-6526 (2020).
30. Li C. et al. Asymmetric Photocatalysis over Robust Covalent Organic Frameworks with Tetrahydroquinoline Linkage. *Chinese J. Catal.* **41**, 1288-1297 (2020).
31. Li X. et al. Facile Transformation of Imine Covalent Organic Frameworks into Ultrastable Crystalline Porous Aromatic Frameworks. *Nat. Commun.* **9**, 2998 (2018).
32. Ren X. R. et al. Constructing Stable Chromenoquinoline-Based Covalent Organic Frameworks Via Intramolecular Povarov Reaction. *J. Am. Chem. Soc.* **144**, 2488-2494 (2022).

33. Nguyen H. L. et al. Hydrazine-Hydrazide-Linked Covalent Organic Frameworks for Water Harvesting. *ACS Cent. Sci.* **8**, 926-932 (2022).
34. Zhu D. et al. Solvent-Induced Incremental Pore Collapse in Two-Dimensional Covalent Organic Frameworks. *ACS Mater. Lett.* **4**, 2368-2374 (2022).
35. Feriante C. H. et al. Rapid Synthesis of High Surface Area Imine-Linked 2d Covalent Organic Frameworks by Avoiding Pore Collapse During Isolation. *Adv. Mater.* **32**, e1905776 (2020).
36. Zhu D., Verduzco R. Ultralow Surface Tension Solvents Enable Facile Cof Activation with Reduced Pore Collapse. *ACS Appl. Mater. Interfaces* **12**, 33121-33127 (2020).
37. Stahler C. et al. Light-Driven Molecular Motors Embedded in Covalent Organic Frameworks. *Chem. Sci.* **13**, 8253-8264 (2022).
38. Johnson R. L., Schmidt-Rohr K. Quantitative Solid-State ^{13}C Nmr with Signal Enhancement by Multiple Cross Polarization. *J. Magn. Reson.* **239**, 44-49 (2014).

3 Research Objective

To date an ever increasing variety of covalent organic frameworks with different linkages, building block compositions and different topologies has been developed. This progress is fueled by a broad diversity of appealing applications, while their organic, and thus tunable backbone forms the foundation for these developments. Since the early days of COF chemistry the range of applications has significantly been extended beyond gas capture and storage enabled by their intrinsic structural porosity. Modern applications, such as sensing, electrochemical energy storage, or heterogeneous (photo-)catalysis, also utilize the (covalent) organic backbone, for example as embedded redox-active building blocks in the material to store electrons, as light absorbers or as an “active” porous support for covalent anchoring of catalysts in heterogeneous (photo)catalysis. Taking advantage of these unique properties pushes the utility of COFs far beyond the capabilities of many other porous materials.

However, these increasingly complex applications are also exploiting the limitations of existing synthesis strategies, as intrinsic limitations of as-synthesized materials become more apparent. These include incompatibility of required functional groups during synthesis or limited stability of the frameworks under application conditions, e.g. hydrolysis in aqueous media at elevated temperature. Although research has led to the *de-novo* synthesis of novel COFs with higher chemical resistance, the demand for these highly complex but also stable and crystalline systems with high permanent porosity and excellent ability for functionalization is far from being met. In turn, the rush for diverse applications requires innovative synthetic methods to satisfy the need for tailorabile complex materials.

The scope of this thesis is (I) to provide access to these tailored COFs by novel synthetic methods focusing on post-synthetic linkage modification. We develop these linkage chemistries on the basis of multiple two-dimensional imine-linked frameworks with different topologies and building block compositions, with the aim to tackle the *COF trilemma* between crystallinity, stability and complexity/function in these frameworks, as introduced in Chapter 2.

To this end, we introduce a simple, but effective post-synthetic reduction of imine linkages to secondary amine linked covalent organic frameworks, presented in Chapter 4, which locks, i.e. stabilizes, and simultaneously activates the connectivity of the framework for further functionalization.

In addition to this method, endowing the pore channels with reactivity and reinforced stability, we present a post-synthetic oxidation strategy that modulates the polarity of the pore channels in Chapter 5. The constructed nitrone-linkages, formed in a topochemical reaction from imine-linkages, render the linkage centers at the pore walls more polar, enhancing interactions with polar molecules, such as water vapor. This property allows them to harvest water vapor from ambient air at reduced relative humidity.

Another aim of this thesis is (II) to integrate stimuli-responsive dynamics in the pore channels of COFs. In Chapter 6, light-driven molecular motors are embedded as building blocks into two-dimensional frameworks to imprint dynamic function in these materials, to investigate dynamics with *in-situ* spectroscopic methods and, to develop design criteria for the integration of light-driven molecular motors in porous solids.

Furthermore, this thesis intends (III) to experimentally probe motion of molecules in pore channels of COFs, which is a prerequisite for post-synthetic linkage modifications, but also for utilizing heterogeneous confinement effects of molecules confined in the pore system. Thus, we present a combined experimental and simulation study of acetonitrile self-diffusion in COFs, combining Pulsed Field Gradient NMR spectroscopy, Molecular Dynamics and Grand Canonical Monte Carlo simulations in Chapter 7.

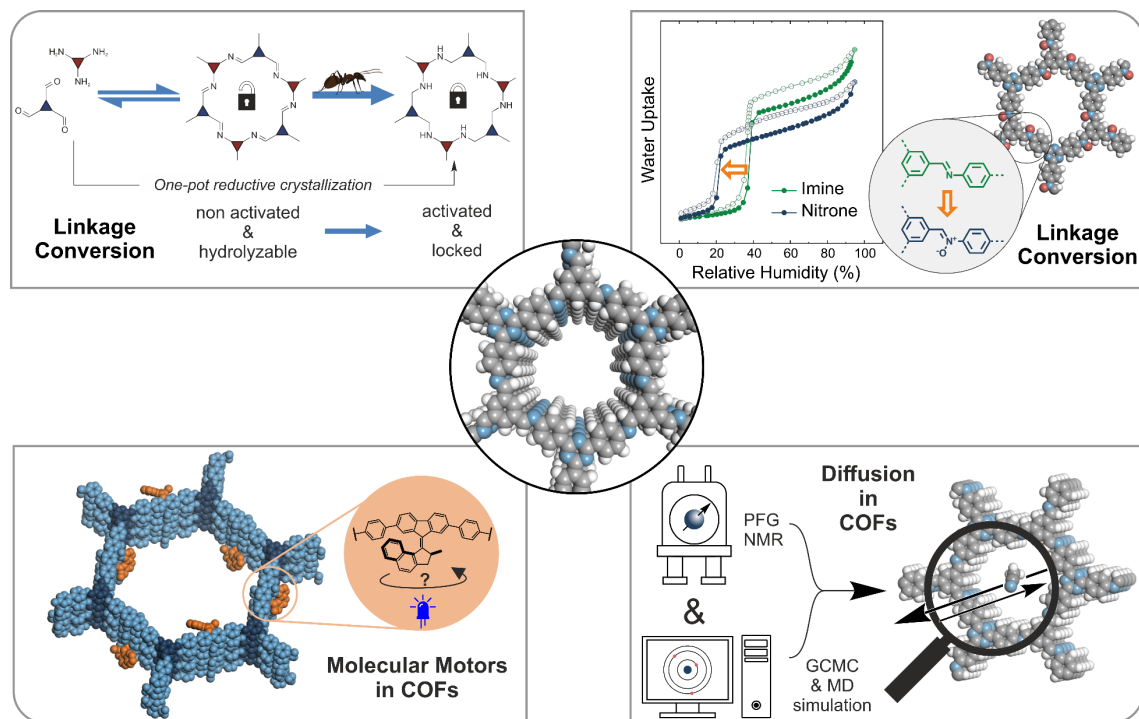
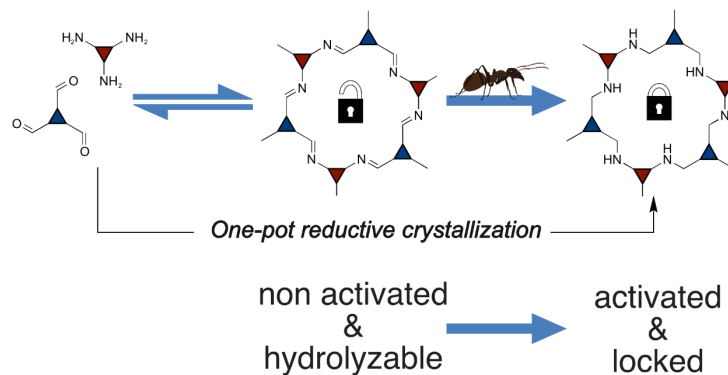


Figure 3-1: Overview about the topics addressed in this thesis: synthetic modification of complexity in covalent organic frameworks and dynamic processes in their pore channels.

4 Amine-Linked COFs: A Platform for Post-Synthetic Structure Interconversion and Modification



The presented work of this chapter was published, adapted and reproduced from:

Amine-Linked Covalent Organic Frameworks as a Platform for Postsynthetic Structure Interconversion and Pore-Wall Modification

Lars Grunenbergs, Gökçen Savascı, Maxwell W. Terban, Viola Duppel, Igor Moudrakovski, Martin Etter, Robert E. Dinnebier, Christian Ochsenfeld, and Bettina V. Lotsch, *J. Am. Chem. Soc.* **2021**, *143*, 3430–3438. doi: 10.1021/jacs.0c12249

L.G. conceived the idea, performed and interpreted experiments, led the project and wrote the manuscript. G.S. performed quantum-chemical calculations. M.W.T. performed synchrotron X-ray measurements and PDF analysis. M.E. helped with synchrotron measurements. R.E.D. helped with measurements and modelling. V.D. recorded SEM and TEM data. I.M. recorded solid-state NMR spectra. B.V.L. supervised the research. All authors wrote and commented on the manuscript.

This article was highlighted in:

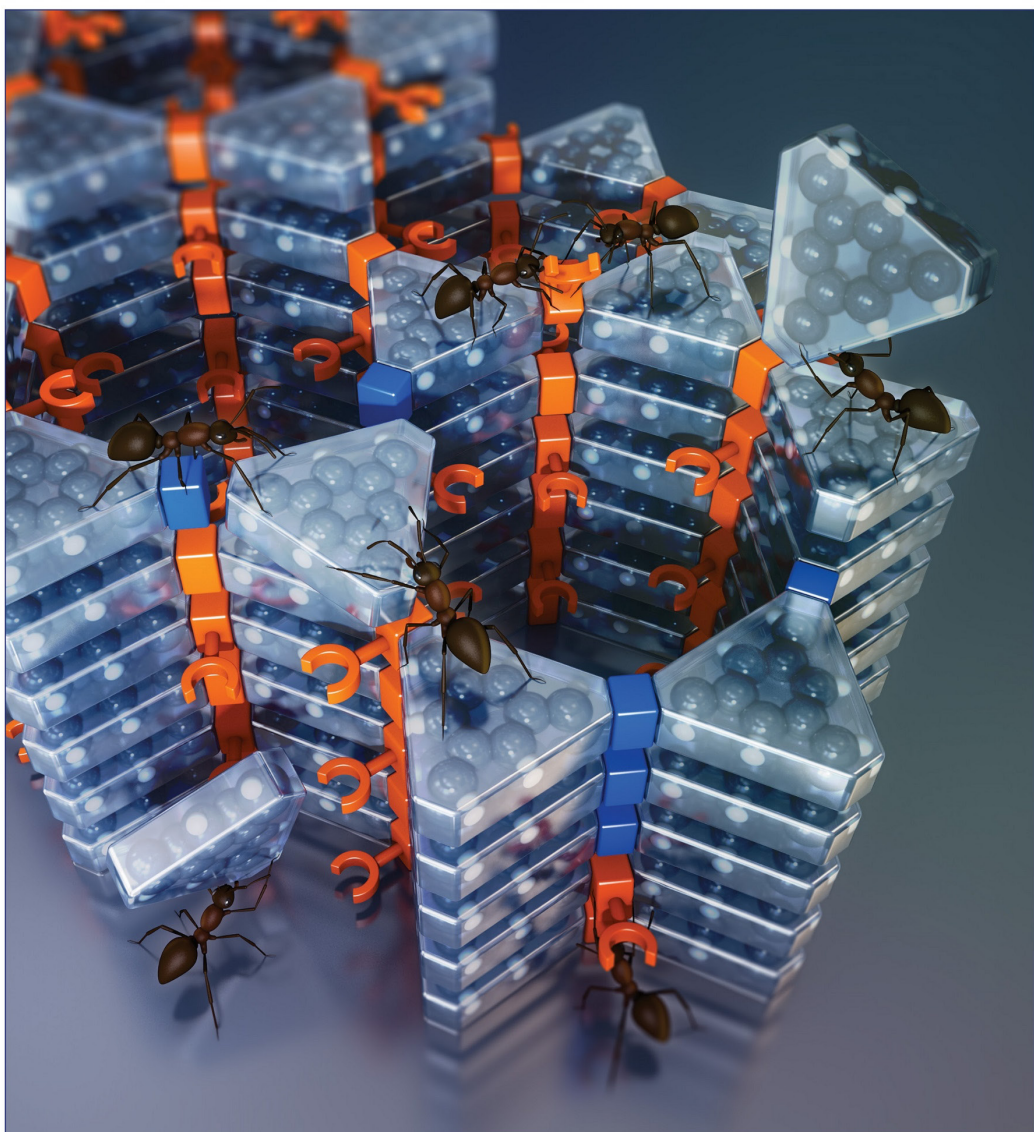
Spotlights on Recent JACS Publications. *J. Am. Chem. Soc.* **2021**, *143*, 4083-4084.

Ashworth C. Overcoming the COF Trilemma. *Nat. Rev. Chem.* **2021**, *5*, 220.

March 10, 2021
Volume 143
Number 9
pubs.acs.org/JACS

J|A|C|S

JOURNAL OF THE AMERICAN CHEMICAL SOCIETY



 ACS Publications
Most Trusted. Most Cited. Most Read.

www.acs.org

Supplementary Cover Image designed by Vera Hiendl (e-conversion).

Abstract: Covalent organic frameworks have emerged as a powerful synthetic platform for installing and interconverting dedicated molecular functions on a crystalline polymeric backbone with atomic precision. Here, we present a novel strategy to directly access amine-linked covalent organic frameworks, which serve as a scaffold enabling pore-wall modification and linkage-interconversion by new synthetic methods based on Leuckart–Wallach reduction with formic acid and ammonium formate. Frameworks connected entirely by secondary amine linkages, mixed amine/imine bonds, and partially formylated amine linkages are obtained in a single step from imine-linked frameworks or directly from corresponding linkers in a one-pot crystallization-reduction approach. The new, 2D amine-linked covalent organic frameworks, rPI-3-COF, rTTI-COF, and rPy1P-COF, are obtained with high crystallinity and large surface areas. Secondary amines, installed as reactive sites on the pore wall, enable further post-synthetic functionalization to access tailored covalent organic frameworks, with increased hydrolytic stability, as potential heterogeneous catalysts.

4.1 Introduction

In recent years, covalent organic frameworks (COFs) have emerged as a versatile class of crystalline porous polymers, which have been pushing the frontiers of single-site heterogeneous catalysis ever since. The unique combination of ordered and tunable pore structures, with high surface areas and versatile (opto-)electronic properties, offers great opportunities beyond gas storage and separation, including sensing, electrochemical energy storage, optoelectronics, and heterogeneous (photo)catalysis.^[1-4]

Imine-linked COFs constitute the most widely studied subclass of COFs owing to their broad synthetic scope and facile building block synthesis. The dichotomy of dynamic covalent chemistry in COF synthesis implies that, while reversible bond formation is critical for crystallization, the reversibility of imine bond formation also causes its limited stability against hydrolysis. To address this issue, several post-synthetic locking strategies have been developed in the past, e.g., converting labile imine-linked COFs into stable benzothiazole-,^[5, 6] amide-,^[7] or quinoline-linked frameworks.^[4, 8-13] Although these methods significantly increase the material's hydrolytic stability, most do not activate but rather deactivate potential reactivity of the linkages for further pore-wall modification. To achieve the latter, reactive centers have to be installed into the linker moieties, which are often incompatible with synthesis conditions. This incompatibility requires an additional pore-wall activation step, e.g., the reduction of nitro groups to amines^[14] or the deprotection of ethers to alcohols.^[15] In essence, a typical synthetic route would consist of at least four sequential steps, including (a) framework crystallization, (b) linkage transformation, (c) pore-wall activation, and (d) pore-wall functionalization, to obtain both stable and decorated frameworks. Being faced with varying conversion yields and a loss of material between each step, innovative synthetic methods condensing these transformations into fewer steps, or even a single synthetic step, are highly desirable.

As a solution to the challenges discussed, we here demonstrate amine-linked covalent organic frameworks as a powerful platform for facile pore-wall modification and linkage interconversion enabled by new synthetic methods based on Leuckart–Wallach^[16, 17] reduction with formic acid and ammonium formate. By fine-tuning reaction conditions, frameworks connected entirely by secondary amine linkages, mixed amine/imine bonds, and partially formylated amine-linkages are accessible in a single step from imine-linked frameworks or directly from the corresponding linkers in a one-pot crystallization-reduction approach. We thus present a novel strategy enabling direct access to amine-linked covalent organic frameworks. In addition, we reveal correlations between topologically equivalent disordered and crystalline frameworks, which are not accessible by typical X-ray powder diffraction (XRPD) analysis, using pair distribution function (PDF) analysis, solid-state nuclear magnetic resonance spectroscopy (ssNMR), and quantum-chemical calculations. These findings enable us to identify unique pH-dependent amorphization pathways and hence expand our fundamental understanding of amine-linked covalent organic frameworks as an important yet underexplored class of heterogeneous catalysts.

4.2 Results

4.2.1 Previous Strategies and Drawbacks

During our studies, we found that a reduction of imine-linkages would both increase the hydrolytic stability of the framework and introduce secondary amine-linkages as reactive centers for further functionalization of the pore wall. This transformation, familiar from small organic molecules as well as molecular cages, is usually achieved using borohydride-based reducing agents, such as sodium borohydride or sodium cyanoborohydride.^[18-20]

Borohydride-based reduction has successfully been used for robust and rigid 3D systems, while 2D frameworks have only been obtained with diminished crystallinity and low surface areas at best.^[11, 15, 21]

While highly reactive, reactions with sodium borohydride, in particular, suffer from limited selectivity and low functional group tolerance.^[5, 22] With these shortcomings in mind, we sought an alternative, mild reduction procedure affording crystalline and porous amine-linked covalent organic frameworks. To this end, we identified the Leuckart–Wallach reduction with formic acid, reported for small organic molecules by Leuckart in 1885 and further developed by Wallach, as a suitable reduction strategy.^[16, 17]

4.2.2 Synthesis of Amine-Linked COFs

As a model system, we first synthesized the imine-linked PI-3-COF from 1,3,5-triformyl benzene (TFB) and 4,4',4''-(1,3,5-triazine-2,4,6-triyl)trianiline (TTA) under solvothermal

conditions in a 2:1 mesitylene/1,4-dioxane mixture with aqueous 6 M AcOH at 120 °C for 72 h, according to a modified literature procedure.^[23]

Upon reacting the imine-linked PI-3 framework in a sequential step with 19 equiv of formic acid in the same solvent, a new vibration appeared at 3405 cm⁻¹ as probed by Fourier transform infrared spectroscopy (FT-IR), attributed to a secondary amine (v_{N—H}) stretching mode. The intensity of the imine vibration (v_{C=N}) at 1630 cm⁻¹ gradually decreased over prolonged reaction time at 120 °C (Figure S 9.1-1, Figure S 9.1-2). Extensive screening for the highest relative intensities of the secondary amine vibrations in the IR spectrum yielded optimal synthetic conditions at 21 equiv of formic acid in a 2:1 mesitylene/1,4-dioxane mixture and a reaction time of 24 h at 120 °C. Under these conditions, the samples did not show any residual imine stretch vibration (v_{C=N}), hinting at the complete transformation of the parent PI-3-COF structure (Figure 4-1b). ¹³C cross-polarization magic angle spinning (CP-MAS) solid-state NMR (ssNMR) spectroscopy similarly shows the disappearance of the characteristic imine carbon signal at 155.3 ppm, while a new aliphatic carbon signal at 45.4 ppm is visible for the reduced PI-3-COF (rPI-3-COF). Besides that, new signals at 119 and 114 ppm become visible for rPI-3-COF, assigned to the aromatic carbons next to the amine bond (Figure 4-1c). ¹⁵N ssNMR of rPI-3-COF shows distinct signals at -313.3 ppm for the secondary amine nitrogen and at -141.4 ppm for the triazine (Figure S 9.1-30). The absence of the imine nitrogen at -59.0 ppm further suggests a quantitative reduction of imine into amine linkages in rPI-3-COF. The measured ssNMR chemical shifts are in good agreement with values obtained by quantum-chemical calculations of representative molecular and single-pore models (Table S 9.1-5).

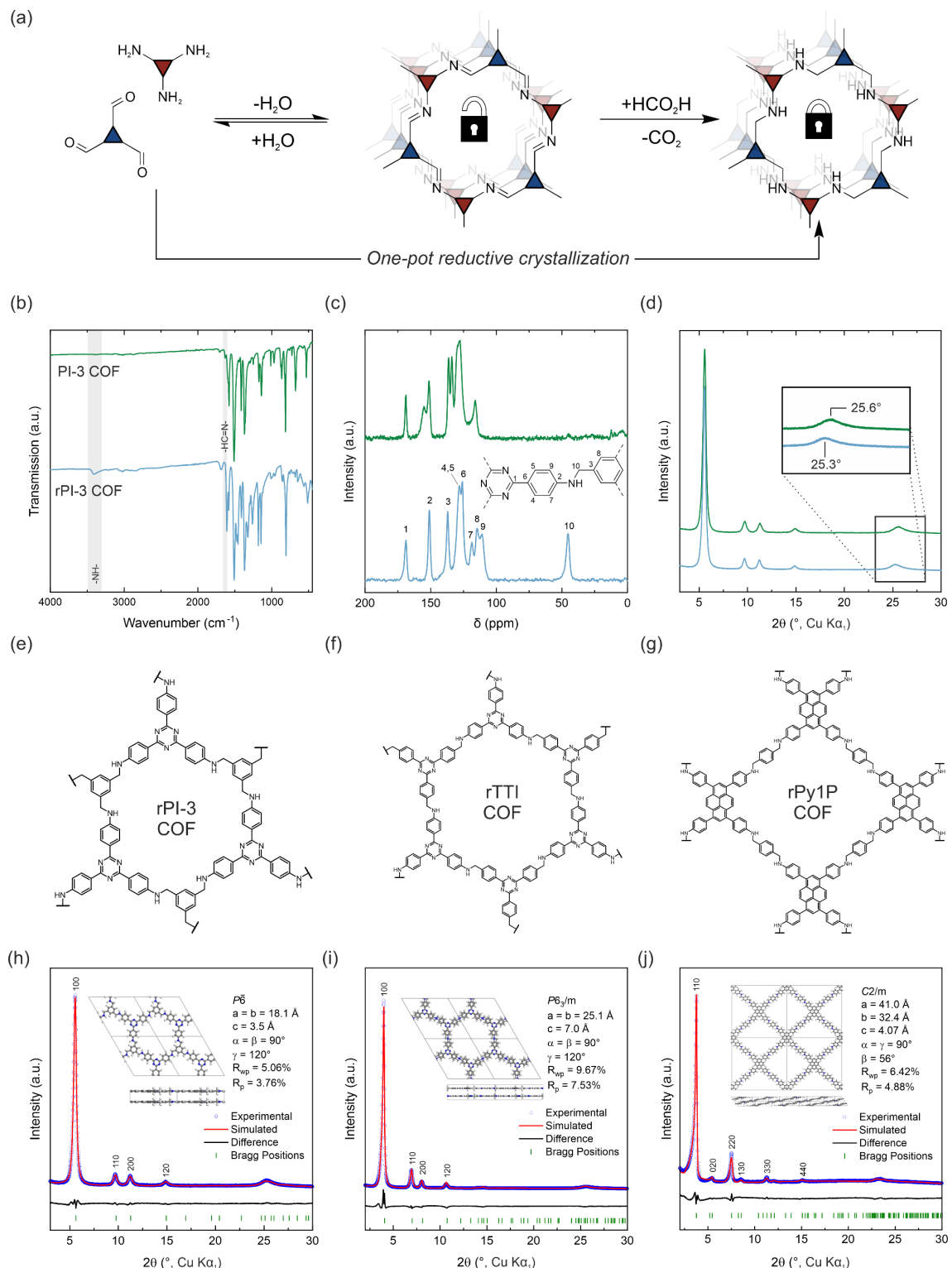


Figure 4-1: (a) Synthesis of amine-linked covalent organic frameworks. (b) FT-IR spectra, (c) ¹³C CP-MAS ssNMR spectra, and (d) XRPD pattern comparison of PI-3-COF (green) and rPI-3-COF (blue). (e and f) Chemical structure of a single pore of (e) rPI-3, (f) rTTI, and (g) rPy1P-COF. (h–j) Rietveld refinements for (h) rPI-3, (i) rTTI, and (j) rPy1P-COF.

Structural analysis of rPI-3-COF via XRPD reveals high crystallinity (Table S 9.1-3), represented by four narrow reflections at $2\theta = 5.6^\circ, 9.7^\circ, 11.2^\circ$, and 14.9° , indexed as 100, 110, 200, and 210 reflections (space group $P\bar{6}$), and a broad stacking reflection at $2\theta = 25.3^\circ$.

Compared to its parent imine structure (PI-3-COF), the apparent hexagonal symmetry and crystallinity are retained, while a significant shift of the broad stacking reflection at $2\theta = 25.6^\circ$ (PI-3-COF) toward smaller angles appears. Rietveld^[24] refinement gives a larger in-plane unit cell parameter of $a = 18.090(7)$ Å and an increased stacking distance of $c = 3.5425(12)$ Å in rPI-3-COF ($a = 18.034(7)$ Å and $c = 3.5058(12)$ Å for PI-3-COF) (Table S 9.1-1). While the cell parameter a is affected by increased C—N (149 pm) vs C=N (127 pm)^[25] bond lengths, the stacking distance (c parameter) is also influenced by both enhanced steric repulsion of the benzylic (CH₂) protons of adjacent layers and higher flexibility of the secondary amine bond in rPI-3-COF. Notably, sorption isotherms reveal the complete retention of porosity and pore-size distributions (Figure S 9.1-54, Figure S 9.1-64) of the materials with Brunauer–Emmett–Teller (BET) surface areas of 1395 m²g⁻¹ for rPI-3-COF (Figure S 9.1-74) and 1404 m²g⁻¹ for PI-3-COF (Figure S 9.1-71), even exceeding those previously published for PI-3-COF (~ 1000 m²g⁻¹).^[23] It must be noted, however, that the porosity of rPI-3-COF is strongly influenced by the drying procedure: Simple vacuum-drying from dichloromethane resulted in a reduced BET surface area of 966 m²g⁻¹ (Figure S 9.1-77), while solvent exchange to methanol (Soxhlet extractor) and subsequent activation with supercritical CO₂ (scCO₂) gave the best results for rPI-3-COF with 1395 m²g⁻¹ (Figure S 9.1-69, Figure S 9.1-74). While this effect was not observed for the rigid imine PI-3 framework, an increased flexibility in rPI-3-COF and a modulated pore-wall polarity upon reduction are expected to enhance solvent interactions and capillary effects, potentially intensifying drying-induced disorder and pore collapse.^[26,27] Scanning electron microscopy (SEM) and transmission electron microscopy (TEM) images reveal intergrown, coral-shaped particle morphologies with sizes between 600 to 1000 nm, decorated with 200 nm long and 60 nm wide stings, for both imine-linked and reduced PI-3-COF (Figure S 9.1-82, Figure S 9.1-85). The similarity of the morphology before and after reduction renders intermediate recrystallization processes unlikely to be at play. TEM images show uniformly distributed crystallinity and extended porous channels of hexagonal symmetry in the materials, which are consistent with the structural model derived from XRPD data and Rietveld refinement (Figure S 9.1-91, Figure S 9.1-96).

To demonstrate the general applicability of this protocol, we applied it to two additional imine COFs with larger pores, different linker compositions, and pore geometry. Both TTI-COF and Py1P-COF were successfully reduced to their new amine-linked derivatives rTTI-COF and rPy1P-COF with high crystallinity as evident from sharp reflections at $2\theta = 4.0^\circ$ (100), 6.9° (110), 8.1° (200), and 25.6° (stacking) for rTTI and $2\theta = 3.7^\circ$ (110), 5.4° (020), 7.5° (220), 8.5° (130), 11.3° (330), and 23.2° (stacking) for rPy1P-COF, respectively. During our screenings to find the optimum reduction conditions for rPy1P-COF, we noticed palladium contamination in both the building blocks and the framework, introduced by palladium-based cross-coupling reactions during linker synthesis. The TEM images of an initial sample of Py1P-COF (Pd contaminated) show unevenly distributed palladium nanoparticles in the material (Figure S 9.1-94, Figure S 9.1-95).^[28] While this contaminant did

not affect the crystallization step of Py1P-COF, the metal particles “overcatalyzed” the reduction with formic acid, causing a partial digestion of the framework. To avoid this contamination, the 4,4',4'',4'''-(pyrene-1,3,6,8-tetrayl)tetraaniline linker was further purified on a metal scavenger (Biotage Isolute Si-TMT). A purified imine-linked Py1P-COF was then crystallized and reduced with formic acid to form rPy1P-COF without any noticeable decomposition. The SEM and TEM images of rTTI and rPy1P-COF thus show full retention of the porous, crystalline features of their parent frameworks (Figure S 9.1-84, Figure S 9.1-89, Figure S 9.1-93, Figure S 9.1-100).

Similar to the rPI-3-COF model system, new N–H vibrations at 3407 (rTTI) or 3398 cm^{-1} (rPy1P) in the FT-IR spectra and secondary amine nitrogen signals at -314.9 (rTTI) and -317.6 ppm (rPy1P) in the ^{15}N -ssNMR spectra prove the conversion into amine-linked frameworks (Figure S 9.1-3, Figure S 9.1-4, Figure S 9.1-35, Figure S 9.1-38). Although both samples show good porosity ($1419 \text{ m}^2\text{g}^{-1}$ rTTI, $1042 \text{ m}^2\text{g}^{-1}$ rPy1P), the BET surface area of rPy1P is reduced, compared to $1883 \text{ m}^2\text{g}^{-1}$ in Py1P-COF (Figure S 9.1-72, Figure S 9.1-73, Figure S 9.1-75, Figure S 9.1-76). By comparing linker geometries in small-pore hexagonal rPI-3, large-pore hexagonal rTTI, and square-net rPy1P-COF, those frameworks consisting of more rigid tritopic + tritopic [3 + 3] linker combinations (rPI-3 and rTTI-COF) show full retention of the BET surface area, while the tetratopic + bitopic [4 + 2] linker combination in rPy1P-COF was obtained with a slightly reduced surface area. This is in line with the expected additional flexibility around the molecular axis of the bitopic terephthalaldehyde linker, which facilitates local distortions in the network, causing reduced accessibility of the pores and thus a smaller surface area in rPy1P-COF.

Upon reduction, the in-plane cell parameters of larger-pore square-net rPy1P-COF were barely influenced, with C–N bond lengths contributing only a small percentage to the overall pore-to-pore distance. On the contrary, the increased stacking distance caused an expansion of the unit cell from $c = 3.818(4) \text{ \AA}$ to $c = 4.069(9) \text{ \AA}$, similar to the small-pore rPI-3-COF. At first sight, these trends cannot be found for the rTTI framework in direct comparison to TTI-COF. Apparent symmetry^[29] changes (peak splitting) in the XRPD pattern, however, show that upon reduction the stacking behavior of TTI-COF changes from antiparallel slip-stacked TTI ($P1$) to more eclipsed-like stacking in rTTI with an average crystallographic symmetry of $P6_3/m$ (Figure S 9.1-9, Figure S 9.1-13, Table S 9.1-1, Table S 9.1-2). Similar symmetry correlations have been described for the TTI-COF system by Haase et al. in comparison to its randomly stacked TTI (rsTTI) framework, resulting in both in-plane and interlayer contractions.^[29, 30] This trend is also observed with rTTI-COF: The increase in symmetry is accompanied by a pore contraction ($a = 25.786(12) \text{ \AA}$ (TTI) vs $a = 25.147(9) \text{ \AA}$ (rTTI)), caused by changed bond angles of antiparallel amine bonds, resulting in overall reduced intralayer cell parameters for rTTI. Furthermore, enhanced interlayer interactions in the eclipsed-stacked rTTI-COF compensate repulsive steric effects of benzylic protons, and thus, stacking distances decrease from $3.578(9) \text{ \AA}$ in TTI to $3.504(2) \text{ \AA}$ in the reduced framework (Table S 9.1-1, Table S 9.1-2).

4.2.3 One-Pot Procedure: Reductive Crystallization

When comparing the conditions needed for the synthesis of the imine framework and the following reduction, acids and the same solvent mixture are used in both cases and only the amount and type of acid changes. Thus, we expected that formic acid could act as a catalyst for both the formation and reduction of the framework, condensing the individual steps into a single one-pot crystallization-reduction approach.

Indeed, with 21 equiv of formic acid in a 2:1 mixture of mesitylene/1,4-dioxane at 120 °C for 72 h, a crystalline sample of rPI3-COF was obtained directly from its corresponding aldehyde and amine building blocks (Figure S 9.1-15). Compared to its two-step analogue, it was obtained in a different, spherical morphology (Figure S 9.1-87). As visible from broadened signals in the ¹³C ssNMR and FT-IR spectra (Figure S 9.1-7, Figure S 9.1-49), this sample is structurally less well-defined with a major impact on the resulting porosity (BET area of 174 m²g⁻¹, Figure S 9.1-79), which may also be reduced by trapped oligomers in the pores of the framework, besides structural defects. During our studies, we noticed a significant impact of the reaction temperature on the obtained product. While formic acid catalyzes the imine condensation both at high (120 °C) and already at low (60 °C) temperatures, the subsequent reduction is fast only at an elevated temperature (Figure S 9.1-16). As such, the one-pot protocol can be used to *thermally* switch between the reversible synthesis of an imine-linked COF at a low temperature or the irreversible “locking” of the framework structure by simultaneous reduction to the amine-linked COF using otherwise identical reaction conditions. We expect this unique property to be key for the adaptation to other covalent organic frameworks. Besides this “thermo-switchability”, it highlights formic acid as a versatile yet underexplored catalyst for the synthesis of imine-linked COFs at a reduced temperature.

4.2.4 Reductive Formylation: Combined Reduction and Protection

Solid ammonium formate as a green, less toxic, and less corrosive alternative to formic acid was also effective for the reduction of imine bonds under solvent-free conditions. Reacting a salt-melt of ammonium formate and PI-3-COF for 3 h at 170 °C in a closed vessel afforded a product with broadened secondary amine vibrations at $\nu_{\text{N}-\text{H}} = 3370 \text{ cm}^{-1}$ and carbonyl stretching modes at $\nu_{\text{C}=\text{O}} = 1669 \text{ cm}^{-1}$ in the FT-IR spectrum (Figure S 9.1-6). An additional signal at 162.8 ppm in the ¹³C ssNMR spectrum, referring to an N-formyl-carbon (Figure S 9.1-43, Figure S 9.1-46), shows that, besides the reduction, a subsequent N-formylation resulted in a partially formylated, reduced PI-3 framework (pfrPI-3-COF). A comparison of FT-IR and ssNMR spectra excludes a degradation of the chemical connectivity. The XRPD pattern shows a substantial reduction in the long-range order reminiscent of an amorphous solid, although a small feature corresponding to the 100 peak further suggests that the intralayer connectivity is maintained (Figure S 9.1-17). When reacting pfrPI-3-COF with 2,3-dichloro-5,6-dicyano-1,4-benzoquinone (DDQ) in dichloromethane, the secondary

amine linkages are oxidized back to the imine linkages, affording reoxidized, partially formylated reduced PI-3-COF (opfrPI-3-COF).^[15] Remarkably, after this treatment, sharp signals in the XRPD pattern similar to the parent PI-3 framework become visible (Figure S 9.1-11, Figure S 9.1-17). The feasibility of this amorphous-to-crystalline conversion suggests a significant topological and structural similarity of the reduced, amorphous COF to the crystalline compound and led us to further investigate the correlations between the crystalline and non-crystalline amine-linked frameworks.

4.2.5 Crystalline vs. Disordered

During our screenings to find optimal reduction conditions for the imine-linked frameworks, we noticed that a large excess of formic acid can decrease the crystallinity of the product, suggesting a profound role of protonation on the layer structure. Using 59.5 equiv. of formic acid with PI-3-COF under the same conditions as above leads to a practically X-ray amorphous structure with slightly broadened but otherwise essentially identical signals as rPI-3-COF in the FT-IR and ssNMR spectra (Figure S 9.1-5, Figure S 9.1-48). SEM and TEM did not show any morphological changes of the particles (Figure S 9.1-86, Figure S 9.1-97). Stability tests of rPI-3-COF, e.g., under acidic conditions, show similar effects on the reflections in the XRPD patterns. In contrast to the imine-linked PI-3-COF, the amine-linked rPI-3-COF does not show any hydrolytic decomposition, though sharp reflections in the XRPD pattern broaden or disappear completely upon treatment with excess acid—illustrating local structural changes and distortion of the stacked 2D layers (Figure S 9.1-101, Figure S 9.1-102).

To elucidate conformational changes in the structure of PI-3-COF upon reduction, quantum-chemical calculations on the PBE0-D3/def2-TZVP level of theory were performed to obtain optimized structures for model compounds.^[31-34] The surface plot for combined rotations around dihedral angles U and Z in molecular models PI-3 M and rPI-3 M (Figure S 9.1-103, Figure S 9.1-104, Figure S 9.1-105) shows an increased flexibility for the amine-linked molecular model, apparent from a broad range of low energy conformations (Figure 4-2a-c). Optimized single-pore models PI-3 SP and rPI-3 SP (Figure S 9.1-106, Figure S 9.1-107) depict discrete points on the surface close to the lowest energy conformations of their molecular models with dihedral angles (U) of 27.4° (PI-3 SP) and 6.46° (rPI-3 SP). Although interlayer steric repulsion in the amine framework is increased due to additional benzylic protons (C-10, Figure 4-1c) that align perpendicular to the 2D surface, reduced 1,4-repulsion between protons at C-9 and C-10 causes a flattening of the dihedral angle U, albeit combined with increased flexibility of the structure. These results corroborate the cell parameter changes upon reduction as observed by Rietveld analysis of the crystalline rPI-3-COF. To elucidate possible amorphization pathways, resulting in a disordered structure of rPI-3 if synthesized with an excess of formic acid, additional protonation must be considered. When protonated at the amine nitrogen, the dihedral angle U undergoes a significant widening to 86.6° in the molecular model H+rPI-3 M (Figure S

9.1-105)—a rotation associated with an energy barrier of approximately 50 kJ/mol in the molecular model rPI-3 M (without protonation). Considering conformational restrictions in the layer geometry of the rPI-3-COF, less pronounced but still substantial conformational changes, combined with interlayer charge repulsion, are expected, leading to a significant disruption of the periodicity of the stacked layers as a function of the pH. This effect is further supported by a vast signal broadening at 119 ppm (C-7) in the ^{13}C ssNMR spectrum with increasing disorder in rPI-3-COF (Figure S 9.1-48), whereas in the actual, well-ordered rPI-3-COF structure, a narrow statistical distribution of dihedral angles indicates a preferred conformation and thus a fairly sharp signal for this carbon (C-7). A protonation-dependent broad distribution in the disordered rPI-3-COF causes this signal to broaden and, ultimately, to vanish, however without disrupting the overall connectivity of the layer.

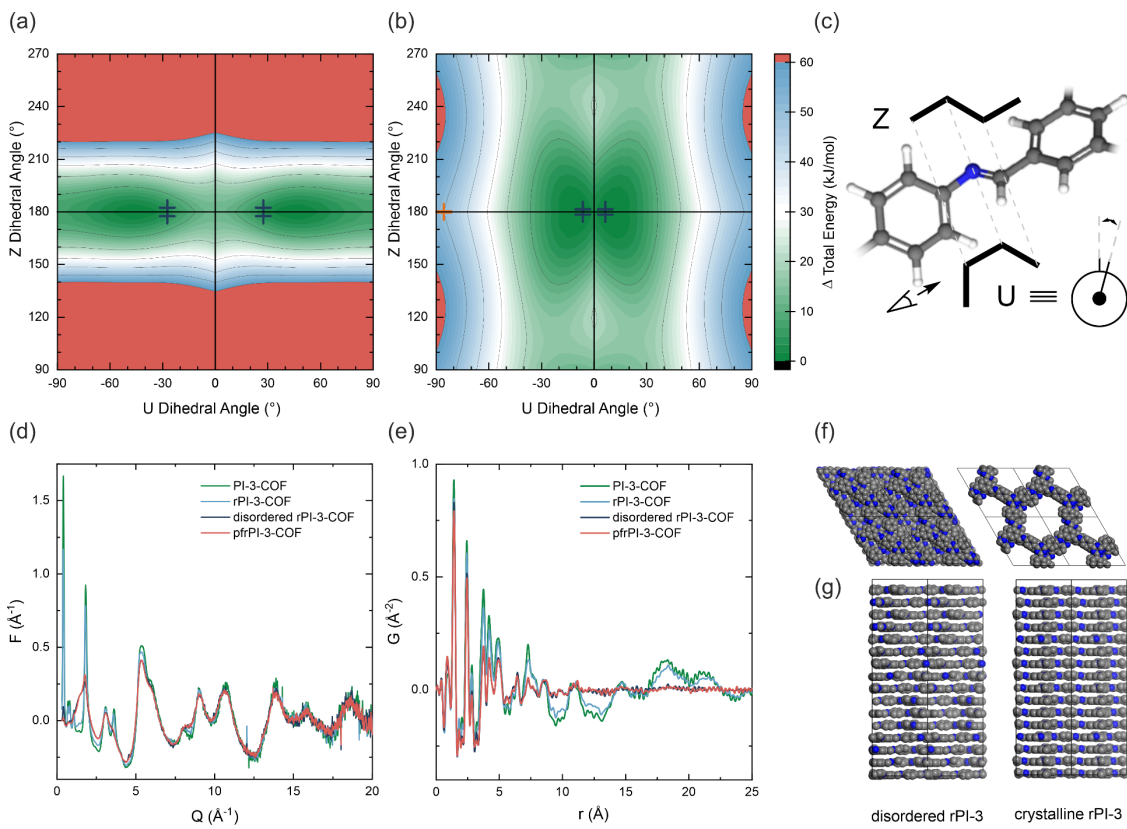


Figure 4-2 (a) Energy surface plot for different values of dihedral angles U and Z in the molecular model PI-3 M. The blue crosses highlight the lowest energy conformation for the single-pore model PI-3 SP. (b) Energy surface plot for the molecular model rPI-3 M. The blue crosses highlight the lowest energy conformation for the single-pore model rPI-3 SP. As a comparison, the conformation of a protonated molecular model H+rPI-3 M is shown on the surface (red cross). Notably, in this simple molecular model, the effect of the anion and charge repulsion, occurring in the layered real structure, are neglected. (c) Dihedral angles U and Z shown in a section of PI-3 M. (d) Reduced total scattering patterns and (e) pair distribution functions for crystalline and disordered materials are overlaid. (f and g) Sixteen-layer structure models derived from PDF analysis for disordered rPI-3-COF (left) and rPI-3-COF (right) considering random translational disorder in 1–10 directions are shown.

To determine the local and intermediate length-scale structure modifications due to conformation-induced disordering, we performed pair distribution function (PDF) analysis on X-ray total scattering synchrotron data. Notably, a high similarity in the reduced total scattering patterns (Figure 4-2d) from $\sim 5\text{--}20 \text{ \AA}^{-1}$ and peak positions up to approximately 7 \AA in the PDFs of all samples evidence intact, imine or amine bonded layer connectivity in the disordered state. The PDFs of PI-3-COF and rPI-3-COF (Figure 4-2e) show distinct medium- and long-range ordered structuring, consisting of two primary oscillations due to the ordering of the stacked layers (higher frequency) and porous channels (lower frequency). The structural correlations are more strongly damped for disordered rPI-3-COF and pfrPI-3-COF, becoming relatively flat around 12 \AA . This indicates that the spatial relationships of atoms in stacked layers and across porous channels are largely reduced, although, as seen in the diffraction patterns, there are still weakly correlated motifs over at least a few layers or pore distances (Figure 4-2e). Distinct differences could be visualized between crystalline and disordered structures by the refinement of a 16-layer structure model to the PDFs for rPI-3-COF and disordered rPI-3-COF PDFs, with random translations allowed in a single direction (Figure 4-2f,g). For the disordered sample, much larger translations were required to damp out the interlayer and ordered pore channel structure signals. It must be noted that these models may overpredict layer translations due to undersampling the number of layers. Furthermore, the interlayer correlations could also be damped by larger and random torsions of the amine or phenyl moieties, as shown in quantum-chemical single-pore models. Average stacking offsets were estimated by refining models to the PDFs in the range of neighboring layers, i.e., $r < 6 \text{ \AA}$, using PDFgui.^[29, 35] The values obtained are 1.0 (PI-3-COF), 1.2 (rPI-3-COF), 3.3 (disordered rPI-3-COF), and 3.3 \AA (pfrPI-3-COF). As visible from the disordered model, random layer translations drastically reduce the pore accessibility and thus help to explain reduced BET surface areas for the disordered models.

4.2.6 Hybrid Materials and Functionalization

Besides frameworks containing only amine or imine linkages, hybrid materials with varying imine/amine linkage content can also be obtained with our method by adjusting reaction time and the amount of formic acid (Figure 4-3a and Figure S 9.1-1). As an example, partially reduced Py1P-COF (prPy1P-COF) was synthesized, showing distinct signals at 149.0 (imine) and 146.4 ppm (amine) in the ^{13}C ssNMR spectrum for the aromatic carbon next to the nitrogen (approximately 42% amine sites, Figure S 9.1-40). Another example, already introduced, is partially formylated reduced PI-3-COF (pfrPI-3-COF) obtained from PI-3-COF via salt-melt reduction with ammonium formate. The presence of *N*-formyl groups opens up further avenues for additional framework functionalization. For instance, partially functionalized frameworks may be generated by reacting the partially formylated framework with an electrophile, since formyl groups act as a protecting group for secondary amine sites. Partial functionalization can avoid reduced pore accessibility and diffusion

limitations, which is critical, for example, in catalysis.^[36] In a more complex case, bifunctionalized frameworks may be synthesized in a subsequent step, after exposing previously protected amine sites. The deprotection of *N*-formyl groups in pfrPI-3-COF was achieved under acidic conditions (aqueous 1 M HCl, 120 °C, 20 min), affording rPI-3-COF as evident from a vanishing formyl signal at 162.8 ppm in the ¹³C ssNMR spectrum (Figure S 9.1-46), while acid chlorides or isocyanates have proven as strong and effective electrophiles to derivatize secondary amines in rTTI-COF (Figure 4-3b, c).

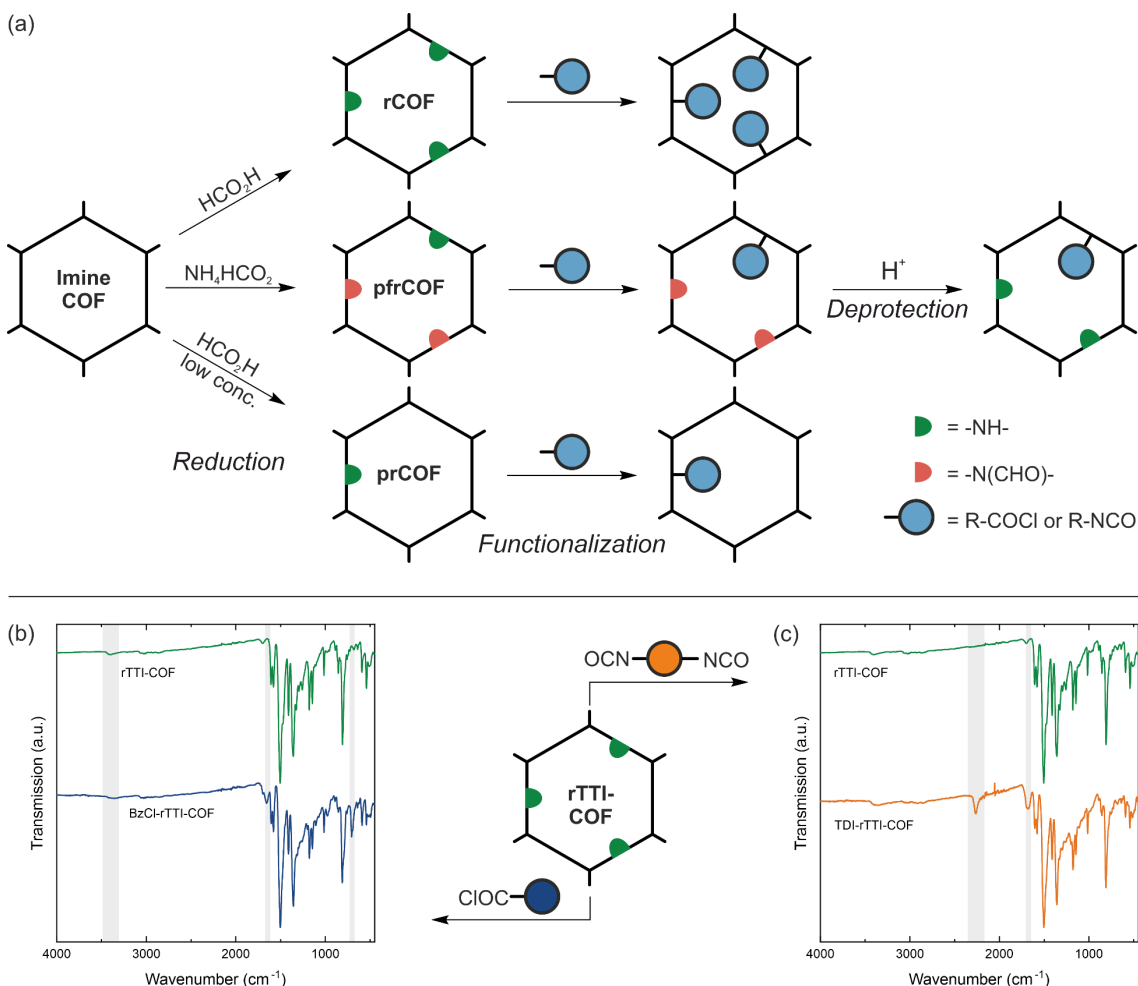


Figure 4-3 (a) Reaction sequence for post-synthetic functionalization of amine-linked covalent organic frameworks. Frameworks entirely connected by secondary amine linkages (rCOF) or hybrid materials with mixed amine/imine bonds (prCOF) and partially formylated amine-linkages (pfrCOF) are accessible in a single step from imine COFs. As experimentally shown with pfrPI-3-COF (middle), *N*-formyl groups in pfrCOFs can be deprotected under acidic conditions. Released secondary amine linkages may allow two-step functionalization to afford bifunctionalized frameworks. The amine/*N*-formyl amine ratio is arbitrary. (b and c) FT-IR spectra of rTTI-COF samples functionalized with (b) benzoyl chloride (BzCl) and (c) toluenediisocyanate (TDI) are shown and compared to rTTI-COF. Gray areas in (b) highlight reduced N—H, emerging C=O, and characteristic C=C vibrations in BzCl-rTTI-COF. For TDI-rTTI-COF, vibrations of dangling -NCO and emerging C=O vibrations are highlighted (gray).

4.3 Conclusion

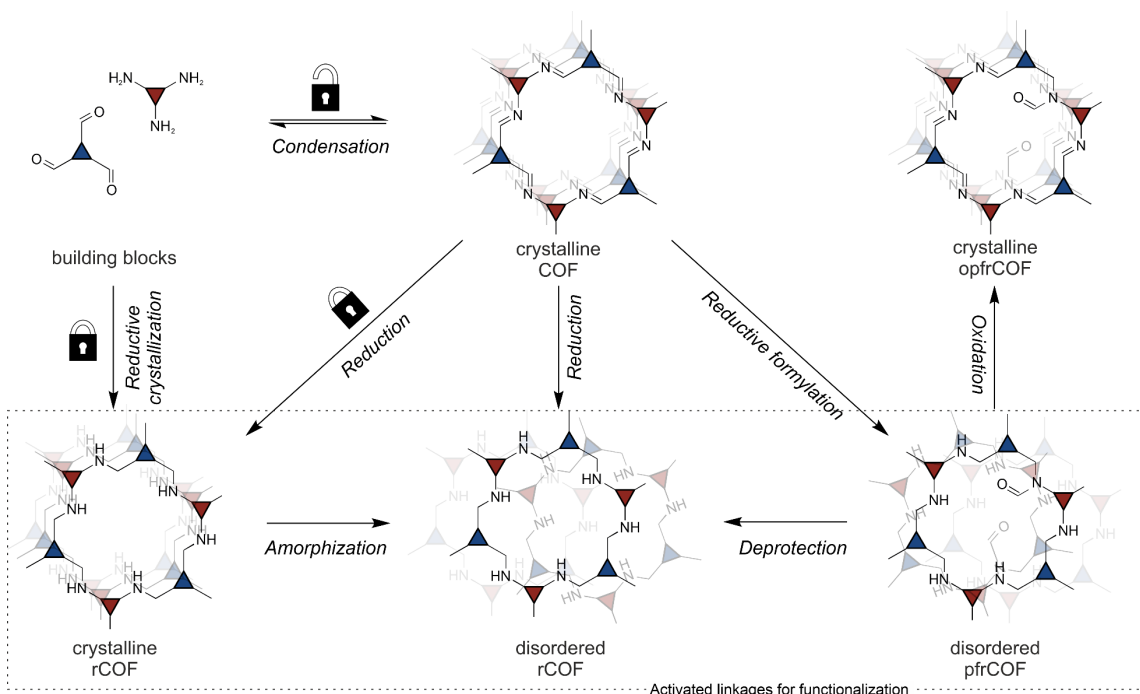


Figure 4-4 Pathways leading to a set of amine-linked covalent organic frameworks as demonstrated with the PI-3 COF system.

In summary, amine-linked frameworks were introduced as a hydrolytically stable and tailorabile system for further post-synthetic modification, which can be accessed from imine-linked frameworks or directly from their corresponding amine and aldehyde building blocks (Figure 4-4). In contrast to many earlier locking strategies, generating amide-, benzoxazole-, or benzothiazole-linked frameworks, our approach locks and simultaneously activates the connectivity of the framework for further functionalization.^[5, 7, 11, 37] The introduced reduction methods using either formic acid or ammonium formate give access to a range of fully amine-linked or intermediate amine-/imine-linked crystalline frameworks with large surface areas or topologically identical, disordered analogues with reduced pore-accessibility. Importantly, the degree of amine functionalization can be rationally controlled by adjusting the amount of acid and the reaction time. For the first time, we demonstrate amine-linked frameworks as a modular platform enabling the facile interconversion of chemically and structurally distinct frameworks, including reduction–reoxidation cycles and crystalline-to-disordered and disordered-to-crystalline conversions. Finally, we show that the obtained amine linkages readily react with electrophiles such as acid chlorides and isocyanates, opening new avenues to the facile post-synthetic functionalization of COFs at the linkage site with a built-in protection–deprotection strategy and without the need for additional building block engineering. In essence, the demonstrated methods enable hitherto undiscovered functionalization strategies that are widely applicable to all imine-linked covalent organic frameworks, the largest family of COFs to date.

4.4 Acknowledgements

The authors would like to thank Sebastian Emmerling for performing sorption measurements. M.W.T. gratefully acknowledges support from BASF. Financial support by an ERC Starting Grant (project COF Leaf, Grant No. 639233), the Deutsche Forschungsgemeinschaft (DFG, Project-ID 358283783 - SFB 1333), the Max Planck Society, the Cluster of Excellence e-conversion (Grant No. EXC2089), and the Center for Nanoscience (CeNS) is gratefully acknowledged. The authors acknowledge DESY (Hamburg, Germany), a member of the Helmholtz Association HGF, for the provision of experimental facilities. Parts of this research were carried out at beamline P02.1.

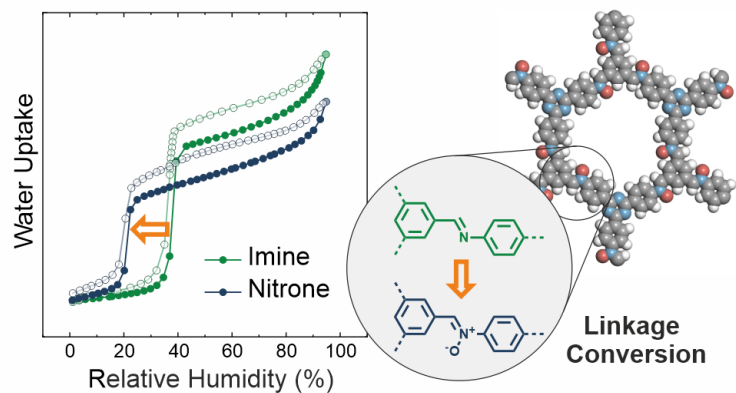
4.5 Bibliography

1. Cote A. P. et al. Porous, Crystalline, Covalent Organic Frameworks. *Science* **310**, 1166-1170 (2005).
2. Lohse M. S., Bein T. Covalent Organic Frameworks: Structures, Synthesis, and Applications. *Adv. Funct. Mater.* **28** (2018).
3. Song Y., Sun Q., Aguila B., Ma S. Opportunities of Covalent Organic Frameworks for Advanced Applications. *Adv. Sci.* **6**, 1801410 (2019).
4. Geng K. et al. Covalent Organic Frameworks: Design, Synthesis, and Functions. *Chem. Rev.* **120**, 8814-8933 (2020).
5. Haase F. et al. Topochemical Conversion of an Imine- into a Thiazole-Linked Covalent Organic Framework Enabling Real Structure Analysis. *Nat. Commun.* **9**, 2600 (2018).
6. Wang K. et al. Synthesis of Stable Thiazole-Linked Covalent Organic Frameworks Via a Multicomponent Reaction. *J. Am. Chem. Soc.* **142**, 11131-11138 (2020).
7. Waller P. J. et al. Chemical Conversion of Linkages in Covalent Organic Frameworks. *J. Am. Chem. Soc.* **138**, 15519-15522 (2016).
8. Li X. et al. Facile Transformation of Imine Covalent Organic Frameworks into Ultrastable Crystalline Porous Aromatic Frameworks. *Nat. Commun.* **9**, 2998 (2018).
9. Segura J. L., Royuela S., Mar Ramos M. Post-Synthetic Modification of Covalent Organic Frameworks. *Chem. Soc. Rev.* **48**, 3903-3945 (2019).
10. Ding H., Mal A., Wang C. Tailored Covalent Organic Frameworks by Post-Synthetic Modification. *Mater. Chem. Front.* **4**, 113-127 (2020).
11. Yan Q. et al. Post-Synthetic Modification of Imine Linkages of a Covalent Organic Framework for Its Catalysis Application. *RSC Adv.* **10**, 17396-17403 (2020).
12. Li X. T. et al. Construction of Covalent Organic Frameworks Via Three-Component One-Pot Strecker and Povarov Reactions. *J. Am. Chem. Soc.* **142**, 6521-6526 (2020).
13. Li C. et al. Asymmetric Photocatalysis over Robust Covalent Organic Frameworks with Tetrahydroquinoline Linkage. *Chinese J. Catal.* **41**, 1288-1297 (2020).
14. Lohse M. S. et al. Sequential Pore Wall Modification in a Covalent Organic Framework for Application in Lactic Acid Adsorption. *Chem. Mater.* **28**, 626-631 (2016).

15. Lyle S. J. et al. Multistep Solid-State Organic Synthesis of Carbamate-Linked Covalent Organic Frameworks. *J. Am. Chem. Soc.* **141**, 11253-11258 (2019).
16. Leuckart R. Ueber Eine Neue Bildungsweise Von Tribenzylamin. *Ber. Dtsch. Chem. Ges.* **18**, 2341-2344 (1885).
17. Wallach O. Zur Kenntniss Der Terpene Und Der Ätherischen Öle; Zweiundzwanzigste Abhandlung. I. Über Die Bestandtheile Des Tujaöls. *Liebigs Ann. Chem.* **272**, 99-122 (1893).
18. Billman J. H., Diesing A. C. Reduction of Schiff Bases with Sodium Borohydride. *J. Org. Chem.* **22**, 1068-1070 (1957).
19. Francesconi O. et al. A Self-Assembled Pyrrolic Cage Receptor Specifically Recognizes Beta-Glucopyranosides. *Angew. Chem. Int. Ed.* **45**, 6693-6696 (2006).
20. Liu M. et al. Acid- and Base-Stable Porous Organic Cages: Shape Persistence and Ph Stability Via Post-Synthetic "Tying" of a Flexible Amine Cage. *J. Am. Chem. Soc.* **136**, 7583-7586 (2014).
21. Liu H. et al. Covalent Organic Frameworks Linked by Amine Bonding for Concerted Electrochemical Reduction of Co₂. *Chem* **4**, 1696-1709 (2018).
22. Boechat N. et al. A Simple Reduction of Methyl Aromatic Esters to Alcohols Using Sodium Borohydride–Methanol System. *Tetrahedron Lett.* **45**, 6021-6022 (2004).
23. Bai L. et al. Nanoscale Covalent Organic Frameworks as Smart Carriers for Drug Delivery. *Chem. Commun.* **52**, 4128-4131 (2016).
24. Rietveld H. M. A Profile Refinement Method for Nuclear and Magnetic Structures. *J. Appl. Crystallogr.* **2**, 65-71 (1969).
25. Breitmaier E., Jung G. *Organische Chemie: Grundlagen, Stoffklassen, Reaktionen, Konzepte, Molekülstrukturen*, (Thieme, Stuttgart, 2005).
26. Sick T. et al. Switching on and Off Interlayer Correlations and Porosity in 2d Covalent Organic Frameworks. *J. Am. Chem. Soc.* **141**, 12570-12581 (2019).
27. Feriante C. H. et al. Rapid Synthesis of High Surface Area Imine-Linked 2d Covalent Organic Frameworks by Avoiding Pore Collapse During Isolation. *Adv. Mater.* **32**, e1905776 (2020).
28. Romero-Muñiz I. et al. Unveiling the Local Structure of Palladium Loaded into Imine-Linked Layered Covalent Organic Frameworks for Cross-Coupling Catalysis. *Angew. Chem.* **132**, 13113-13120 (2020).
29. Pütz A. M. et al. Total Scattering Reveals the Hidden Stacking Disorder in a 2d Covalent Organic Framework. *Chem. Sci.* **11**, 12647-12654 (2020).
30. Haase F. et al. Tuning the Stacking Behaviour of a 2d Covalent Organic Framework through Non-Covalent Interactions. *Mater. Chem. Front.* **1**, 1354-1361 (2017).
31. Schäfer A., Huber C., Ahlrichs R. Fully Optimized Contracted Gaussian Basis Sets of Triple Zeta Valence Quality for Atoms Li to Kr. *J. Chem. Phys.* **100**, 5829-5835 (1994).
32. Adamo C., Barone V. Toward Reliable Density Functional Methods without Adjustable Parameters: The Pbe0 Model. *J. Chem. Phys.* **110**, 6158-6170 (1999).
33. Ernzerhof M., Scuseria G. E. Assessment of the Perdew–Burke–Ernzerhof Exchange-Correlation Functional. *J. Chem. Phys.* **110**, 5029-5036 (1999).

34. Grimme S., Antony J., Ehrlich S., Krieg H. A Consistent and Accurate Ab Initio Parametrization of Density Functional Dispersion Correction (Dft-D) for the 94 Elements H-Pu. *J. Chem. Phys.* **132**, 154104 (2010).
35. Farrow C. L. et al. Pdffit2 and Pdfgui: Computer Programs for Studying Nanostructure in Crystals. *J. Phys.: Condens. Matter* **19**, 335219 (2007).
36. Sun Q. et al. Pore Environment Control and Enhanced Performance of Enzymes Infiltrated in Covalent Organic Frameworks. *J. Am. Chem. Soc.* **140**, 984-992 (2018).
37. Wei P. F. et al. Benzoxazole-Linked Ultrastable Covalent Organic Frameworks for Photocatalysis. *J. Am. Chem. Soc.* **140**, 4623-4631 (2018).

5 Post-Synthetic Transformation of Imine- into Nitrone-linked COFs for Water Harvesting



The presented work of this chapter was published, adapted and reproduced from:

Postsynthetic Transformation of Imine- into Nitrone-linked Covalent Organic Frameworks for Atmospheric Water Harvesting at Decreased Humidity

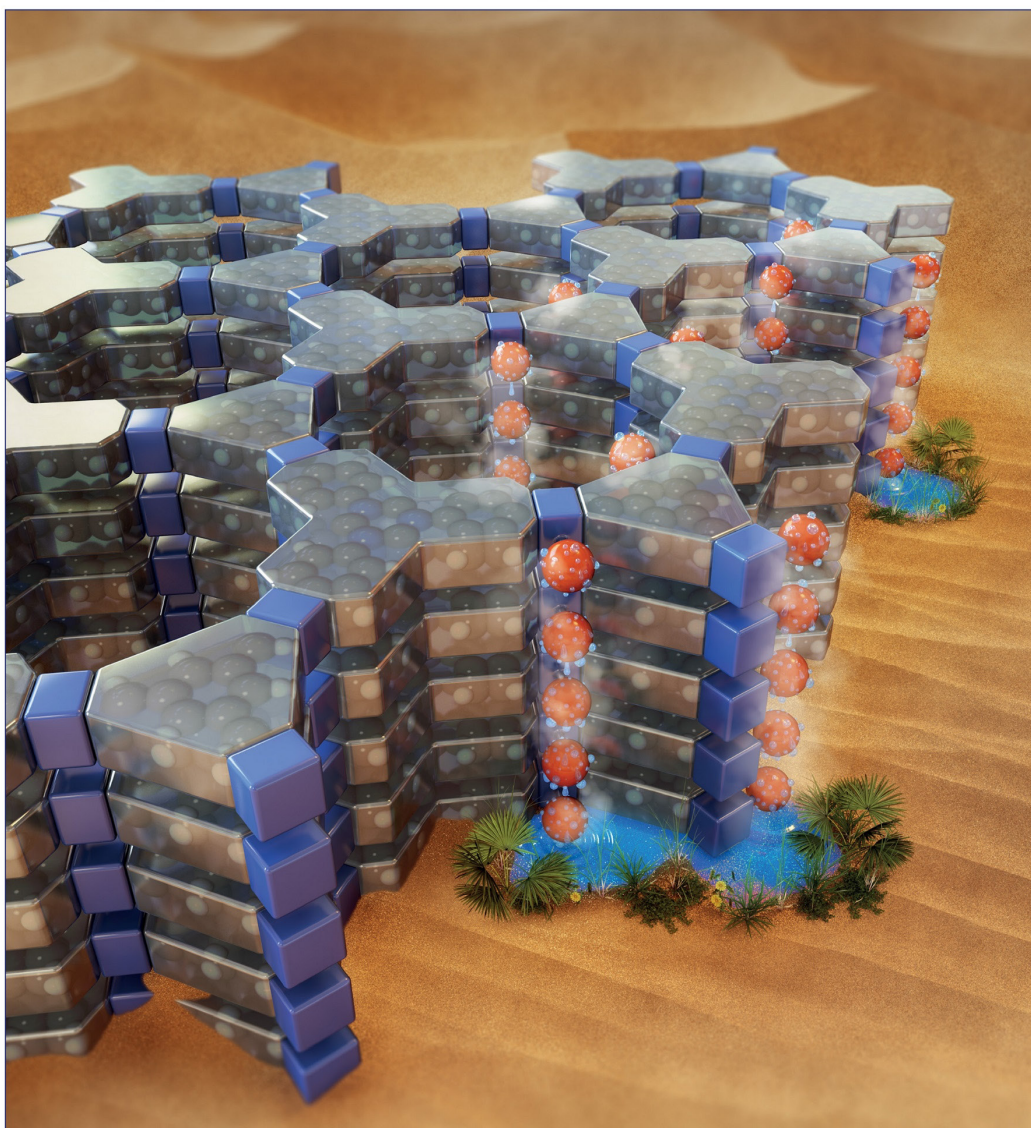
Lars Grunenberg, Gökçen Savascı, Sebastian T. Emmerling, Fabian Heck, Sebastian Bette, Afonso Cima Bergesch, Christian Ochsenfeld and Bettina V. Lotsch, *J. Am. Chem. Soc.* **2023**, *145*, 13241–13248. doi: 10.1021/jacs.3c02572

L.G. conceived the idea, performed and interpreted experiments, led the project and wrote the manuscript. G.S. performed quantum-chemical calculations. S.T.E. and F.H. performed gas and vapor sorption experiments. S.B. performed and analyzed *in-situ* XRPD experiments. A.C.G supported material synthesis at an initial stage. B.V.L. and C.O. supervised the research.

June 21, 2023
Volume 145
Number 24
pubs.acs.org/JACS

J|A|C|S

JOURNAL OF THE AMERICAN CHEMICAL SOCIETY



 **ACS Publications**
Most Trusted. Most Cited. Most Read.

www.acs.org

Supplementary Cover Image designed by Vera Hiendl (e-conversion).

Abstract: Herein, we report a facile post-synthetic linkage conversion method giving synthetic access to nitrone-linked covalent organic frameworks from imine- and amine-linked COFs. The new, 2D nitrone-linked covalent organic frameworks, NO-PI-3-COF and NO-TTI-COF are obtained with high crystallinity and large surface areas. Nitrone-modified pore channels induce condensation of water vapor at 20% lower humidity compared to their amine- or imine-linked precursor COFs. Thus, the topochemical transformation to nitrone linkages constitutes an attractive approach to post-synthetically fine-tune water adsorption properties in framework materials.

5.1 Introduction

In recent years, covalent organic frameworks have received increasing attention as sorbents for water vapor from the atmosphere.^[1-7] Similar to already well-established materials such as metal-organic frameworks,^[8, 9] COFs offer ideal structural capabilities for this application, given their typically large specific surface areas and permanent porosity.^[10] The structural diversity of COF building blocks and linkages, coupled with their regular ordering in the crystalline material, also allow for almost infinite variation and optimization possibilities, and provide the basis for application-targeted engineering of these materials.^[11-14] Despite this adaptability of their structures, water capture in many evaluated COFs systems, especially in those with pore diameters larger than 1.5 nm, is typically characterized by high uptake pressures and large hysteresis, limiting their potential for application as water harvesting materials.^[15] This implies that the water uptake performance of many existing COFs often cannot compete with the best-in-class MOFs, although their variety in building blocks, and in particular linkage composition, and the fact that COFs are not based on potentially toxic, or cost-prohibitive metals, offer great potential.^[7] Thus, several approaches have been made to improve the sorption properties of COFs. For example, the change in hydrophilicity of the pore channel surface in two-dimensional (2D) COFs was investigated as a function of the chemical structure of COF building blocks, the linkers. Here, hydroxyl or nitro groups in the chemical structure of the linkers resulted in improved water uptake at lower relative pressures, as presented for small-pored materials with ketoamine linkages.^[6, 16] Likewise, an isoreticular series of hydroxy-functionalized azine-linked COFs showed a shift in the steep uptake region of the sorption isotherm to lower relative humidities.^[5] Uptake at low relative pressures (i.e., low humidity) is particularly desirable for water harvesting materials, and should ideally occur between 10% and 30% relative humidity.^[9] Besides functional surface groups on the pore channels, the framework topology and the pore-diameter were also shown to modulate water adsorption properties. Multivalent linker combinations affording microporous trigonal^[15] or voided square-lattice^[17] materials with small pore diameters support the condensation of water and thus exhibit attractive water sorption properties.

While these concepts are generally based on the modification of the chemical structure of the building blocks, which is always related to a bottom-up or *de novo* synthesis of new COFs,

post-synthetic strategies targeting the connectivity, (i.e., linkage) in existing frameworks have rarely been addressed as systematic approaches to improve water adsorption properties.^[7]

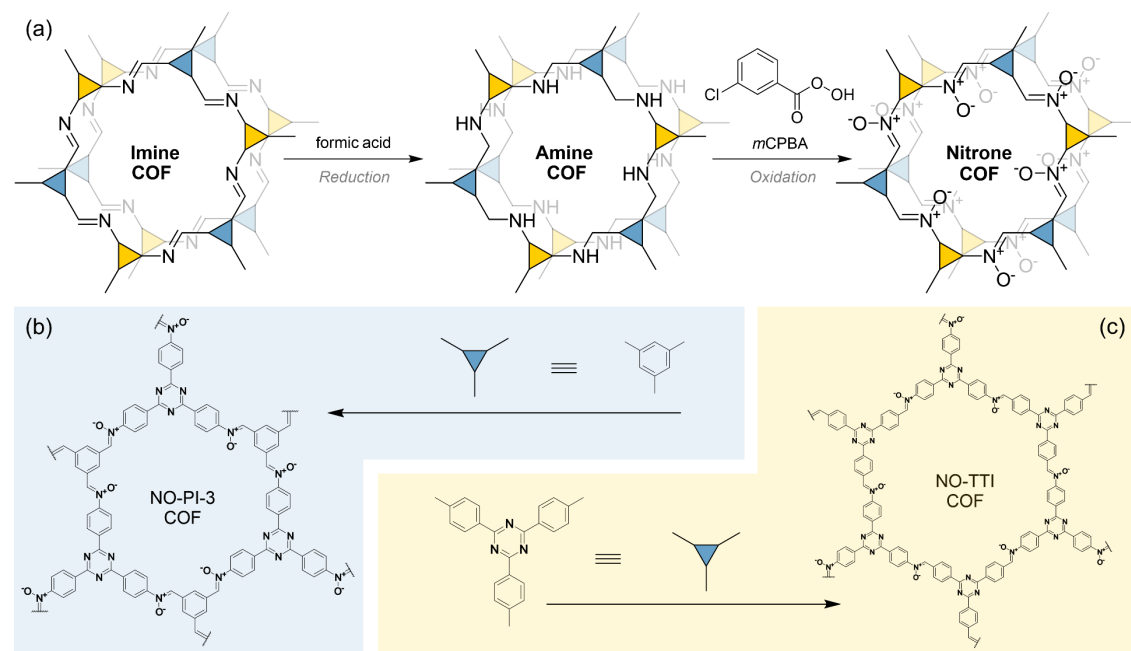


Figure 5-1: (a) Synthesis scheme for the post-synthetic transformation of imine- into nitrone-linked covalent organic frameworks. (b) Chemical structure of a single pore of (b) NO-PI-3-COF and (c) NO-TTI-COF.

Herein, we present a new post-synthetic linkage conversion protocol, applicable to imine- and amine-linked COFs, to obtain a novel class of nitrone-linked COFs with improved water adsorption capabilities at reduced humidity (Figure 5-1a). Compared to earlier reports, our method constitutes a selective top-down strategy to imprint desired properties into these frameworks through an atom-precise topochemical modification of their chemical structure. Our approach circumvents tedious optimization of crystallization conditions and costly material losses of precious building blocks, typically associated with *de novo* synthesis of COFs.

To demonstrate the generality of our post-synthetic oxidation method, we apply this novel approach to the synthesis of two hexagonal COFs with different pore diameters, namely NO-PI-3-COF (1.6 nm) and NO-TTI-COF (2.1 nm), from their imine-linked parent materials (Figure 5-1b, c). We characterize changes in the material by utilizing a comprehensive suite of analytical techniques including Fourier transform infrared (FT-IR) spectroscopy, ¹³C and ¹⁵N solid-state nuclear magnetic resonance spectroscopy (ssNMR), and X-ray powder diffraction (XRPD) and correlate the COFs' ability of adsorbing water vapor, assessed by water vapor sorption experiments, to the targeted modification of the linkage chemistry.

5.2 Results

5.2.1 Material Synthesis and Analysis

As a model system for our reaction sequence, we first synthesized the imine-linked PI-3-COF from 1,3,5-triformyl benzene (TFB) and 4,4',4''-(1,3,5-triazine-2,4,6-triyl)trianiline (TTA) under solvothermal conditions, according to our previously reported method (see details in the Supporting Information).^[18] In a following step, the imine-linked PI-3-COF was reduced to its amine-linked derivative rPI-3-COF using formic acid, following our recently developed protocol.^[18] In a second post-synthetic linkage conversion, we employed *m*-chloroperoxybenzoic acid (mCPBA) to oxidize secondary amine linkages in rPI-3-COF to nitrone linkages.

Upon reaction of rPI-3-COF with mCPBA, characteristic secondary amine vibrations at $\nu_{\text{N-H}} = 3405 \text{ cm}^{-1}$ in the Fourier transform infrared (FT-IR) spectrum disappeared, suggesting a conversion of the linkage in the material (Figure S 9.2-1). Concomitant changes of relative intensities in the finger-print region of the spectrum, among which a very weak vibration at $\nu_{\text{N-O}} = 1079 \text{ cm}^{-1}$, point at a successful oxidation to nitrone linkages.^[19] Notably, relative intensities of apparent vibrations in the spectrum of NO-PI-3-COF differ from those visible for the parent imine-linked PI-3-COF and exclude that secondary amines were simply re-oxidized to imines (Figure S 9.2-1).

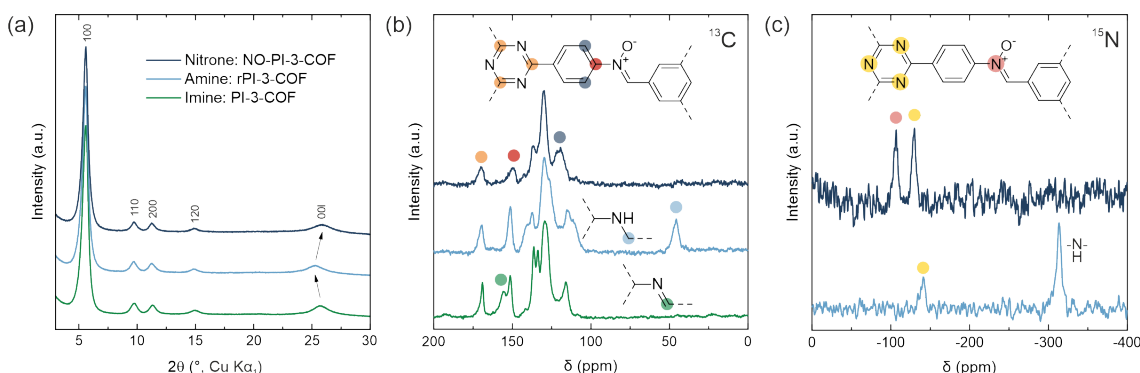


Figure 5-2: (a) XRPD pattern comparison of PI-3 (green), rPI-3 (blue) and NO-PI-3-COF (dark blue) obtained from multi-step linkage conversion. As indicated by arrows, the position of the stacking reflection shifts depending on the linkage type in the framework. (b) ^{13}C CP-MAS ssNMR spectra of these materials with characteristic signals highlighted by arrows. (c) ^{15}N CP-MAS ssNMR spectra of rPI-3 and NO-PI-3-COF.

The ^{13}C cross-polarization magic angle spinning (CP-MAS) solid-state NMR (ssNMR) spectrum of NO-PI-3-COF further corroborates this finding, lacking a characteristic imine carbon signal at $\delta = 155.3 \text{ ppm}$ (PI-3-COF) and signals for the benzylic CH_2 carbon of rPI-3-COF at $\delta = 45.4 \text{ ppm}$. The ^{15}N ssNMR spectrum of NO-PI-3-COF shows distinct signals at -106.3 ppm for the nitrone and at -129.4 ppm for the triazine nitrogen. The absence of the imine and amine nitrogens at -57.4 ppm (Figure S 9.2-17) and -313.3 ppm , respectively, suggest a quantitative oxidation of amine linkages to nitrones in NO-PI-3-COF.

Likewise, the data show that the oxidation treatment did not affect the nitrogen atoms of the triazine ring, and proves a selective oxidation of the linkages. The observed ssNMR chemical shifts are in line with values obtained by quantum-chemical calculations of representative molecular models (Figure S 9.2-47, Figure S 9.2-48, Figure S 9.2-49, Figure S 9.2-50, Figure S 9.2-51, Figure S 9.2-52).

A structural analysis of NO-PI-3-COF and its precursors via XRPD reveals high crystallinity, represented by four narrow reflections in the diffraction pattern of NO-PI-3-COF at $2\theta = 5.6^\circ, 9.7^\circ, 11.3^\circ$, and 14.9° , indexed as 100, 110, 200, and 120 reflections (space group $P\bar{6}$), and a broad stacking reflection 00 $\bar{1}$ at $2\theta = 25.8^\circ$ (Figure 5-2a). Compared to its parent imine and amine structures, both the apparent hexagonal symmetry and crystallinity are retained during the multi-step conversion, while a significant shift of the broad stacking reflection (00 $\bar{1}$) toward larger angles appears in NO-PI-3-COF at $2\theta = 25.8^\circ$. Notably, the individual steps of linkage modification can be traced by a characteristic shift of the broad stacking reflection. For the reduction from imine to amine linkages a shift towards lower angles, namely from $2\theta = 25.7^\circ$ to 25.2° , is visible.¹⁸ The following oxidation to the nitrone shifts this reflection in the reverse direction, to a higher angle of $2\theta = 25.8^\circ$, hinting at a contraction of the stacking distance in NO-PI-3-COF compared to the imine and amine derivative.

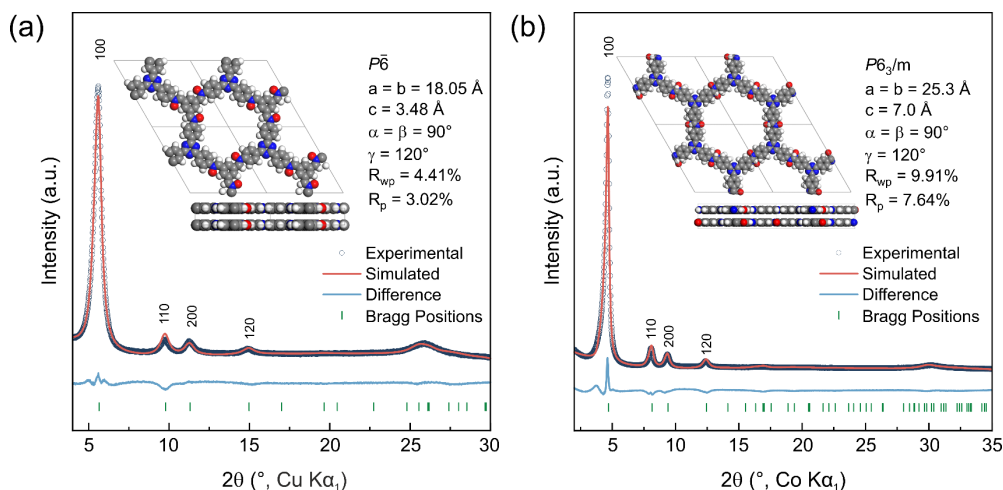


Figure 5-3: Rietveld refinements for NO-PI-3-COF (a) and NO-TTI-COF (b).

A Rietveld^[20] refinement (Figure 5-3) gives slightly larger in-plane unit cell parameters of $a = b = 18.049(14) \text{ \AA}$ and a decreased stacking distance of $c = 3.484(2) \text{ \AA}$ in NO-PI-3-COF ($a = 18.034(7) \text{ \AA}$ and $c = 3.5058(12) \text{ \AA}$ for PI-3-COF)^[18] (Table S 9.2-1). While reduction to rPI-3-COF has been previously described to increase both in-plane (a, b) and stacking (c) cell parameters, due to increased C—N single- vs. double-bond lengths and steric repulsion of the benzylic (CH_2) protons of adjacent layers in the amine-linked material, the oxidation of amine to nitrone-linkages causes the reverse effect, giving reduced in-plane and stacking cell parameters for NO-PI-3-COF. The in-plane cell parameter a is approximately 0.02 \AA larger, which is in line with the steric demand of the oxygen substituent in the nitrone. The stacking

distance c is reduced by 0.03 Å in the nitrone, suggesting a closer packing of the layers in the c -direction. On the other hand, a comparison of the pore size distributions obtained from N₂ gas adsorption experiments (Figure S 9.2-19) shows a small contraction of the average pore size from 1.7 nm (PI-3-COF) to 1.6 nm in NO-PI-3-COF (Figure S 9.2-20). In contrast to the increased cell parameter a , the slight reduction in pore diameter might be affected by increasing stacking disorder, e.g. random offset-stacking of the layers^[18, 21, 22] upon oxidation to the nitrone, likely introduced by the reorganization of the local structure of the linkages affecting interlayer interactions.^[23, 24] Despite these changes in the structure, the material shows porosity after the conversion of the linkage, evident from a BET surface area of 664 m²g⁻¹ for NO-PI-3-COF (Figure S 9.2-22). Drying of the as-synthesized material in a desiccator (CaCl₂), instead of applying high vacuum at 120°C, reduces drying-induced stress in the material and allowed us to obtain NO-PI-3-COF with a larger surface area of 1186 m²g⁻¹ (Figure S 9.2-30).

Motivated by these promising results, we further attempted a direct conversion of the imine-linkages in PI-3-COF to nitrones with mCPBA under similar conditions (see SI). As reported for small molecular imines, oxidation with mCPBA usually leads to a product mixture, containing the oxaziridine as a major product.^[25] Depending on the substituents, the three-membered ring of the oxaziridine rearranges under light or thermal stimulation to the nitrone or amide moiety.^[26, 27] In many cases, these circumstances lead to a complex mixture of these compounds in the crude reaction mixture, which need to be separated by tedious chromatographic techniques. Due to the incompatibility of a solid-state material such as a COF to chromatographic purification, a post-synthetic linkage transformation requires a selective and efficient reaction to a single product, which would clearly exclude this synthetic strategy to obtain nitrone-linked COFs. Surprisingly, treating PI-3-COF with 1.0 equiv. mCPBA (see SI for details) led to a clean and direct conversion of the imine linkages to nitrones. This intriguing observation highlights that pre-organizing molecules in the solid-state, and thereby restricting their mobility and accessibility, can confine the reaction environment and lead to unexpected selectivity of reactions of or with solid-state materials.^[28, 29] Likewise, the mechanism of oxidation seems to occur *via* direct oxygen transfer to the imine nitrogen in PI-3-COF by mCPBA, contrary to the nucleophilic Baeyer-Villiger reaction or concerted oxidation mechanisms considered to yield oxaziridines from small molecule imines.^[30] Furthermore, we believe that the presence of an oxaziridine linkage intermediate is unlikely, because the highly strained three-membered oxaziridine heterocycle would require a drastic deformation, i.e. corrugation, of the layers. Likewise, oxaziridines pointing into the interlayer space, towards the neighboring layers, would cause an expansion of the interlayer stacking distance, which is in stark contrast to the observed reduction of the stacking distance in the nitrone (Figure 5-2a). The absence of any aliphatic carbon signals in the ¹³C ssNMR spectrum (Figure 5-2b) and nitrogen signals in the ¹⁵N ssNMR spectrum (Figure 5-2c) relating to oxaziridine formation supports our hypothesis that, in the sterically crowded COF pore, oxidation likely occurs through an electrophilic attack of mCPBA on

the nitrogen,^[31] as similarly observed for sterically hindered small molecule N-alkyl imines.^[32] The electrophilic attack mechanism involves an equatorial advance of the mCPBA reagent towards the linkage nitrogen, *i.e.* from within the pores, perpendicular to the stacking direction of the layers. In contrast, the intermediate formation of oxaziridines would involve an axial approach of mCPBA, which is sterically blocked by the neighboring layers in the 2D COF and thus rather unlikely to occur.

To further demonstrate the general transferability of our oxidation method, we successfully applied it to another imine-linked COF with a larger pore diameter, namely the TTI-COF system (Figure S 9.2-3). Analogous to the oxidation of PI-3-COF, XRPD patterns of NO-TTI-COF show retention of crystalline order throughout the reduction and oxidation steps (Figure S 9.2-5). As earlier reported for the reduction of TTI-COF to amine-linked rTTI-COF, changes of the apparent symmetry occur, as evident from the disappearance of peak splitting in the XRPD pattern (Figure S 9.2-5).^[18] A change from antiparallel slip-stacked TTI-COF^[33] to more eclipsed-like stacking in rTTI-COF, due to a randomization of stacking offset upon reduction, is even preserved during subsequent oxidation to NO-TTI-COF. The interlayer distance of the randomly stacked rTTI-COF (3.504(2) Å)^[18] is further reduced to 3.478(25) Å in NO-TTI-COF, following similar trends as described for NO-PI-3-COF. A comparison of the N₂ adsorption isotherms (Figure S 9.2-24) reveals retention of porosity during oxidation of rTTI to NO-TTI-COF, attested by an almost unaltered BET surface area of 1325 m²g⁻¹ for NO-TTI-COF (from 1397 m²g⁻¹ for rTTI-COF). Similar to NO-PI-3-COF, pore size distribution analysis shows a contraction of the pore diameter by 0.2 nm to 2.1 nm in NO-TTI-COF (Figure S 9.2-25).

5.2.2 Water Adsorption Properties

After synthesizing NO-PI-3-COF and handling it in ambient air, we noticed a broad signal centered at $\nu \approx 3350$ cm⁻¹ in the FT-IR spectrum (Figure S 9.2-2), which disappeared after extensive drying of the material under reduced pressure. Likewise, an intense signal at $\delta = 4.5$ ppm in the ¹H ssNMR spectrum of NO-PI-3-COF, as well as minor intensity changes in the ¹³C ssNMR spectrum around $\delta = 150$ and 119 ppm were visible, referring to carbons in close proximity to the nitrone center (Figure 5-2b, Figure S 9.2-18). Due to the characteristic vibration in the FT-IR spectrum, we attributed the signal to water in NO-PI-3-COF, which was captured from ambient air. This observation encouraged us to study the water adsorption properties of the nitrone-linked frameworks.

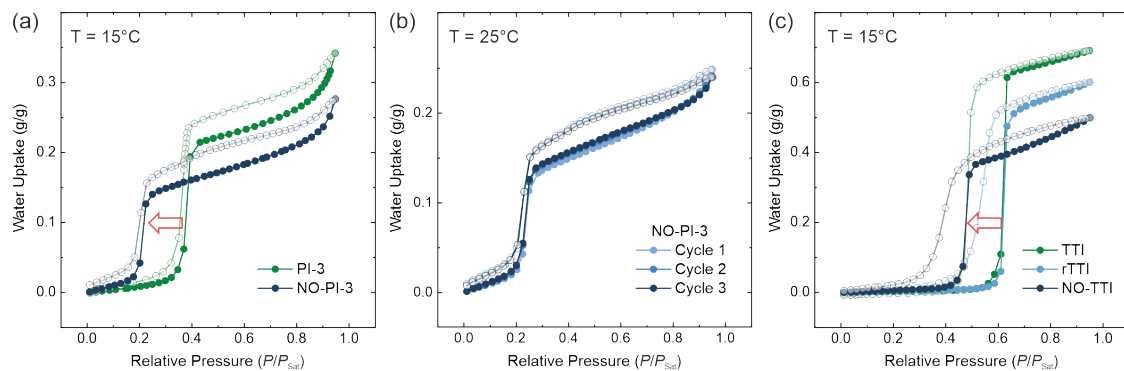


Figure 5-4: (a) Comparison of water vapor adsorption isotherms of PI-3- and NO-PI-3-COF. (b) Water adsorption-desorption cycles of NO-PI-3-COF. (c) Adsorption isotherms of TTI-, rTTI-, and NO-TTI-COF.

Water vapor adsorption experiments of NO-PI-3-COF and PI-3-COF at 15°C (Figure 5-4a) show S-shaped isotherms with a steep uptake step as an effect of nucleated condensation in the pore channels.^[7, 34] Relative pressures, i.e. relative humidity, at which steep pore filling occurs, shift from $P/P_{\text{sat}} \approx 0.38$ (PI-3-COF) to $P/P_{\text{sat}} \approx 0.21$ upon oxidation of the nitrone-linked material. The total uptake at $P/P_{\text{sat}} = 0.95$ is slightly reduced in NO-PI-3-COF with an adsorbed mass of 0.27 g per gram of material (compared to 0.34 g/g of PI-3-COF), which correlates with the structural rearrangement as well as the increase in molecular mass of the material during oxidation. Besides a small hysteresis of the isotherm, low induction pressures are a prerequisite for efficient harvesting of atmospheric water.^[9] In contrast to a limited capacity, which is less relevant for the applicability of a material for water uptake, the induction pressure for the pore-filling step is a strongly limiting factor for harvesting water under arid conditions if the material is capable of performing multiple cycles per day.^[35] To better understand the impact of oxidation on the interaction of water with the material's surface, we determined the heats of adsorption (Q_{st}) for the pristine and NO-functionalized COF based on the Clausius-Clapeyron equation by measuring additional adsorption isotherms at 25°C and 35°C (Figure S 9.2-34, Figure S 9.2-36). Isotherms measured at higher temperature show a retention of the adsorption properties observed for 15°C, accompanied by a gradual shift of the pore-filling step to $P/P_{\text{sat}} \approx 0.26$ at 35°C. Values for Q_{st} calculated from the kinetically limited adsorption process for small adsorbed amounts (Figure S 9.2-36) suggest a predominantly hydrophobic pore channel in NO-PI-3-COF, as similarly observed for PI-3-COF (Figure S 9.2-36). In contrast, higher values for the desorption process in NO-PI-3-COF indicate a stronger interaction of water molecules with dedicated sites in the material, visible from increased Q_{st} towards small loadings during desorption.^[15] Likewise, the heats of adsorption reach a plateau for amounts corresponding to the pore-filling steps in both materials and stabilize at $Q_{\text{st}} \approx 47 \text{ kJ/mol}$ for the imine and $Q_{\text{st}} \approx 50 \text{ kJ/mol}$ for the nitrone, respectively, which are close to bulk water ($Q_{\text{st}} = 44 \text{ kJ/mol}$).^[15] Together with increasing heats of adsorption towards zero loading during desorption (Figure S 9.2-36), this hints at an increased interaction of water with the more polar nitrone sites in NO-PI-3-COF. Heats of adsorption at zero coverage calculated from CO₂ adsorption isotherms at different temperatures (Figure S 9.2-39, Figure S 9.2-40) further corroborate this finding, giving

increased values for NO-PI-3-COF ($Q_{st} \approx 30 \text{ kJ/mol}$) compared to PI-3-COF ($Q_{st} \approx 21 \text{ kJ/mol}$). Our observations suggest that the nitrone-linkages act as hydrophilic centers, which support the coordination of water molecules. With increasing water vapor pressures, clustered water molecules at the linkage centers act as nucleation sites for water condensation in the pore channels.^[15] Consecutive volumetric adsorption/desorption cycles of NO-PI-3-COF at 25°C (Figure 5-4b) do not show any signs of material degradation.

In order to gain more insights into the water uptake and release behavior and cycling stability of NO-PI-3-COF we performed *in-situ* XRPD measurements at 25 °C in a dynamic atmosphere with adjustable relative humidity (Figure 5).

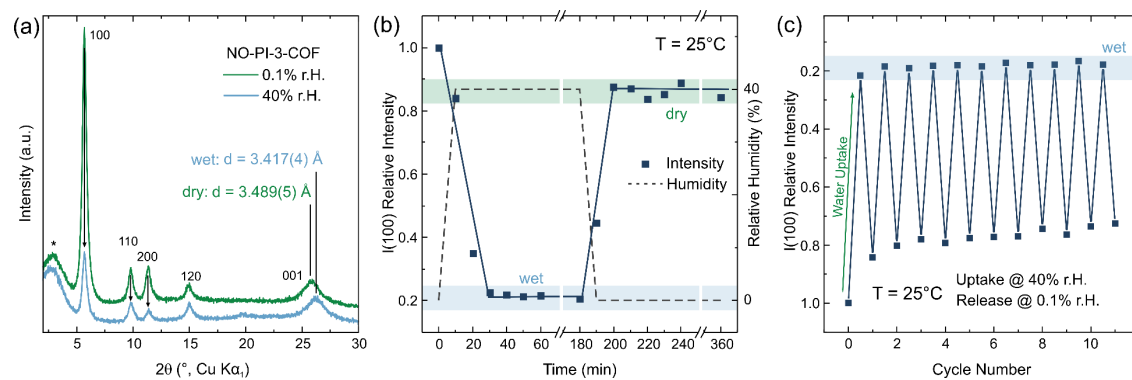


Figure 5-5: *In situ* XRPD measurements of NO-PI-3-COF (a): XRPD patterns in dehydrated (green) and hydrated states (blue) including the background diffraction signal attributed to the sample holder and the humidity chamber (asterisks) and selected reflection indices. (b) Time-dependent intensity of the 100 reflection obtained from *in situ* XRPD patterns during hydration and dehydration. (c) Modulation of the 100 intensity during multiple hydration and dehydration cycles.

A gradual change of 100, 110 and 200 reflection intensity and significant upshift of the 001 reflection position occurs upon hydration (Figure 5a, S55b), which is attributed to a reduced scattering contrast and stacking distance of the layers, in agreement with simulated diffraction patterns of a refined model at different water loadings (Figure S 9.2-55). Although a contraction of the interlayer distance and thus unit cell volume upon filling the pores with water molecules (Figure S 9.2-54c, Figure S 9.2-56c) might appear counterintuitive, increased interlayer interactions and/or conformational changes of linker related groups can lead to a denser packing of the COF layers. When the relative humidity is subsequently decreased, the peak intensities of 100, 110 or 200 increase again (Figure 5-5b, S55b), corresponding to a reversible hydration of NO-PI-3-COF analogous to the observations from volumetric water adsorption experiments (Figure 5-4a, b). Motivated by these results we conjectured to use the prominent changes in 100 reflection intensity as a proxy to trace the kinetics and reversibility of the adsorption process (Figure 5-5b). The change in 100 intensity occurs gradually upon hydration at 25°C (40% R.H.) and stabilizes after 30-40 minutes. Subsequent reduction of the relative humidity (0.1%) to trigger the isothermal desorption shows a similarly fast response to the signal intensity, indicating that both ad- and desorption of water

vapor occur fast enough to perform multiple cycles per day. However, the 100 intensity (i.e. the dried state) does not fully recover after the first hydration cycle, hinting at an incomplete water release under the applied isothermal desorption conditions. During consecutively performed cycles (Figure 5-5c) an induction period of 3-4 cycles becomes evident, after which the 100 signal intensity of the dehydrated state stabilizes. On the other hand, the corresponding relative intensity in the hydrated (i.e. wet) state stays constant at around ~ 0.2 throughout the entire experiment, corroborating the observed cycling stability of the material from volumetric sorption experiments (Figure 5-4b) throughout an increased number of cycles.

Adsorption isotherms for NO-TTI-COF (Figure 5-4c) show a similar shift of the steep pore condensation step by $\Delta(P/P_{sat}) \approx 0.15$ towards lower relative pressures. Due to the larger pore diameter of 2.1 nm water condensation in the TTI-COF system requires higher humidity compared to PI-3-COFs, evident from the inflection point of the pore-filling step at $P/P_{sat} \approx 0.47$ for NO-TTI-COF (Figure 5-4c). Notably, this shift is only visible after oxidation to NO-TTI-COF and does not occur after the initial reduction from TTI-COF to amine-linked rTTI-COF, highlighting the necessity of the nitrone linkage and the transferability of the observed water adsorption effect in NO-PI-3-COF to other COF systems. On the other hand, water vapor isotherms successively collected at different temperatures for TTI-, rTTI-, and NO-TTI-COF show a decrease in adsorption capacity for both post-modified TTI materials (Figure S 9.2-35). In contrast to the behavior of NO-PI-3-COF, the uptake capacity of rTTI- and NO-TTI-COF is halved during the second measurement with the same material (Figure S 9.2-35). XRPD (Figure S 9.2-8) analysis of NO-TTI-COF after water adsorption experiments suggest that the reduction is caused by partial pore-collapse, evident from a shift of the reflections towards higher angles accompanied by a loss of scattering intensity. Notably, FT-IR spectra of this material before and after water adsorption experiments do not show signs of chemical decomposition of the material such as hydrolysis (Figure S 9.2-4). Solvent-induced pore collapse is a common phenomenon observed especially during the drying process of large pore COFs,^[36] which can be reduced with decreasing polarity of the solvent^[37] or by enhanced interlayer interactions.^[23, 38] As previously reported for certain MOF water harvesting materials,^[4] this observation further points to a strong interaction of polar nitrone moieties in NO-TTI-COF with adsorbed water and recalls the necessity for orchestrating different types of interactions to further optimize adsorption properties of COFs. More specifically, fine-tuning of pore channel hydrophilicity can only lead to efficient water adsorption materials if interlayer interactions—as the “opponent” in 2D COFs—are likewise adjusted or, as described for NO-PI-3-COF, are strong enough to withstand drying-induced stress during water desorption.

Nevertheless, the water adsorption characteristics of NO-PI-3-COF fulfill the criteria for water harvesting materials. Besides stability under the required conditions, these materials should preferably exhibit an S-shaped water adsorption isotherm with a steep uptake step

between $P/P_{\text{sat}} = 0.1$ and 0.3 to allow adsorption at low humidity.^[9, 17] To enable energy efficient water desorption by a small temperature swing, the isotherms should only show minor hysteresis and low heats of adsorption.^[39] Accordingly, the adsorption isotherm profile, and cycling stability of NO-PI-3-COF together with only minor hysteresis between ad-/desorption and a Q_{st} close to bulk water ($Q_{\text{st}} = 44 \text{ kJ/mol}$)^[15] at the pore-filling step, bodes well for the use as the active material in water harvesting applications.

5.3 Conclusion

In summary, we present a new, facile topochemical oxidation method to obtain nitrone-linked covalent organic frameworks *via* solid-state synthesis starting from readily available imine-linked COFs. In contrast to earlier post-synthetic oxidation methods affording amide-linked COFs,^[40, 41] our protocol, makes use of the electrophilic oxidation capabilities of mCPBA,^[32] and thus allows to selectively oxidize nitrogen centers in the presented materials, while both crystalline order and porosity of the scaffolds are retained. Converting imine or amine linkages to nitrones introduces polar centers into the pore wall surface and thus modulates the interaction with polar adsorbates, such as water vapor. Both post-synthetically modified small and larger pore diameter nitrone COFs adsorb water vapor at reduced relative pressures compared to their parent COFs. The condensation of water vapor in the nitrone decorated pore channels is significantly shifted by $\sim 20\%$ relative humidity compared to the corresponding amine- or imine-linked precursor COFs. This makes COFs based on this novel linkage attractive candidates for atmospheric water harvesting. Due to an early onset at lower humidity, nitrone-linked COFs could be promising candidates for water vapor adsorbents in areas where arid atmospheric conditions prevail.

5.4 Acknowledgements

The authors thank Igor Moudrakovski for supporting ssNMR measurements. Financial support by the Max Planck Society and the Cluster of Excellence e-conversion (Grant No. EXC2089) is gratefully acknowledged. Funded by the Deutsche Forschungsgemeinschaft (DFG, German Research Foundation) – Project-ID 358283783 – SFB 1333/2 2022.

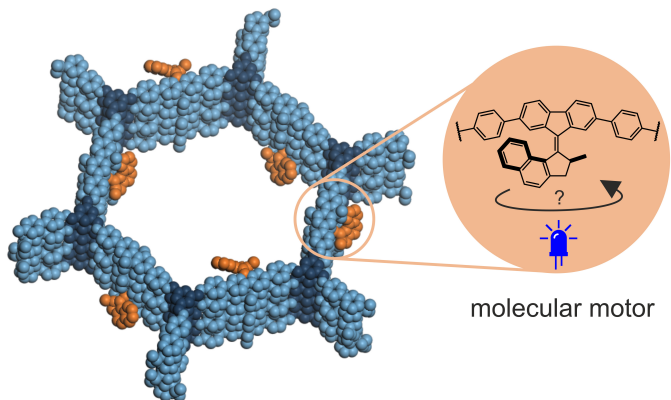
5.5 Bibliography

1. Byun Y., Je S. H., Talapaneni S. N., Coskun A. Advances in Porous Organic Polymers for Efficient Water Capture. *Chem. Eur. J.* **25**, 10262-10283 (2019).
2. Jiang S. et al. Dual-Functional Two-Dimensional Covalent Organic Frameworks for Water Sensing and Harvesting. *Mater. Chem. Front.* **5**, 4193-4201 (2021).
3. Gilmanova L. et al. Chemically Stable Carbazole-Based Imine Covalent Organic Frameworks with Acidochromic Response for Humidity Control Applications. *J. Am. Chem. Soc.* **143**, 18368-18373 (2021).

4. Furukawa H. et al. Water Adsorption in Porous Metal-Organic Frameworks and Related Materials. *J. Am. Chem. Soc.* **136**, 4369-4381 (2014).
5. Stegbauer L. et al. Tunable Water and CO₂ Sorption Properties in Isostructural Azine-Based Covalent Organic Frameworks through Polarity Engineering. *Chem. Mater.* **27**, 7874-7881 (2015).
6. Biswal B. P. et al. Pore Surface Engineering in Porous, Chemically Stable Covalent Organic Frameworks for Water Adsorption. *J. Mater. Chem. A* **3**, 23664-23669 (2015).
7. Nguyen H. L. et al. Hydrazine-Hydrazide-Linked Covalent Organic Frameworks for Water Harvesting. *ACS Cent. Sci.* **8**, 926-932 (2022).
8. Xu W., Yaghi O. M. Metal-Organic Frameworks for Water Harvesting from Air, Anywhere, Anytime. *ACS Cent. Sci.* **6**, 1348-1354 (2020).
9. Kalmutzki M. J., Diercks C. S., Yaghi O. M. Metal-Organic Frameworks for Water Harvesting from Air. *Adv. Mater.* **30**, e1704304 (2018).
10. Lohse M. S., Bein T. Covalent Organic Frameworks: Structures, Synthesis, and Applications. *Adv. Funct. Mater.* **28** (2018).
11. Cusin L., Peng H., Ciesielski A., Samorì P. Chemical Conversion and Locking of the Imine Linkage: Enhancing the Functionality of Covalent Organic Frameworks. *Angew. Chem. Int. Ed.* **133**, 14356-14370 (2021).
12. Helweh W. et al. Layered Structures of Assembled Imine-Linked Macrocycles and Two-Dimensional Covalent Organic Frameworks Give Rise to Prolonged Exciton Lifetimes. *J. Mater. Chem. C* **10**, 3015-3026 (2022).
13. Tan K. T. et al. Covalent Organic Frameworks. *Nat. Rev. Methods Primers* **3** (2023).
14. Feng J. et al. Fused-Ring-Linked Covalent Organic Frameworks. *J. Am. Chem. Soc.* **144**, 6594-6603 (2022).
15. Tan K. T., Tao S., Huang N., Jiang D. Water Cluster in Hydrophobic Crystalline Porous Covalent Organic Frameworks. *Nat. Commun.* **12**, 6747 (2021).
16. Karak S. et al. Constructing Ultraporous Covalent Organic Frameworks in Seconds Via an Organic Terracotta Process. *J. Am. Chem. Soc.* **139**, 1856-1862 (2017).
17. Nguyen H. L. et al. A Porous Covalent Organic Framework with Voided Square Grid Topology for Atmospheric Water Harvesting. *J. Am. Chem. Soc.* **142**, 2218-2221 (2020).
18. Grunenberg L. et al. Amine-Linked Covalent Organic Frameworks as a Platform for Postsynthetic Structure Interconversion and Pore-Wall Modification. *J. Am. Chem. Soc.* **143**, 3430-3438 (2021).
19. Shindo H., Umezawa B. Infrared Absorption Spectra of Aldonitrones. I. Infrared Spectra of Benzaldehyde N-Methyl and N-Phenyl Nitrones. *Chem. Pharm. Bull.* **10**, 492-503 (1962).
20. Rietveld H. M. A Profile Refinement Method for Nuclear and Magnetic Structures. *J. Appl. Crystallogr.* **2**, 65-71 (1969).
21. Pütz A. M. et al. Total Scattering Reveals the Hidden Stacking Disorder in a 2d Covalent Organic Framework. *Chem. Sci.* **11**, 12647-12654 (2020).
22. Stahler C. et al. Light-Driven Molecular Motors Embedded in Covalent Organic Frameworks. *Chem. Sci.* **13**, 8253-8264 (2022).

23. Emmerling S. T. et al. Interlayer Interactions as Design Tool for Large-Pore Cofs. *J. Am. Chem. Soc.* **143**, 15711-15722 (2021).
24. Song X. et al. Design Rules of Hydrogen-Bonded Organic Frameworks with High Chemical and Thermal Stabilities. *J. Am. Chem. Soc.* **144**, 10663-10687 (2022).
25. Krimm H. Über Isonitrone. *Chem. Ber.* **91**, 1057-1068 (1958).
26. Williamson K. S., Michaelis D. J., Yoon T. P. Advances in the Chemistry of Oxaziridines. *Chem. Rev.* **114**, 8016-8036 (2014).
27. Duhamel P., Bénard D., Plaquevent J.-C. Isomérisation Oxaziridine-Amide Sur Gel De Silice Obtention Non Classique D'une Liaison Peptidique. *Tetrahedron Lett.* **26**, 6065-6066 (1985).
28. Grunenberg L., Lotsch B. V. Escaping the Horns of the Cof Dilemma. *Matter* **5**, 2482-2484 (2022).
29. Zhang W. et al. Reconstructed Covalent Organic Frameworks. *Nature* **604**, 72-79 (2022).
30. Kraiem J., Ben Othman R., Ben Hassine B. Synthesis of Oxaziridines by Oxidation of Imines with the Trichloroacetonitrile–Hydrogen Peroxide System. *C. R. Chim.* **7**, 1119-1126 (2004).
31. Ogata Y., Sawaki Y. Peracid Oxidation of Imines. Kinetics and Mechanism of Competitive Formation of Nitrones and Oxaziranes from Cyclic and Acyclic Imines. *J. Am. Chem. Soc.* **95**, 4692-4698 (2002).
32. Boyd D. R. et al. Imines and Derivatives. Part 24. Nitrone Synthesis by Imine Oxidation Using Either a Peroxyacid or Dimethyldioxirane. *J. Chem. Soc., Perkin Trans. 1*, doi: 10.1039/p19900000301, 301-306 (1990).
33. Haase F. et al. Tuning the Stacking Behaviour of a 2d Covalent Organic Framework through Non-Covalent Interactions. *Mater. Chem. Front.* **1**, 1354-1361 (2017).
34. Hanikel N. et al. Evolution of Water Structures in Metal-Organic Frameworks for Improved Atmospheric Water Harvesting. *Science* **374**, 454-459 (2021).
35. Hanikel N. et al. Rapid Cycling and Exceptional Yield in a Metal-Organic Framework Water Harvester. *ACS Cent. Sci.* **5**, 1699-1706 (2019).
36. Mu Z. et al. Covalent Organic Frameworks with Record Pore Apertures. *J. Am. Chem. Soc.* **144**, 5145-5154 (2022).
37. Zhu D. et al. Solvent-Induced Incremental Pore Collapse in Two-Dimensional Covalent Organic Frameworks. *ACS Mater. Lett.* **4**, 2368-2374 (2022).
38. Diwakara S. D. et al. Supramolecular Reinforcement of a Large-Pore 2d Covalent Organic Framework. *J. Am. Chem. Soc.* **144**, 2468-2473 (2022).
39. Zhou X., Lu H., Zhao F., Yu G. Atmospheric Water Harvesting: A Review of Material and Structural Designs. *ACS Mater. Lett.* **2**, 671-684 (2020).
40. Waller P. J. et al. Chemical Conversion of Linkages in Covalent Organic Frameworks. *J. Am. Chem. Soc.* **138**, 15519-15522 (2016).
41. Zhou Z. B. et al. A Facile, Efficient, and General Synthetic Method to Amide-Linked Covalent Organic Frameworks. *J. Am. Chem. Soc.* **144**, 1138-1143 (2022).

6 Light-Driven Molecular Motors Embedded in Covalent Organic Frameworks



The presented work of this chapter was published, adapted and reproduced from:

Light-Driven Molecular Motors Embedded in Covalent Organic Frameworks

Cosima Stähler,[‡] Lars Grunenberg,[‡] Maxwell W. Terban, Wesley R. Browne, Daniel Doellerer, Michael Kathan, Martin Etter, Bettina V. Lotsch, Ben L. Feringa and Simon Krause, *Chem. Sci.* **2022**, *13*, 8253-8264. DOI: 10.1039/d2sc02282f

[‡] Authors contributed equally.

C.S. synthesized and analyzed the light-responsive molecular motors, imines, amines and derived polymers. L.G. synthesized and characterized the COF materials and established their structural models. C.S. and L.G. wrote the manuscript. M.W.T. and M.E. performed PDF analysis. W.R.B. performed Raman analysis. D.D. performed DFT analysis of the molecular motors. M.K. supported synthesis and spectroscopic analysis of the molecular motors. B.V.L., B.L.F. and S.K. supervised the project and supported writing of the manuscript.

This article is part of the themed collections: *Most popular 2022 materials and energy articles* and *2022 Chemical Science HOT Article Collection*

Volume 13
Number 28
28 July 2022
Pages 8209-8446

Chemical Science

rsc.li/chemical-science



ISSN 2041-6539

**ROYAL SOCIETY
OF CHEMISTRY**

EDGE ARTICLE
Bettina V. Lotsch, Ben L. Feringa, Simon Krause *et al.*
Light-driven molecular motors embedded in covalent
organic frameworks

Front Cover Image designed by Vera Hiendl (e-conversion).

Abstract: The incorporation of molecular machines into the backbone of porous framework structures will facilitate nano actuation, enhanced molecular transport, and other out-of-equilibrium host-guest phenomena in well-defined 3D solid materials. In this work, we detail the synthesis of a diamine-based light-driven molecular motor and its incorporation into a series of imine-based polymers and covalent organic frameworks (COF). We study structural and dynamic properties of the molecular building blocks and derived self-assembled solids with a series of spectroscopic, diffraction, and theoretical methods. Using an acid-catalyzed synthesis approach, we are able to obtain the first crystalline 2D COF with stacked hexagonal layers that contains 20 mol% molecular motors. The COF features a specific pore volume and surface area of up to $0.45 \text{ cm}^3 \text{ g}^{-1}$ and $604 \text{ m}^2 \text{ g}^{-1}$, respectively. Given the molecular structure and bulkiness of the diamine motor, we study the supramolecular assembly of the COF layers and detail stacking disorders between adjacent layers. We finally probe the motor dynamics with *in situ* spectroscopic techniques revealing current limitations in the analysis of these new materials and derive important analysis and design criteria as well as synthetic access to new generations of motorized porous framework materials.

6.1 Introduction

Light-driven molecular motors have emerged as promising platforms to achieve stimuli-responsive motion at a molecular scale.^[1-6] Incorporating these into porous, heterogeneous structures promises new generations of dynamic, light-responsive, smart materials with unique properties that allow control over molecular motion in their surrounding space and pore volume.^[7-11] Maximizing dynamic effects and achieving molecular motion along length scales to create nano- or macroscopic function requires specific designs and diverse conditions, which is a challenging area of contemporary research.^[5, 12-16] Besides the control of molecular dynamics, cooperative interactions on a spatiotemporal level and structural aspects of the matrix are also critical design criteria. These include the ratio of dynamically active and passive components in confined space, the three-dimensional structure, adaptivity of the matrix and sufficient void space.

High packing densities of bistable rotaxanes^[17] and catenanes embedded in self-assembled monolayers^[18-20] and polymers^[21] result in a significant decrease in the rate of rotational and translational motion. Similar effects were observed for the intramolecular rotational motion of molecular motors embedded in polymers^[7, 22] or grafted onto surfaces^[23, 24]. Strategies to avoid these effects include incorporation into low-viscous fluids^[25, 26] as well as spatial separation by co-assembly or immobilization of molecular motors into the backbone of porous frameworks^[8] and polymers.^[27] In particular, the latter is a critical innovation towards the transfer of controlled motion of a molecular machine onto a guest species.^[28] The Feringa group recently demonstrated that light driven molecular motors can be embedded in the backbone of metal-organic frameworks by applying a motor-based stator unit.^[8] The rotational frequency of the molecular motors in these nanoporous crystals did not change

compared to the molecules' behavior in solution, indicating that the rotor units perform unrestricted motion. In principle, the pore space allows for dynamic confinement effects and unusual transport or adsorption phenomena.^[29] Castiglioni and Feringa *et al.* demonstrated that the porosity of a nanoporous polymer with backbone-embedded, light-driven molecular motors changes reversibly upon irradiation as a result of photoswitch dynamics.^[27] In a computational study, Kolodzeiski *et al.* predicted collective dynamics of framework-embedded molecular motors^[30] and Evans *et al.* were able to show that such properties can lead to activated, directed transport of a confined fluid mimicking a macroscopic pump.^[31] A critical design criterion of such activated directed transport is the presence of pore channels in which the fluid is confined and translational motion is forced in a preferred direction.

A class of materials that feature such intrinsic pore channels and combines it with exceptional structural tunability are 2D Covalent Organic Frameworks (COFs).^[32] The unique properties, such as high porosity, large surface areas, light-absorption, and ordered structuring, are combined within a crystalline polymeric material. COFs have been used for diverse applications, including gas storage and separation, sensing, electrochemical energy storage, and heterogeneous (photo)catalysis.^[33-39]

Recently the incorporation of light-responsive moieties in COFs has gained interest for modifying their properties, e.g. pore-accessibility, by external stimulation. To this end, various polymers^[40] and COFs comprising azobenzene-^[41, 42] or dithienylethene-switches^[43] as building blocks have been synthesized. Apart from these switches, rotaxanes have also recently been introduced into COF-like polymers.^[44, 45] A major challenge in these structures is the compromise between structural complexity, functionality and crystallinity of the material,^[46] with a loss of structural order evident in the X-ray diffraction pattern and low surface area with geometrically more complex building blocks.^[44, 45] In contrast to MOFs, COFs are connected entirely by covalent bonds, and many COFs exhibit a higher chemical stability than MOFs.^[47] The combination of low density, structural tunability and stability makes COFs more attractive for the integration of molecular machines. As an example, many MOF structures are sensitive to solvent removal, drastically limiting their potential for applications.^[48] COFs furthermore perform better in terms of processability and in principle allow for hierarchical structuring, such as thin-film fabrication, required for advanced (photo-)electrochemical applications.^[49, 50] Despite its structural elegance and advantages, molecular motors have not been embedded in COFs to date.

Contrary to amorphous polymeric materials, COFs allow, in principle, for precise arrangement of responsive molecules within their crystalline framework, similar to the arrangement demonstrated in MOFs.^[8] The spatial arrangement of molecular machines is crucial to amplify and coordinate their movement across multiple length and time scales.^[12] Molecular motors arranged in amphiphiles could be used as artificial muscles, able to lift macroscopic objects.^[51] Motors as dopants in liquid crystals, for example, are able to move micrometer sized objects through spatial rearrangement of the liquid crystal matrix.^[26] In

these systems only small amounts of molecular motors were embedded, demonstrating that the quantity of machines integrated is less relevant than the quality of their arrangement to obtain responsive function.

Herein we detail design principles and synthetic strategies of COFs featuring backbone-embedded light-driven molecular motors. To the best of our knowledge, this is the first report of a light-driven molecular motor covalently incorporated in 2D COFs, in which both crystallinity and porosity are preserved. We synthesize a new diamine light driven molecular motor and investigate its dynamics with *in-situ* spectroscopic methods. By utilizing different reaction conditions, we synthesize amorphous polymers as well as crystalline 2D COFs, constructed from this diamine molecular motor *via* imine condensation. The structural features of the self-assembled frameworks with respect to composition, local and long-range structure, structural disorder, and porosity were investigated. We elucidate the stacking mechanism of adjacent 2D layers in the framework and examine the motor behavior with FT-IR, Raman and UV/Vis spectroscopy. From this, we derive design principles and methodologies that in the future will help to establish dynamic COFs to be used as light-responsive smart materials.

6.2 Results

The rotational cycle of overcrowded alkene-based molecular motors consists of four distinct steps.^[52, 53] First, the C-C double bond connecting the two halves of the molecule functions as the rotary axle. It undergoes an *E*-*Z* isomerization upon irradiation with light in the UV/Vis region. The molecule adopts a metastable state, in which the methyl group of the upper half (Figure 6-1a, orange) converts from a pseudo axial to an energetically less favored pseudo equatorial position. Subsequently, the molecule relaxes through a thermal helix inversion, completing a 180° rotation. This step is irreversible, in contrast to the double bond isomerization step in which a photochemical equilibrium is established. The thermal helix inversion therefore ensures the unidirectionality of the motor rotation. The half-life of the metastable state is furthermore the main determining factor for the rotational speed of the motor. Repetition of the photochemical and thermal steps fulfills a full 360° rotation (Figure 6-1a).

Depending on the structural features of overcrowded alkene-based molecular motors, their properties like absorption wavelength, rotational speed, or thermal half-life of the metastable state can vary tremendously.^[5] The half-life of the metastable state is primarily determined by the ring size of the two moieties connected by the central C-C double bond. For our studies, we chose a synthetically easily accessible molecular motor structurally related to the MOF-embedded, pyridine-derived motor detailed by Danowski *et al.*^[8] This molecular motor features a half-life in the range of minutes to be able to conveniently study the rotation at room temperature.^[54]

Imine based dynamic covalent chemistry^[55, 56] has emerged as the most popular handle for making functional COFs,^[57] as boronic acids are prone to hydrolysis.^[58] This approach requires amine or aldehyde-based building blocks and we selected the aniline-based bisfunctional molecular motor **1** (Figure 6-1a, R = NH₂) as a suitable building block for the synthesis of COFs and 1,3,5-triformyl benzene (**3**) as the aldehyde counterpart (Figure 6-2a). Due to steric bulk of the motor unit, we used a larger amine building block, which is extended by aniline moieties, compared to recent examples of fluorene based COFs,^[59, 60] creating a larger pore size in the condensed network and void volume in the motor plane. The selected building block combination allows condensation into a 2D layered COF, which is not prone to form interpenetrated structures as reported for many 3D COFs. Although 3D COFs may appear structurally more related to MOF structures, these materials are often obtained with reduced pore volume due to interpenetration, detrimental for the rotation of the motor unit.^[61]

In order to study framework formation and properties independent of molecular motors, we chose to establish a structurally similar dimethyl fluorene spacer without motor functionality. This spacer mimics the lower half of the motor (Figure 6-1a, blue), also allowing integration of both molecular building blocks within the same framework. Co-condensation in a single framework^[62] enhances the free space in which the motor can rotate. The methyl groups of the spacer further assist in increasing free volume for the motor rotation by favoring an antiparallel arrangement between neighboring fluorene units.^[63-65]

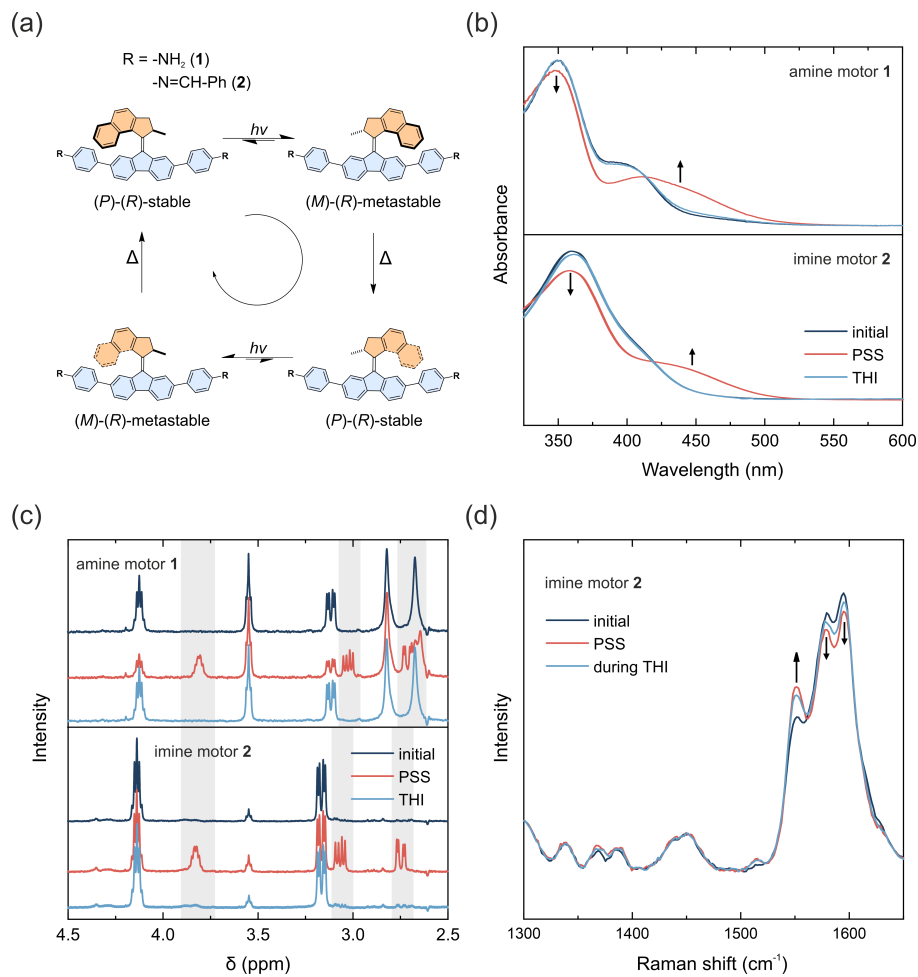


Figure 6-1: (a) Configurational changes upon photoswitching and thermal helix inversion of motors **1** and **2**. (b) UV/Vis absorption spectra upon irradiation of motors **1** and **2** in acetonitrile at 5 °C. The initial absorption spectra are shown in dark blue. The red spectra correspond to the photostationary state (PSS) at 395 nm for motor **1** and 365 nm for motor **2**. The spectra after thermal helix inversion (THI) are shown in light blue. (c) ¹H NMR spectra of motors **1** and **2** in the dark (blue) and after irradiation (red) in deuterated benzene at 10 °C. Spectra of the PSS show an additional set of signals for the metastable states (grey). (d) Raman spectra (785 nm) of motor **2** in toluene in the dark (blue), after irradiation with 365 nm (red) and after thermal helix inversion (light blue).

6.2.1 Synthesis and Characterization of the Building Blocks

The amine-functionalized spacer **4** and motor **1** were synthesized following a convergent strategy. A motor precursor was synthesized in a Barton-Kellogg olefination between the respective thioketone and 2,7-dibromo-9-diazafluorene following our reported procedure.^[8] The amine functionality in the motor **1** was subsequently introduced in a Suzuki-cross coupling reaction with 4-aminophenylboronic pinacol ester (for synthetic details, see SI). The same procedure was followed to afford the amine-functionalized spacer **4**. A model imine compound **2** (Figure 6-1a) was prepared and investigated additionally to study the rotary behavior of the motor **1** after imine condensation in solution. This model compound also mimics the chemistry of the motor and local molecular sterics when incorporated into the backbone of the COF. The model compound **2** was prepared by reaction of the amine building block **1** with benzaldehyde in toluene with 3 Å molecular sieves.

The light-induced rotational behavior of molecular motors **1** and **2** was monitored *in situ* using UV/Vis absorption and proton nuclear magnetic resonance (¹H NMR) spectroscopy (Figure 6-1b, c, d). We additionally investigated a solution of imine functionalized motor **2** by Raman spectroscopy to probe the dynamics of molecular motors in solution and in the solid state as previously shown for MOFs.^[8, 11]

A solution of amine functionalized motor **1** in acetonitrile initially shows a local absorption maximum at 400 nm (Figure 6-1b). Upon irradiation at 395 nm at 5 °C, a new band with a bathochromic shift formed at 450 nm, indicating the formation of a metastable state typically observed for second generation light-driven molecular motors.⁴ An isosbestic point at 415 nm indicates that a single step process takes place (Figure S 9.3-2). Relaxation of the sample at 5 °C after irradiation led to the reversible recovery of the stable isomer. Eyring analysis yielded an activation barrier for the thermal helix inversion of 87.9 kJ/mol, which corresponds to a thermal half-life of the metastable state of 8.6 min at 20 °C (Figure S 9.3-2).

A solution of imine functionalized model motor **2** in acetonitrile exhibited a absorption maximum at 360 nm, and irradiation at 365 nm led to the formation of a new band at 440 nm, indicating the formation of the metastable state, while maintaining an isosbestic point at 420 nm (Figure 6-1b, Figure S 9.3-3). The stable state was fully recovered after relaxation in the dark for approximately 2 h (Figure S 9.3-26). The activation energy of the thermal helix inversion was determined to be 88.3 kJ/mol, which corresponds to a thermal half-life of the metastable state of 10.3 min at 20 °C (Figure S 9.3-3). Based on this analysis we have confirmed both motors **1** and **2** to exhibit light-responsive rotational dynamics that are observable under ambient conditions.

The nature of the isomers formed was further investigated by ¹H NMR spectroscopy (Figure 6-1c). Solutions of both motors **1** and **2** dissolved in deuterated benzene were irradiated *in situ* at 10 °C. Irradiation of motor **1** at 385 nm led to the formation of a new set of signals, indicating the formation of the metastable isomer at a photostationary state with a ratio of 54:46 (metastable:stable). Leaving the sample at 10 °C without irradiation led to recovery of the initial spectrum of the stable state (Figure S 9.3-23, Figure S 9.3-24). Imine functionalized motor **2** was irradiated at 365 nm and reached a ratio of 22:78 (metastable:stable) at the photostationary state. After leaving the sample at 10 °C in the dark, the spectrum of the stable state was fully recovered (Figure S 9.3-25, Figure S 9.3-26).

Investigation of motor **2** by Raman spectroscopy in toluene showed the appearance of a band at 1550 cm⁻¹ upon irradiation at 365 nm, which is typical for the stretching of the central C-C double bond of the metastable isomer (Figure 6-1d).^[66] The band diminishes while leaving the sample without irradiation at room temperature, demonstrating reversible thermal helix inversion. The energy barriers for the thermal helix inversion of metastable motors **1** and **2** are in line with values computed by DFT (Table S 9.3-2, Table S 9.3-3). In both cases, the geometry of the fluorenyl moiety, which is embedded in the framework backbone, undergoes only a minor deformation upon isomerization and should allow

rotation while preserving the framework. The imine functionalized motor **2** has a half-life of several minutes at room temperature (Figure S 9.3-3, Figure S 9.3-26), which is ideal to follow the motor rotation at room temperature in solution and in the solid framework. Motor **2** however, exhibits a less favorable ratio between the stable and metastable state at PSS, with a preference towards the stable state. DFT studies show that the lower halves of the building blocks are bend by ca. 18° (Table S 9.3-4) and the motor adds structural complexity and bulkiness, making their condensation into a crystalline COF challenging. Consequently, we followed two different approaches for the condensation of building blocks into COFs.

6.2.2 Materials Synthesis

The amine building blocks were condensed with 1,3,5-triformyl benzene (**3**) under either of two reaction conditions. Reaction of the building blocks **1** and **4** with 1,3,5-triformyl benzene (**3**) with $\text{Sc}(\text{OTf})_3$ catalysis^[67, 68] in mesitylene:1,4-dioxane (1:4) at room temperature led to fast precipitation of an amorphous, polymeric material. Three different polymers with varying amount of motor were prepared: a pure motor polymer (**m₁₀₀-P**), in a 1:1 ratio with the spacer (**m₅₀-P**), and a pure spacer polymer (**m₀-P**). After the condensation, the materials were washed with ethanol and centrifuged several times to remove residual building blocks and dried with supercritical CO_2 . The formation of the imine backbone of the polymer and the consumption of trisaldehyde **3** and amine building blocks **1** and **4** is confirmed by Fourier transform infrared (FT-IR) spectroscopy, showing the characteristic imine band ($\nu_{\text{C}=\text{N}}$) at 1623 cm^{-1} (Figure S 9.3-4). All three IR spectra show similar bands in the finger-print region, underlining the structural similarity of the polymers.

Solid-state nuclear magnetic resonance spectroscopy (ssNMR) was performed to confirm the incorporation of the building blocks and preservation of motor integrity within the polymer backbone. The ¹³C ssNMR spectrum of **m₀-P** shows three characteristic signals for the imine carbon atom (156.4 ppm), the aliphatic bridging atom (48.3 ppm) and the methyl groups (28.3 ppm) (Figure S 9.3-27, Figure S 9.3-28). **m₁₀₀-P** shows two characteristic peaks in the aliphatic region at 41.6 ppm and 18.2 ppm and a broad signal at 148.5 ppm for the imine carbon (Figure S 9.3-29, Figure S 9.3-30). The two sets of signals can be identified in the spectrum of **m₅₀-P** confirming that both building blocks are incorporated within the polymer and the motor molecules are intact (Figure S 9.3-31, Figure S 9.3-32). X-ray powder diffraction (XRPD) revealed that all three materials are missing long-range order with only the **m₀-P** exhibiting a single broad, poorly defined reflection at $2\theta = 2\text{--}4^\circ$ ($\text{Co-K}_{\alpha 1}$), indicative of only weak structural coherence within the material (Figure S 9.3-13). These findings are consistent with the low Brunauer-Emmett-Teller (BET) surface areas of 25.3 $\text{m}^2 \text{ g}^{-1}$ (**m₁₀₀-P**) and 10.2 $\text{m}^2 \text{ g}^{-1}$ (**m₅₀-P**) for the motor containing polymers, and moderate values of 713 $\text{m}^2 \text{ g}^{-1}$ for the pure-spacer polymer **m₀-P**, probed by N_2 sorption analysis at 77 K (Figure S 9.3-39, Figure S 9.3-40, Figure S 9.3-41, Figure S 9.3-44, Figure S 9.3-45, Figure S 9.3-46). Furthermore, the total pore volumes for these materials are 0.04 $\text{cm}^3 \text{ g}^{-1}$, 0.03 $\text{cm}^3 \text{ g}^{-1}$ and 0.42 $\text{cm}^3 \text{ g}^{-1}$, respectively, showing porosity only for the non-motor containing polymer

m₀-P. However, given the lack of long-range order, the local molecular environment in these polymers is unknown.

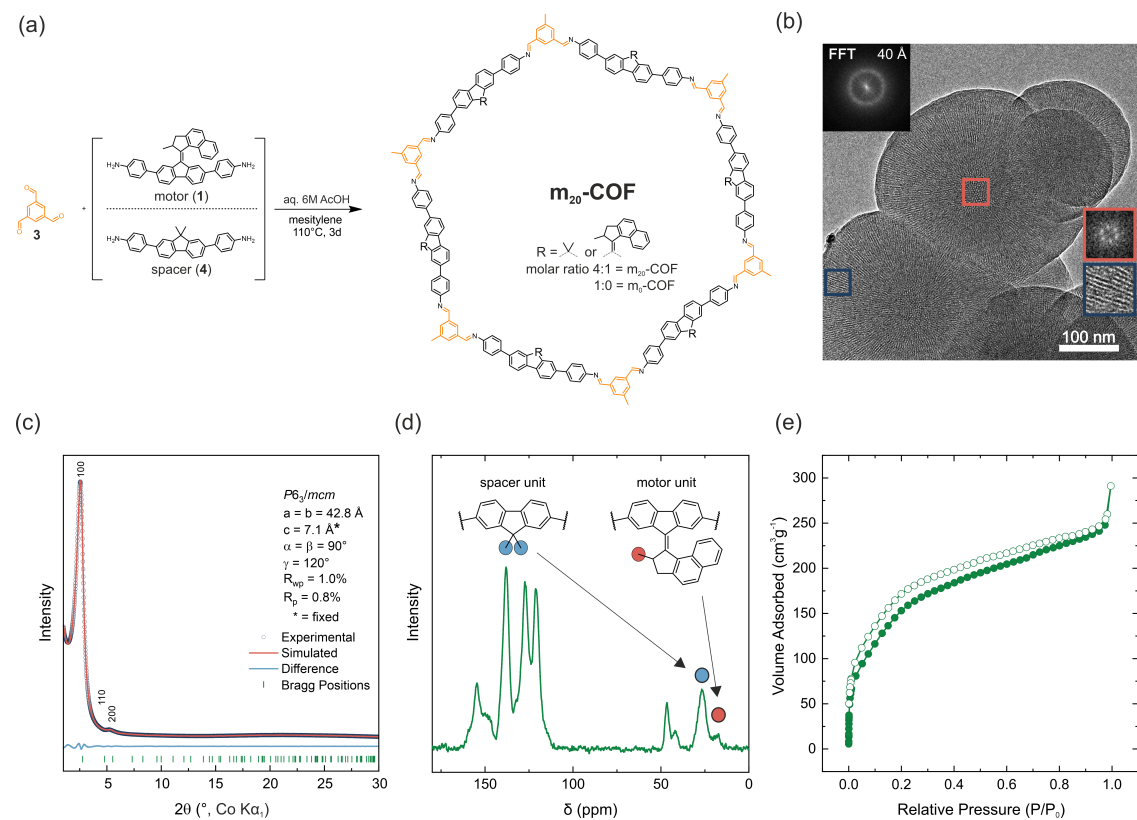


Figure 6-2: (a) Synthesis of **m₂₀-COF** from mixtures of spacer and motor building blocks with triformylbenzene (3) under solvothermal conditions. (b) Transmission electron microscopy (TEM) image of **m₂₀-COF** with visible pore channels along [001] pointing towards the surface of the spherical particle (blue inset). Fast Fourier transformed (FFT) insets show a hexagonal pattern (red box, viewing direction [001]). (c) XRPD pattern and unit cell parameters of **m₂₀-COF** obtained by Pawley refinement with a simplified unit cell proxy model (see Table S 9.3-1) (d) ¹³C-CPMAS ssNMR spectrum of **m₂₀-COF** containing signals of the motor and spacer building blocks. (e) N₂ adsorption isotherm of **m₂₀-COF**.

To realize a porous, motor-containing material, we made use of an orthogonal solvothermal synthesis approach with aqueous 6 M acetic acid as catalyst to enhance crystallinity.^[69] With this approach **m₂₀-COF** was crystallized from motor **1** and spacer **4** amine building blocks (4:1 molar ratio) and 1,3,5-triformyl benzene (**3**) in mesitylene as the solvent at 110 °C for 72 h (Figure 6-2a). This ratio of spacer and motor building blocks refers to a statistical loading of 1.2 motors per hexagonal pore in two layers, and thus ensures free void for the motor rotation. XRPD with Co-K_{α1} radiation shows two Bragg-like peaks at $2\theta = 2.6^\circ$ and 5.3° , indexed as 100 and 200 reflections using a crystalline eclipsed stacked structure as a proxy model (Figure 6-2c, Figure S 9.3-12) (space group $P6_3/mcm$). This supports the in-plane order of the layers, in spite of the random motor distribution. A Pawley refinement gives unit cell parameters $a = b = 42.8 \text{ \AA}$ (Figure 6-2c). Notably, due to the absence of any stacking reflections, the cell parameter c could not be refined and was fixed to an arbitrary

value of $c = 7.1$ Å, representing the calculated value of the lowest energy unit cell model (Table S 9.3-1).

The absence of amine ($\nu_{\text{N-H}}$) stretching bands in the FT-IR spectrum and the presence of the imine bands ($\nu_{\text{C=N}}$) at 1623 cm⁻¹ indicate condensation of the framework as previously described for the amorphous polymer (Figure S 9.3-6). ¹³C cross-polarization magic angle spinning (CP-MAS) ssNMR spectra support this finding as well, showing a characteristic signal for the imine carbon at $\delta = 154.6$ ppm (Figure 6-2d, S36). Additional signals in the aliphatic region were assigned with the aid of ¹H/¹³C heteronuclear correlation (HETCOR) spectroscopy (Figure S 9.3-37) and correspond to the spacer ($\delta = 46.5, 26.6$ ppm) and the motor unit ($\delta = 41.9, 26.6, 17.8$ ppm) incorporated into the framework. ¹³C direct-excitation (DE) experiments (Figure S 9.3-38) were carried out to obtain quantitative information about the motor/spacer ratio in the material. The signals at $\delta = 26.6$ (spacer), and 17.8 ppm (motor) in the ¹³C-DE spectrum were found to be sufficiently resolved (Figure 6-2d) and reveal a motor content of approximately 20% relative to spacer units (1.2 motors per pore in two layers). This value matches well with the theoretical content of 20%, indicating quantitative incorporation of the motor building block into the COF (relative to the starting ratio). Scanning electron microscopy (SEM) images show spherical, intergrown particles sized between 150 and 300 nm in diameter (Figure S 9.3-51) with uniform crystallinity and visible pore channels along [001] as evident from transmission electron microscopy (TEM) analysis (Figure S 9.3-52). The hexagonal pattern of the fast Fourier transformed TEM image (Figure 6-2b) further corroborates the symmetry and unit cell parameters obtained from Pawley refinement of the XRPD data. We performed N₂ adsorption experiments to gain insights into the porosity of **m₂₀-COF**. From the adsorption isotherms a BET surface area of $S_{\text{BET}} = 604$ m² g⁻¹ (0.45 cm³ g⁻¹ total pore volume) and an average pore size centered at 2.7 nm was observed, derived by the QSDFT model for cylindrical pores (Figure S 9.3-42, Figure S 9.3-47, Figure S 9.3-49). Interestingly, the value found for the average pore size is rather small and would be expected to be at least 3 nm for an idealized eclipsed stacking, compared to COFs with similar topology and lattice parameters.^[70] Recent reports showed weak interlayer interactions to cause a decrease in apparent pore diameter in similar COFs,^[71,72] due to a poor registry of the layers in the stacking direction.^[73] As this property also depends on the orientation of the building blocks in neighboring layers, we modeled different orientations of the amine building blocks in the framework and additionally assessed the local structure with the help of pair distribution function (PDF) analysis.^[74]

Since the large majority of the **m₂₀-COF** backbone consists of the spacer building block, we chose to simplify structure modeling by omitting the motor moiety in the model (Figure 6-3). A closer look at the molecular structure of the spacer building block (Figure 6-2a) reveals two characteristics of the amine building blocks that can influence the layer stacking: the curvature of the linker and two benzylic methyl groups of the dimethylfluorene core, oriented

perpendicularly to the aromatic system. These factors have a profound effect on the relative orientation of the building blocks in a condensed three-dimensional structure (Figure S 9.3-10). The steric demand of the methyl groups (and in the case of motor **1** the rotor parts alike), pointing into the interlayer space, can complicate the structure's ability to lower its energy based on the optimization between π - π interactions and dispersion forces.^[75, 76] This is particularly the case in structures with a parallel spacer orientation (Figure 6-3a), rendering parallel models energetically unfavorable.^[77] With an antiparallel orientation of the unit, a regular conformation of the imine linkages is equally needed to construct evenly shaped pore channels, but due to the curvature of the fluorene unit, the imine conformation also determines the possibility for sufficient stacking interactions across the layers.^[78-81] This constraint led to the development of three possible unit cell structure models, which differ mainly in their imine configuration (Figure S 9.3-11). A comparison of the total energies, obtained from Forcite geometry- and cell optimization in *Material Studio*, revealed the most favorable model with antiparallel stacking of the fluorene core and synchronized imine bonds pointing away from the dimethyl group (AA-1_EE, Table S 9.3-1) combining the least interlayer steric repulsion with best stacking interactions.

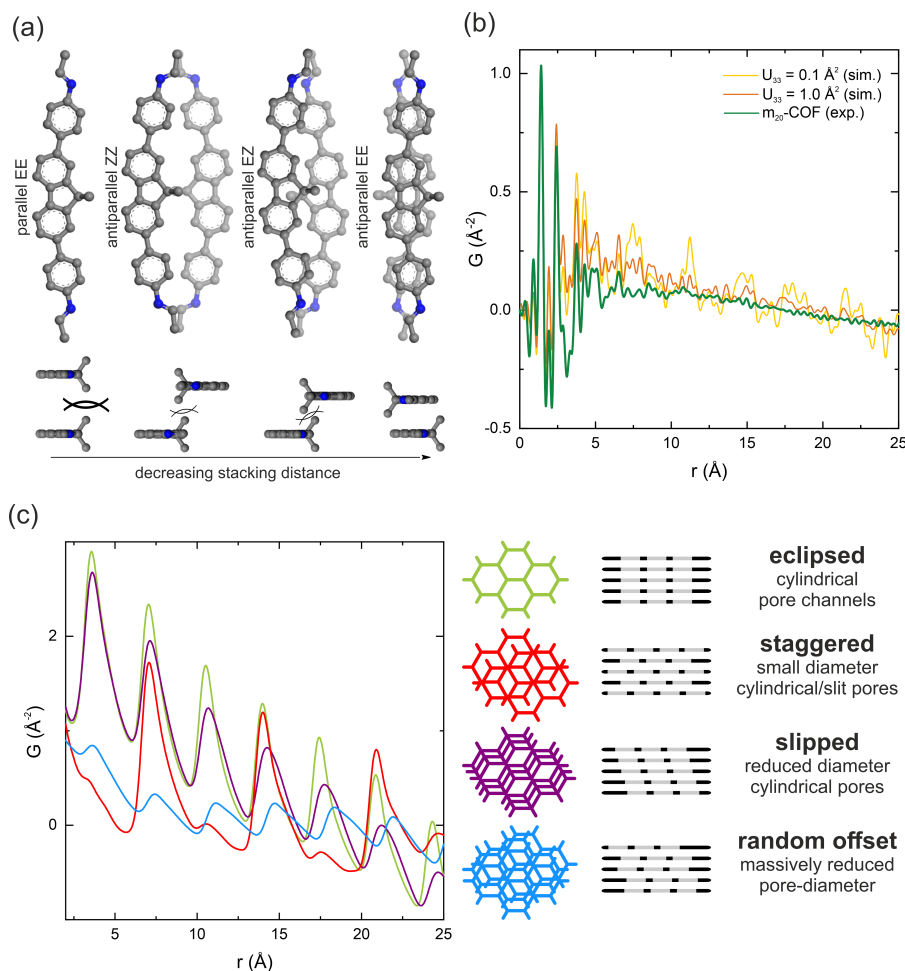


Figure 6-3: (a) Schematic illustration of molecular models probing the relative orientation and interlayer distance of the spacer moiety with respect to the imine bond configuration in a condensed framework. The antiparallel EE model combines the least steric repulsion of the methyl groups with best π overlap. (b) Experimental pair distribution function (PDF) for m_{20} -COF and simulated PDFs with different values of the

displacement parameter U_{33} , simulating the effects of stacking and conformational disorder, are overlaid. (c) Interlayer density distributions simulated for different layer offset scenarios in 2D honeycomb layered COFs are shown to demonstrate the specific impact of different relative stacking offsets on the PDF profile ($U_{11} = U_{22} = 1.0 \text{ \AA}^2$; $U_{33} = 0.05 \text{ \AA}^2$).

We employed PDF analysis on X-ray total scattering synchrotron data (Figure 6-3b, Figure S 9.3-17) to gain further insights into the local and intermediate length scale structure of the framework. The experimental PDF profile shows characteristic sharp peak profiles for atom-pair distances below $r = 5 \text{ \AA}$, provided by intralayer molecular connectivity, and a sloping baseline ($> 5 \text{ \AA}$) indicative of intralayer pore-pore correlations. Unlike other 2D COFs, interlayer correlations are not observed, indicating the relationship between the stacked, and even neighboring layers is not coherent, due to a broadened distribution of interatomic distances between neighboring layers.^[73, 82] Hence, a good qualitative agreement to the simulated pair distribution functions (AA-1_EE model) is obtained by implementing large atomic displacement parameters in the [001] direction (U_{33}), simulating different levels of reduction in interlayer coherence (Figure 6-3b). This agreement is not noticeably impacted if the motor unit is considered in the structural model, indicating that the motor units cannot be distinctly resolved without long-range ordering, since the bond distances in the motor units are too similar to the backbone of the material (Figure S 9.3-16).

Simple models have been developed to demonstrate how the interlayer correlations are modified to understand the absence of any stacking reflection (00l) and associated correlations of interlayer density.^[83] These are illustrated for the associated layered honeycomb structures in Figure 6-3c. In these models, large atomic displacement parameters (U_{11} , U_{22}) have been applied to wash out specific atom-pair correlations, resulting in effectively continuous density honeycombs. A shift from eclipsed to slipped stacking, for example, results in a broadening and effective shift of the interlayer density distribution (the distance of closest approach between neighboring branches does not change, but the maximum distance increases), while a staggered relationship decreases the amount of nearest neighbor correlations but maintains the second neighbor correlations still sitting in an eclipsed position. With completely randomized layer offsets, the intensity of the interlayer peaks for the model are substantially diminished, but still present due to the remaining equidistant spacing and thus cannot explain the absence of interlayer correlations as experimentally observed for **m₂₀-COF**. However, in the presented material conformational distortions are expected to be coupled with offsets, thus allowing the atoms in the layers to also move off their ideal positions in the stacking direction, resulting in a distribution of different interlayer distances. The combination of both offsets and conformational flexibility can lead to the extinction of the interlayer coherence, and no modulation in stacking density remains. This is further supported by simulated diffraction patterns for **m₂₀-COF** as a function of randomized layer offset magnitude (lateral) and interlayer displacement parameter using DIFFaX^[84] (Figure S 9.3-72). This is in contrast to continuous layered materials like graphite, because interlayer offsets lead to a wider distribution of possible

interlayer interaction environments due to the intrinsic porosity in the layers. In certain cases, with drastic offsets and additional factors, e.g. flexibility, causing out-of-plane distortions of the layers, this effect can lead to a practically X-ray amorphous, non-porous structure.^[82] However, in the case of **m₂₀-COF**, interlayer offsets and conformational distortions only decrease the apparent pore-diameter, while retaining an overall porous framework, as probed by N₂ sorption experiments.

Additional materials with 0%, 5%, and 10% motor-content (**m_{0/5/10}-COF**) were prepared under identical synthetic conditions as spectroscopic reference materials for COFs without motor-units (**m₀-COF**) and with reduced pore-occupancy. Notably, these materials showed essentially identical XRPD patterns and FT-IR spectra to **m₂₀-COF** (Figure S 9.3-7, Figure S 9.3-14). Due to the absence of motor units, **m₀-COF** exhibited a slightly increased BET surface area and pore volume of 938 m² g⁻¹ and 0.63 cm³ g⁻¹, respectively, and pore diameters of 2.9 nm vs. 2.7 nm in **m₂₀-COF** (Figure S 9.3-47, Figure S 9.3-48, Figure S 9.3-49, Figure S 9.3-50).

This comprehensive analysis suggests that additional functional groups (methyl or motor) drastically impact the formation of ordered layered COF materials. Nevertheless, the residual porosity and pore channels may in principle allow for movement of the rotor units and potential intra-framework dynamic processes.

6.2.3 Irradiation of Solid-State Materials

In situ Raman spectroscopy of the dried powdered materials under irradiation was carried out to investigate light-driven dynamics of the molecular motors in the polymers and COFs. In previous reports on metal-organic frameworks, this technique enabled the detection of light-stimulated formation of the metastable isomer as well as the thermal relaxation of the metastable state of the motor after photoexcitation.^[8, 11] With a half-life of 10.3 min for the imine functionalized motor **2**, the isomerization process is expected to be observable at ambient temperature as confirmed by the switching of the motor **2** in toluene (Figure 6-1d).

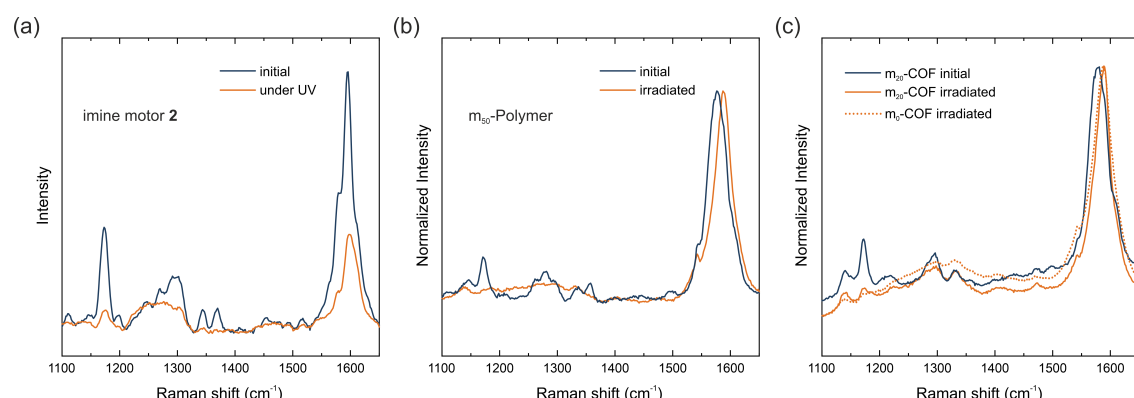


Figure 6-4: Raman spectra of the imine motor **2** as a thin-film (a), **m₅₀-P** (b), and **m₂₀-COF**. The thin-film of the molecular imine motor **2** was recorded at 785 nm and irradiated at 365 nm with a UV-LED. Raman

spectra of **m₅₀-P** (b), **m₂₀-COF** and **m₀-COF** (c) were recorded with a Raman laser at 355 nm for simultaneous excitation of the motor.

To identify motor-related signals in the Raman spectra, polymers were initially measured at 785 nm (Figure S 9.3-8). Primary signals at 1590, 1305, 1153 and 1178 cm⁻¹ for all polymers were identified. The motor containing polymers **m₅₀-P** and **m₁₀₀-P** additionally show weak bands at 1517, 1370, 1268 and 1115 cm⁻¹, attributed to the molecular motor.^[8] Due to the absorption of the motors, Raman measurements at 355 nm allowed for the simultaneous Raman scattering and excitation of the motor within the materials with a more intense light source (Figure 6-4b, c). Under these conditions, however, an irreversible decrease in signal strength and signal broadening occurred, identical to the behavior of a thin-film of the molecular imine functionalized motor **2** irradiated with a 365 nm LED (Figure 6-4a). This irreversible change of the spectrum caused a total loss of signals assigned to the motor moiety and thus prevents a detailed study of the rotary behavior of the motor in the material.

Raman spectra at 785 nm of the COF samples show similar signals as the polymers (Figure S 9.3-9). The spectra of all COF samples are almost identical irrespective of the amount of motor integrated in the material. Signals referring to the motors cannot be identified likely because the motor concentration in the materials is below the limit of detection. Nonetheless, a spectrum of **m₂₀-COF** was recorded at 355 nm and again a loss in signal intensity as well as broadening was observed during prolonged irradiation (Figure 6-4c). A comparison of the Raman spectra of **m₀-COF** and **m₂₀-COF** under irradiation shows that this observation is independent of the motor content, and occurs similarly with the amorphous polymers. To understand the unexpected intensity losses during the Raman measurements, we conducted additional experiments to probe changes in the chemical and long-range order. FT-IR spectra of the imine motor **2** thin film and **m₂₀-COF** (Figure 6-5a,b) show drastic changes for the molecular thin film **2** already after 5 min of irradiation with a UV-LED at 365 nm, whereas the spectrum for **m₂₀-COF** remained essentially unchanged even for prolonged irradiation (Figure 6-5b). The appearance of an intense, irreversible signal centered at 1697 cm⁻¹, attributed to an aldehyde C=O vibration, shows that the molecular imine motor **2** readily hydrolyzed under irradiation of a desolvated thin film. On the other hand, this is not observed for the porous framework, highlighting an increased hydrolytic stability of the imine if incorporated in the condensed COF-network.

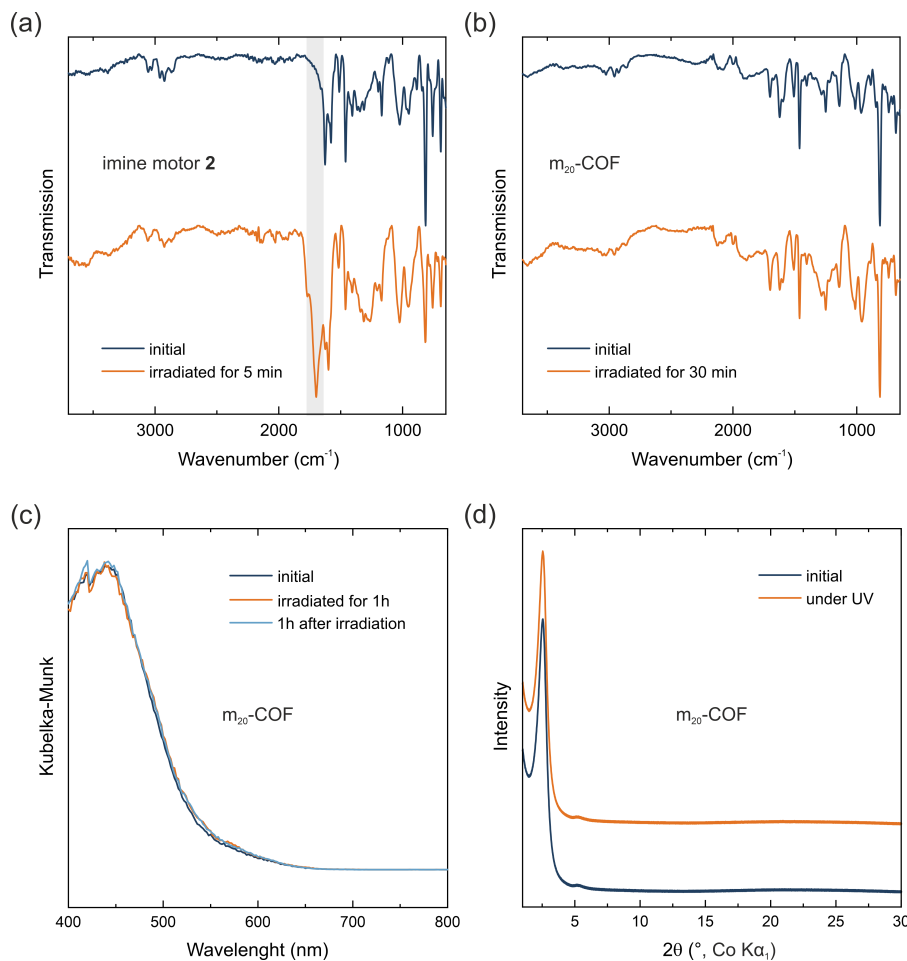


Figure 6-5: FT-IR spectra of a thin film of the imine motor **2** (a) and **m**₂₀-COF (b) under prolonged irradiation at 365 nm (UV-LED). Grey area highlights appearing C=O vibrations during irradiation of imine motor **2**. Direct reflectance UV/Vis spectra (c) and XRPD patterns of **m**₂₀-COF before and during irradiation (>1.5h) at 365 nm are shown. The patterns are stacked with an arbitrary offset to aid visibility.

Similar to the FT-IR spectra, UV/Vis absorption spectra and XRPD patterns of **m**₂₀-COF (Figure 6-5c, d) do not indicate any long-range structural changes or decomposition of the material even under irradiation at 365 nm with an LED for several hours. We thus attribute the observed intensity loss during Raman measurements to local heating effects under high intensity, focused light irradiation of the Raman laser. However, changes in the local structure, such as interlayer slipping/layer bending, or even local decomposition, perhaps driven or enhanced by local heating effects, may also occur and remain invisible to the available analytical techniques. Whereas these data clearly demonstrate the increased stability of the molecular building blocks in the condensed COF materials under irradiation, they also highlight that the applied spectroscopic and diffraction techniques are not sensitive to monitor motor excitation in the solid state at low motor loadings and consequently low fraction of the metastable state, emphasizing the need for local structural probes, such as PDF, to pinpoint the effects of interlayer shifting or strain formation on rotor dynamics.

6.3 Conclusion

Herein we present the first example of a molecular motor integrated within the backbone of an imine-based polymer and mesoporous COF using a novel diamine light-driven molecular motor. We detail synthesis strategies to enhance crystallinity by using an acid catalyst under solvothermal conditions and demonstrate that the motors are preserved under such harsh reaction conditions. Using a wide range of methods such as FT-IR, NMR, SEM, TEM, XRPD, PDF, DFT and nitrogen adsorption, we detail the composition, porosity, molecular, and framework structure of a series of motorized polymers and COFs. By this, we are able to identify the long-range and local structure of the motor-containing COF, building the basis for future investigations of such machine containing solids. As such, the materials described in this work can act as model compounds from which we identified two major challenges with respect to integration, operation and observation of light-driven molecular motors and photo-responsive dynamics in 2D layered covalent organic frameworks: i) sensitivity of analytical techniques towards low concentration of light-responsive functionality, and ii) local and long-range structural disorder induced by the interaction of adjacent layers.

In a 2D COF, curved building blocks such as motor **1** and spacer **4** affect the self-assembled structure drastically. The curvature results in different conformational combinations, which reduce the average periodicity of the stacked layers. The conformation of the imine linkage as well as the steric demand of perpendicularly oriented methyl groups or rotor parts in spacer **4** and motor **1**, respectively affect the stacking additionally. This has detrimental influence on interlayer stacking correlations and the available pore volume as well as the local environment of the motor. Yet, the accessible pore size is still found to exceed the radius of motor rotation. However, intermolecular interactions from adjacent layers may hamper or restrict motor movement even if commonly applied benchmarks for accessible void indicate otherwise. We thus conclude that local structural characteristics, such as interlayer interactions and stacking offset, which are invisible to most employed analytical methods, need to be considered for the development of analytical tools and the material's design to establish and investigate unrestricted motor dynamics in porous layered solids. Integrating molecular motors into three-dimensional COFs could circumvent this challenge. These materials are however challenging to synthesize and are prone to form interpenetrated structures, which can again constrain the available free volume for motor rotation.^[85]

Beyond these structural influences and design criteria, the commonly available and applied analytical techniques including solid-state NMR, FT-IR, and Raman spectroscopy did not allow us to draw a definite conclusion on the rotation ability of the motor in the solid polymer and COF materials. In the presented COF materials the motor signals could not be detected due to the low concentration in the solid. An increased motor content, however, concomitantly reduces the available pore void and thus interferes with the free rotation of the motor units, as demonstrated with the motor-containing polymer (**m₁₀₀-P**). Our study

thus highlights that new analytical techniques with high local sensitivity and *in-situ* operation have to be developed to study the behavior of motor dynamics in this class of porous materials further. Advanced *in-situ* ssNMR techniques under irradiation with abundant heteroatoms like fluorine and also ¹³C enriched motor units may enable to observe the rotation of embedded motors in these materials – if considered with structural characteristics, e.g. interlayer interactions and stacking offset, arising from the stacked layers. We envision that such analytical tools will also allow studies of interlayer dynamics and dynamic host-guest properties caused by the light-responsive dynamics of framework-embedded molecular motors. The synthetic procedures and in-depth structural characterization demonstrated herein provide access to these materials as model compounds and structural model systems. Furthermore, these can be used for in depth molecular dynamics simulations to probe design criteria for the operation of light-driven molecular motors in porous solids.

6.4 Acknowledgements

The authors thank Sebastian Emmerling for support with sorption measurements, Igor Moudrakovski for supporting ssNMR measurements and Viola Duppel for TEM and SEM analysis. C.S. and B.L.F. gratefully acknowledge support from the European Research Council (ERC Advanced grant no: 694345) and the Dutch Ministry of Education, Culture and Science (Gravitation program No. 024.001.035) (B.L.F and W.R.B.). Financial support by the Deutsche Forschungsgemeinschaft (DFG, German Research Foundation) – Project-ID 358283783 – SFB 1333, the Max Planck Society and the Cluster of Excellence e-conversion (Grant No. EXC2089) is gratefully acknowledged. S.K. and M.K. are grateful for financial support by the Alexander von Humboldt Foundation. S.K. gratefully acknowledges the Fonds der Chemischen Industrie for financial support. The authors acknowledge DESY (Hamburg, Germany), a member of the Helmholtz Association HGF, for the provision of experimental facilities. Parts of this research were carried out at beamline P02.1.

6.5 Bibliography

1. Browne W. R., Feringa B. L. Making Molecular Machines Work. *Nat. Nanotechnol.* **1**, 25-35 (2006).
2. Feringa B. L. The Art of Building Small: From Molecular Switches to Motors (Nobel Lecture). *Angew. Chem. Int. Ed.* **56**, 11060-11078 (2017).
3. Kassem S. et al. Artificial Molecular Motors. *Chem. Soc. Rev.* **46**, 2592-2621 (2017).
4. Iino R., Kinbara K., Bryant Z. Introduction: Molecular Motors. *Chem. Rev.* **120**, 1-4 (2020).
5. Pooler D. R. S., Lubbe A. S., Crespi S., Feringa B. L. Designing Light-Driven Rotary Molecular Motors. *Chem. Sci.* **12**, 14964-14986 (2021).
6. Kathan M. et al. A Light-Fuelled Nanoratchet Shifts a Coupled Chemical Equilibrium. *Nat. Nanotechnol.* **17**, 159-165 (2022).

7. Li Q. et al. Macroscopic Contraction of a Gel Induced by the Integrated Motion of Light-Driven Molecular Motors. *Nat. Nanotechnol.* **10**, 161-165 (2015).
8. Danowski W. et al. Unidirectional Rotary Motion in a Metal-Organic Framework. *Nat. Nanotechnol.* **14**, 488-494 (2019).
9. Moulin E., Faour L., Carmona-Vargas C. C., Giuseppone N. From Molecular Machines to Stimuli-Responsive Materials. *Adv. Mater.* **32**, e1906036 (2020).
10. Corra S. et al. Photoactivated Artificial Molecular Machines That Can Perform Tasks. *Adv. Mater.* **32**, e1906064 (2020).
11. Danowski W. et al. Visible-Light-Driven Rotation of Molecular Motors in a Dual-Function Metal-Organic Framework Enabled by Energy Transfer. *J. Am. Chem. Soc.* **142**, 9048-9056 (2020).
12. Coskun A. et al. Great Expectations: Can Artificial Molecular Machines Deliver on Their Promise? *Chem. Soc. Rev.* **41**, 19-30 (2012).
13. Baroncini M. et al. Making and Operating Molecular Machines: A Multidisciplinary Challenge. *ChemistryOpen* **7**, 169-179 (2018).
14. Dattler D. et al. Design of Collective Motions from Synthetic Molecular Switches, Rotors, and Motors. *Chem. Rev.* **120**, 310-433 (2020).
15. Krause S., Feringa B. L. Towards Artificial Molecular Factories from Framework-Embedded Molecular Machines. *Nat. Rev. Chem.* **4**, 550-562 (2020).
16. Grommet A. B., Lee L. M., Klajn R. Molecular Photoswitching in Confined Spaces. *Acc. Chem. Res.* **53**, 2600-2610 (2020).
17. Feng L. et al. Active Mechanisorption Driven by Pumping Cassettes. *Science* **374**, 1215-1221 (2021).
18. Payer D. et al. Toward Mechanical Switching of Surface-Adsorbed [2]Catenane by in Situ Copper Complexation. *J. Am. Chem. Soc.* **129**, 15662-15667 (2007).
19. Lu T., Zhang L., Gokel G. W., Kaifer A. E. The First Surface-Attached Catenane: Self-Assembly of a Two-Component Monolayer. *J. Am. Chem. Soc.* **115**, 2542-2543 (2002).
20. Norgaard K. et al. Structural Evidence of Mechanical Shuttling in Condensed Monolayers of Bistable Rotaxane Molecules. *Angew. Chem. Int. Ed.* **44**, 7035-7039 (2005).
21. Flood A. H. et al. The Role of Physical Environment on Molecular Electromechanical Switching. *Chem. Eur. J.* **10**, 6558-6564 (2004).
22. Foy J. T. et al. Dual-Light Control of Nanomachines That Integrate Motor and Modulator Subunits. *Nat. Nanotechnol.* **12**, 540-545 (2017).
23. van Delden R. A. et al. Unidirectional Molecular Motor on a Gold Surface. *Nature* **437**, 1337-1340 (2005).
24. Pollard M. M. et al. Light-Driven Rotary Molecular Motors on Gold Nanoparticles. *Chem. Eur. J.* **14**, 11610-11622 (2008).
25. Elkema R. et al. Rotational Reorganization of Doped Cholesteric Liquid Crystalline Films. *J. Am. Chem. Soc.* **128**, 14397-14407 (2006).
26. Elkema R. et al. Molecular Machines: Nanomotor Rotates Microscale Objects. *Nature* **440**, 163 (2006).

27. Castiglioni F. et al. Modulation of Porosity in a Solid Material Enabled by Bulk Photoisomerization of an Overcrowded Alkene. *Nat. Chem.* **12**, 595-602 (2020).
28. Martinez-Bulit P., Stirk A. J., Loeb S. J. Rotors, Motors, and Machines inside Metal-Organic Frameworks. *Trends Chem.* **1**, 588-600 (2019).
29. Krause S., Hosono N., Kitagawa S. Chemistry of Soft Porous Crystals: Structural Dynamics and Gas Adsorption Properties. *Angew. Chem. Int. Ed.* **59**, 15325-15341 (2020).
30. Kolodzeiski E., Amirjalayer S. Collective Structural Properties of Embedded Molecular Motors in Functionalized Metal-Organic Frameworks. *Phys. Chem. Chem. Phys.* **23**, 4728-4735 (2021).
31. Evans J. D., Krause S., Feringa B. L. Cooperative and Synchronized Rotation in Motorized Porous Frameworks: Impact on Local and Global Transport Properties of Confined Fluids. *Faraday Discuss.* **225**, 286-300 (2021).
32. Cote A. P. et al. Porous, Crystalline, Covalent Organic Frameworks. *Science* **310**, 1166-1170 (2005).
33. Stegbauer L., Schwinghammer K., Lotsch B. V. A Hydrazone-Based Covalent Organic Framework for Photocatalytic Hydrogen Production. *Chem. Sci.* **5**, 2789-2793 (2014).
34. Wei P. F. et al. Benzoxazole-Linked Ultrastable Covalent Organic Frameworks for Photocatalysis. *J. Am. Chem. Soc.* **140**, 4623-4631 (2018).
35. Liu X. et al. Recent Advances in Covalent Organic Frameworks (Cofs) as a Smart Sensing Material. *Chem. Soc. Rev.* **48**, 5266-5302 (2019).
36. Nguyen H. L. et al. A Porous Covalent Organic Framework with Voided Square Grid Topology for Atmospheric Water Harvesting. *J. Am. Chem. Soc.* **142**, 2218-2221 (2020).
37. Zhao X., Pachfule P., Thomas A. Covalent Organic Frameworks (Cofs) for Electrochemical Applications. *Chem. Soc. Rev.* **50**, 6871-6913 (2021).
38. Keller N., Bein T. Optoelectronic Processes in Covalent Organic Frameworks. *Chem. Soc. Rev.* **50**, 1813-1845 (2021).
39. Liu R. et al. Covalent Organic Frameworks: An Ideal Platform for Designing Ordered Materials and Advanced Applications. *Chem. Soc. Rev.* **50**, 120-242 (2021).
40. Zhu Y., Zhang W. Reversible Tuning of Pore Size and Co₂ Adsorption in Azobenzene Functionalized Porous Organic Polymers. *Chem. Sci.* **5**, 4957-4961 (2014).
41. Zhang J. et al. A Novel Azobenzene Covalent Organic Framework. *CrystEngComm* **16**, 6547-6551 (2014).
42. Das G. et al. Azobenzene-Equipped Covalent Organic Framework: Light-Operated Reservoir. *J. Am. Chem. Soc.* **141**, 19078-19087 (2019).
43. Sun N. et al. Photoresponsive Covalent Organic Frameworks with Diarylethene Switch for Tunable Singlet Oxygen Generation. *Chem. Mater.* **34**, 1956-1964 (2022).
44. Das G. et al. A Polyrotaxanated Covalent Organic Network Based on Viologen and Cucurbit[7]Uril. *Commun. Chem.* **2** (2019).

45. Ruan X. et al. Mechanical Bond Approach to Introducing Self-Adaptive Active Sites in Covalent Organic Frameworks for Zinc-Catalyzed Organophosphorus Degradation. *ACS Cent. Sci.* **7**, 1698-1706 (2021).
46. Haase F., Lotsch B. V. Solving the Cof Trilemma: Towards Crystalline, Stable and Functional Covalent Organic Frameworks. *Chem. Soc. Rev.* **49**, 8469-8500 (2020).
47. Feng L. et al. Destruction of Metal-Organic Frameworks: Positive and Negative Aspects of Stability and Lability. *Chem. Rev.* **120**, 13087-13133 (2020).
48. Rauche M. et al. New Insights into Solvent-Induced Structural Changes of (13)C Labelled Metal-Organic Frameworks by Solid State Nmr. *Chem. Commun.* **55**, 9140-9143 (2019).
49. Bessinger D. et al. Fast-Switching Vis-Ir Electrochromic Covalent Organic Frameworks. *J. Am. Chem. Soc.* **143**, 7351-7357 (2021).
50. Dey K. et al. Self-Assembly-Driven Nanomechanics in Porous Covalent Organic Framework Thin Films. *J. Am. Chem. Soc.* **143**, 955-963 (2021).
51. Chen J. et al. Artificial Muscle-Like Function from Hierarchical Supramolecular Assembly of Photoresponsive Molecular Motors. *Nat. Chem.* **10**, 132-138 (2018).
52. Koumura N. et al. Light-Driven Monodirectional Molecular Rotor. *Nature* **401**, 152-155 (1999).
53. Koumura N. et al. Second Generation Light-Driven Molecular Motors. Unidirectional Rotation Controlled by a Single Stereogenic Center with near-Perfect Photoequilibria and Acceleration of the Speed of Rotation by Structural Modification. *J. Am. Chem. Soc.* **124**, 5037-5051 (2002).
54. Vicario J., Meetsma A., Feringa B. L. Controlling the Speed of Rotation in Molecular Motors. Dramatic Acceleration of the Rotary Motion by Structural Modification. *Chem. Commun.* , 5910-5912 (2005).
55. Lehn J. M. From Supramolecular Chemistry Towards Constitutional Dynamic Chemistry and Adaptive Chemistry. *Chem. Soc. Rev.* **36**, 151-160 (2007).
56. Belowich M. E., Stoddart J. F. Dynamic Imine Chemistry. *Chem. Soc. Rev.* **41**, 2003-2024 (2012).
57. Li Y. et al. New Synthetic Strategies toward Covalent Organic Frameworks. *Chem. Soc. Rev.* **49**, 2852-2868 (2020).
58. Lohse M. S., Bein T. Covalent Organic Frameworks: Structures, Synthesis, and Applications. *Adv. Funct. Mater.* **28** (2018).
59. Mokhtari N., Afshari M., Dinari M. Synthesis and Characterization of a Novel Fluorene-Based Covalent Triazine Framework as a Chemical Adsorbent for Highly Efficient Dye Removal. *Polymer* **195** (2020).
60. Wang L. et al. Fluorene-Based Two-Dimensional Covalent Organic Framework with Thermoelectric Properties through Doping. *ACS Appl. Mater. Interfaces* **9**, 7108-7114 (2017).
61. Ma T. et al. Observation of Interpenetration Isomerism in Covalent Organic Frameworks. *J. Am. Chem. Soc.* **140**, 6763-6766 (2018).
62. Li R. L. et al. Two-Dimensional Covalent Organic Framework Solid Solutions. *J. Am. Chem. Soc.* **143**, 7081-7087 (2021).

63. Xue Y.-J. et al. Isomeric Effect of Fluorene-Based Fused-Ring Electron Acceptors to Achieve High-Efficiency Organic Solar Cells. *J. Mater. Chem. A* **8**, 5315-5322 (2020).

64. Chen X., Fu X., Qiu Y., Yuan J. 2,7-Dibromo-9,9-Dimethyl-9h-Fluorene. *Acta Cryst.* **66**, o1034 (2010).

65. Durka K., Kazimierczuk K., Luliński S. Dipole-Dipole Interactions of Sulfone Groups as a Tool for Self-Assembly of a 2d Covalent Organic Framework Derived from a Non-Linear Diboronic Acid. *Microporous Mesoporous Mater.* **337** (2022).

66. Conyard J. et al. Ultrafast Dynamics in the Power Stroke of a Molecular Rotary Motor. *Nat. Chem.* **4**, 547-551 (2012).

67. Giuseppone N., Schmitt J. L., Schwartz E., Lehn J. M. Scandium(Iii) Catalysis of Transimination Reactions. Independent and Constitutionally Coupled Reversible Processes. *J. Am. Chem. Soc.* **127**, 5528-5539 (2005).

68. Matsumoto M. et al. Rapid, Low Temperature Formation of Imine-Linked Covalent Organic Frameworks Catalyzed by Metal Triflates. *J. Am. Chem. Soc.* **139**, 4999-5002 (2017).

69. Emmerling S. T. et al. In Situ Monitoring of Mechanochemical Covalent Organic Framework Formation Reveals Templating Effect of Liquid Additive. *Chem* **7**, 1639-1652 (2021).

70. Evans A. M. et al. Trends in the Thermal Stability of Two-Dimensional Covalent Organic Frameworks. *Faraday Discuss.* **225**, 226-240 (2021).

71. Emmerling S. T. et al. Interlayer Interactions as Design Tool for Large-Pore Cofs. *J. Am. Chem. Soc.* **143**, 15711-15722 (2021).

72. Xu H., Gao J., Jiang D. Stable, Crystalline, Porous, Covalent Organic Frameworks as a Platform for Chiral Organocatalysts. *Nat. Chem.* **7**, 905-912 (2015).

73. Pütz A. M. et al. Total Scattering Reveals the Hidden Stacking Disorder in a 2d Covalent Organic Framework. *Chem. Sci.* **11**, 12647-12654 (2020).

74. Terban M. W., Billinge S. J. L. Structural Analysis of Molecular Materials Using the Pair Distribution Function. *Chem. Rev.* **122**, 1208-1272 (2022).

75. Koo B. T., Dichtel W. R., Clancy P. A Classification Scheme for the Stacking of Two-Dimensional Boronate Ester-Linked Covalent Organic Frameworks. *J. Mater. Chem.* **22**, 17460-17469 (2012).

76. Fan Y. et al. A Case Study on the Influence of Substitutes on Interlayer Stacking of 2d Covalent Organic Frameworks. *Chemistry* **23**, 5668-5672 (2017).

77. Martinez-Abadia M., Mateo-Alonso A. Structural Approaches to Control Interlayer Interactions in 2d Covalent Organic Frameworks. *Adv. Mater.* **32**, 2002366 (2020).

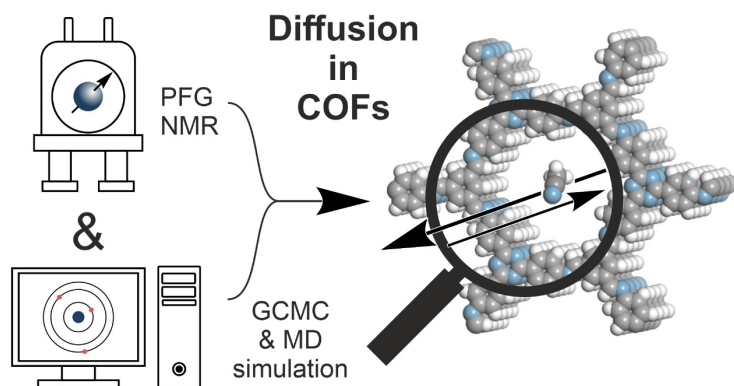
78. Albacete P. et al. Layer-Stacking-Driven Fluorescence in a Two-Dimensional Imine-Linked Covalent Organic Framework. *J. Am. Chem. Soc.* **140**, 12922-12929 (2018).

79. Yin H. Q., Yin F., Yin X. B. Strong Dual Emission in Covalent Organic Frameworks Induced by Esipt. *Chem. Sci.* **10**, 11103-11109 (2019).

80. Haase F. et al. Tuning the Stacking Behaviour of a 2d Covalent Organic Framework through Non-Covalent Interactions. *Mater. Chem. Front.* **1**, 1354-1361 (2017).

81. Xun S., Li H., Sini G., Bredas J. L. Impact of Imine Bond Orientations on the Geometric and Electronic Structures of Imine-Based Covalent Organic Frameworks. *Chem. Asian J.* **16**, 3781-3789 (2021).
82. Grunenberg L. et al. Amine-Linked Covalent Organic Frameworks as a Platform for Postsynthetic Structure Interconversion and Pore-Wall Modification. *J. Am. Chem. Soc.* **143**, 3430-3438 (2021).
83. Warren B. E. X-Ray Diffraction in Random Layer Lattices. *Phys. Rev.* **59**, 693-698 (1941).
84. Treacy M. M. J., Newsam J. M., Deem M. W. A General Recursion Method for Calculating Diffracted Intensities from Crystals Containing Planar Faults. *Proc. R. Soc. Lond. A* **433**, 499-520 (1991).
85. Gao C. et al. Redox-Triggered Switching in Three-Dimensional Covalent Organic Frameworks. *Nat. Commun.* **11**, 4919 (2020).

7 Self-Diffusion of Acetonitrile in a Covalent Organic Framework: Simulation and Experiment



The presented work of this chapter will be submitted for publication as:

Self-Diffusion of Acetonitrile in a Covalent Organic Framework: Simulation and Experiment

Lars Grunenberg[‡], Christopher Keßler,[‡] Tiong Wei Teh, Robin Schuldt, Fabian Heck, Johannes Kästner, Joachim Groß, Niels Hansen and Bettina V. Lotsch.

[‡] Authors contributed equally.

L.G. synthesized and analyzed the materials and precursors, performed PFG-NMR diffusion experiments and interpreted experimental data. C.K. performed GCMC and MD simulations with support by T.W.T. R.S. performed DFT calculations. F.H. performed gas and vapor sorption experiments. L.G. wrote the manuscript with input from C.K. and N.H. J.K., J.G., B.V.L. and N.H. supervised the research. All authors read and commented on the manuscript.

Abstract: Covalent Organic Frameworks have emerged as a promising class of porous materials. Quantifying the self-diffusion of guest molecules in the interior of their nanometer-sized pores is of relevance for a rational enhancement of performance in their various prospective technical applications. By means of pulsed field gradient nuclear magnetic resonance measurements and molecular dynamics simulations we probe the self-diffusion of acetonitrile in the 1.7 nm diameter pore channels of the imine-linked PI-3-COF between 270 K and 300 K. The molecular dynamics simulations predict a reduction of the self-diffusion coefficient on the single pore level by a factor of 5.4 compared to the bulk liquid value. The measurements are carried out in two samples of the material differing in their porosity. In the sample showing higher crystallinity and porosity anisotropic diffusion, i.e. parallel to the pore channel direction, is observed as characterized by a diffusion coefficient of $D_{par} = 6.1 \times 10^{-10} \text{ m}^2\text{s}^{-1}$, with $\Delta = 20 \text{ ms}$ at $T = 300 \text{ K}$. Self-diffusion in the material vs. bulk liquid is thus observed to be reduced by a factor of 7.4, which is in good agreement with the simulated values.

7.1 Introduction

2D covalent organic frameworks (COFs) are a unique class of materials, combining a high level of tunability with intrinsic structural porosity on a crystalline, covalently linked polymeric backbone. Their chemical structure can be tuned with atomic precision, rendering these materials an attractive scaffold for diverse applications, including gas storage and separation, sensing, electrochemical energy storage, and heterogeneous (photo)catalysis.^[1-9]

The typically large specific surface areas of these materials, and in particular the spatial arrangement of building blocks as encoded in the shape of the pore channels featuring adjustable diameters in the nanometer range, enables the utilization of confinement effects in heterogeneous catalysis, similar to those well-known from enzymes as biological catalysts.^[10] Spatial confinement in these pores allows a precise arrangement and relative orientation of catalytic centers and substrates in the pore channels and modulates the local concentration of reactants in the cavities.^[11, 12] These effects can be used as a handle to tailor product selectivity in catalytic reactions, e.g. by suppressing oligomerization in L-lactide synthesis from lactic acid.^[13] Recently, Lotsch, Buchmeiser, Plietker, Bauer and co-workers demonstrated that the ordered structural porosity of COFs enhances selectivity for (mono)macrocyclization during a ruthenium catalyzed olefin metathesis reaction, favoring ring closing over oligomerization.^[14] While the variation of pore size forms the basis for these effects, interactions between the reactants as well as of other molecules in the reaction mixture with the pore wall, become more dominant with a reduction in pore size.^[15] Acid/base interactions between catalytic substrates and reaction intermediates can affect the reaction rate, while collision events with the pore walls alter the in- and outflow of reactants.^[16, 17] This can lead either to localized concentration gradients affecting selectivity or, in the limiting case for very small pore diameters that exclude (competing) molecules

entirely, open up further areas of application, such as molecular sieving, or nanofiltration with these materials.^[18-22]

Computer simulations are well established in the field of porous media. Molecular dynamics (MD) simulations are a versatile tool to study self- and collective diffusion in crystalline porous media such as zeolites, MOFs and COFs^[23] or carbon nanotubes,^[24] but also in complex amorphous materials if a reasonable structural model is available.^[25] In contrast to zeolites^[26-30] and MOFs^[31-34] the investigation of self-diffusion in COFs so far focused on light gases such as hydrogen, nitrogen, carbon dioxide, methane and ethane.^[35-39] Molecular simulations in conjunction with experimental investigations leads to a fundamental understanding of nano-confinement effects,^[40] but such combined studies so far exclusively focused on MOFs^[41] and zeolites^[42]. Therefore, we herein present a combined experimental and computational study of the self-diffusion of acetonitrile in the two-dimensional covalent organic network PI-3-COF using Pulsed Field Gradient Nuclear Magnetic Resonance (PFG-NMR) spectroscopy and Grand Canonical Monte Carlo (GCMC) and MD simulations.

7.2 Results

7.2.1 Synthesis and Characterization of COFs

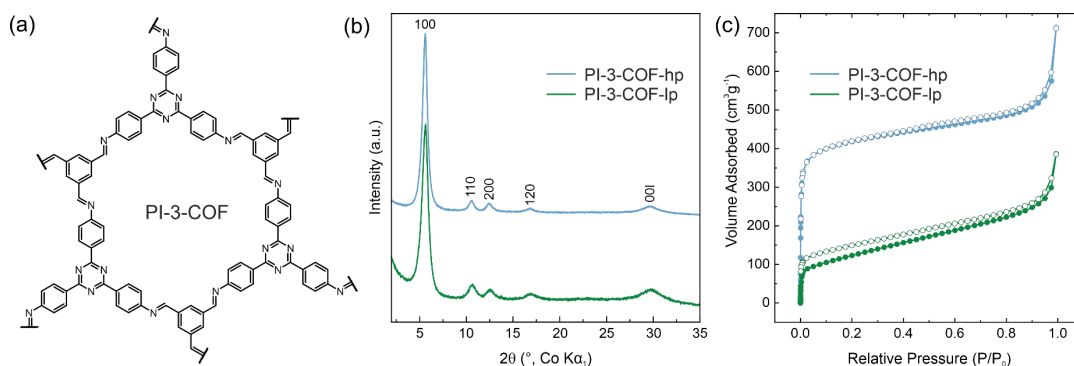


Figure 7-1: (a) Chemical structure of a single pore of PI-3-COF. (b) XRPD pattern and (c) N₂ adsorption isotherm comparison of PI-3-COF-lp (green) and PI-3-COF-hp (blue).

We first synthesized the imine-linked PI-3-COF from 1,3,5-triformyl benzene and 4,4',4''-(1,3,5-triazine-2,4,6-triyl)trianiline under solvothermal conditions, according to a previously reported procedure.^[43] We synthesized two samples of PI-3-COF, named PI-3-COF-lp (low porosity) and PI-3-COF-hp (high porosity), depending on the selected drying procedure (see SI for details). Fourier transform infrared (FT-IR) spectra of the yellow powdered materials indicate a successful condensation to the imine-linked frameworks, represented by the imine bond vibration ($\nu_{C=N}$) at 1630 cm⁻¹ (Figure S 9.4-2). The spectra for both samples appear essentially indistinguishable due to their identical chemical composition. Structural analysis by X-ray powder diffraction (XRPD) with Co-K_{α1} radiation shows four narrow reflections

at $2\theta = 6.6^\circ$, 11.5° , 13.2° , and 17.8° , indexed as 100, 110, 200, and 120 reflections (space group $P\bar{6}$), and a broad stacking reflection (00l) centered at $2\theta \approx 30^\circ$ (Figure S 9.4-3, Figure S 9.4-4). Bragg peaks in the XRPD pattern appear at identical positions for both hp- and lp-materials, but with a reduced full width at half maximum (FWHM) for the hp sample, hinting at a better structural definition and long-range order, i.e. crystallinity, of PI-3-COF-hp compared to its lp derivative. A Pawley refinement gives unit cell parameters of $a = b = 17.9 \text{ \AA}$ and $c = 3.55 \text{ \AA}$, which is in good agreement with previous reports.^[44] Scanning electron and transmission electron microscopy (SEM/TEM) images show agglomerated polycrystalline spherical particles and a polydisperse distribution of (secondary) particle sizes, approximately centered at $\sim 300 \text{ nm}$ in diameter (Figure S 9.4-5, Figure S 9.4-6) for both samples. Some agglomerates show sizes of multiple μm . The surface of these particles is decorated with stings, consisting of crystallites with average diameters of a few tens of nanometers (Figure S 9.4-7, Figure S 9.4-8). Nitrogen gas sorption experiments (Figure 7-1c) show a limited nitrogen uptake of PI-3-COF-lp and reveal BET surface areas of $S_{\text{BET}} = 442 \text{ m}^2\text{g}^{-1}$ and $1620 \text{ m}^2\text{g}^{-1}$ for PI-3-COF-lp and hp, respectively (Figure S 9.4-9, Figure S 9.4-10). Calculated pore size distributions by quenched solid density functional theory (QSDFT) based on a carbon model for cylindrical pores are centered at 1.7 nm for both PI-3-COF-lp and hp (Figure S 9.4-9b, Figure S 9.4-10b). With respect to the characterization data shown, we find that the difference between lp and hp lies in the extent of crystallinity, i.e. structural definition of the two samples, caused for example by inaccessible pores or disorder in PI-3-COF-lp and is not attributed to a difference in chemical composition. This leads to a reduced porosity in the case of PI-3-COF-lp compared to PI-3-COF-hp. Based on these findings we envisaged using these samples as a basis for PFG-NMR diffusion experiments to investigate the effect of porosity on the diffusivity.

7.2.2 Probing Diffusion Experimentally by PFG NMR

Due to its abundant use as an organic solvent in synthesis and its sufficiently long T_2 relaxation time (s.b., Table S 9.4-1), acetonitrile was selected to probe self-diffusion in the COFs. Acetonitrile thus acts as a proxy for probing self-diffusion of molecular reactants or intermediates in the pore system of a COF. Excess amounts of liquid on the outer particle surface or in the interparticle space distort the diffusion experiment and result in a major signal in the $^1\text{H-NMR}$ spectrum with bulk liquid-like mobility. To allow more selective filling of the pores in the materials, we exposed the vacuum-dried materials to saturated acetonitrile vapor in air. Consequently, condensation of acetonitrile into the pores of the material occurred. As indicated by a single, broadened and downfield shifted signal for acetonitrile due to confinement,^[45] which is centered at $\delta = 3.7 \text{ ppm}$ in the $^1\text{H-NMR}$ spectrum compared to the narrow signal for the isolated liquid at $\delta = 1.9 \text{ ppm}$ (Figure S 9.4-15), the liquid mainly condensed into the pores, instead of interparticle voids which would yield signals closer to the free liquid. The mass of the samples increased after this solvent vapor treatment, corresponding to loadings of 25 wt% (PI-3-COF-lp) and 39 wt% (PI-3-COF-hp) of

acetonitrile, respectively. Despite these high loadings, the appearance of the loaded materials were identical to the (dry) pristine materials. No liquid was visible on the surface.

PFG-NMR is a useful, non-destructive spectroscopic technique capable of tracking molecular motion and transport on a broad range of distances, varying from nanometers to hundreds of micrometers. By probing NMR signal attenuations at different diffusion times (Δ), spatial decoding of different diffusion regions and thus, localized as well as long-range information on the structure of porous materials, can be obtained.^[46, 47] Fitting of the NMR signal obtained by the pulsed field gradient method using the Stejskal-Tanner^[48] equation (Eq. 1), yields the diffusion coefficient (D) as a function of the gradient field strength (g), the gradient pulse duration (δ) and the gyromagnetic ratio of the probed nuclei (γ).

$$I = I_0 \exp \left[-\gamma^2 g^2 \delta^2 \left(\Delta - \frac{\delta}{3} \right) D \right] = I_0 \exp[-BD] \quad (\text{Eq. 1})$$

To select appropriate gradient strengths and observation parameters, the relaxation times of the molecules under study are required.^[49] Both longitudinal relaxation times ($T_{1,\text{lp}} = 1.8$ s) and transverse relaxation times ($T_{2,\text{lp}} = 0.54$ ms) of acetonitrile loaded onto PI-3-COFs were between one and three orders of magnitude shorter compared to the bulk liquid at 300 K (Table S 9.4-1), characteristic of smaller molecular mobility within the pores.^[50] On the one hand, this observation provides further evidence that MeCN is primarily located in the pores of the material, while on the other hand, short spin-spin relaxation times (T_2) lead to a fast decay of signal intensity in NMR experiments. This sets an experimental upper limit for the gradient pulse duration δ , as well as the diffusion time Δ . Long pulse durations and observation times lead to a bad signal-to-noise ratio, because most of the signal has decayed due to relaxation^[49] before the signal can be measured. At the same time, uniform and stable gradients in the spectrometer require a technically limited minimum duration for the gradient pulse, setting the lower limits for δ during a PFG experiment.^[46]

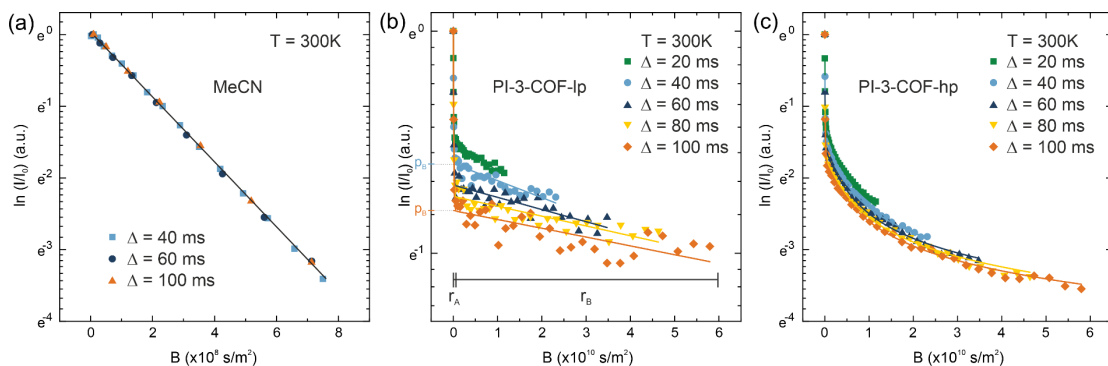


Figure 7-2: PFG-NMR spin-echo attenuation for (a) liquid MeCN, (b) MeCN loaded PI-3-COF-IP, (c) MeCN loaded PI-3-COF-hp with varying diffusion times (Δ) at $T = 300\text{K}$. Lines represent fits with a mono- or bi-exponential model for MeCN and MeCN loaded COFs, respectively.

For the presented PFG experiments, we chose the minimum technically possible value with our spectrometer of $\delta = 0.3$ ms (at high gradients $g_{\max} = 900 \text{ Gs}^1\text{cm}^{-1}$) to acquire PFG spin-echoes for diffusion times $\Delta = 20\text{--}100$ ms using a stimulated echo (ste) pulse sequence (see SI for details). As shown in Figure 7-2, the spin-echo attenuations appear non-linear for both samples, although linearity in the semi-logarithmic representation would be expected for regular isotropic diffusion of acetonitrile (Figure 7-2a, Figure S 9.4-13). The course of the signals can be separated into two regimes: A steeply decreasing initial range for small gradients (r_A) and then a slowly decaying range towards large gradients (r_B) at a fixed pulse duration $\delta = 0.3$ ms. This behavior is characteristic for a distribution of diffusion coefficients, for example observed in porous materials^[51] including zeolites^[52, 53] and MOFs,^[54] where regions with different translational mobilities are found. This behavior can be observed in these materials for example for molecules diffusing inside versus outside of crystallites.^[55] A bi-exponential model (Eq. 2) can fit attenuations with this behavior, where p_i reflects the population of the region (i) with diffusivity D_i .^[51, 56] The diffusivities of both regions appear as linear ranges in the semi-logarithmic plot.

$$\frac{I}{I_0} = p_A \exp[-BD_A] + p_B \exp[-BD_B] \quad (\text{Eq. 2})$$

The observed signal attenuations in PI-3-COF-lp (b) are in good agreement with this simple bi-exponential model. For varying diffusion times, different slopes are visible in the range r_B towards high gradients (Figure 7-2b), indicating a dependence of the diffusivity D_B on diffusion time Δ . With variation of Δ also the population p_i , which can be interpreted as the y-intercept of the linear, slowly decaying intensity extrapolated to $B = 0$ (Figure 7-2b), changes. The population p_B decreases with longer observation times (Figure 7-2b). This phenomenon indicates a molecular exchange between both regions in the material, expected for open pore channels in PI-3-COF, and can be used by the NMR tracer exchange method^[57] to determine the fraction of molecules and their mean lifetime τ_i within these regions.^[58, 59] With a defined macroscopic particle geometry, e.g. in single-crystals, or for spherical particles, their diffusivity and average lifetime allows to estimate mean particle/crystallite sizes.^[54, 60, 61] Unfortunately, the distribution of particles sizes and shapes in our materials, as observed by electron microscopy (Figure S 9.4-5, Figure S 9.4-6) does not allow for this analysis. Applying the simple bi-exponential model to PI-3-COF-lp yields two diffusion coefficients of $D_A = 1.7 \times 10^{-8} \text{ m}^2\text{s}^{-1}$ and $D_B = 1.4 \times 10^{-11} \text{ m}^2\text{s}^{-1}$, with $\Delta = 20$ ms at $T = 300$ K. A comparison of the exchange behavior between these regions at reduced temperature down to $T = 280$ K shows that the population p_A drops at reduced temperatures and the exchange between both regions becomes less prominent (Figure S 9.4-16). Analysis of the population p_B at these temperatures as a function of Δ further corroborates this finding, evident from a slower decrease of p_B vs. Δ at reduced temperature (Figure S 9.4-18). The diffusivity D_A exceeds the self-diffusion coefficient of pure acetonitrile

($D_s = 4.5 \times 10^{-9} \text{ m}^2\text{s}^{-1}$, Figure S 9.4-14) at $T = 300 \text{ K}$ by one order of magnitude. This observation and the strong temperature dependence of p_B (Figure S 9.4-18) suggest that D_A corresponds to an averaged diffusion of liquid acetonitrile molecules, which exchanged with the gas phase during the time of the NMR experiment.^[62, 63] With reduced temperature, the vapor pressure of acetonitrile and thus the partial pressure of MeCN in the gas phase, as well as the probability for a phase exchange during the observation time, is reduced. Contrary to p_A , we conclude that the molecules of the population p_B have not exchanged with the gas phase during the time of the NMR experiment, and can be labeled as the fraction of molecules remaining within the particle. Their diffusivity D_B thus denotes intraparticle diffusion of acetonitrile within the pore channels of the polycrystalline particles of PI-3-COF. A comparison of D_B at constant temperature (Figure S 9.4-19) shows a decrease of D_B with increasing diffusion times Δ . In contrast to this, diffusion in the non-confined, isotropic bulk-liquid is independent of Δ (Figure 7-2a, Figure S 9.4-13). Similar to observations in lithium ion conductors^[64] and polycrystalline faujasite crystals,^[65] long-range diffusion of MeCN in PI-3-COF-lp is limited by transport barriers (e.g. grain boundaries or surface effects^[52, 66]), whereas at small displacements these defects have less effect on the diffusion coefficient.^[52] To solely observe intracrystalline diffusion and reduce the influence of intercrystallite or interparticle diffusion resistances, D_B should ideally be measured at short diffusion times, where the mean square displacements ($\langle z^2 \rangle \approx 2D\Delta$) for most diffusing molecules in this time interval are smaller than the average crystallite diameter. However, due to technical limitations, Δ cannot be chosen arbitrarily small for high gradient values.^[46] Because the accessible isotropic diffusion lengths in the presented materials (μm range, Table S 9.4-2) exceed the observed crystallite size of a few tens of nanometers by SEM/TEM analysis (s. a.), only effective long-range diffusion coefficients can be obtained from the experiments. To estimate the order of magnitude for short-range diffusion in the pores of PI-3-COF, we extrapolated the experimental values for D_B towards short diffusion times in a phenomenological log(D)-log(Δ) plot, which has been used to describe for example restricted diffusion in zeolites (Figure S 9.4-20).^[52] The extrapolation suggests that D_B may approach values up to the order of $10^{-10} \text{ m}^2\text{s}^{-1}$ for PI-3-COF-lp. The extrapolated values, however, should be interpreted with care as they might overestimate short-range diffusivity: The experimental diffusion coefficients for D_B may still contain a contribution of a fraction of acetonitrile diffusing in textural mesopores or small voids between individual crystallites, the presence of which can be inferred from acetonitrile vapor sorption experiments with PI-3-COF-lp (Figure S 9.4-11). The vapor sorption isotherm at 300 K shows a steep uptake at low relative pressures ($P/P_{\text{sat}} < 0.13$), corresponding to the filling of micropores, i.e. pore channels (structural pores). Towards higher relative pressure, a further but less steep uptake with pronounced hysteresis is visible. This uptake is attributed to the filling of textural mesopores. In turn, we conclude that some signal intensity during the NMR experiments may be caused by acetonitrile molecules in small textural pores, besides those in structural pores (pore channels of PI-3-COF). In addition, the linearity of the signal corresponding to

intraparticle mobility D_B (Figure 7-2) as well as the absence of additional signals during relaxation experiments suggests that the obtained PFG attenuation is not amenable to further quantitative differentiation of structural and textural pores. Relaxation times (Table S 9.4-1) as well as diffusion coefficients of molecules in these different pore regimes may appear superimposed and thus indistinguishable, likely influenced by a fast exchange between them relative to the NMR experiment timescale.

The PFG NMR signal attenuation curves for MeCN loaded PI-3-COF-hp (Figure 7-2b) similarly show two separated ranges and exchange between the corresponding regions, evident from an offset of the slowly decaying range (r_B). In contrast to PI-3-COF-lp, however, the signal attenuation appears to be non-linear. This phenomenon indicates a contribution of anisotropic diffusion, which is in-line with a diffusion along the 1D pore channels of PI-3-COF. Similar attenuations have been observed for anisotropic diffusion in pore channels of aluminum fumarate MOFs^[55, 67] and mesoporous silica SBA-15.^[68] To address this effect of anisotropy to the observed PFG signal attenuation, the second term of the simple bi-exponential model was adjusted to a previously developed anisotropic model for hierarchically porous SBA-15 catalysts (Eq. 3).^[69] Notably, this model uses a simplified approximation to account for the molecular exchange between the different regions (p_A and p_{aniso}) in the material, based on the more complex solution developed by Spith *et. al.*^[55], which requires a negligibly small population p_A of the region with isotropic diffusion. Similar to the assumptions for the hierarchically ordered SBA-15 materials, however, we need to consider a fraction of MeCN present in small textural pores at the respective loadings of MeCN in the PI-3-COF samples under study, which is in contrast to the boundary conditions of the model by Spith *et. al.*

$$\frac{I}{I_0} \approx p_A \exp[-BD_A] + p_{aniso} \exp[-BD_{perp}] \left[\frac{\sqrt{\pi}}{2} \frac{\operatorname{erf}\{\sqrt{B(D_{par} - D_{perp})}\}}{\sqrt{B(D_{par} - D_{perp})}} \right] \quad (\text{Eq. 3})$$

Applying Eq. 3 to the observed signal attenuations for PI-3-COF-hp gives an isotropic diffusion coefficient D_A , and two different anisotropic diffusion coefficients for movement of molecules parallel (D_{par}) and perpendicular (D_{perp}) to the channel direction. The fit shows excellent agreement with experimental data (Figure 7-2c) and yields two diffusion coefficients of $D_A = 2.2 \times 10^{-8} \text{ m}^2\text{s}^{-1}$ and $D_{par} = 6.1 \times 10^{-10} \text{ m}^2\text{s}^{-1}$, with $\Delta = 20 \text{ ms}$ at $T = 300 \text{ K}$ and $D_{perp} \rightarrow 0$, which is in-line with the structural model of PI-3-COF consisting of closely stacked 2D layers that restrict diffusion between the layers, e.g. perpendicular to the channel direction. Analogous to the exchange behavior observed for PI-3-COF-lp, the material shows temperature-dependent molecular exchange between both regions, with D_A comprising contributions of gas diffusion through gas-liquid exchange during the observation time (Figure S 9.4-17). Extrapolation of the experimental values for D_{par} in the log(D)-log(Δ) plot^[52] gives values up to the order of $10^{-9} \text{ m}^2\text{s}^{-1}$, similar to diffusion in the bulk liquid, towards short diffusion times. In summary, diffusion in the high porosity sample is

less affected by defects or limited pore accessibility, resulting in an observable anisotropic diffusion parallel to the channel direction that is on average one to two orders of magnitude faster compared to PI-3-COF-lp.

7.2.3 Computational Modelling

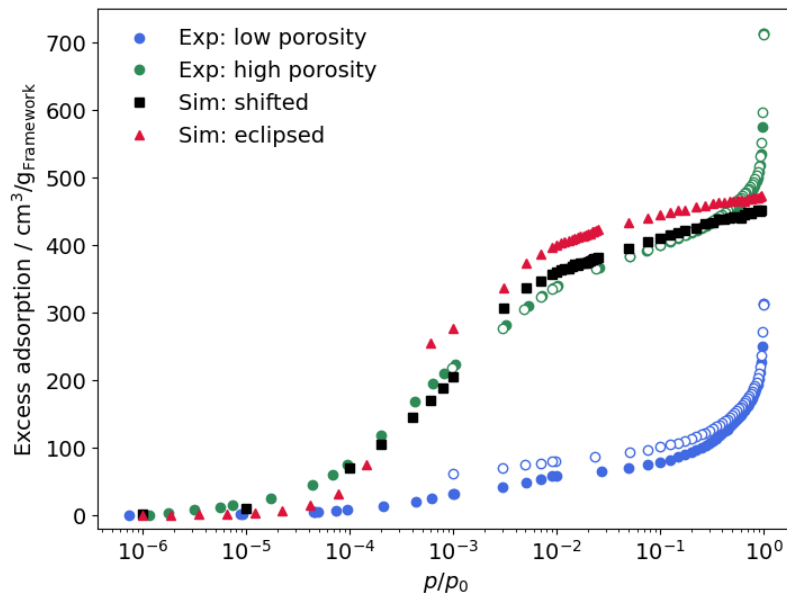


Figure 7-3 Comparison between experimental N_2 adsorption isotherms at 77K (low porosity in blue, high porosity in green) and simulated ones. The isotherm resulting from the shifted structure is depicted in black squares, the one of the eclipsed stacked structure in red triangles.

Following previous work^[70] the structural model obtained from X-ray powder diffraction experiments was refined by density functional calculations under periodic boundary conditions as described in more detail in the Supporting Information. Figure 7-3 shows simulated and experimental excess nitrogen adsorption isotherms for PI-3-COF. The two experimental curves correspond to the lp and hp samples while the two simulated curves correspond to a model structure in which the layers are perfectly eclipsed (red triangles) and one model structure in which two adjacent layers are slightly shifted by approx. 1.7 Å in an alternating way (black squares) such that the first and the third layer as well as the second and the fourth layer and so on are eclipsed. In both cases the interlayer distance was fixed to a value of 3.65 Å resulting from the DFT optimization for the shifted structure. The two structures are visualized in Figure 7-4. The good agreement between the simulated isotherms and the experimental curve of the hp sample indicates a high degree of crystallinity and accessibility of the experimental sample. In contrast to our previous work,^[70] no scaling factor was required to account for the finding that the simulation usually overestimated the experimental isotherm. The divergence of the experimental isotherms close to the saturation pressure results from condensation of nitrogen in textural macropores and is therefore not captured in the simulation, which is based on an infinite ideal structure. As found

previously,^[70] the isotherm corresponding to the shifted structure shows a smoother increase in loading with increasing pressure compared to the eclipsed structure. Given the qualitative difference between the two simulated isotherms in the medium pressure range between $p/p_0 = 10^{-4}$ and 10^{-2} despite rather small structural differences in the two model COFs, the good agreement between experiment and simulation over the entire pressure range is remarkable and suggests that the real structure in the material is characterized by small shifts between the different layers, likewise.

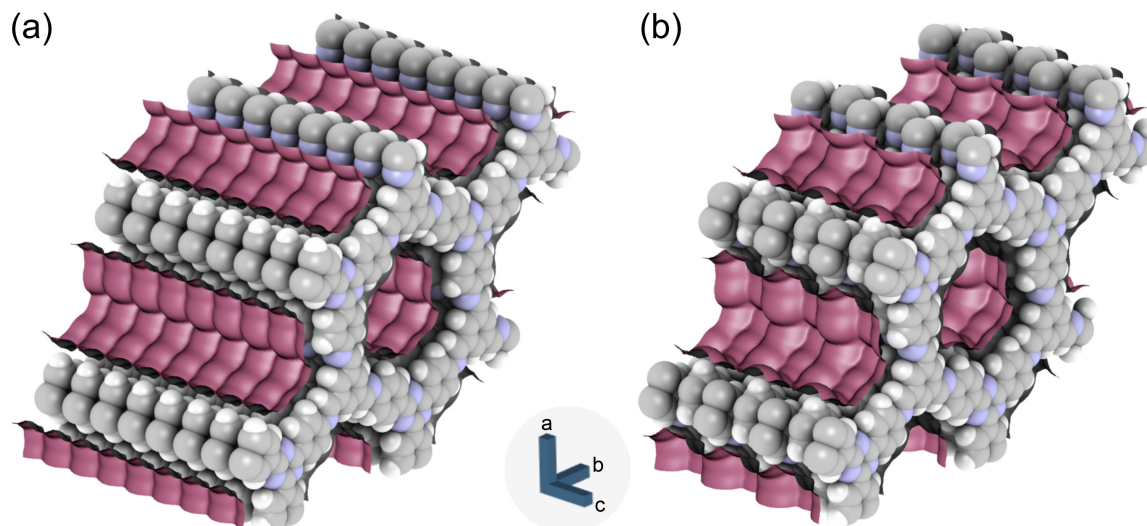


Figure 7-4 Visualization of the eclipsed (a) and the shifted structure (b) of PI 3-COF. Violet surfaces depict the N_2 accessible pore surface based on Van der Waals parameters.

The self-diffusion coefficient of acetonitrile in the two structures at 300 K amounts to $1.02 \times 10^{-9} \text{ m}^2\text{s}^{-1}$ in the perfectly eclipsed structure and to $0.7 \times 10^{-9} \text{ m}^2\text{s}^{-1}$ in the shifted structure, which corresponds to a reduction by a factor of 3.7 and 5.4, respectively, compared to the bulk liquid value of $3.76 \times 10^{-9} \text{ m}^2\text{s}^{-1}$ at 298 K, predicted by the molecular model. This bulk value is close to the experimentally determined self-diffusion coefficients reported in the literature ($D \approx 4.2 \times 10^{-9} \text{ m}^2\text{s}^{-1}$)^[71, 72] and measured in the present study ($D \approx 4.5 \times 10^{-9} \text{ m}^2\text{s}^{-1}$). However, since the simulated value of bulk diffusion does not exactly match experiment, it is reasonable to compare the ratios of the bulk and pore diffusion coefficients in addition to the absolute values. The ratio between the diffusion coefficients of liquid MeCN in bulk (this study) vs. PI-3-COF-hp (PFG) of 7.4 obtained in the present work is in good agreement with the ratio of 5.4 for the bulk value vs. the simulation result for the shifted structure at 300 K.

In other simulation works ratios of 2.0 and 3.2 were reported for diffusion of MeCN in a carbon nanotube of 1.5 nm diameter^[73] and an amorphous silica sample of 2.4 nm diameter^[74], respectively. Experimental studies reporting the self-diffusion of acetonitrile under confinement show a diverse picture. In pores smaller than 1 nm self-diffusion

coefficients on the order of $10^{-11} \text{ m}^2\text{s}^{-1}$ were measured for zeolite NaX^[58] and porous carbon^[75], respectively. In a sol-gel glass with a reported diameter of 2.9 nm a diffusion coefficient of $1.1 \times 10^{-9} \text{ m}^2\text{s}^{-1}$ was obtained^[76], i.e. similar to the diffusion coefficient reported for a mesoporous MCM-41 sample (pore size 3.6 nm, $D = 9.9 \times 10^{-10} \text{ m}^2\text{s}^{-1}$)^[77] and larger than the diffusion coefficient reported for a porous carbon (pore size 4.8 nm, $D = 6.0 \times 10^{-10} \text{ m}^2\text{s}^{-1}$)^[75]. Experiments probing a pore size similar to the one in the present work are scarce. For a MCM-41 sample with a pore size of 2 nm a diffusion coefficient of $2.7 \times 10^{-10} \text{ m}^2\text{s}^{-1}$ was reported^[77], which is relatively close to the value obtained for the hp sample in the present work.

7.3 Conclusion

The present work aims at clarifying the comparability of the self-diffusion coefficient of acetonitrile in a covalent organic framework obtained from MD simulations and PFG NMR measurements. For this purpose, two model structures were investigated in conjunction with a fluid model that captures the bulk diffusion coefficient reasonably well. The theoretical model, applied to ideal structural models of an isolated pore channel, suggests a comparably fast diffusion within the structural pore channels of PI-3-COF in both fully eclipsed and offset stacked cases, albeit with slightly reduced diffusivity in the offset stacked case. The obtained diffusion coefficients are slightly lower, yet roughly of the same order of magnitude as isotropic diffusion in the bulk liquid. We complemented our simulation studies with experimental data obtained by PFG NMR experiments. We observed short T_2 relaxation times for the confined liquid in the pores of PI-3-COF. This limits diffusion times and pulse durations applicable during PFG experiments. Due to the limited crystallite sizes in the polycrystalline COF particles, the experimentally observed diffusion coefficients were limited to mid-to-long range diffusion processes across multiple crystallites, given the technical limits for short pulse durations at high gradient strengths. By deconvolution of the obtained NMR signal attenuation, we identified multicomponent diffusion with open pore channels allowing the equilibrium exchange of molecules between surrounding vapor phase and liquid in pores. PFG measurements at reduced temperature helped to pinpoint these contributions by limiting the gas-liquid exchange. The experimental diffusivity in PI-3-COF samples was obtained as effective diffusion coefficients, decreasing for long diffusion times. This behavior points at real structure effects, e.g. defects and surface barriers at crystal boundaries within and between the particles.^[65, 78] For a sample of PI-3-COF with lower porosity these effects are more dominating compared to a sample with higher porosity, and led to the observation of effective diffusivities of the order of $10^{-11} \text{ m}^2\text{s}^{-1}$ and $10^{-10} \text{ m}^2\text{s}^{-1}$ for lp and hp samples, respectively. Extrapolation of the obtained diffusivities toward short diffusion times, i.e. small mean square displacements, indicate that short-range diffusion may be one (hp) to two orders (lp) of magnitude faster than the observable long-range diffusion. The high porosity sample of PI-3-COF showed anisotropy in diffusion, characterized by diffusivities which agree well with the simulated values for the offset stacked model, both being in the order of

$10^{-10} \text{ m}^2\text{s}^{-1}$. In contrast, the reduced structural definition of the lp sample merely led to the observation of isotropic diffusion only. This observation hints at strongly dominating diffusion barriers in the material restricting the diffusion of acetonitrile to shorter displacements and reducing its mobility, compared to the hp sample. Thus, we point out that a limited structural order not only reduces the accessible pore volume, i.e. porosity, but also restrict the mobility of molecules *via* diffusion barriers. As these are essentially invisible to typical analytical techniques, including gas sorption experiments, PFG NMR spectroscopy should be considered as a complementary method to assess diffusivity dependent parameters, such as turnover frequency or selectivity of reactions with COFs as heterogeneous catalysts.

Comparing the experimental to the simulated results, we obtained important findings for the real structure of the material. Our comparison between calculated nitrogen gas adsorption isotherms for eclipsed und offset structures in a pressure range $p/p_0 = 10^{-4}$ and 10^{-2} shows profound sensitivity for localized differences in the stacking and suggests small displacements of the layers in the material, since the experimentally observed isotherm of PI-3-COF-hp essentially resembles the simulated isotherms of the offset stacked structure with remarkable agreement. Thus, simulated isotherms may serve as a handle to pinpoint local characteristics in the real structure of the material, although these simulations are generally based on artificial, idealized structural models.

The combined experiments and simulations shine light on prevalent diffusion mechanisms and issues associated with the experimental determination of diffusion coefficients in covalent organic frameworks. However, the direct observation of pure short-range, i.e. undisturbed intracrystalline diffusion within the pore channels, requires large (ideally single crystalline) particles with pore channel lengths in the μm range. Powdered COF materials obtained from most established synthetic procedures do not meet this requirement, and obtaining crystallite-sizes in this range is a rarely tackled and challenging task for imine and other COFs.^[79] Nevertheless, our systematic computational and experimental study sets the stage for future exploration of diffusion processes in covalent organic frameworks. We propose that optimizing synthesis conditions to obtain domain sizes in the μm range should be the basis for future studies. With these requirements in mind, studies on the effect of pore sizes, chemical structure of the pore walls and their surface polarity, as well as the impact of meso/macro porosity on diffusion processes are expected to become accessible.

7.4 Acknowledgements

The authors thank Viola Duppel for supporting this work with SEM and TEM images. We also thank Igor Moudrakovski for introducing L.G. to PFG NMR experimentation. This work was funded by the Deutsche Forschungsgemeinschaft (DFG, German Research Foundation), Germany - Project-ID 358283783 - SFB 1333/2 2022. We also thank the DFG for supporting this work by funding EXC 2075/1 - 390740016 and EXC 2089/1 -

390776260 under Germany's Excellence Strategy. Financial support by the Max Planck Society is gratefully acknowledged. We appreciate the support by the Stuttgart Center for Simulation Science (SimTech), Germany. Monte Carlo and molecular dynamics simulations were performed on the computational resource BinAC at High Performance and Cloud Computing Group at the Zentrum für Datenverarbeitung of the University of Tübingen, funded by the state of Baden-Württemberg through bwHPC and the German Research Foundation (DFG) through grant no INST 37/935-1 FUGG.

7.5 Bibliography

1. Keller N., Bein T. Optoelectronic Processes in Covalent Organic Frameworks. *Chem. Soc. Rev.* **50**, 1813-1845 (2021).
2. Lohse M. S., Bein T. Covalent Organic Frameworks: Structures, Synthesis, and Applications. *Adv. Funct. Mater.* **28** (2018).
3. Lyu H. et al. Covalent Organic Frameworks for Carbon Dioxide Capture from Air. *J. Am. Chem. Soc.* **144**, 12989-12995 (2022).
4. Xu F. et al. Energy-Storage Covalent Organic Frameworks: Improving Performance Via Engineering Polysulfide Chains on Walls. *Chem. Sci.* **10**, 6001-6006 (2019).
5. Xu F. et al. Radical Covalent Organic Frameworks: A General Strategy to Immobilize Open-Accessible Polyradicals for High-Performance Capacitive Energy Storage. *Angew. Chem. Int. Ed.* **54**, 6814-6818 (2015).
6. Furukawa H., Yaghi O. M. Storage of Hydrogen, Methane, and Carbon Dioxide in Highly Porous Covalent Organic Frameworks for Clean Energy Applications. *J. Am. Chem. Soc.* **131**, 8875-8883 (2009).
7. Diercks C. S. et al. Reticular Electronic Tuning of Porphyrin Active Sites in Covalent Organic Frameworks for Electrocatalytic Carbon Dioxide Reduction. *J. Am. Chem. Soc.* **140**, 1116-1122 (2018).
8. Wang X. et al. Sulfone-Containing Covalent Organic Frameworks for Photocatalytic Hydrogen Evolution from Water. *Nat. Chem.* **10**, 1180-1189 (2018).
9. Biswal B. P. et al. Sustained Solar H(2) Evolution from a Thiazolo[5,4-D]Thiazole-Bridged Covalent Organic Framework and Nickel-Thiolate Cluster in Water. *J. Am. Chem. Soc.* **141**, 11082-11092 (2019).
10. Mitschke B., Turberg M., List B. Confinement as a Unifying Element in Selective Catalysis. *Chem* **6**, 2515-2532 (2020).
11. Tan K. T., Tao S., Huang N., Jiang D. Water Cluster in Hydrophobic Crystalline Porous Covalent Organic Frameworks. *Nat. Commun.* **12**, 6747 (2021).
12. Zeng W. J. et al. Covalent Organic Frameworks as Micro-Reactors: Confinement-Enhanced Electrochemiluminescence. *Chem. Sci.* **11**, 5410-5414 (2020).
13. Zhao J. et al. A "One-Step" Approach to the Highly Efficient Synthesis of Lactide through the Confinement Catalysis of Covalent Organic Frameworks. *Green Chem.* **25**, 3103-3110 (2023).
14. Emmerling S. T. et al. Olefin Metathesis in Confinement: Towards Covalent Organic Framework Scaffolds for Increased Macrocyclization Selectivity. *Chemistry* **28**, e202104108 (2022).

15. Gao W. Y., Cardenal A. D., Wang C. H., Powers D. C. In Operando Analysis of Diffusion in Porous Metal-Organic Framework Catalysts. *Chem. Eur. J.* **25**, 3465-3476 (2019).
16. Fang Q. et al. 3d Microporous Base-Functionalized Covalent Organic Frameworks for Size-Selective Catalysis. *Angew. Chem. Int. Ed.* **53**, 2878-2882 (2014).
17. North A. M. Diffusion-Controlled Reactions. *Q. Rev. Chem. Soc.* **20**, 421 (1966).
18. Shinde D. B. et al. Crystalline 2d Covalent Organic Framework Membranes for High-Flux Organic Solvent Nanofiltration. *J. Am. Chem. Soc.* **140**, 14342-14349 (2018).
19. Shi X. et al. Design of Three-Dimensional Covalent Organic Framework Membranes for Fast and Robust Organic Solvent Nanofiltration. *Angew. Chem. Int. Ed.* **61**, e202207559 (2022).
20. Karak S., Dey K., Banerjee R. Maneuvering Applications of Covalent Organic Frameworks Via Framework-Morphology Modulation. *Adv. Mater.* **34**, e2202751 (2022).
21. Wang R., Guo J., Xue J., Wang H. Covalent Organic Framework Membranes for Efficient Chemicals Separation. *Small Struct.* **2**, 2100061 (2021).
22. Yang Y. et al. Constructing Chemical Stable 4-Carboxyl-Quinoline Linked Covalent Organic Frameworks Via Doeblner Reaction for Nanofiltration. *Nat. Commun.* **13**, 2615 (2022).
23. Krishna R. Describing the Diffusion of Guest Molecules inside Porous Structures. *J. Phys. Chem. C* **113**, 19756-19781 (2009).
24. Jakobtorweihen S. et al. Understanding the Loading Dependence of Self-Diffusion in Carbon Nanotubes. *Phys. Rev. Lett.* **95**, 044501 (2005).
25. Obliger A., Bousige C., Coasne B., Leyssale J.-M. Development of Atomistic Kerogen Models and Their Applications for Gas Adsorption and Diffusion: A Mini-Review. *Energy Fuels* **37**, 1678-1698 (2023).
26. Dubbeldam D., Snurr R. Q. Recent Developments in the Molecular Modeling of Diffusion in Nanoporous Materials. *Mol. Simul.* **33**, 305-325 (2007).
27. Jobic H., Theodorou D. N. Quasi-Elastic Neutron Scattering and Molecular Dynamics Simulation as Complementary Techniques for Studying Diffusion in Zeolites. *Microporous Mesoporous Mater.* **102**, 21-50 (2007).
28. Demontis P., Suffritti G. B. Structure and Dynamics of Zeolites Investigated by Molecular Dynamics. *Chem. Rev.* **97**, 2845-2878 (1997).
29. Sholl D. S. Understanding Macroscopic Diffusion of Adsorbed Molecules in Crystalline Nanoporous Materials Via Atomistic Simulations. *Acc. Chem. Res.* **39**, 403-411 (2006).
30. Smit B., Maesen T. L. Molecular Simulations of Zeolites: Adsorption, Diffusion, and Shape Selectivity. *Chem. Rev.* **108**, 4125-4184 (2008).
31. Skouidas A. I. Molecular Dynamics Simulations of Gas Diffusion in Metal-Organic Frameworks: Argon in Cubtc. *J. Am. Chem. Soc.* **126**, 1356-1357 (2004).
32. Skouidas A. I., Sholl D. S. Self-Diffusion and Transport Diffusion of Light Gases in Metal-Organic Framework Materials Assessed Using Molecular Dynamics Simulations. *J. Phys. Chem. B* **109**, 15760-15768 (2005).

33. Yang Q., Zhong C. Molecular Simulation of Adsorption and Diffusion of Hydrogen in Metal-Organic Frameworks. *J. Phys. Chem. B* **109**, 11862-11864 (2005).
34. Düren T., Snurr R. Q. Assessment of Isoreticular Metal-Organic Frameworks for Adsorption Separations: A Molecular Simulation Study of Methane/N-Butane Mixtures. *J. Phys. Chem. B* **108**, 15703-15708 (2004).
35. Garberoglio G., Vallauri R. Adsorption and Diffusion of Hydrogen and Methane in 2d Covalent Organic Frameworks. *Microporous Mesoporous Mater.* **116**, 540-547 (2008).
36. Keskin S. Adsorption, Diffusion, and Separation of Ch4/H2 Mixtures in Covalent Organic Frameworks: Molecular Simulations and Theoretical Predictions. *J. Phys. Chem. C* **116**, 1772-1779 (2012).
37. Yang Z., Cao D. Effect of Li Doping on Diffusion and Separation of Hydrogen and Methane in Covalent Organic Frameworks. *J. Phys. Chem. C* **116**, 12591-12598 (2012).
38. Zeng H., Liu Y., Liu H. Adsorption and Diffusion of Co2 and Ch4 in Covalent Organic Frameworks: An Mc/Md Simulation Study. *Mol. Simul.* **44**, 1244-1251 (2018).
39. Altundal O. F., Haslak Z. P., Keskin S. Combined Gcmc, Md, and Dft Approach for Unlocking the Performances of Cofs for Methane Purification. *Ind. Eng. Chem. Res.* **60**, 12999-13012 (2021).
40. Bukowski B. C. et al. Connecting Theory and Simulation with Experiment for the Study of Diffusion in Nanoporous Solids. *Adsorption* **27**, 683-760 (2021).
41. Ford D. C. et al. Self-Diffusion of Chain Molecules in the Metal-Organic Framework Irmof-1: Simulation and Experiment. *J. Phys. Chem. Lett.* **3**, 930-933 (2012).
42. Dutta S. et al. Molecular Diffusion in Hierarchical Zeolites with Ordered Mesoporosity: Pulsed Field Gradient Nuclear Magnetic Resonance Combined with Thermodynamic Modeling. *J. Phys. Chem. C* **127**, 1548-1559 (2023).
43. Grunenberg L. et al. Postsynthetic Transformation of Imine- into Nitrone-Linked Covalent Organic Frameworks for Atmospheric Water Harvesting at Decreased Humidity. *J. Am. Chem. Soc.* **145**, 13241-13248 (2023).
44. Grunenberg L. et al. Amine-Linked Covalent Organic Frameworks as a Platform for Postsynthetic Structure Interconversion and Pore-Wall Modification. *J. Am. Chem. Soc.* **143**, 3430-3438 (2021).
45. Das A. et al. Single-File Diffusion of Confined Water inside Swnts: An Nmr Study. *ACS Nano* **4**, 1687-1695 (2010).
46. Kärger J. et al. Pulsed Field Gradient Nmr Diffusion Measurement in Nanoporous Materials. *Adsorption* **27**, 453-484 (2021).
47. Kärger J., Chmelik C., Heinke L., Valiullin R. A New View of Diffusion in Nanoporous Materials. *Chem. Ing. Tech.* **82**, 779-804 (2010).
48. Tanner J. E. Use of the Stimulated Echo in Nmr Diffusion Studies. *J. Chem. Phys.* **52**, 2523-2526 (1970).
49. Kärger J., Pfeifer H., Heink W. Principles and Application of Self-Diffusion Measurements by Nuclear Magnetic Resonance. In: Waugh JS (ed). *Advances in Magnetic and Optical Resonance*, vol. 12. Academic Press, 1988, pp 1-89.
50. Hertel S. et al. Nmr Studies of Benzene Mobility in Metal-Organic Framework Mof-5. *The European Physical Journal Applied Physics* **55** (2011).

51. Valiullin R. R., Skirda V. D., Stapf S., Kimmich R. Molecular Exchange Processes in Partially Filled Porous Glass as Seen with Nmr Diffusometry. *Phys. Rev. E* **55**, 2664-2671 (1997).
52. Hedin N. et al. Intracrystalline Transport Barriers Affecting the Self-Diffusion of Ch(4) in Zeolites $|\text{Na}(12)|\text{-a}$ and $|\text{Na}(12-\text{X})\text{K}(\text{X})|\text{-A}$. *Langmuir* **35**, 12971-12978 (2019).
53. Morgan M., Cosgrove T., Richardson R. The Diffusion of Benzene in High Silica Zeolite Zsm5 Studied by Pfgnmr and Quens. *Colloids Surf.* **36**, 209-219 (1989).
54. Stallmach F. et al. Nmr Studies on the Diffusion of Hydrocarbons on the Metal-Organic Framework Material Mof-5. *Angew. Chem. Int. Ed.* **45**, 2123-2126 (2006).
55. Splith T., Frohlich D., Henninger S. K., Stallmach F. Development and Application of an Exchange Model for Anisotropic Water Diffusion in the Microporous Mof Aluminum Fumarate. *J. Magn. Reson.* **291**, 40-46 (2018).
56. Kärger J. Zur Bestimmung Der Diffusion in Einem Zweibereichsystem Mit Hilfe Von Gepulsten Feldgradienten. *Ann. Phys.* **479**, 1-4 (1969).
57. Kärger J. A Study of Fast Tracer Desorption in Molecular Sieve Crystals. *AIChE J.* **28**, 417-423 (1982).
58. Kärger J., Pfeifer H. N.M.R. Self-Diffusion Studies in Zeolite Science and Technology. *Zeolites* **7**, 90-107 (1987).
59. Zeigermann P. et al. Diffusion in Hierarchical Mesoporous Materials: Applicability and Generalization of the Fast-Exchange Diffusion Model. *Langmuir* **28**, 3621-3632 (2012).
60. Loskutov V. V., Sevriugin V. A. A Novel Approach to Interpretation of the Time-Dependent Self-Diffusion Coefficient as a Probe of Porous Media Geometry. *J. Magn. Reson.* **230**, 1-9 (2013).
61. Latour L. L., Mitra P. P., Kleinberg R. L., Sotak C. H. Time-Dependent Diffusion Coefficient of Fluids in Porous Media as a Probe of Surface-to-Volume Ratio. *J. Magn. Reson.* **101**, 342-346 (1993).
62. Forse A. C. et al. Influence of Pore Size on Carbon Dioxide Diffusion in Two Isoreticular Metal-Organic Frameworks. *Chem. Mater.* **32**, 3570-3576 (2020).
63. Vasenkov S., Geir O., Karger J. Gas Diffusion in Zeolite Beds: Pfg Nmr Evidence for Different Tortuosity Factors in the Knudsen and Bulk Regimes. *Eur Phys J E Soft Matter* **12 Suppl 1**, S35-38 (2003).
64. Holzmann T. et al. Li0.6[Li0.2sn0.8s2] – a Layered Lithium Superionic Conductor. *Energy & Environmental Science* **9**, 2578-2585 (2016).
65. Beckert S. et al. Tracing Water and Cation Diffusion in Hydrated Zeolites of Type Li-Lsx by Pulsed Field Gradient Nmr. *J. Phys. Chem. C* **117**, 24866-24872 (2013).
66. Krutyeva M. et al. Surface Barriers on Nanoporous Particles: A New Method of Their Quantitation by Pfg Nmr. *Microporous Mesoporous Mater.* **104**, 89-96 (2007).
67. Peksa M., Lang J., Stallmach F. 13c Nmr Study of Diffusion Anisotropy of Carbon Dioxide Adsorbed in Nanoporous Dmof-1. *Microporous Mesoporous Mater.* **205**, 11-15 (2015).
68. Naumov S. et al. Tracing Pore Connectivity and Architecture in Nanostructured Silica Sba-15. *Microporous Mesoporous Mater.* **110**, 37-40 (2008).

69. Isaacs M. A. et al. Unravelling Mass Transport in Hierarchically Porous Catalysts. *J. Mater. Chem. A* **7**, 11814-11825 (2019).
70. Kessler C. et al. Influence of Layer Slipping on Adsorption of Light Gases in Covalent Organic Frameworks: A Combined Experimental and Computational Study. *Microporous Mesoporous Mater.* **336**, 111796 (2022).
71. Viel S. et al. Pulsed Field Gradient Magic Angle Spinning Nmr Self-Diffusion Measurements in Liquids. *J. Magn. Reson.* **190**, 113-123 (2008).
72. Cohen S. R. et al. Structure and Dynamics of Acetonitrile: Molecular Simulation and Neutron Scattering. *J. Mol. Liq.* **348**, 118423 (2022).
73. Kalugin O. N., Chaban V. V., Loskutov V. V., Prezhdo O. V. Uniform Diffusion of Acetonitrile inside Carbon Nanotubes Favors Supercapacitor Performance. *Nano Lett.* **8**, 2126-2130 (2008).
74. Norton C. D., Thompson W. H. On the Diffusion of Acetonitrile in Nanoscale Amorphous Silica Pores. Understanding Anisotropy and the Effects of Hydrogen Bonding. *J. Phys. Chem. C* **117**, 19107-19114 (2013).
75. Borchardt L., Leistenschneider D., Haase J., Dvoyashkin M. Revising the Concept of Pore Hierarchy for Ionic Transport in Carbon Materials for Supercapacitors. *Adv. Energy Mater.* **8**, 1800892 (2018).
76. Koone N., Shao Y., Zerda T. W. Diffusion of Simple Liquids in Porous Sol-Gel Glass. *J. Phys. Chem.* **99**, 16976-16981 (2002).
77. Kittaka S. et al. Low Temperature Properties of Acetonitrile Confined in Mcm-41. *J. Phys. Chem. B* **109**, 23162-23169 (2005).
78. Nivarthi S. S., McCormick A. V., Davis H. T. Diffusion Anisotropy in Molecular Sieves. *Chem. Phys. Lett.* **229**, 297-301 (1994).
79. Natraj A. et al. Single-Crystalline Imine-Linked Two-Dimensional Covalent Organic Frameworks Separate Benzene and Cyclohexane Efficiently. *J. Am. Chem. Soc.* **144**, 19813-19824 (2022).

8 Summary and Conclusions

The introductory chapter about post-synthetic modifications in covalent organic frameworks, gives an educational overview about the motivation for performing PSM reactions with framework materials. It was shown how different sites in the materials can be utilized to endow the modified frameworks with improved stability, complex and tailored chemical functionalities or function by modification of material properties. On the basis of reported examples for post-synthetic modifications of imine linkages in COFs we explained the superior role of linkages as the intrinsically reversible, and thus, weakest link in the COF structure for addressing these targets. Recently reported synthetic strategies for converting imine linkages were analyzed systematically and categorized by reaction classes to convey the general concept behind these transformations and to show how they originate from fundamental reactivity of imine bonds. A comparison of this reactivity between imine bonds in small organic molecules and imines as linkages in COFs highlighted that general concepts of (small-molecular) organic synthesis still apply to solid-state organic materials. Indeed small molecular imines may serve as a blue-print for the design of linkage modification reactions in COFs, albeit with additional considerations taking into account characteristic changes in the reaction environment such as confinement in the pore channels of the framework. We highlighted these influencing factors, summarized as *accessibility* aspects, *steric-shielding* of linkage centers, and modulated *flexibility* emerging from the three dimensional arrangement, i.e. layer stacking, in two-dimensional covalent organic frameworks to elucidate fundamental aspects of changes in reactivity in these materials. An understanding of these principles lays the basis for a successful design of post-synthetic linkage modification reactions. Furthermore, we detailed practical aspects for performing PSM of COFs, including a step-by-step guide for reaction design and necessary considerations for the practical conduction of experiments. We covered complications occurring when performing these experiments, subsequent workup, and analysis, and depicted possible solutions to these, supplemented by a prototypical workflow for decision making during optimization of PSM reaction conditions. The detailed reactivity concepts, design principles and guides for conducting post-synthetic linkage modifications will support students as well as researcher to understand challenges in this field of research and give ideas on how to tackle them.

As part of this thesis, the scope of post-synthetic linkage conversion in COFs was successfully extended by two strategies, namely a reduction of imine linkages to secondary amine-linked frameworks, as detailed in Chapter 4, and an oxidative strategy giving access to nitrone-linked COFs in Chapter 5.

The reduction to secondary amine linked frameworks under Leuckart-Wallach conditions, with formic acid as the reducing agent was presented as a robust and versatile method to synthesize three new amine linked 2D COFs with different topologies (hexagonal and

tetragonal) and pore sizes, in both typical *ex-situ* as well as *in-situ* post-synthetic linkage transformation reactions, employing the imine-linked COF or the building blocks in a reductive crystallization, respectively. The obtained materials showed increased hydrolytic stability, and excellent functionalization capabilities, with secondary amine linkages serving as anchoring sites at the pore wall for covalent immobilization of molecules in the pore channels. This functionalization approach was successfully presented by reacting the secondary amine linkage centers with electrophilic reagents, such as acid chlorides and isocyanates. Furthermore a judicious variation of the amount of formic acid, or utilization of ammonium formate as a reductive salt-melt in a solvent-free procedure, afforded partially reduced or fully reduced, partially formylated amine-linked frameworks, respectively. After this combined reduction-protection procedure *N*-formyl groups proved to be deprotectable on demand using dilute acid, presenting unparalleled possibilities for stepwise functionalization strategies with this reaction platform. Furthermore, correlations between crystalline amine-linked frameworks and topologically identical disordered materials with reduced pore accessibility were investigated by a combination of synthetic structure interconversion and pair-distribution function analysis. We demonstrated crystalline-to-amorphous, as well as amorphous-to-crystalline transformations, proving the topological identity between these materials. In summary, the presented combination of chemical and combined structural modification capabilities promises an unprecedented level of control for the functionalization and stabilization of imine-linked COFs, the largest class of COFs to date.

Nitrone-linked frameworks were obtained by topochemical oxidation of imine- or amine-linked frameworks using the electrophilic oxidizing reagent *m*CPBA. In contrast to previous oxidations of imine linkages yielding amide linked frameworks, this strategy allowed to selectively oxidize the nitrogen center of the imine bonds with atomic precision in the solid-state. Nitrone linkages carved polar centers into the pore walls of the materials, improving interactions with polar sorbents, such as water vapor. We studied the adsorption process of water vapor with a set of analytical techniques, such as isothermal vapor adsorption and *in-situ* XRPD at controlled humidity levels. Both nitrone linked COFs showed adsorption at 20% decreased humidity compared to their imine-linked precursors. However, in depth analysis of the cycling performance revealed that only the microporous nitrone COF remained structurally intact over multiple adsorption/desorption cycles, whereas the mesoporous material suffered from pore collapse induced by stress on the material upon water desorption. This study highlights the necessity of well-balanced interlayer vs. sorbent-sorptive interactions to maintain the material's stability over multiple cycles. Since water uptake in the structurally more robust material already occurred at low humidity levels of approximately 20% r.H., nitrone linked COFs could be promising candidates as active materials in water harvesting devices.

Besides post-synthetic modification of linkages, another goal of this thesis was the integration of stimuli-responsive functionality in COFs by embedding light-driven molecular

motors in their backbone (Chapter 6). To address this, we designed a light-driven molecular motor with diamine functional groups as a building block for the synthesis of an imine-linked two-dimensional COF. We successfully synthesized crystalline and porous frameworks and amorphous polymers with rational control over the amount of motors by a mixed building block approach of non-functional spacers and molecular motor building blocks. In contrast to physisorbed molecular motors on a material support, this rational approach of embedding the motor moiety by building block design featured a defined localization and orientation in the pore channels of the COF and structural integration by “strong” covalent bonds. A diverse set of analytical techniques including gas sorption analysis, transmission electron microscopy, XRPD, in-depth structural analysis using the pair-distribution function and quantitative solid-state NMR spectroscopy was used to study and quantify the successful integration of motors into the materials. On the other hand, we found that the complex geometry of the building blocks has detrimental influence on interlayer stacking correlations and the available pore volume as well as the local environment of the motor. Although common requirements, including permanent porosity and void space for motor rotation were met in the obtained crystalline COF, isomerization of the motors could not be probed by available techniques including Raman, FT-IR and UV-Vis spectroscopy. From these observations we conclude that the incorporated motors may be (partially) restricted by geometric factors in the stacked layers. Given the technically limited motor loadings to avoid further restrictive motor-motor interactions in the confined pore channels, these factors may reduce the amount of rotatable motors in the real structure below the limits of detection by the employed techniques. Our study thus extends the design criteria for establishing unrestricted motor dynamics in porous layered solids by local structural characteristics, such as interlayer interactions and stacking offset. By providing valuable insights into these effects in two-dimensional COFs, our findings constitute a step towards realization of light responsive functions, such as nano actuation or triggered directional motion through pore channels in solid-state porous materials.

Besides these synthetic approaches to modify properties of frameworks, we presented a combined simulation and experimental study on self-diffusion of acetonitrile in COFs, using PFG-NMR experiments and MD simulations, in Chapter 7. A fundamental understanding of diffusion processes in these materials, and especially understanding their relation to real-structure characteristics, is an important goal for an efficient utilization of confinement effects in these materials. Despite experimental challenges summarized as small crystallite sizes in the materials, fast transverse relaxation of the confined liquid probed by PFG NMR, and both gas-liquid as well as exchange processes between different regions in the polycrystalline samples, we observed an excellent agreement of experimentally observed effective diffusion coefficients for a structurally defined, high porosity sample with those obtained from MD simulation. As expected for directional diffusion in the 1D pore channels of the material, we also observed an anisotropic contribution to the derived effective diffusivities in the order of $10^{-10} \text{ m}^2\text{s}^{-1}$. On the other hand, a structurally less defined sample

with decreased porosity showed diffusivities that are between one and two orders of magnitude smaller, further decreasing for increased diffusion times which is indicative that diffusion in this sample is restricted by diffusion barriers such as defects or surface boundaries between the crystallites. Our combined report thus sheds light on prevalent diffusion mechanisms and challenges in experimental determination of diffusion coefficients in COFs, while the described methods provide the foundation for further studies of diffusion and confinement effects in framework materials.

From the sum of the various results presented in this thesis it may be concluded that fundamental molecular concepts, such as conversion of functional groups, dynamics, and mobility in the sense of diffusion, can also be transferred to solid-state framework materials, such as COFs, which thus indeed keep their promise of structural diversity and nearly unlimited possibilities for functionalization, which give access to a broad range of diverse applications.

9 Appendix

9.1 Supporting Information to Chapter 4 Amine-Linked COFs: A Platform for Post-Synthetic Structure Interconversion and Modification

9.1.1 Methods and Equipment

General Methods: All reactions, unless otherwise noted, were performed with magnetic stirring under Ar atmosphere using standard Schlenk techniques. Reaction temperatures were electronically monitored as external heating block temperatures. Reagents were purchased from different commercial sources and used without further purification. The removal of solvent under reduced pressure was carried out on a standard rotary evaporator.

Solvents: THF was distilled with sodium and benzophenone under inert gas prior to use. Degassed solvents were degassed by purging with Ar for at least 10 min. Solvents for flash column chromatography were purified by distillation under reduced pressure.

Chromatography: Analytical thin-layer chromatography was carried out on pre-coated aluminum plates (silica gel 60 F254) from Merck. Compound spots were visualized under ultra violet light (UV, 254 nm) for fluorescent compounds or KMnO₄ stain solutions. For flash column chromatography, silica gel 60 from Merck, with a particle size between 40 and 63 μm , was used.

NMR Spectroscopy: Liquid state ¹H-NMR spectra were recorded on a JEOL ECZ 400S 400 MHz spectrometer or a Bruker Avance III HD 400 at 400 MHz, respectively, and are reported as follows: chemical shift δ in ppm (multiplicity, coupling constants J in Hz, number of protons, assignment). Couplings are expressed as: s (singlet), d (doublet), t (triplet), q (quartet), m (multiplet) or combinations. All chemical shifts δ are reported to the nearest 0.01 ppm with the residual solvent peak as the internal reference (chloroform-d = 7.26 ppm, dimethylsulfoxide-d⁶ = 2.50 ppm). ¹³C-NMR spectra were recorded on the same spectrometers at 101 MHz with ¹H decoupling, respectively. All ¹³C resonances are reported to the nearest 0.1 ppm with the central resonance of the solvent peak as the internal reference (chloroform-d = 77.16 ppm, dimethylsulfoxide-d⁶ = 39.52 ppm). In order to allocate proton and carbon spectra, several 2D NMR spectra (COSY, HSQC, and HMQC) were used. The numbering of the proton and carbon atoms does not match the IUPAC nomenclature. Diastereotopic protons in the ¹H NMR spectra are referenced with a and b: this nomenclature is arbitrary and does not correspond to the spin system.

Solid-state NMR spectra were recorded at room temperature in 4 mm or 2.5 mm OD ZrO₂ rotors on a Bruker Avance III 400 MHz spectrometer using Bruker BL4 or BL2.5 double resonance MAS probes. Standard instrument library pulse sequences were used. Chemical shifts were referenced relative to TMS (¹H, 0.0 ppm), adamantane (¹³C, 38.52 ppm and 29.47 ppm), and CH₃NO₂ (¹⁵N, 0.0 ppm).

Infrared Spectroscopy: IR spectra were recorded on a Perkin Elmer UATR Two FT-IR spectrometer equipped with an attenuated total reflection (ATR) measuring unit. IR data are reported in wavenumbers (cm^{-1}) of normalized absorption. The IR bands are characterized as w (weak), m (medium), s (strong), or br (broad).

High-Resolution Mass Spectrometry (HRMS): High-resolution electron spray ionization (ESI) mass spectra were recorded on a Varian MAT 711 MS spectrometer.

SEM/EDX: SEM SE (secondary electron) detector images were obtained on either a Zeiss Merlin or a VEGA TS 5130MM (TESCAN) with a SEM-EDX using a Si/Li detector (Oxford).

TEM/EDX was performed with a Philips CM30 ST (300kV, LaB6 cathode). The samples were prepared dry onto a copper lacy carbon grid (Plano). EDX was obtained on a Noran System Seven (NSS) Si(Li) detector.

Sorption: Sorption measurements were performed on a Quantachrome Instruments Autosorb iQ MP with Nitrogen at 77 K. The samples were degassed for 12 h at 120 °C under vacuum prior to the gas adsorption studies. Pore size distribution was determined from Nitrogen adsorption isotherms using the QSDFT cylindrical pores in carbon model for nitrogen at 77 K. For multipoint BET surface area calculations, pressure ranges were chosen with the help of the BET assistant in the ASiQwin software, which chooses BET tags in accordance with the ISO recommendations equal or below the maximum in grams per square meter.

X-Ray Powder Diffraction (XRPD): X-ray powder diffraction experiments were performed on a Stoe Stadi P diffractometer (Cu-K α 1, Ge(111) in Debye-Scherrer geometry. The samples were measured in sealed glass capillaries (OD = 0.7 mm) and spun for improved particle statistics.

Rietveld Refinements: Rietveld refinements were performed using TOPAS v6. The background was corrected with Chebychev polynomials (Order 5). Simple axial and zero-error corrections were used together with additional corrections for Gaussian and Lorentzian crystallite size and strain broadening.

Synchrotron X-Ray Total Scattering Measurements: Total scattering measurements were carried out using the high energy Powder Diffraction and Total Scattering Beamline P02.1 of PETRA III at the Deutsches Elektronen-Synchrotron (DESY). X-ray total scattering data were collected in rapid acquisition mode (RAPDF) [1]. A large-area 2D PerkinElmer XRD1621 detector (2048×2048 pixels, 200×200 μm^2 each) was used at a sample-to-detector distance of approximately 304 mm. Samples were loaded into 1.8 mm ID/1.9 mm OD polyimide capillaries (Cole-Parmer) and measured at room temperature. The incident energy of the X-rays was 59.858 keV ($\lambda = 0.20713 \text{ \AA}$). A measurement of Si was collected at room temperature as a standard for calibration of the setup. Calibration was performed, and the raw 2D intensity was corrected for polarization and azimuthally

integrated and converted to 1D intensity versus Q ($Q = 4\pi \sin \theta/\lambda$ is the magnitude of the scattering momentum transfer, with 2θ scattering angle) using the software Fit2D^[2].

Further correction and normalization of the integrated 1D diffraction intensities were carried out to obtain the total scattering structure function, $F(Q)$, which was Fourier transformed to obtain the pair distribution function (PDF), $G(r)$ using PDFgetX3^[3] within xPDFsuite^[4]. The maximum value used in the Fourier transform of the total scattering data (Q_{max}) was 22.0 \AA^{-1} . Real-space structure model refinements to the PDF data were carried out using PDFgui^[5]. The resolution parameters due to Q -space resolution, $Q_{\text{damp}} = 0.0340 \text{ \AA}^{-1}$, and due to variable Q -resolution and high- Q noise, $Q_{\text{broad}} = 0.0064 \text{ \AA}^{-1}$, were determined from Si and used for further fitting.

Supercritical CO₂ Activation: Activation of the methanol-soaked COF samples with supercritical CO₂ was performed on a Leica EM CPD300 critical point dryer.

Quantum-Chemical Calculations: Atom positions and lattices of all periodic structures were optimized on RI-PBE-D3/def2-TZVP^[6-9] level of theory using an acceleration scheme based on the resolution of the identity (RI) technique and the continuous fast multipole method (CFMM)^[10-12] implemented^[13, 14] in Turbomole^[15] version V7.3.

The CFMM uses multipole moments of maximum order 20, together with a well-separateness value of 3 and a basis function extent threshold of 10^9 a.u. Grid 7 was used for the numerical integration of the exchange-correlation term. The norm of the gradient was converged to 10^{-4} a.u. and the total energy to 10^{-8} Hartree within the structure optimization using the gamma point approximation.

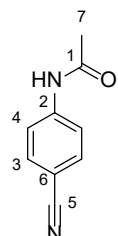
Structures for all investigated molecular compounds were optimized on PBE0-D3/def2-TZVP^[7, 8, 16, 17] level of theory. Subsequent frequency calculations were performed on the same level of theory to ensure all minima to be true minima on the potential energy hypersurface.

NMR chemical shifts were obtained on B97-2/pcS-2^[18, 19] level of theory using the FermiONs++^[18, 20, 21] program package.

9.1.2 Synthetic Procedures

9.1.2.1 Starting Material Syntheses

N-(4-cyanophenyl)acetamide



4-aminobenzonitrile (2.00 g, 16.8 mmol, 1.0 eq.) was dissolved in 1.2 M aqueous HCl (20 mL) and cooled to 0°C in an ice bath. After addition of 4.2 M aqueous NaOAc (7 mL) and acetic anhydride (7.4 mL, 78.3 mmol, 4.1 eq.), the solution was stirred at 0°C for 20 min. The reaction mixture was diluted with water (50 mL). Suction filtration of the precipitate and washing with water (2 x 50 mL) afforded *N*-(4-cyanophenyl)acetamide (2.53 g, 15.8 mmol, 93%) as a white solid.

¹H NMR (400 MHz, CDCl₃): δ = 7.68 – 7.57 (m, 4H, H-3, H-4), 7.39 (s, 1H, NH), 2.22 (s, 3H, H-7) ppm.

¹³C NMR (101 MHz, CDCl₃): δ = 168.6 (C-1), 142.0 (C-2), 133.5 (C-3), 119.6 (C-4), 118.9 (C-5), 107.3 (C-6), 24.9 (C-7) ppm.

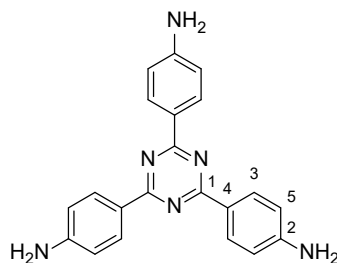
IR (ATR): $\tilde{\nu}$ = 3300 (w), 3258 (w), 3184 (w), 3114 (w), 3054 (w), 2222 (m), 1667 (s), 1598 (s), 1541 (s), 1506 (m), 1404 (m), 1362 (m), 1322 (s), 1265 (m), 833 (s) cm⁻¹.

HRMS (ESI): calculated for C₉H₇N₂O⁺ ([M-H]⁺): 159.05639.

found:	159.05635.
--------	------------

The analytical data matched those previously described in the literature.^[22]

4,4',4''-(1,3,5-triazine-2,4,6-triyl)trianiline



Procedure A from N-(4-cyanophenyl)acetamide:

A heat-dried round-bottom flask was equipped with chlorosulfonic acid (5.4 mL, 80.1 mmol, 5.0 eq.) and cooled to -15°C . *N*-(4-cyanophenyl)acetamide (2.50 g, 15.6 mmol, 1.0 eq.) was added to the stirring acid in small portions. The resulting slurry was allowed to warm to room temperature under stirring for 16 h. The reaction mixture was poured on ice and neutralized to pH 7 with 4 M aqueous NaOH. Suction filtration of the precipitate and washing with water (2 x 50 mL) afforded crude *N,N',N''*-(1,3,5-triazine-2,4,6-triyl)tris(benzene-4,1-diyl)triacetamide (2.50 g) as an orange solid, which was used without further purification in the next step.

To a solution of the crude triacetamide (2.50 g) in EtOH (32 mL) conc. aqueous HCl (12 mL) was added and the reaction mixture was heated to 110°C for 16 h. The reaction mixture was neutralized to pH 7 with 4 M aqueous NaOH. Suction filtration of the precipitate and washing with water (2 x 30 mL) afforded 4,4',4''-(1,3,5-triazine-2,4,6-triyl)trianiline (665 mg, 1.88 mmol, 36%) as a yellow solid.

Procedure B from 4-aminobenzonitrile:

A heat-dried round-bottom flask was equipped with 4-aminobenzonitrile (772 mg, 6.54 mmol, 1.0 eq.) and cooled to 0°C . Trifluoromethanesulfonic acid (2.0 mL, 22.6 mmol, 3.5 eq.) was added slowly through a Teflon cannula. The resulting slurry was allowed to warm to room temperature for 24 h. The reaction mixture was diluted with water (20 mL) and neutralized to pH 7 with 2 M aqueous NaOH. Suction filtration of the precipitate and washing with water (2 x 30 mL) afforded 4,4',4''-(1,3,5-triazine-2,4,6-triyl)trianiline (494 mg, 1.39 mmol, 64%) as a yellow solid.

^1H NMR (400 MHz, DMSO- d_6): δ = 8.35 (d, J = 8.8 Hz, 6H, H-3), 6.69 (d, J = 8.8 Hz, 6H, H-5), 5.89 (s, 6H, NH_2) ppm.

^{13}C NMR (101 MHz, DMSO- d_6): δ = 170.0 (C-1), 153.4 (C-2), 130.6 (C-3), 123.4 (C-4), 113.6 (C-5) ppm.

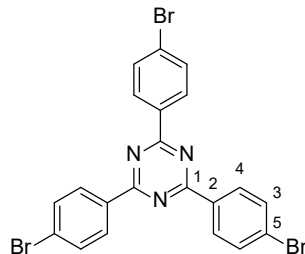
IR (ATR): $\tilde{\nu}$ = 3462 (w), 3325 (w), 3210 (w), 1632 (m), 1605 (m), 1578 (m), 1495 (s), 1431 (m), 1309 (m), 1295 (m), 1179 (m), 1148 (m), 812 (s) cm^{-1} .

HRMS (ESI): calculated for $C_{21}H_{19}N_6^+$ ($[M+H]^+$): 355.16657

found: 355.16649.

The analytical data matched those previously described in the literature.^[22, 23]

2,4,6-tris(4-bromophenyl)-1,3,5-triazine



A heat-dried round-bottom flask was equipped with 4-Bromobenzonitrile (1.0 g, 5.5 mmol, 0.3 eq.) and cooled to 0°C. Trifluoromethanesulfonic acid (2.0 mL, 22 mmol, 4.0 eq.) was added slowly through a Teflon cannula. The resulting slurry was allowed to warm to room temperature for 24 h. The reaction mixture was diluted with water (20 mL) and neutralized to pH 7 with 2 M aqueous NaOH. Suction filtration of the precipitate and washing with water (2 x 10 mL) afforded 2,4,6-tris(4-bromophenyl)-1,3,5-triazine (0.93 g, 1.8 mmol, 93%) as a white solid.

1H NMR (400 MHz, $CDCl_3$): δ = 8.59 (d, J = 8.5 Hz, 6H, H-4), 7.70 (d, J = 8.5 Hz, 6H, H-3) ppm.

^{13}C NMR (101 MHz, $CDCl_3$): δ = 171.3 (C-1), 135.0 (C-2), 132.2 (C-3), 130.7 (C-4), 123.7 (C-5) ppm.

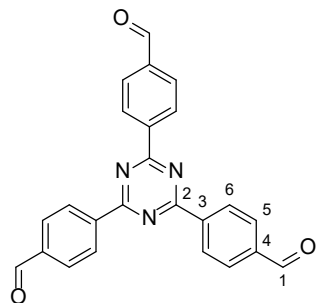
IR (ATR): $\tilde{\nu}$ = 1579 (m), 1511 (s), 1401 (m), 1354 (m), 1172 (m), 1148 (w), 1101 (w), 1067 (m), 1009 (s), 842 (m), 802 (s), 629 (w), 495 (s) cm^{-1} .

HRMS (EI): calculated for $C_{21}H_{12}Br_3N_3^-$ ($[M]^-$): 542.8587

found: 542.8578.

The analytical data matched those previously described in the literature.^[24]

4,4',4''-(1,3,5-triazine-2,4,6-triyl)tribenzaldehyde



To a suspension of 2,4,6-tris(4-bromophenyl)-1,3,5-triazine (0.50 g, 0.92 mmol, 1.0 eq.) in THF (50 mL), *n*-BuLi (2.5 M in hexane, 1.2 mL, 3.0 mmol, 3.3 eq.) was added dropwise at -78°C. The mixture was stirred at -78°C for 90 min, then 1-formylpiperidine (0.34 mL, 3.0 mmol, 3.3 eq.) was added dropwise at -78°C. The mixture was stirred at -78°C for 30 min and allowed to warm to room temperature. Aqueous concentrated NH₄Cl solution (1 mL) was added and the solvent was removed under reduced pressure. The residue was suspended in a mixture of EtOH (3 mL) and water (3 mL). Suction filtration of the suspension and washing with water (10 mL) and EtOH (10 mL) afforded 4,4',4''-(1,3,5-triazine-2,4,6-triyl)tribenzaldehyde (0.35 g, 0.91 mmol, 97 %) as an off-white solid.

¹H NMR (400 MHz, CDCl₃): δ = 10.18 (s, 3H, H-1), 8.92 (d, *J* = 8.2 Hz, 6H, H-6), 8.37 – 7.82 (m, 6H, H-5) ppm.

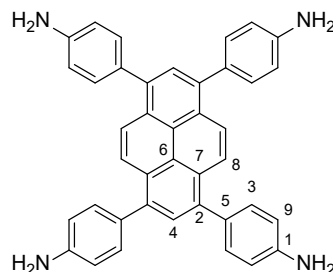
¹³C NMR (101 MHz, CDCl₃): δ = 192.0 (C-1), 140.9 (C-2), 139.5 (C-3), 130.1 (C-4), 129.8 (C-5) ppm.

IR (ATR): $\tilde{\nu}$ = 1699 (m), 1582 (w), 1515 (s), 1359 (m), 1298 (w), 1201 (m), 1105 (w), 1013 (w), 805 (s), 692 (w), 498 cm⁻¹.

HRMS (EI): calculated for C₂₄H₁₅N₃O₃⁺ ([M]⁺): 393.1108

found: 393.1107.

The analytical data matched those previously described in the literature.^[25]

4,4',4'',4'''-(pyrene-1,3,6,8-tetrayl)tetraaniline

Tetrakis(triphenylphosphine)palladium(0) (0.40 g, 0.35 mmol, 1.0 meq.) was added to a mixture of (1,3,6,8-tetrabromopyrene (3.00 g, 5.8 mmol, 1.0 eq.), 4-aminophenylboronic acid pinacol ester (5.98 g, 27.3 mmol, 4.0 eq.) and K_2CO_3 (4.40 g, 31.8 mmol, 5.5 eq.) in 1,4-dioxane (135 mL) and water (45 mL). After refluxing at 110°C for 72 h, the mixture was allowed to cool to room temperature. Suction filtration of the suspension and washing with water (50 mL) and MeOH (50 mL) afforded 4,4',4'',4'''-(pyrene-1,3,6,8-tetrayl)tetraaniline (2.83 g, 5.78 mmol, 86 %) as a yellow solid.

1H NMR (400 MHz, DMSO-d₆): δ = 8.12 (s, 4H, H-8), 7.78 (s, 2H, H-4), 7.34 (d, J = 7.9 Hz, 8H, H-3), 6.77 (d, J = 7.9 Hz, 8H, H-9), 5.30 (s, 8H, NH₂).ppm.

^{13}C NMR (101 MHz, DMSO-d₆): δ = 148.2 (C-1), 137.1 (C-2), 131.0(C-3), 129.0(C-4), 127.6(C-5), 126.7(C-6), 126.1(C-7), 124.4(C-8), 113.9 (C-9) ppm.

IR (ATR): $\tilde{\nu}$ = 3438 (w), 3417 (w), 3338 (w), 3210 (w), 2858 (w), 1605 (m), 1517 (m), 1493 (m), 1459 (w), 1275 (m), 1176 (m), 1061 (m), 904 (w), 834 (vs), 738 (w), 638 (m), 606 (m), 577 (m), 530 (s), 497 (s) cm^{-1} .

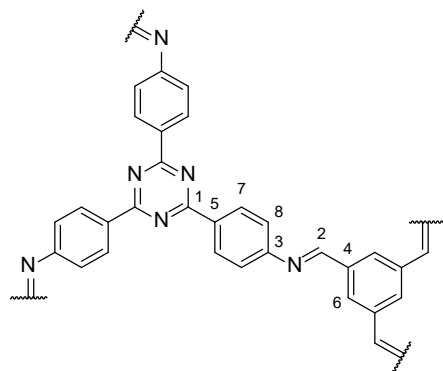
HRMS (ESI): calculated for $C_{40}H_{31}N_4^+$ ([M+H]⁺): 567.2543

found: 567.2591.

The analytical data matched those previously described in the literature.^[26]

9.1.2.2 Syntheses of Imine-linked COFs

PI-3-COF



To a mixture of benzene-1,3,5-tricarbaldehyde (22.1 mg, 0.13 mmol, 1.0 eq.) and 4,4',4''-(1,3,5-triazine-2,4,6-triyl)trianiline (46.8 mg, 0.13 mmol, 1.0 eq.) in mesitylene (2.7 mL) and 1,4-dioxane (1.3 mL), aqueous 6 M AcOH (0.5 mL) was added. The suspension was heated at 120°C for 72 h. Suction filtration of the precipitate and washing with DMF (20 mL), THF (20 mL) and DCM (20 mL) afforded PI-3-COF (55.5 mg, 91%) as a yellow solid.

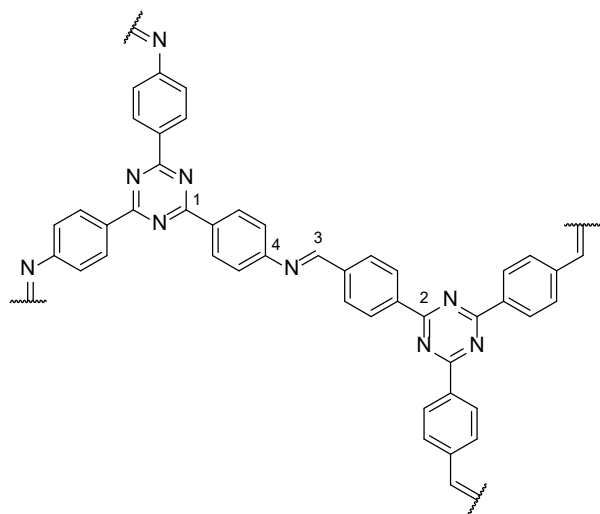
¹H ssNMR (MAS, 400 MHz): $\delta = 7.1$ (H-2, H-6, H-7, H-8) ppm.

¹³C ssNMR (CP-MAS, 101 MHz): $\delta = 169.1$ (C-1), 155.3 (C-2), 151.5 (C-3), 136.6 (C-4), 134.0 (C-5), 129.6 (C-6), 127.7 (C-7), 116.3 (C-8) ppm.

¹⁵N ssNMR (CP-MAS, 41 MHz): $\delta = -59.0$ (N-2), -131.8 (N-1) ppm.

IR (ATR): $\tilde{\nu} = 1579$ (m), 1511 (s), 1413 (m), 1370 (s), 1174 (w), 1141 (w), 1013 (w), 968 (w), 864 (w), 813 (s), 678 (w), 531 (w), 415 (w) cm^{-1} .

The analytical data matched those previously described in the literature.^[27]

TTI-COF

To a mixture of 4,4',4''-(1,3,5-triazine-2,4,6-triyl)tribenzaldehyde (25.0 mg, 63.5 μ mol, 1.0 eq.) and 4,4',4''-(1,3,5-triazine-2,4,6-triyl)trianiline (22.5 mg, 63.5 μ mol, 1.0 eq.) in mesitylene (2.5 mL) and 1,4-dioxane (2.5 mL), aqueous 6 M AcOH (0.13 mL) was added. The suspension was heated at 120°C for 72 h. Suction filtration of the precipitate and washing with DMF (5 mL), THF (5 mL) and DCM (5 mL) afforded TTI-COF (26.8 mg, 61%) as a yellow solid.

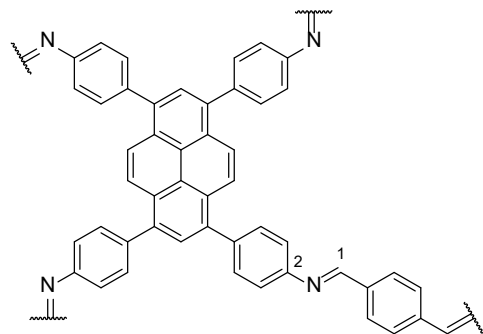
^1H ssNMR (MAS, 400 MHz): $\delta = 7.1$ (H-2, H-Ar) ppm.

^{13}C ssNMR (CP-MAS, 101 MHz): $\delta = 169.1$ (C-1, C-2), 157.4 (C-3), 151.7 (C-4), 138.5 (C-Ar), 133.9 (C-Ar), 128.2 (C-Ar), 114.8 (C-Ar) ppm.

^{15}N ssNMR (CP-MAS, 41 MHz): $\delta = -55.7$ (N-3), -131.3 (N-1, N-2) ppm.

IR (ATR): $\tilde{\nu} = 1576$ (w), 1505 (vs), 1414 (m), 1362 (s), 1173 (w), 1145 (w), 1014 (w), 857 (w), 814 (m), 595 (w), 544 (w) cm^{-1} .

The analytical data matched those previously described in the literature.^[28]

Py1P-COF

To a mixture of 4,4',4'',4'''-(pyrene-1,3,6,8-tetrayl)tetraaniline (34.0 mg, 60.0 μ mol, 1.0 eq.) and terephthalaldehyde (16.1 mg, 0.12 mmol, 2.0 eq.) in mesitylene (2 mL) and 1,4-dioxane (1 mL), aqueous 6 M AcOH (0.3 mL) was added. The suspension was heated at 120°C for 7 days. Suction filtration of the precipitate and washing with MeOH (5 mL), DMF (5 mL), THF (5 mL) and DCM (5 mL) afforded Py1P-COF (37.9 mg, 83%) as an orange solid.

^1H ssNMR (MAS, 400 MHz): δ = 6.9 (H- 1, H-Ar) ppm.

^{13}C ssNMR (CP-MAS, 101 MHz): δ = 156.5 (C-1), 149.8 (C-2), 138.7 (C-Ar), 137.3 (C-Ar), 132.8 (C-Ar), 131.5 (C-Ar), 129.4 (C-Ar), 127.8 (C-Ar), 124.9 (C-Ar), 121.7 (C-Ar), 119.4 (C-Ar) ppm.

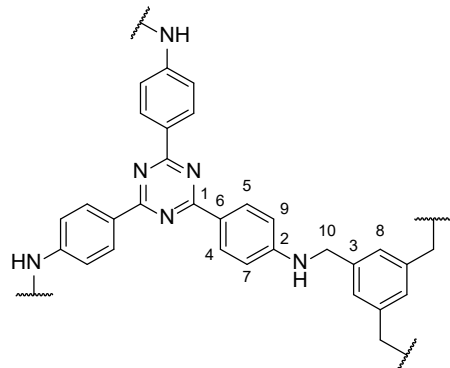
^{15}N ssNMR (CP-MAS, 41 MHz): δ = -48.8 (N-1) ppm.

IR (ATR): $\tilde{\nu}$ = 3031 (w), 1699 (w), 1625 (m), 1597 (w), 1489 (m), 1460 (w), 1303 (w), 1198 (w), 1169 (w), 1104 (w), 1005 (w), 967 (w), 882 (w), 831 (s), 737 (w), 613 (w), 585 (w), 538 (w) cm^{-1} .

The analytical data matched those previously described in the literature.^[26]

9.1.2.3 Syntheses of Amine-linked COFs

rPI-3-COF



Procedure A: Reduction of PI-3-COF

To a suspension of PI-3-COF (30.0 mg) in mesitylene (2 mL) and 1,4-dioxane (1 mL), formic acid (97%, 53.0 μ L) was added. The suspension was heated at 120°C for 48 h. The precipitate was collected via suction filtration and extracted with MeOH in a Soxhlet extractor for 12 h. Extraction with supercritical CO₂ afforded rPI-3-COF (28.0 mg, 92%) as a yellow solid.

Procedure B: One-pot strategy

To a mixture of benzene-1,3,5-tricarbaldehyde (9.7 mg, 60 μ mol, 1.0 eq.) and 4,4',4''-(1,3,5-triazine-2,4,6-triyl)trianiline (21 mg, 60 μ mol, 1.0 eq.) in mesitylene (2 mL) and 1,4-dioxane (1 mL), formic acid (97%, 49 μ L) was added. The suspension was heated at 60°C for 48 h and at 120°C for 24 h. Suction filtration of the precipitate and washing with DMF, THF and DCM (3 x 5 mL) afforded rPI-3-COF (26 mg, 92%) as a yellow solid.

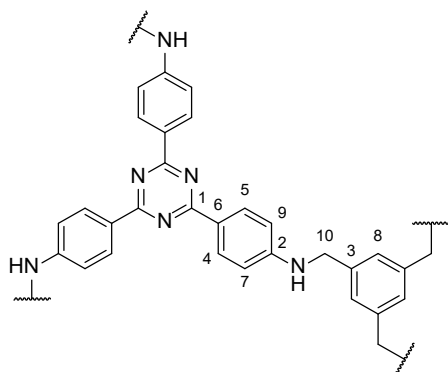
¹H ssNMR (MAS, 400 MHz): δ = 7.8 (H-4, H-5), 5.9 (H-7, H-8, H-9), 2.6 (H-10) ppm.

¹³C ssNMR (CP-MAS, 101 MHz): δ = 168.8 (C-1), 151.0 (C-2), 137.3 (C-3), 128.7 (C-4, C-5), 126.1 (C-6), 119.0 (C-7), 114.4 (C-8), 111.2 (C-9), 45.4 (C-10) ppm.

¹⁵N ssNMR (CP-MAS, 41 MHz): δ = -141.4 (N-1), -313.3 (N-10) ppm.

IR (ATR): $\tilde{\nu}$ = 3412 (w), 1607 (w), 1581 (w), 1509 (s), 1412 (m), 1369 (s), 1326 (w), 1261 (w), 1182 (m), 1145 (m), 1012 (w), 863 (w), 809 (m), 682 (w), 651 (w), 512 (w) cm^{-1} .

disordered rPI-3-COF



Procedure A: To a suspension of PI-3-COF (10.0 mg) in mesitylene (666 μ L) and 1,4-dioxane (333 μ L), formic acid (97%, 50.0 μ L) was added. The suspension was stirred at 120°C for 48 h. The precipitate was collected via suction filtration, washed with DMF, THF, and DCM (3 x 2 mL) and dried under high vacuum. Disordered rPI-3-COF (9.9 mg, 98%) was obtained as a yellow solid.

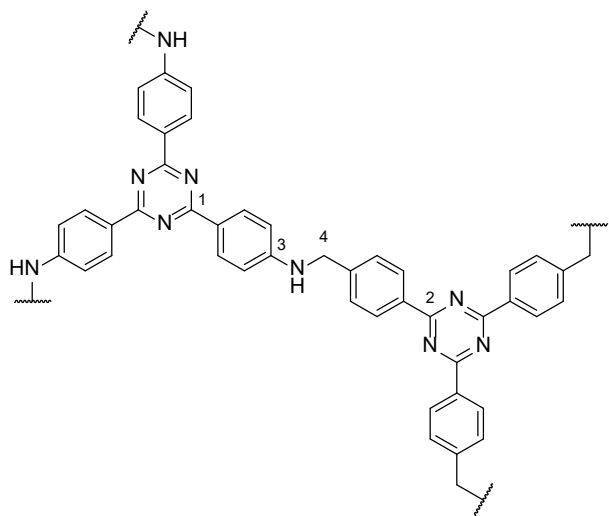
Procedure B: A suspension of pfrPI-3-COF (10.0 mg) in aqueous 1M HCl (2 mL) was stirred at 120°C for 20 min. Suction filtration, washing with water, THF, DCM (3 x 2 mL) and drying under high vacuum afforded disordered rPI-3-COF (9.2 mg) as a yellow solid.

^1H ssNMR (MAS, 400 MHz): δ = 7.3 (H-4, H-5, H-7, H-9, H-8), 3.4 (H-10) ppm.

^{13}C ssNMR (CP-MAS, 101 MHz): δ = 170.3 (C-1), 151.5 (C-2), 139.9 (C-3), 130.0 (C-4, C-5, C-6), 114.5 (C-7, C-8, C-9), 46.5 (C-10) ppm.

IR (ATR): $\tilde{\nu}$ = 3371 (w), 1606 (m), 1509 (vs), 1472 (s), 1367 (s), 1321 (m), 1263 (m), 1181 (m), 1145 (m), 807 (s), 573 (w), 521 (w) cm^{-1} .

rTTI-COF



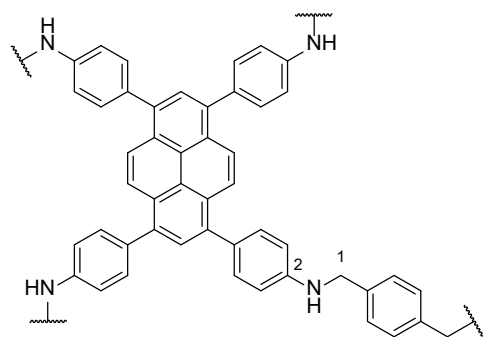
To a suspension of TTI-COF (30.0 mg) in mesitylene (2 mL) and 1,4-dioxane (1 mL), formic acid (97%, 19.3 μ L) was added. The suspension was heated at 120°C for 48 h. The precipitate was collected via suction filtration and extracted with MeOH in a Soxhlet extractor for 12 h. Extraction with supercritical CO₂ afforded rTTI-COF (27.1 mg, 90%) as a yellow solid.

¹H ssNMR (MAS, 400 MHz): δ = 7.4 (H-Ar), 3.0 (H-4) ppm.

¹³C ssNMR (CP-MAS, 101 MHz): δ = 170.5 (C-1, C-2), 151.5 (C-3), 138.8 (C-Ar), 134.5 (C-Ar), 128.9 (C-Ar), 114.0 (C-Ar), 46.7 (C-4) ppm.

¹⁵N ssNMR (CP-MAS, 41 MHz): δ = -134.0 (N-1, N-2), -314.8 (N-4) ppm.

IR (ATR): $\tilde{\nu} = 3403$ (w), 1607 (w), 1581 (w), 1505 (s), 1412 (m), 1359 (s), 1258 (w), 1180 (w), 1145 (w), 1016 (w), 855 (w), 809 (m), 592 (w), 541 (w) cm^{-1} .

rPy1P-COF

To a suspension of Py1P-COF (15.0 mg) in mesitylene (2 mL) and 1,4-dioxane (1 mL), formic acid (97%, 13.0 μ L) was added. The suspension was heated at 120°C for 24 h. The precipitate was collected via suction filtration and extracted with MeOH in a Soxhlet extractor for 12 h. Extraction with supercritical CO₂ afforded rPy1P-COF (14.2 mg, 94%) as an orange solid.

¹H ssNMR (MAS, 400 MHz): δ = 6.9 (C-Ar), 2.9 (C-1) ppm.

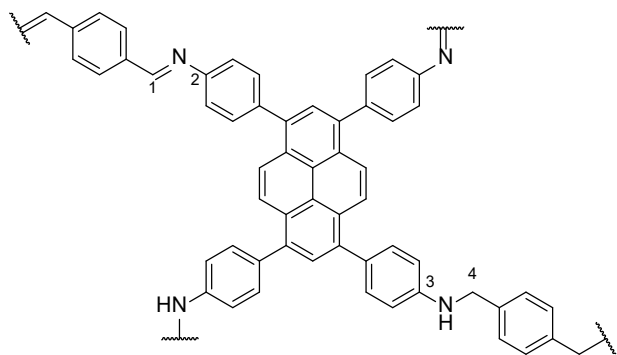
¹³C ssNMR (CP-MAS, 101 MHz): δ = 147.6 (C-2), 137.5 (C-Ar), 129.6 (C-Ar), 127.8 (C-Ar), 114.5 (C-Ar), 112.2, 48.2 (C-1) ppm.

¹⁵N ssNMR (CP-MAS, 41 MHz): δ = -317.6 (N-1) ppm.

IR (ATR): $\tilde{\nu}$ = 3397 (w), 3028 (w), 1609 (s), 1520 (m), 1491 (s), 1461 (w), 1319 (w), 1291 (w), 1250 (w), 1180 (w), 1016 (w), 980 (w), 821 (vs), 732 (w), 611 (w), 579 (w), 545 (w), 524 (w) cm^{-1} .

9.1.2.4 Syntheses of Hybrid Materials

prPy1P-COF



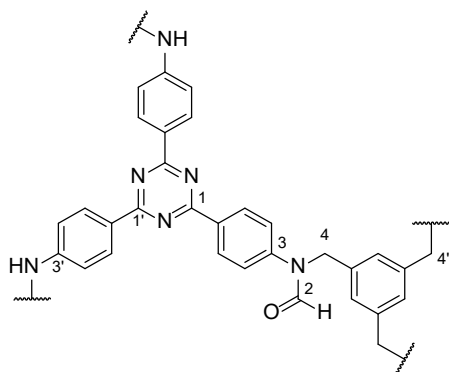
In a representative example, partial reduction of Py1P-COF (15.0 mg) was performed according to the procedure for rPy1P-COF with a reduced amount of formic acid (97%, 12.3 μ L) at 120°C for 24h, affording prPy1P-COF (14.2 mg, 94%) as an orange solid. Estimated from the relative integrals of C-2 and C-3 in the ^{13}C -ssNMR spectrum (see Figure S 9.1-40 for details), approximately 42% of the imine-bonds were reduced.

^1H ssNMR (MAS, 400 MHz): $\delta = 7.1$ (C-1, C-Ar), 3.01 (C-4) ppm.

^{13}C ssNMR (CP-MAS, 101 MHz): $\delta = 156.7$ (C-1), 149.0 (C-2), 146.4 (C-3), 142.1 (C-Ar), 138.4 (C-Ar), 135.9 (C-Ar), 132.1 (C-Ar), 130.1 (C-Ar), 127.7 (C-Ar), 125.1 (C-Ar), 121.3 (C-Ar), 112.7 (C-Ar), 48.1 (C-4) ppm.

^{15}N ssNMR (CP-MAS, 41 MHz): $\delta = -48.3$ (N-1), -316.8 (N-4) ppm.

IR (ATR): $\tilde{\nu} = 3397$ (w), 3029 (w), 1610 (s), 1521 (m), 1492 (s), 1461 (w), 1319 (w), 1292 (w), 1250 (w), 1180 (w), 1108 (w), 1017 (w), 982 (w), 821 (vs), 732 (w), 611 (w), 580 (w), 543 (w), 519 (w) cm^{-1} .

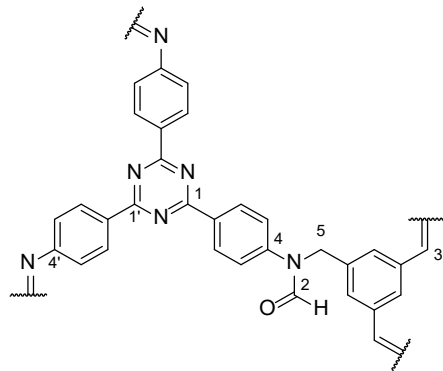
pfrPI-3-COF

A mixture of PI-3-COF (30.1 mg) and ammonium formate (257 mg, 40.8 mmol) was heated under autogenous pressure at 170°C for 3 h. The solid residue was collected via suction filtration, washed with water, DMF, THF, and DCM (4 x 2 mL) and dried under high vacuum, affording pfrPI-3-COF (31.6 mg) as a yellow solid.

¹H ssNMR (MAS, 400 MHz): δ = 7.5 (H-2, H-Ar), 3.7 (H-4, H-4') ppm.

¹³C ssNMR (CP-MAS, 101 MHz): δ = 170.4 (C-1, C-1'), 162.8 (C-2), 151.9 (C-3, C-3'), 138.0 (C-Ar), 130.2 (C-Ar), 114.9 (C-Ar), 46.5 (C-4, C-4') ppm.

IR (ATR): $\tilde{\nu}$ = 3366 (w), 1669 (w), 1606 (m), 1505 (vs), 1365 (vs), 1327 (m), 1263 (w), 1180 (m), 1145 (m), 811 (m), 640 (w), 587 (w), 520 (w) cm^{-1} .

opfrPI-3-COF

A suspension of pfrPI-3-COF (5.0 mg) and 2,3-Dichloro-5,6-dicyano-p-benzoquinone (15 mg, 64 mmol) in DCM (1 mL) was stirred at r.t. for 24 h. The precipitate was collected via suction filtration, washed with DMF, THF, and DCM (3 x 2 mL) and dried under high vacuum, affording opfrPI-3-COF (4.5 mg) as an orange solid.

¹H ssNMR (MAS, 400 MHz): δ = 7.8 (H-2, H-Ar), 5.1 (H-3, H-5) ppm.

¹³C ssNMR (CP-MAS, 101 MHz): δ = 169.6 (C-1, C-1'), 159.0 (C-2, C-3), 151.8 (C-4, C-4'), 130.30 (C-Ar), 116.73 (C-Ar), 45.64 (C-5) ppm.

IR (ATR): $\tilde{\nu}$ = 1694 (w), 1628 (w), 1579 (w), 1509 (vs), 1413 (m), 1363 (s), 1178 (w), 1144 (w), 1012 (w), 865 (w), 814 (m), 675 (w), 528 (w) cm^{-1} .

BzCl-rTTI-COF

To a suspension of rTTI-COF (3.5 mg) in THF (1 mL), triethylamine (23 μL , 0.17 mmol) and benzoyl chloride (18 μL , 0.15 mmol) was added and the suspension was heated at 60°C for 18h. The precipitate was collected via suction filtration, washed with water, DMF, THF, and DCM (3 x 2 mL) and dried under high vacuum, affording BzCl-rTTI-COF (4.4 mg) as a yellow solid.

TDI-rTTI-COF

A suspension of rTTI-COF (5.0 mg) and toluene diisocyanate (15 μL , 0.11 mmol) in THF (1 mL) was heated at 60°C for 18h. The precipitate was collected via suction filtration, washed with DMF, THF, and DCM (3 x 2 mL) and dried under high vacuum, affording TDI-rTTI-COF (7.1 mg) as a yellow solid.

9.1.3 FT-IR Spectroscopy

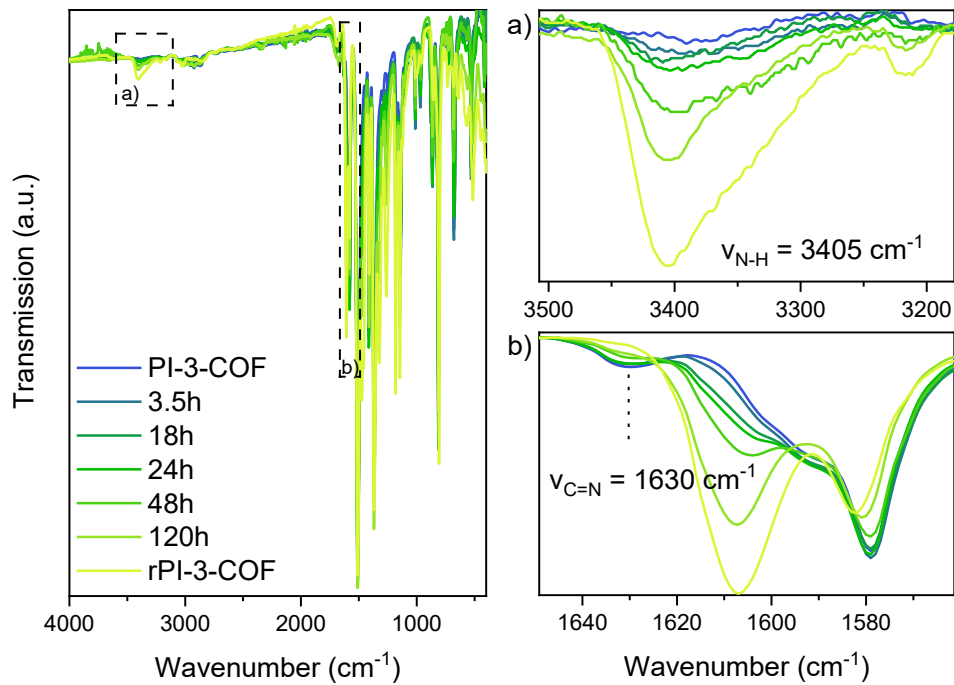


Figure S 9.1-1: Ex-situ FT-IR analysis of PI-3-COF samples under reductive conditions (19 eq. formic acid, mesitylene:dioxane 2:1, 120°C).

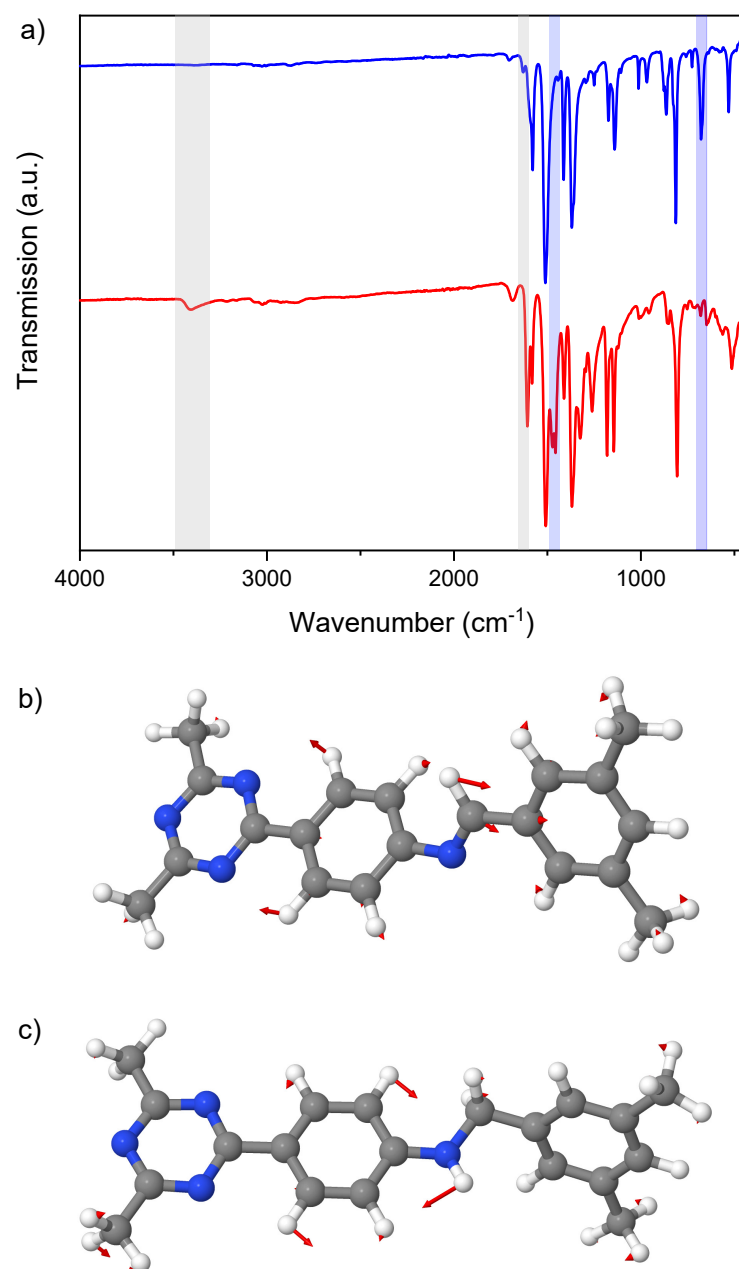


Figure S 9.1-2: (a) Comparison of FT-IR spectra of PI-3-COF (blue) and rPI-3-COF (red). Grey areas highlight appearing secondary amine and disappearing imine vibrations upon reduction. Blue areas highlight complex vibrations in the fingerprint region, which cannot clearly be assigned to an isolated vibration mode. Calculated IR modes for the molecular models PI-3 M (b) and rPI-3 M (c) in these regions suggest a contribution of imine C-H (b), or amine N-H (c), bending vibrations, respectively.

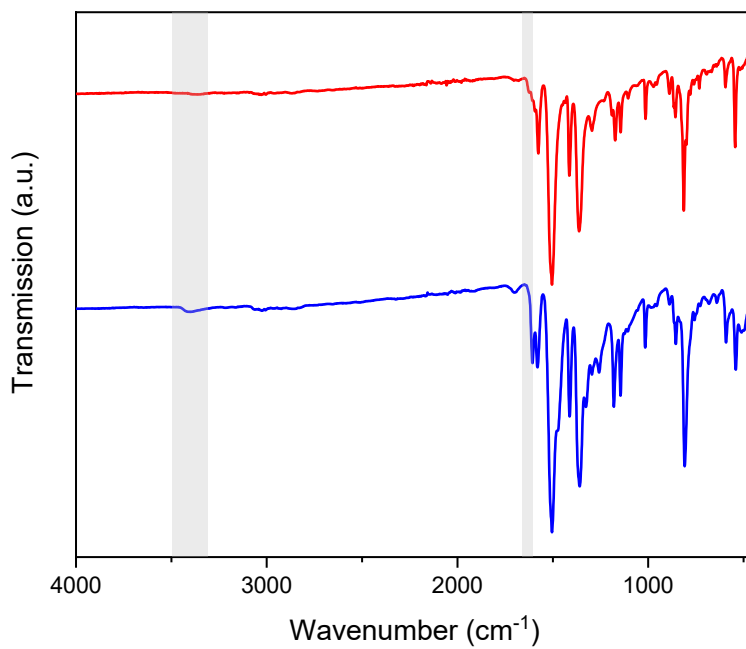


Figure S 9.1-3: Comparison of FT-IR spectra of TTI-COF (red) and rTTI-COF (blue). Grey areas highlight appearing secondary amine and disappearing imine vibrations upon reduction.

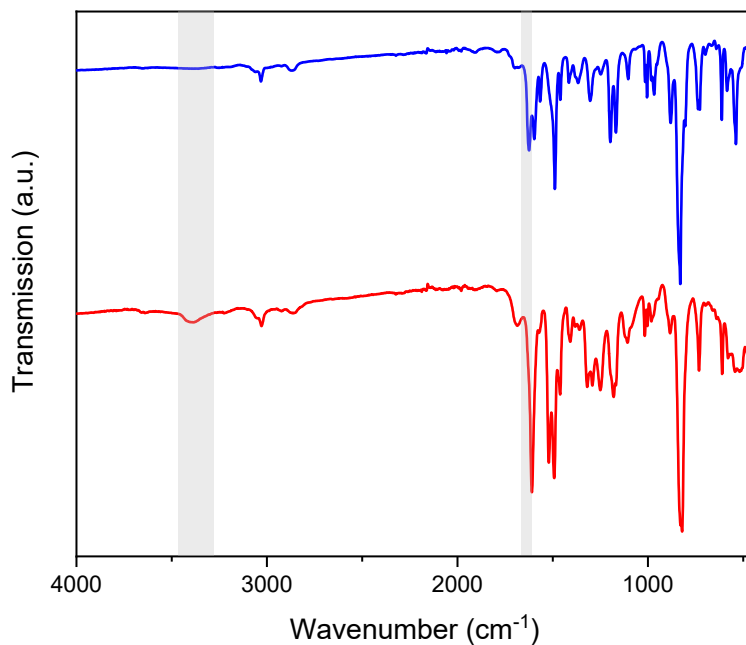


Figure S 9.1-4: Comparison of FT-IR spectra of Py1P-COF (blue) and rPy1P-COF (red). Grey areas highlight appearing secondary amine and disappearing imine vibrations upon reduction.

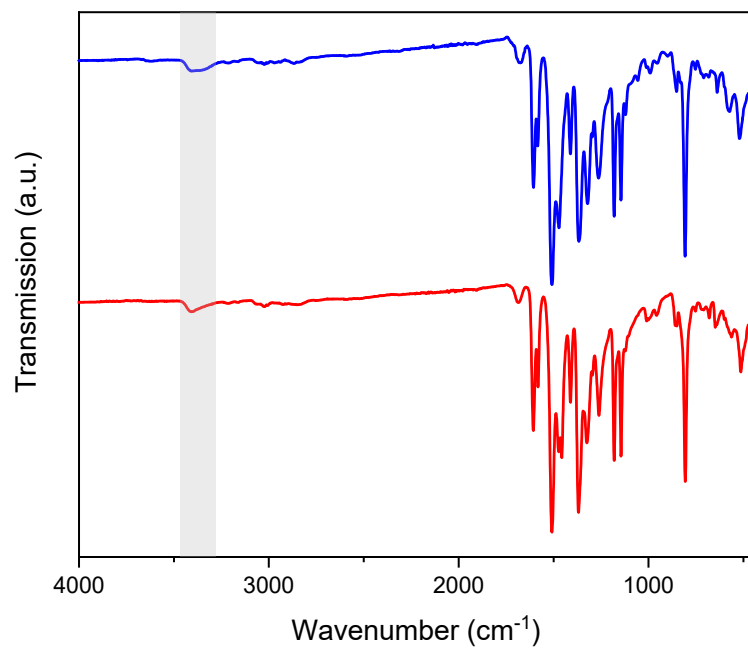


Figure S 9.1-5: Comparison of FT-IR spectra of disordered rPI-3-COF (blue) and rPI-3-COF (red). Grey area highlights broadened secondary amine vibrations in disordered rPI-3-COF.

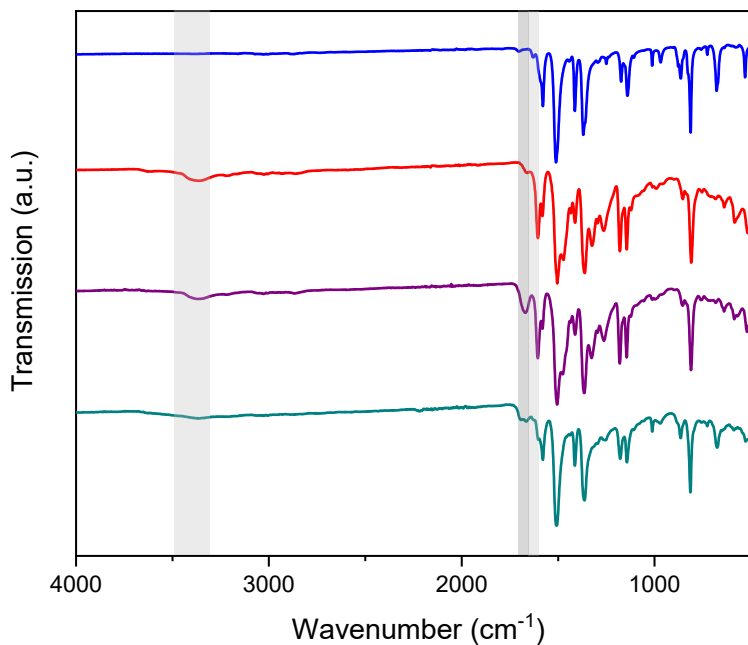


Figure S 9.1-6: Comparison of FT-IR spectra of PI-3-COF (blue), disordered rPI-3-COF (red), pfrPI-3-COF (purple) and opfrPI-3-COF (cyan). Grey areas highlight secondary amine as well as C=N (imine) and C=O vibrations (dark grey).

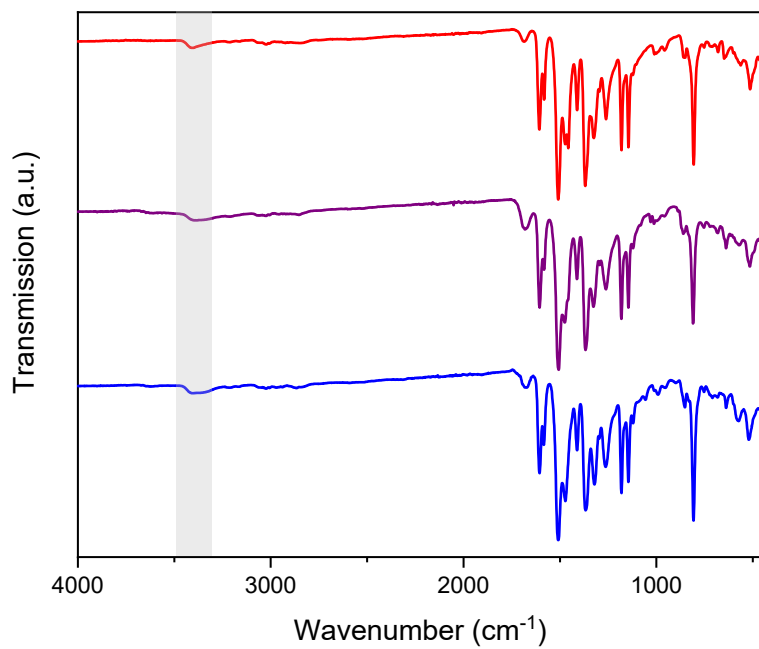


Figure S 9.1-7: Comparison of FT-IR spectra of rPI-3-COF (red), one-pot synthesized rPI-3-COF (purple) and disordered rPI-3-COF. Grey area highlights broadened secondary amine vibrations in disordered and one-pot rPI-3-COF.

9.1.4 X-Ray Powder Diffraction

9.1.4.1 Rietveld Refinements for Imine-linked COFs

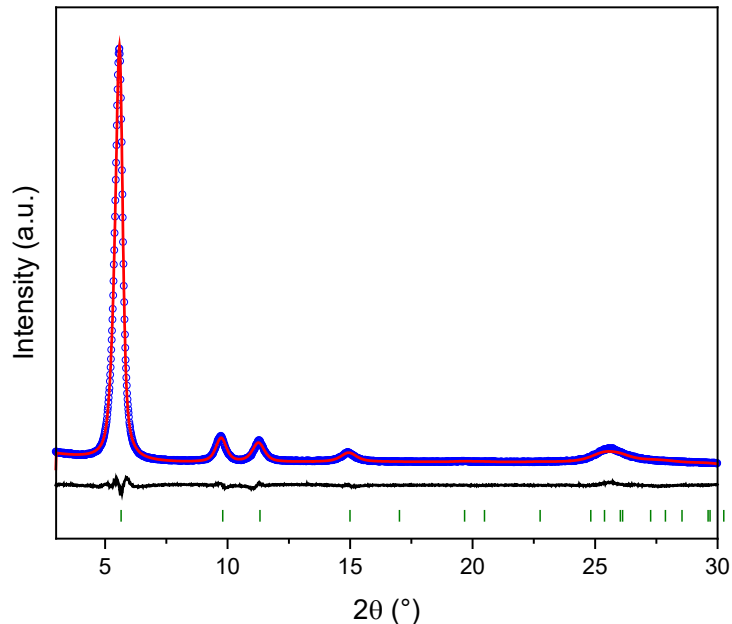


Figure S 9.1-8: Experimental (blue) and simulated XRPD (Cu-K α 1) diffractogram (red) of PI-3-COF after Rietveld refinement.

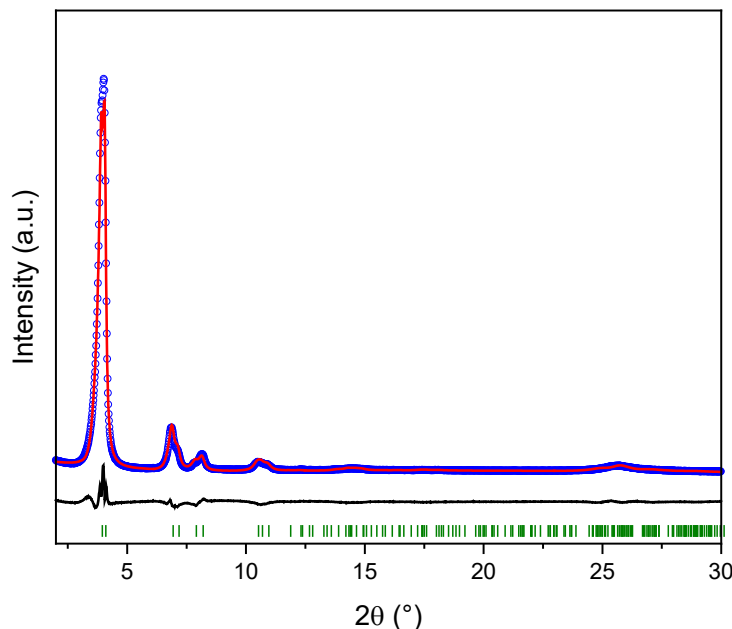


Figure S 9.1-9: Experimental (blue) and simulated XRPD (Cu-K α 1) diffractogram (red) of TTI-COF after Rietveld refinement.

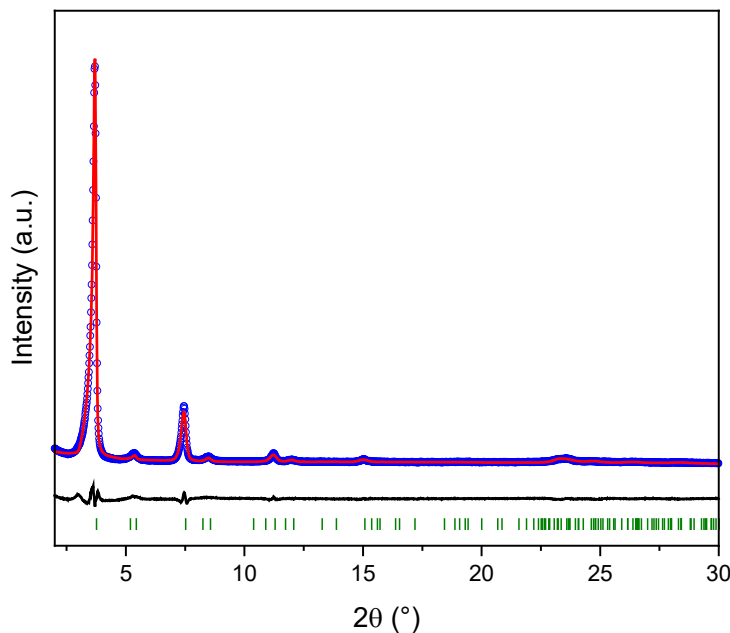


Figure S 9.1-10: Experimental (blue) and simulated XRPD (Cu-K α 1) diffractogram (red) of Py1P-COF after Rietveld refinement.

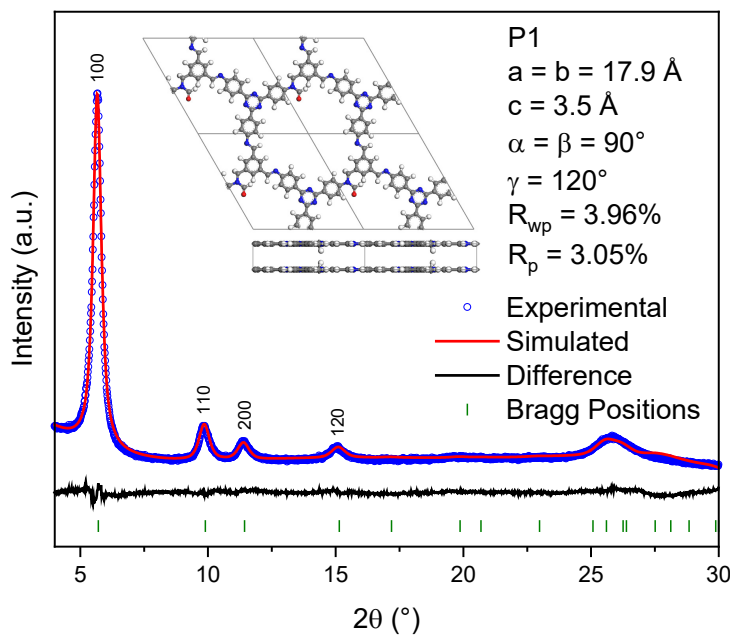


Figure S 9.1-11: Experimental (blue) and simulated XRPD (Cu-K α 1) diffractogram (red) of opfrPI-3-COF after Rietveld refinement. The conformation and concentration of *N*-formyl groups is arbitrarily and might not represent the real structure influenced by steric effects. The rather small scattering contrast does not allow to refine the exact torsion angle and amount per pore.

Table S 9.1-1: Cell parameters of Rietveld refined imine-linked COFs. OpfrPI-3-COF was fitted in a constrained *P1* space group to account for a non-symmetric occurrence of formyl groups in the structure model despite the high apparent symmetry in XRPD diffractogram.

Fitted Pattern	PI-3-COF ^[27]	opfrPI-3-COF	TTI-COF ^[29]	Py1P-COF ^[26]
Space group	<i>P</i> 6	<i>P</i> 1	<i>P</i> 1	<i>C</i> 2/ <i>m</i>
Constraints	-	$a = b; \alpha = \beta =$ $90; \gamma = 120^\circ$	$a = b; \alpha = \beta; \gamma =$ 120°	-
R_{wp} (%)	5.11	3.96	8.60	7.08
R_p (%)	3.61	3.05	6.51	5.24
a (Å)	18.034(7)	17.859(7)	25.786(12)	38.06(7)
b (Å)	18.034(7)	17.859(7)	25.786(12)	32.47(3)
c (Å)	3.5058(12)	3.4764(14)	7.239(5)	3.818(2)
α (°)	90	90	81.38(3)	90
β (°)	90	90	81.38(3)	63.34(18)
γ (°)	120	120	120	90

9.1.4.2 Rietveld Refinements for Amine-linked COFs

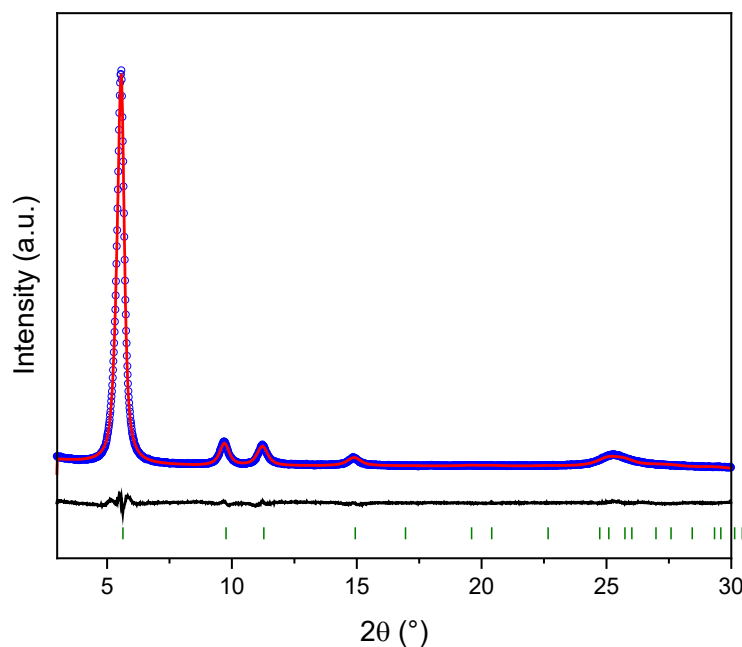


Figure S 9.1-12: Experimental (blue) and simulated XRPD (Cu-K α 1) diffractogram (red) of rPI-3-COF after Rietveld refinement.

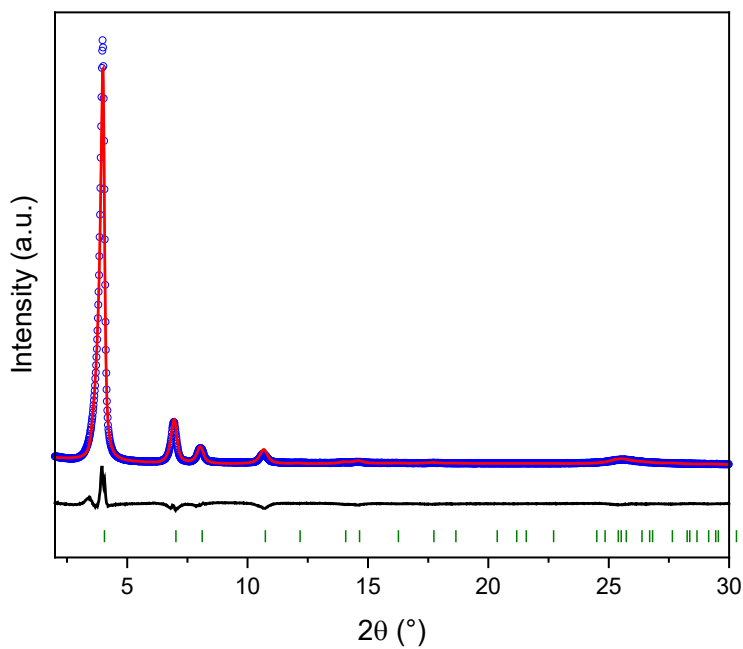


Figure S 9.1-13: Experimental (blue) and simulated XRPD (Cu-K α 1) diffractogram (red) of rTTI-COF after Rietveld refinement.

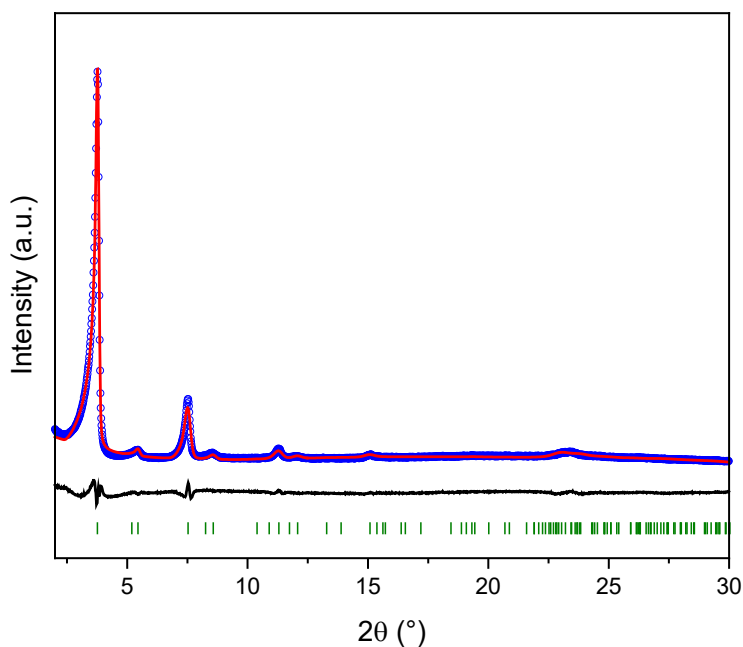


Figure S 9.1-14: Experimental (blue) and simulated XRPD (Cu-K α 1) diffractogram (red) of rPy1P-COF after Rietveld refinement.

Table S 9.1-2: Cell parameters of Rietveld refined amine-linked COFs. PrPy1P-COF was fitted in a constrained *P*1 space group to account for a non-symmetric occurrence of amine groups in the structure model despite the high apparent symmetry in XRPD diffractogram.

Fitted Pattern	rPI-3-COF	rPI-3-COF	rTTI-COF	rPy1P-COF	prPy1P-COF
Space group	<i>P</i> 3	<i>P</i> 6	<i>P</i> 6 ₃ / <i>m</i>	<i>C</i> 2/ <i>m</i>	<i>P</i> 1
Constraints	-	-	-	-	$\alpha = \gamma = 90^\circ$
R_{wp} (%)	6.68	5.06	9.67	6.42	5.52
R_p (%)	4.83	3.75	7.53	4.88	4.11
a (Å)	18.087(9)	18.090(7)	25.147(9)	41.04(17)	38.34(8)
b (Å)	18.087(9)	18.090(7)	25.147(9)	32.43(4)	32.50(3)
c (Å)	3.550(2)	3.5425(12)	7.008(4)	4.069(9)	3.876(3)
α (°)	90	90	90	90	90
β (°)	90	90	90	56.0(3)	62.6(2)
γ (°)	120	120	120	90	90

9.1.4.3 Coherence Length Analysis

Table S 9.1-3: Lateral and vertical crystallite coherence lengths for imine and amine linked COFs.

	Lateral crystallite coherence	Vertical crystallite coherence
	length (nm)	length (nm)
	100/010 peak	Stacking reflection (~001)
PI-3-COF	26(2)	4(1)
rPI-3-COF	30(8)	4(2)
disordered	10(2)	2(1)
rPI-3-COF	8(2)	2(1)
pfrPI-3-COF	24(2)	4(1)
opfrPI-3-COF		

Coherence lengths were estimated by single line fits of the apparent 100/010 peak for the lateral direction and the apparent stacking peak observed around 25.5° 2 θ for the vertical direction. For the second feature, this assumes that the peak is predominantly only from the periodicity of locally disordered layers in the stacking direction, and does not contain strong

contributions from the other allowed reflections suggested by the apparent crystallographic space group. The instrumental profile was accounted for by Rietveld refinement to a measurement of Silicon standard using constant Gaussian, Lorentzian, and exponential convolutions using TOPAS v6.^[30] An additional exponential convolution was refined to the sharpest 100 peak of sample rPI-3-COF, to account for additional asymmetry in the much broader diffraction patterns observed for the COFs that could not be accounted for with the standard profile. This was not found to have a large impact on the crystallite sizes obtained from the refinement of this sample, and was fixed for the other samples for comparison. Then, peak broadening from the samples was accounted for by an additional Lorentzian broadening term, and the crystallite sizes in the respective directions were estimated from the resulting volume averaged column heights (LVol-IB). The errors were estimated as the refinement uncertainties multiplied by a factor of ten. It is important to note that these values roughly estimate the minimum crystallite coherence lengths of the respective directions, and can result from either discrete crystallites or the buildup of defects resulting in an uncorrelated relationship between atoms at longer distances.

The values are in excellent agreement with the measured PDF data, i.e. that the lateral coherence of the disordered samples is significantly smaller than the ordered samples. Also, the coherence of the stacked layers is much smaller in all samples, likely due to random local layer offsets. The stacking coherence of the samples appears slightly longer from the PDF data, about 4 nm for disordered samples and 6 nm for ordered samples. It is further worth noting that, by the relative peak intensities, disordered rPI-3-COF appears to have relatively more content with ordered lateral dimensions while pfrPI-3-COF appears to have relatively more content with ordered stacking.

9.1.4.4 Additional XRPD Patterns

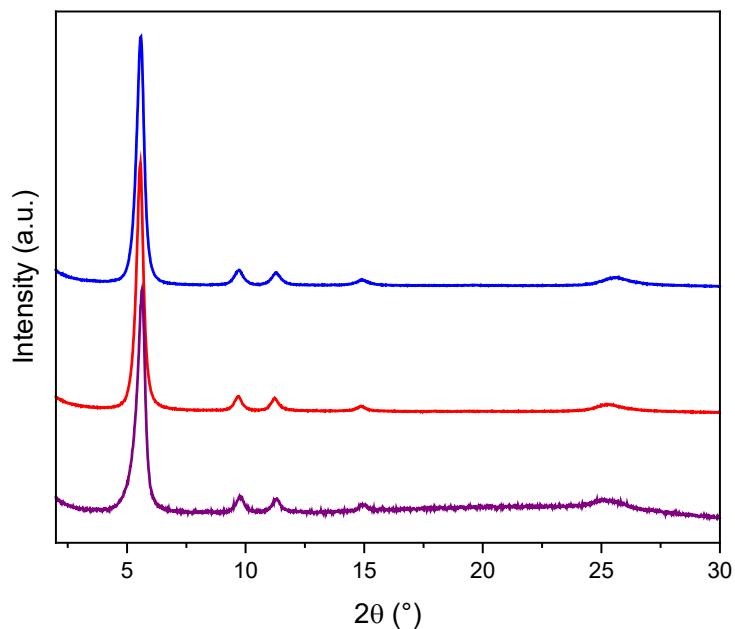


Figure S 9.1-15: XRPD (Cu-K α 1) patterns of PI-3-COF (blue) and rPI-3-COF obtained by reduction of PI-3-COF (red) in comparison to rPI-3-COF obtained by one-pot crystallization/reduction approach.

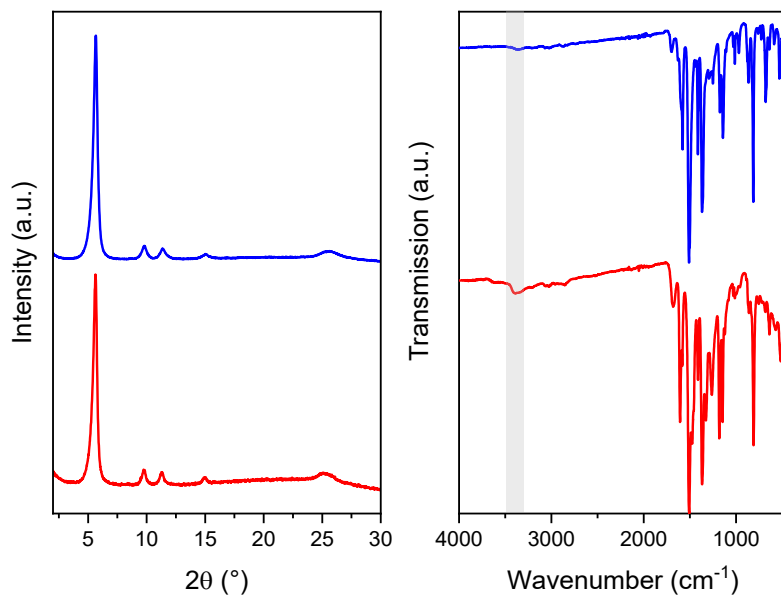


Figure S 9.1-16: XRPD (Cu-K α 1) patterns and FT-IR spectra of one-pot synthesized rPI-3 COF at 60°C (after 2 days, blue line) and 120°C (after 3d, red line). Grey area highlights secondary amine vibrations caused by reduction of imine linkages. A comparison of both reaction temperatures shows that formic acid catalyzes the crystallization process already at 60°C, while higher temperatures are needed for fast reduction of the framework.

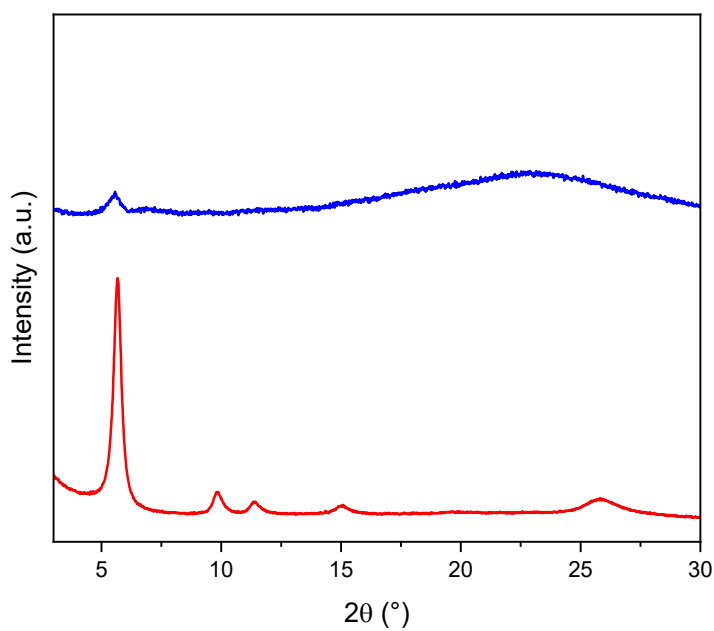


Figure S 9.1-17: XRPD (Cu-K α 1) patterns of pfrPI-3-COF (blue) and opfrPI-3-COF (red) - same sample after oxidation with DDQ. Increased crystallinity after oxidation supports the hypothesis that disorder in pfrPI-3-COF is influenced by structural disorder, while the molecular structure of the framework is kept intact.

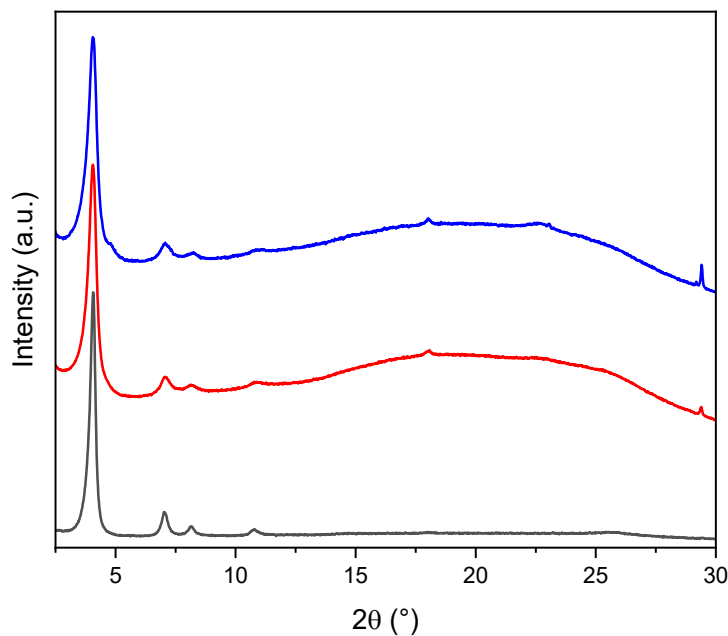


Figure S 9.1-18: XRPD (Cu-K α 1) pattern comparison of BzCl-rTTI-COF (blue), TDI-rTTI-COF (red) and rTTI-COF (black). Increased background and broadened, but defined reflections indicate that the structure of the functionalized COFs is principally retained, but may also be influenced by steric interactions of the immobilized moieties.

9.1.5 ssNMR Spectroscopy

9.1.5.1 ssNMR Spectra of Imine-linked COFs

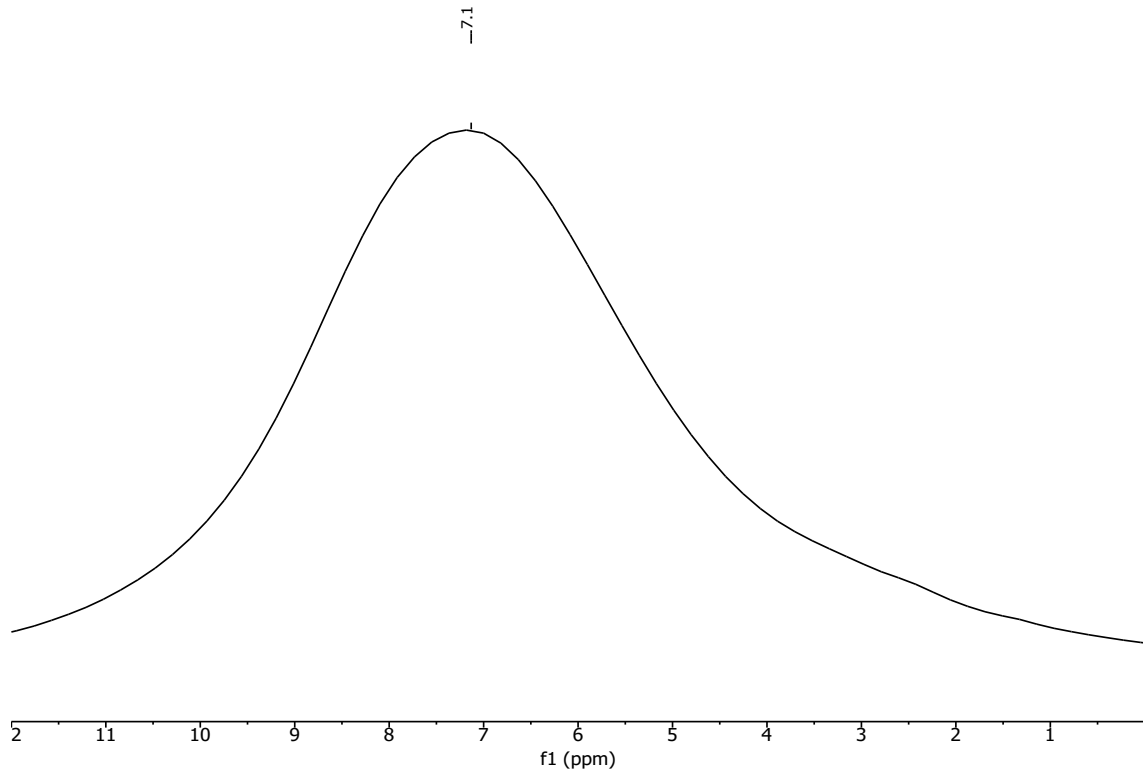


Figure S 9.1-19: ^1H ssNMR MAS spectrum of PI-3-COF.

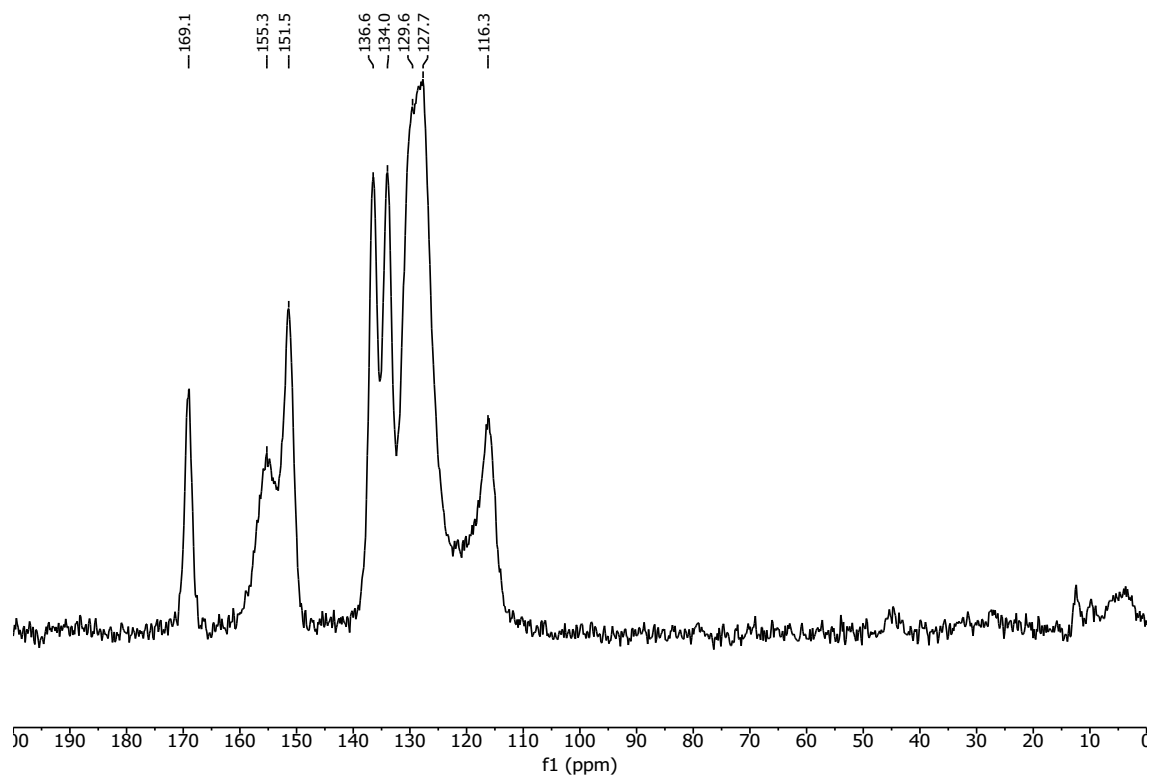


Figure S 9.1-20: ¹³C ssNMR CP-MAS spectrum of PI-3-COF.

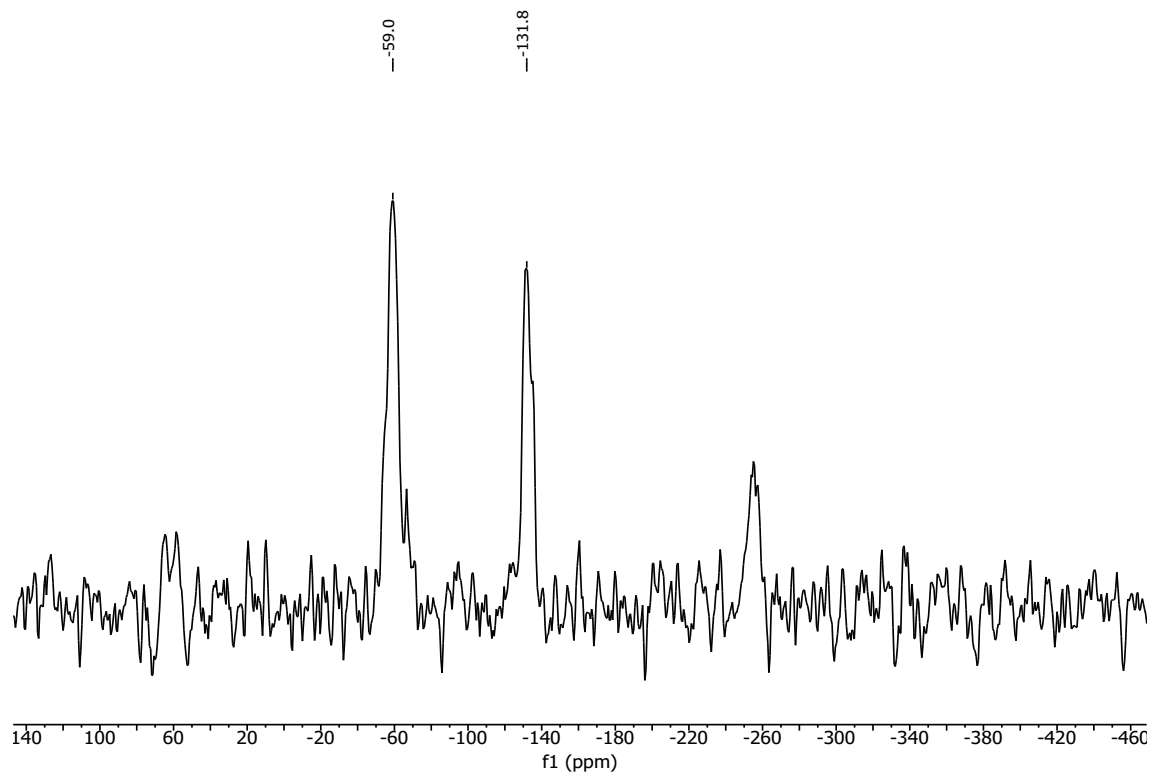


Figure S 9.1-21: ¹⁵N ssNMR CP-MAS spectrum of PI-3-COF.

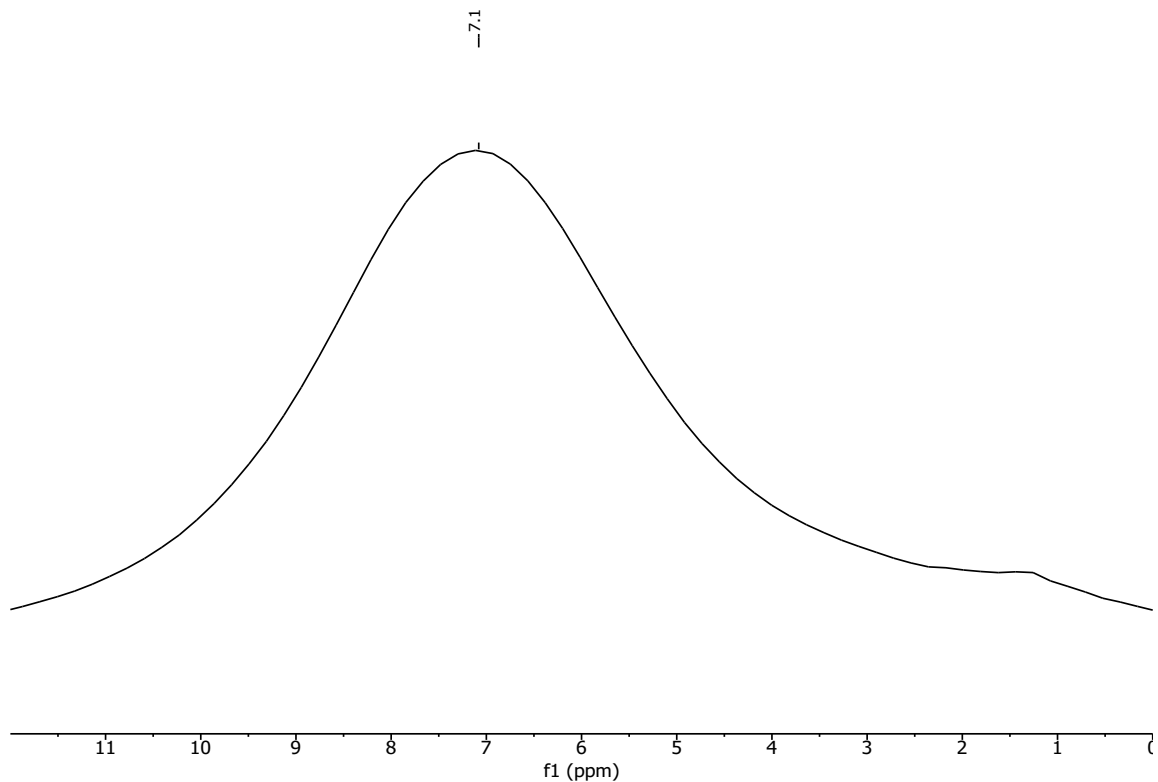


Figure S 9.1-22: ¹H ssNMR MAS spectrum of TTI-COF.

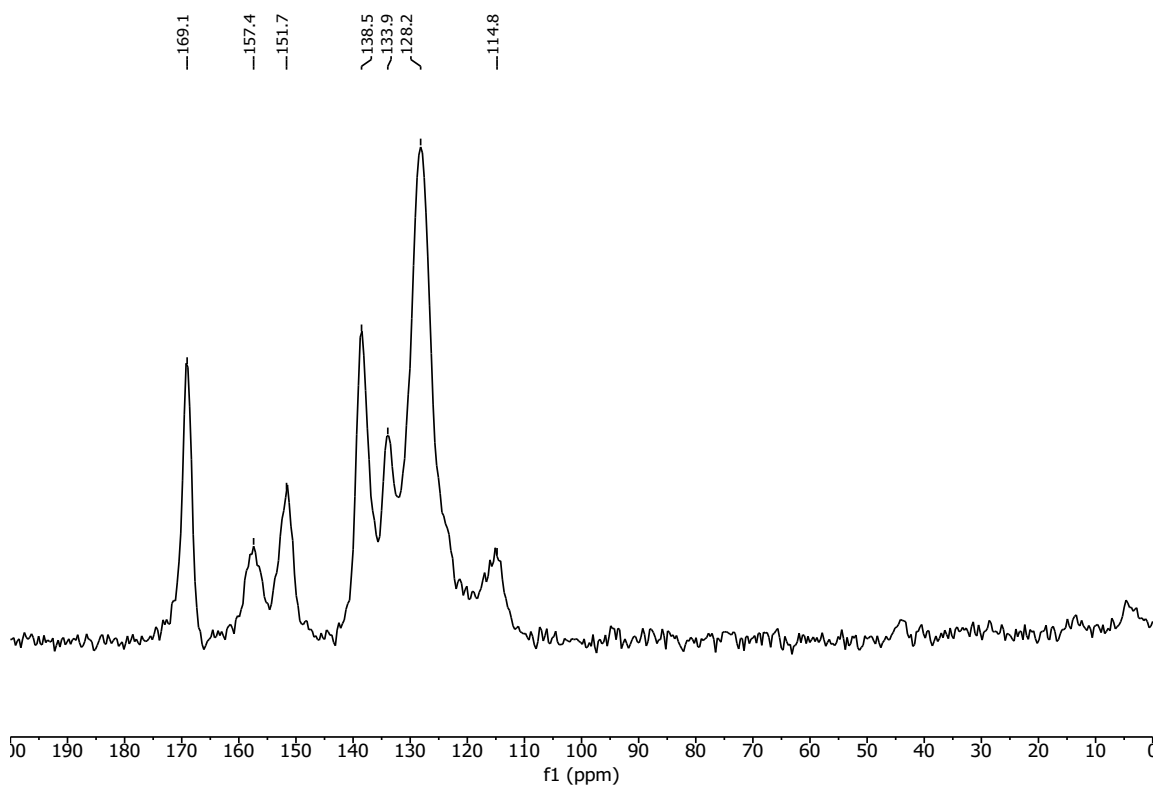


Figure S 9.1-23: ¹³C ssNMR CP-MAS spectrum of TTI-COF.

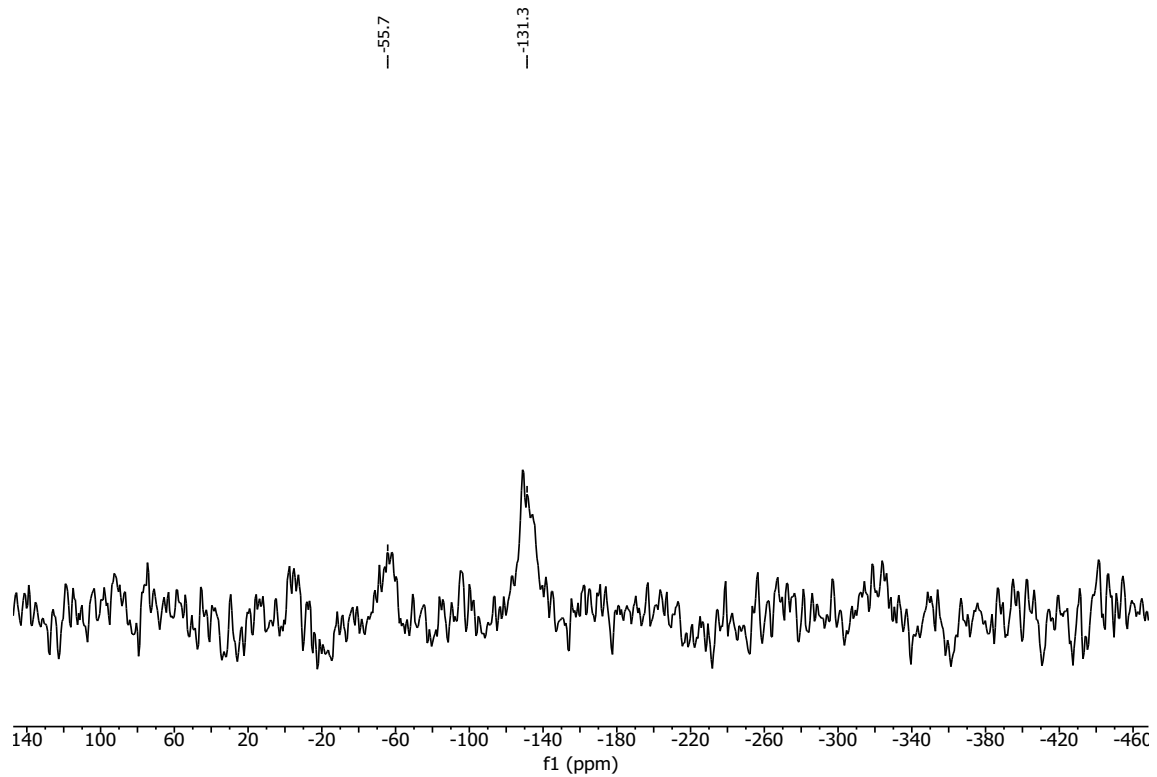


Figure S 9.1-24: ^{15}N ssNMR CP-MAS spectrum of TTI-COF.

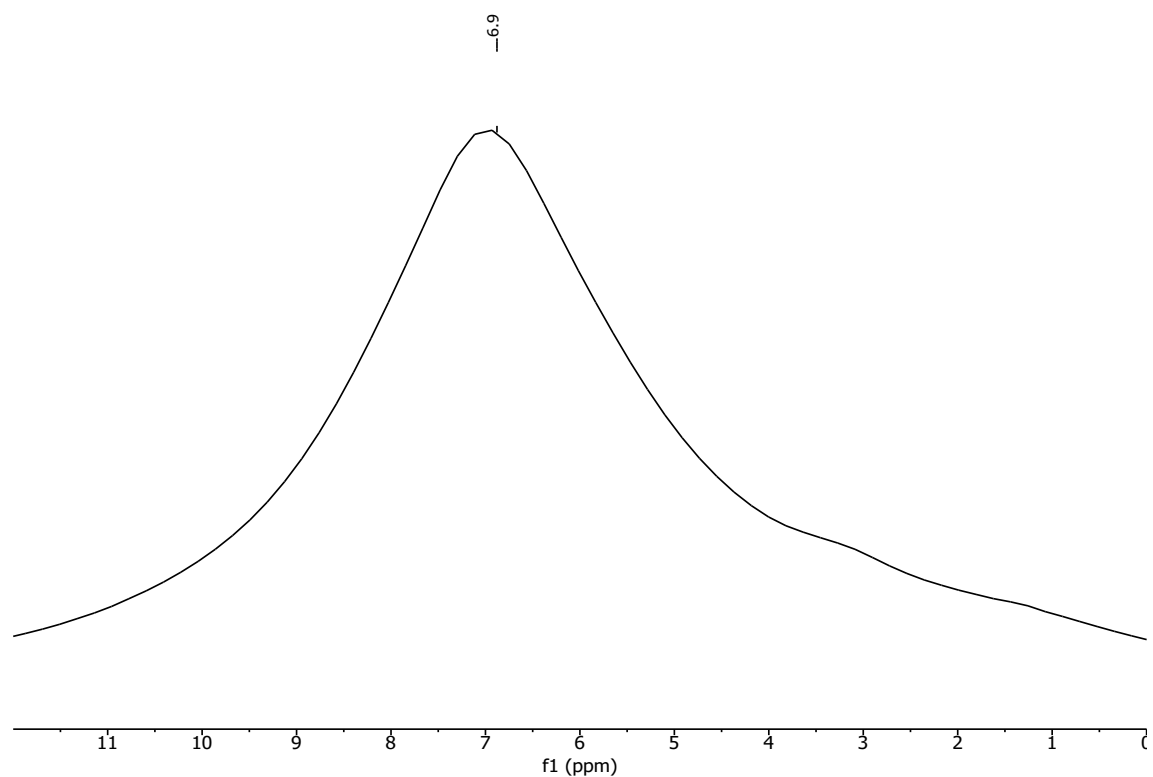


Figure S 9.1-25: ^1H ssNMR MAS spectrum of Py1P-COF.

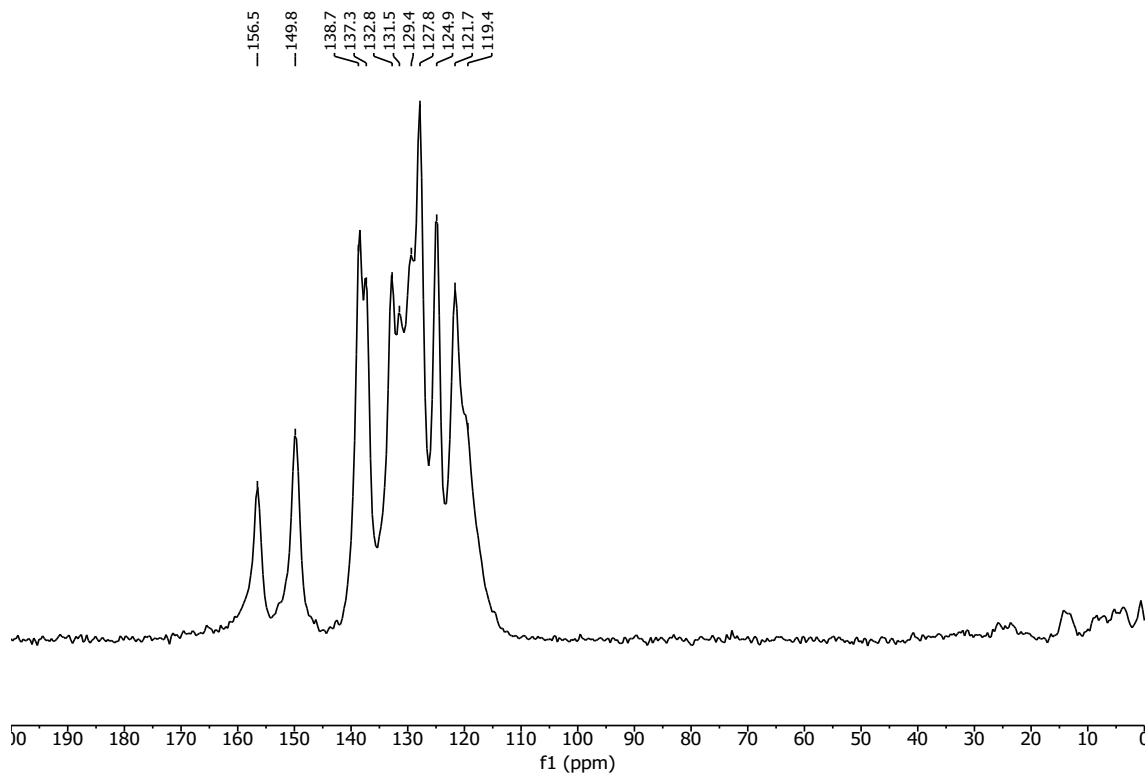


Figure S 9.1-26: ¹³C ssNMR CP-MAS spectrum of Py1P-COF.

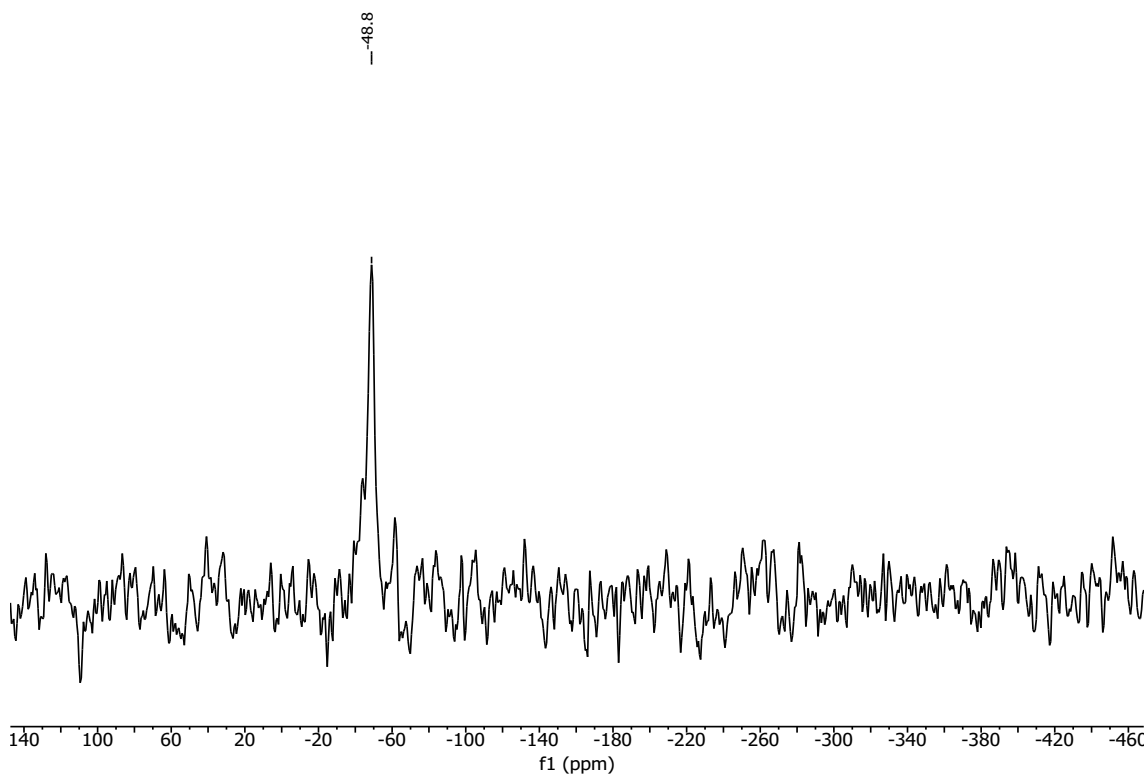


Figure S 9.1-27: ¹⁵N ssNMR CP-MAS spectrum of Py1P-COF.

9.1.5.2 ssNMR Spectra of Amine-linked COFs

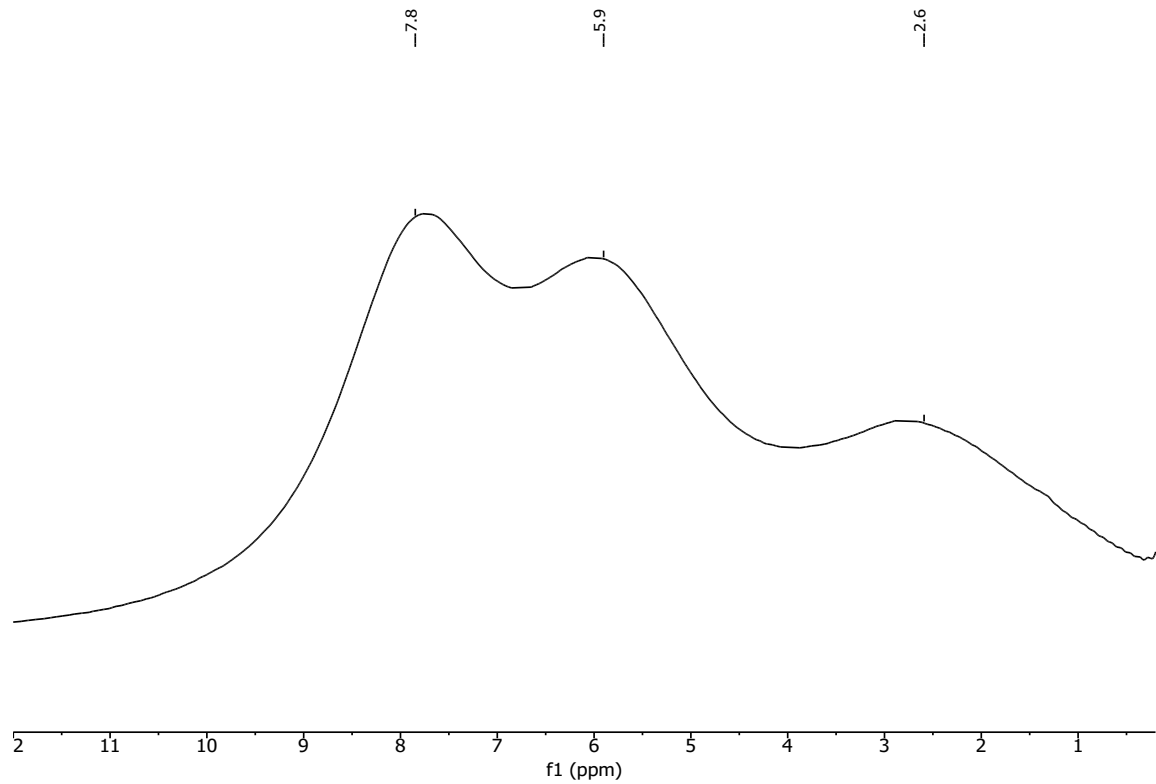


Figure S 9.1-28: ¹H ssNMR MAS spectrum of rPI-3-COF.

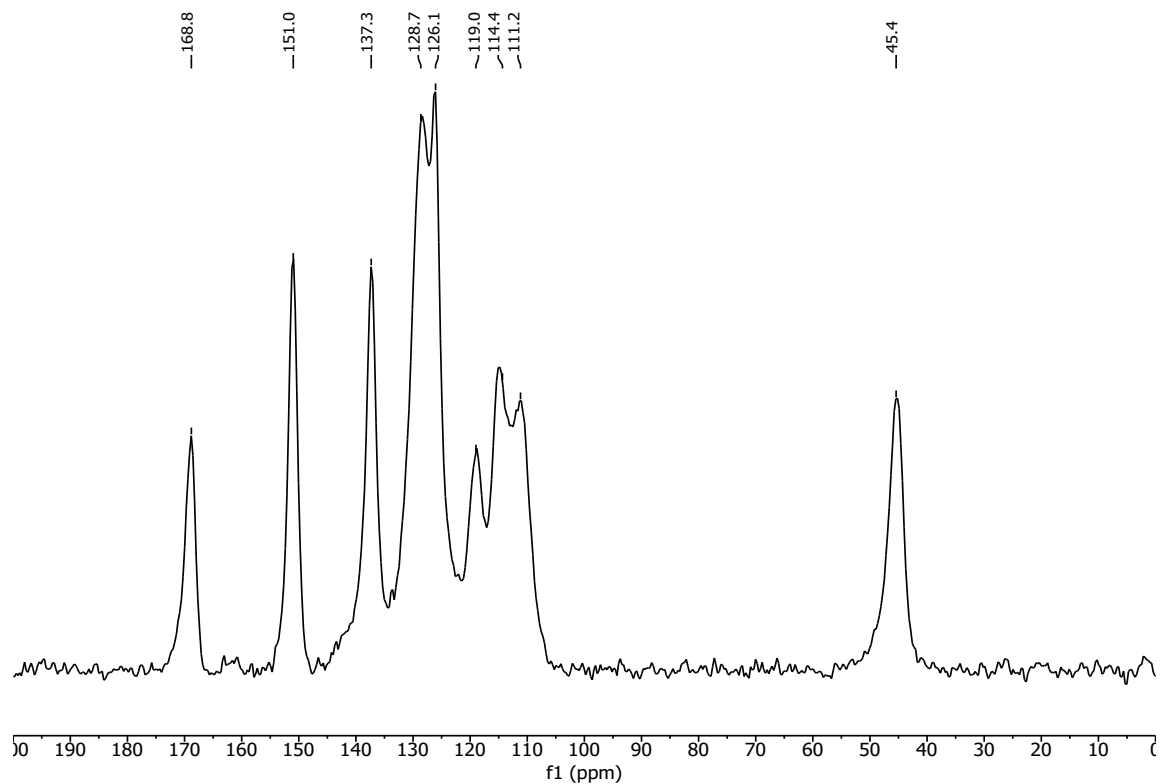


Figure S 9.1-29: ¹³C ssNMR CP-MAS spectrum of rPI-3-COF.

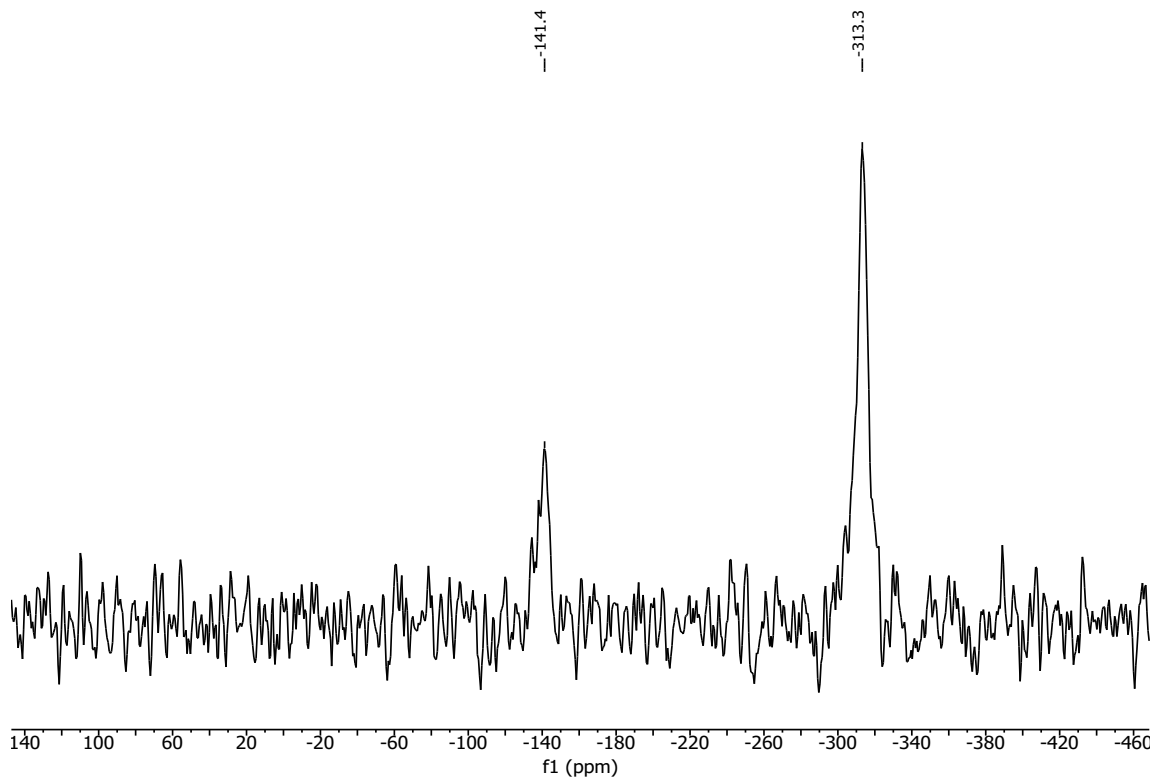


Figure S 9.1-30: ^{15}N ssNMR CP-MAS spectrum of rPI-3-COF.

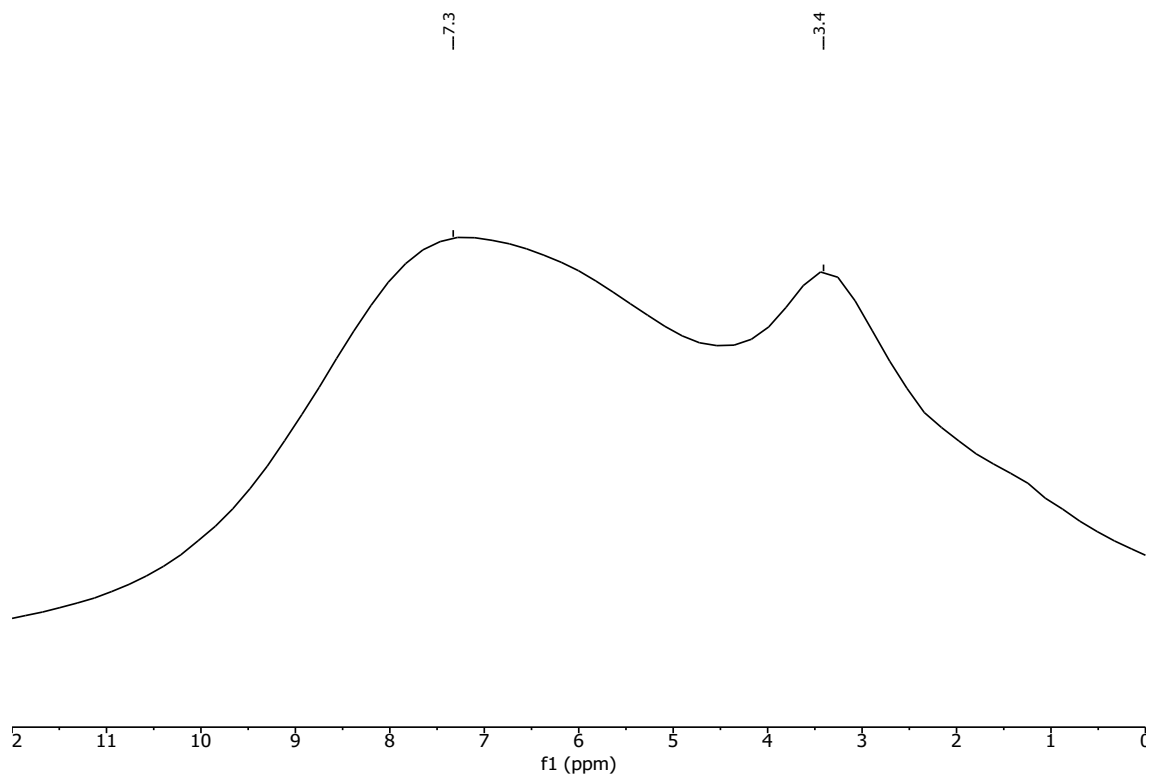


Figure S 9.1-31: ^1H ssNMR MAS spectrum of disordered rPI-3-COF.

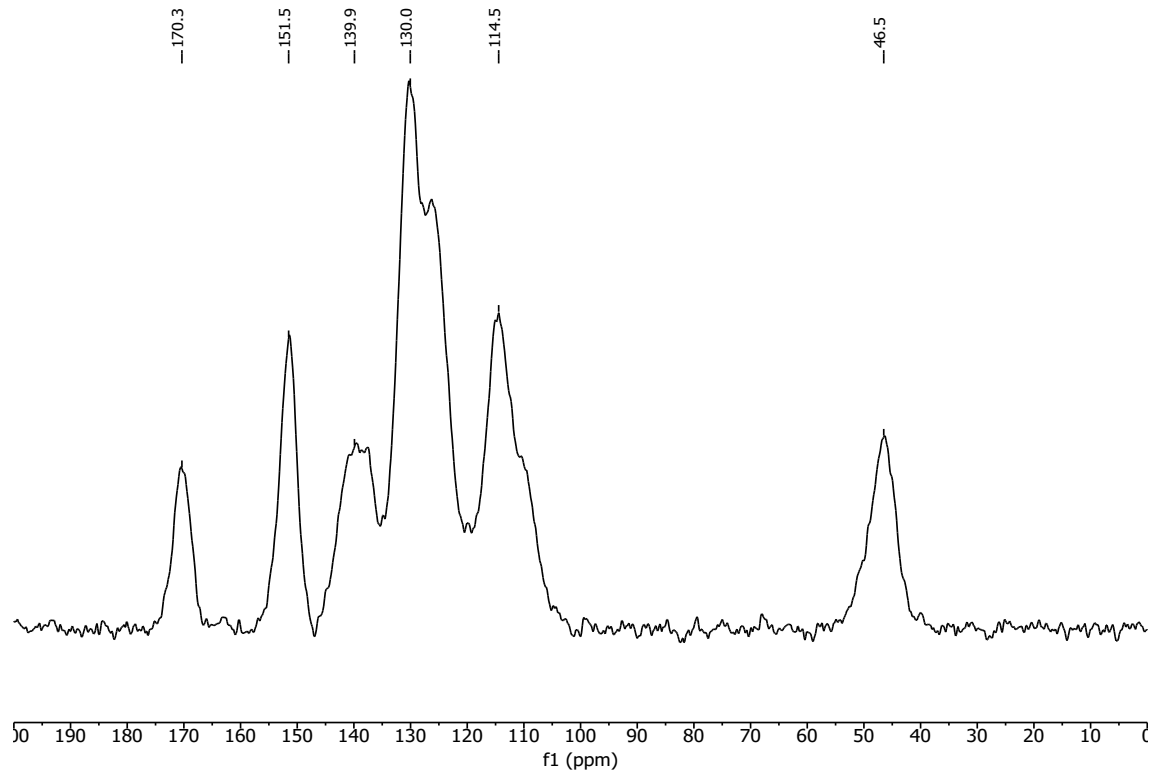


Figure S 9.1-32: ^{13}C ssNMR CP-MAS spectrum of disordered rPI-3-COF.

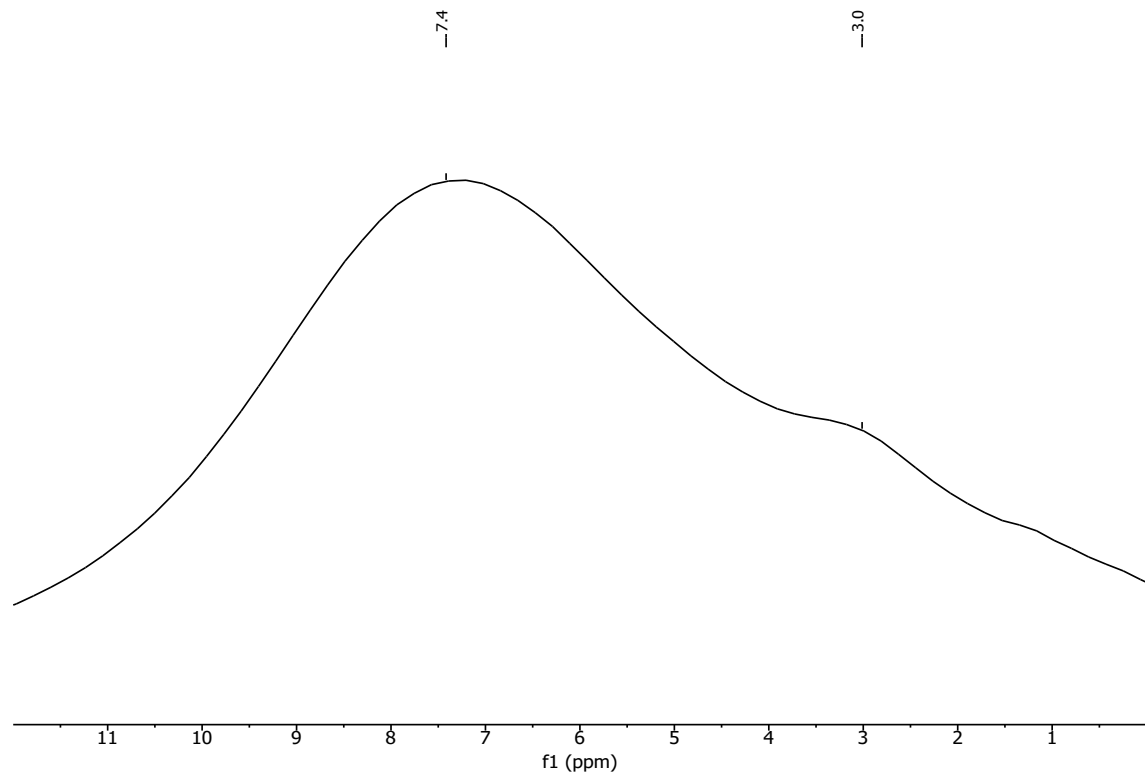


Figure S 9.1-33: ^1H ssNMR MAS spectrum of rTTI-COF.

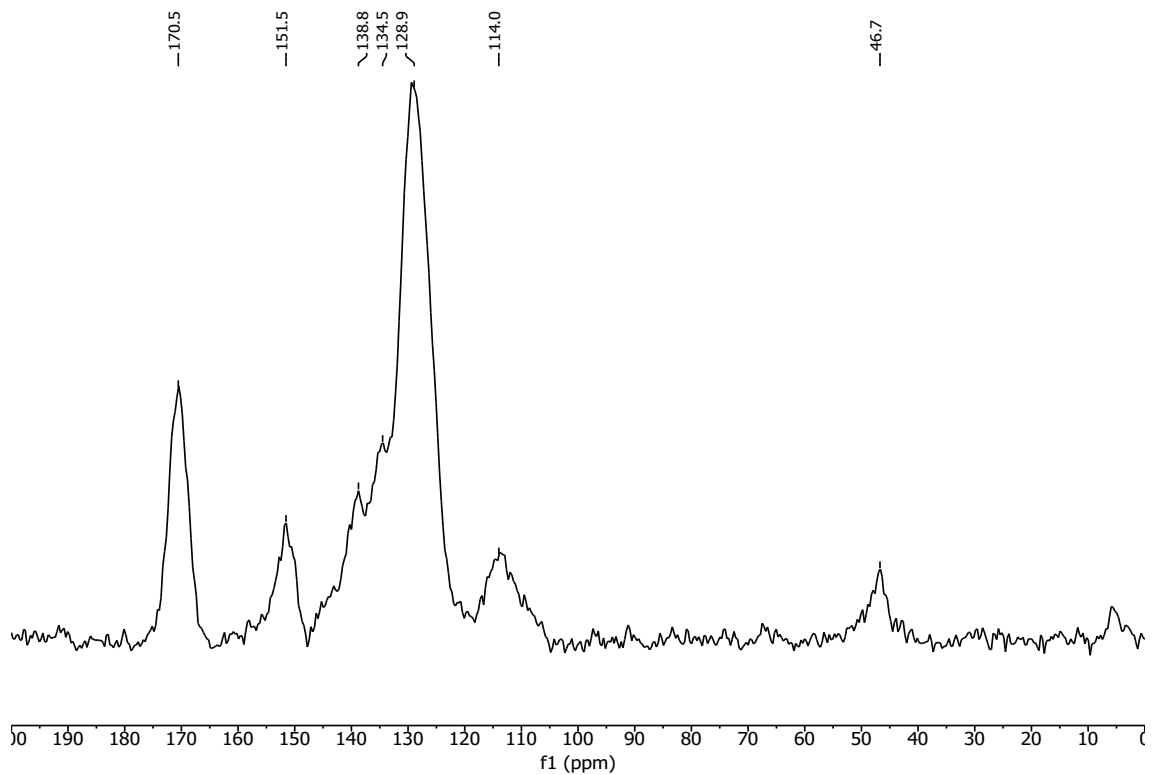


Figure S 9.1-34: ¹³C ssNMR CP-MAS spectrum of rTTI-COF.

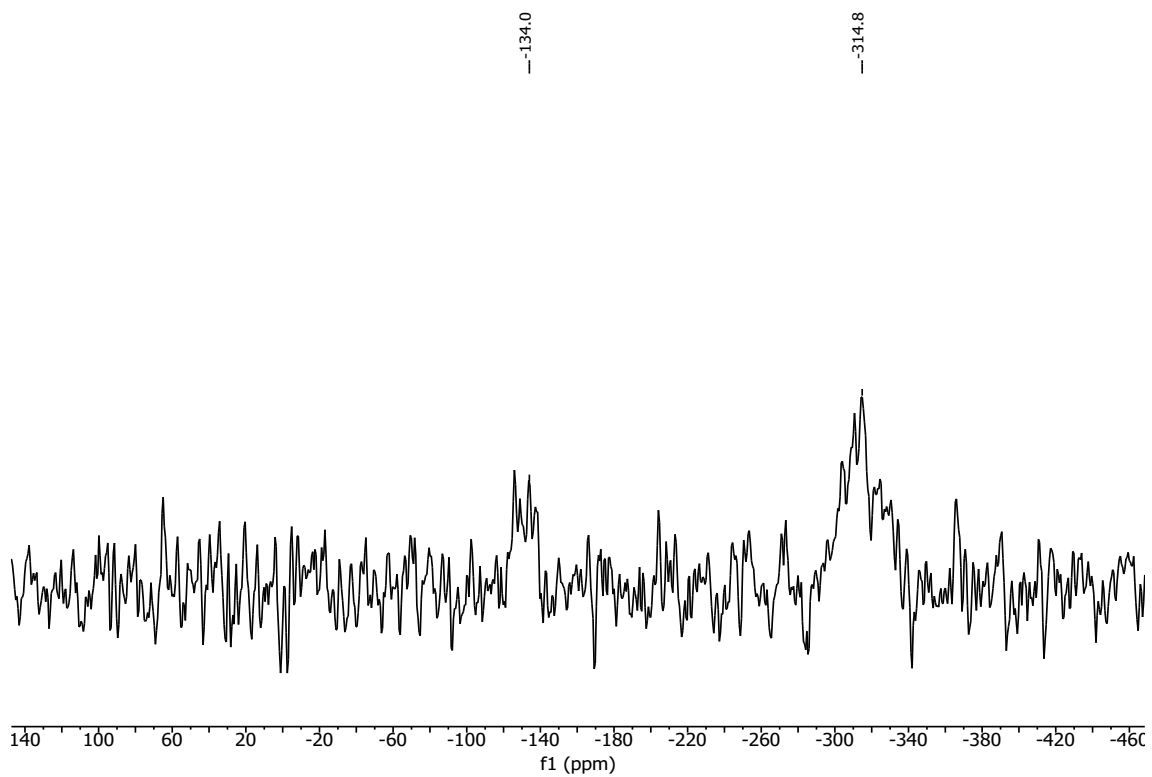


Figure S 9.1-35: ¹⁵N ssNMR CP-MAS spectrum of rTTI-COF.

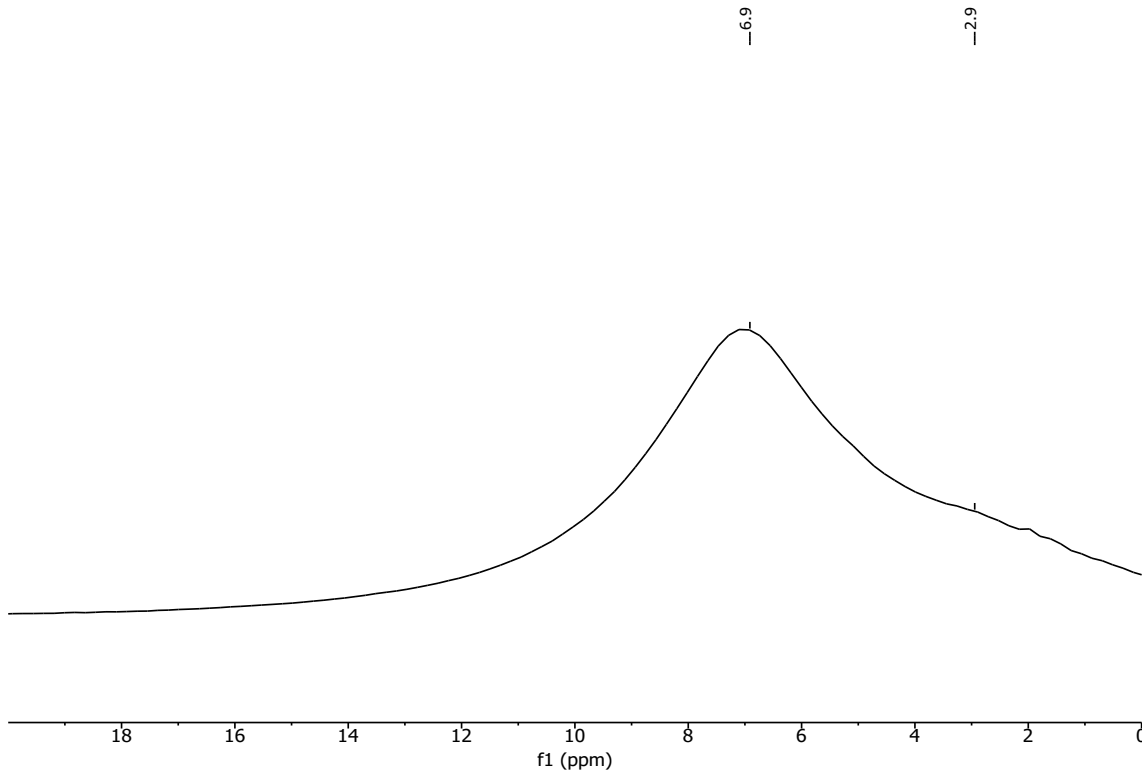


Figure S 9.1-36: ¹H ssNMR MAS spectrum of rPy1P-COF.

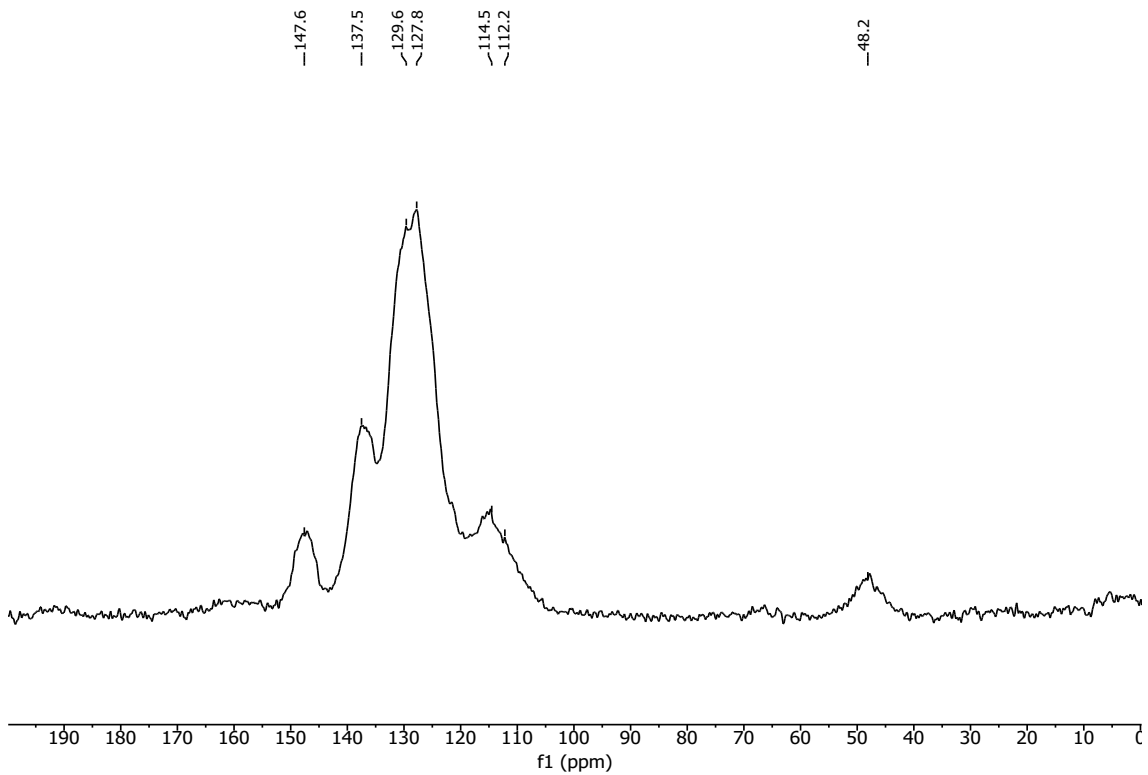


Figure S 9.1-37: ¹³C ssNMR CP-MAS spectrum of rPy1P-COF.

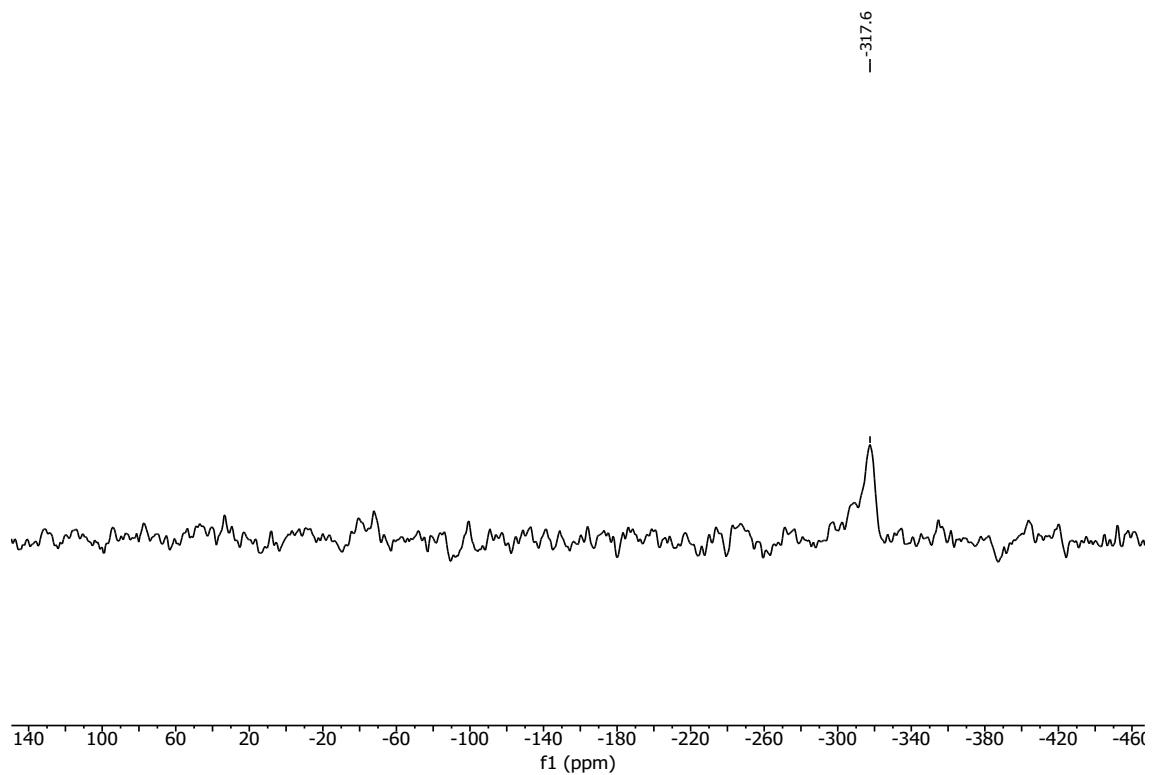


Figure S 9.1-38: ^{15}N ssNMR CP-MAS spectrum of rPy1P-COF.

9.1.5.3 ssNMR Spectra of Hybrid Materials

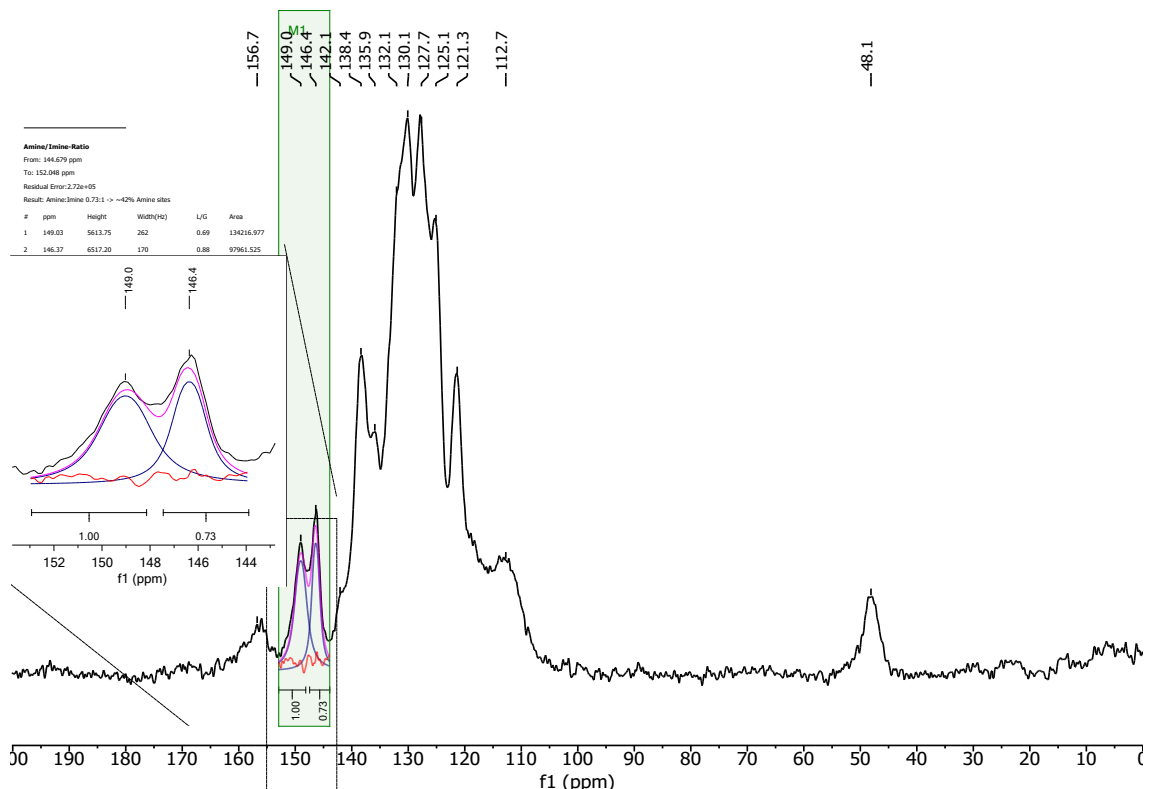
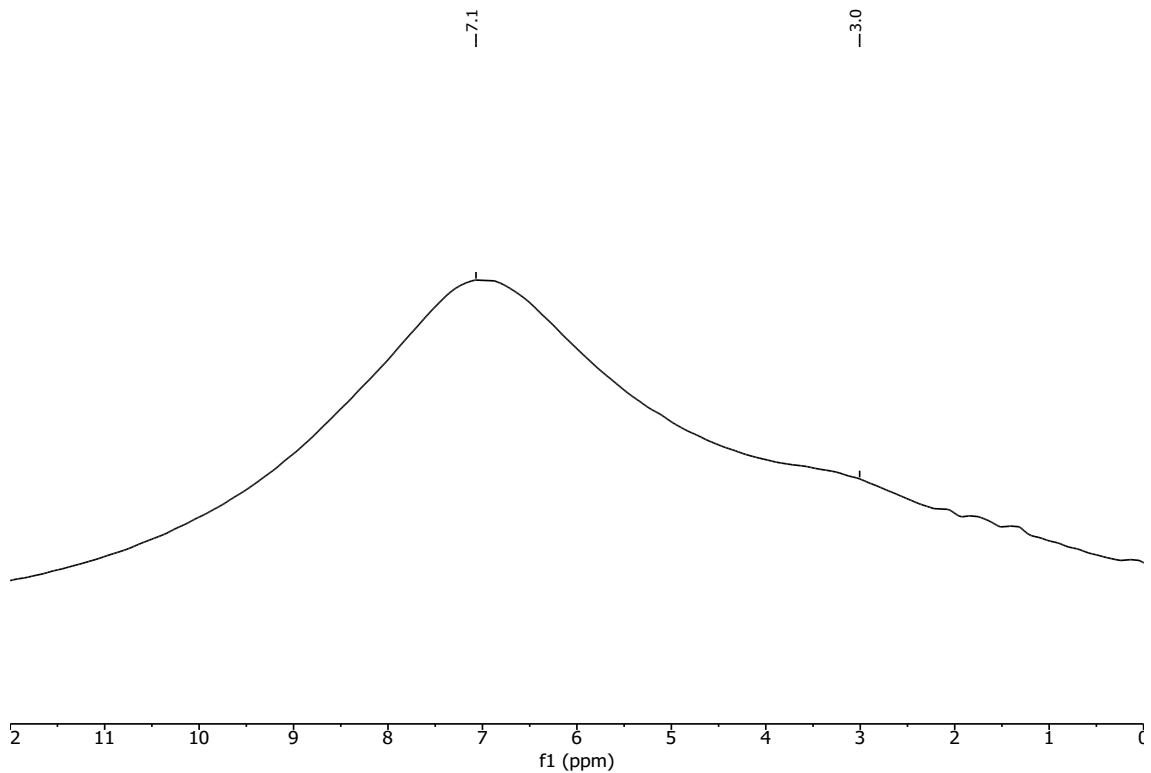


Figure S 9.1-40: ^{13}C ssNMR CP-MAS spectrum of prPy1P-COF including line fitting to determine amine/imine ratio. Note that this approximation can only be done from this CP experiment, because relaxation times of the quaternary carbons (orange, red) are expected to be similar.

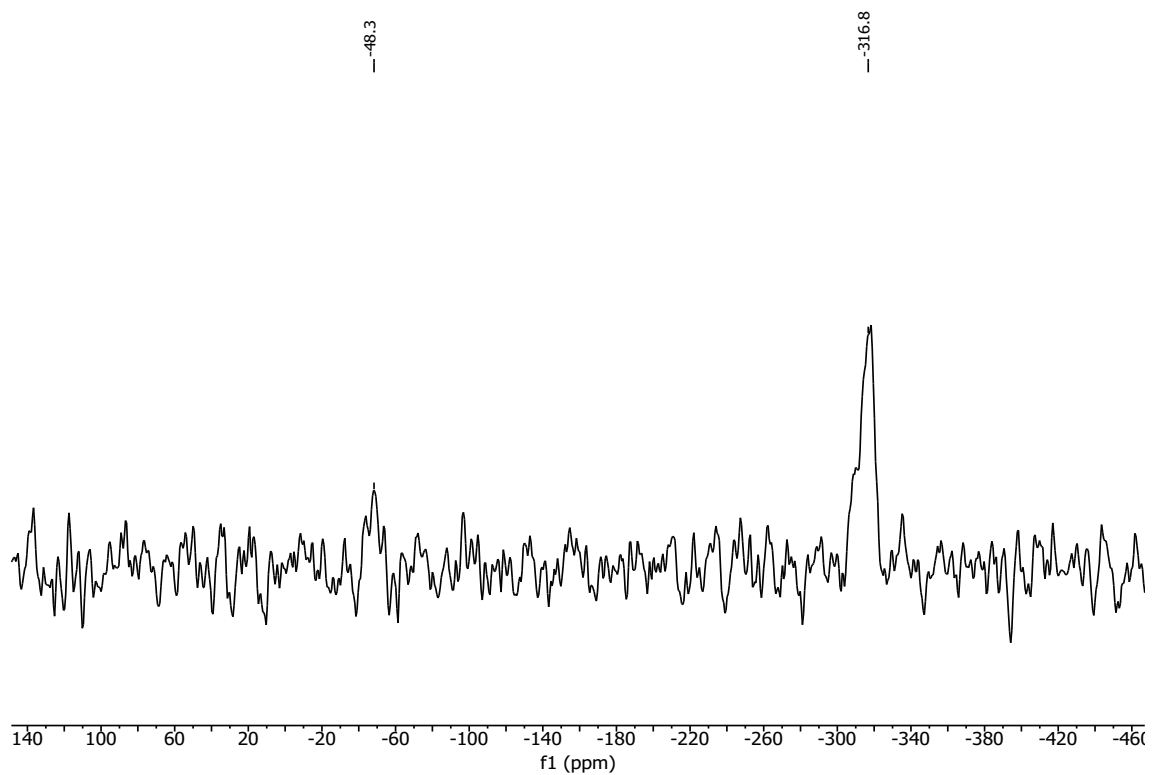


Figure S 9.1-41: ¹⁵N ssNMR CP-MAS spectrum of prPy1P-COF

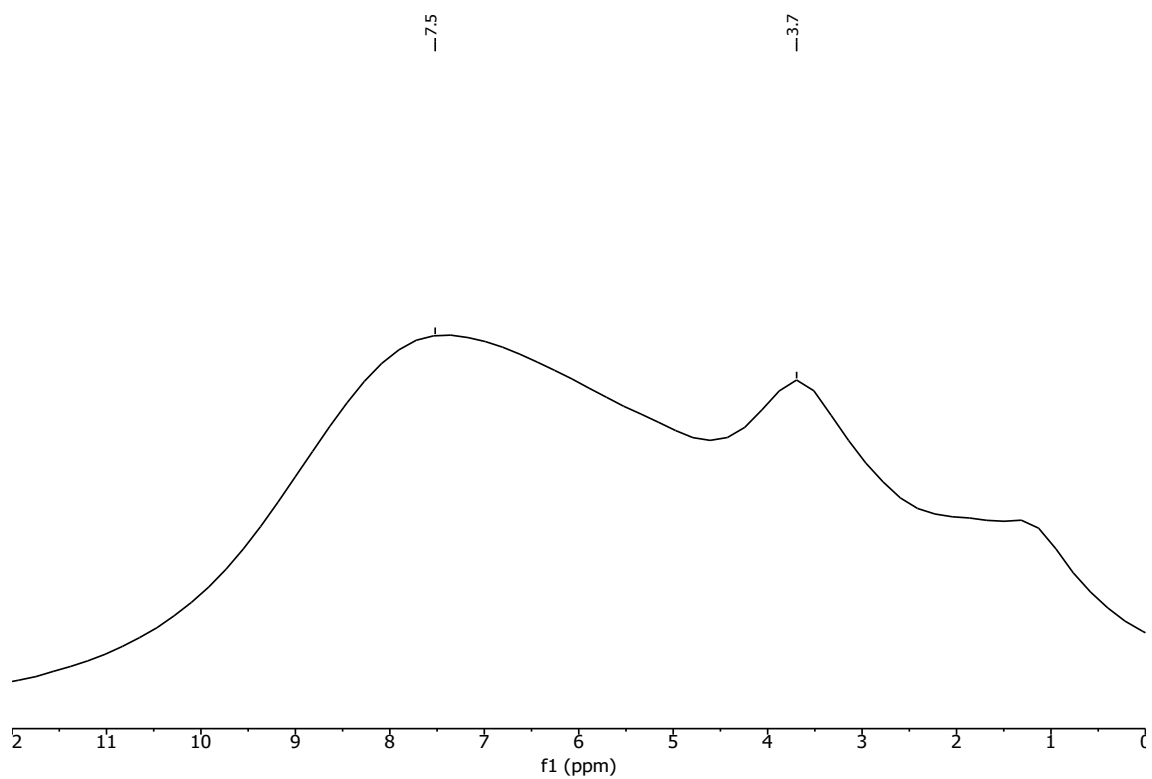


Figure S 9.1-42: ¹H ssNMR MAS spectrum of pfrPI-3-COF.

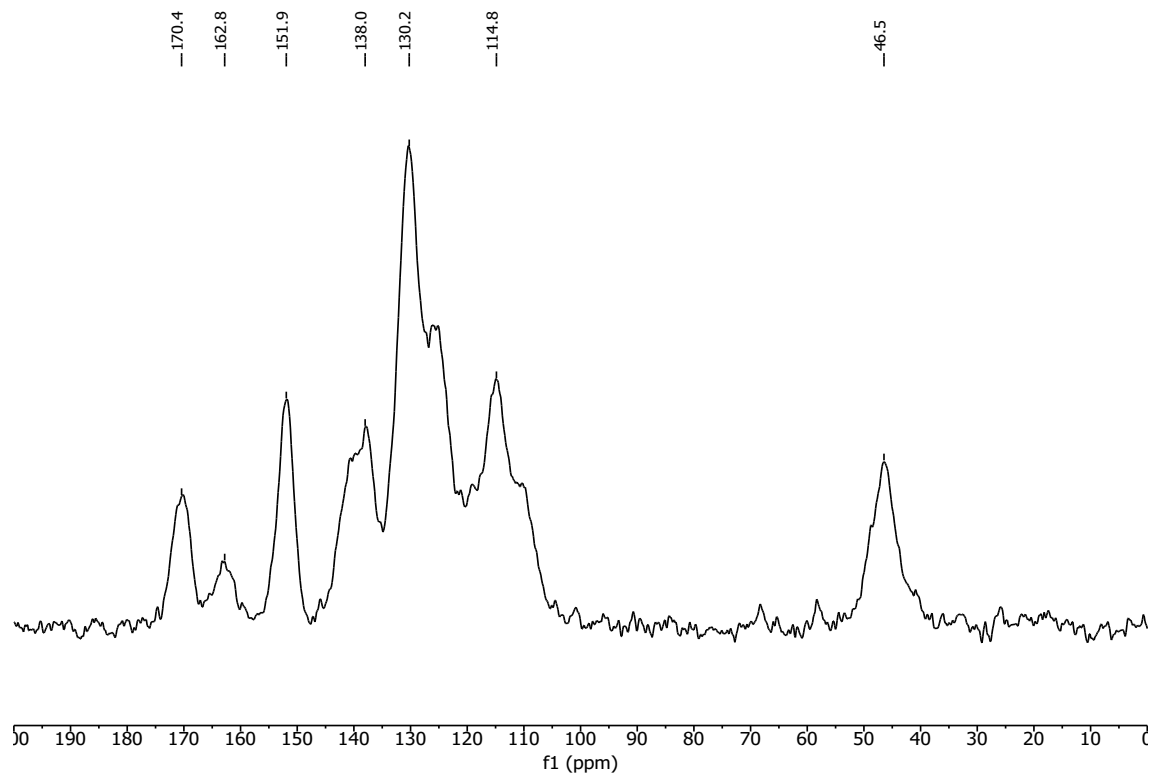


Figure S 9.1-43: ^{13}C ssNMR MAS spectrum of pfrPI-3-COF.

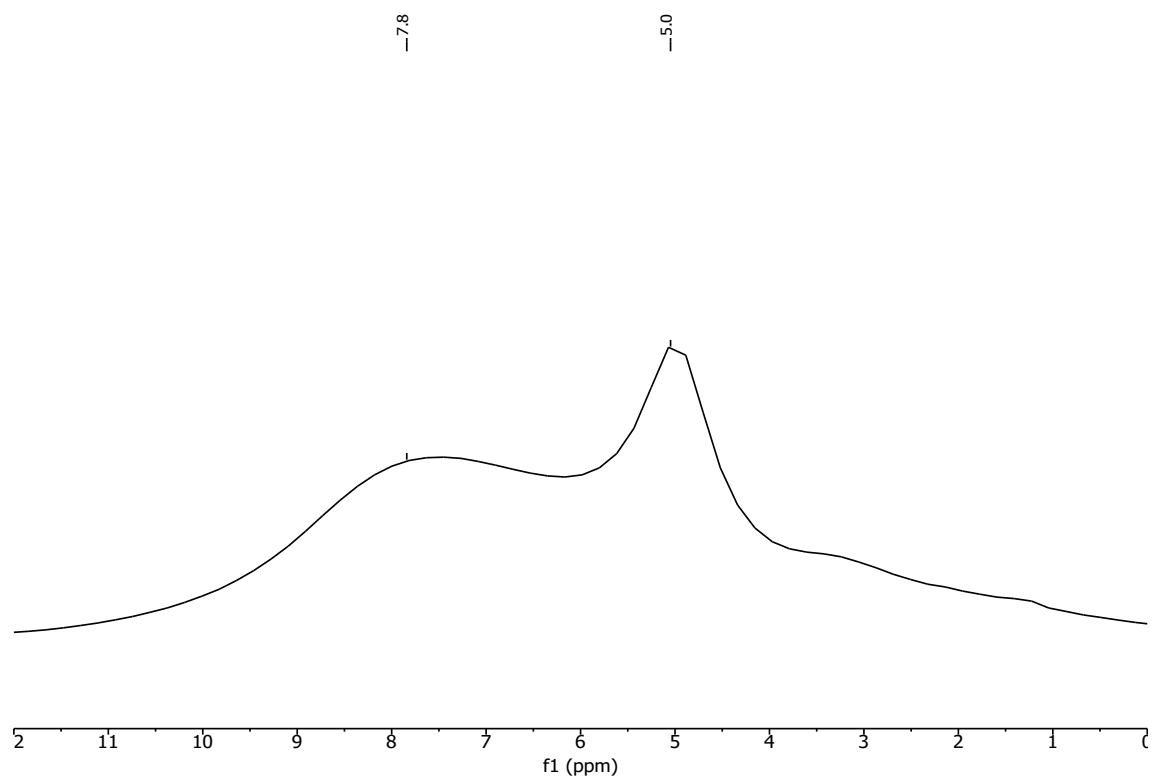


Figure S 9.1-44: ^1H ssNMR MAS spectrum of opfrPI-3-COF.

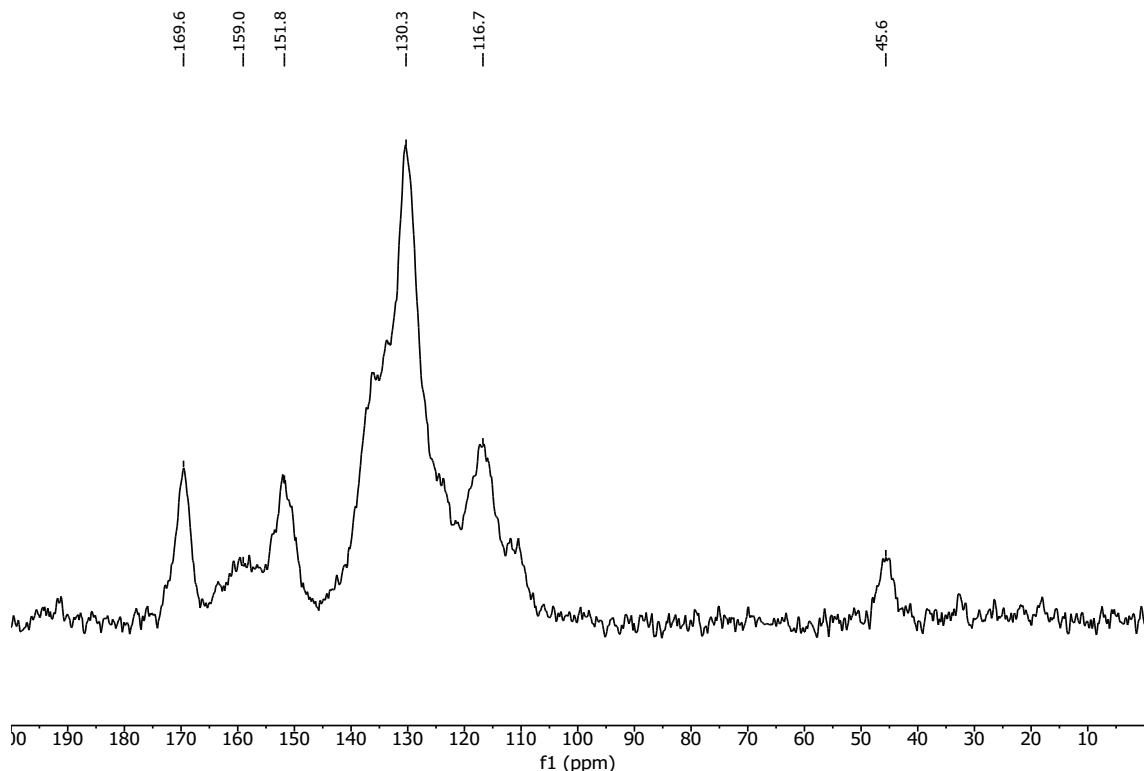


Figure S 9.1-45: ^{13}C ssNMR MAS spectrum of opfrPI-3-COF.

9.1.5.4 Additional ssNMR Spectra

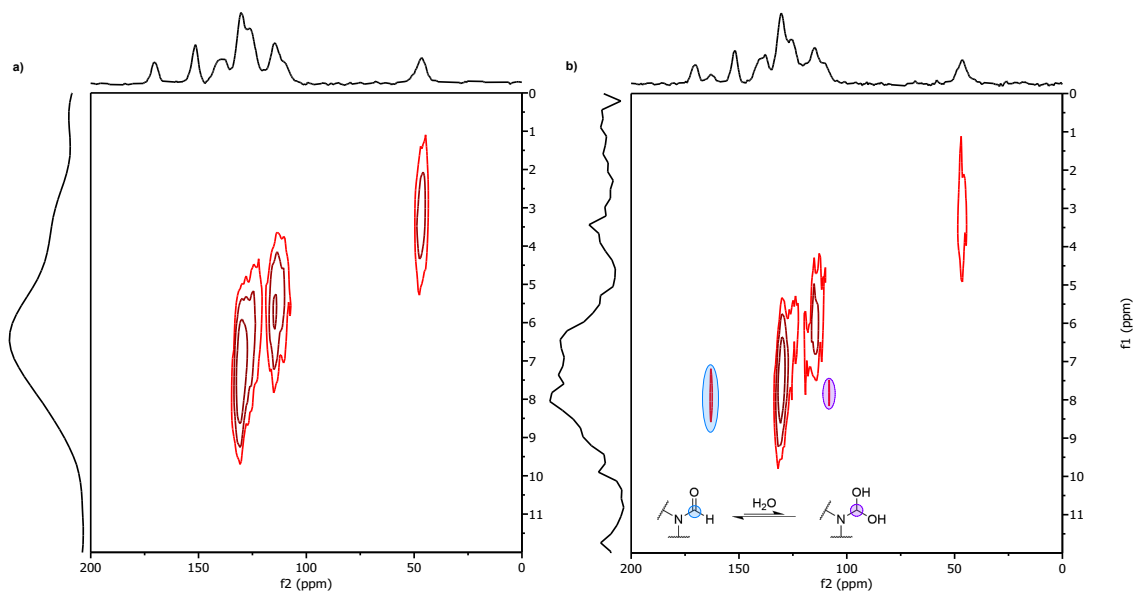


Figure S 9.1-46: $^1\text{H}/^{13}\text{C}$ -HETCOR ssNMR spectra of disordered rPI-3-COF (a) and pfPI-3-COF (b) in comparison. The spectra are plotted against ^{13}C -CP MAS spectra (horizontal trace) and internal projection (vertical trace). N-Formyl groups (blue) form hydrates (purple) with residual pore water, bound as hydrate in pfPI-3-COF, resulting in an additional but weak signal at 108 ppm in the carbon spectrum. After treatment with aqueous acid, the signals disappear, suggesting a deprotection of the secondary amines under these conditions – affording disordered rPI-3-COF (a).

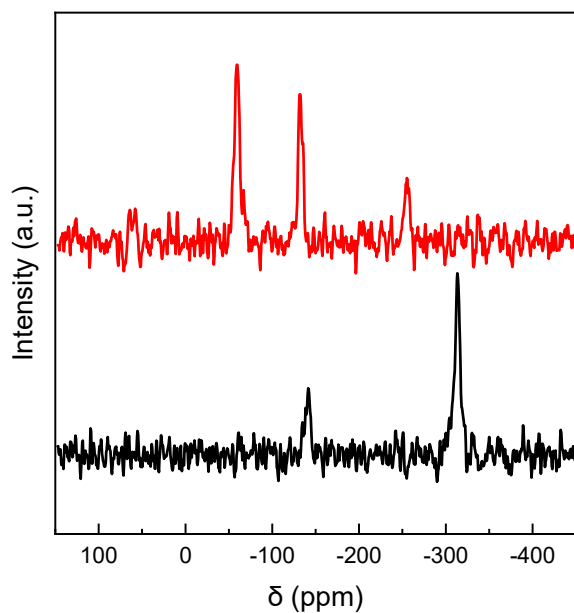


Figure S 9.1-47: Comparison of ¹⁵N-CPMAS ssNMR spectra of PI-3-COF (red) and rPI-3-COF (black).

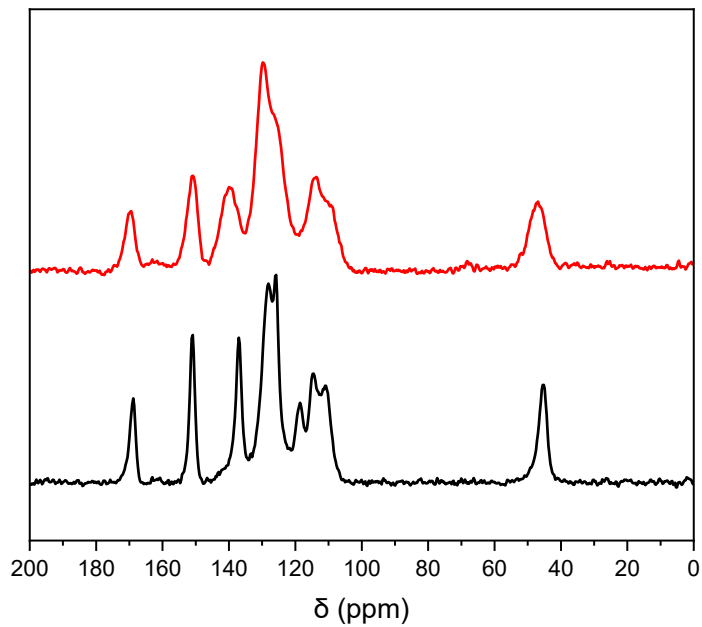


Figure S 9.1-48: Comparison of ¹³C-CPMAS ssNMR spectra of disordered rPI-3-COF (red) and rPI-3-COF (black). Broadened signals indicate disorder in the framework. Note that signal at 119 ppm refers to planar orientation of phenyl rings in the crystalline, well ordered material.

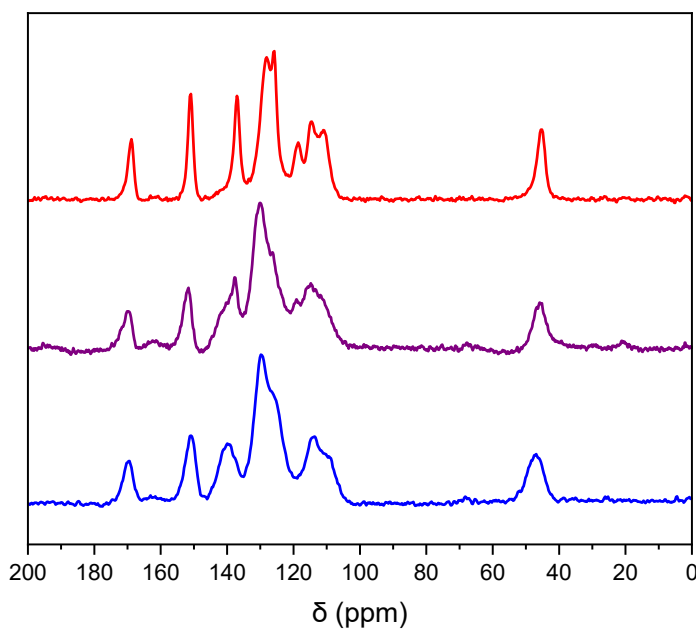


Figure S 9.1-49: Comparison of ^{13}C -CPMAS ssNMR spectra of rPI-3-COF obtained by reduction of PI-3-COF (red), rPI-3-COF obtained by one-pot reductive crystallization (purple) and disordered rPI-3-COF (blue).

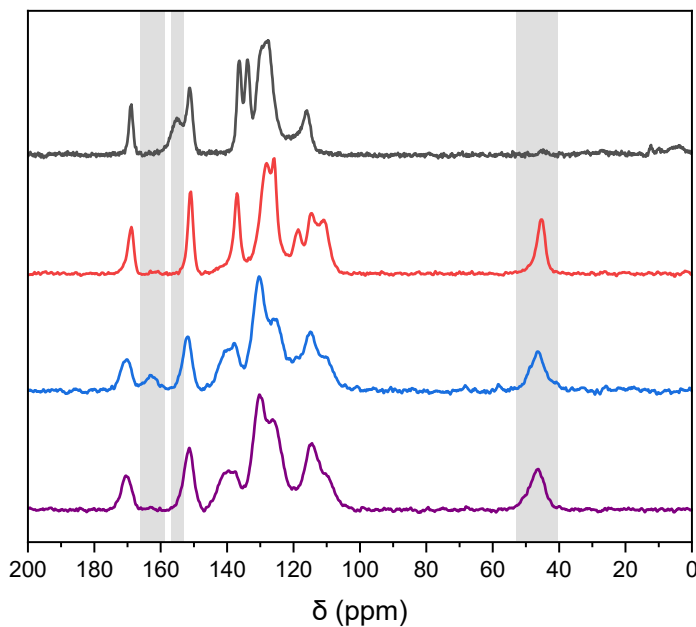


Figure S 9.1-50: Comparison of ^{13}C -CPMAS ssNMR spectra of PI-3-COF (black), rPI-3-COF (red), pfrPI-3-COF (blue) and disordered rPI-3-COF (purple). Grey areas indicate N-formyl, imine, and secondary amine carbons, respectively.

9.1.6 Nitrogen Gas Adsorption Data

9.1.6.1 Sorption Isotherms of Imine-linked COFs

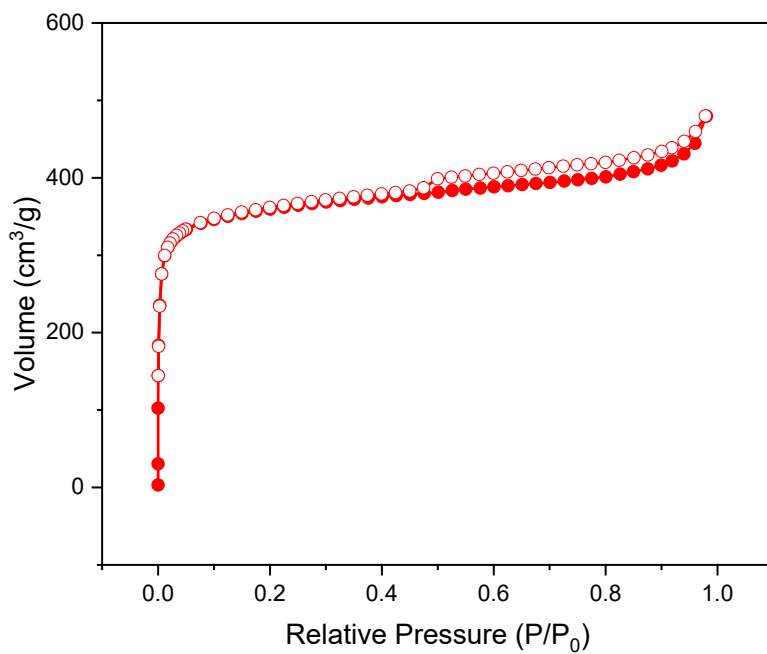


Figure S 9.1-51: N₂ sorption isotherm of PI-3-COF. Filled dots represent data points of the adsorption branch, hollow dots those of the desorption branch, respectively.

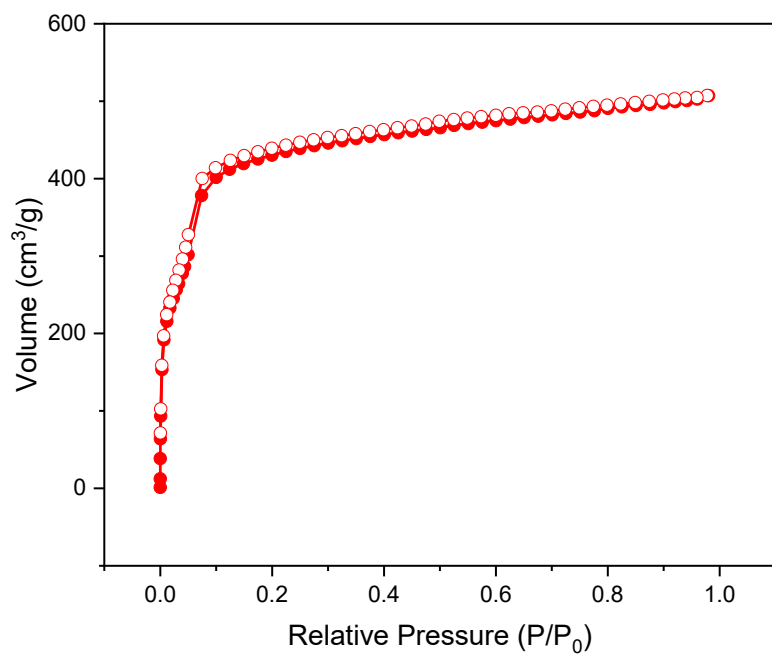


Figure S 9.1-52: N_2 sorption isotherm of TTI-COF. Filled dots represent data points of the adsorption branch, hollow dots those of the desorption branch, respectively.

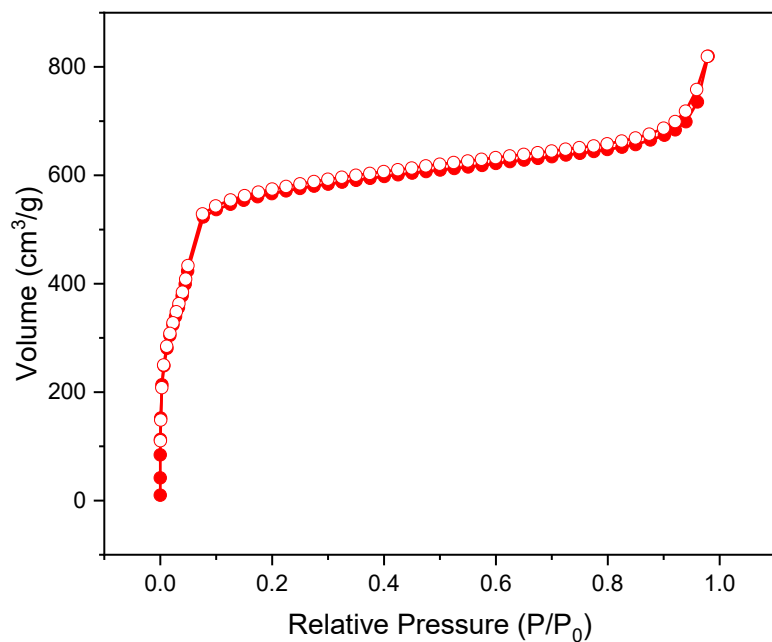


Figure S 9.1-53: N_2 sorption isotherm of Py1P-COF. Filled dots represent data points of the adsorption branch, hollow dots those of the desorption branch, respectively.

9.1.6.2 Sorption Isotherms of Amine-linked COFs

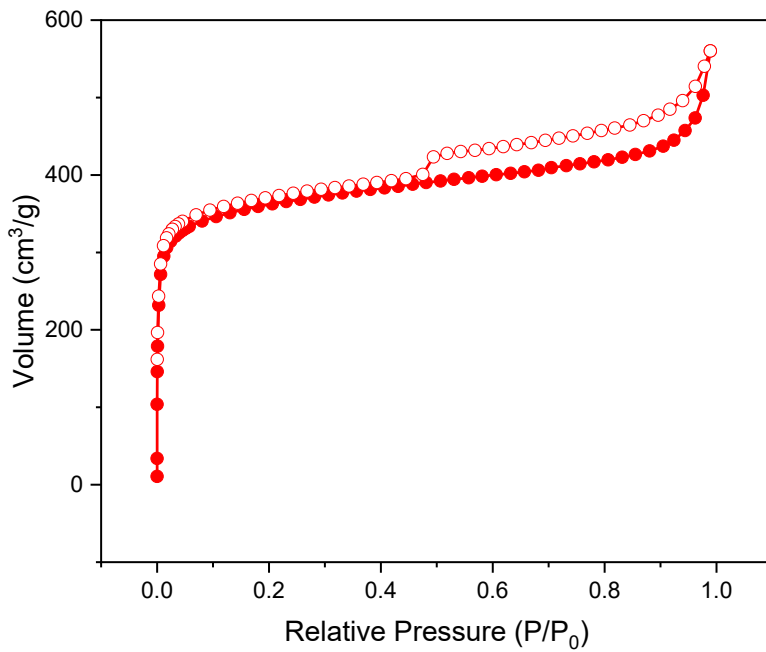


Figure S 9.1-54: N_2 sorption isotherm of rPI-3-COF. Filled dots represent data points of the adsorption branch, hollow dots those of the desorption branch, respectively.

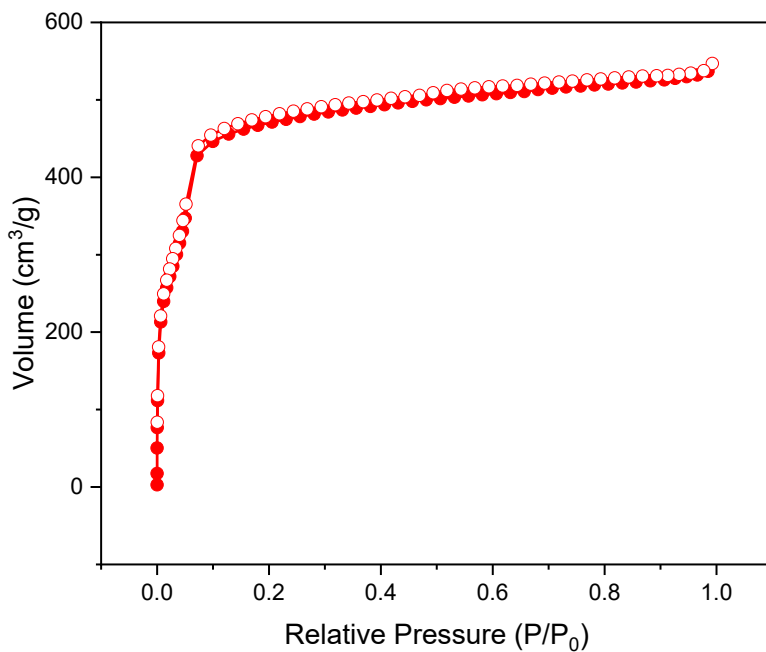


Figure S 9.1-55: N_2 sorption isotherm of rTTI-COF. Filled dots represent data points of the adsorption branch, hollow dots those of the desorption branch, respectively.

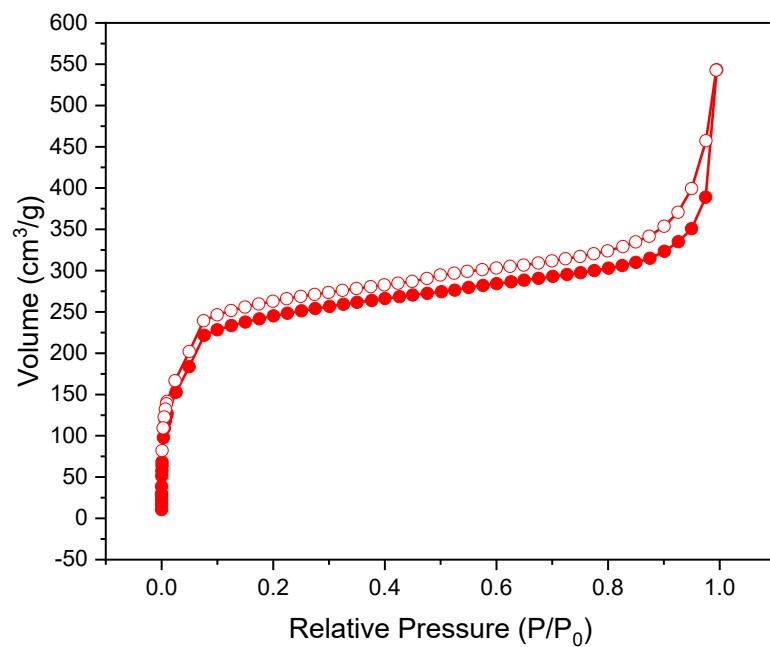


Figure S 9.1-56: N₂ sorption isotherm of rPy1P-COF. Filled dots represent data points of the adsorption branch, hollow dots those of the desorption branch, respectively.

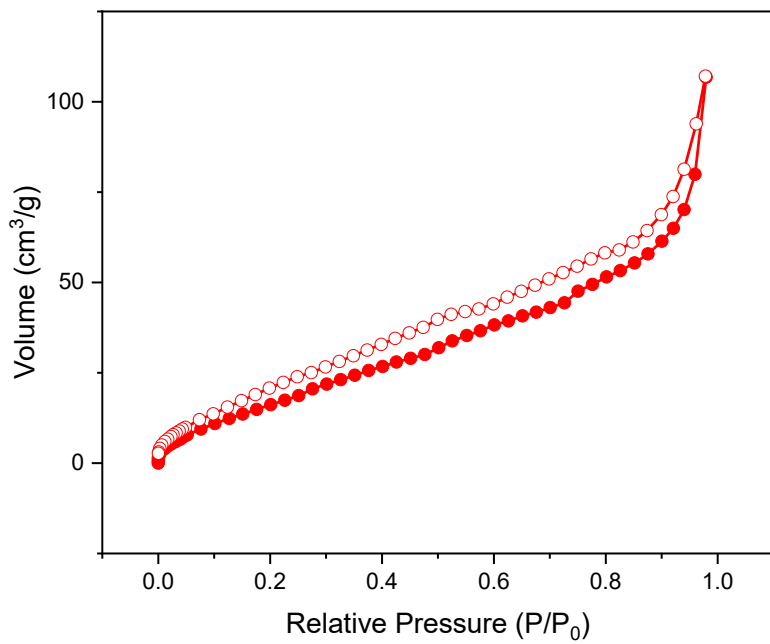


Figure S 9.1-57: N₂ sorption isotherm of disordered rPI-3-COF. Filled dots represent data points of the adsorption branch, hollow dots those of the desorption branch, respectively.

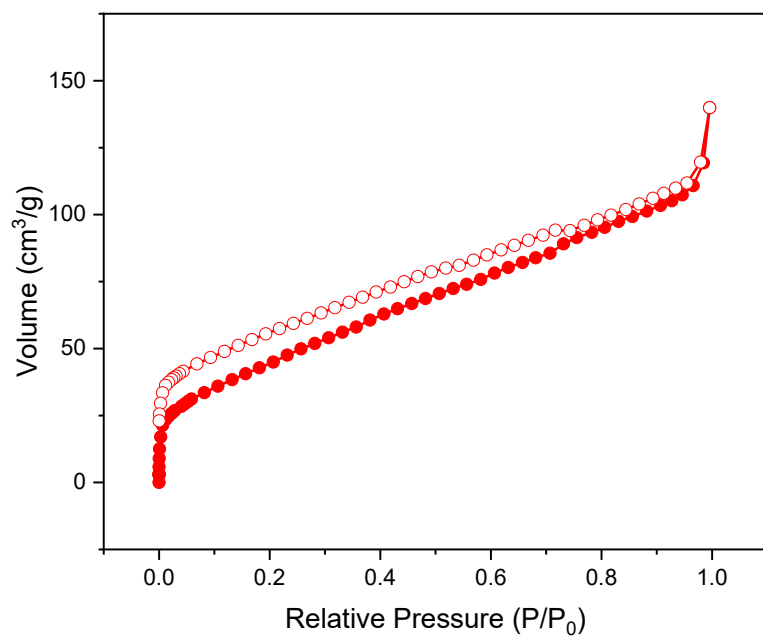


Figure S 9.1-58: N_2 sorption isotherm of rPI-3-COF obtained from one-pot crystallization/reduction. Filled dots represent data points of the adsorption branch, hollow dots those of the desorption branch, respectively.

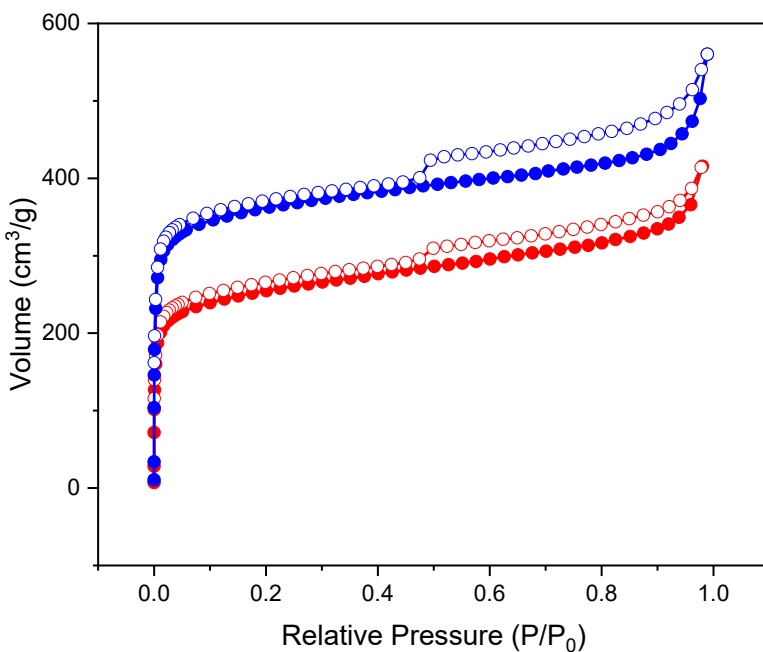


Figure S 9.1-59: N_2 sorption isotherm comparison of different samples of rPI-3-COF. The activated sample (scCO₂ extraction; blue) shows a significant increase in nitrogen adsorption volume, compared to the non-activated sample (red). Filled dots represent data points of the adsorption branch, hollow dots those of the desorption branch, respectively.

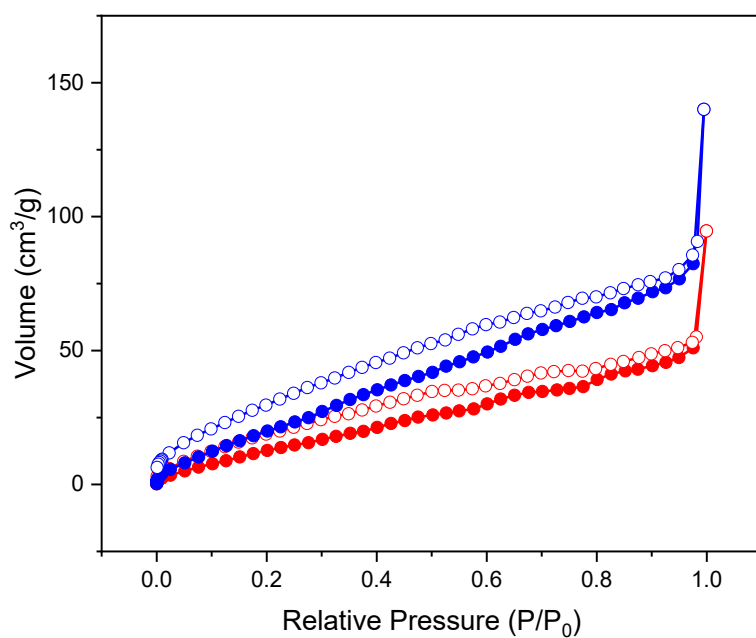


Figure S 9.1-60: N₂ sorption isotherm comparison of BzCl-rTTI (blue) and TDI-rTTI (red). Both samples show a significantly reduced N₂ uptake, due to clogged pores after functionalization with an excess of the corresponding reagent. Filled dots represent data points of the adsorption branch, hollow dots those of the desorption branch, respectively.

9.1.6.3 Pore Size Distribution in Imine-Linked COFs

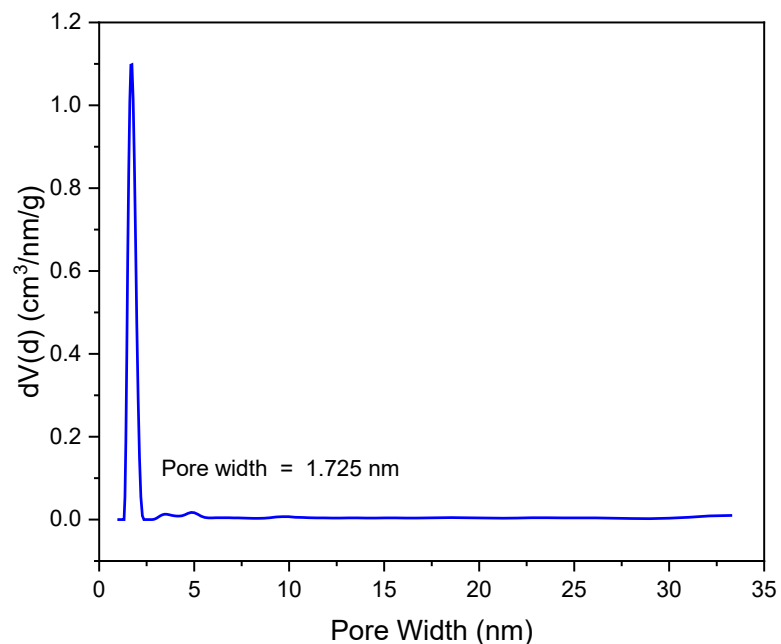


Figure S 9.1-61: Pore size distribution in PI-3-COF.

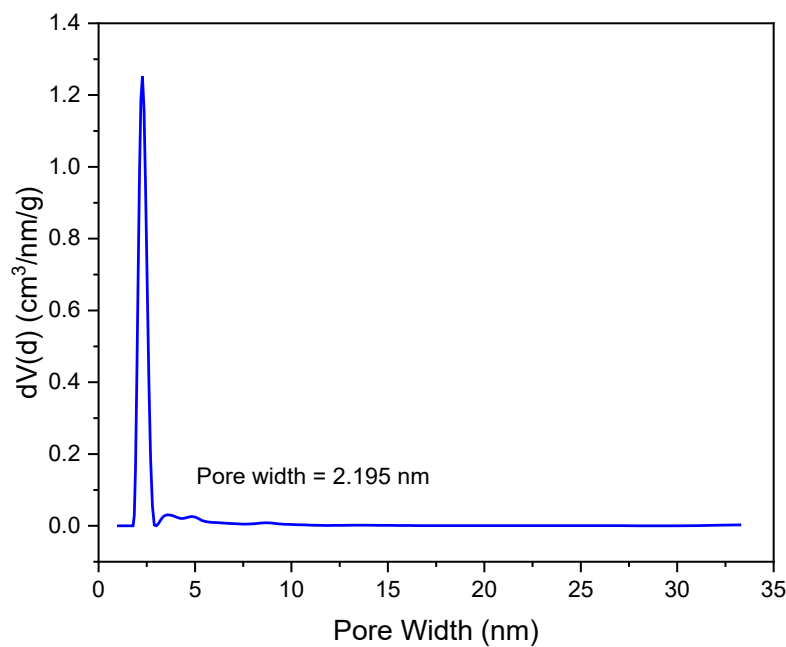


Figure S 9.1-62: Pore size distribution in TTI-COF.

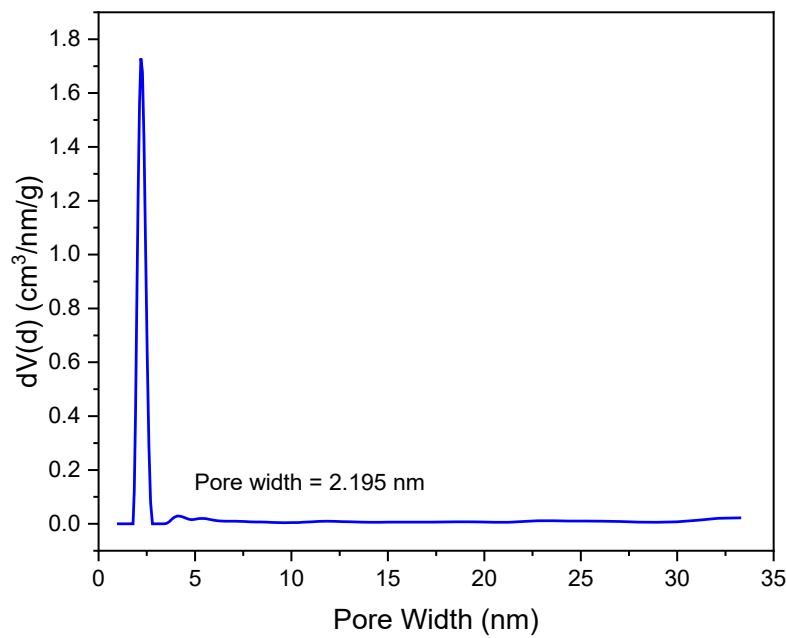


Figure S 9.1-63: Pore size distribution in Py1P-COF.

9.1.6.4 Pore Size Distribution in Amine-linked COFs

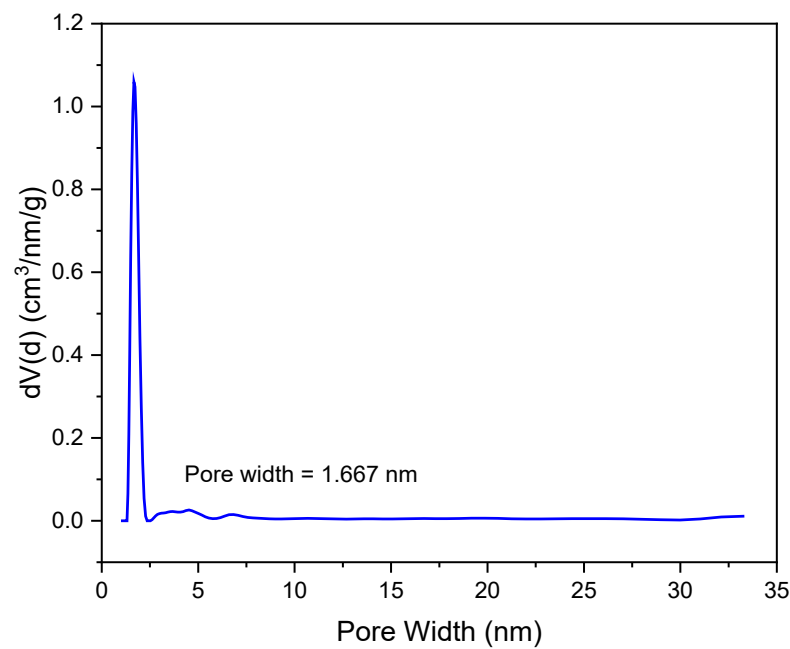


Figure S 9.1-64: Pore size distribution in rPI-3-COF.

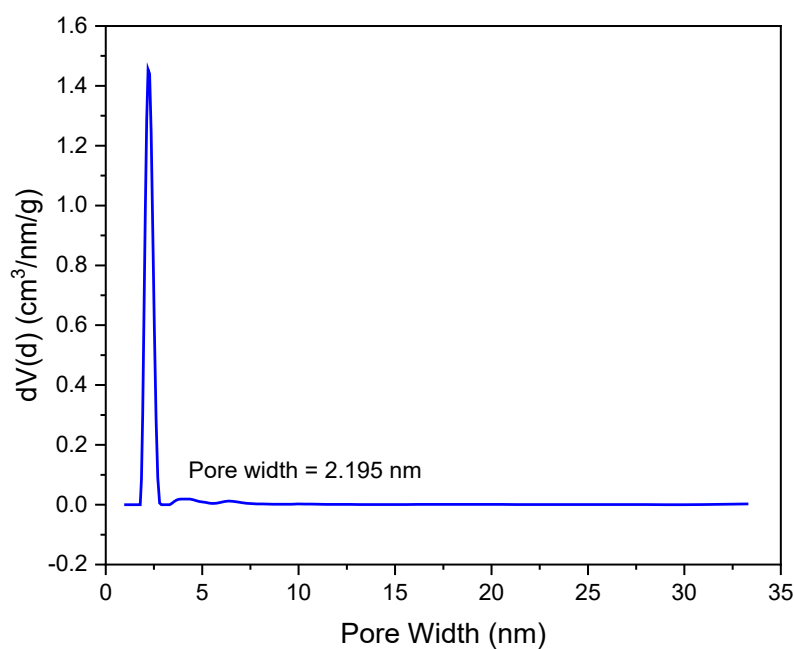


Figure S 9.1-65: Pore size distribution in rTTI-COF.

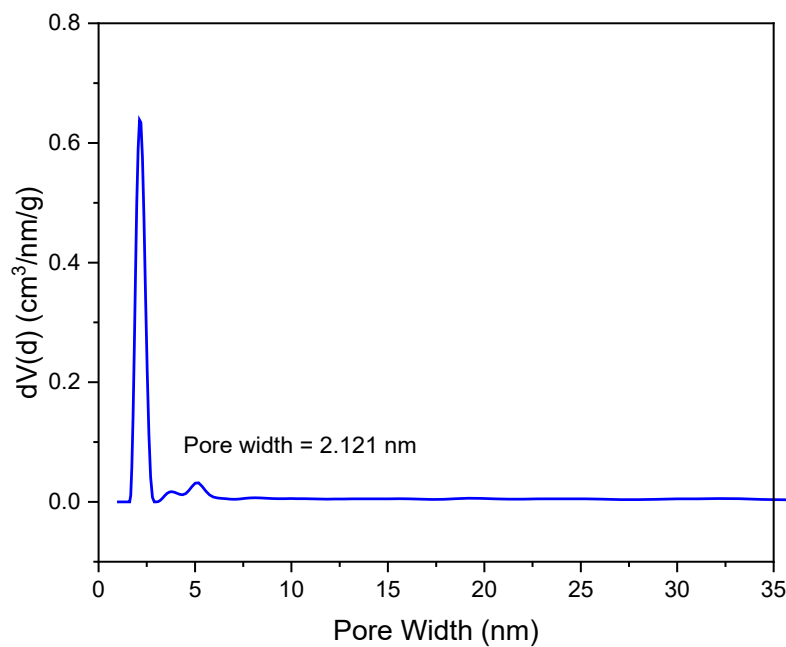


Figure S 9.1-66: Pore size distribution in rPy1P-COF.

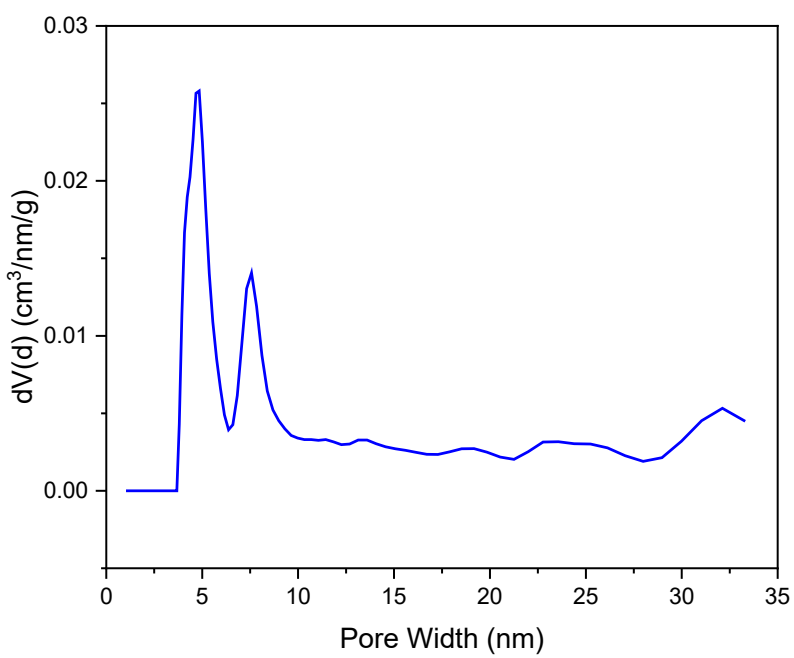


Figure S 9.1-67: Pore size distribution in disordered rPI-3-COF.

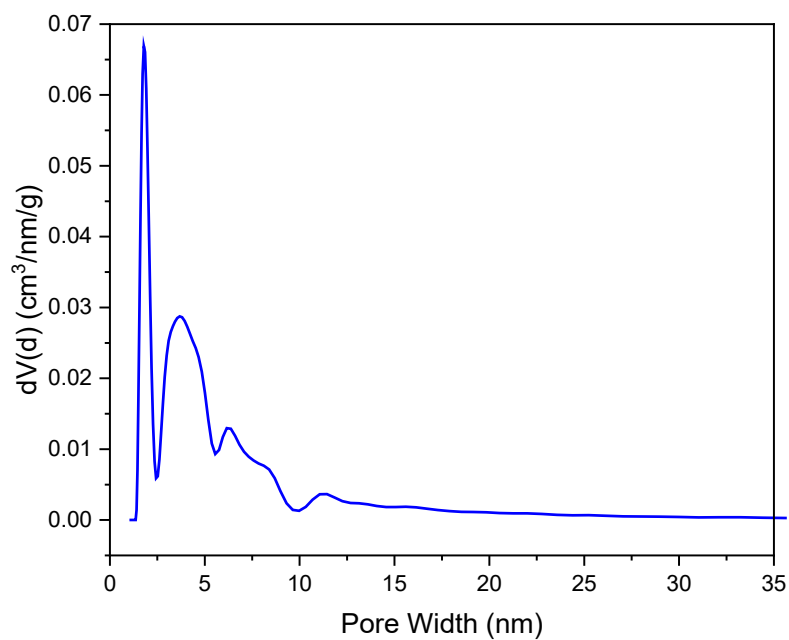


Figure S 9.1-68: Pore size distribution rPI-3-COF obtained from one-pot crystallization/reduction.

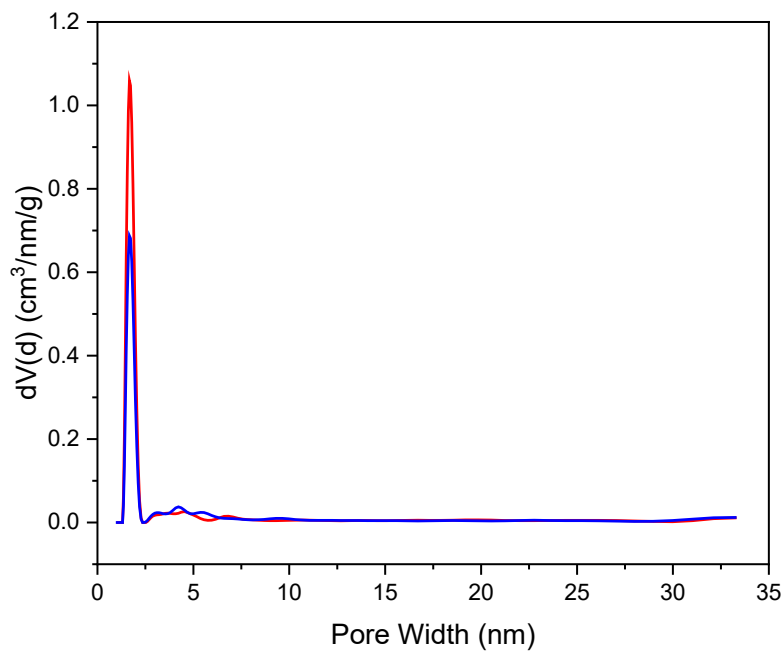


Figure S 9.1-69: Pore size distribution comparison of different samples of rPI-3-COF. The activated sample (scCO₂ extraction; red) shows a significant increase in nitrogen adsorption volume, compared to the non-activated sample (blue).

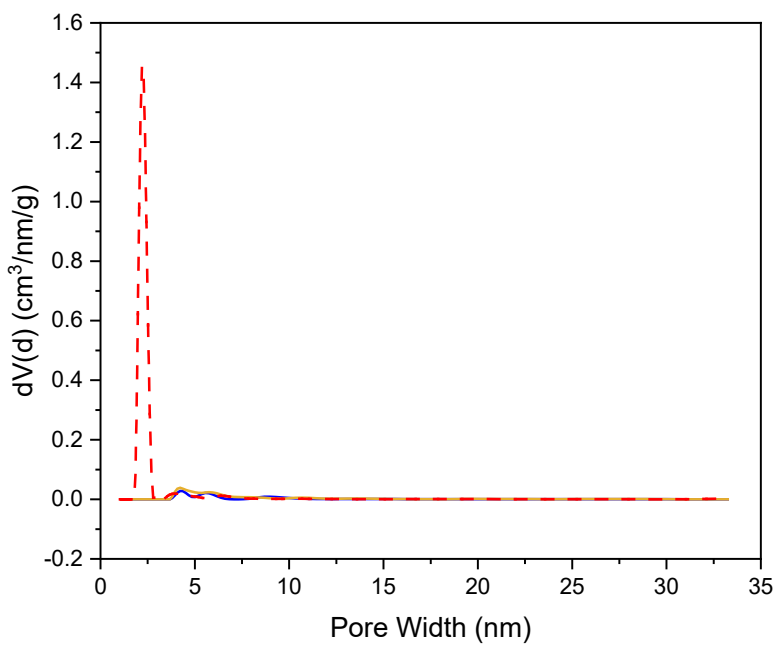


Figure S 9.1-70: Pore size distribution comparison of rTTI-COF (red) and its functionalized derivatives BzCl-rTTI-COF (orange) and TDI-rTTI-COF (blue), which show a significant decrease in nitrogen adsorption volume around the pore-diameter of 2.195 nm, due to pore clogging.

9.1.6.5 BET Plots

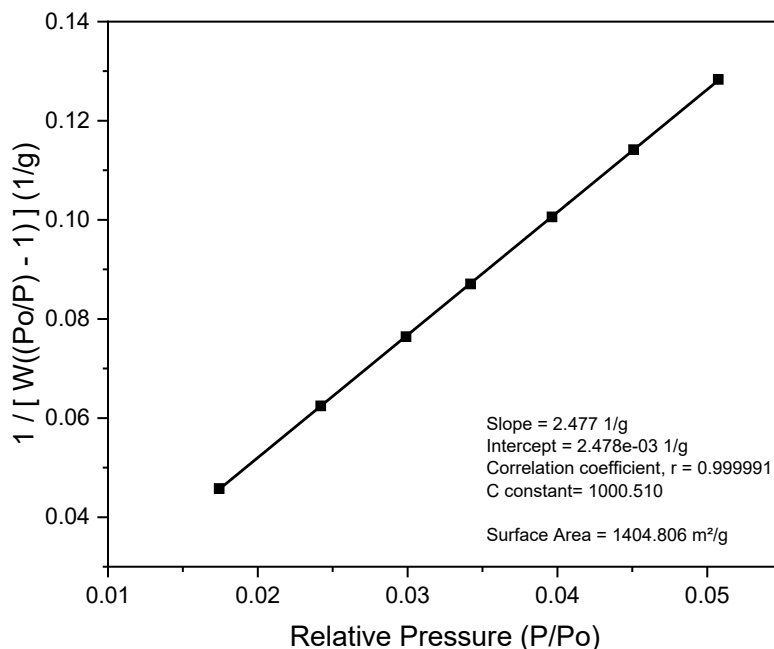


Figure S 9.1-71: BET-Plot of PI-3-COF.

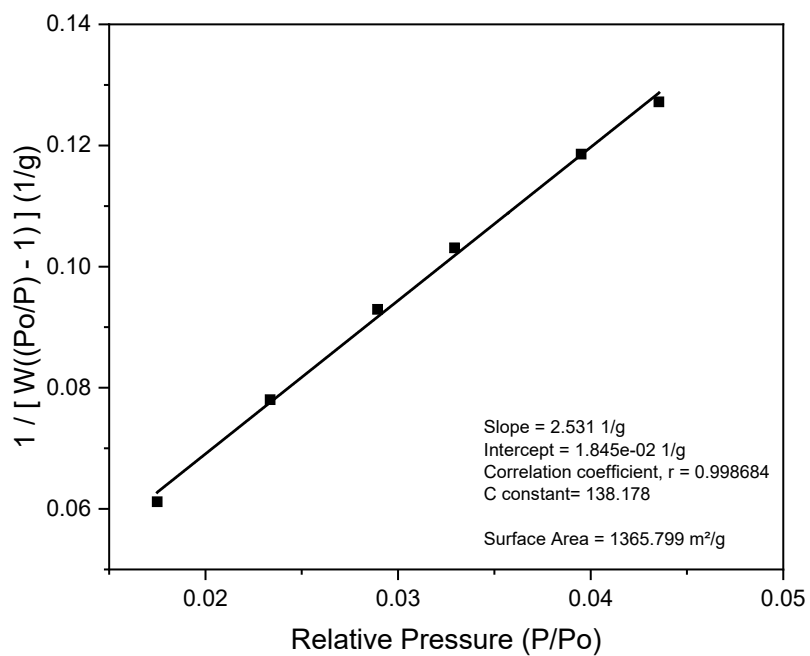


Figure S 9.1-72: BET-Plot of TTI-COF.

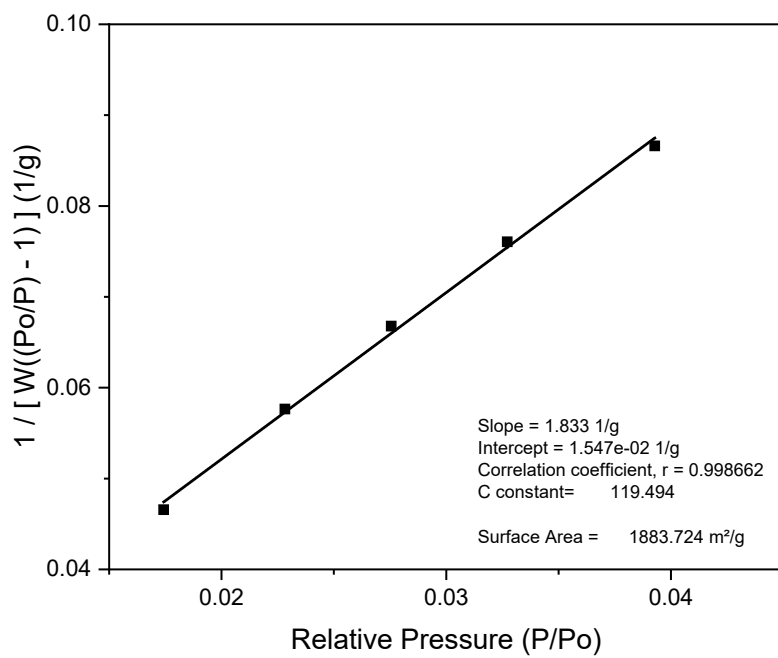


Figure S 9.1-73: BET-Plot of Py1P-COF.

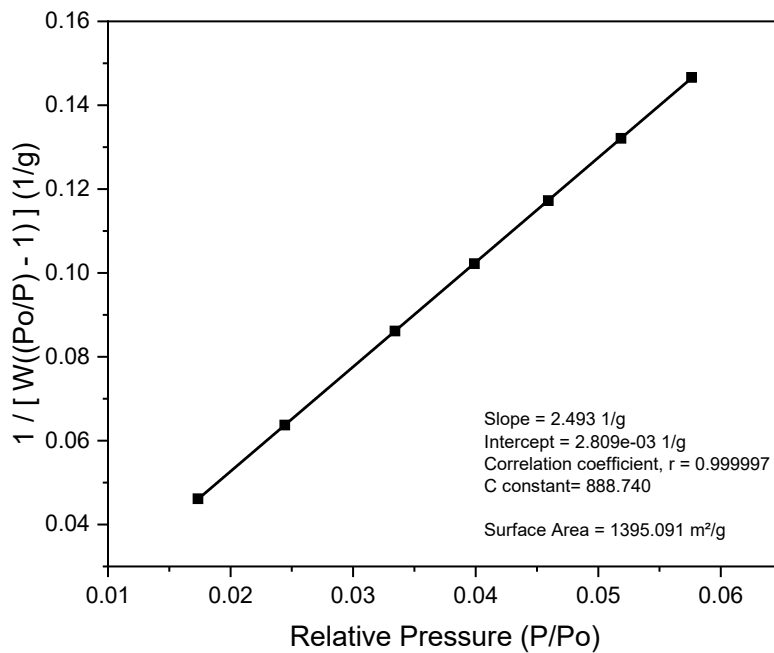


Figure S 9.1-74: BET-Plot of rPI-3-COF.

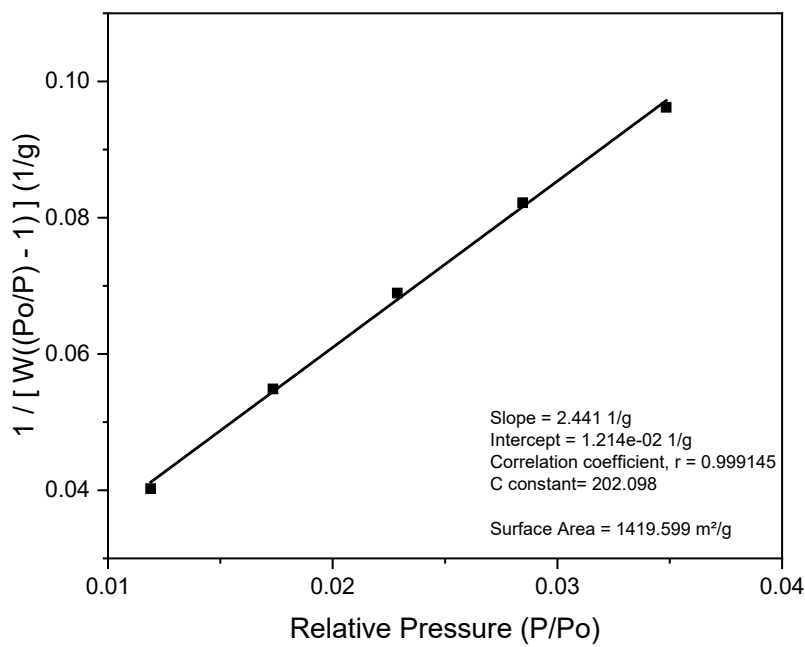


Figure S 9.1-75: BET-Plot of rTTI-COF.

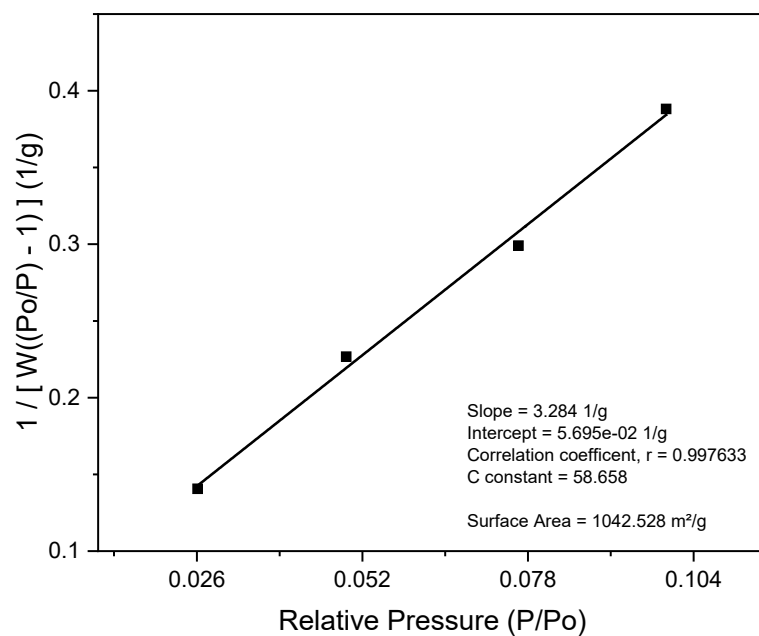
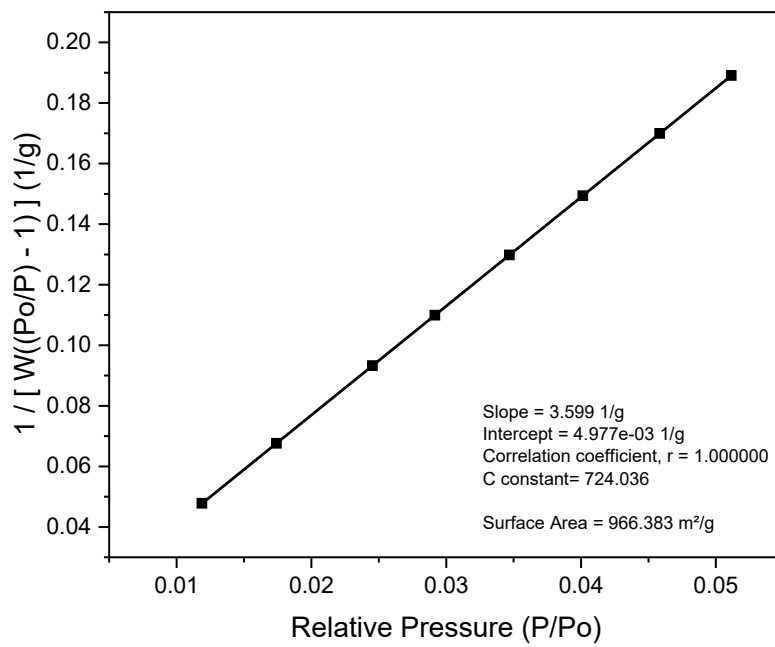


Figure S 9.1-76: BET-Plot of rPy1P-COF.

Figure S 9.1-77: BET-Plot of rPI-3-COF, without scCO₂ activation.

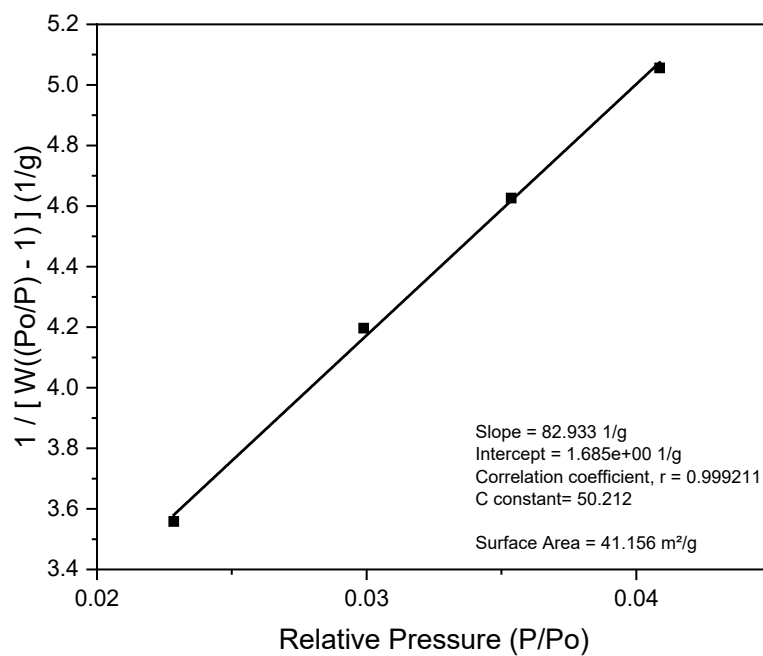


Figure S 9.1-78: BET-Plot of disordered rPI-3-COF.

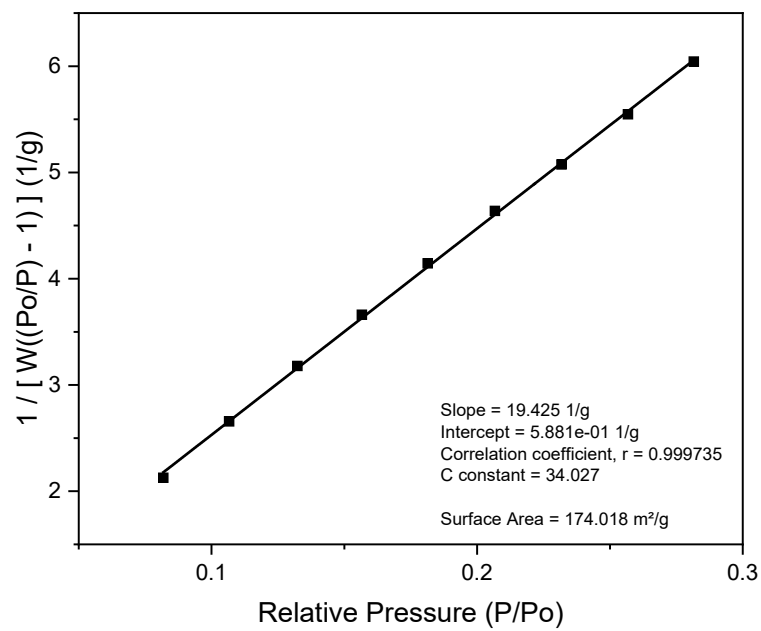


Figure S 9.1-79: BET-Plot of rPI-3-COF obtained from one-pot crystallization/reduction.

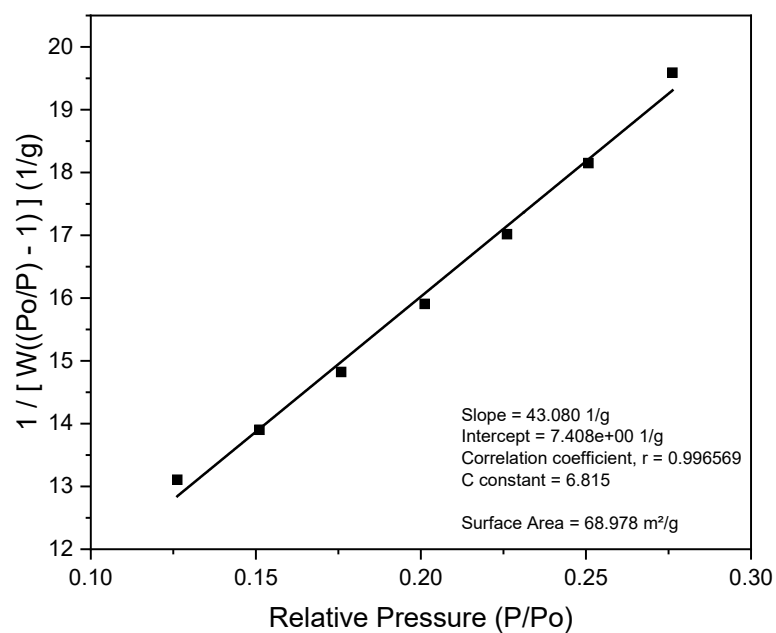


Figure S 9.1-80: BET-Plot of TDI-rTTI-COF.

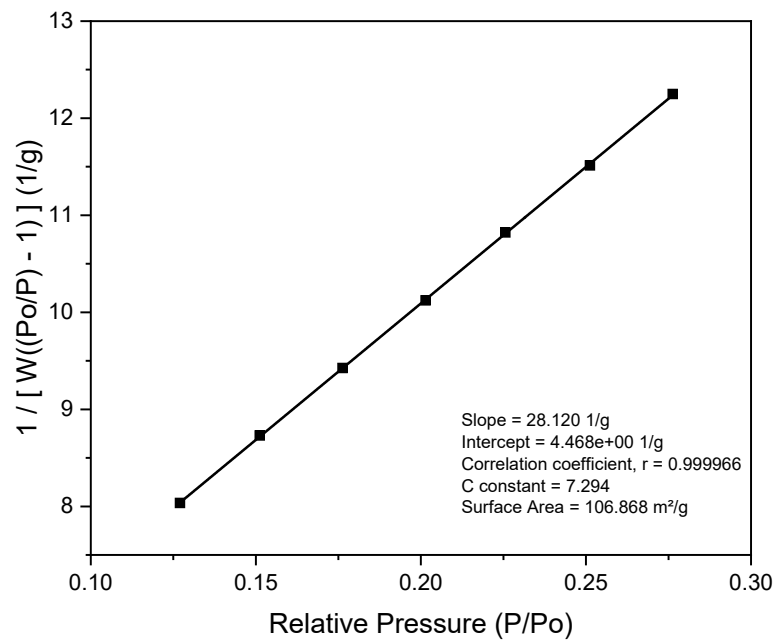


Figure S 9.1-81: BET-Plot of BzCl-rTTI-COF.

9.1.7 Scanning Electron Microscopy

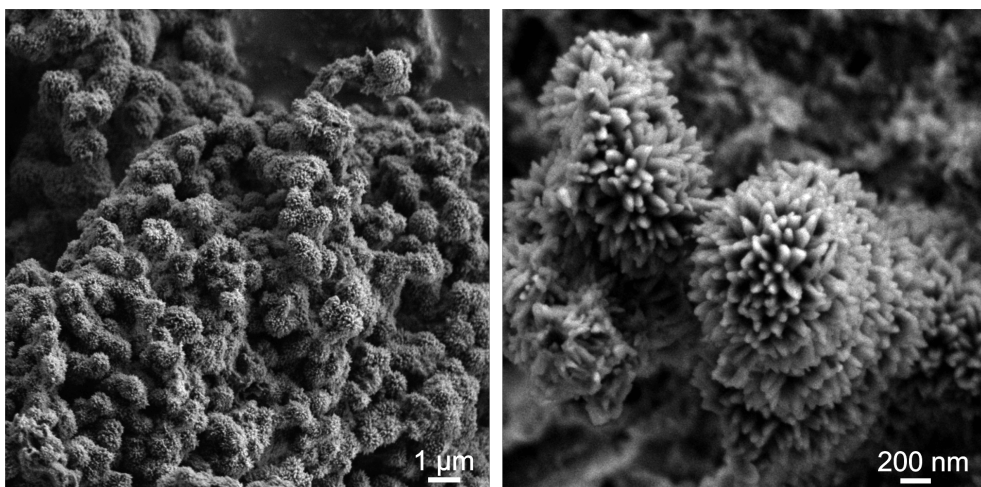


Figure S 9.1-82: SEM images of PI-3-COF.

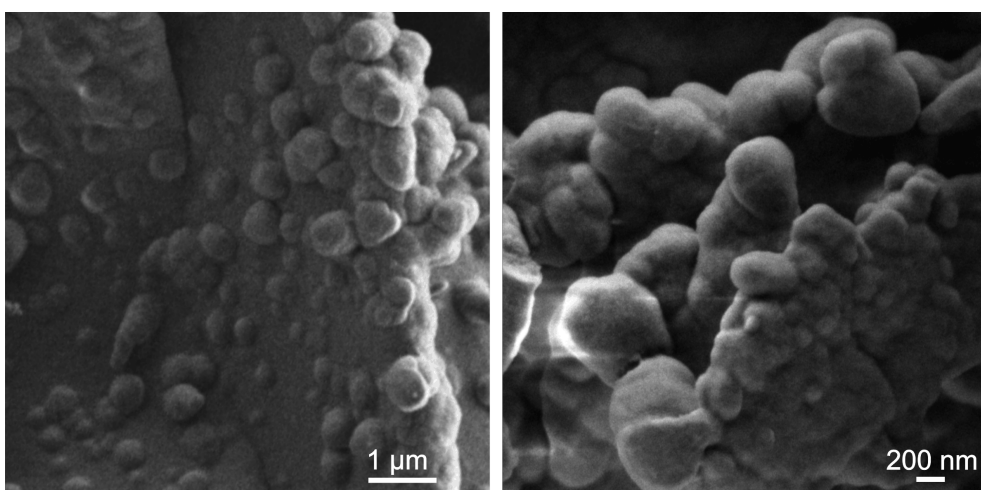


Figure S 9.1-83: SEM images of TTI-COF.

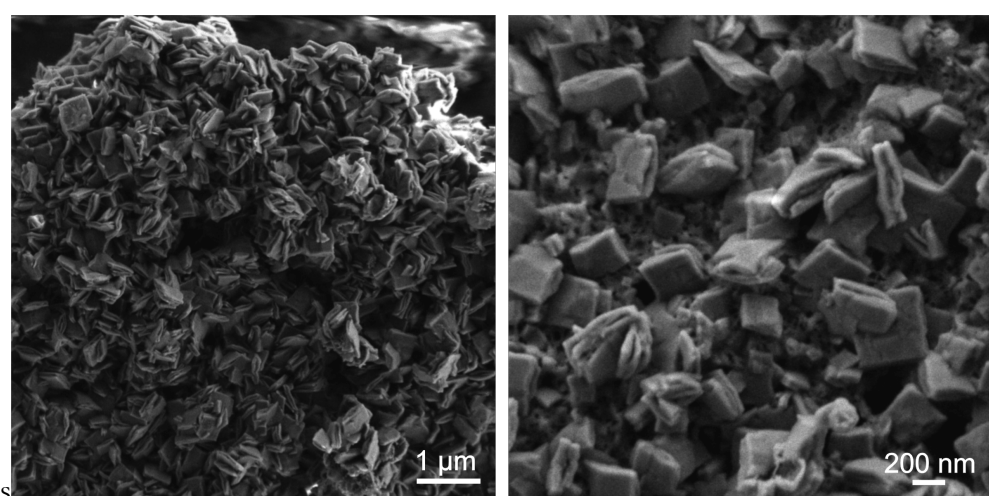


Figure S 9.1-84: SEM images of Py1P-COF.

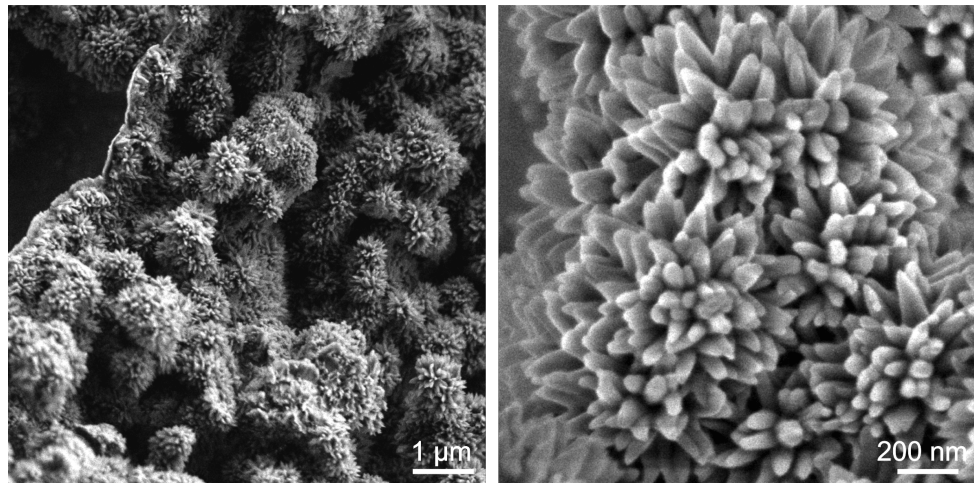


Figure S 9.1-85: SEM images of rPI-3-COF.

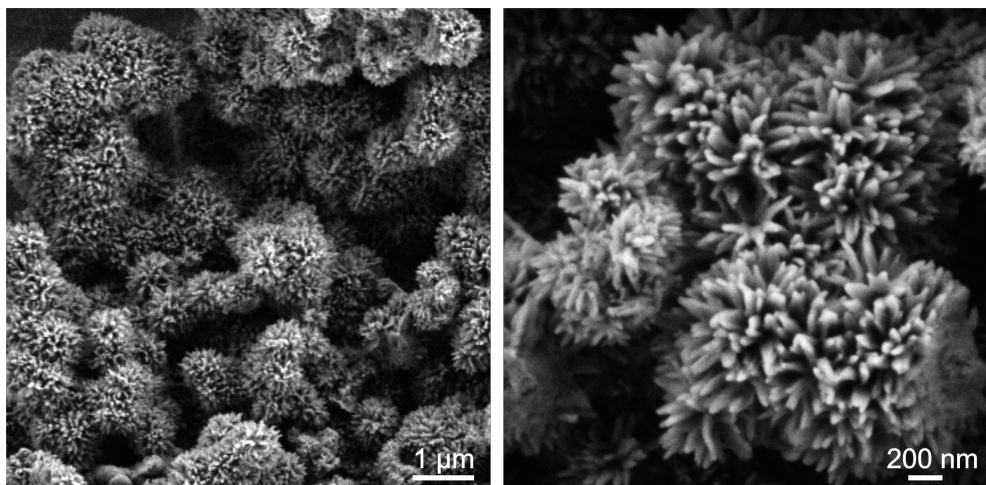


Figure S 9.1-86: SEM images of disordered rPI-3-COF.

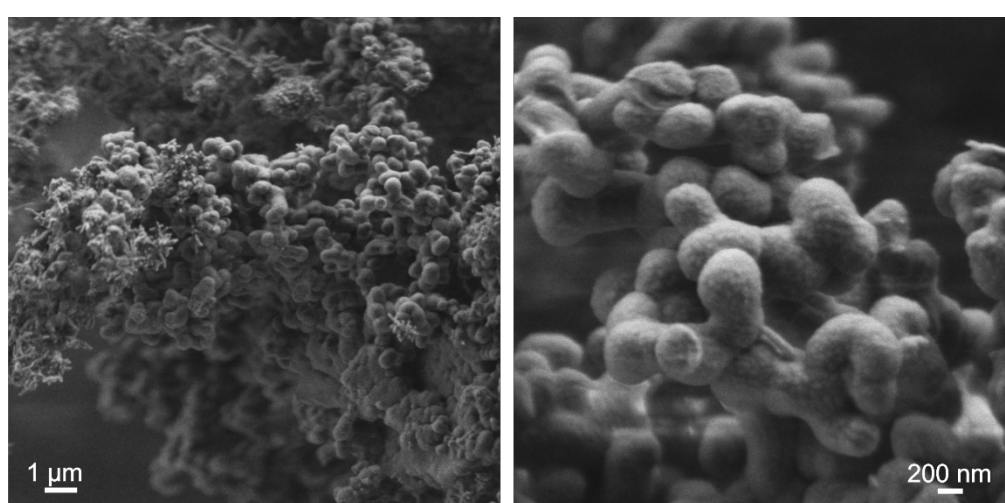


Figure S 9.1-87: SEM images of rPI-3-COF obtained by one-pot crystallization/reduction.

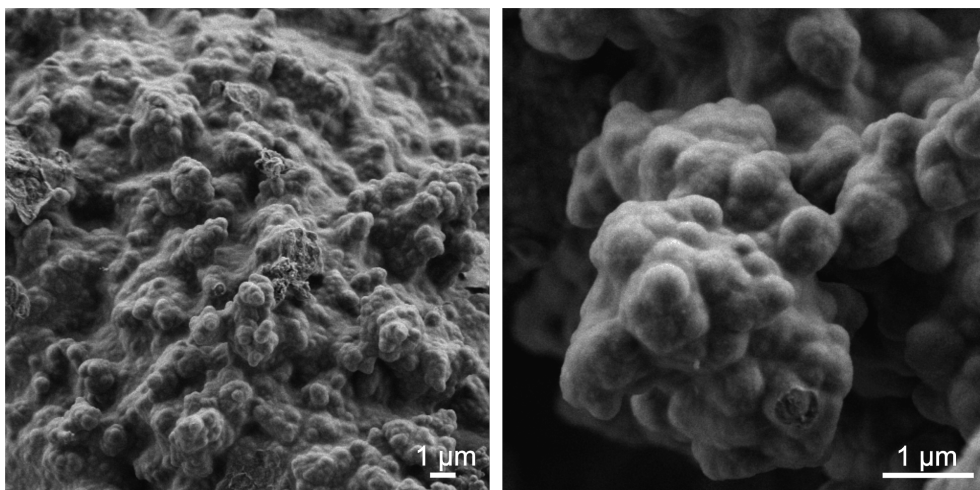


Figure S 9.1-88: SEM images of rTTI-COF.

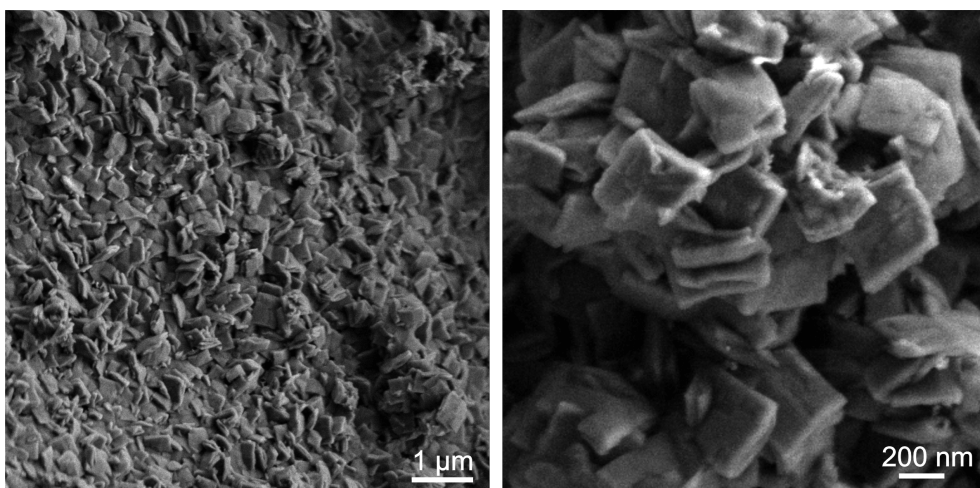


Figure S 9.1-89: SEM images of rPy1P-COF.

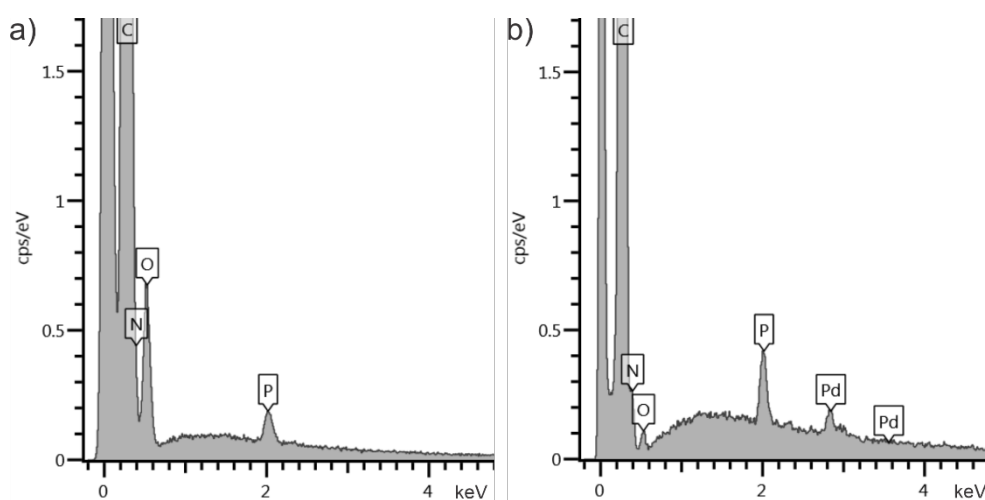


Figure S 9.1-90: SEM-EDX spectra of a purified (a) and Pd-contaminated sample of 4,4',4'',4'''-(pyrene-1,3,6,8-tetrayl)tetraaniline measured at 20kV.

9.1.8 Transmission Electron Microscopy

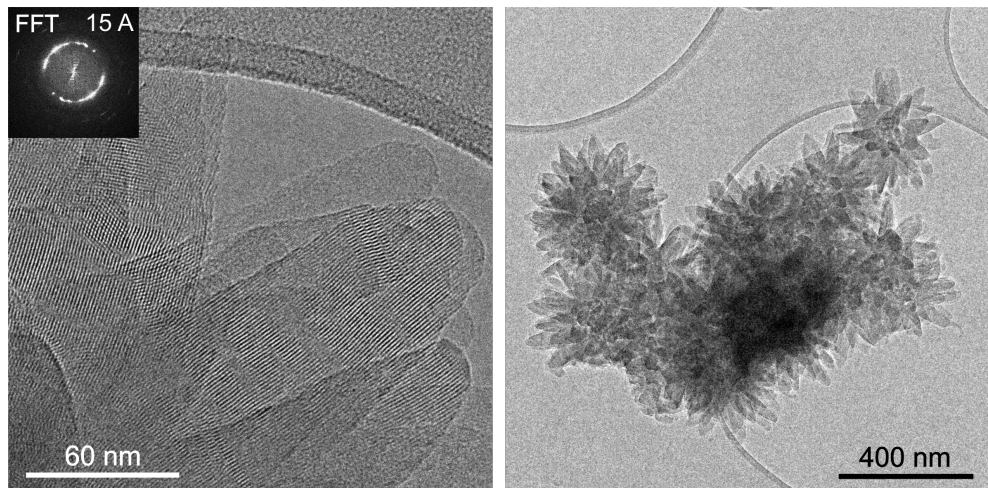


Figure S 9.1-91: TEM images of PI-3-COF.

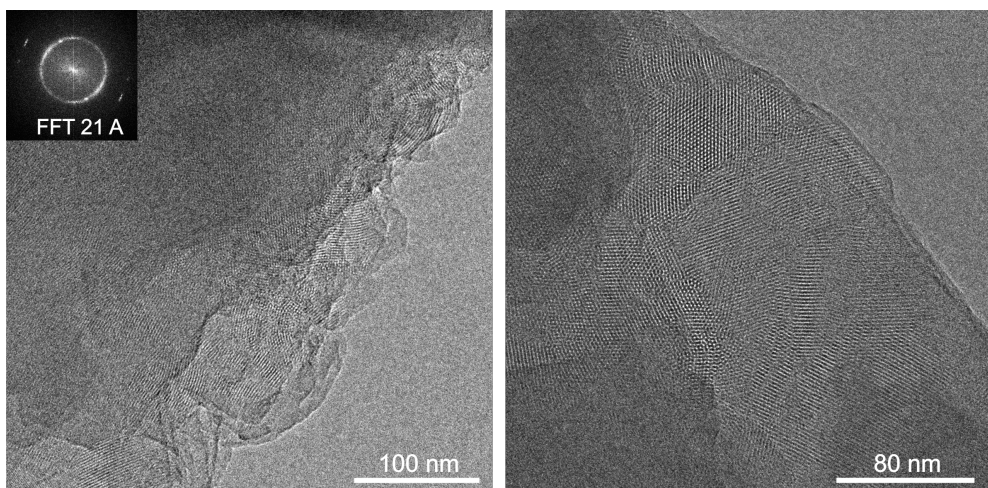


Figure S 9.1-92: TEM images of TTI-COF.

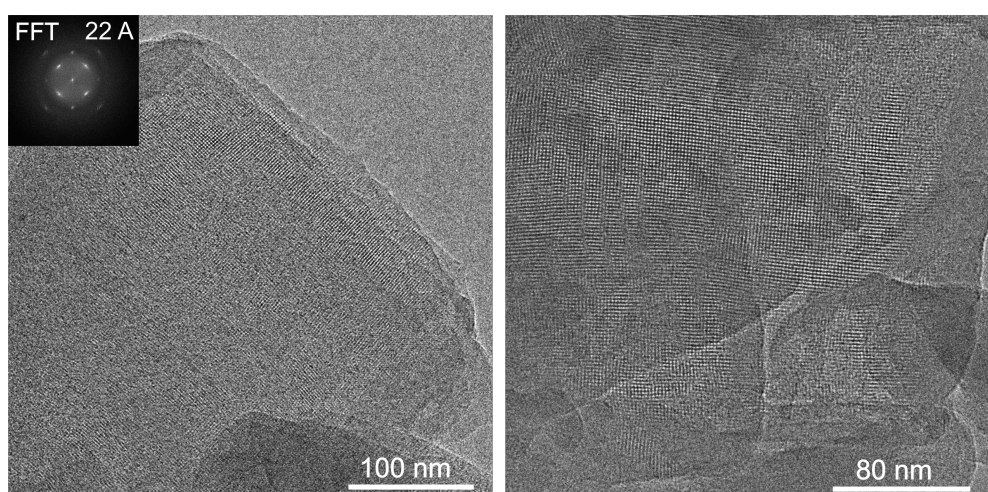


Figure S 9.1-93: TEM images of Py1P-COF.

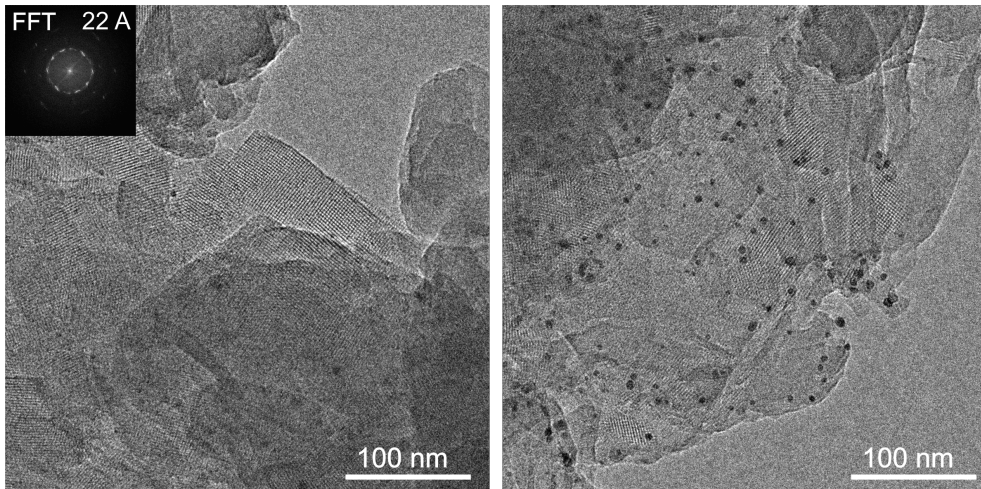


Figure S 9.1-94: TEM images of a Pd-contaminated (black dots) Py1P-COF sample.

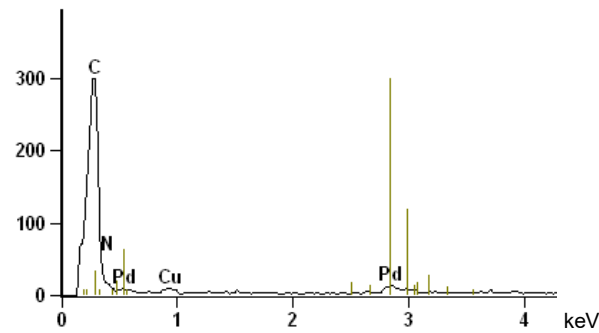


Figure S 9.1-95: TEM-EDX spectrum (point analysis) of a Pd-contaminated Py1P-COF sample (black). For comparison, a spectrum for palladium is shown in green.

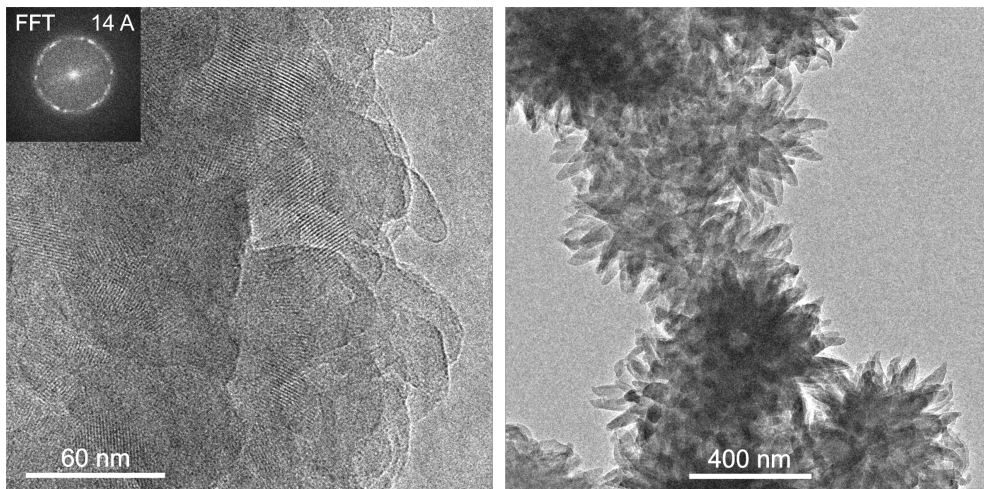


Figure S 9.1-96: TEM images of rPI-3-COF.

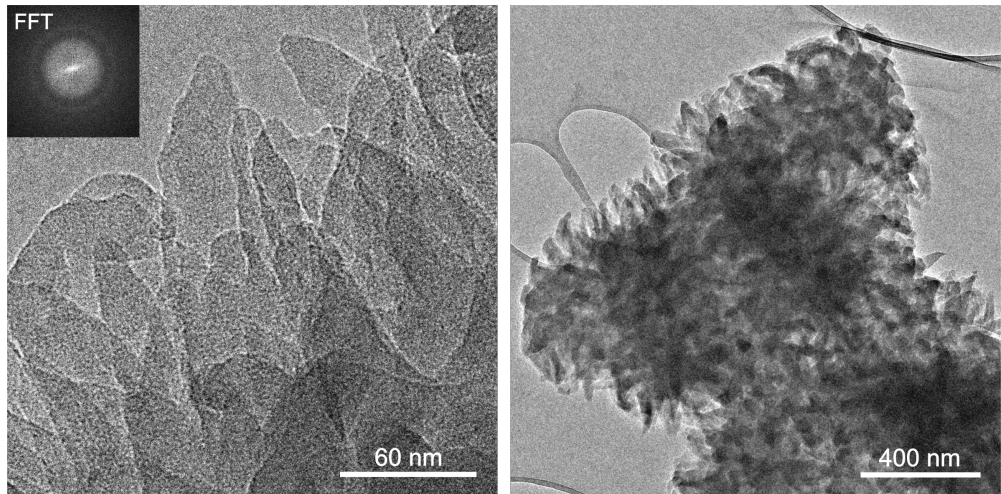


Figure S 9.1-97: TEM images of disordered rPI-3-COF.

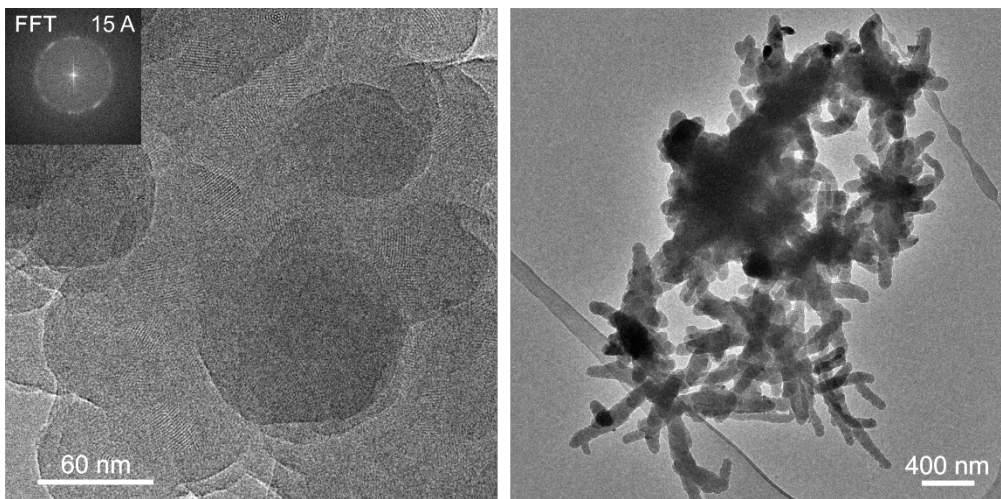


Figure S 9.1-98: TEM images of rPI-3-COF obtained by one-pot crystallization/reduction.

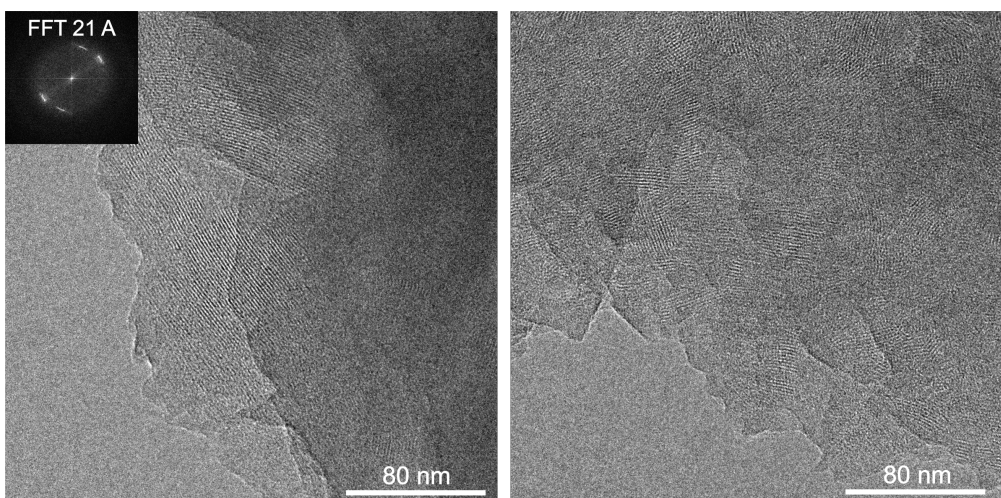


Figure S 9.1-99: TEM images of rTTI-COF.

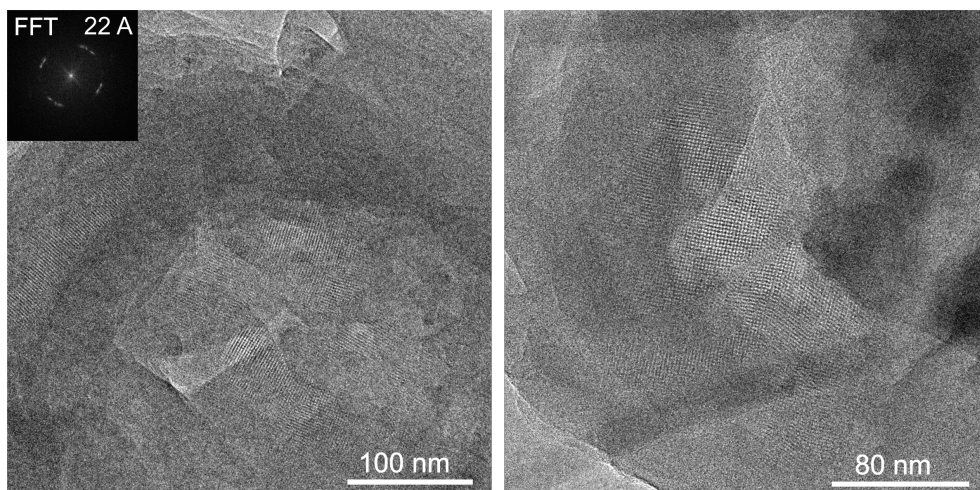


Figure S 9.1-100: TEM images of rPy1P-COF.

9.1.9 Stability Tests

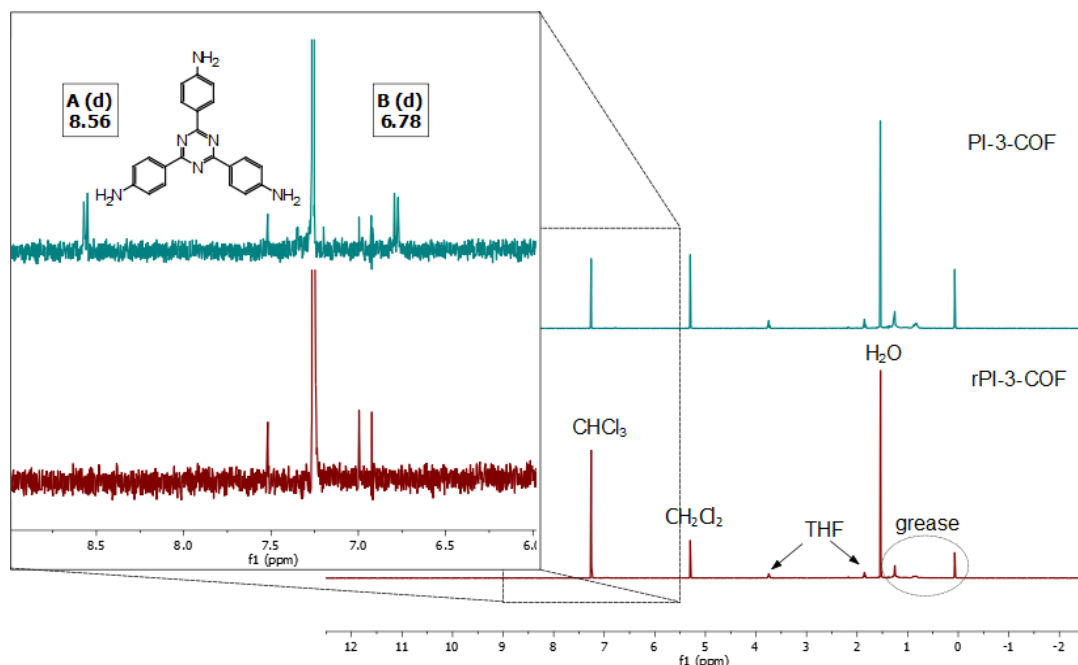


Figure S 9.1-101: ^1H -NMR spectrum (400 MHz, CDCl_3) of degradation products from hydrolysis of PI-3-COF and rPI-3-COF samples treated with 3M NaOH in a THF:Water (1:1) mixture. Only the imine-linked framework (PI-3-COF) decomposed partially (hydrolysis) and shows signals of the amine monomer.

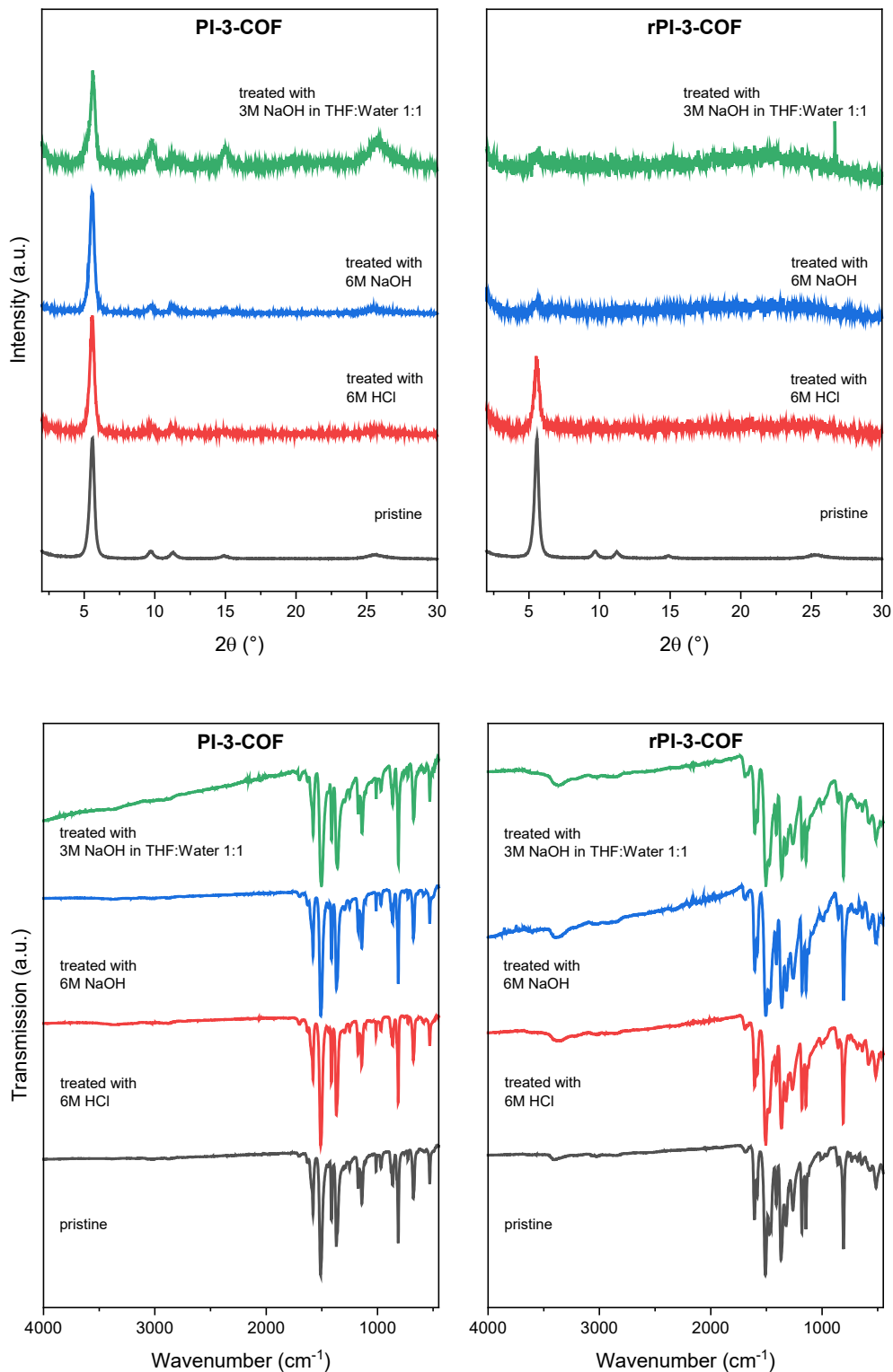


Figure S 9.1-102: XRPD and FT-IR comparison of amine- and imine-linked COF samples stirred in acidic and basic solutions for 24h. Note that reduced crystallinity for rPI-3-COF is caused by increasing disorder in the framework instead of hydrolytic decomposition (see Figure S 9.1-101).

9.1.10 Quantum-Chemical Calculations

9.1.10.1 Geometry Optimization

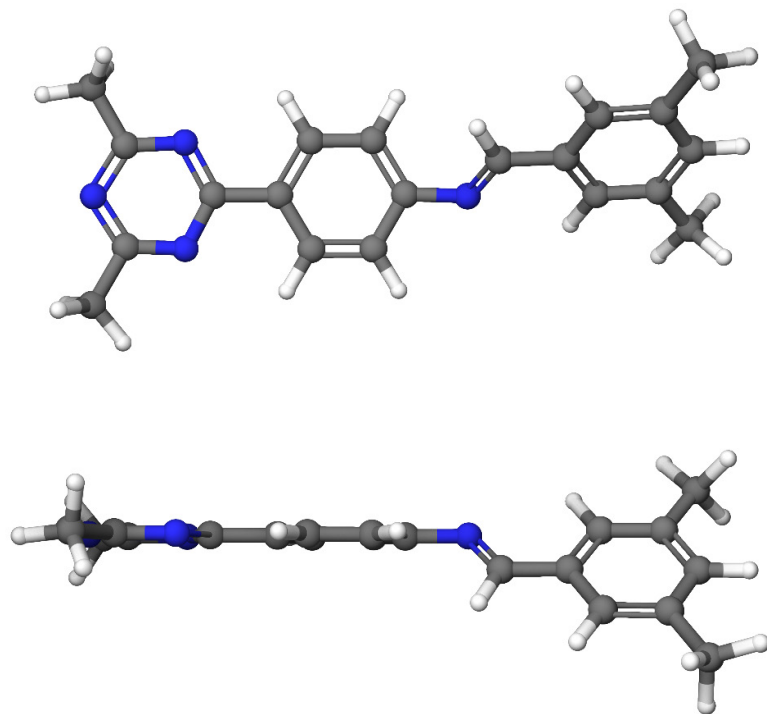


Figure S 9.1-103: Optimized structure for a representative molecular model system of PI-3-COF (PI 3 M), obtained on PBE0 D3/def2 TZVP level of theory.

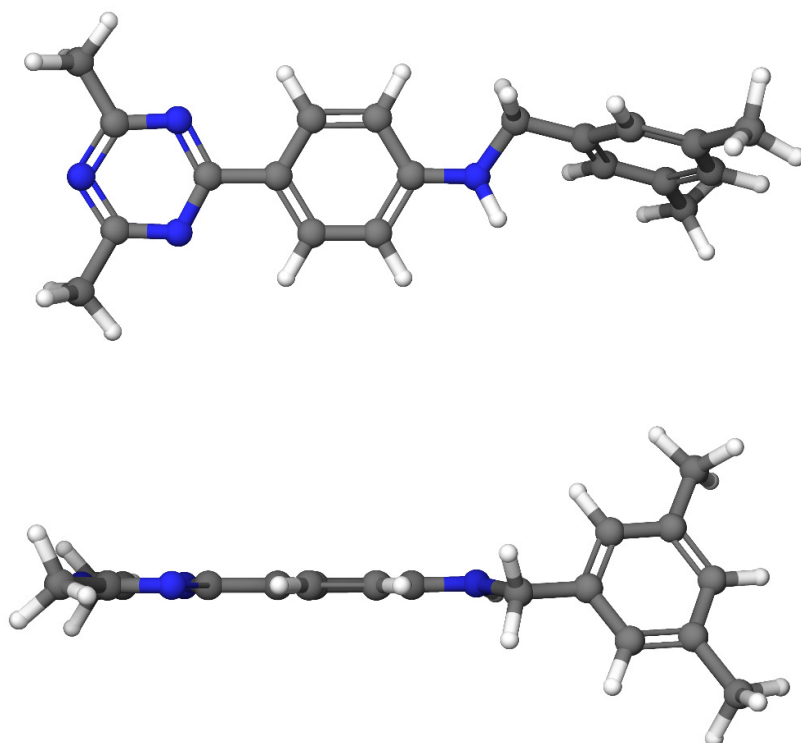


Figure S 9.1-104: Optimized structure for a representative molecular model system of rPI-3-COF (rPI-3 M), obtained on PBE0-D3/def2-TZVP level of theory

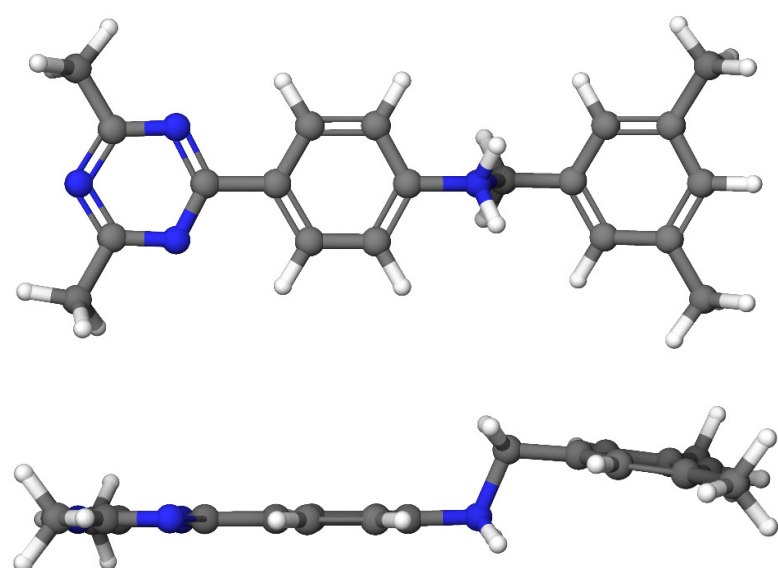


Figure S 9.1-105: Optimized structure for a protonated representative molecular model system of rPI-3-COF (H+rPI-3 M), obtained on PBE0-D3/def2-TZVP level of theory. Note that the effect of the counter ion is neglected in this model.

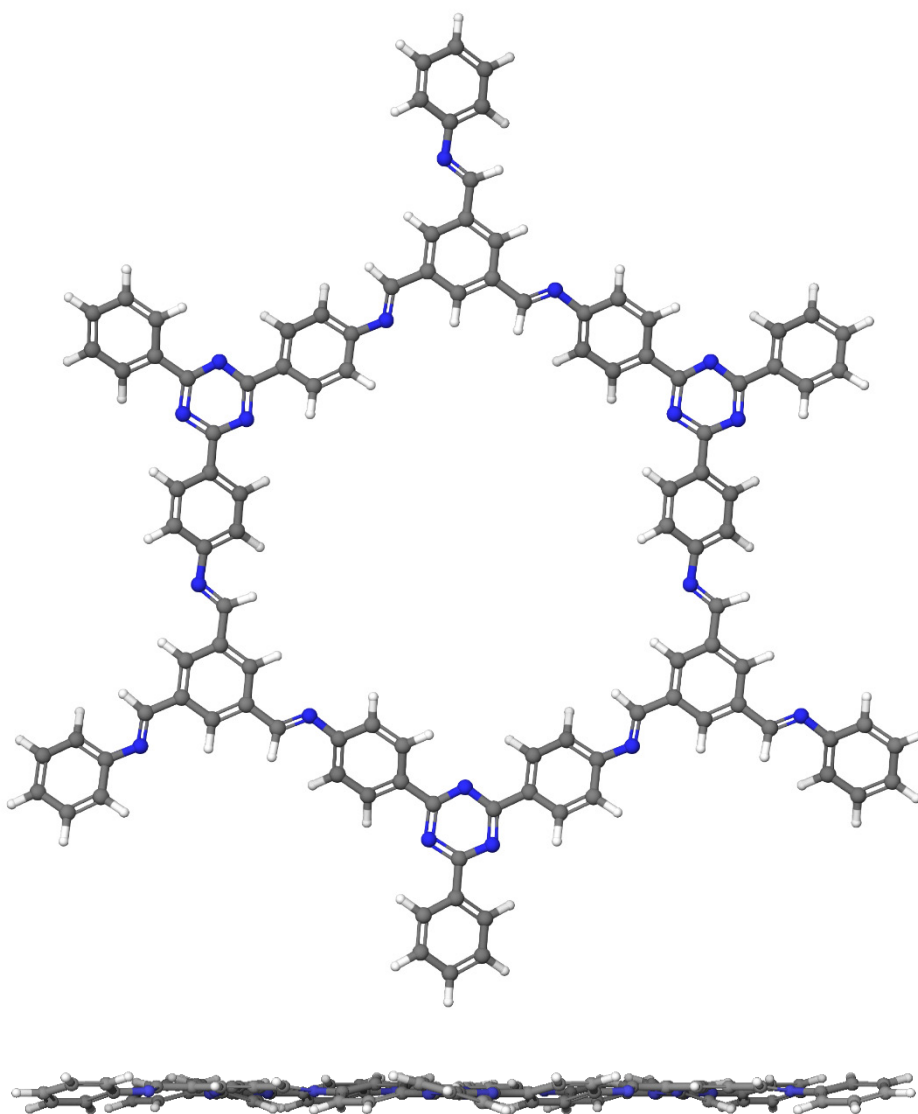


Figure S 9.1-106: Optimized structure for a representative single-pore model system of PI-3-COF (PI-3 SP), obtained on RI-PBE-D3/def2-TZVP level of theory.

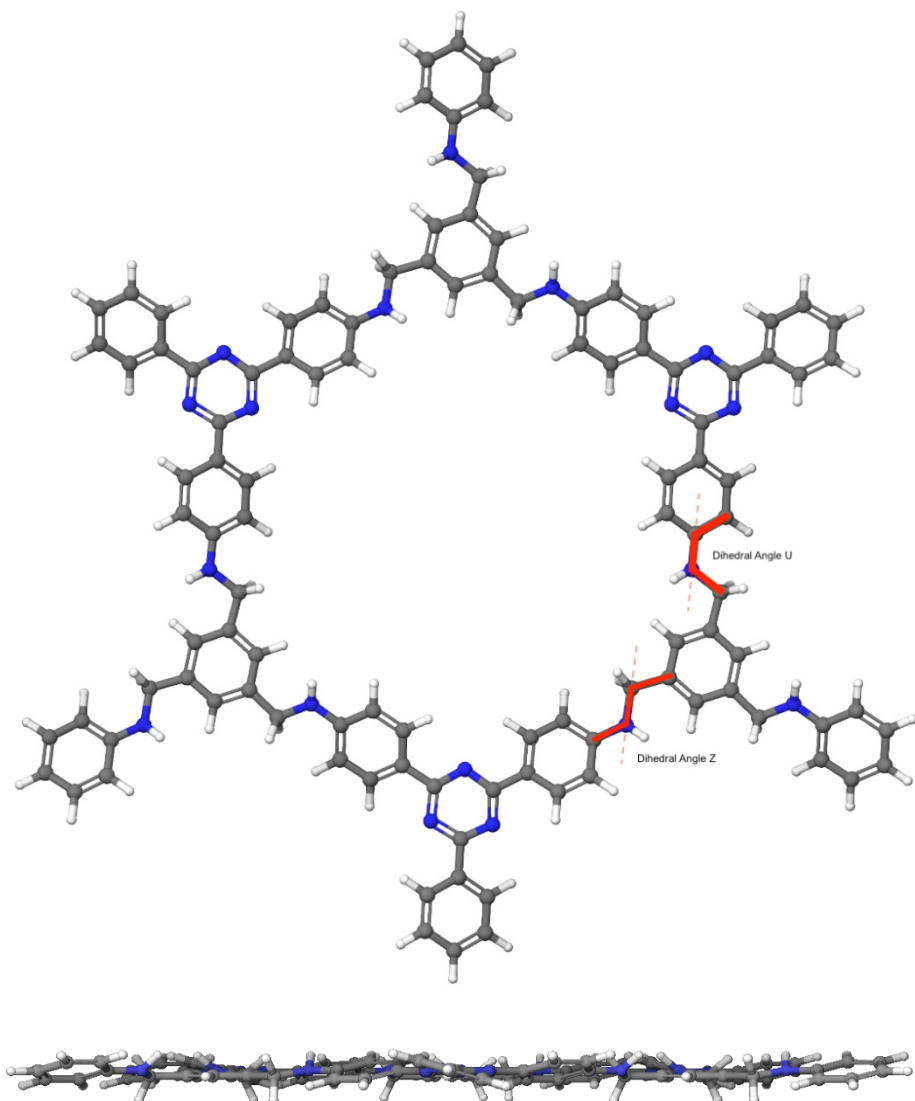


Figure S 9.1-107: Optimized structure for a representative single-pore model system of rPI-3-COF (rPI-3 SP), obtained on RI-PBE-D3/def2-TZVP level of theory.

Table S 9.1-4: Comparison of **U** and **Z** dihedral angles [°], obtained from optimized geometries for the presented model systems.

Model System	Level of Theory	U (CCNC)	ΔU (CCNC)	Z (CNCC)	ΔZ (CNCC)
PI-3 M	PBE0-D3/def2-TZVP	43.59		-176.82	
PI-3 M	RI-PBE-D3/def2-TZVP	43.29	-0.30	-175.80	1.02
PI-3 SP	RI-PBE-D3/def2-TZVP	27.40	-15.89	-177.64	-1.84
rPI-3 M	PBE0-D3/def2-TZVP	10.18		-179.68	
rPI-3 M	RI-PBE-D3/def2-TZVP	8.97	-1.21	-179.55	0.13
rPI-3 SP	RI-PBE-D3/def2-TZVP	6.46	-2.51	-178.51	1.04
H+rPI-3 M		-85.71		-179.57	
		-86.6	-0.89	-179.48	0.09

9.1.10.2 NMR Chemical Shifts

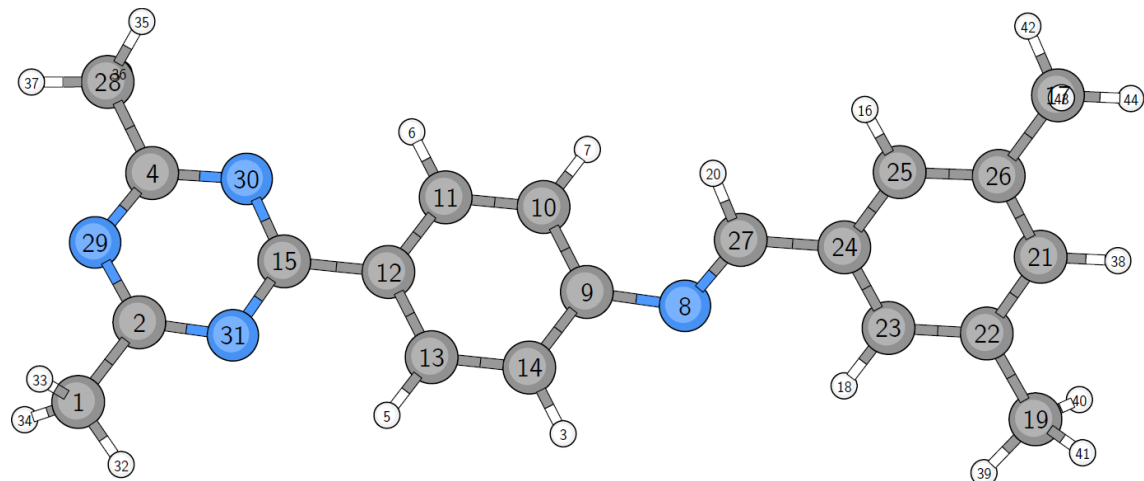


Figure S 9.1-108: Atom labels for the PI-3 M model.

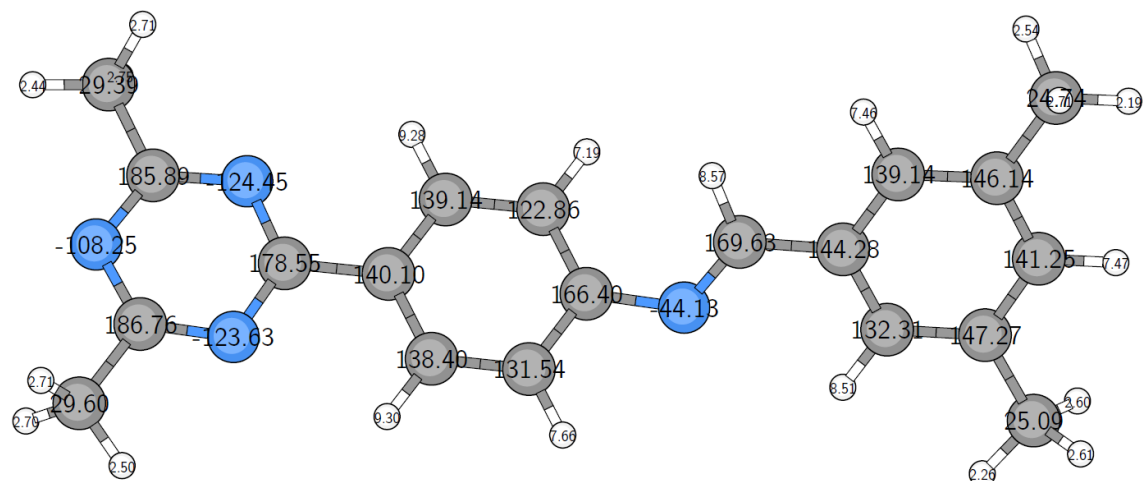


Figure S 9.1-109: Calculated NMR Chemical Shifts for the PI-3 M model system, obtained on B97-2/pcS-2//PBE0-D3/def2-TZVP level of theory.

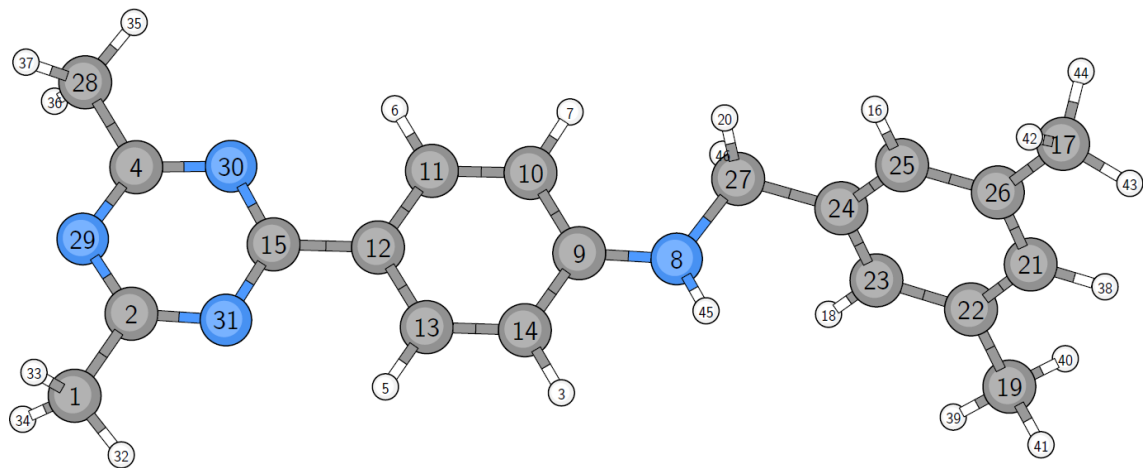


Figure S 9.1-110: Atom labels for the rPI-3 M model.

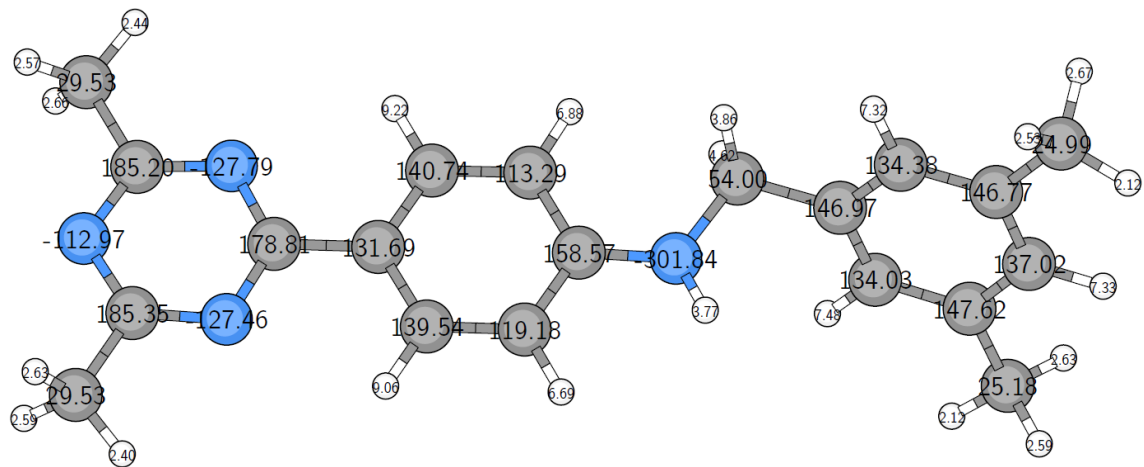


Figure S 9.1-111: Calculated NMR Chemical Shifts for the rPI-3 M model system, obtained on B97-2/pcS-2//PBE0-D3/def2-TZVP level of theory.

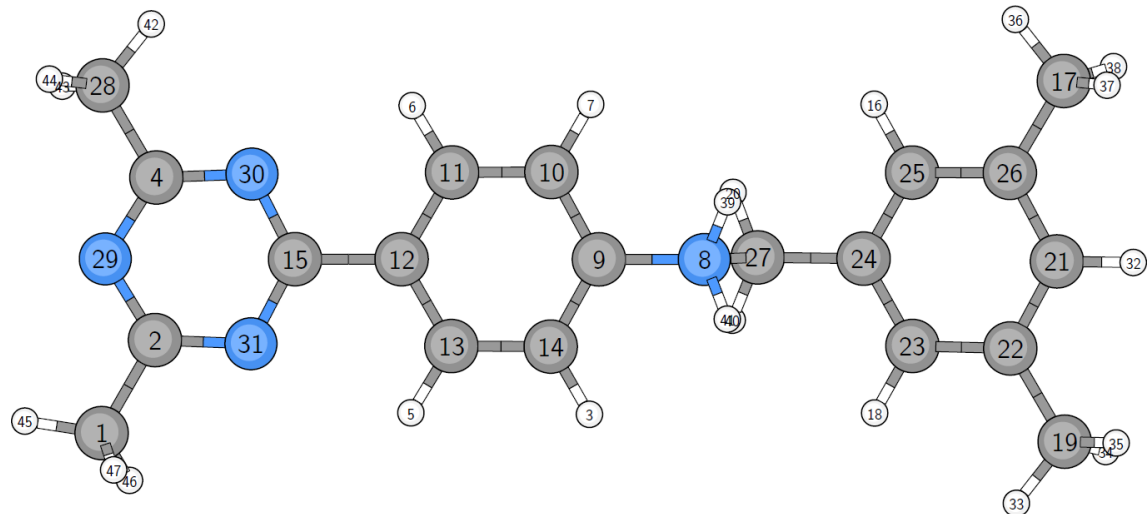


Figure S 9.1-112: Atom labels for the H+rPI-3 M model.

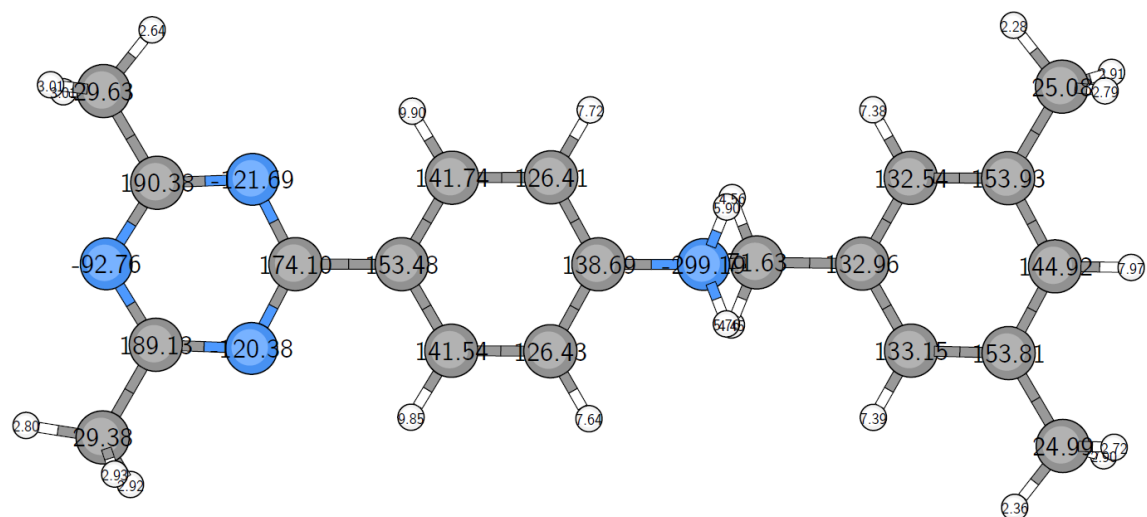


Figure S 9.1-113: Calculated NMR Chemical Shifts for the H+rPI-3 M model system, obtained on B97-2//pcS-2//PBE0-D3/def2-TZVP level of theory.

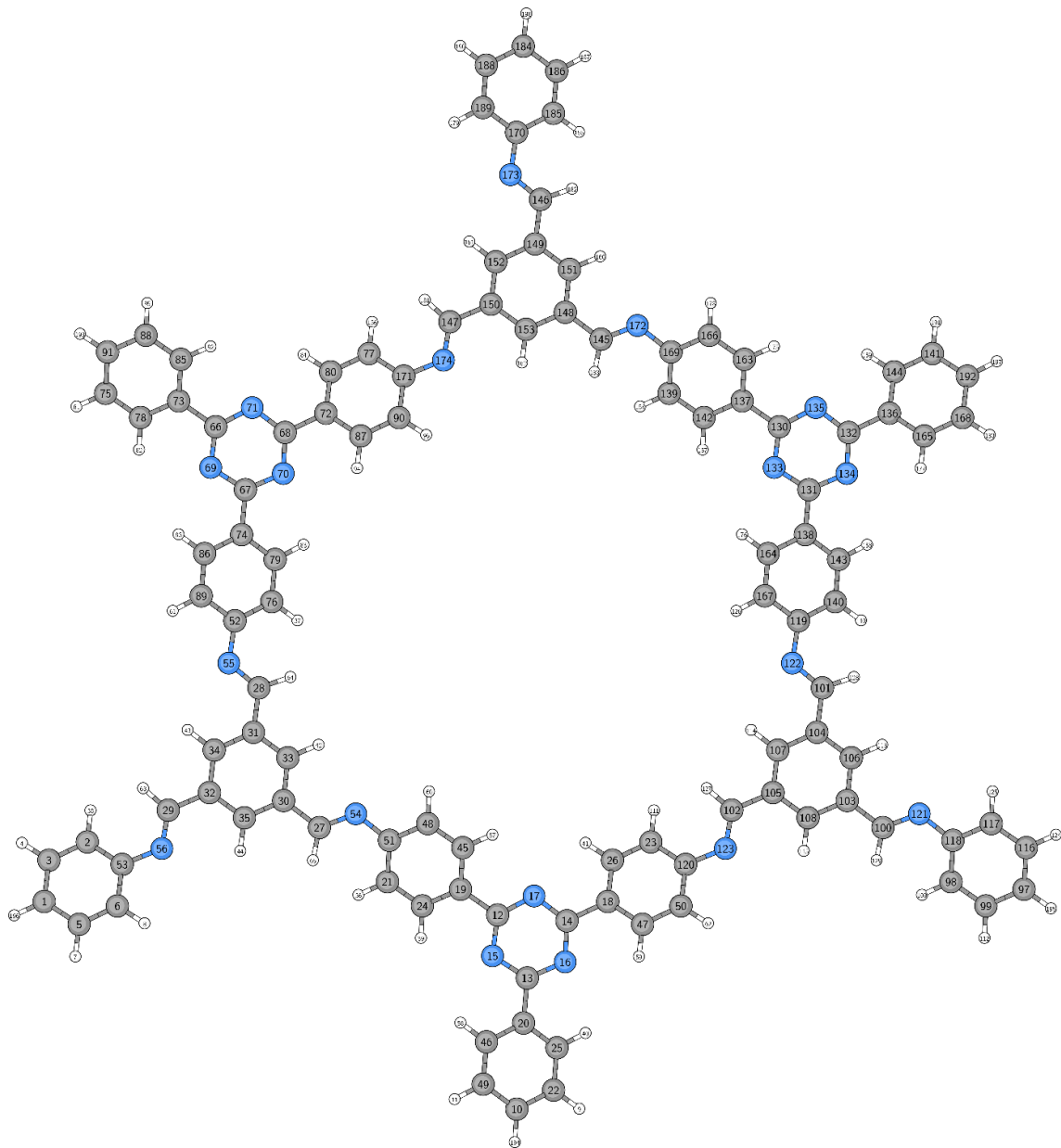


Figure S 9.1-114: Atom labels for the PI-3 SP model.

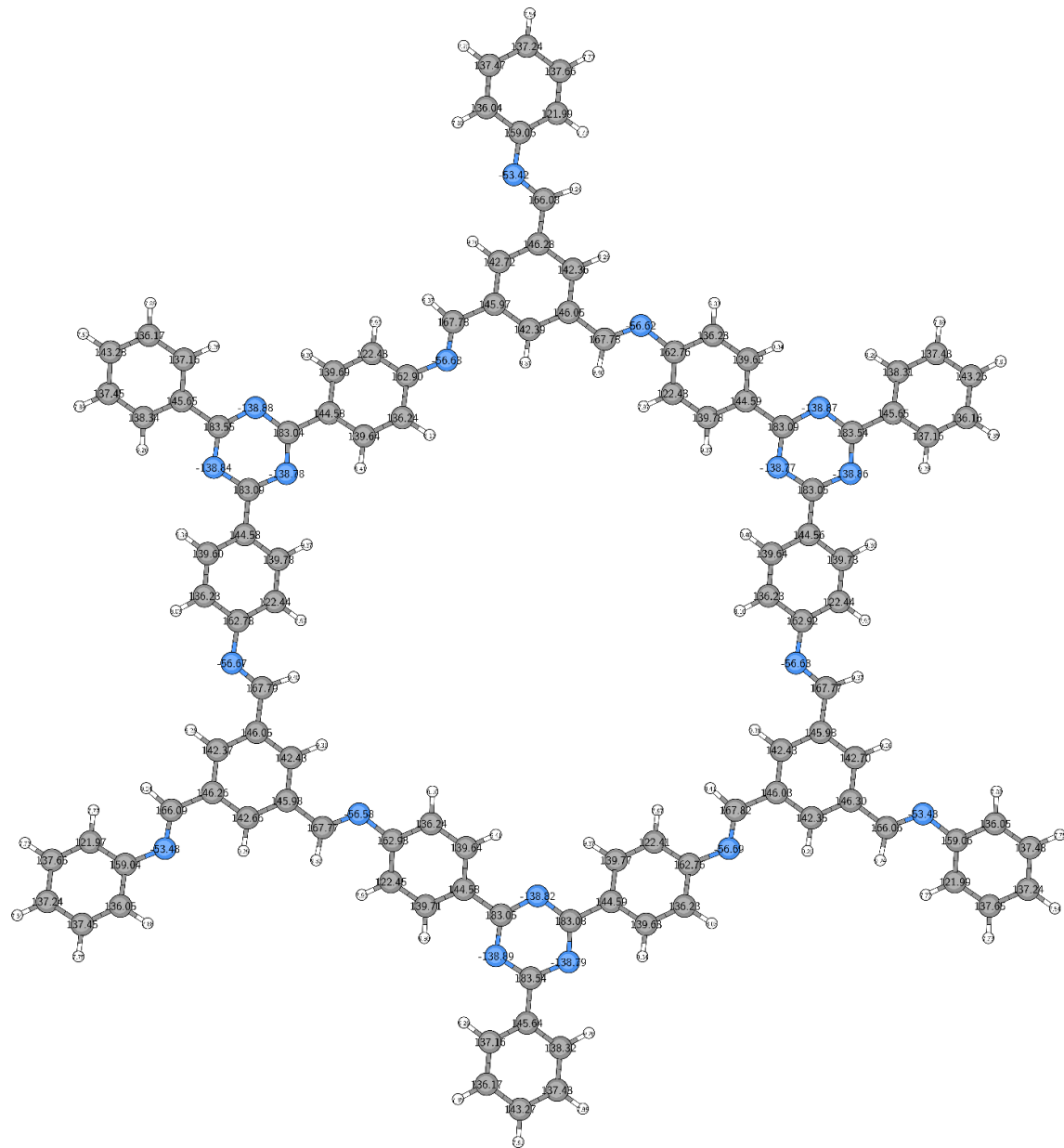


Figure S 9.1-115: Calculated NMR Chemical Shifts for the PI-3 SP model system, obtained on B97-2/pcS-2//PBE0-D3/def2-TZVP level of theory.

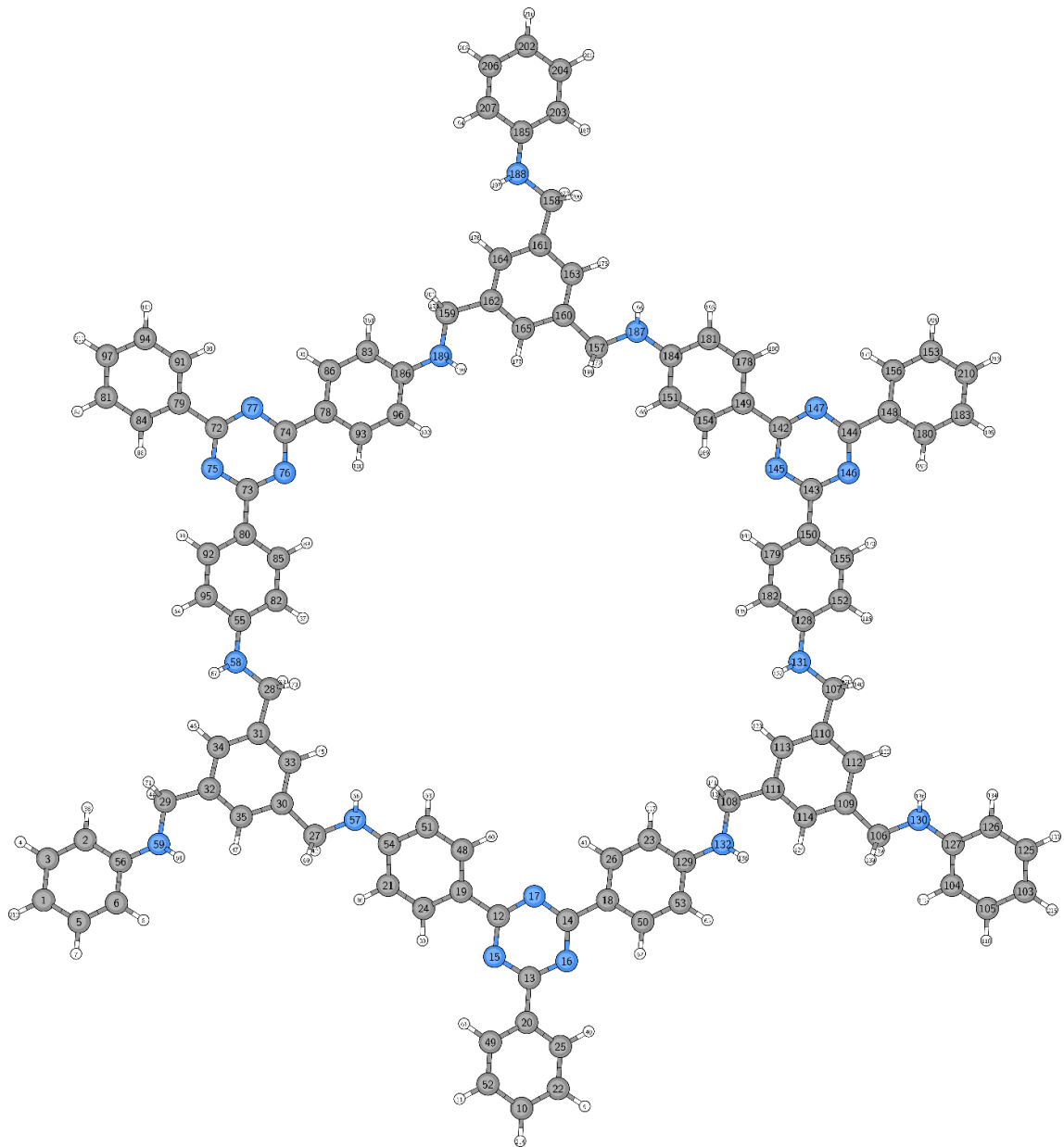


Figure S 9.1-116: Atom labels for the rPI-3 SP model.

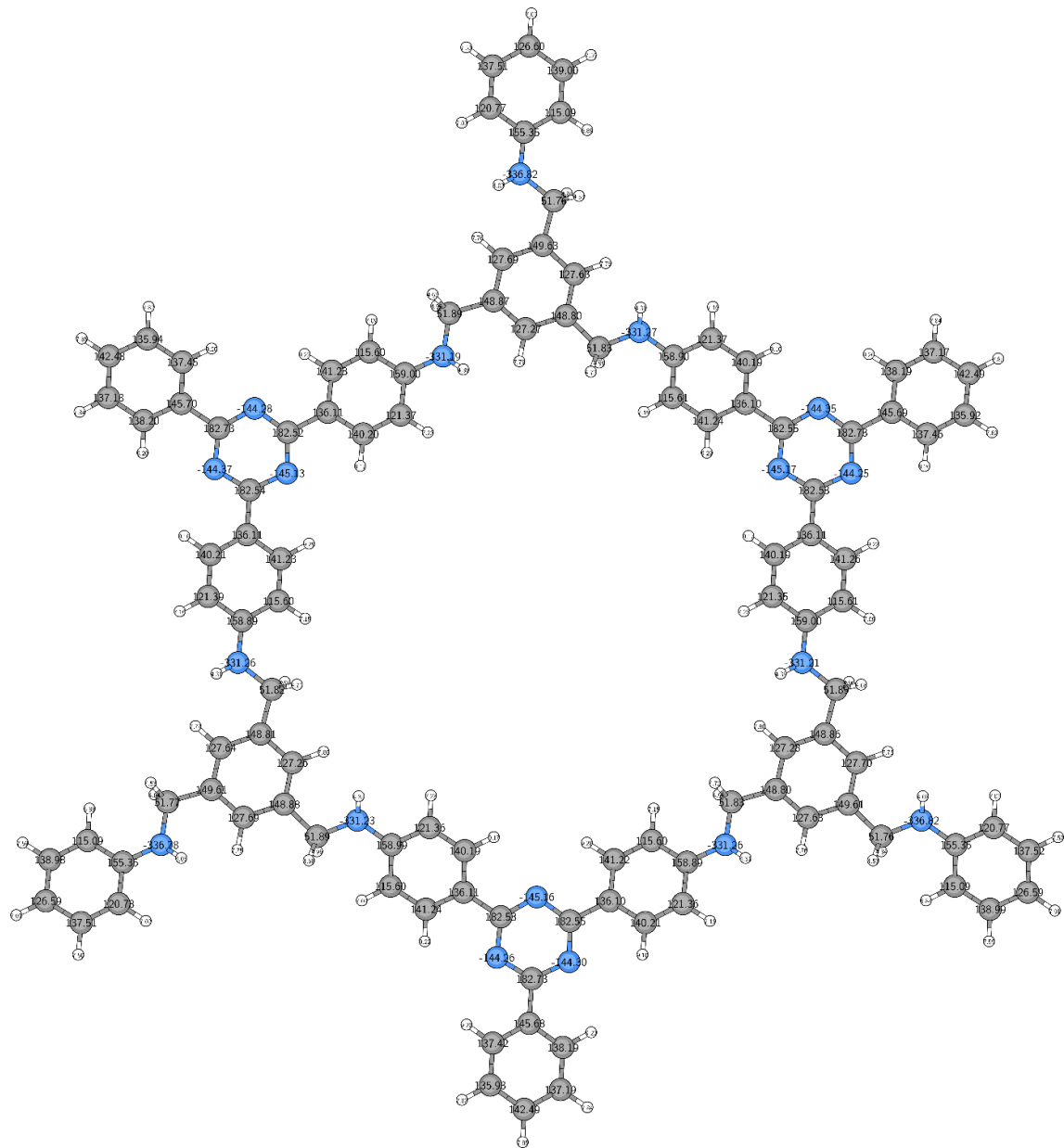


Figure S 9.1-117: Calculated NMR Chemical Shifts for the rPI-3 SP model system, obtained on PBE0-D3/def2-TZVP level of theory.

Table S 9.1-5: Calculated imine/amine ^{15}N NMR chemical shifts [ppm] obtained from optimized geometries for the presented model systems. Note that an overestimation of ring strain in the single pore calculation can cause deviations of the calculated NMR shifts, as these are influenced by the conformation of the dihedral angle U (Table S 9.1-6).

Model	Level of Theory	Atom Number	NMR Shift	Delta
PI-3 M	PBE0-D3/def2-TZVP// B97-2/pcS-2	8	-44.13	
PI-3 M	RI-PBE-D3/def2-TZVP// B97-2/pcS-2	8	-54.63	-10.50
PI-3 SP	RI-PBE-D3/def2-TZVP// B97-2/pcS-2	172	-56.62	
		122	-56.63	
		123	-56.69	
		54	-56.58	
		55	-56.67	
		174	-56.68	
		Average =	-56.65	-2.01
rPI-3 M	PBE0-D3/def2-TZVP// B97-2/pcS-2	8	-301.84	
rPI-3 M	RI-PBE-D3/def2-TZVP// B97-2/pcS-2	8	-314.69	
rPI-3 SP	RI-PBE-D3/def2-TZVP// B97-2/pcS-2	187	-331.27	
		131	-331.21	
		132	-331.26	
		57	-331.23	
		58	-331.26	
		189	-331.19	
		Average =	-331.24	-16.54
H+rPI-3 M	PBE0-D3/def2-TZVP// B97-2/pcS-2	8	-299.19	
H+rPI-3 M	RI-PBE-D3/def2-TZVP// B97-2/pcS-2	8	-312.52	-13.33

Table S 9.1-6: Calculated ^{15}N NMR chemical shifts [ppm] and dihedral angles U [$^\circ$], obtained from optimized geometries for the presented model systems.

Model	Level of Theory	NMR Shift	Delta	Dihedral Angle	Delta
PI-3 M	PBEO-D3/def2-TZVP// B97-2/pcS-2	-44.13		43.59	
PI-3 M	RI-PBE-D3/def2-TZVP// B97-2/pcS-2	-54.63	-10.50	43.29	-0.30
PI-3 SP	RI-PBE-D3/def2-TZVP// B97-2/pcS-2	-56.65	-2.01	27.40	-15.89
rPI-3 M	PBEO-D3/def2-TZVP// B97-2/pcS-2	-301.84		10.18	
rPI-3 M	RI-PBE-D3/def2-TZVP// B97-2/pcS-2	-314.69	-12.85	8.97	-1.21
rPI-3 SP	RI-PBE-D3/def2-TZVP// B97-2/pcS-2	-331.24	-16.54	6.46	-2.51

9.1.11 Pair Distribution Function (PDF) Analysis

9.1.11.1 Data Processing

Analysis of the PDF provides a useful method for interpreting structure information from total scattering data. It provides a sensitive probe of the local structure in amorphous and nanostructured materials, because it does not require symmetry, and treats both Bragg and diffuse scattering equally^[31]. A diffraction measurement over a wide range of momentum transfer and with good statistics is required to obtain suitable PDFs for structure analysis. Starting with a 2D data collection of diffracted intensities, azimuthal integration results in the 1D, isotropic powder pattern $I(Q)$, which includes all coherent scattering interferences from the atoms in the sample, defined by the Debye equation, ^[32] as

$$I_c(Q) = \sum_i \sum_j f(Q)_i f(Q)_j \frac{\sin(Qr_{ij})}{Qr_{ij}}. \quad (1)$$

In order to obtain the pair distribution function, by the formalism of Egami and Billinge^[31], the measured powder diffraction intensities are first normalized by the average form factor squared to obtain the total scattering structure function $S(Q)$, defined as

$$S(Q) = \frac{I_c(Q) - \langle f(Q)^2 \rangle + \langle f(Q) \rangle^2}{\langle f(Q) \rangle^2}. \quad (2)$$

The experimental PDF, denoted $G(r)$, is the truncated Fourier transform of the reduced, total scattering structure function, $F(Q) = Q[S(Q) - 1]$, as

$$G(r) = \frac{2}{\pi} \int_{Q_{min}}^{Q_{max}} F(Q) \sin(Qr) dQ, \quad (3)$$

where $G(r)$ is the magnitude of the scattering momentum transfer for elastic scattering,

$$Q = 4\pi \sin\theta/\lambda, \quad (4)$$

where λ is the probe wavelength and 2θ is the scattering angle. In practice, values of Q_{min} and Q_{max} are determined by the experimental setup, and Q_{max} is often reduced below the experimental maximum to reduce the effects of low signal-to-noise in the high- Q region on the Fourier transformation. To aid in qualitative assessment of the long-distance structural correlations, a modification function can be applied to $F(Q)$ prior to Fourier transformation by,

$$G(r) = \frac{2}{\pi} \int_{Q_{min}}^{Q_{max}} M(Q) F(Q) \sin(Qr) dQ \quad (5)$$

and,

$$M(Q) = \frac{\sin(Qr_{ij})}{Qr_{ij}}. \quad (6)$$

$M(Q)$ is called a modification function, in this case a Lorch function^[33, 34], which damps the intensity of $F(Q)$ to 0 at Q_{max} . This reduces the effects of termination from high- Q signal and noise intensities in the reduced structure function, which suppresses non-structural high frequency oscillations in the PDF.

9.1.11.2 Real-Space Structure Refinement

The PDF gives the scaled probability of finding two atoms in a material a distance r apart and is relative to the average density of atom pairs in the material. For a macroscopic scatterer, $G(r)$ is calculated from a known structure model according to

$$G(r) = 4\pi r [\rho(r) - \rho_0], \quad (7)$$

$$\rho(r) = \frac{1}{4\pi r^2 N} \sum_i \sum_{j \neq i} \frac{f_i f_j}{\langle f \rangle^2} \delta(r - r_{ij}). \quad (8)$$

Here, ρ_0 is the average number density of the material and $\rho(r)$ is the local atomic pair density, which is the mean weighted density of neighbor atoms at distance r from an atom at the origin. The sums in $\rho(r)$ run over all atoms in the sample, f_i is the scattering factor of atom i , $\langle f \rangle$ is the average scattering factor and r_{ij} is the distance between atoms i and j . In this study, Eqs. (4) and (5) were used to fit the PDF generated from a structure model to the

experimental PDFs in using the program PDFgui.^[5] The delta functions in Eq. (5) were broadened to account for atom displacements and a finite Q-range in the experiment, and the equation was modified to account for signal damping and broadening due to experimental effects. PDF modelling was performed by adjusting the lattice parameters $a=b$ and c , atomic displacement parameters (ADPs) $U_{11} = U_{22} \neq U_{33}$, correlated motion of neighbouring atoms $\delta 2$, domain size (*spdiameter*), and a global scale factor. The refinements were run by minimizing R_w , calculated as

$$R_w = \sqrt{\frac{\sum_{i=1}^n [G_{obs}(r_i) - G_{calc}(r_i, P)]^2}{\sum_{i=1}^n G_{obs}(r_i)^2}}, \quad (9)$$

Where P is the set of refined parameters, which was used to quantify the goodness-of-fit for the model. The model was constructed in each case, for the amine and imine structures, with 2D layers which had been relaxed by quantum chemical calculations (see Section 9.1.10.1). The relaxed layer was then placed into a starting cell based on the repeat distances in the relaxed layer, and the approximate stacking distance from XRPD analysis. Additional supercells were constructed with 2, 4, 8 and 16 layers to test the effects of random interlayer translational disorder.

9.1.11.3 Results

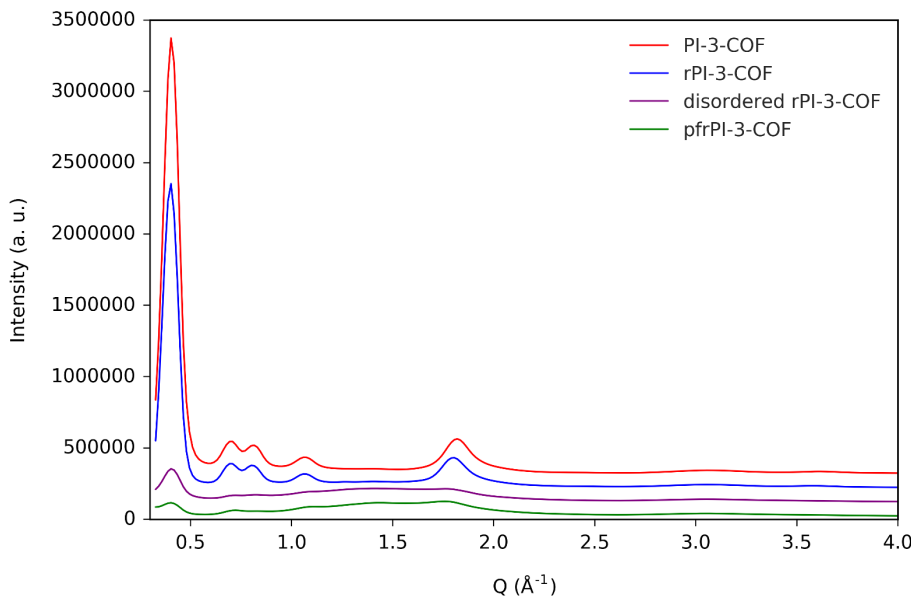


Figure S 9.1-118: The XRPD patterns for all samples are plotted in intensity versus Q. The patterns were rescaled by normalization of the diffuse, high-Q intensities and are offset for clarity. The ordered COFs, PI-3-COF and rPI-3-COF, show sharp Bragg diffraction peaks indexed by $P\bar{6}$ symmetry to 100, 2-10, 200, 3-20, and primarily 001 from low to high, respectively. The disordered COFs, disordered rPI-3-COF and pfrPI-3-COF, also show features for the same peak indexing, though significantly reduced in intensity, indicating that at least some content maintains intralayer connectivity and an ordered stacking arrangement.

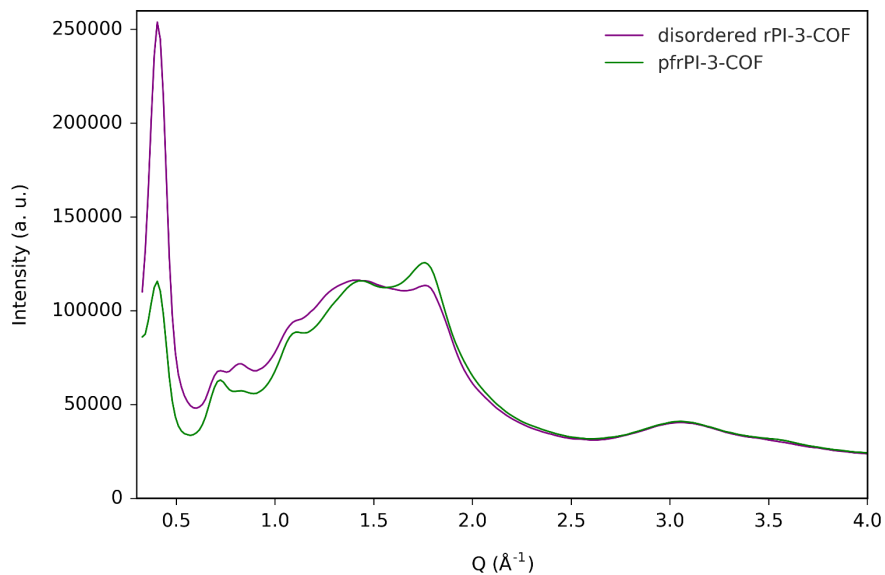


Figure S 9.1-119: The XRPD patterns for disordered samples are overlayed in intensity versus Q . The patterns were rescaled by normalization of the diffuse, high- Q intensities. The 100 and 200 peaks are substantially more prominent in the disordered rPI-3-COF, while the 001 peak is more prominent in pfrPI-3-COF, relative to the 100 peak. This indicates differences in the disordered sample structures, possibly larger lateral intralayer coherence in the in disordered rPI-3-COF, but more layers contributing to ordered stacking domains in pfrPI-3-COF. Formyl groups in pfrPI-3-COF may also play a role in decreasing the planarity of the layers, which could decrease in-plane coherence, i.e. 100 peak. However, differences in relative intensities may also be due to the presence of formyl groups sticking into the pores in pfrPI-3-COF, which reduces the scattering contrast between pore and framework.

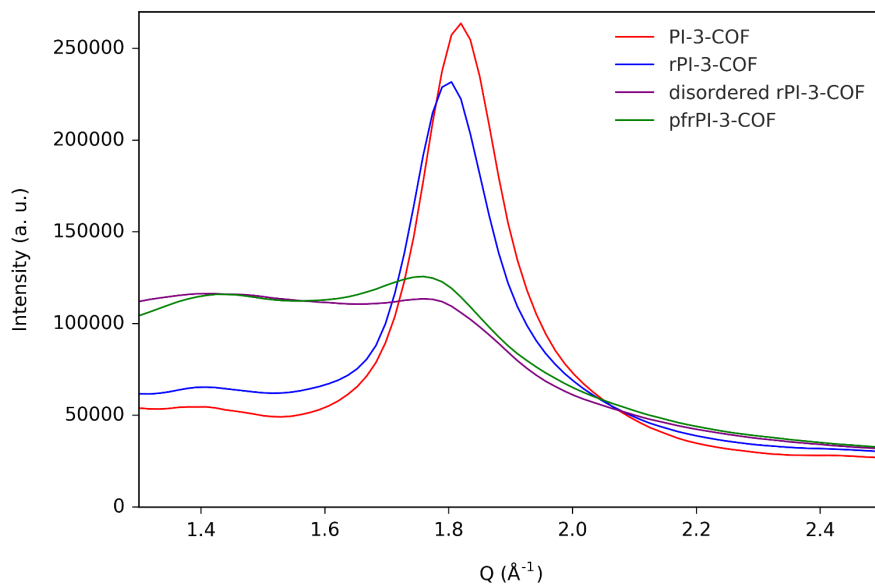


Figure S 9.1-120: The XRPD patterns for all samples are overlayed in intensity versus Q , focused on the 001 peaks. The patterns were rescaled by normalization of the diffuse, high- Q intensities. It is clear that at least some content in every sample exists in a state of ordered interlayer stacking along the [001] direction. However, the stacking distances are not equivalent. Pseudo-Voigt functions with a linear baseline were fit to the peaks to determine their positions. PI-3-COF (red) shows the shortest interlayer distance at $3.4528(9)$ Å which is likely due to stronger bonding and more planar conformation of the imine bonding leading to a more ordered framework structure, therefore allowing closer stacking. rPI-3-COF (blue) stacking distance is slightly longer at $3.485(1)$ Å, which is likely due to increased disorder of the framework due to larger torsions

of the amine bonding. The next largest stacking distance is disordered rPI-3-COF (purple) at 3.515(3) Å, and the largest, pfrPI-3-COF (green) 3.547(2) Å. The larger stacking distances in the disordered forms makes sense due to reduced stacking coherence and likely increased disorder in the amine torsion angles. Furthermore, interactions of the formyl groups in pfrPI-3-COF may also play a role in increasing the stacking distance between layers. A similar peak fitting analysis was performed on the 100 peak. In this case, the positions resulted in *d*-spacings of 15.50(1) (PI-3-COF), 15.66(1) (rPI-3-COF), 15.415(7) (disordered rPI-3-COF), 15.361(8) (pfrPI-3-COF). This could suggest, for the segments of all samples which are coherently ordered in the *ab* plane, that the imine to amine conversion results in a larger pore-to-pore spacing due to the expanded N-C bond lengths, but that the disordering process leads to a contracted pore-to-pore spacing, which may have to do with larger and more random out-of-plane torsions due to larger neighbor-layer offsets.

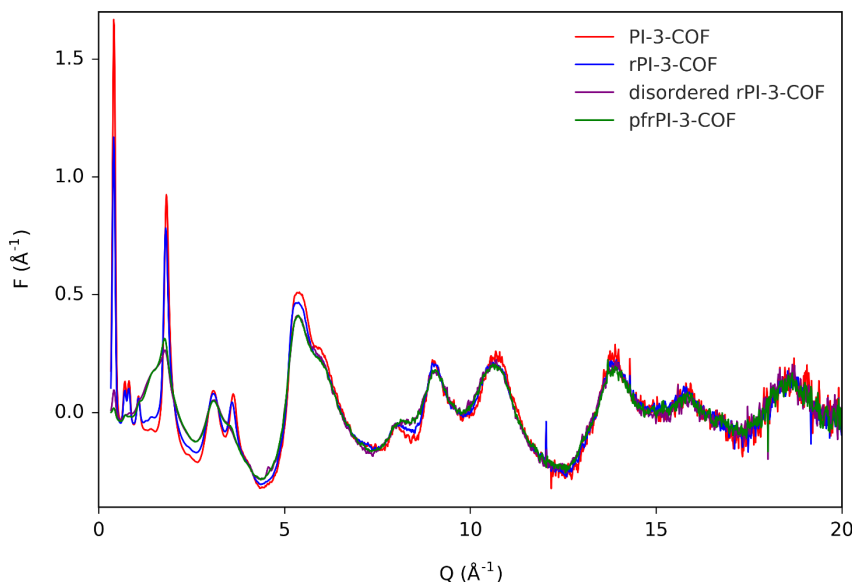


Figure S 9.1-121: The reduced total scattering patterns for all samples are overlaid. Distinct structural information, not clearly visible in the raw diffraction patterns, is evident out to high *Q* values, which is made apparent by the normalization procedure. High similarity in the patterns from approximately 5-20 Å⁻¹ is a good indicator of similarity in local molecular motifs present in the structure, e.g. imine versus amine bonded layers. For example a shift to lower *Q* (longer *d*-spacing) of the feature at 10-12 Å⁻¹ is present in all amine-based samples.

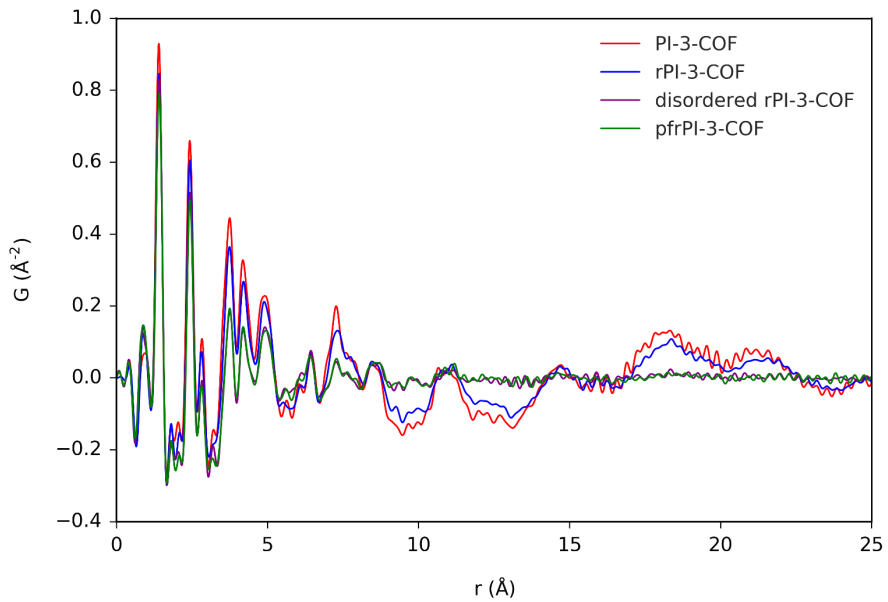


Figure S 9.1-122: The PDFs, $G(r)$, for all samples are overlaid. All samples show high similarity in the peak positions and relative amplitudes up to approximately 7 Å, which is further evidence that that layer connectivity is still intact in the disordered state. Beyond this, there is some similarity in positions but drastic differences in the relative amplitude between ordered and disordered sample structures. There are distinct medium- and long-range order structuring in PI-3-COF and rPI-3-COF, which consists of two primary oscillations, one with shorter wavelength due to the ordering of the stacked layers, and one with longer wavelength due to the ordering of the porous channels. There is an apparent loss of structural coherence beyond approximately 12 Å for the disordered samples, indicating that the spatial relationships of the stacked layers, and of the porous channels, are significantly reduced.

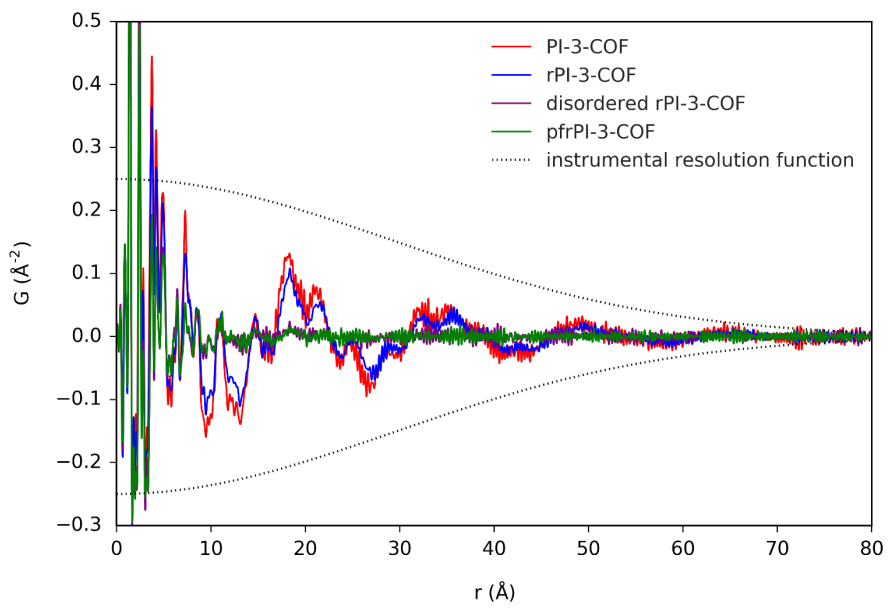


Figure S 9.1-123: The PDFs, $G(r)$, for all samples are overlaid and plotted over a longer distance range. Here, density modulations due to stacked layers and porous channels can be observed for the crystalline samples out to much higher distances, whereas the disordered samples are flat, indicating no long range order. The long range signals are damped due to the limited reciprocal space resolution of the measurement.

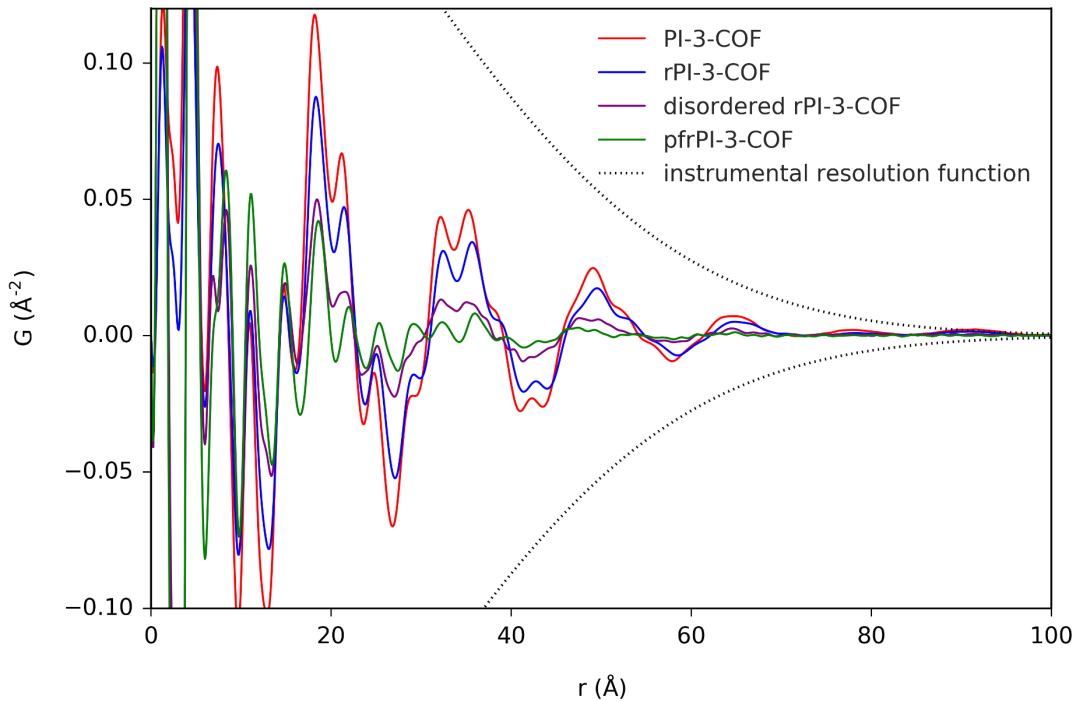


Figure S 9.1-124: The PDFs, $G(r)$, for all samples are again overlaid and plotted over a longer distance range. However, the data have been reprocessed using a $Q_{\text{max}} = 5.0 \text{ \AA}^{-1}$ and a Lorch function as described in the methods section to remove effects of noise and termination on the resulting PDF data. The plot is also magnified close into the low amplitude signals at higher distances. Here, we can see the structural signals from the 100 and 001 Bragg peaks, previously noted in the diffraction patterns of the disordered samples. First, an oscillation distinctly coming from stacked layers is present for pfrPI-3-COF (green) up to at least 50-60 Å (14-17 layers). It is also present in disordered rPI-3-COF (purple), but broadened and with reduced amplitude. As with the diffraction data, the roles are reversed for ordering of the porous channels, distinct oscillations between pore and framework in disordered rPI-3-COF to at least 60 Å (4-5 channels).

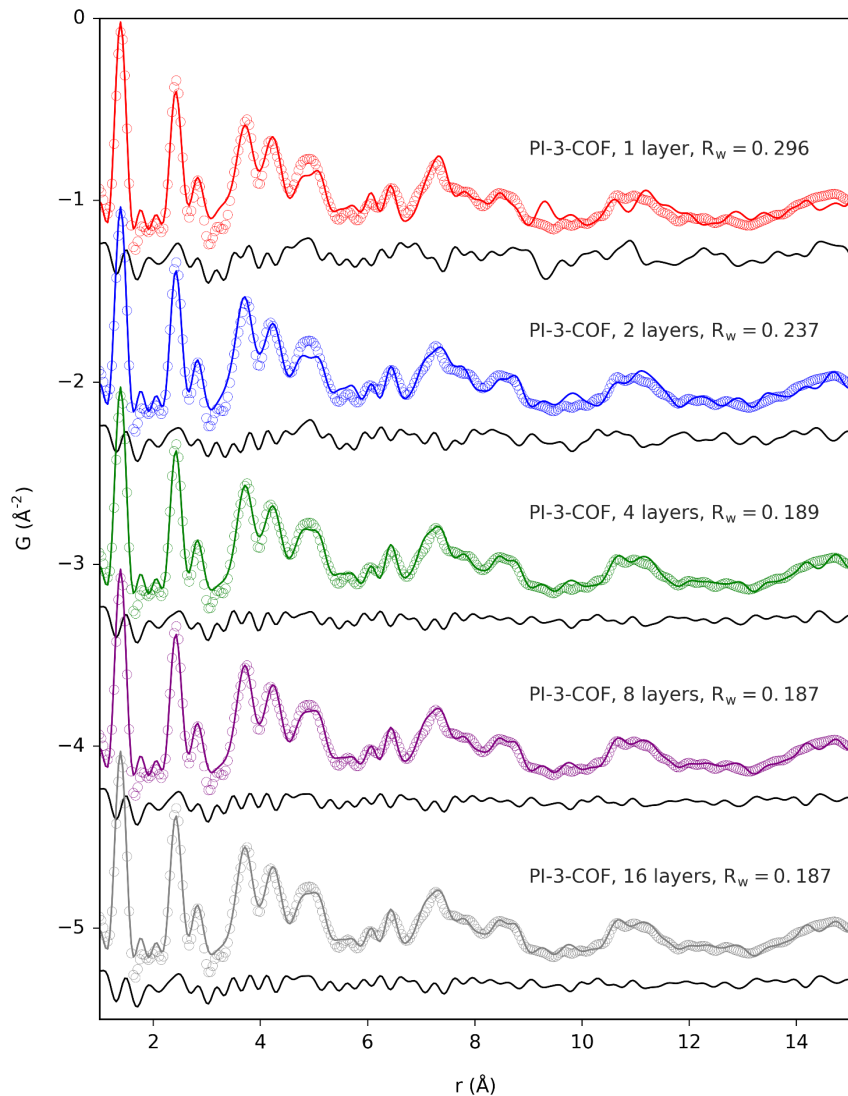


Figure S 9.1-125: Structure refinement (solid line) to the PDF from PI-3-COF (dots) for models with 1, 2, 4, 8, and 16 layers. The layers allowed to randomly translate forward or backward along the 1-10 direction. Difference curves are shown offset below the fit (black).

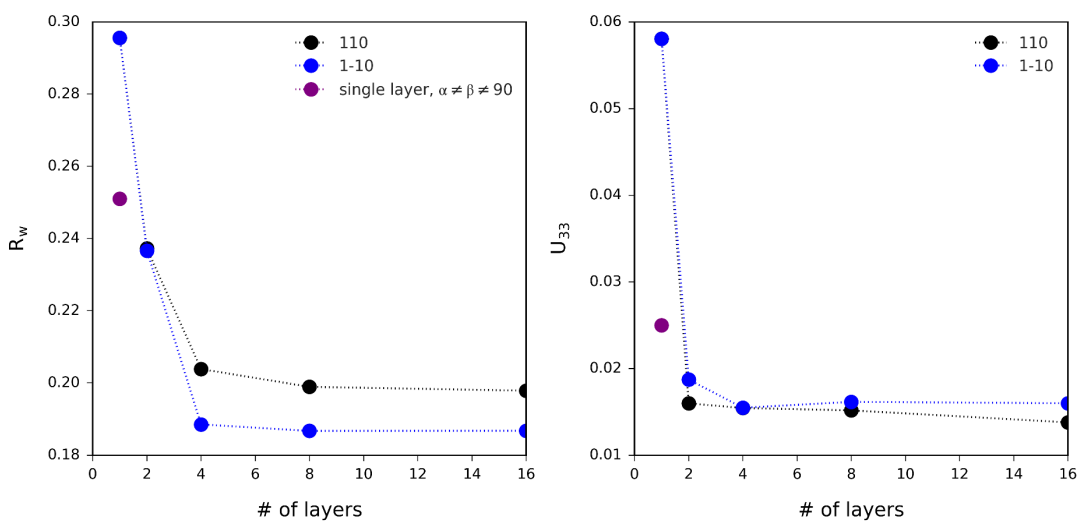


Figure S 9.1-126: R_w (left) and U_{33} (right) values resulting from fitting of structural models with increasing numbers of layers allowed to translate forward and backward along either 110 or 1-10 directions to the PDF

data from PI-3-COF. The R_w value decreases dramatically on adding a single or few layers, indicating that the structuring prefers a staggered relationship between neighboring layers rather than perfectly eclipsed stacking as indicated by the average structure. Furthermore, disorder in the stacking vectors can also account for the very large interlayer ADP (U_{33}) observed when modelling with only a single layer, which is artificially enlarged to reduce the contribution from non-preferred, eclipsed interlayer atom-pair distances. The data appears to prefer translation along the 1-10 direction as opposed to 110, although this does not account for the possibility of combining random displacements along the other two equivalent directions, which could be equally likely. In addition, the model with a single layer was also refined allowing the α and β angles to assume non-90° angles which also significantly increased the goodness-of-fit, supporting the preference for locally slipped stacking of the neighboring layers.

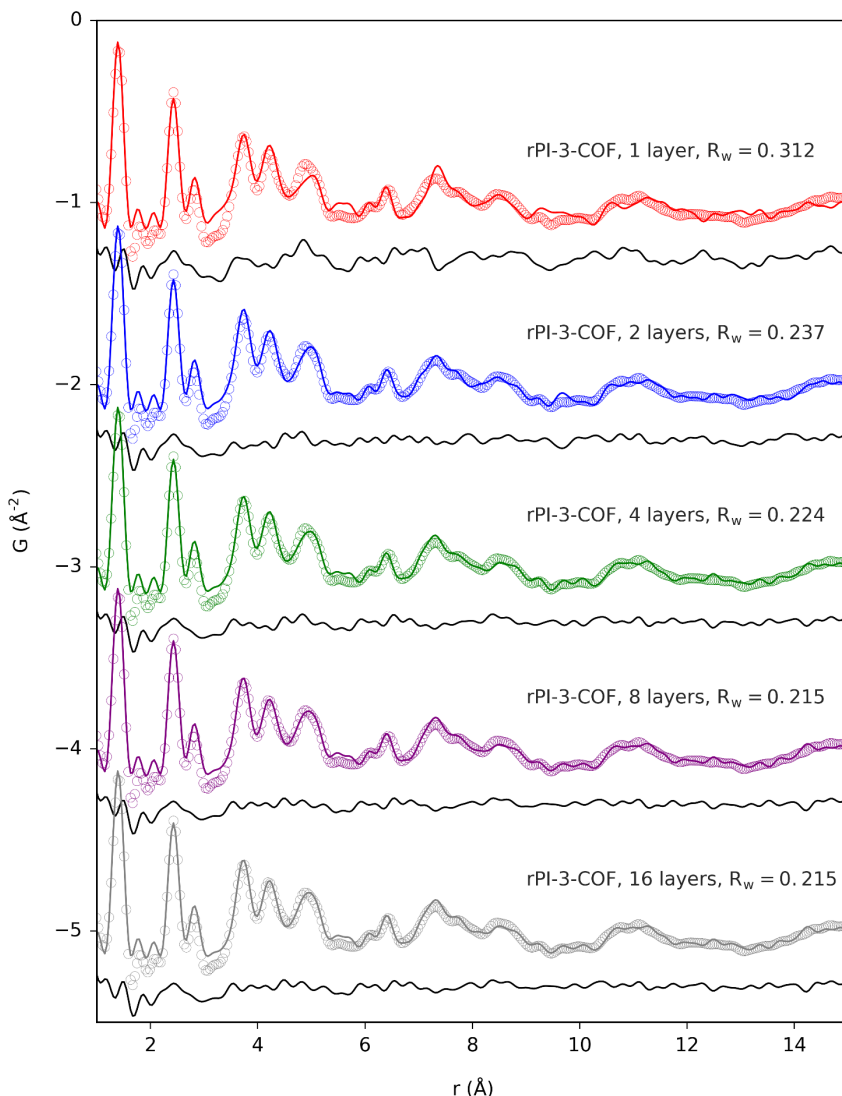


Figure S 9.1-127: Structure refinement (solid line) to the PDF from rPI-3-COF (dots) for models with 1, 2, 4, 8, and 16 layers. The layers allowed to randomly translate forward or backward along the 1-10 direction. Difference curves are shown offset below the fit (black).

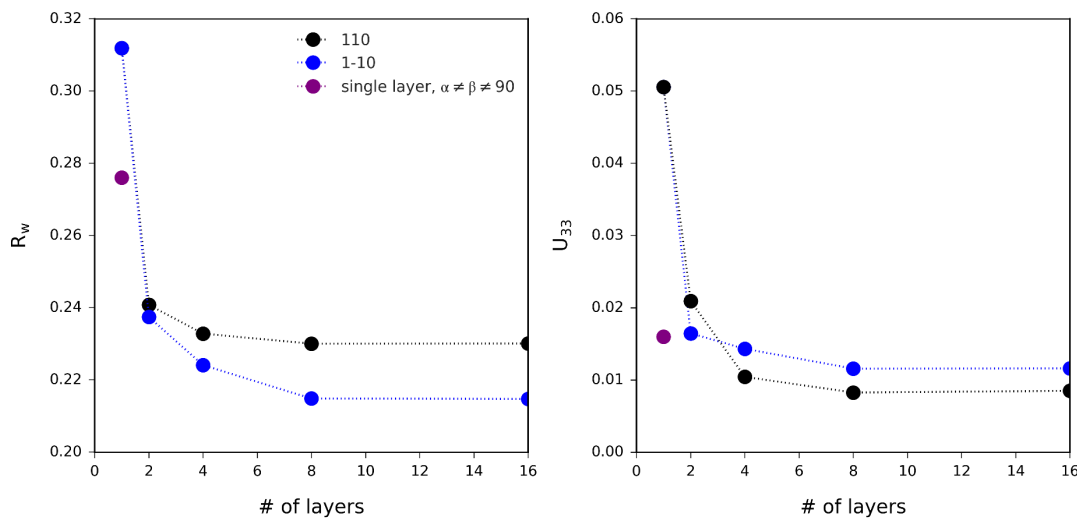


Figure S 9.1-128: R_w (left) and U_{33} (right) values resulting from fitting of structural models with increasing numbers of layers allowed to translate forward and backward along either 110 or 1-10 directions to the PDF data from rPI-3-COF. The R_w value decreases dramatically on adding a single or few layers, indicating that the structuring prefers a staggered relationship between neighboring layers rather than perfectly eclipsed stacking as indicated by the average structure. Furthermore, disorder in the stacking vectors can also account for the very large interlayer ADP (U_{33}) observed when modeling with only a single layer, which is artificially enlarged to reduce the contribution from non-preferred, eclipsed interlayer atom-pair distances. The data appears to prefer translation along the 1-10 direction as opposed to 110, although this does not account for the possibility of combining random displacements along the other two equivalent directions, which could be equally likely. In addition, the model with a single layer was also refined allowing the α and β angles to assume non-90° angles which also significantly increased the goodness-of-fit, supporting the preference for locally slipped stacking of the neighboring layers.

We consider the stacking vector to be the translation of one layer along the ab plane from an eclipsed position with respect to the neighboring layer in the hexagonal cell, $\alpha=\beta=90^\circ$. For the 1-10 direction, the shift can be calculated by $2*f*a*\cos(30^\circ)$ where f is the fractional shift value, and then relative shifts can be obtained from the difference between subsequent neighbor shifts. Thus the average shifts obtained from the 16 layer models are 1.48(58) and 1.88(99) Å for the imine and amine PDF refinements, respectively, which match well within the ranges suggested by Spitzer et al. 1.7-1.8 Å^[35] and Koo, Dichtel & Clancy i.e. 1.5-2.8 Å^[36], giving direct experimental evidence for random local shifting of neighboring layers despite the fact that the average crystallographic structure appears eclipsed.

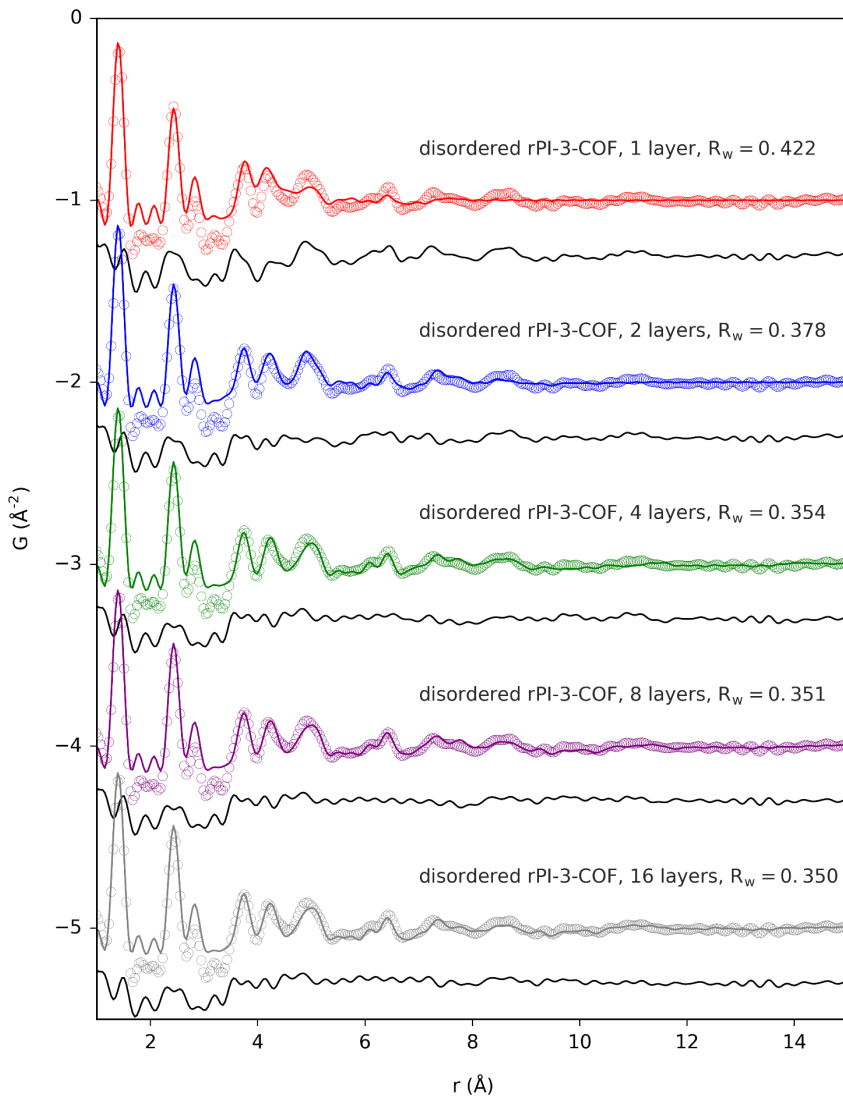


Figure S 9.1-129: Structure refinement (solid line) to the PDF from disordered rPI-3-COF (dots) for models with 1, 2, 4, 8, and 16 layers. The layers allowed to freely translate in the *ab* plane. Difference curves are shown offset below the fit (black).

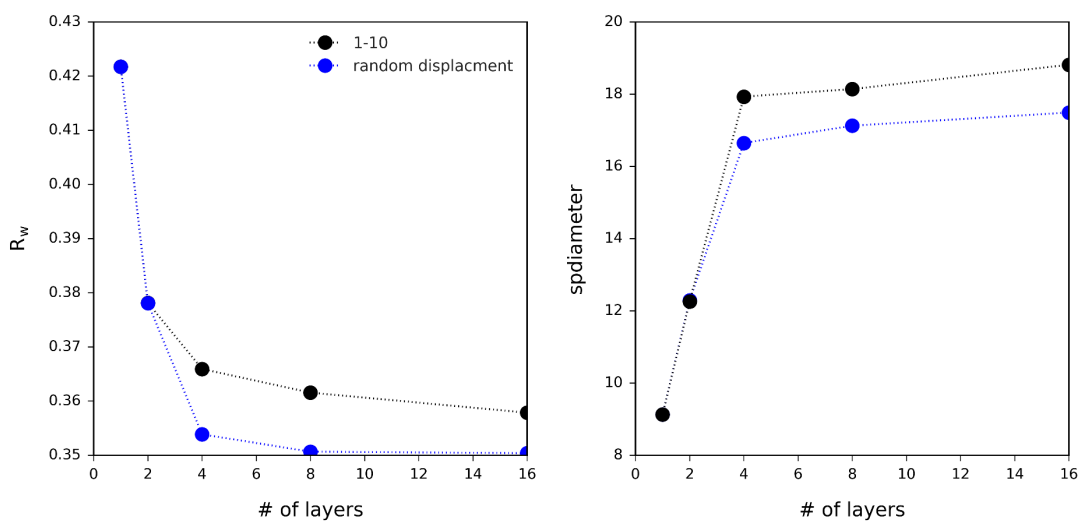


Figure S 9.1-130: R_w (left) and the coherence length (spdiameter from PDFgui program) (right) values resulting from fitting of structural models with increasing numbers of layers allowed to translate forward and

backward along the 1-10 direction as in the previous model, and freely in the *ab* plane, to the PDF data from disordered rPI-3-COF. This refinement prefers larger magnitude, and random direction, translations to reduce the contribution of coherent intermolecular atom-pairs to the simulated PDF. As the intermolecular signal is reduced by random translations, the dampening of the simulated signal by spdiameter is reduced, eventually returning \sim 17-19 Å, which is approximately the in-plane coherence we might expect given the distances in which sharp features exist in the measured PDF.

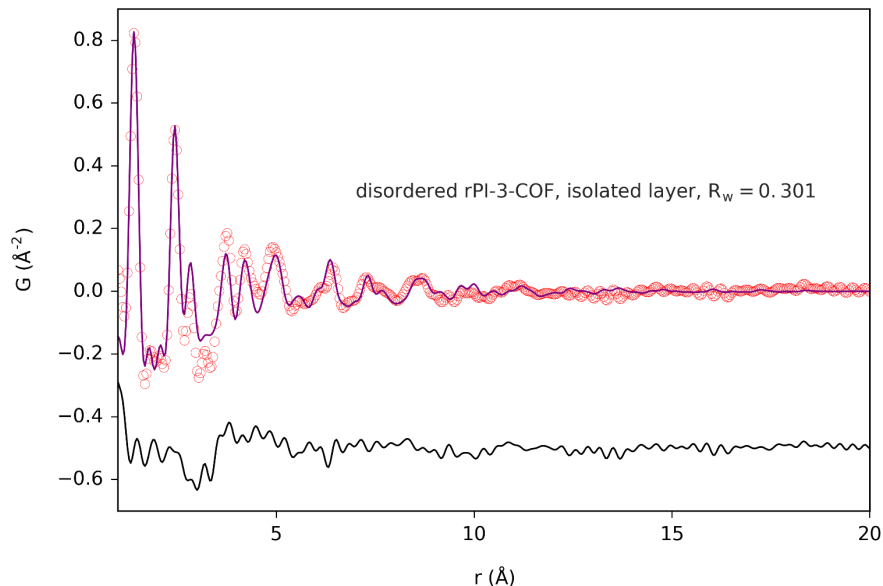


Figure S 9.1-131: An additional refinement of a single, isolated layer of the amine structure was attempted to completely eliminate all intermolecular structural correlations from the simulated PDF. This gives the best fit, further supporting that all sharp features in the disordered sample PDFs come from intramolecular correlations from a connected layer, at least up to \sim 20 Å.

9.1.12 References

1. Chupas P. J. et al. Rapid-Acquisition Pair Distribution Function (Ra-Pdf) Analysis. *J. Appl. Crystallogr.* **36**, 1342-1347 (2003).
2. Hammersley A. P. et al. Two-Dimensional Detector Software: From Real Detector to Idealised Image or Two-Theta Scan. *High Pressure Research* **14**, 235-248 (1996).
3. Juhás P., Davis T., Farrow C. L., Billinge S. J. L. Pdfgetx3: A Rapid and Highly Automatable Program for Processing Powder Diffraction Data into Total Scattering Pair Distribution Functions. *J. Appl. Crystallogr.* **46**, 560-566 (2013).
4. Yang X., Juhas P., Farrow C. L., Billinge S. J. Xpdfsuite: An End-to-End Software Solution for High Throughput Pair Distribution Function Transformation, Visualization and Analysis. Preprint at <https://arxiv.org/abs/1402.3163> (2015).
5. Farrow C. L. et al. Pdfit2 and Pdfgui: Computer Programs for Studying Nanostructure in Crystals. *J. Phys.: Condens. Matter* **19**, 335219 (2007).
6. Perdew J. P., Burke K., Ernzerhof M. Generalized Gradient Approximation Made Simple. *Phys. Rev. Lett.* **77**, 3865-3868 (1996).

7. Grimme S., Antony J., Ehrlich S., Krieg H. A Consistent and Accurate Ab Initio Parametrization of Density Functional Dispersion Correction (Dft-D) for the 94 Elements H-Pu. *J. Chem. Phys.* **132**, 154104 (2010).
8. Schäfer A., Huber C., Ahlrichs R. Fully Optimized Contracted Gaussian Basis Sets of Triple Zeta Valence Quality for Atoms Li to Kr. *J. Chem. Phys.* **100**, 5829-5835 (1994).
9. Eichkorn K., Weigend F., Treutler O., Ahlrichs R. Auxiliary Basis Sets for Main Row Atoms and Transition Metals and Their Use to Approximate Coulomb Potentials. *Theor. Chem. Acc.* **97**, 119-124 (1997).
10. Burow A. M., Sierka M. Linear Scaling Hierarchical Integration Scheme for the Exchange-Correlation Term in Molecular and Periodic Systems. *J. Chem. Theory Comput.* **7**, 3097-3104 (2011).
11. Burow A. M., Sierka M., Mohamed F. Resolution of Identity Approximation for the Coulomb Term in Molecular and Periodic Systems. *J. Chem. Phys.* **131**, 214101 (2009).
12. Grajciar L. Low-Memory Iterative Density Fitting. *J. Comput. Chem.* **36**, 1521-1535 (2015).
13. Lazarski R., Burow A. M., Grajciar L., Sierka M. Density Functional Theory for Molecular and Periodic Systems Using Density Fitting and Continuous Fast Multipole Method: Analytical Gradients. *J. Comput. Chem.* **37**, 2518-2526 (2016).
14. Lazarski R., Burow A. M., Sierka M. Density Functional Theory for Molecular and Periodic Systems Using Density Fitting and Continuous Fast Multipole Methods. *J. Chem. Theory Comput.* **11**, 3029-3041 (2015).
15. Turbomole V7.3 2018, a Development of University of Karlsruhe and Forschungszentrum Karlsruhe GmbH, 1989-2007, Turbomole GmbH, since 2007; Available from [Http://Www.Turbomole.Com](http://Www.Turbomole.Com).
16. Adamo C., Barone V. Toward Reliable Density Functional Methods without Adjustable Parameters: The Pbe0 Model. *J. Chem. Phys.* **110**, 6158-6170 (1999).
17. Ernzerhof M., Scuseria G. E. Assessment of the Perdew–Burke–Ernzerhof Exchange-Correlation Functional. *J. Chem. Phys.* **110**, 5029-5036 (1999).
18. Wilson P. J., Bradley T. J., Tozer D. J. Hybrid Exchange-Correlation Functional Determined from Thermochemical Data and Ab Initio Potentials. *J. Chem. Phys.* **115**, 9233-9242 (2001).
19. Jensen F. Basis Set Convergence of Nuclear Magnetic Shielding Constants Calculated by Density Functional Methods. *J. Chem. Theory Comput.* **4**, 719-727 (2008).
20. Kussmann J., Ochsenfeld C. Preselective Screening for Linear-Scaling Exact Exchange-Gradient Calculations for Graphics Processing Units and General Strong-Scaling Massively Parallel Calculations. *J. Chem. Theory Comput.* **11**, 918-922 (2015).
21. Kussmann J., Ochsenfeld C. Pre-Selective Screening for Matrix Elements in Linear-Scaling Exact Exchange Calculations. *J. Chem. Phys.* **138**, 134114 (2013).
22. Gattuso G. et al. Amino Surface-Functionalized Tris(Calix[4]Arene) Dendrons with Rigid C3-Symmetric Propeller Cores. *Eur. J. Org. Chem.* **2011**, 5696-5703 (2011).
23. Gomes R., Bhaumik A. A New Triazine Functionalized Luminescent Covalent Organic Framework for Nitroaromatic Sensing and Co2 Storage. *RSC Adv.* **6**, 28047-28054 (2016).

24. Tanaka H., Shizu K., Nakanotani H., Adachi C. Twisted Intramolecular Charge Transfer State for Long-Wavelength Thermally Activated Delayed Fluorescence. *Chem. Mater.* **25**, 3766-3771 (2013).
25. Li S.-H., Huang H.-P., Yu S.-Y., Li X.-P. Design and Synthesis of Polypyrazolyl Compounds as a New Type of Versatile Building Blocks. *Chin. J. Chem.* **24**, 1225-1229 (2006).
26. Auras F. et al. Synchronized Offset Stacking: A Concept for Growing Large-Domain and Highly Crystalline 2d Covalent Organic Frameworks. *J. Am. Chem. Soc.* **138**, 16703-16710 (2016).
27. Bai L. et al. Nanoscale Covalent Organic Frameworks as Smart Carriers for Drug Delivery. *Chem. Commun.* **52**, 4128-4131 (2016).
28. Haase F. et al. Topochemical Conversion of an Imine- into a Thiazole-Linked Covalent Organic Framework Enabling Real Structure Analysis. *Nat. Commun.* **9**, 2600 (2018).
29. Haase F. et al. Tuning the Stacking Behaviour of a 2d Covalent Organic Framework through Non-Covalent Interactions. *Mater. Chem. Front.* **1**, 1354-1361 (2017).
30. Coelho A. A. Topasandtopas-Academic: An Optimization Program Integrating Computer Algebra and Crystallographic Objects Written in C++. *J. Appl. Crystallogr.* **51**, 210-218 (2018).
31. Egami T., Billinge S. J. L. *Underneath the Bragg Peaks: Structural Analysis of Complex Materials*, (Pergamon, Oxford, 2012).
32. Debye P. Zerstreuung Von Röntgenstrahlen. *Ann. Phys.* **351**, 809-823 (1915).
33. Lorch E. Neutron Diffraction by Germania, Silica and Radiation-Damaged Silica Glasses. *J. Phys. C* **2**, 229-237 (1969).
34. Soper A. K., Barney E. R. On the Use of Modification Functions When Fourier Transforming Total Scattering Data. *J. Appl. Crystallogr.* **45**, 1314-1317 (2012).
35. Spitler E. L. et al. A 2d Covalent Organic Framework with 4.7-Nm Pores and Insight into Its Interlayer Stacking. *J. Am. Chem. Soc.* **133**, 19416-19421 (2011).
36. Koo B. T., Dichtel W. R., Clancy P. A Classification Scheme for the Stacking of Two-Dimensional Boronate Ester-Linked Covalent Organic Frameworks. *J. Mater. Chem.* **22**, 17460-17469 (2012).

9.2 Supporting Information to Chapter 5 Post-Synthetic Transformation of Imine- into Nitrone-linked COFs for Water Harvesting

9.2.1 Methods and Equipment

General Methods: All reactions, unless otherwise noted, were performed with magnetic stirring under inert gas (N₂ or Ar) atmosphere using standard Schlenk techniques. Reaction temperatures were electronically monitored as external heating block temperatures. Unless otherwise noted, reagents were purchased from different commercial sources and used without further purification. Commercial *m*-CPBA was purified according to a procedure described below.

Infrared Spectroscopy: IR spectra were recorded on a Perkin Elmer UATR Two FT-IR spectrometer equipped with an attenuated total reflection (ATR) measuring unit. IR data are reported in wavenumbers (cm⁻¹) of normalized absorption. The IR bands are characterized as w (weak), m (medium), s (strong), or br (broad).

Gas Sorption Measurements: Sorption measurements for COFs were performed on a Quantachrome Instruments Autosorb iQ MP with Nitrogen at 77 K or CO₂ at designated temperature. The samples were degassed for 12 h at 120 °C under vacuum prior to the gas adsorption studies. Pore size distributions were determined from Nitrogen adsorption isotherms using the QSDFT cylindrical pores in carbon model for nitrogen at 77 K. For multipoint BET surface area calculations, pressure ranges were chosen with the help of the BET assistant in the ASiQwin software, which chooses BET tags in accordance with the ISO recommendations equal or below the maximum in grams per square meter.

Values of the adsorbed amount of CO₂ in V_{STP} [cm³g⁻¹] were converted to molar amount adsorbed per gram of material [mmol¹g⁻¹] = V_{STP}/22.414. Heats of adsorption at zero coverage (θ) were estimated from CO₂ adsorption isotherms measured at 273 K, 288 K and 298 K using Henry's law (Eq. 1). The low pressure region ($0 < p < 50$ Torr) of the isotherms was fitted linearly to derive the Henry coefficient (k_H) normalized to a proportionality factor (α) from the slope ($=k_H\alpha^{-1}$) of the fit, according to Eq. 2. The normalized Henry coefficients at respective temperatures (T) were then plotted semi logarithmically vs. T⁻¹. Heats of adsorption (ΔQ_{ST}) were then calculated from the slope of the linear fits (Eq. 3).

$$\theta = \alpha V_{STP} = \frac{k_H p}{1+k_H p} \approx k_H p \text{ (for small pressures)} \quad (1)$$

$$V_{STP} \approx \frac{k_H}{\alpha} p \quad (2)$$

$$\ln\left(\frac{k_H}{\alpha}\right) = -\frac{\Delta Q_{ST}}{R} \cdot \frac{1}{T} - \ln(\alpha) \quad (3)$$

Vapor Sorption Measurements: Vapor sorption experiments were performed on a Quantachrome Instruments Autosorb iQ MP with water at different temperatures. The samples were degassed for 12 h at 120 °C under vacuum prior adsorption studies. Values of the adsorbed amount V_{STP} [cm³g⁻¹] were converted to gravimetric amount adsorbed per gram of material [g¹g⁻¹] = $V_{STP}/22414*18.015$.

X-Ray Powder Diffraction (XRPD): X-ray powder diffraction experiments were performed on a Stoe Stadi P diffractometer (Co-/Cu-K α_1 , Ge(111)) in Debye-Scherrer geometry. The samples were measured in sealed glass capillaries (OD = 0.7 mm) and spun for improved particle statistics.

Rietveld refinements: Rietveld refinements were performed using TOPAS v6. The background was corrected with Chebychev polynomials (Order 5). Simple axial and zero-error corrections were used together with additional corrections for Lorentzian crystallite size and/or strain broadening.

Supercritical CO₂ Activation: Activation of the methanol-soaked COF samples with supercritical CO₂ was performed on a Leica EM CPD300 critical point dryer.

Thermogravimetric Analysis: Thermogravimetric analysis (TGA) was performed on a NETZSCH STA 449 F3 Jupiter. Measurements were carried out with 3-6 mg of sample in an Al₂O₃ crucible under Ar flow (60 mL/min) a temperature range between 30 and 800 °C and a heating rate of 5 K/min. Deviating buoyancy effects between the reference crucible and the sample-loaded crucible were compensated by a correction of y-offsets. Baseline correction was achieved by subtracting reference measurements with an empty crucible.

Quantum-Chemical Calculations: Atom positions and lattices of all periodic structures were optimized on RI-PBE-D3/def2-TZVP^[1-4] level of theory using an acceleration scheme based on the resolution of the identity (RI) technique and the continuous fast multipole method (CFMM)^[5-7] implemented^[8, 9] in Turbomole version V7.3.^[10]

The CFMM uses multipole moments of maximum order 20, together with a well-separateness value of 3 and a basis function extent threshold of 10⁹ a.u. Grid 7 was used for the numerical integration of the exchange-correlation term. The norm of the gradient was converged to 10⁻⁴ a.u. and the total energy to 10⁻⁸ Hartree within the structure optimization using the gamma point approximation.

Structures for all investigated molecular compounds were optimized on PBE0-D3/def2-TZVP^[2, 3, 11, 12] level of theory. Subsequent frequency calculations were performed on the same level of theory to ensure all minima to be true minima on the potential energy hypersurface.

NMR chemical shifts were obtained on B97-2/pcS-2^[13, 14] level of theory using the FermiONs++ program package.^[13, 15, 16]

Purification of Commercial *m*CPBA: *meta*-Chloroperbenzoic acid (*m*CPBA) was obtained from *Merck KGaA, Darmstadt*. Commercial grade *m*CPBA contains water and impurities of benzoic acid, which were removed following a previously reported procedure.^[17] *m*CPBA (25 g) was dissolved in Et₂O (200 mL) and washed with an aqueous buffer solution (pH 7, 3 x 100 mL). The organic phase was dried (MgSO₄). The solvent was removed under reduced pressure to afford pure *m*CPBA as white crystals. To avoid decomposition, the purified material was stored at -30°C under inert atmosphere in the dark.

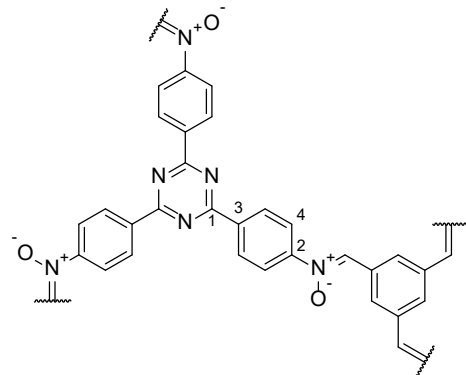
9.2.2 Synthetic Procedures

9.2.2.1 COF Synthesis

Synthesis of PI-3-COF: PI-3-COF was synthesized according to a previously described procedure.^[18] To a mixture of benzene-1,3,5-tricarbaldehyde (21.4 mg, 0.13 mmol, 1.0 equiv.) and 4,4',4''-(1,3,5-triazine-2,4,6-triyl)trianiline (46.8 mg, 0.13 mmol, 1.0 equiv.) in mesitylene (2.7 mL) and 1,4-dioxane (1.3 mL), aqueous 6 M AcOH (0.5 mL) was added. The suspension was heated at 120°C for 72 h. The precipitate was collected via suction filtration, washed with DMF (20 mL), THF (20 mL) and DCM (20 mL) and extracted with MeOH in a Soxhlet extractor for 12 h. Activation with supercritical CO₂ afforded PI-3-COF (55.0 mg, 90%) as a yellow solid.

Synthesis of rPI-3-COF: rPI-3-COF was synthesized according to a previously described procedure.^[18] To a suspension of PI-3-COF (30.0 mg) in mesitylene (2 mL) and 1,4-dioxane (1 mL), formic acid (97%, 53.0 µL) was added. The suspension was heated at 120°C for 48 h. The precipitate was collected via suction filtration and extracted with MeOH in a Soxhlet extractor for 12 h. Activation with supercritical CO₂ afforded rPI-3-COF (28.0 mg, 92%) as a yellow solid.

Synthesis of NO-PI-3-COF:



(a) from rPI-3-COF: To a cooled suspension of rPI-3-COF (10.4 mg, 22.2 μ mol, 1.0 equiv.) in DCM (1.0 mL), a solution of mCPBA (21.1 mg, 134 μ mol, 6.0 equiv.) in DCM (3.0 mL) was added at 0°C. The reaction mixture was stirred for 24 h at room temperature. The solid was filtered and washed with acetone and methanol (3 x 10 mL each). Soxhlet extraction with methanol, supercritical drying (CO_2) and drying under high vacuum afforded NO-PI-3-COF (8.40 mg, 75%) as a yellow-orange solid.

(b) from PI-3-COF: To a cooled suspension of PI-3-COF (30.0 mg, 64.9 μ mol, 1.0 equiv.) in DCM (4.0 mL), a solution of mCPBA (33.9 mg, 195 μ mol, 3.0 equiv.) in DCM (2.0 mL) was added dropwise at 0°C. The reaction mixture was stirred for 18 h, during which the mixture was allowed to warm to room temperature. The crude product was filtered and washed with acetone (3 x 10 mL) and methanol (3 x 10 mL). Soxhlet extraction with methanol for 24 h, supercritical drying with CO_2 and drying under high vacuum afforded NO-PI-3-COF (27.1 mg, 82%) as a yellow-orange powder. Notably, drying of the material in a desiccator (CaCl_2) allowed to obtain NO-PI-3-COF with higher porosity (Figure S 9.2-30).

^1H ssNMR (MAS, 400 MHz): $\delta = 7.7$ (C-4, C-Ar) ppm.

^{13}C ssNMR (CP-MAS, 101 MHz): $\delta = 169.2$ (C-1), 149.7 (C-2), 136.3 (C-3), 129.5 (C-Ar), 121.2 (C-Ar), 117.3 (C-4) ppm.

^{15}N ssNMR (CP-MAS, 61 MHz): $\delta = -106.3$ (N-2), -129.5 (N-1) ppm.

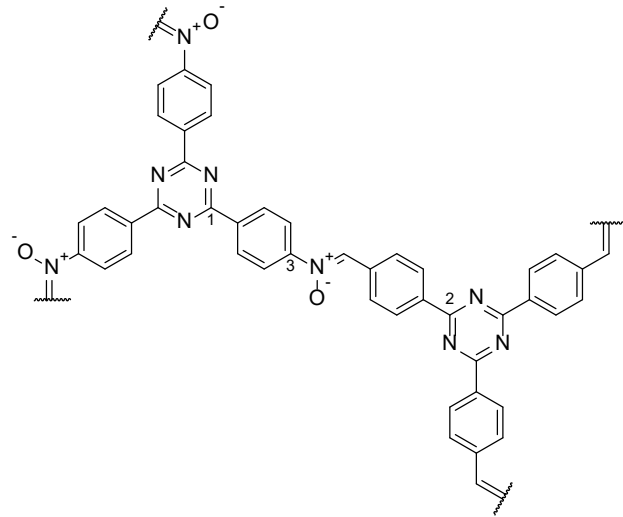
FT-IR (ATR): $\nu = 1596$ (w), 1514 (s), 1413 (w), 1367 (m), 1180 (w), 1145 (w), 1013 (w), 867 (w), 812 (m), 676 (w), 524 (w) cm^{-1} .

Synthesis of TTI-COF: TTI-COF was synthesized according to a previously described procedure.^[18] A mixture of 4,4',4''-(1,3,5-triazine-2,4,6-triyl)tribenzaldehyde (25.0 mg, 63.5 μ mol, 1.0 equiv.) and 4,4',4''-(1,3,5-triazine-2,4,6-triyl)trianiline (22.5 mg, 63.5 μ mol, 1.0 equiv.) in mesitylene/1,4-dioxane 1:1 (5 mL) and aqueous 6 M AcOH (0.13 mL) was heated at 120°C for 72 h. The precipitate was collected via suction filtration, washed with DMF (20 mL), THF (20 mL) and DCM (20 mL) and extracted with MeOH in a Soxhlet

extractor for 12 h. Activation with supercritical CO_2 afforded TTI-COF (26.4 mg, 60%) as a yellow solid.

Synthesis of rTTI-COF: rTTI-COF was synthesized according to a previously described procedure.^[18] To a suspension of TTI-COF (100.0 mg) in mesitylene (6 mL) and 1,4-dioxane (6 mL), formic acid (97%, 64.9 μL) was added. The suspension was heated at 120°C for 48 h. The precipitate was collected via suction filtration and extracted with MeOH in a Soxhlet extractor for 12 h. Activation with supercritical CO_2 afforded rTTI-COF (97.0 mg, 96%) as a yellow solid.

Synthesis of NO-TTI-COF:



To a cooled suspension of rTTI-COF (30.0 mg, 42.9 μmol , 1.0 equiv.) in acetone (3.0 mL), a solution of mCPBA (45.6 mg, 0.26 mmol, 6.0 equiv.) in acetone (2.0 mL) was added dropwise at 0°C. The reaction mixture was stirred for 24 h, during which the mixture was allowed to warm to room temperature. The crude product was filtered and washed with acetone (3 x 10 mL) and methanol (3 x 10 mL). Soxhlet extraction with methanol for 24 h and supercritical drying with CO_2 afforded NO-TTI-COF (23.0 mg, 72%) as a yellow-orange powder.

^1H ssNMR (MAS, 400 MHz): $\delta = 7.2$ (C-Ar) ppm.

^{13}C ssNMR (CP-MAS, 101 MHz): $\delta = 168.9$ (C-1, C-2), 149.6 (C-3), 136.4 (C-Ar), 128.0 (C-Ar), 119.5 (C-Ar) ppm.

^{15}N ssNMR (CP-MAS, 61 MHz): $\delta = -95.4$ (N-3), -128.0 (N-1, N-2) ppm.

FT-IR (ATR): $\nu = 1596$ (w), 1580 (w), 1511 (s), 1364 (m), 1315 (w), 1244 (w), 1179 (w), 1015 (w), 868 (w), 812 (m), 523 (w) cm^{-1} .

9.2.3 FT-IR Spectra

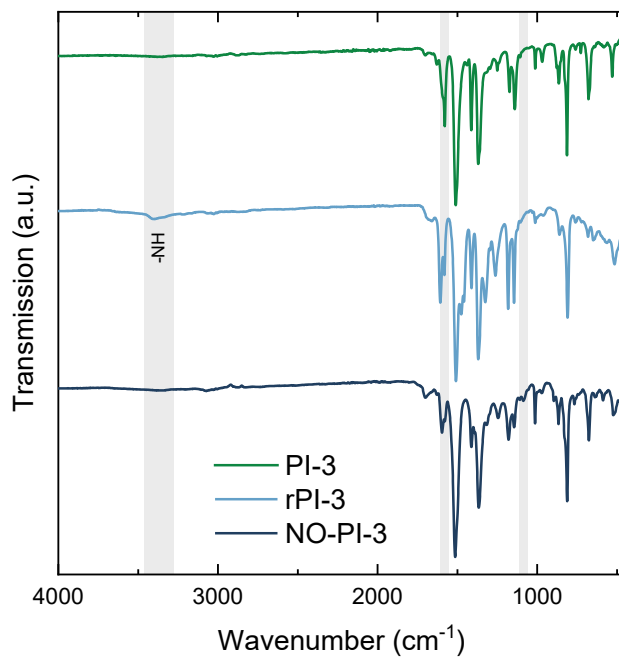


Figure S 9.2-1: FT-IR spectra comparison of NO-PI-3-COF and its parent amine-linked (rPI-3) and imine-linked (PI-3) covalent organic frameworks. Secondary amine vibrations present in rPI-3-COF vanish upon oxidation to nitrone-linkages in NO-PI3-COF. Further but less prominent changes in the finger print region (gray) differentiate NO-PI-3-COF from PI-3-COF.

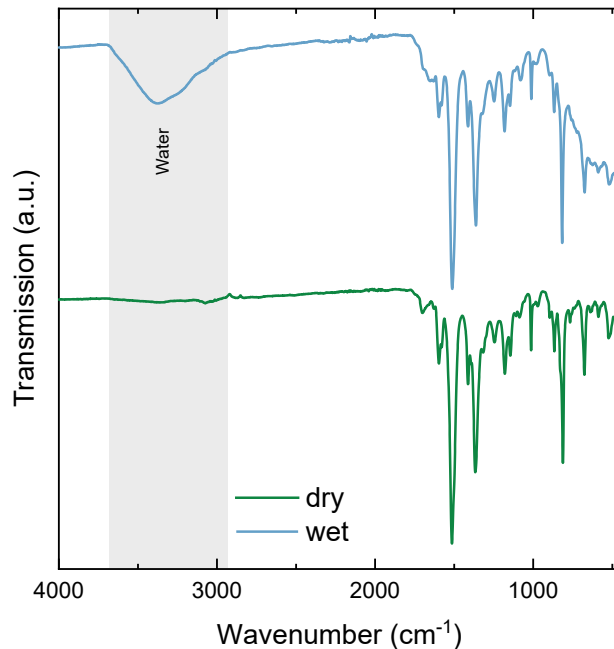


Figure S 9.2-2: FT-IR spectra comparison of NO-PI-3-COF after exposing it to air (wet) and after drying under high vacuum (dry). The broad and intense vibration centered at ~3400 cm⁻¹ suggests that the framework adsorbs water vapor from the atmosphere.

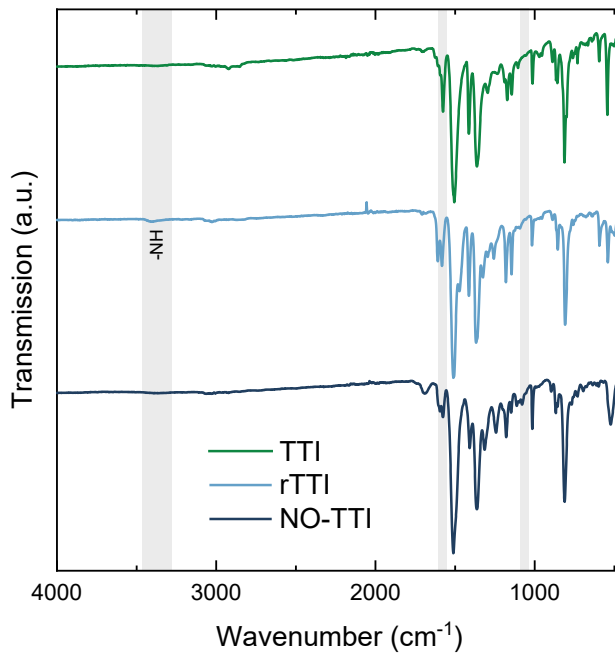


Figure S 9.2-3: FT-IR spectra comparison of NO-TTI-COF and its parent amine-linked (rTTI) and imine-linked (TTI) covalent organic frameworks. Secondary amine vibrations present in rTTI-COF vanish upon oxidation to nitroso-linkages in NO-TTI-COF. Further, but less prominent changes in the fingerprint region (gray) differentiate NO-TTI-COF from TTI-COF.

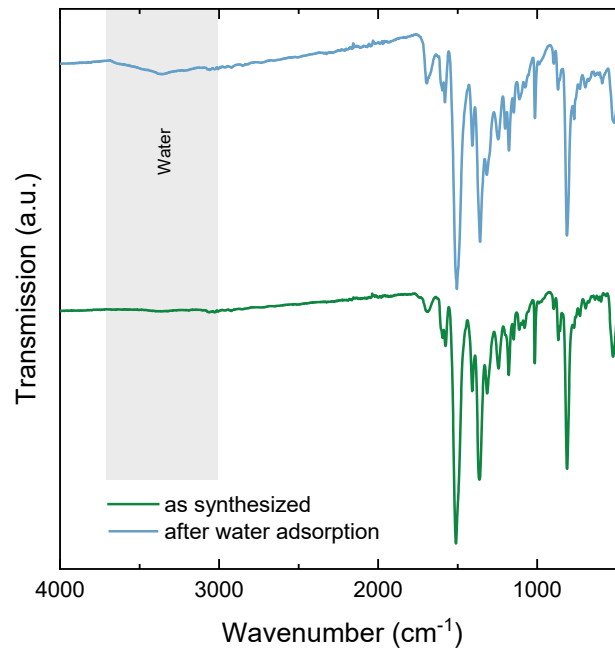


Figure S 9.2-4: FT-IR spectra comparison of NO-TTI-COF as-synthesized and after water vapor adsorption experiments. Despite the vibrations related to adsorbed water, especially the fingerprint region of the spectrum remained largely unchanged, suggesting that changes in the properties are rather related to structural changes in the material, instead of changes in the chemical connectivity.

9.2.4 XRPD Data and Structure Refinement

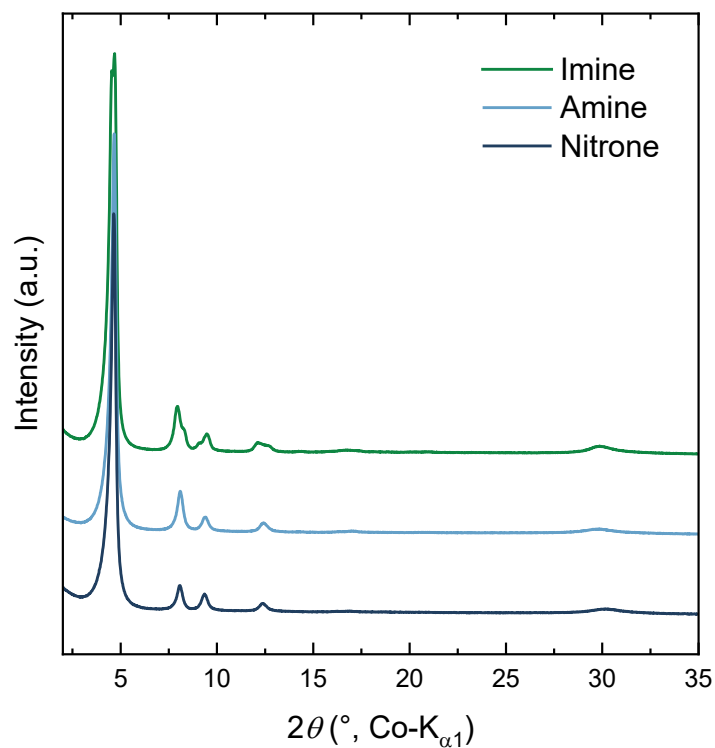


Figure S 9.2-5: XRPD comparison of TTI, rTTI and NO-TTI-COF. Peak splitting in TTI-COF occurs due to antiparallel slip-stacking of the layers. After reduction and oxidation more eclipsed-like stacking occurs, due to a randomization of stacking offset.^[18]

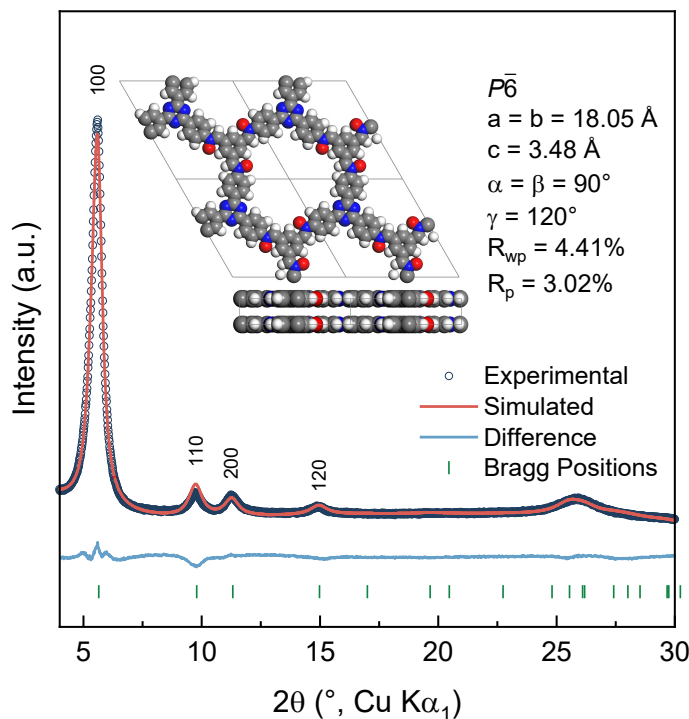


Figure S 9.2-6: Experimental XRPD pattern and Rietveld refinement for NO-PI-3-COF.

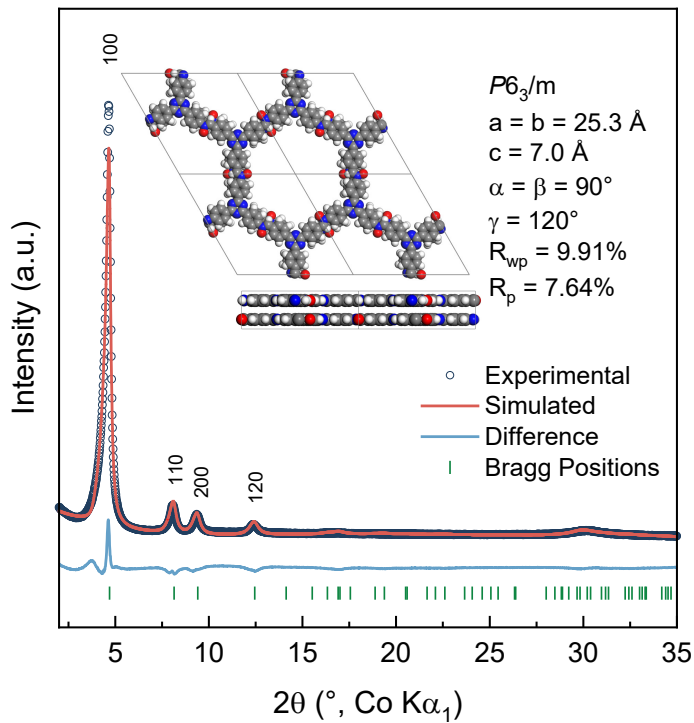


Figure S 9.2-7: Experimental XRPD pattern and Rietveld refinement for NO-TTI-COF.

Table S 9.2-1: Cell parameters of Rietveld refined nitrone-linked COFs.

Fitted Pattern	NO-PI-3-COF	NO-TTI-COF
Space group	$P\bar{6}$	$P6_3/m$
R_{wp} (%)	4.41	9.91
R_p (%)	3.02	7.64
a (Å)	18.049(14)	25.209(4)
b (Å)	18.049(14)	25.209(4)
c (Å)	3.484(2)	6.956(5)
α (°)	90	90
β (°)	90	90
γ (°)	120	120

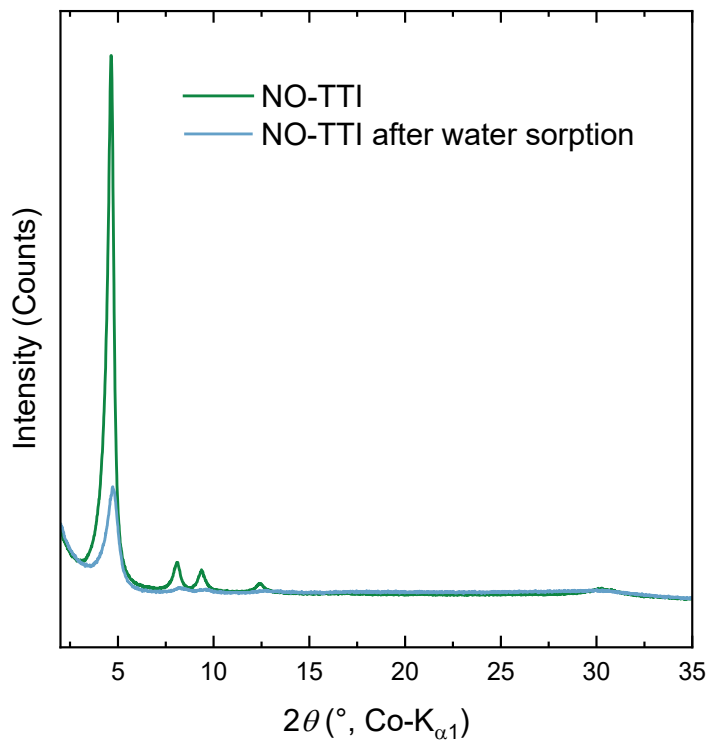


Figure S 9.2-8: XRPD patterns of NO-TTI before and after water vapor adsorption experiments (same sample). The observed decrease in uptake capacity (Figure S 9.2-35) is related to a decrease in structural definition of the sample, due to pore collapse.

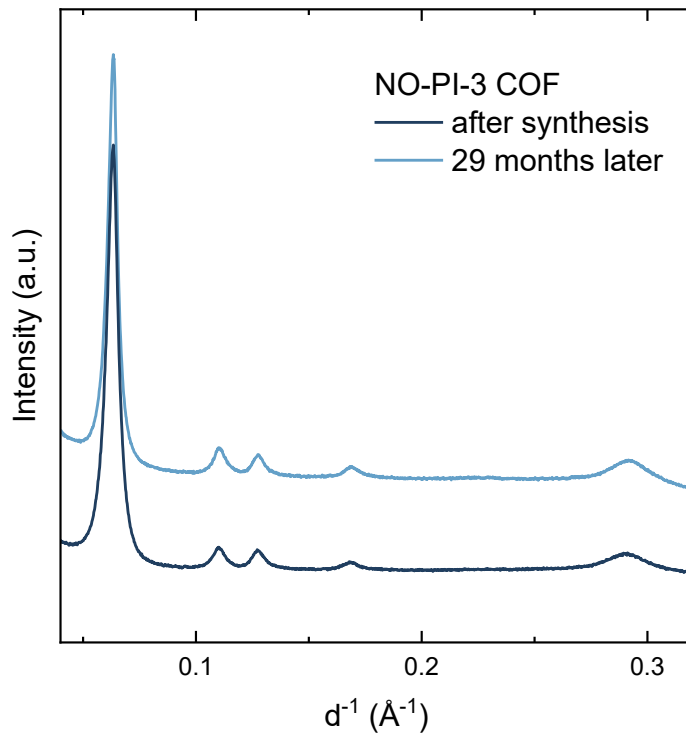


Figure S 9.2-9: XRPD patterns of NO-PI-3 COF before and after storing the sample in hydrated state under ambient conditions for 29 months.

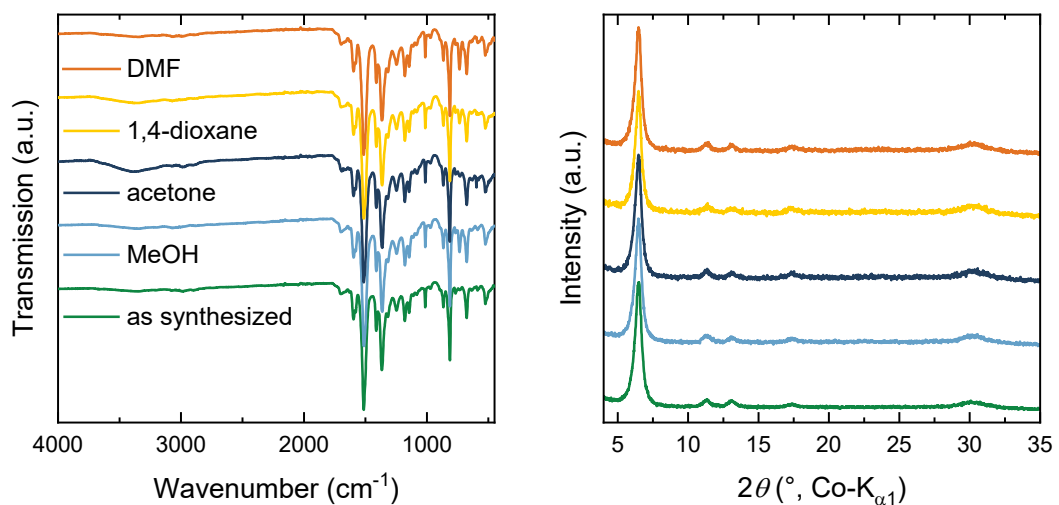


Figure S 9.2-10: FT-IR spectra (left) and XRPD patterns of NO-PI-3-COF treated with common organic solvents for 24h. The samples were subsequently extracted with DCM and dried under slowly reduced pressure. After this treatment, the samples do not show any signs of decomposition. The broad vibration at $\sim 3400 \text{ cm}^{-1}$ refers to adsorbed water from the atmosphere during the FT-IR experiment.

9.2.5 ssNMR Spectra

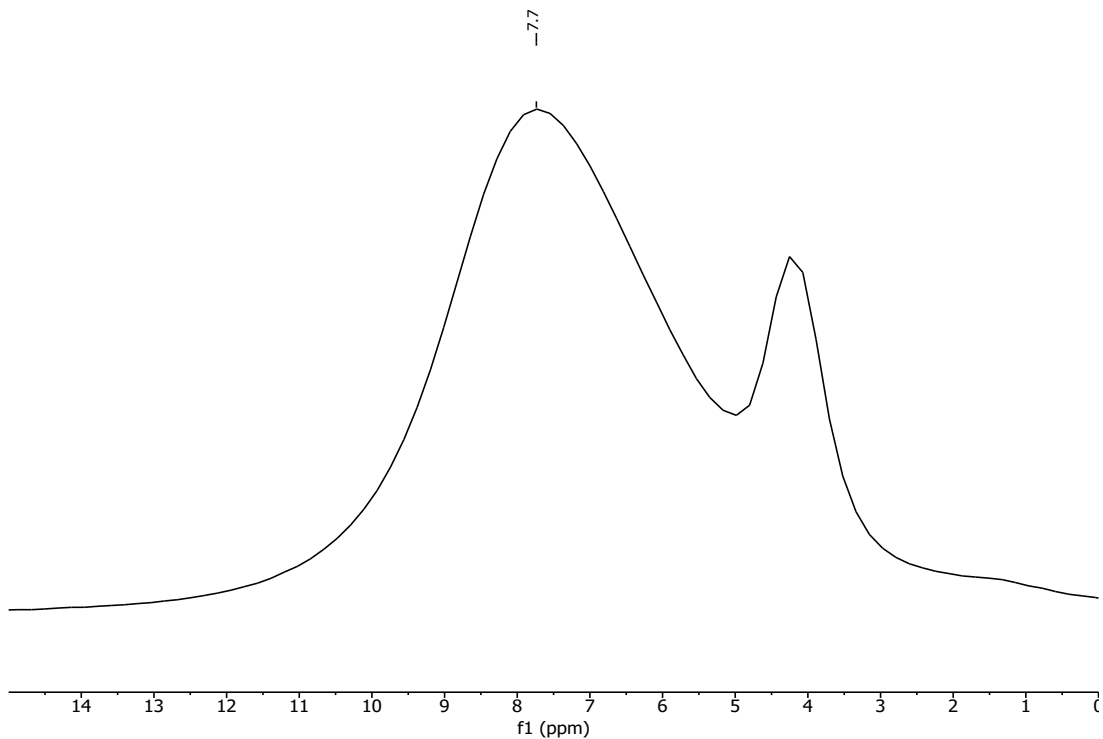


Figure S 9.2-11: ^1H -ssNMR spectrum of NO-PI-3-COF. Signal centered at $\delta \approx 4 \text{ ppm}$ is caused by residual adsorbed water.

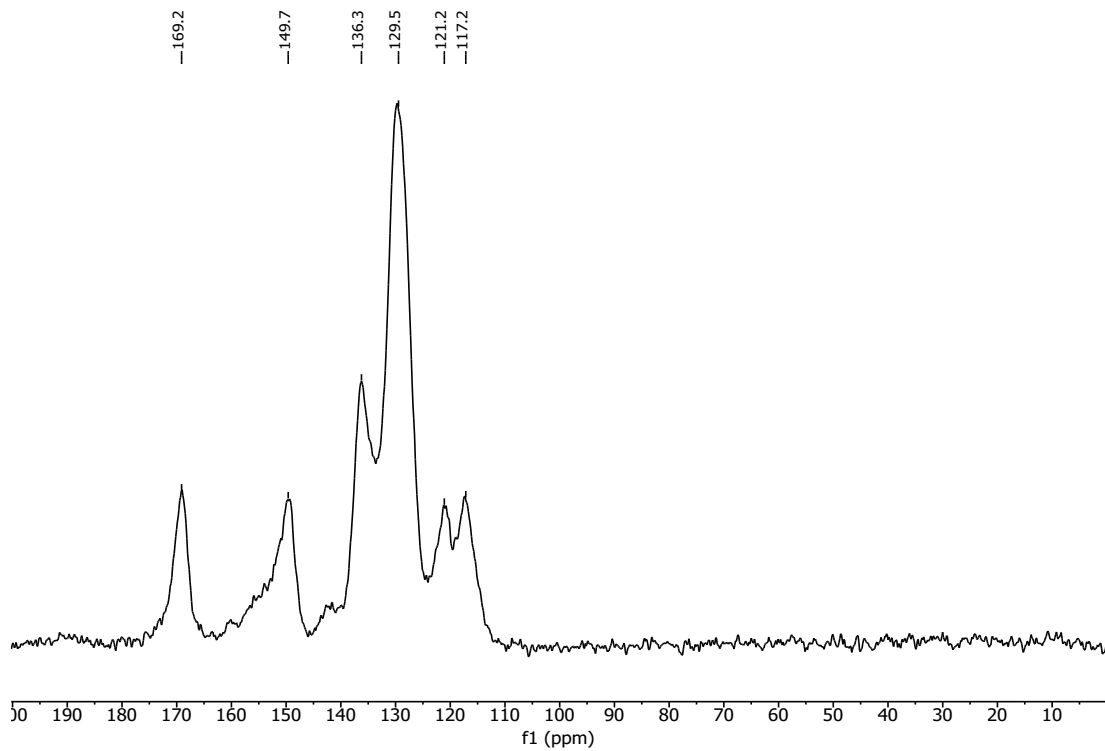


Figure S 9.2-12: ¹³C-ssNMR spectrum of NO-PI-3-COF.

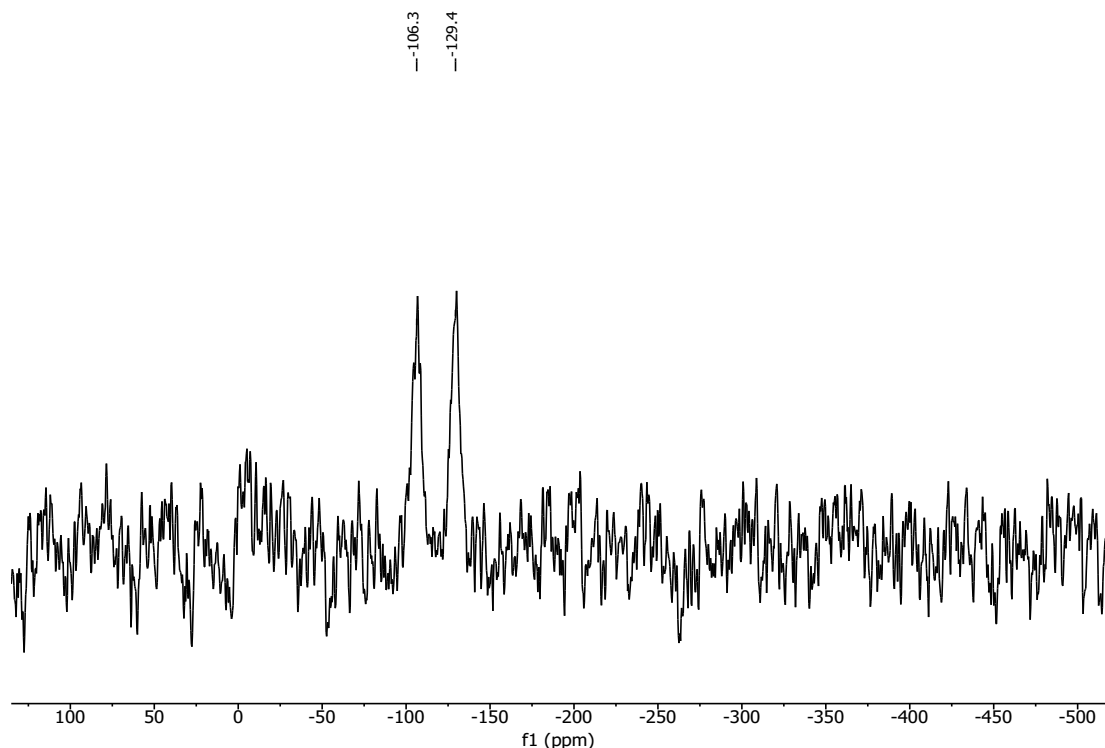


Figure S 9.2-13: ¹⁵N-ssNMR spectrum of NO-PI-3-COF. The signals at $\delta = -129.4$ ppm is assigned to the triazine-, and -106.3 ppm to the nitrone-nitrogen atoms.

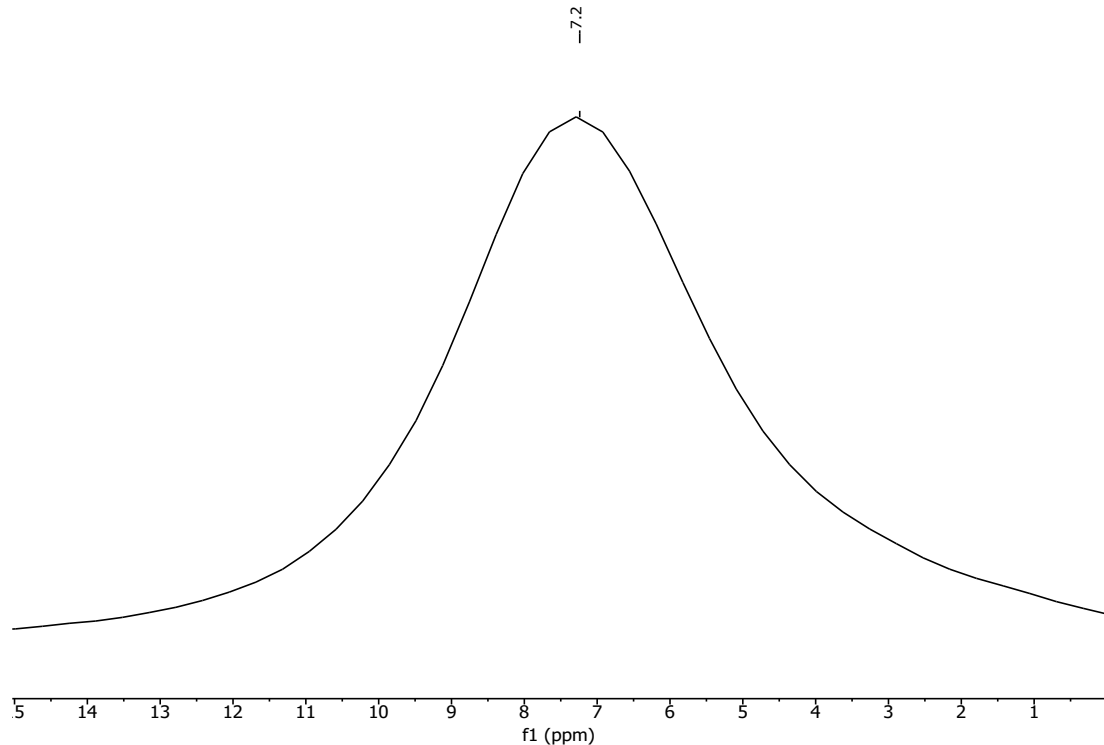


Figure S 9.2-14: ¹H-ssNMR spectrum of NO-TTI-COF.

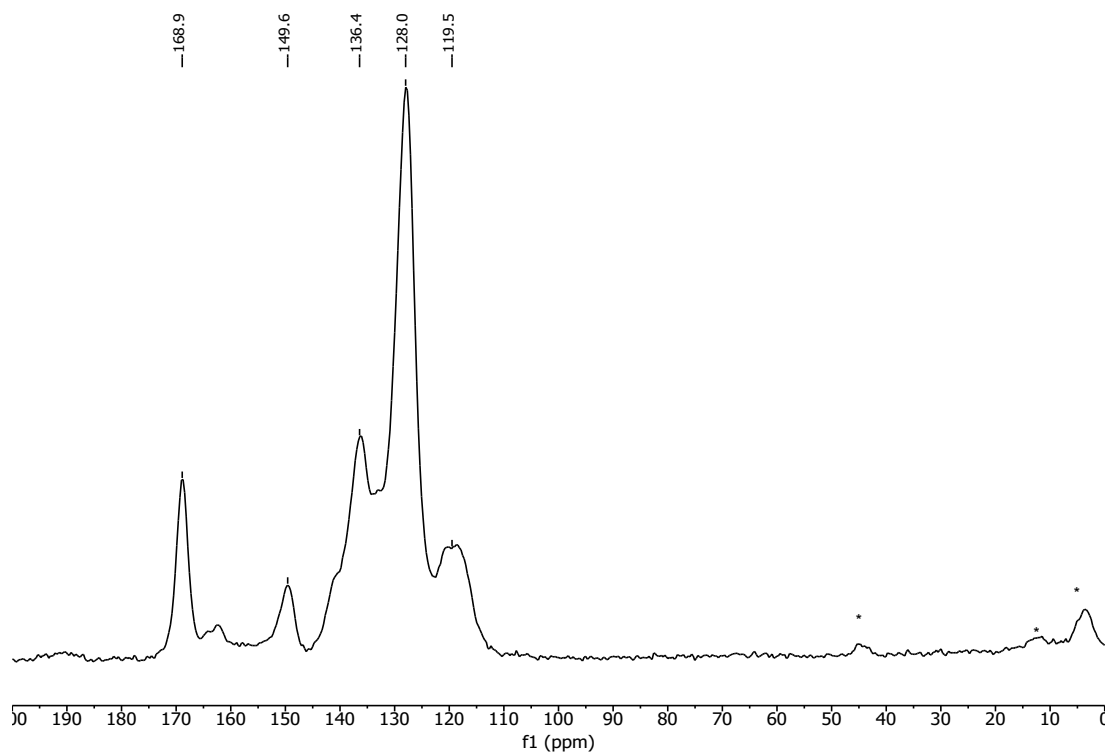


Figure S 9.2-15: ¹³C-CP-ssNMR spectrum of NO-TTI-COF. Asterisks denote spinning sidebands.

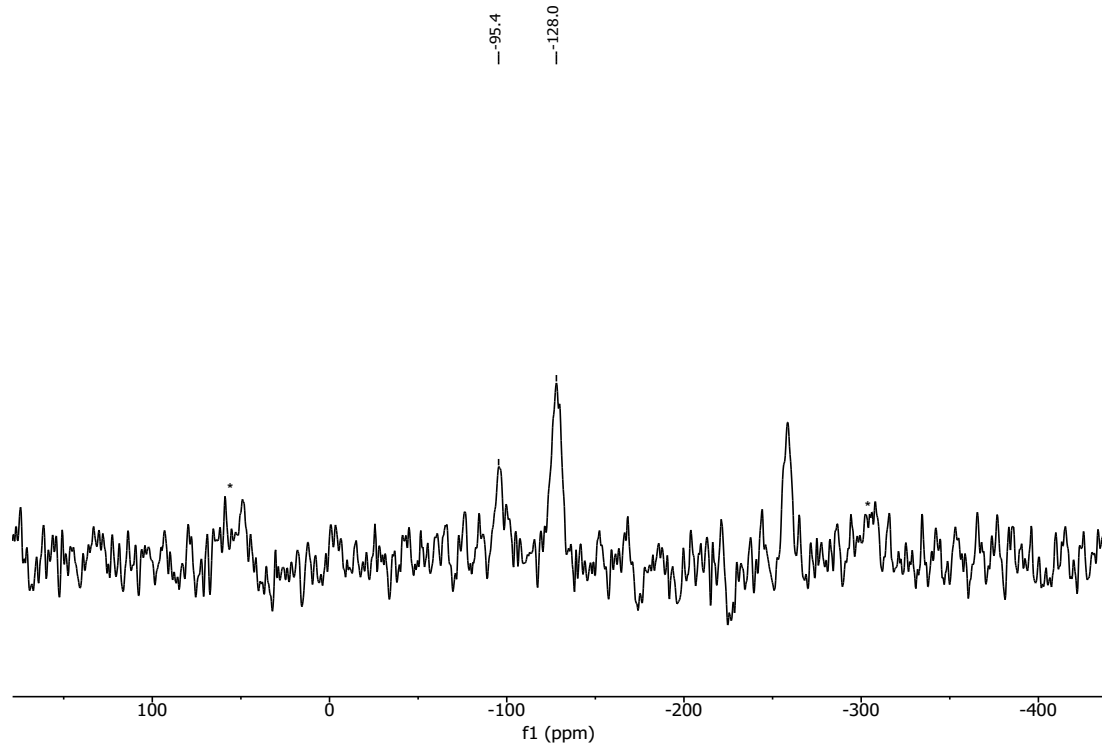


Figure S 9.2-16: ¹⁵N-CP-ssNMR spectrum of NO-TTI-COF. The signal at $\delta \approx -260$ ppm refers to traces of amide groups in the material, occurring as an impurity after oxidation. Note that their intensity is (over)amplified compared to nitrogen atoms without proton substitution, due to the N-H cross-polarization experiment. Asterisks denote spinning sidebands.

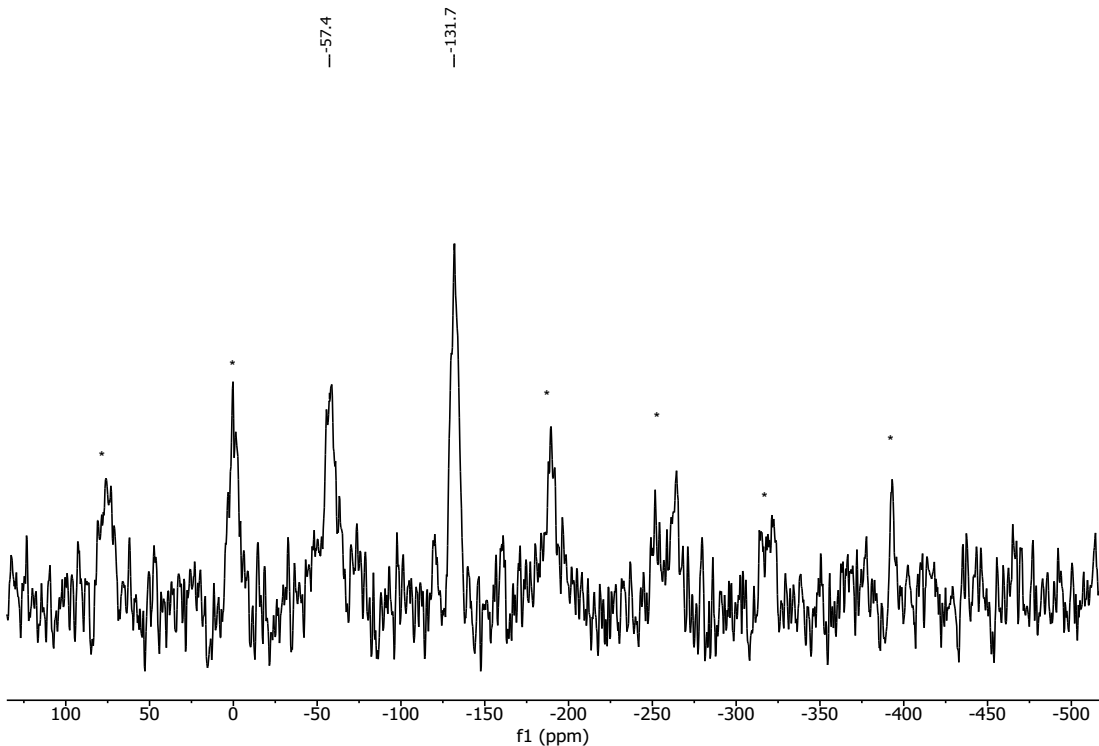


Figure S 9.2-17: ¹⁵N-ssNMR spectrum of PI-3-COF. The signals at $\delta = -131.7$ ppm are assigned to the triazine-, and -57.4 ppm to the imine-nitrogen atoms. Asterisks denote spinning sidebands.

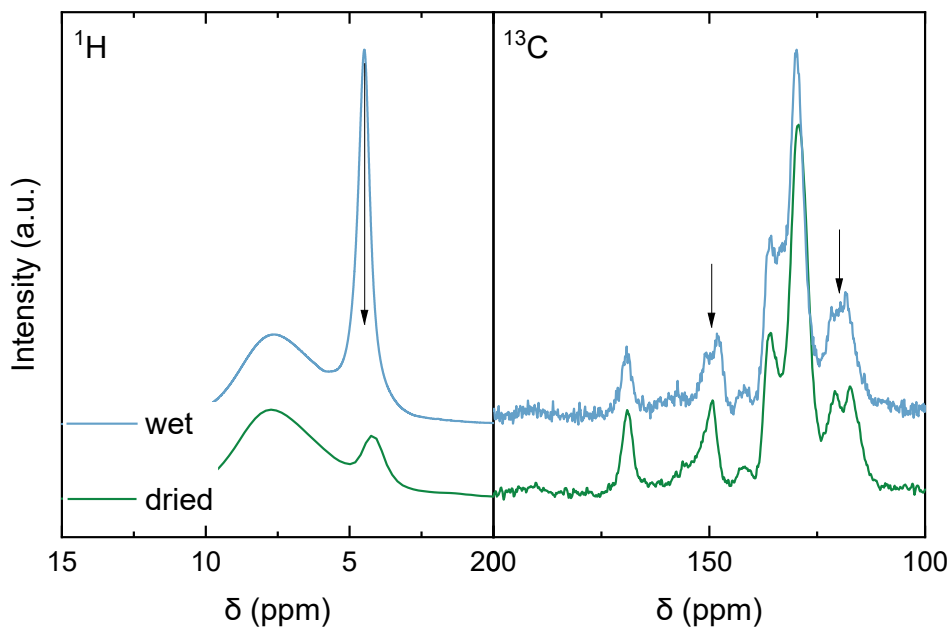


Figure S 9.2-18: ^1H and ^{13}C -ssNMR comparison of wet, and dried NO-PI-3-COF with only minor residual water adsorbed. Both spectra were recorded on the same sample before and after drying under high vacuum. Arrows serve as a guide to the eye and indicate regions with differences between both spectra.

9.2.6 Nitrogen Gas Sorption Experiments

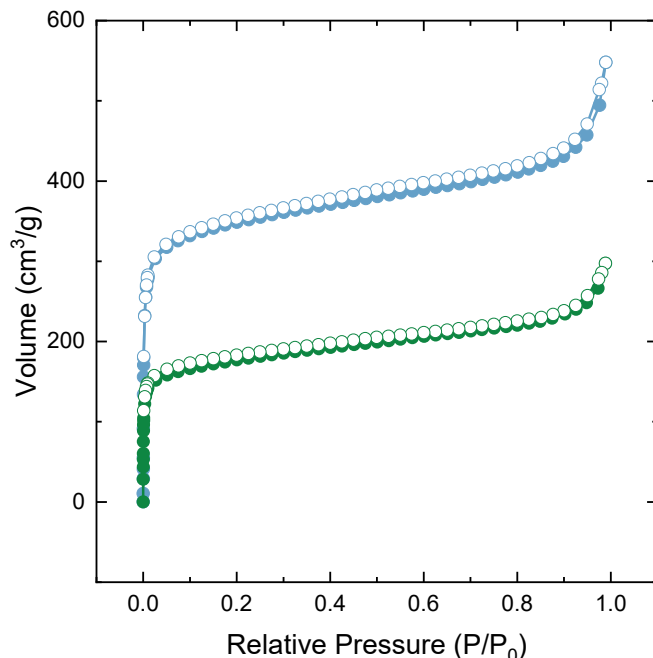


Figure S 9.2-19: N_2 sorption isotherms of PI-3-COF (blue) and NO-PI-3-COF (green), synthesized by direct oxidation of PI-3-COF. Filled dots represent data points of the adsorption branch, hollow dots those of the desorption branch, respectively.

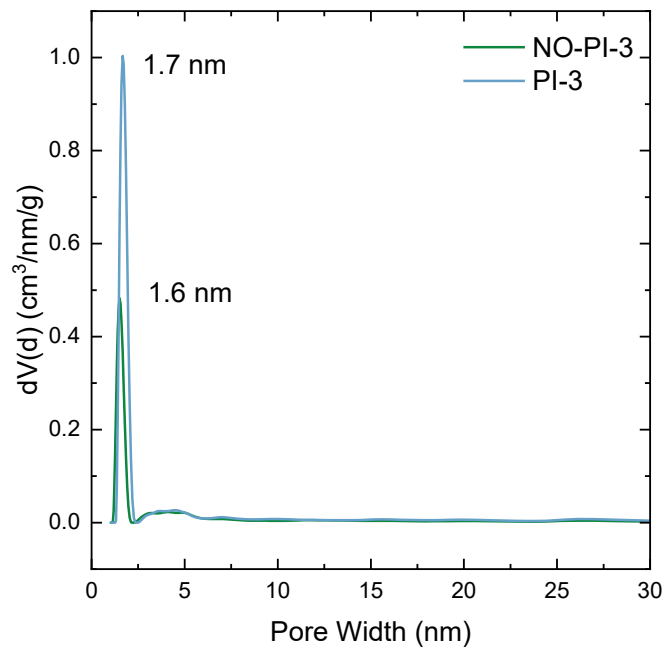


Figure S 9.2-20: Pore-size distribution of PI-3-COF and NO-PI-3-COF.

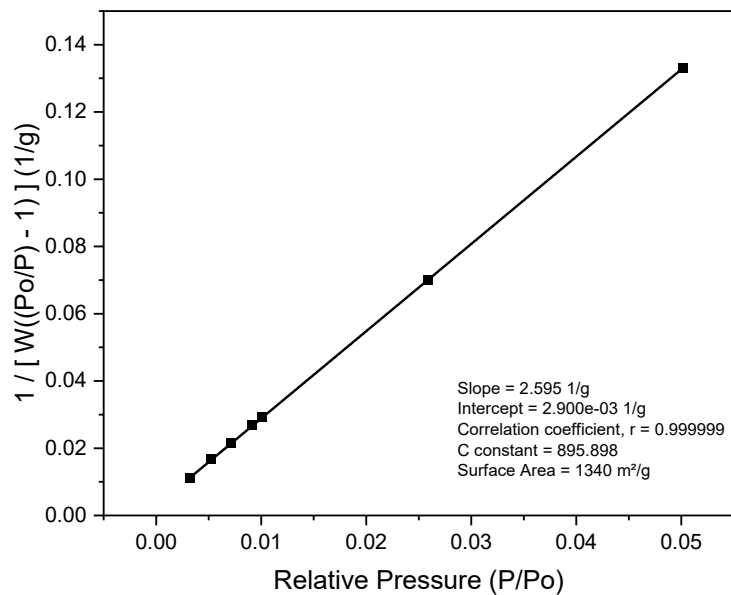


Figure S 9.2-21: BET plot for PI-3-COF.

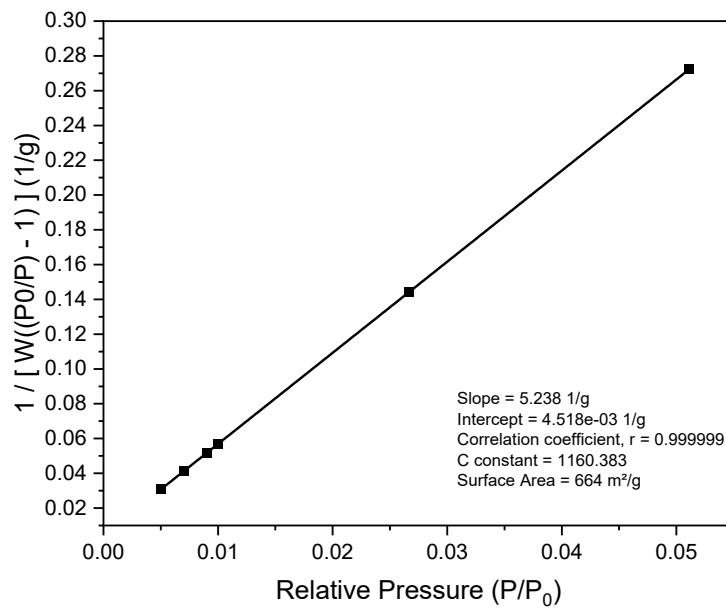
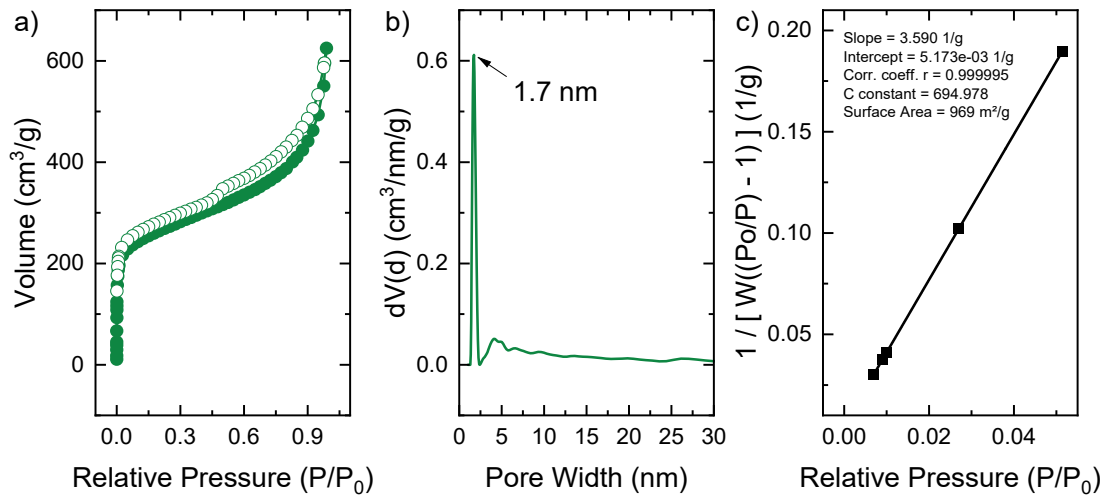


Figure S 9.2-22: BET plot for NO-PI-3-COF.

Figure S 9.2-23: N₂ sorption isotherm (a), pore-size distribution (b), and BET plot (c) for rPI-3-COF.

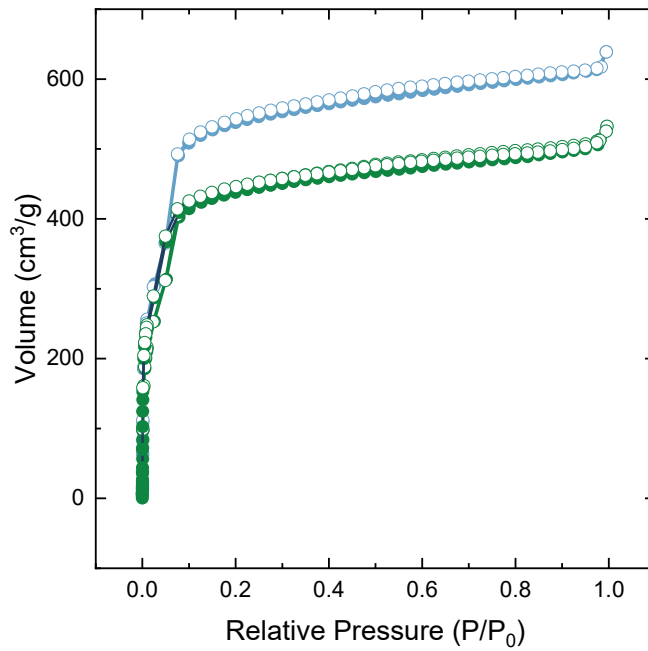


Figure S 9.2-24: N_2 sorption isotherms of TTI-COF (blue), rTTI-COF (green), and NO-TTI-COF (dark blue) are overlaid. Filled dots represent data points of the adsorption branch, hollow dots those of the desorption branch, respectively.

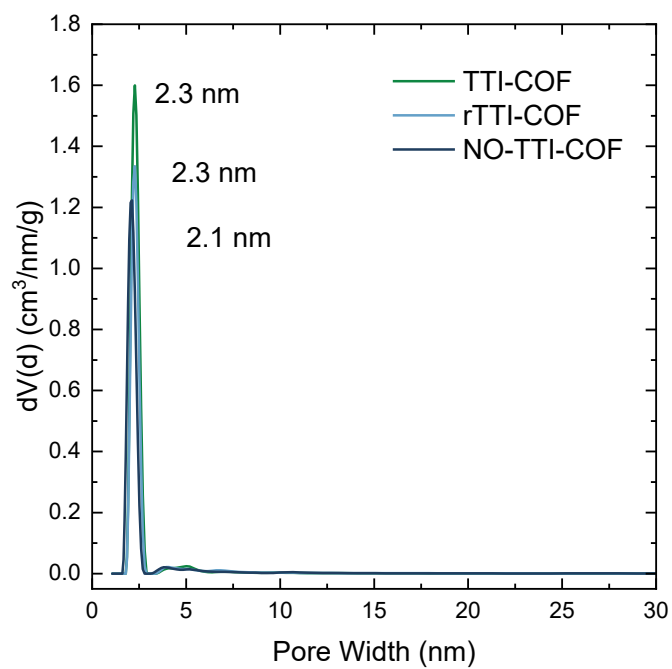


Figure S 9.2-25: Pore-size distribution of TTI-COF, rTTI-COF and NO-TTI-COF.

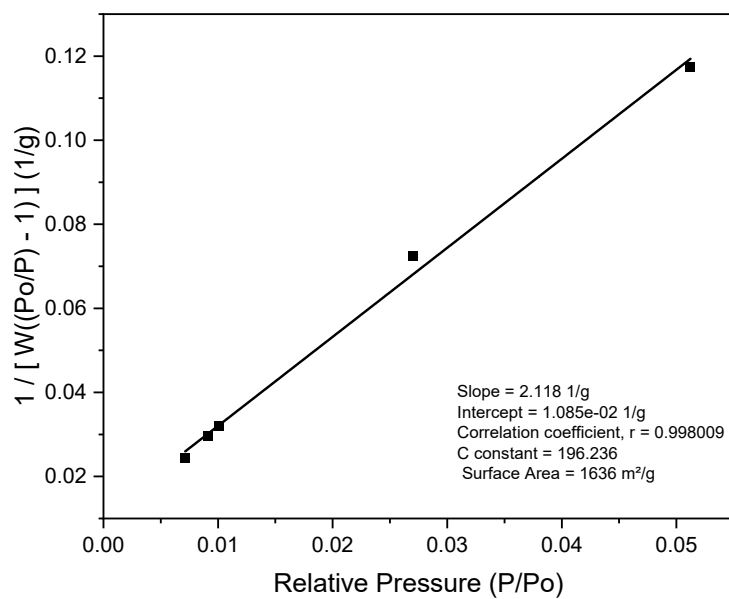


Figure S 9.2-26: BET plot for TTI-COF.

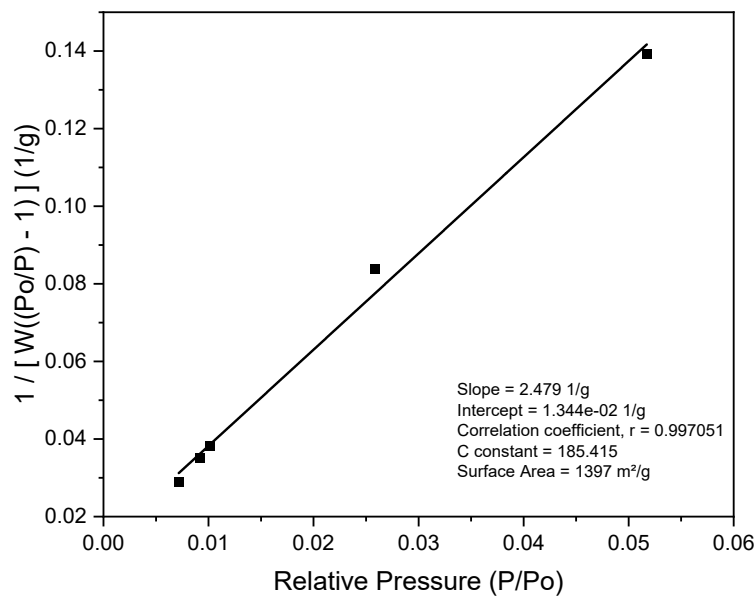


Figure S 9.2-27: BET plot for rTTI-COF.

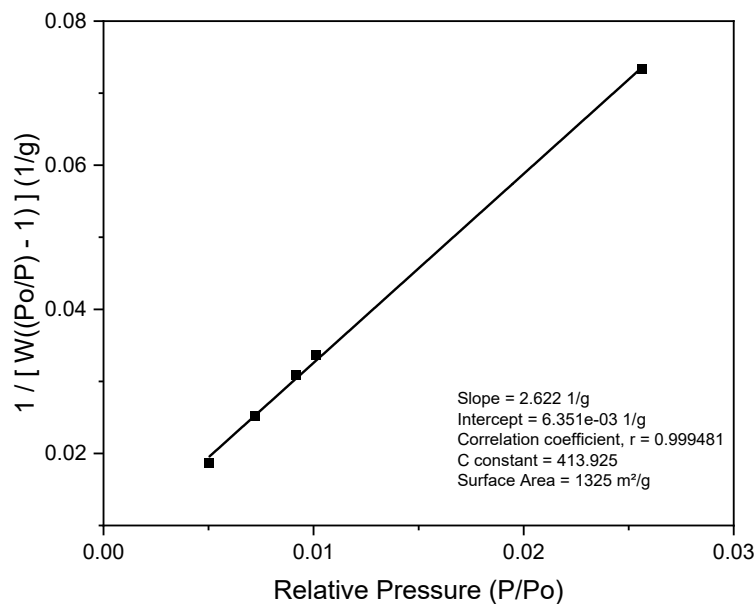


Figure S 9.2-28: BET plot for NO-TTI-COF.

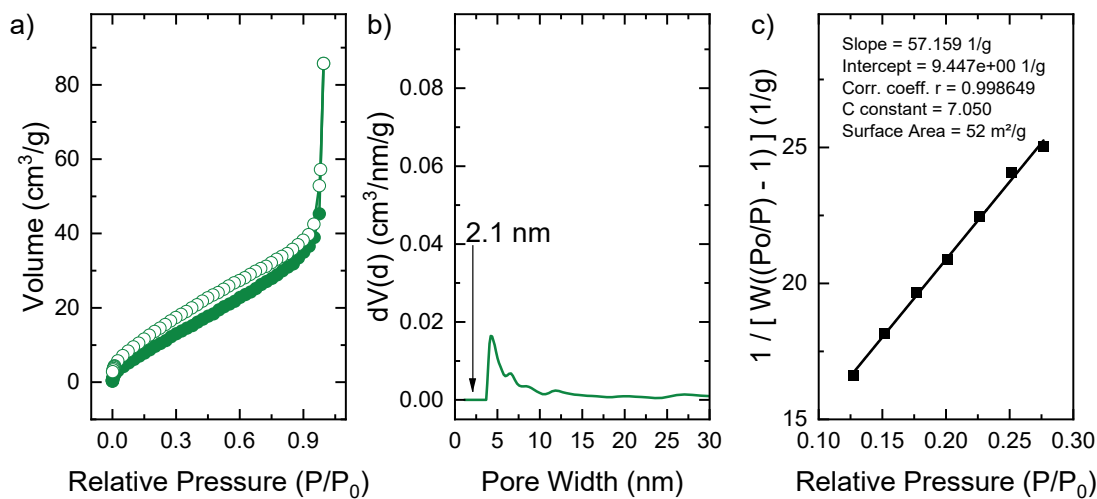


Figure S 9.2-29: N₂ sorption isotherm (a), pore-size distribution (b), and BET plot (c) for NO-TTI-COF after water adsorption. The data shows that the initial porosity of the material is lost due to drying-induced collapse of the 2.1 nm pore channels. Only a small fraction of textural porosity remains, which is responsible for a comparably small residual surface area.

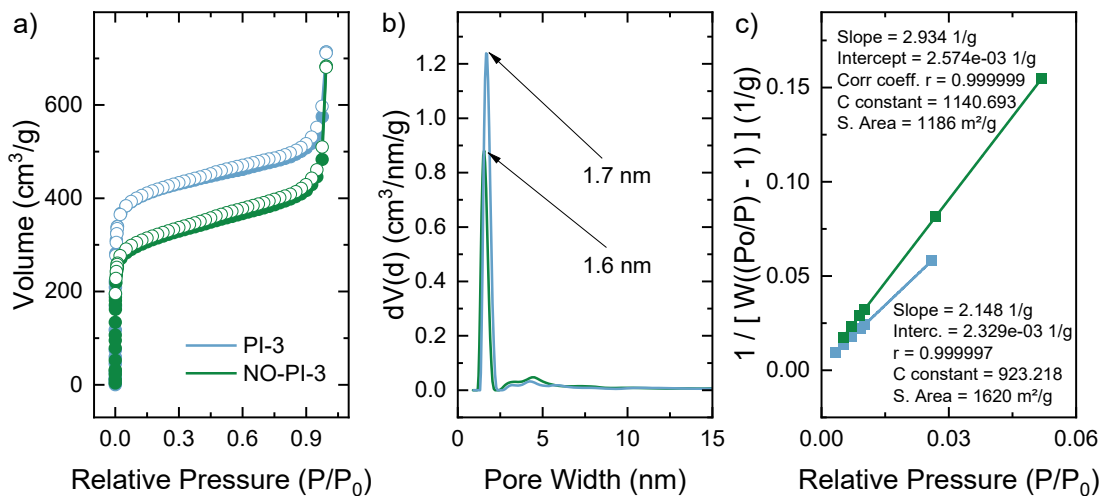


Figure S 9.2-30: N₂ sorption isotherm (a), pore-size distribution (b), and BET plot (c) for PI-3-COF and NO-PI-3-COF obtained via direct oxidation of PI-3-COF (reproduction experiment). NO-PI-3-COF was treated with scCO₂ and residual adsorbed water was removed by storing the sample in a desiccator over CaCl₂. Compared to a previous sample (Figure S 9.2-19, heated under dynamic vacuum) the loss in porosity after oxidation of PI-3-COF was reduced and allowed to obtain a sample of NO-PI-3 COF with larger surface area of S_{BET} = 1186 m²g⁻¹.

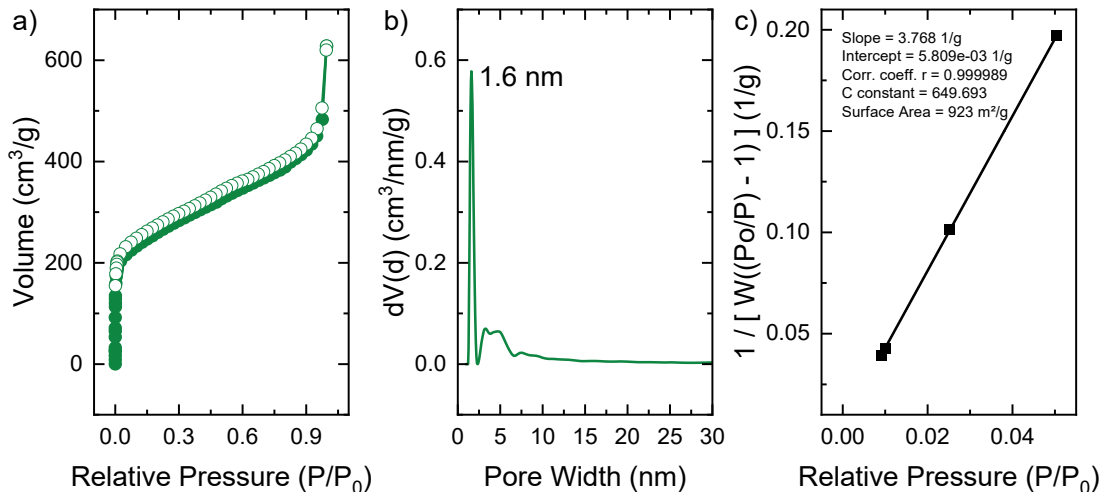


Figure S 9.2-31: N₂ sorption isotherm (a), pore-size distribution (b), and BET plot (c) for NO-PI-3-COF after in-situ XRPD experiments with humidity control. Compared to the initial value (S_{BET} = 1186 m²g⁻¹) the surface area of the material is slightly reduced, which is in contrast to the observed cycling performance (Figure S 9.2-56) and long-term moisture stability (Figure S 9.2-9) of the material. Note that the amount of sample available for the analysis was only ~3 mg, due to the limited capacity of the sample holder (see Figure S 9.2-53c), which might impact the experimental and weighting accuracy. In addition, remaining moisture after the water vapor desorption might have caused stress on the material during the heated vacuum treatment performed prior to the N₂ adsorption measurement.

9.2.7 Water Vapor Sorption Experiments

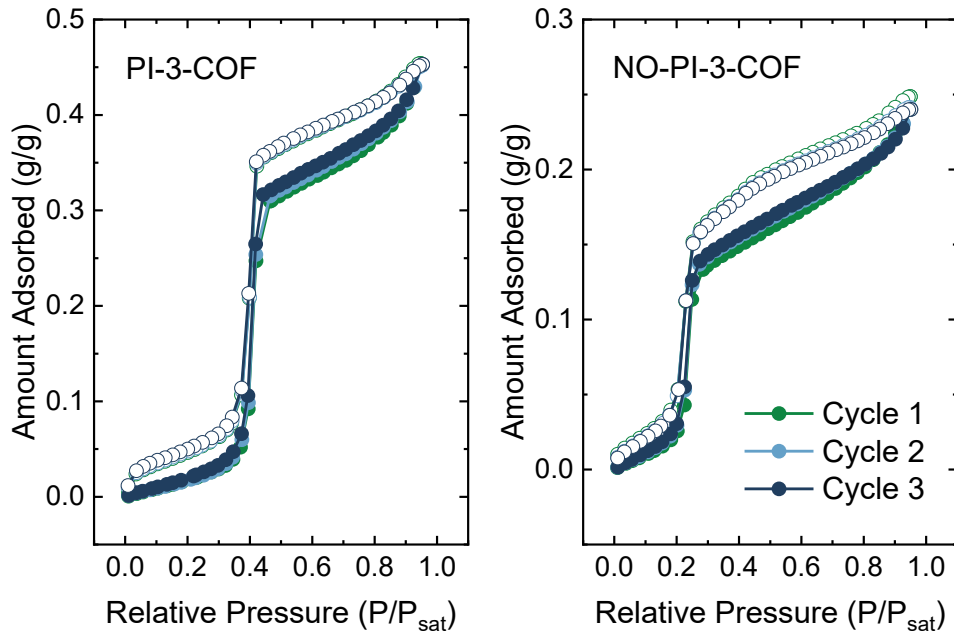


Figure S 9.2-32: Water vapor sorption isotherms of three consecutive cycles measured at $T = 25^\circ\text{C}$ for PI-3-COF and NO-PI-3-COF. Within the experimental error, no reduction in uptake capacity within these cycles is observed.

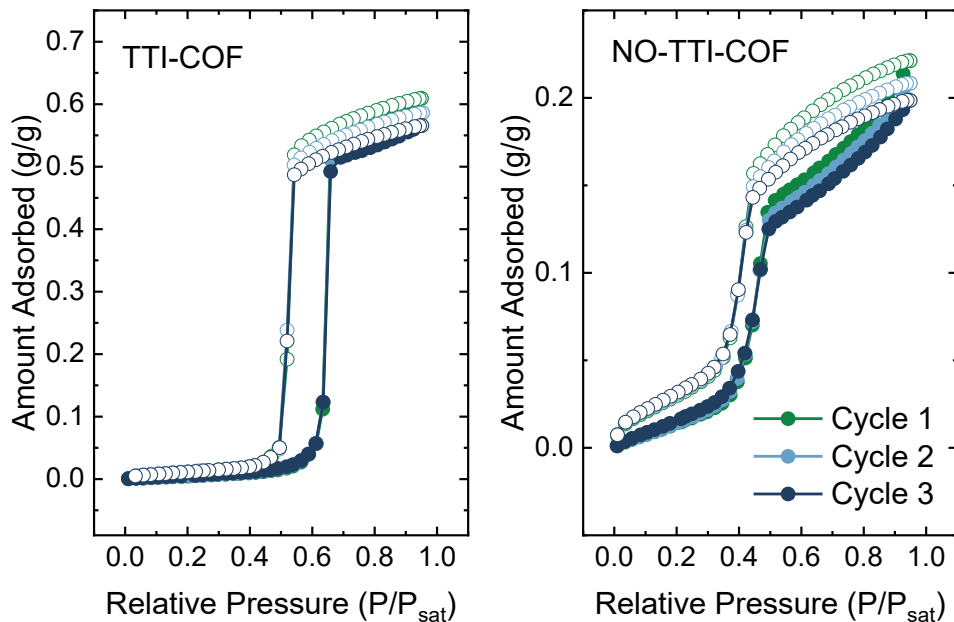


Figure S 9.2-33: Water vapor sorption isotherms of three consecutive cycles measured at $T = 25^\circ\text{C}$ for TTI-COF and NO-TTI-COF. A small but minor gradual decrease in maximum uptake capacity within these cycles is observed. Cycling measurements were performed after variable temperature measurements presented in Figure S 9.2-35.

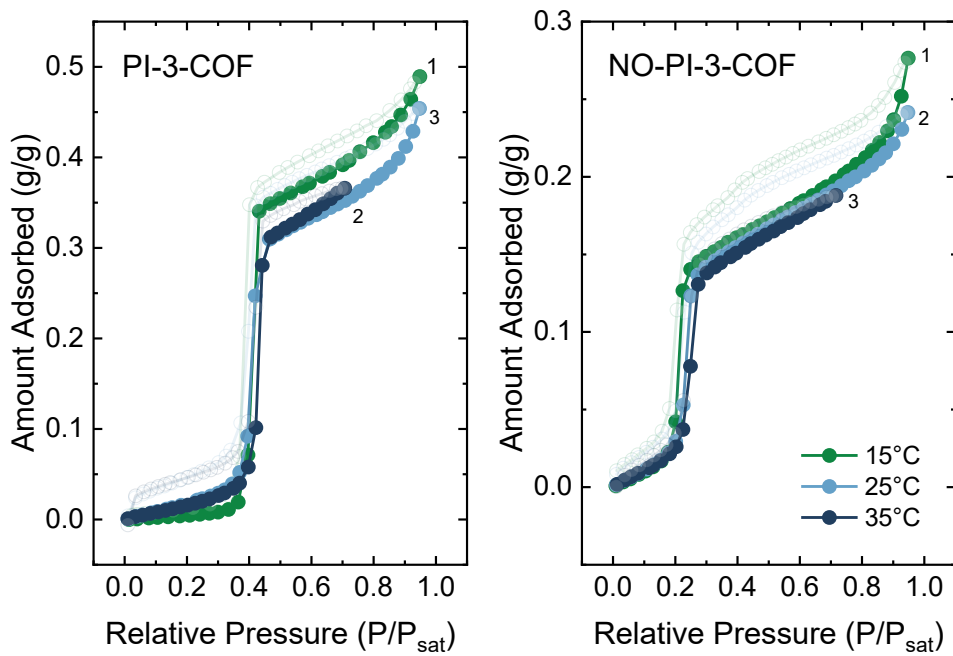


Figure S 9.2-34: Water vapor sorption isotherms of PI-3-COF and NO-PI-3-COF at different temperatures. Numbering denotes the order of measurement.

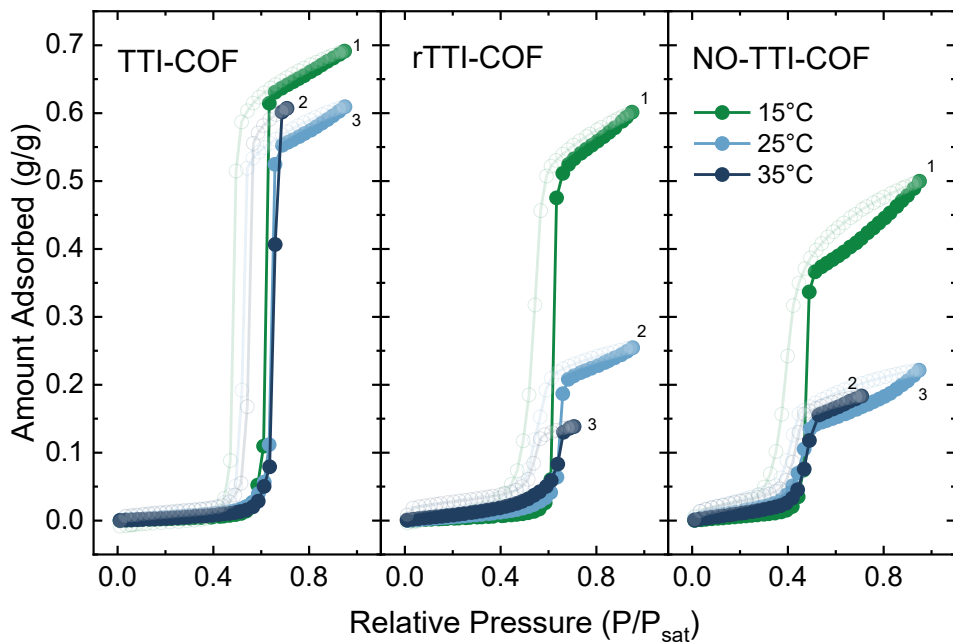


Figure S 9.2-35: Water vapor sorption isotherms of TTI-COF, rTTI and NO-TTI-COF at different temperatures. Numbers next to the isotherm denote the order of measurement. A major reduction in uptake capacity is visible for the second measurement of rTTI- and NO-TTI-COF, following the order of measurement. This indicates that the pore volume decreases after each adsorption-desorption cycle, which is related to a collapse of the pores in the material.

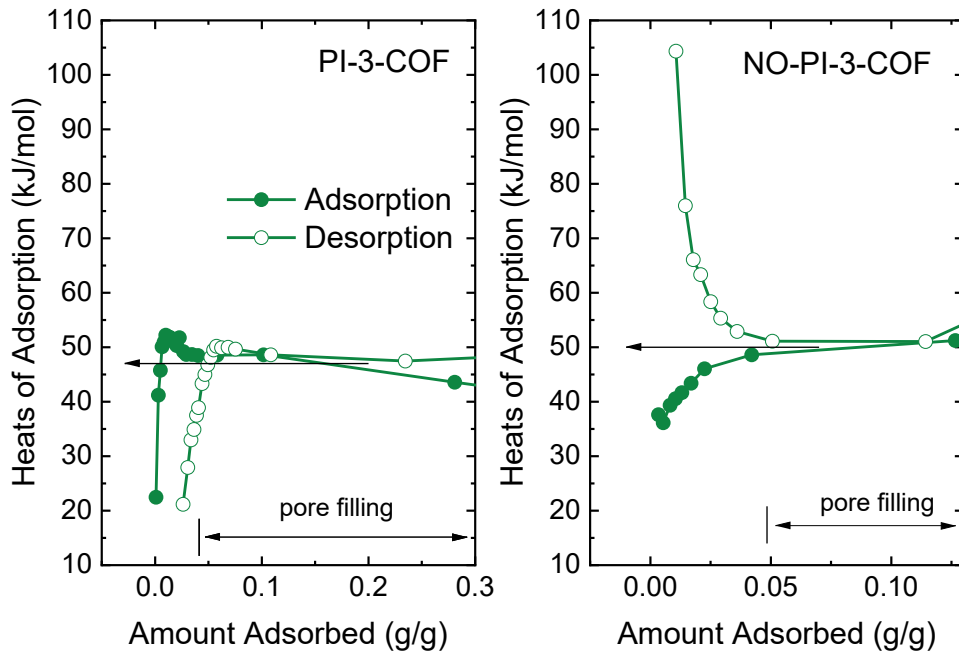


Figure S 9.2-36: Isosteric heats of adsorption at small loadings of adsorbed water vapor, approaching the pore condensation step, in PI-3-COF and NO-PI-3-COF. Values were calculated from vapor sorption isotherms at different temperatures. Note that calculated values at small loadings are associated with a larger error, caused by limited measurement accuracy, as well as kinetic influences during the sorption process (e.g. hysteresis) differing from ideal conditions.

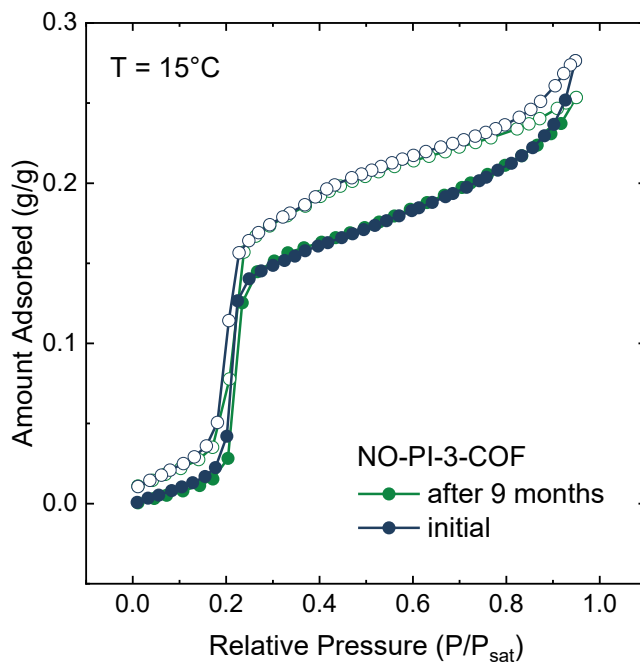


Figure S 9.2-37: Water vapor adsorption isotherms of NO-PI-3-COF at 15°C before and after storing the sample under ambient conditions i.e. in the hydrated state. The isotherms show a negligible difference indicating long-term stability of the material under exposure to moisture, which is in line with the cycling stability experiments presented in Figure S 9.2-32.

Table S 9.2-2: Comparison of reported COF water uptake capacities at low relative humidity.

COF	Water uptake (g/g) at $P/P_{\text{sat}} = 0.3$ @ 298K	BET surface area (m^2/g)	Linkage	Synthesis	Reference
AB-COF	0.34	1209	azine	de-novo	19
COF-480 hydrazide	0.33	989	azine/hydrazide	PSM of azine	19
TpPa-1	0.30	984	keto-enamine	de-novo	20
DHTa-Pa	0.49	2099	imine/keto-enamine	de-novo	21
NO-PI-3	0.15 0.27 (288K)	664 1186	nitrone	PSM of imine	This work

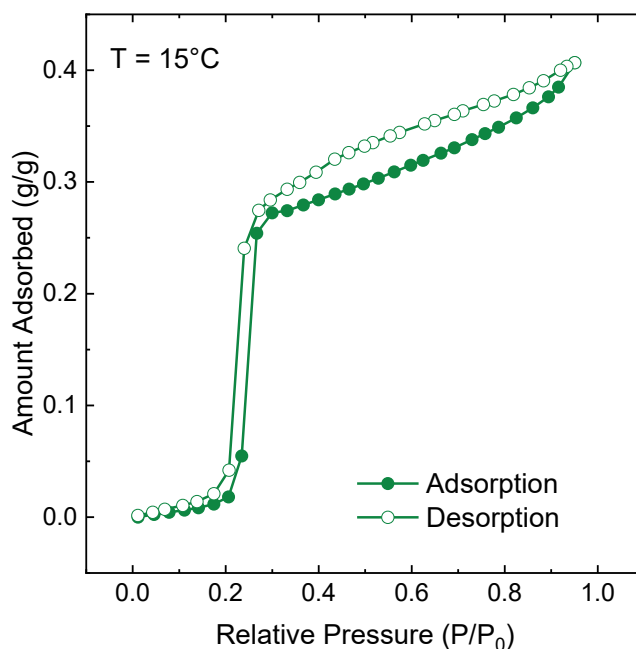


Figure S 9.2-38: Water vapor adsorption isotherms of NO-PI-3-COF (reproduction) at 15°C. This sample was obtained with larger BET surface area by careful drying in a desiccator to avoid vacuum induced stress (see Figure S 9.2-30). The increased porosity also results in a higher water uptake capacity.

9.2.8 CO₂ Gas Sorption Experiments

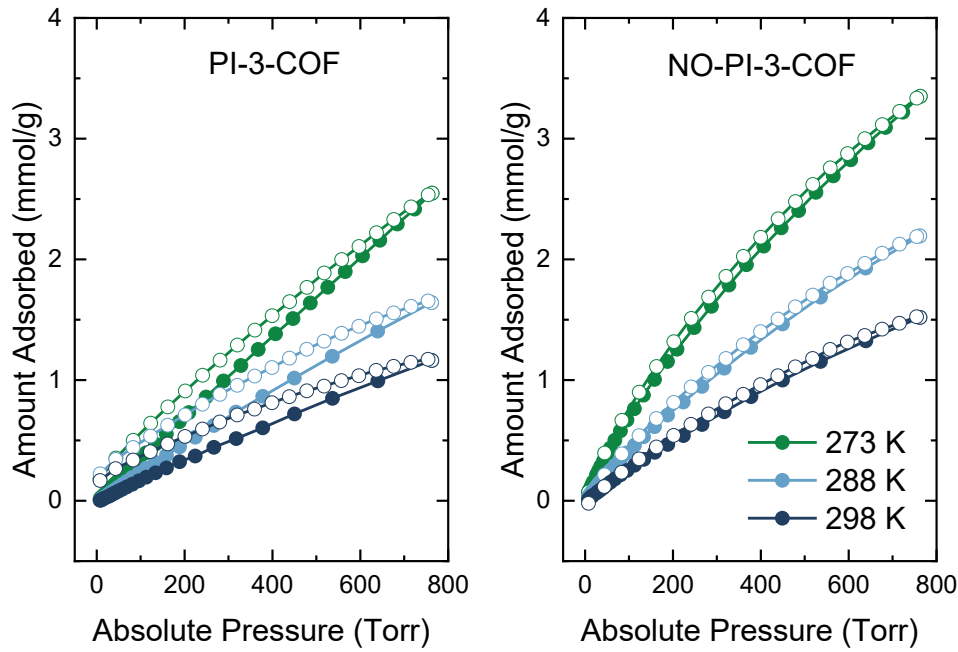


Figure S 9.2-39: CO₂ sorption isotherms of PI-3 and NO-PI-3-COF at different temperatures. Filled dots represent data points of the adsorption branch, hollow dots those of the desorption branch, respectively.

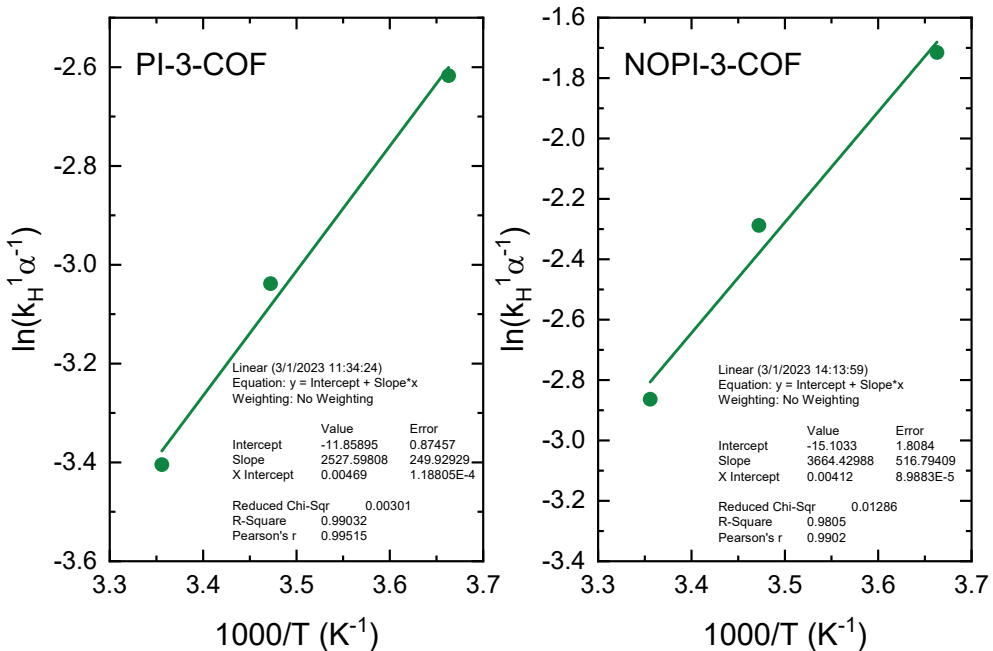


Figure S 9.2-40: Arrhenius plot of $k_H^{-1}\alpha^{-1}$, obtained by a linear fit of the CO₂ adsorption isotherms at low pressures for PI-3- and NO-PI-3-COF vs. temperature. Slopes of the linear fits allow to estimate ΔQ_{st} at zero coverage (see methods for details) and give values of $\Delta Q_{st} = 21 \pm 2 \text{ kJ}^{-1}\text{mol}^{-1}$ (PI-3-COF) and $\Delta Q_{st} = 30 \pm 4 \text{ kJ}^{-1}\text{mol}^{-1}$ (NO-PI-3-COF).

9.2.9 Thermogravimetric Analysis

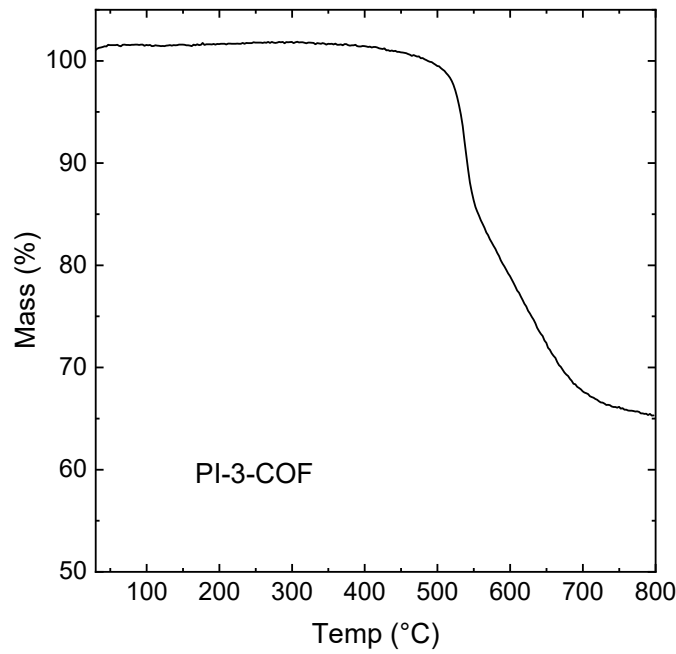


Figure S 9.2-41: Thermogravimetric trace of PI-3-COF under argon flow.

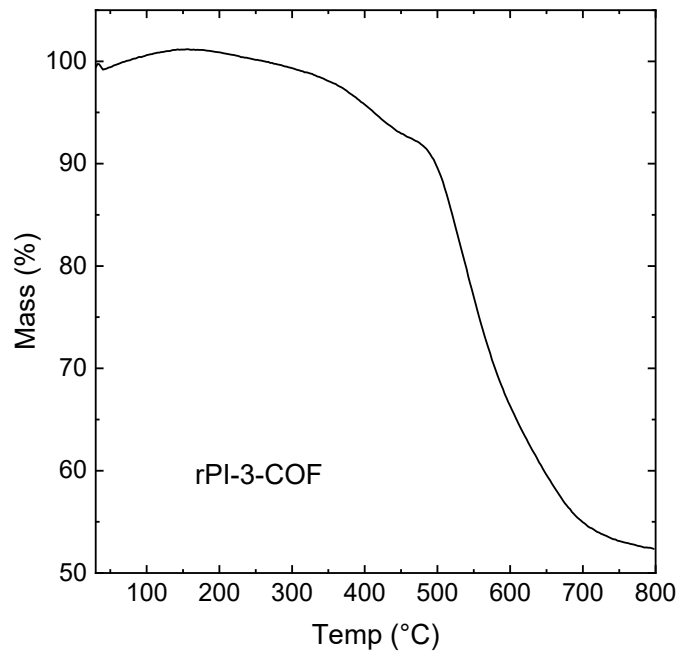


Figure S 9.2-42: Thermogravimetric trace of rPI-3-COF under argon flow.

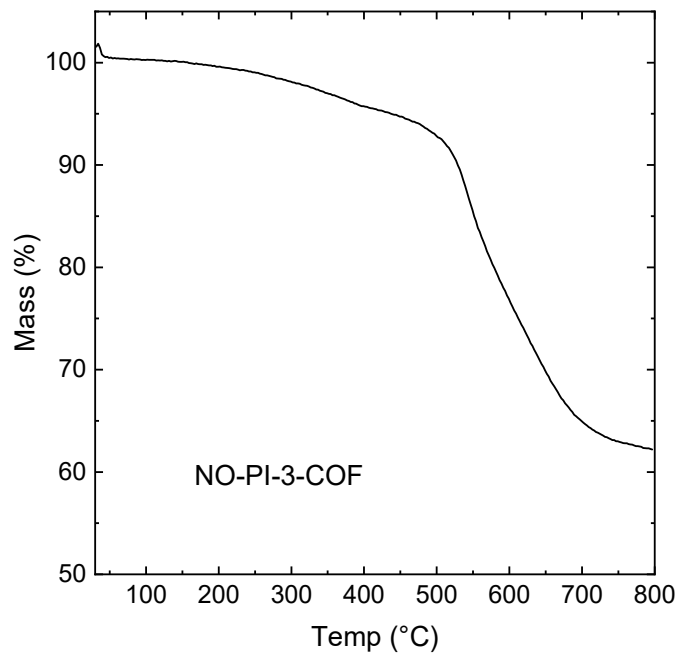


Figure S 9.2-43: Thermogravimetric trace of NO-PI-3-COF under argon flow.

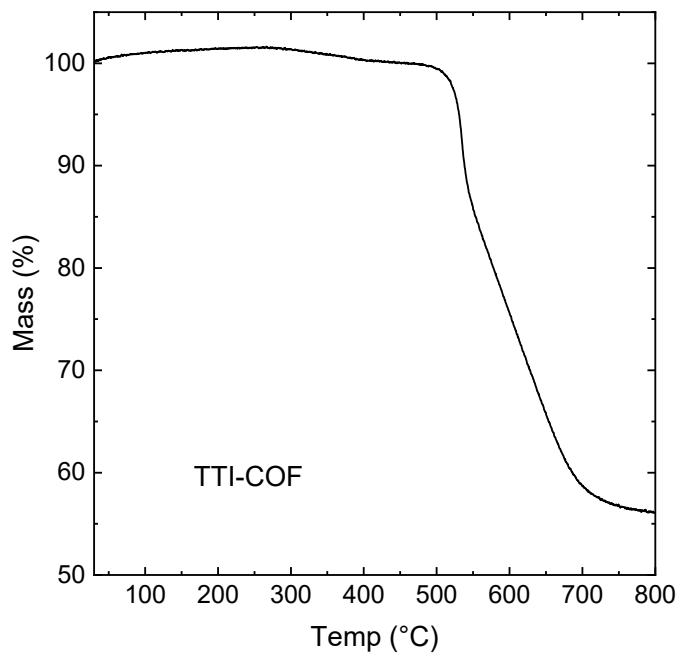


Figure S 9.2-44: Thermogravimetric trace of TTI-COF under argon flow.

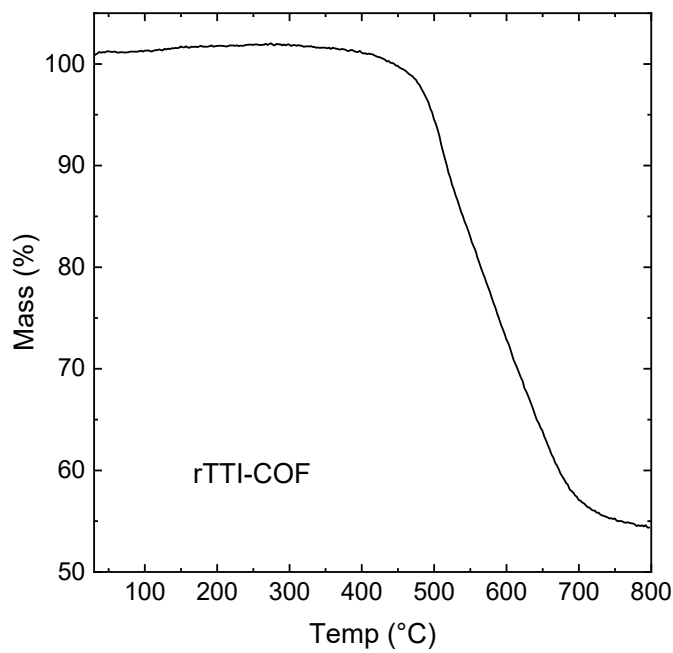


Figure S 9.2-45: Thermogravimetric trace of rTTI-COF under argon flow.

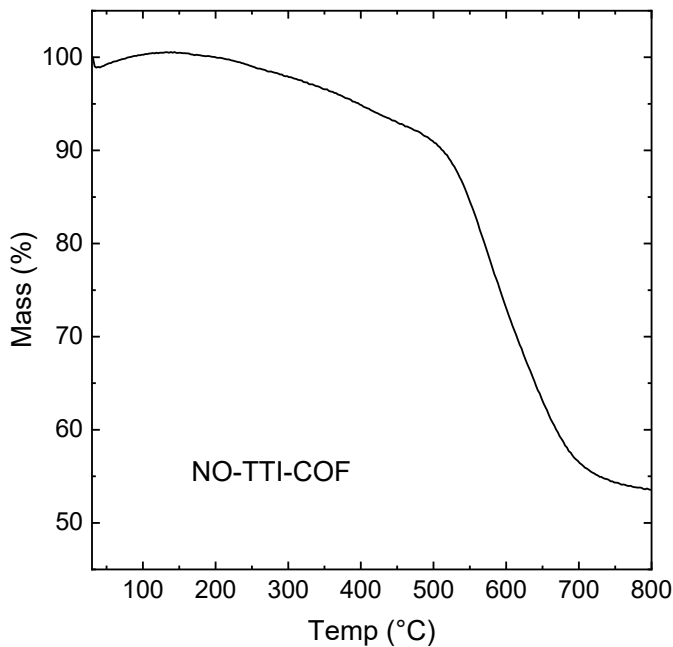


Figure S 9.2-46: Thermogravimetric trace of NO-TTI-COF under argon flow.

9.2.10 Quantum Chemical Calculations

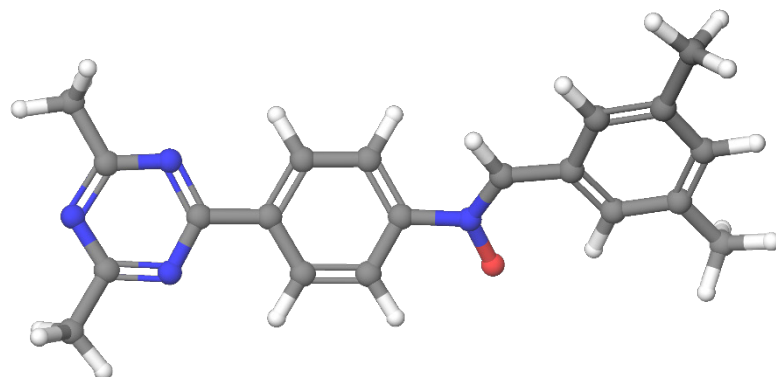


Figure S 9.2-47: Optimized structure for a representative molecular model system of NO-PI-3-COF (NO-PI-3 M), obtained on PBE0-D3/def2-TZVP level of theory.

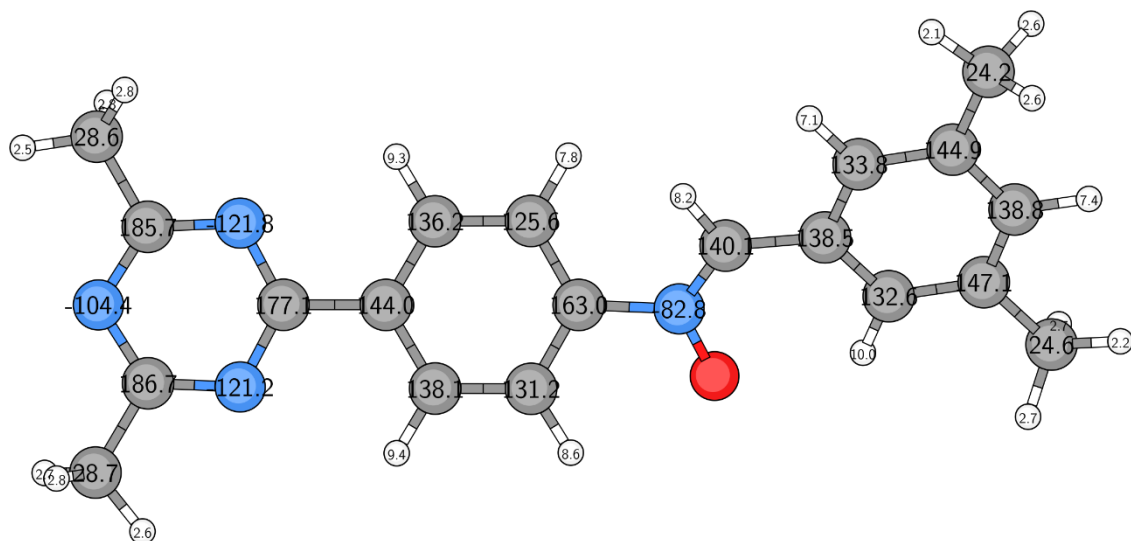


Figure S 9.2-48: Calculated NMR Chemical Shifts for the NO-PI-3 M model system, obtained on B97-2/pcS-2//PBE0-D3/def2-TZVP level of theory.

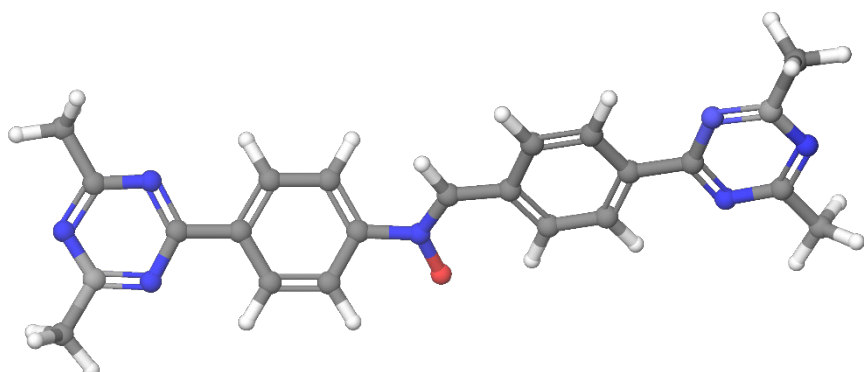


Figure S 9.2-49: Optimized structure for a representative molecular model system of NO-TTI-COF (NO-TTI M), obtained on PBE0-D3/def2-TZVP level of theory.

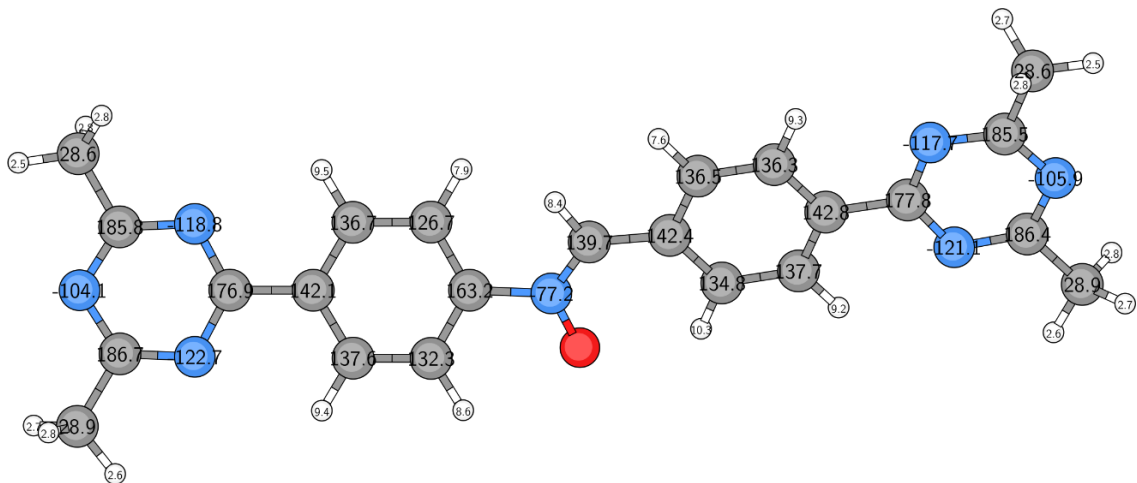


Figure S 9.2-50: Calculated NMR Chemical Shifts for the NO-TTI M model system, obtained on B97-2/pcS-2//PBE0-D3/def2-TZVP level of theory.

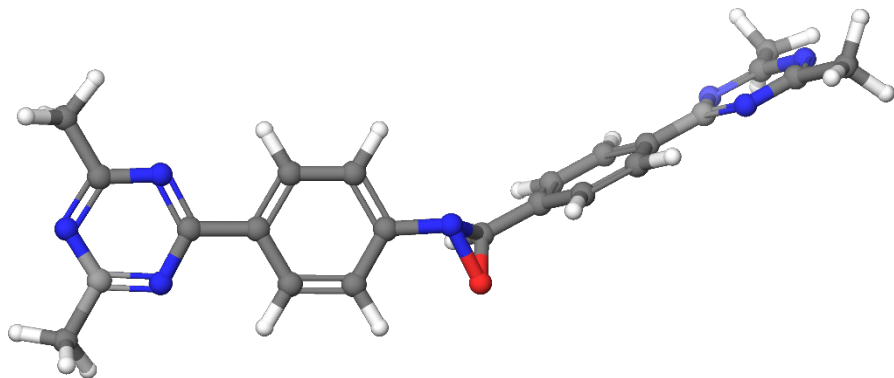


Figure S 9.2-51: Optimized structure for a theoretical oxaziridine-linkage in the TTI M model system, obtained on PBE0-D3/def2-TZVP level of theory.

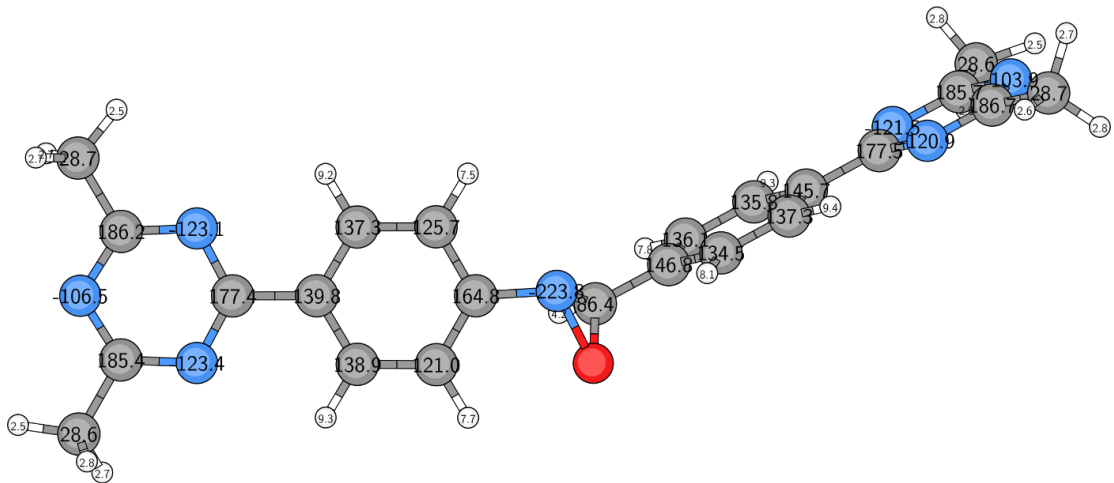


Figure S 9.2-52: Calculated NMR Chemical Shifts for a theoretical oxaziridin-linkage in the TTI M model system, obtained on B97-2/pcS-2//PBE0-D3/def2-TZVP level of theory. The absence of aliphatic carbon signals at ~86 ppm in the experimental carbon ssNMR spectrum excludes the formation of this linkage in the COF.

9.2.11 *In-Situ* X-ray Powder Diffraction

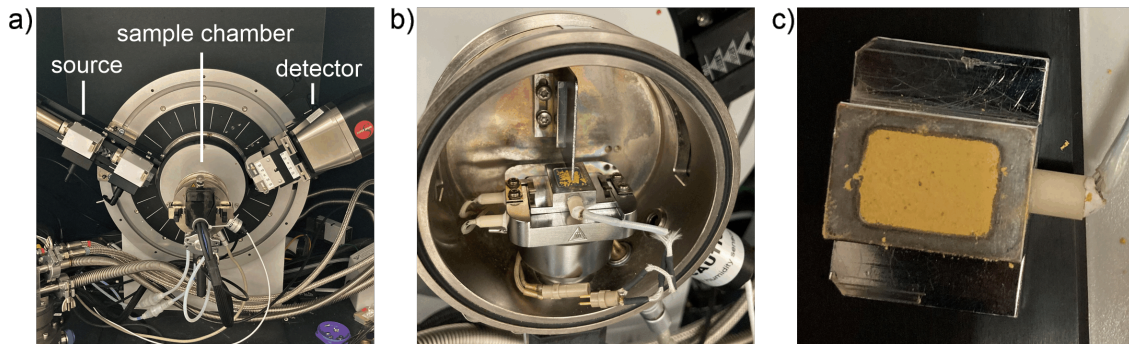


Figure S 9.2-53: Instrumental setup (a) used for in-situ XRPD experiments at controlled humidity. The humidity and temperature of the sample chamber (b) is controlled during the measurement. The sample (NO-PI-3-COF) is spread-out on the flat sample holder (c) to allow vapor exchange with the humidified nitrogen gas stream.

XRPD patterns under humidity controlled atmosphere were collected using a Bruker D8 advanced diffractometer using Cu-K α 1 radiation from a Johann-type Ge111 monochromator and a Lynx Eye detector (Bruker) equipped with a humidity chamber (Anton Paar). The humidity within the chamber was adjusted by mixing a dry and a water vapor saturated nitrogen stream. A total flow rate of 500 mL/min was applied and the temperature of the chamber was constantly kept at 25.0 ± 0.2 °C. NO-PI-3-COF was exposed to 0.1 and 40 % r.H for switching between the dehydrated and hydrated state. For measurements on the hydration and dehydration kinetics a total scan time of 10 minutes was used. The cycling behavior was monitored by exposing NO-PI-3-COF to the “dry” (0.1 % R.H.) and “wet” state (40 % R.H.) for one hour per step. A delay time of 40 minutes, prior to a measurement using a scan time of 20 minutes was applied. The XRPD data analyses was performed using TOPAS v6.^[22]

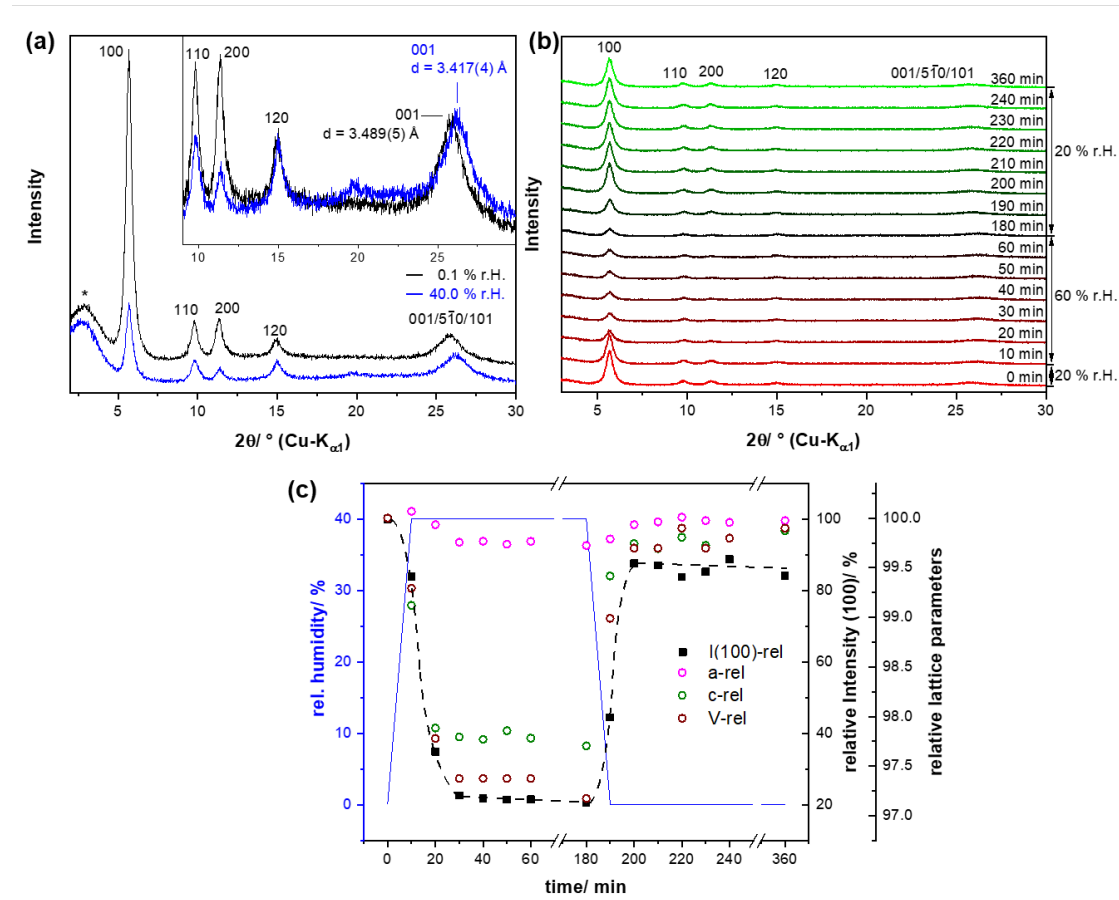


Figure S 9.2-54: In situ XRPD measurements NO-PI-3-COF (a): XRPD patterns in dehydrated (black lines) and hydrated states R.H. (blue lines) including the diffraction signal attributed to the empty sample holder and the humidity chamber (grey line, asterisks) and selected reflection indices, (b) time dependent in situ XRPD patterns during hydration and dehydration, (c) quantitative analyses of the diffraction patterns during hydration and dehydration.

Upon hydration, the diffraction signals of the COF seem to decrease in intensity (Figure S 9.2-54a, blue lines). A close inspection of XRPD patterns, however, reveals that only certain reflections like 100, 110 or 200 become weaker, whereas the intensity of other reflections like 120 stays constant (inset). As the peaks do not become broader, these diffraction effects are attributed to the incorporation of water into the crystal structure (leading to a reduced scattering contrast) rather than to a loss of the crystallinity of the COF (see below). Moreover, the incorporation of water into the structure leads to a significant upshift of the position of the 001 reflection, which corresponds to a decrease of the *c*-lattice parameter from 3.489(5) Å to 3.417(4) Å. When the relative humidity is subsequently decreased, the peak intensities of 100, 110 or 200 increase again (Figure S 9.2-54b, c), which shows that the hydration of the COFs is reversible. We conducted repeated measurements to gain insights into the de- and rehydration kinetics: the change in peak intensities upon de- and rehydration was observed to occur within 30-40 minutes (Figure S 9.2-54b). At the end of the re- and dehydration cycle, the intensities do not fully revert to their initial state, which can be depicted best by monitoring the evolution of the 100 reflection intensity (Figure S 9.2-54c, black squares). After dehydration, the intensity of the 100 reflection only reaches 85 % of its

original value, which suggests that after dehydration some water remains in the pores, even at lower relative humidity. The quality of the diffraction data of the NO-PI-3-COF allowed us to perform a more in depth analyses by fully weighted Rietveld²³ refinements (Figure S 9.2-54c) for tracking the evolution of the lattice parameters. Hydration of the NO-PI-3-COF leads to a significant reduction of the unit cell volume by more than 2.5 % (brown circles), mainly driven by the contraction of the c -lattice parameter of more than 2 % (green circles), whereas the a -axis only slightly shortens by < 0.5 % (magenta circles). In conclusion, an uptake of water leads to a contraction of the mean interlayer distance and therefore to a contraction of the unit cell. This might appear counterintuitive, however by filling the pores with water molecules, the interlayer interactions can be increased mediated by hydrogen bonds among water molecules and neighboring COF layers. In addition, the water incorporation could trigger a conformational change of linker related groups and therefore lead to a more efficient packing of the COF layers.

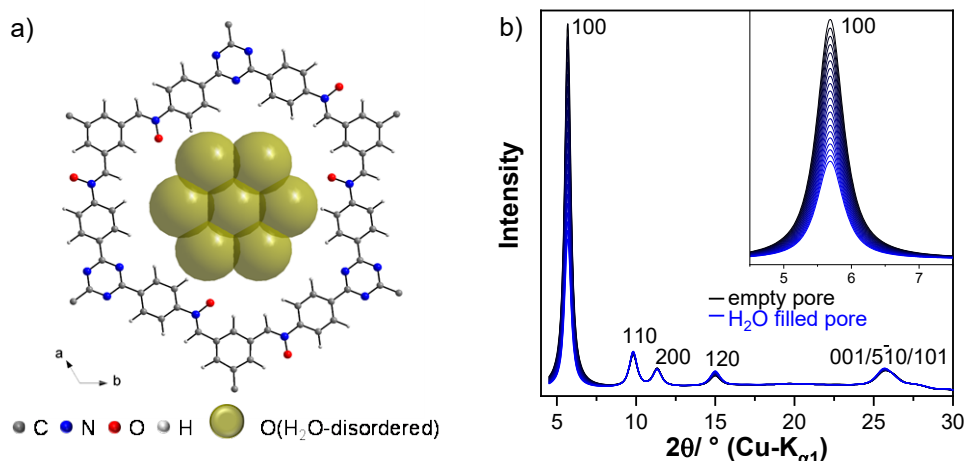


Figure S 9.2-55: Structure model of (a) NO-PI-3-COF filled with seven disordered water molecules per layer represented by oxygen atoms with artificially large thermal displacement parameters (large green balls), series of simulated XRPD patterns of NO-PI-3-COF, and (b) with an incremental increase of pore content starting with empty pores and extending to complete filling.

All XRPD data analyses were performed by fully weighted Rietveld^[23] refinements using idealized models for the COF structures with planar layer and all possible torsion angles of the linker components fixed. The filling of the pores by disordered water molecules was simulated using oxygen atoms with artificially high thermal displacement parameters in a closed packed arrangement (Figure S 9.2-55a, green balls). For the NO-PI-3-COF one pore was filled with seven water molecules per pore and layer. In order to visualize the impact of the pore filling on the diffraction patterns, we performed systematic simulations, where we calculated the XRPD patterns while incrementally increasing the occupancy of the pore water related oxygen sites from 0 (Figure S 9.2-55b, black lines) to 1 (blue lines), simulating a change from empty to water filled pores. An increasing pore content has significant impact on the XRPD pattern, especially on the 100 reflection, which shows a significant decrease in

intensity. This decrease in peak intensity corresponds to the interaction of the increasing amount of diffuse electron density in the pores with the electron density of the COF-framework. All other reflection are not or only effected to lesser extent by this effect. It must be noted that an anisotropic occupation of the possible sites for pore water can change the magnitude of the decrease in the 100 peak intensity and can change the effect on other reflections. For the NO-PI-3-COF a significant decrease of the 110 and 200 peak intensities was noticed upon pore filling, whereas the intensity of the 120 stayed constant. Simulations with an isotropic pore filling, the intensity of the 110 and 200 diffraction lines hardly changes. This can point to an anisotropic filling of the pore in the real structure. In the simulations, the magnitude of the decrease in peak intensity was also impacted by the size of the isothermal displacement parameter that we chose arbitrarily. Given this and the possible change of the stacking order, degree of stacking faulting and torsion of the linkers of the COF framework, we decided to not use this model for quantitative analyses of the pore filling, i.e. for tracking the occupancy of the pore water related oxygen sites.

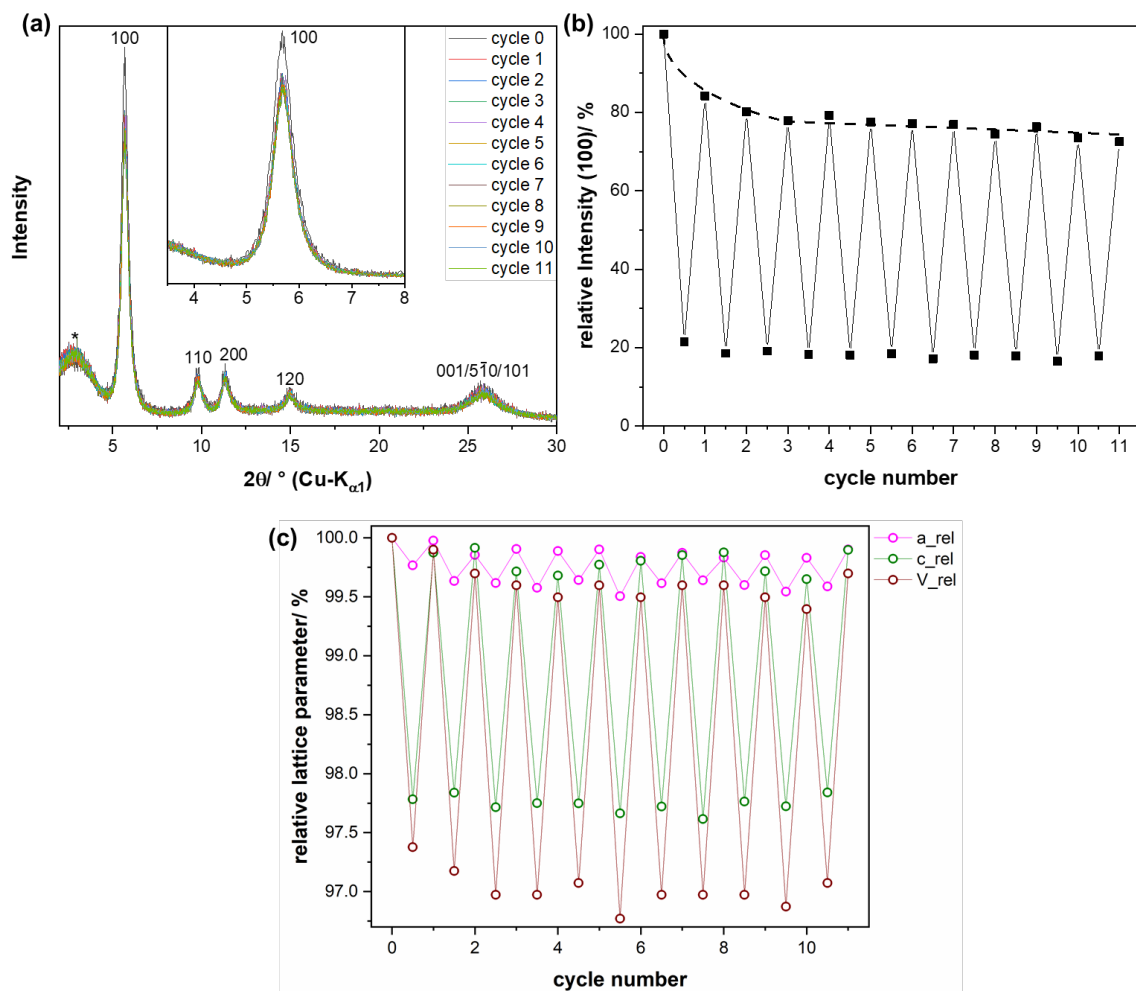


Figure S 9.2-56: XRPD patterns of NO-PI-3-COF (a) collected after different hydration-dehydration cycles, (b) evolution of the 100 peak intensities upon reversible hydration and dehydration, the dashed line visualizes the trend of the 100 peak intensity at the end of each cycle in dehydrated state, (c) evolution of the 100 peak intensity upon pore filling in the simulated XRPD patterns, (c) evolution of the unit cell volume and the a - and c -lattice parameter of the NO-PI-3-COF during hydration-dehydration cycles.

The reversible hydration and dehydration behavior of the COF material was monitored by in situ XRPD. Each hydration and dehydration cycle was started at 0.1 % R.H. Afterwards the humidity was ramped up to 40 % R.H. within one minute, kept constant, and subsequently the humidity was ramped down within one minute again. For every step the relative humidity was kept constant for one hour, which corresponds to a total cycle-length of two hours. The XRPD patterns reveal that the relative peak intensity (100), corresponding to the “dry” state of the COF, decreases during the first 3 cycles. This decrease is most pronounced after completion of the first hydration-cycle (Figure S 9.2-56b) and then the peak intensity stays constant upon continued hydration-dehydration cycles. The 100 reflection intensity in the dehydrated state stabilizes after four cycles at $\approx 75\%$ of its initial value (Figure S 9.2-56b, black dashed line), whereas the corresponding intensity in hydrated state stays constant at around 20 % throughout the entire experiment. This trend is also reflected by the evolution of the lattice parameters and of the unit cell volume (Figure S 9.2-56c). These data show, that after the completion of the hydration-dehydration cycles, water remains in the material that is not easily desorbed by a simple reduction of the relative humidity. On the other hand the constant intensity of the 100 reflection for the hydrated state signifies that the material reaches the same level of hydration in each adsorption cycle – and thus remains chemically and structurally intact throughout the cycles. This conclusion is also in agreement with the observed cycling stability during the presented volumetric water vapor adsorption experiments.

9.2.12 References

1. Perdew J. P., Burke K., Ernzerhof M. Generalized Gradient Approximation Made Simple. *Phys. Rev. Lett.* **77**, 3865-3868 (1996).
2. Grimme S., Antony J., Ehrlich S., Krieg H. A Consistent and Accurate Ab Initio Parametrization of Density Functional Dispersion Correction (Dft-D) for the 94 Elements H-Pu. *J. Chem. Phys.* **132**, 154104 (2010).
3. Schäfer A., Huber C., Ahlrichs R. Fully Optimized Contracted Gaussian Basis Sets of Triple Zeta Valence Quality for Atoms Li to Kr. *J. Chem. Phys.* **100**, 5829-5835 (1994).
4. Eichkorn K., Weigend F., Treutler O., Ahlrichs R. Auxiliary Basis Sets for Main Row Atoms and Transition Metals and Their Use to Approximate Coulomb Potentials. *Theor. Chem. Acc.* **97**, 119-124 (1997).
5. Burow A. M., Sierka M., Mohamed F. Resolution of Identity Approximation for the Coulomb Term in Molecular and Periodic Systems. *J. Chem. Phys.* **131**, 214101 (2009).
6. Burow A. M., Sierka M. Linear Scaling Hierarchical Integration Scheme for the Exchange-Correlation Term in Molecular and Periodic Systems. *J. Chem. Theory Comput.* **7**, 3097-3104 (2011).
7. Grajciar L. Low-Memory Iterative Density Fitting. *J. Comput. Chem.* **36**, 1521-1535 (2015).

8. Łazarski R., Burow A. M., Grajciar L., Sierka M. Density Functional Theory for Molecular and Periodic Systems Using Density Fitting and Continuous Fast Multipole Method: Analytical Gradients. *J. Comput. Chem.* **37**, 2518-2526 (2016).
9. Łazarski R., Burow A. M., Sierka M. Density Functional Theory for Molecular and Periodic Systems Using Density Fitting and Continuous Fast Multipole Methods. *J. Chem. Theory Comput.* **11**, 3029-3041 (2015).
10. Turbomole V7.3 2018, a Development of University of Karlsruhe and Forschungszentrum Karlsruhe GmbH, 1989-2007, Turbomole GmbH, since 2007; Available from <Http://Www.Turbomole.Com>.
11. Adamo C., Barone V. Toward Reliable Density Functional Methods without Adjustable Parameters: The Pbe0 Model. *J. Chem. Phys.* **110**, 6158-6170 (1999).
12. Ernzerhof M., Scuseria G. E. Assessment of the Perdew–Burke–Ernzerhof Exchange-Correlation Functional. *J. Chem. Phys.* **110**, 5029-5036 (1999).
13. Wilson P. J., Bradley T. J., Tozer D. J. Hybrid Exchange-Correlation Functional Determined from Thermochemical Data and Ab Initio Potentials. *J. Chem. Phys.* **115**, 9233-9242 (2001).
14. Jensen F. Basis Set Convergence of Nuclear Magnetic Shielding Constants Calculated by Density Functional Methods. *J. Chem. Theory Comput.* **4**, 719-727 (2008).
15. Kussmann J., Ochsenfeld C. Pre-Selective Screening for Matrix Elements in Linear-Scaling Exact Exchange Calculations. *J. Chem. Phys.* **138**, 134114 (2013).
16. Kussmann J., Ochsenfeld C. Preselective Screening for Linear-Scaling Exact Exchange-Gradient Calculations for Graphics Processing Units and General Strong-Scaling Massively Parallel Calculations. *J. Chem. Theory Comput.* **11**, 918-922 (2015).
17. Horn A., Kazmaier U. Purified Mcpba, a Useful Reagent for the Oxidation of Aldehydes. *Eur. J. Org. Chem.* **2018**, 2531-2536 (2018).
18. Grunenberg L. et al. Amine-Linked Covalent Organic Frameworks as a Platform for Postsynthetic Structure Interconversion and Pore-Wall Modification. *J. Am. Chem. Soc.* **143**, 3430-3438 (2021).
19. Nguyen H. L. et al. Hydrazine-Hydrazide-Linked Covalent Organic Frameworks for Water Harvesting. *ACS Cent. Sci.* **8**, 926-932 (2022).
20. Biswal B. P. et al. Pore Surface Engineering in Porous, Chemically Stable Covalent Organic Frameworks for Water Adsorption. *J. Mater. Chem. A* **3**, 23664-23669 (2015).
21. Sun C. et al. 2d Covalent Organic Framework for Water Harvesting with Fast Kinetics and Low Regeneration Temperature. *Angew. Chem. Int. Ed.* **62**, e202217103 (2023).
22. Coelho A. A. Topasandtopas-Academic: An Optimization Program Integrating Computer Algebra and Crystallographic Objects Written in C++. *J. Appl. Crystallogr.* **51**, 210-218 (2018).
23. Rietveld H. M. A Profile Refinement Method for Nuclear and Magnetic Structures. *J. Appl. Crystallogr.* **2**, 65-71 (1969).

9.3 Supporting Information to Chapter 6 Light-Driven Molecular Motors Embedded in Covalent Organic Frameworks

9.3.1 Methods and Equipment

General Methods: All reactions, unless otherwise noted, were performed with magnetic stirring under inert gas (N_2 or Ar) atmosphere using standard Schlenk techniques. Reaction temperatures were electronically monitored as external heating block temperatures. Reagents were purchased from different commercial sources and used without further purification.

NMR Spectroscopy: NMR spectra were obtained using a Varian Mercury Plus (^1H : 400 MHz, ^{13}C : 100 MHz) or a Bruker Avance NEO (^1H : 600 MHz, ^{13}C : 150 MHz). Chemical shifts are reported in δ units (ppm) relative to the residual solvent signal of CDCl_3 (^1H NMR, δ 7.26 ppm; ^{13}C NMR, δ 77.0 ppm) C_6D_6 (^1H NMR, 7.16 ppm; ^{13}C NMR 128.1 ppm) or $\text{DMSO-}d_6$ (^1H NMR, δ 2.50 ppm; ^{13}C NMR, δ 39.5 ppm). The splitting pattern of peaks is designated as follows: s (singlet), d (doublet), t (triplet), m (multiplet), br (broad), p (quintet) or dd (doublet of doublets).

NMR irradiation experiments were performed on a Varian Innova (^1H : 500 MHz) instrument at 10 °C with a Thorlab model M395F1 and M365F1 LED coupled to a 0.6 mm optical fiber, which sends the light into the NMR tube inside the spectrometer.

Solid-state NMR spectra (ssNMR) were recorded at room temperature in 3.2 mm ZrO_2 rotors on a Bruker Neo 600 MHz spectrometer using Bruker BL3.2 triple resonance MAS probes. Standard instrument library pulse sequences were used. Chemical shifts were referenced relative to TMS (^1H and ^{13}C , 0.0 ppm) and CH_3NO_2 (^{15}N , 0.0 ppm).

High-Resolution Mass Spectrometry (HRMS): HRMS were recorded on an LTQ Orbitrap XL.

Infrared Spectroscopy: IR spectra were recorded on a Perkin Elmer UATR Two FT-IR spectrometer equipped with an attenuated total reflection (ATR) measuring unit. IR data are reported in wavenumbers (cm^{-1}) of normalized absorption. The IR bands are characterized as w (weak), m (medium), s (strong), or br (broad). Irradiated IR samples: A small amount of dried COF powder was deposited on the sample holder. Irradiation was performed with a M365F1 LED by Thorlabs from a distance of a few centimeters for an optimal focus of the light on the sample. The IR spectra were measured *in situ*.

UV/Vis Absorption Spectroscopy: UV-Vis absorption spectra of solutions were recorded in a cm quartz cuvette with a Agilent Technologies Cary 8454 UV-Vis spectrometer, equipped with a Quantum Northwest temperature controller.

DR-UV/Vis: A small amount of dried COF powder was carefully mixed with $\text{Ba}(\text{SO}_4)_2$ and deposited in a sample holder. Irradiation was performed with a Throlabs M365F1 LED

inside the spectrometer, without moving the sample holder. Spectra were taken before and after irradiation and after letting the sample stand in the dark for 1 h.

Raman Spectroscopy: Raman spectra were recorded either using a Raman microscope with optical head from Perkin Elmer with excitation at 785 nm (Ondax, 5-50 mW at sample) typically with a 50x long working distance objective or a Inphotonics low-cost Raman probe with Raman scattering feed to a Shamrock163i spectrograph with a 600 l/mm 750 nm blazed grating and a SMA fiber coupler and correction lens with spectra collected using an Andor Technology iVac-316-LDC-DD or iDus-420-OE CCD, respectively. Spectra were calibrated with polystyrene or cyclohexane (ASTM E 1840). Spectra were typically 0.5 to 1 s acquisitions and 60 accumulations. Raman spectra at 355 nm (10 mW, Cobolot Lasers Zouk) were recorded in 180° backscattering mode with 7.5 mm focal length collection lens at sample and 15 cm focal length lens feeding light into the Shamrock500i (ANDOR technology) spectrograph equipped with a iDUS-420-BU2 CCD detector and 1800 l/mm grating blazed at 300 nm. A Semrock long pass filter was used to reject Rayleigh scattering. Spectra were obtained with ANDOR Solis, processed in Spectragraph 1.2.14 (F. Menges).

Gas Sorption Measurements: Sorption measurements for COFs were performed on a Quantachrome Instruments Autosorb iQ MP with Nitrogen at 77 K. The samples were degassed for 12 h at 120 °C under vacuum prior to the gas adsorption studies. Pore size distribution was determined from Nitrogen adsorption isotherms using the QSDFT cylindrical pores in carbon model for nitrogen at 77 K. For multipoint BET surface area calculations, pressure ranges were chosen with the help of the BET assistant in the ASiQwin software, which chooses BET tags in accordance with the ISO recommendations equal or below the maximum in grams per square meter.

Nitrogen physisorption at 77 K of the polymers was performed on a Micromeritics® ASAP 2420 instruments using the instruments default settings. Previous to the physisorption experiments samples were degassed at 80 °C for 6 h.

X-Ray Powder Diffraction (XRPD): X-ray powder diffraction experiments were performed on a Stoe Stadi P diffractometer (Cu-K α or Co- K α , Ge(111)) in Debye-Scherrer geometry. The samples were measured in sealed glass capillaries (OD = 0.7 mm) and spun for improved particle statistics. A Thorlabs M365LP1-C4 LED light source, equipped with a Thorlabs COP4-A Zeiss lens, was used for irradiated XRPD experiments.

Pawley Refinements: Pawley refinements were performed using TOPAS v6. The background was corrected with Chebychev polynomials (Order 10). Simple axial and zero-error corrections were used together with additional corrections for Lorentzian crystallite size broadening.

Pair Distribution Function (PDF) Analysis: Total scattering measurements were carried out using the high energy Powder Diffraction and Total Scattering Beamline P02.1 of PETRA III at the Deutsches Elektronen-Synchrotron (DESY). X-ray total scattering data were collected in rapid acquisition mode (RAPDF).^[1] A large-area 2D Varex XRD 4343CT

detector (2880×2880 pixels, 150×150 μm^2 each) was used at a sample-to-detector distance of approximately 500 mm. Samples were loaded into 1.0 mm ID/1.1 mm OD polyimide capillaries (Cole-Parmer) and measured at room temperature. The incident energy of the X-rays was 59.792 keV ($\lambda = 0.20736 \text{ \AA}$). A measurement of LaB₆ was collected at room temperature as a standard for calibration of the setup. Calibration was performed, and the raw 2D intensity was corrected for polarization and azimuthally integrated and converted to 1D intensity versus Q ($Q = 4\pi \sin \theta / \lambda$ is the magnitude of the scattering momentum transfer, with 20 scattering angle) using pyFAI^[2] with the xpdtools package^[3].

Further correction and normalization of the integrated 1D diffraction intensities were carried out to obtain the total scattering structure function, F(Q), which was Fourier transformed to obtain the pair distribution function (PDF), G(r) using PDFgetX3^[4] within xPDFsuite^[5]. The maximum value used in the Fourier transform of the total scattering data (Qmax) was 15.0 \AA^{-1} . Simulated PDFs were performed using PDFgui^[5, 6].

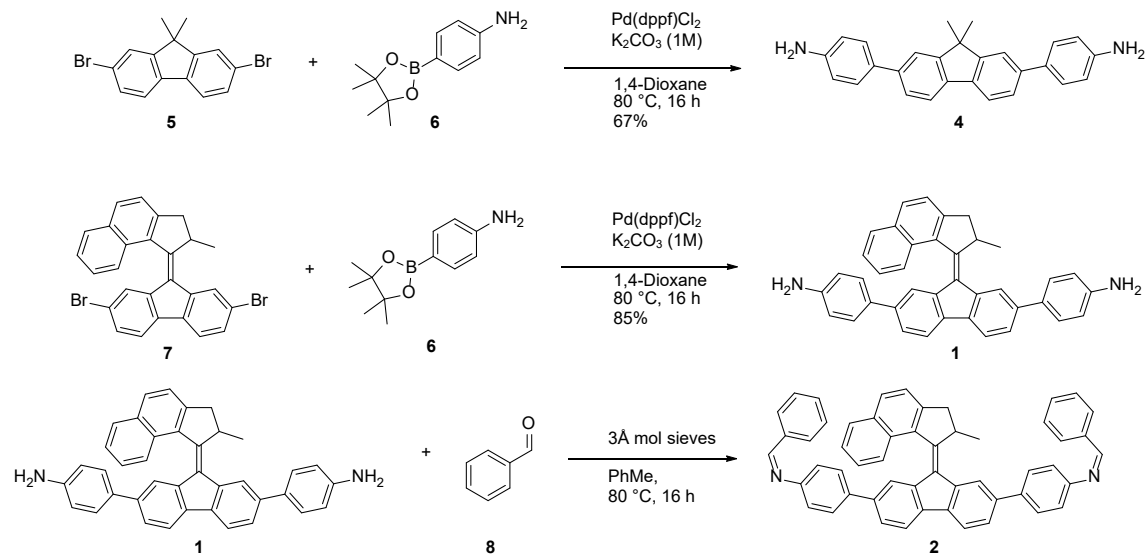
Supercritical CO₂ Activation: Activation of the methanol-soaked COF samples with supercritical CO₂ was performed on a Leica EM CPD300 critical point dryer. Solvent removal from the polymers was performed *via* supercritical CO₂ extraction using a Tousimis Autosamdry-815 Series B Critical Point Dryer. The sample were previously washed and suspended in ethanol.

Scanning Electron Microscopy (SEM): SEM SE (secondary electron) detector images were obtained on a Zeiss Merlin SEM.

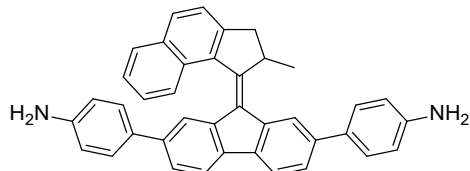
Transmission Electron Microscopy (TEM): TEM analysis was performed with a Philips CM30 ST (300kV, LaB6 cathode). The samples were prepared dry onto a copper lacey carbon grid (Plano).

9.3.2 Synthetic Procedures

9.3.2.1 Building Block Synthesis



4,4'-(9-(2-Methyl-2,3-dihydro-1*H*-cyclopenta[*a*]naphthalen-1-ylidene)-9*H*-fluorene-2,7-diyl)dianiline (1)



Motor 7 (300 mg, 597 μ mol, 1.0 equiv.),^[7] 4-aminophenylboronic pinacol ester (6, 393 mg, 1.79 mmol, 3.0 equiv.) and Pd(dppf)Cl₂ (44.0 mg, 60.0 μ mol, 0.1 equiv.) were mixed with 10 mL 1,4-dioxane and 1M aqueous potassium carbonate solution (2.4 mL, 2.4 mmol, 4.0 equiv.). The mixture was degassed by applying vacuum until the solvent started bubbling and was saturated with N₂. This process was repeated three times. Subsequently the mixture was stirred at 80 °C for 17 h under N₂ atmosphere. The reaction mixture was cooled down to room temperature, ethyl acetate and water were added, the phases were separated and the aqueous phase was extracted with ethyl acetate (3 x 50 mL). The combined organic phase was washed with water (3 x 50 mL) and with brine (50 mL). Finally it was dried over magnesium sulfate and the solvent was removed under reduced pressure. The crude product was purified by flash column chromatography (pentane: EtOAc 10-100%). The product was collected as a brown-orange solid (268 mg, 509 μ mol, 85%).

¹H NMR (600 MHz, C₆D₆) δ = 8.34 (d, *J* = 1.5 Hz, 1H), 8.15 (d, *J* = 8.4 Hz, 1H), 7.82 (dd, *J* = 8.0, 1.5 Hz, 2H), 7.73 (d, *J* = 7.8 Hz, 1H), 7.67 (dd, *J* = 7.8, 1.5 Hz, 1H), 7.65 – 7.61 (m, 3H), 7.53 (dd, *J* = 7.8, 1.6 Hz, 1H), 7.38 (d, *J* = 1.6 Hz, 1H), 7.29 (ddd, *J* = 8.2, 6.7, 1.2 Hz, 1H), 7.26 (d, *J* = 8.1 Hz, 1H), 7.10 (ddd, *J* = 8.3, 6.7, 1.3 Hz, 1H), 6.82 – 6.76 (m, 2H), 6.54 – 6.49 (m, 2H), 6.26 – 6.20 (m, 2H), 4.18 (p, *J* = 6.6 Hz, 1H), 3.18 (dd, *J* = 15.0, 5.6 Hz, 1H), 2.88 (s, 2H), 2.75 (s, 2H), 2.32 (d, *J* = 15.0 Hz, 1H), 1.20 (d, *J* = 6.8 Hz, 3H) ppm.

¹³C NMR (151 MHz, C₆D₆) δ = 150.8, 147.7, 146.6, 146.1, 141.5, 140.8, 139.4, 139.2, 138.6, 138.5, 137.0, 133.2, 132.8, 132.0, 131.8, 131.1, 130.6, 129.0, 128.4, 127.5, 126.2, 125.8, 125.4, 124.7, 124.2, 123.3, 120.4, 119.7, 115.6, 115.2, 45.6, 42.1, 19.1 ppm.

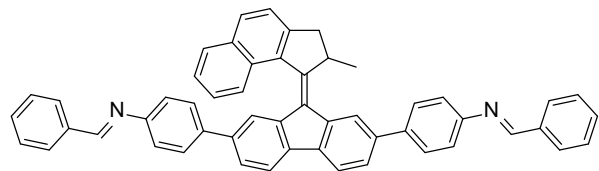
¹H NMR (600 MHz, CDCl₃) δ = 8.17 (d, *J* = 1.5 Hz, 1H), 8.02 (dd, *J* = 8.3, 1.2 Hz, 1H), 7.93 (t, *J* = 8.9 Hz, 2H), 7.84 (d, *J* = 7.9 Hz, 1H), 7.75 (d, *J* = 7.8 Hz, 1H), 7.60 – 7.51 (m, 5H), 7.46 – 7.39 (m, 2H), 6.93 (d, *J* = 1.5 Hz, 1H), 6.87 – 6.80 (m, 2H), 6.60 – 6.54 (m, 2H), 6.49 – 6.44 (m, 2H), 4.44 (p, *J* = 6.6 Hz, 1H), 3.73 (s, 4H), 3.58 (dd, *J* = 15.1, 5.7 Hz, 1H), 2.78 (d, *J* = 15.1 Hz, 1H), 1.47 (d, *J* = 6.8 Hz, 3H) ppm.

¹³C NMR (151 MHz, CDCl₃) δ = 151.0, 147.5, 145.9, 145.4, 140.8, 140.0, 138.6, 138.5, 138.0, 137.8, 136.6, 132.9, 132.6, 131.9, 131.1, 130.9, 130.2, 128.9, 128.2, 127.9, 127.7, 127.1, 125.7, 125.2, 125.2, 124.2, 124.2, 122.5, 119.9, 119.2, 115.7, 115.2, 45.4, 42.1, 19.5 ppm.

IR (ATR): ν = 3456 (w), 3367 (w), 3209 (w), 3024 (w), 2963 (w), 2923 (w) 1616 (m), 1519 (m), 1461 (m), 1410 (w), 1273 (w), 1184 (w), 1057 (w), 811 (vs), 757 (w), 657 (w), 565 (w), 536 (m), 476 (w) cm⁻¹.

HRMS (ESI pos): calculated for C₃₉H₃₁N₂⁺ ([M+H]⁺): 527.2482 found: 527.2487.

***N,N'*-((9-(2-Methyl-2,3-dihydro-1*H*-cyclopenta[*a*]naphthalen-1-ylidene)-9*H*-fluorene-2,7-diyl)bis(4,1-phenylene))bis(1-phenylmethanimine) (2)**



Motor **1** (2.5 mg, 4.7 μ mol, 1.0 equiv.) was dissolved in 0.3 mL toluene and 1 μ L benzaldehyde (**8**, 9.5 μ mol, 2.0 equiv.) was added together with 3 \AA molecular sieves. The mixture was heated to 80 °C for 16 h. The solvent was removed under reduced pressure and the product was obtained as a yellow solid (3.3 mg, 4.7 μ mol, 99%).

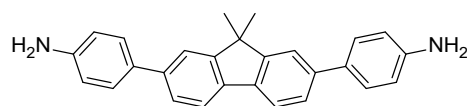
¹H NMR (400 MHz, C₆D₆): δ = 8.39 (s, 1H), 8.33 (s, 1H), 8.14 (d, *J* = 9.5 Hz, 2H), 7.94 – 7.76 (m, 9H), 7.68 (dd, *J* = 11.2, 8.3 Hz, 2H), 7.56 (d, *J* = 8.0 Hz, 1H), 7.45 (s, 1H), 7.39 (d, *J* = 8.0 Hz, 2H), 7.29 (dd, *J* = 11.1, 7.9 Hz, 2H), 7.14 – 7.10 (m, 9H), 6.97 (d, *J* = 8.1 Hz,

2H), 4.20 (t, J = 6.5 Hz, 1H), 3.22 (dd, J = 15.2, 5.5 Hz, 1H), 2.37 (d, J = 15.2 Hz, 1H), 1.22 (d, J = 6.7 Hz, 3H) ppm.

^{13}C NMR (101 MHz, C_6D_6): δ = 159.9, 151.9, 151.7, 151.4, 148.0, 141.6, 140.5, 140.3, 139.6, 139.1, 138.9, 138.7, 137.1, 133.3, 131.5, 131.2, 129.3, 129.3, 129.2, 128.9, 128.9, 128.6, 128.4, 128.2, 128.1, 127.9, 126.7, 126.3, 125.6, 125.3, 124.3, 123.7, 122.2, 121.7, 120.7, 120.0, 45.6, 42.1, 19.1 ppm.

HRMS (ESI pos): calculated for $\text{C}_{53}\text{H}_{39}\text{N}_2^+$ ($[\text{M}+\text{H}]^+$): 703.3108 found: 703.3115.

4,4'-(9,9-Dimethyl-9*H*-fluorene-2,7-diyl)dianiline (4)



Spacer **5** (2.10 g, 5.97 mmol, 1.0 equiv.),^[8] 4-aminophenylboronic pinacol ester (**6**, 2.88 g, 13.1 mmol, 2.2 equiv.) and Pd(dppf)Cl₂ (218 mg, 298 μmol , 5 mol%) were mixed with 10 mL 1,4-dioxane and 1M aqueous potassium carbonate (24 mL, 24 mmol, 4.0 equiv.). The mixture was degassed by applying vacuum until the solvent started bubbling and was saturated with N₂. This process was repeated three times. Subsequently the mixture was stirred at 80 °C for 16 h under N₂ atmosphere. The reaction mixture was cooled down to room temperature, ethyl acetate and water were added, the phases were separated and the aqueous phase was extracted with ethyl acetate (3 x 100 mL). The combined organic phase was washed with half sat. brine (3 x 100 mL). Finally, it was dried over magnesium sulfate and the solvent was removed under reduced pressure. The crude product was purified by flash column chromatography (pentane:EtOAc 10-100%). The product was collected as a brown-orange solid (1.50 g, 3.98 mmol, 67%).

^1H NMR (400 MHz, CDCl_3): δ = 7.74 (d, J = 7.9 Hz, 2H), 7.59 (d, J = 1.6 Hz, 2H), 7.60 – 7.44 (m, 8H), 6.83 – 6.74 (m, 4H), 3.74 (s, 2H), 1.56 (s, 6H) ppm.

^{13}C NMR (101 MHz, CDCl_3): δ = 154.5, 145.9, 140.3, 137.5, 132.2, 128.2, 125.6, 120.7, 120.2, 115.6, 77.5, 77.2, 76.8, 47.1, 27.5 ppm.

IR (ATR): ν = 3206 (w), 3442 (w), 3351 (w), 3021 (w), 2956 (w), 2922 (w), 2863 (w), 1606 (w), 1519 (m), 1463 (m), 1409 (w), 1269 (w), 1183 (w), 1127 (w), 1081 (w), 815 (vs), 745 (w), 633 (w), 560 (w), 529 (m), 470 (m) cm^{-1} .

HRMS (ESI pos) calculated for $\text{C}_{27}\text{H}_{25}\text{N}_2^+$ ($[\text{M}+\text{H}]^+$): 377.2012, found 377.2020.

9.3.2.2 Polymer Synthesis

Motor:Spacer 1:1 Polymer ($m_{50}\text{-P}$)

Motor amine **1** (48.7 mg, 92.5 μmol , 1.5 equiv.) and spacer amine **4** (34.8 mg, 92.5 μmol , 1.5 equiv.) were dissolved in a degassed (freeze-pump-thaw) solvent mixture of dioxane and mesitylene (4:1, 2 mL). Triformylbenzene (20.0 mg, 123 μmol , 2.0 equiv.) and $\text{Sc}(\text{OTf})_3$ (3.00 mg, 6.2 μmol) were dissolved separately in the same solvent mixture (2 mL). The first solution was added to the latter in a sealed vial, stirred briefly and it was kept for three days without light exposure.

$^1\text{H ssNMR}$ (MAS, 600 MHz): $\delta = 6.6, 2.5, 0.9$ ppm.

$^{13}\text{C ssNMR}$ (CP-MAS, 151 MHz): $\delta = 154.1, 149.4, 137.8, 126.8, 120.2, 46.8, 42.6, 26.5, 17.9$ ppm.

IR (ATR): $\nu = 1700$ (w), 1622 (w), 1593 (w), 1507 (w), 1463 (m), 1250 (w), 1137 (w), 1011 (w), 970 (w), 811 (vs), 743 (w), 683 (w), 655 (w), 538 (w) cm^{-1} .

Motor Polymer ($m_{100}\text{-P}$)

The motor polymer was synthesized similar to the above-mentioned procedure, but without the addition of the spacer amine and an increased amount of motor amine **1** (97.4 mg, 185 μmol , 3.0 equiv.).

$^1\text{H ssNMR}$ (MAS, 600 MHz): $\delta = 6.5, 2.4, 0.8$ ppm.

$^{13}\text{C ssNMR}$ (CP-MAS, 151 MHz): $\delta = 148.5, 137.7, 126.6, 41.6, 18.2$ ppm.

IR (ATR): $\nu = 1702$ (w), 1619 (w), 1589 (w), 1508 (w), 1460 (m), 1406 (w), 1249 (w), 1139 (w), 1012 (w), 969 (w), 810 (vs), 756 (w), 683 (w), 656 (w), 538 (w) cm^{-1} .

Spacer Polymer ($m_0\text{-P}$)

The spacer polymer was synthesized similar to the above-mentioned procedure, but without the addition of the motor amine **1** and an increased amount of spacer amine **4** (69.6 mg, 185 μmol , 3.0 equiv.).

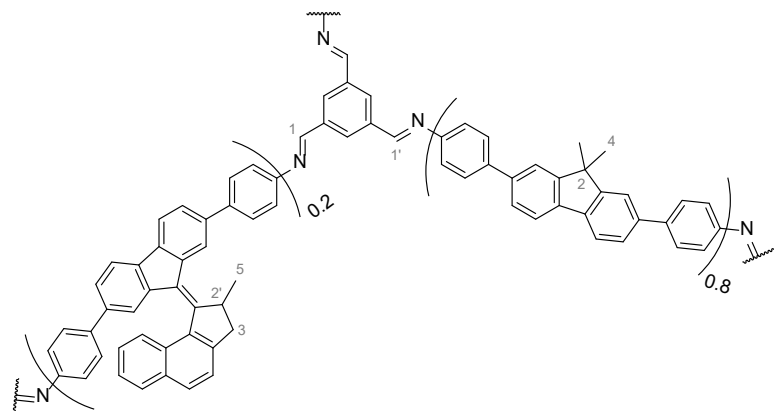
$^1\text{H ssNMR}$ (MAS, 600 MHz): $\delta = 6.7, 0.9$ ppm.

$^{13}\text{C ssNMR}$ (CP-MAS, 151 MHz): $\delta = 156.4, 139.9, 128.8, 122.2, 48.3, 28.3$ ppm.

IR (ATR): $\nu = 1700$ (w), 1623 (w), 1507 (w), 1464 (s), 1250 (w), 1137 (w), 1011 (w), 971 (w), 812 (vs), 743 (w), 683 (w), 654 (w), 566 (w), 538 (w), 467 (w) cm^{-1} .

9.3.2.3 COF Synthesis

m₂₀-COF



A mixture of 1,3,5-triformyl benzene (6.5 mg, 40 μ mol, 2.0 equiv.), spacer **4** (18.1 mg, 48 μ mol, 2.4 equiv.) and motor **1** (6.3 mg, 12 mmol, 0.6 equiv.) in mesitylene (2 mL) and aqueous 6 M AcOH (0.2 mL) was heated at 110 °C for 72 h. The precipitate was collected via suction filtration, washed with DMF (10 mL), THF (10 mL) and MeOH (10 mL) and extracted with MeOH in a Soxhlet extractor for 24 h. Supercritical point drying with CO₂ afforded **m₂₀-COF** (27.1 mg, 90%) as an orange-brown solid.

¹H ssNMR (MAS, 600 MHz): δ = 6.9 (H-1, H-1', H-Ar), 1.1 (H-3, H-4, H-4', H-5) ppm.

¹³C ssNMR (CP-MAS, 151 MHz): δ = 154.6 (C-1, C-1'), 148.9, 137.7, 127.2, 121.2, 46.5 (C-2, C-2'), 41.9 (C-3), 26.6 (C-4), 17.8 (C-5) ppm.

IR (ATR): ν = 3031 (w), 2956 (w), 2863 (w), 1703 (w), 1623 (w), 1592 (w), 1507 (w), 1463 (s), 1250 (w), 1138 (w), 1011 (w), 970 (w), 811 (vs), 743 (w), 683 (w), 655 (w), 565 (w), 539 (w) cm^{-1} .

m₁₀ and **m₅-COF** were synthesized under identical conditions to **m₂₀-COF** with adjusted relative amounts of the motor **1** and spacer **4** building blocks (5% motor **1** for **m₅** and 10% motor **1** for **m₁₀-COF**).

m₀-COF (pure spacer COF)

The spacer COF was synthesized similar to the above-mentioned procedure, but without the addition of the motor **1** and an increased amount of spacer **4** (22.6 mg, 60 μ mol, 3.0 equiv.).

¹H ssNMR (MAS, 600 MHz): δ = 6.8, 0.8 ppm.

¹³C ssNMR (CP-MAS, 151 MHz): δ = 154.2, 150.3, 137.8, 126.8, 120.4, 46.1, 26.1 ppm.

IR (ATR): $\tilde{\nu}$ = 2981 (w), 1701 (w), 1625 (w), 1596 (w), 1508 (w), 1464 (s), 1250 (w), 1139 (w), 1011 (w), 971 (w), 812 (vs), 743 (w), 715 (w), 684 (w), 655 (w), 565 (w), 538 (w), 468 (w) cm^{-1} .

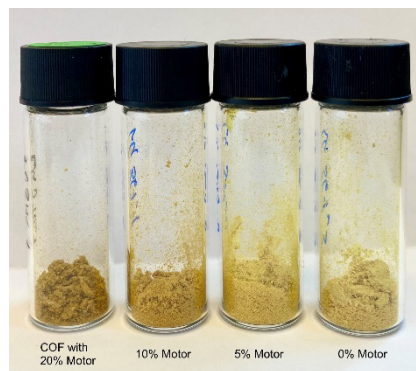


Figure S 9.3-1: Photograph of the synthesized COF samples with different fractions of motor building block. Increased motor content causes a red shift in absorption of the resulting COF.

9.3.3 UV-Vis Spectra

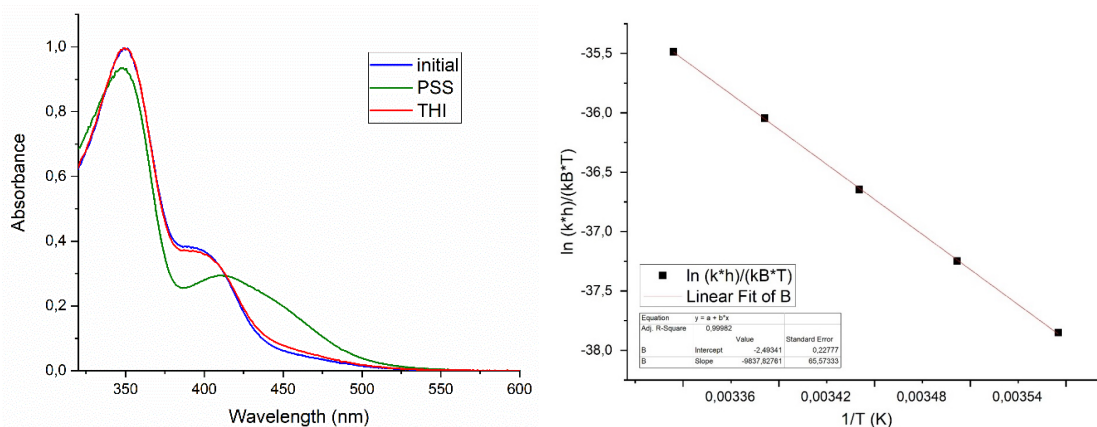


Figure S 9.3-2: **Left:** UV-Vis absorption spectrum of amine motor **1** in acetonitrile (1×10^{-5} M) at 5 °C, initially (blue), after irradiation with 365 nm to the photostationary state (PSS, green) and after thermal relaxation of the metastable state (THI, red). **Right:** Eyring plot analysis of the thermal isomerisation of amine motor **1** from metastable isomer to stable isomer in acetonitrile.

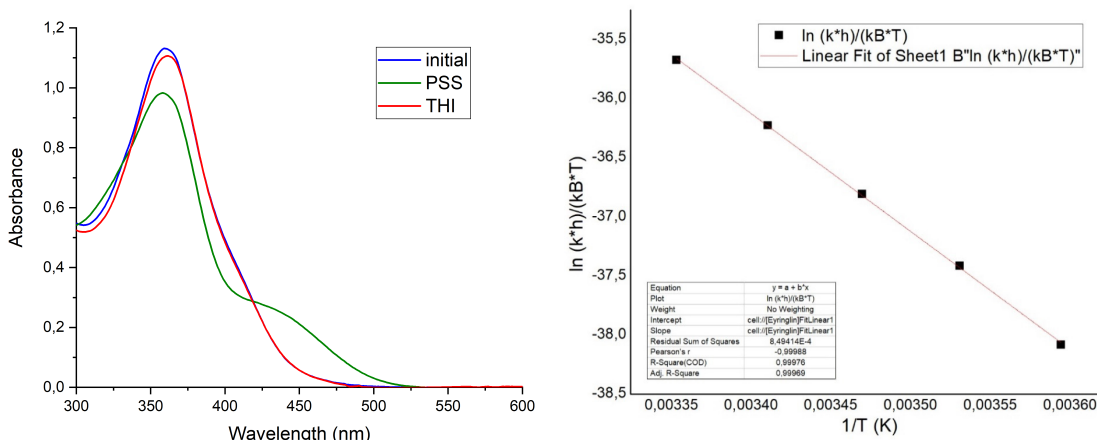


Figure S 9.3-3: **Left:** UV-Vis absorption spectrum of imine motor **2** in acetonitrile (0.7 mm) at 5 °C, initially, after irradiation with 365 nm to the photostationary state and after thermal relaxation of the metastable state. **Right:** Eyring plot analysis of the thermal isomerisation of imine motor **2** from metastable isomer to stable isomer in acetonitrile.

9.3.4 FT-IR Spectra

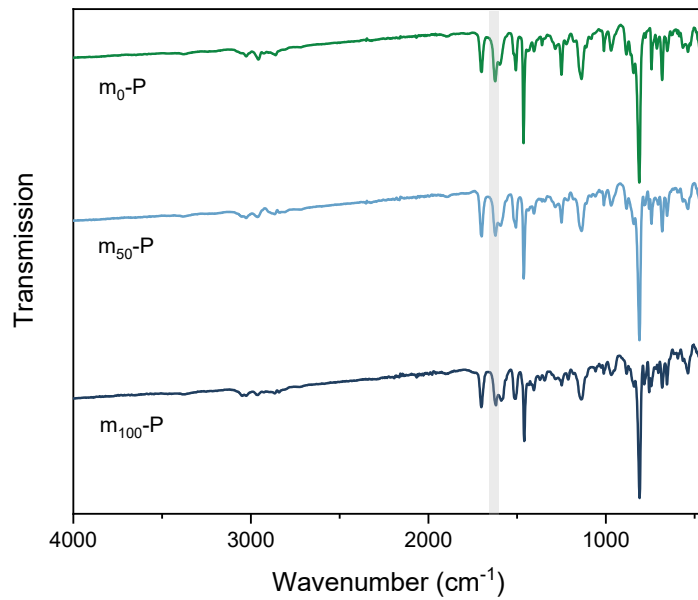


Figure S 9.3-4: FT-IR spectra of **m₀-polymer** (green), **m₅₀- polymer** (light blue) and **m₁₀₀-polymer** (dark blue). Grey area highlights imine C=N vibration bands.

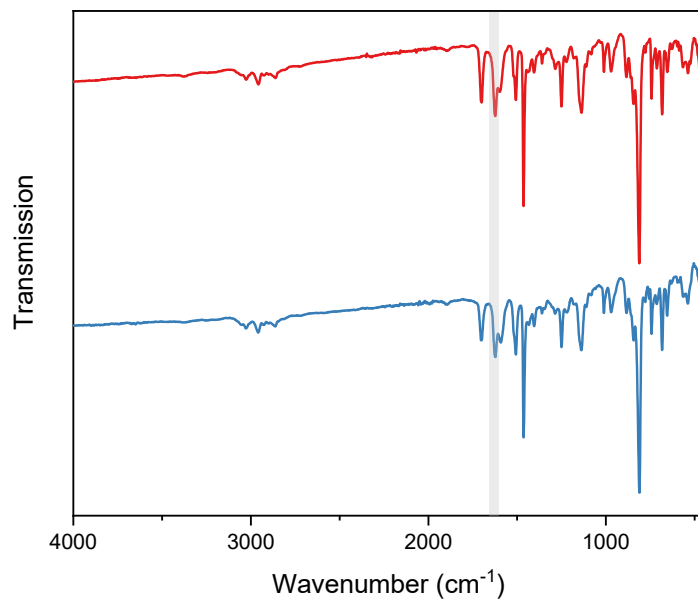


Figure S 9.3-5: FT-IR spectra of **m₀-Polymer** (red) and **m₂₀-COF** (blue). The spectra do not show significant differences, underlining their compositional relation. Grey area highlights imine C=N vibration bands.

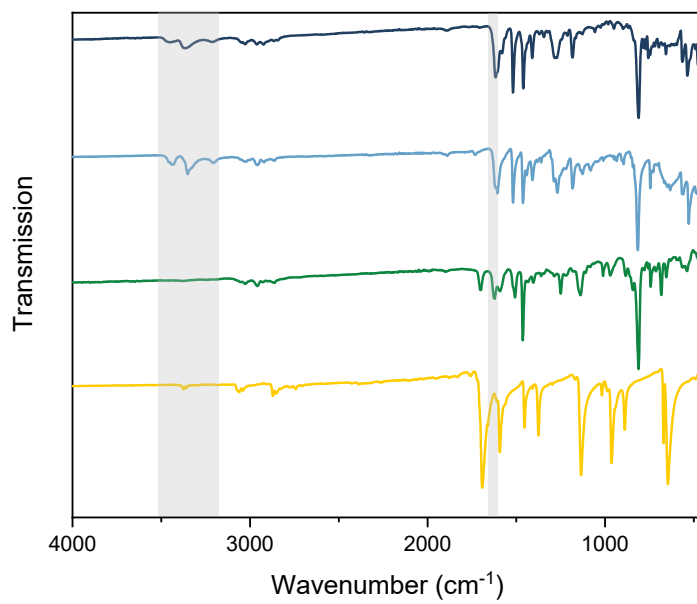


Figure S 9.3-6: FT-IR spectra of motor building block (dark blue), spacer building block (light blue), **m₂₀-COF** (green) and aldehyde building block (yellow). The absence of amine (N-H) and simultaneous appearance of imine (C=N) vibration bands in the COF underlines the successful condensation of the starting materials. Grey areas highlight aldehyde C-H, amine N-H and imine C=N vibration bands.

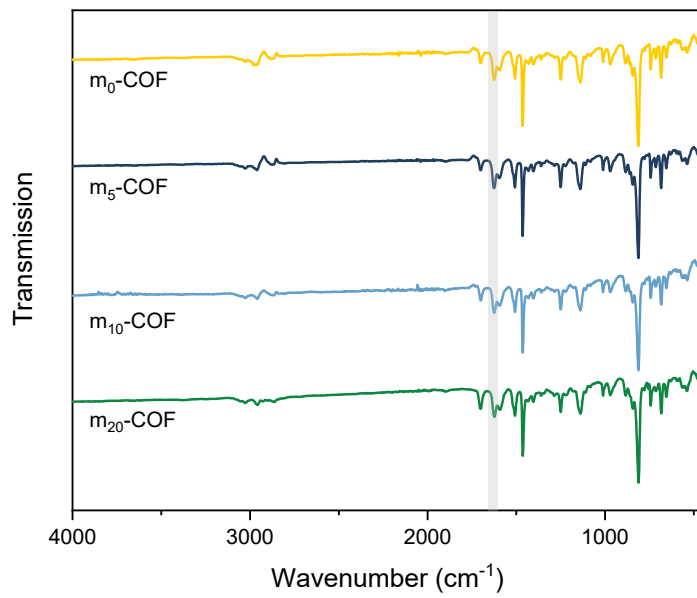


Figure S 9.3-7: FT-IR spectra of COFs with various motor content. Grey area highlights imine C=N vibration bands.

9.3.5 Raman Spectra

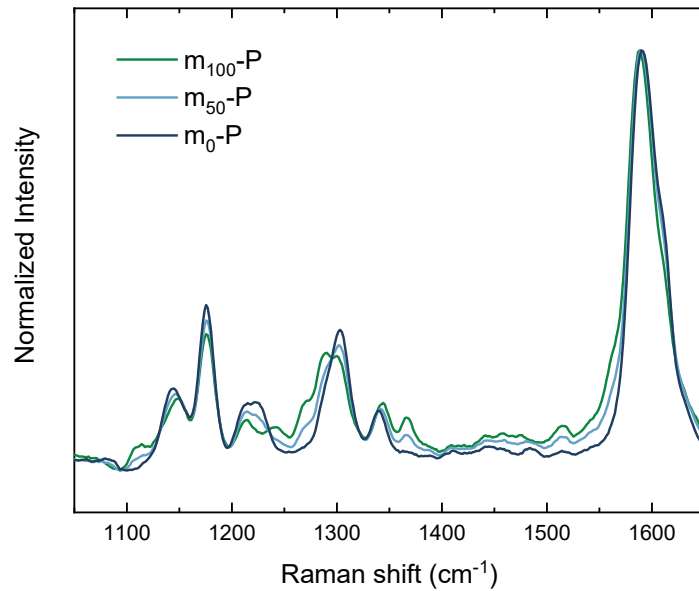


Figure S 9.3-8: Raman spectra (785 nm) of various motor containing polymers.

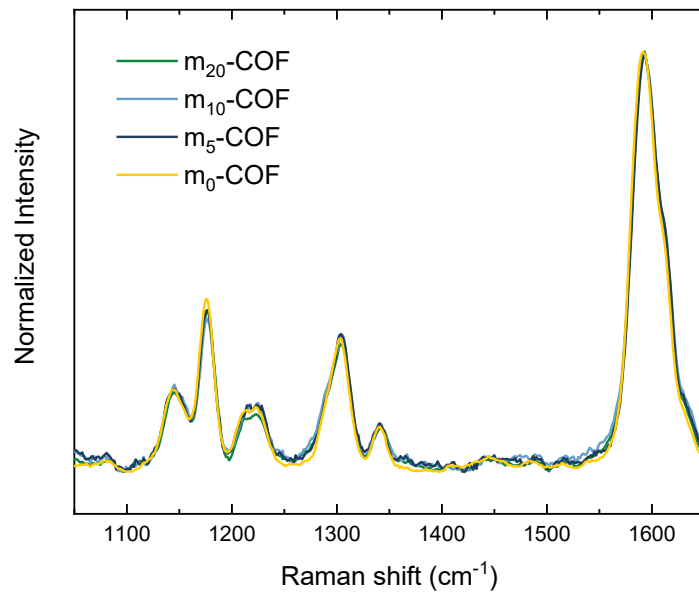


Figure S 9.3-9: Raman spectra (785 nm) of various motor containing COFs. Additional bands could not be attributed to the motor unit, due to the low motor content in the materials.

9.3.6 XRPD Data and Structure Modeling

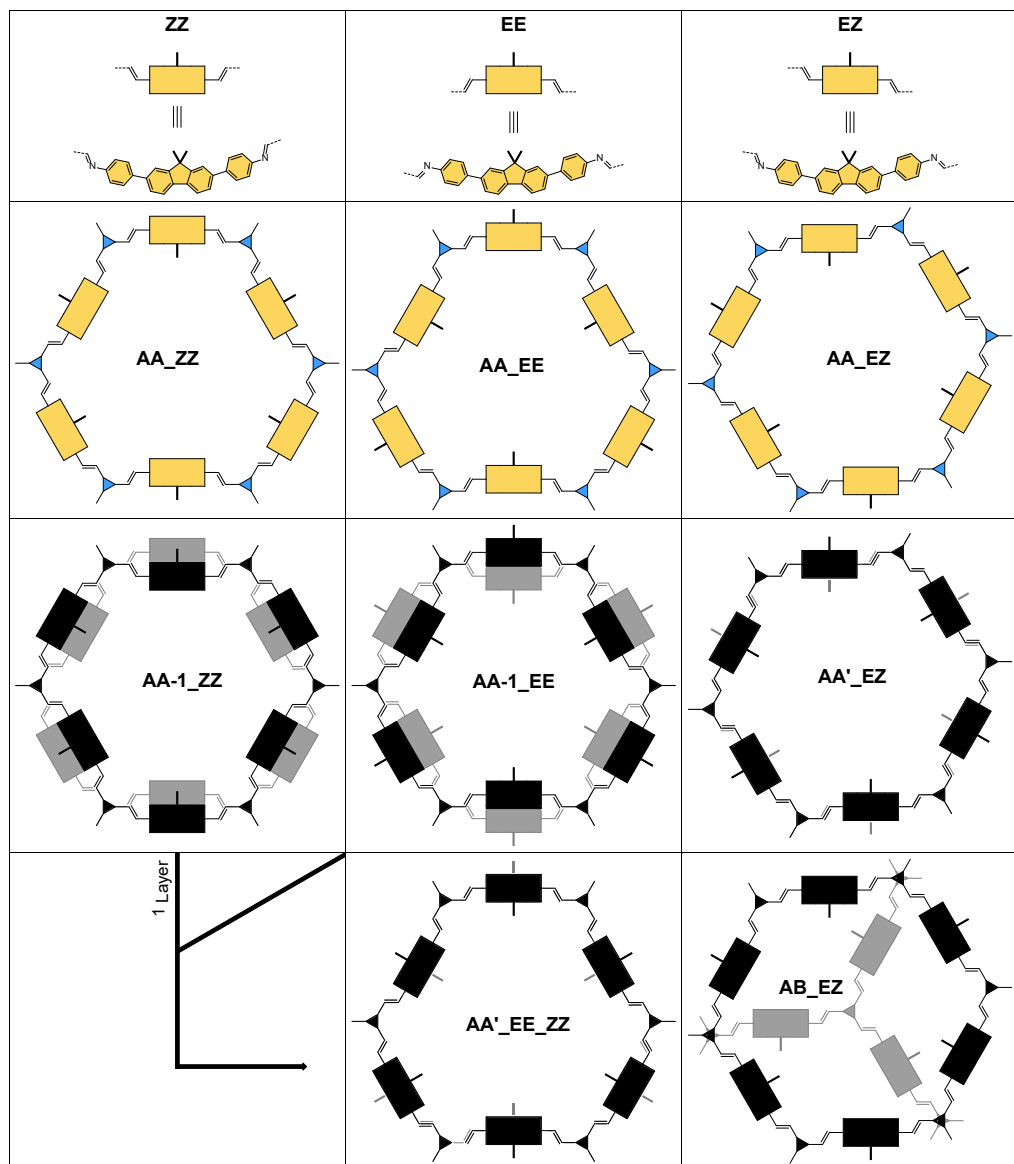


Figure S 9.3-10: A collection of possible stacking modes with a simplified pure-spacer COF pore are shown. The structures differ in imine-bond conformation (EE/ZZ/EZ/EE+ZZ) and eclipsed (AA/AA'/AA-1) or staggered (AB) stacking of the layers. To visualize the effect of imine-conformation on the position of the methyl groups, first (black) and second layer (grey) are colored. Depending on the conformation, sterically demanding methyl groups of the building block can either point in the same direction (AA structures) or in opposite directions, impacting interlayer π - π interactions which are mostly inhibited in AA structures, AA-1_ZZ and weak for AB_EZ. AA-1_EE as well as both AA' structures benefit from an alternating configuration of methyl groups pointing towards the pore channel, which enables interaction of the aromatic systems across the layers. A comparison of these structures also highlights that the apparent pore-diameter is not only defined by the building blocks but also based on imine-bond orientation and stacking of the layers. In AA and AA' the imine bonds between layers are fully eclipsed (parallel), whereas in AA-1 structures these bonds point in opposite directions.

Table S 9.3-1: Comparison of selected stacking models for a simplified pure-spacer COF. The cell parameters, pore-diameters (smallest carbon-carbon distance across the pore) and total energies, as obtained from Forcite geometry and cell optimization in Material Studio are shown. The AA-1_EE was selected as the model for the structure refinement.

Model	Cell parameter a/b [Å]	Cell parameter c [Å]	Space group	Pore diameter [Å]	Total energy [kcal/mol]
AA-1_EE	44.35	7.09	$P6_3mcm$	38.63	366.96
AA'_EE_ZZ	44.27	7.17	$P6_2m$	38.74	405.46
AA'_EZ	44.36	7.16	$P6_3m$	38.80	404.65

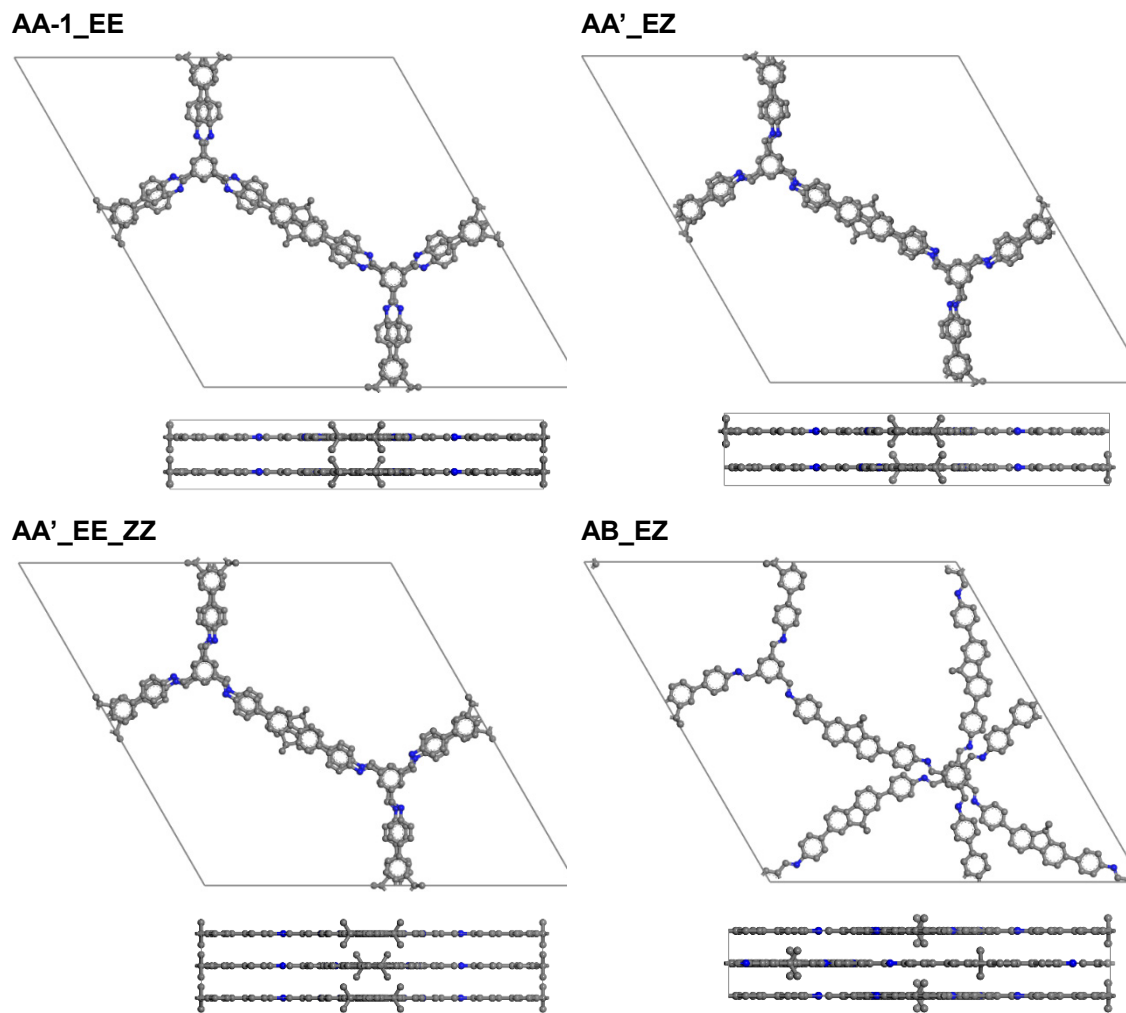
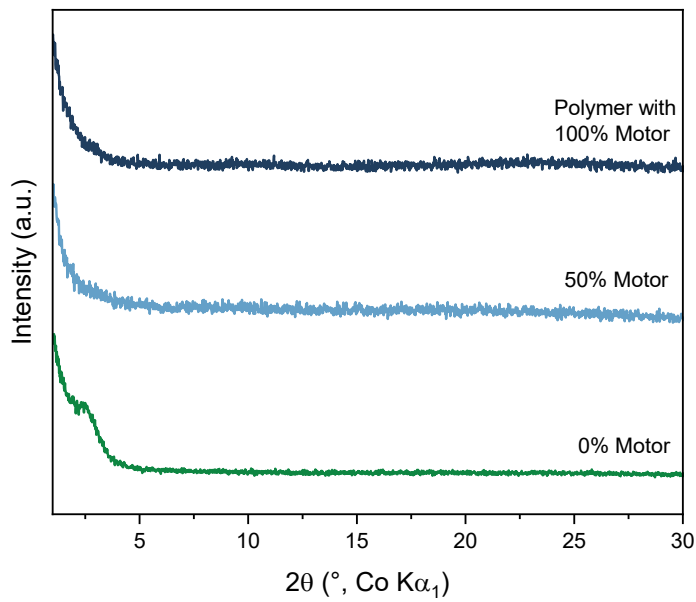
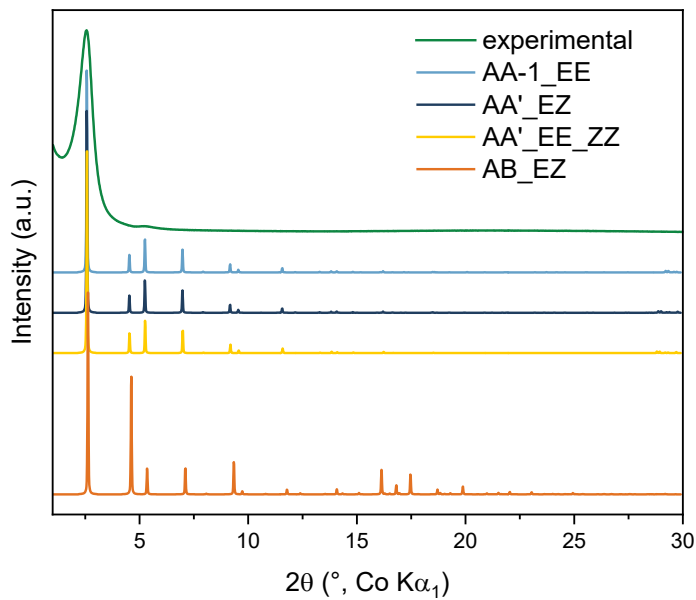


Figure S 9.3-11: Comparison of selected stacking models (unit cells, hydrogen omitted for clarity) for a simplified pure-spacer COF. In all cases except AB_EZ, the synchronization of imine-bonds across the layers allows for acceptable stacking interaction despite the curvature of the substituted fluorene building block. The trade-off between sterically demanding methyl groups and stacking interactions is best met in the AA-1_EE model with lowest total energy. In AA and AA' the imine bonds between layers are fully eclipsed (parallel), whereas in AA-1 structures these bonds point in opposite directions. The curvature of the fluorene fragment together with the steric demand of the methyl groups create different stacking environments and thus imine configurations in the material energetically less favorable (see Table S 9.3-1). In contrast to straight aldehydes in other materials adopting an EZ imine bond configuration, the AA-1_EE configuration is energetically favored for our materials and allows optimal interlayer interactions.



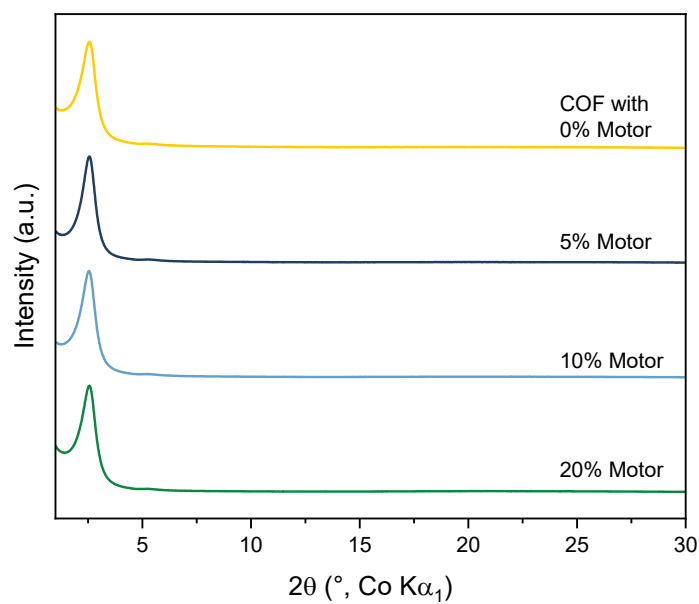


Figure S 9.3-14: XRPD patterns of COFs with various motor content.

9.3.7 Pair Distribution Function (PDF) Analysis

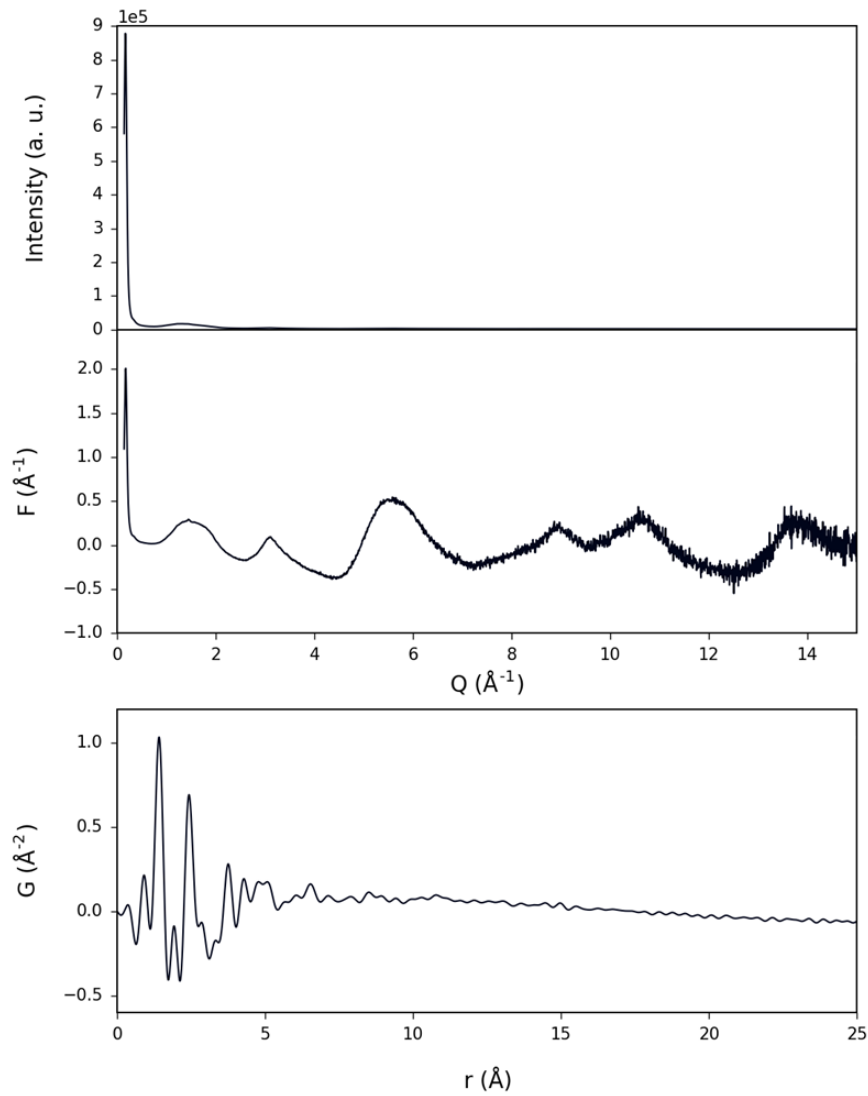


Figure S 9.3-15: Visualization of total scattering intensities (top), reduced structure function (middle), and the resulting pair distribution function (bottom). The 100 Bragg peak indicates in-plane crystallinity of the 2D layers. The resulting PDF shows the characteristic intralayer local structure, and a sloping baseline indicating the presence of some pore structure. Unlike other 2D COFs, we do not observe any interlayer correlations, indicating that there is no coherent relationship between different layers.

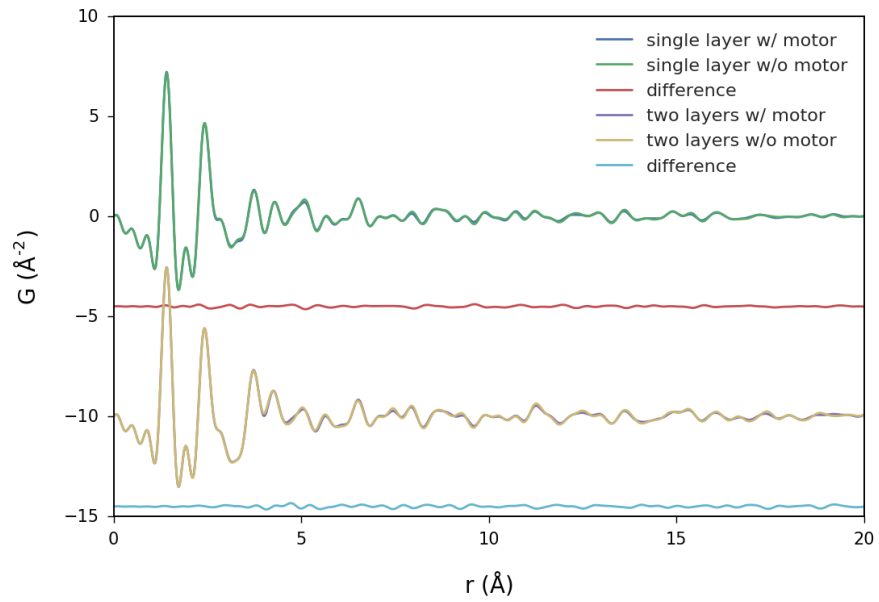


Figure S 9.3-16: Simulations of individual layers (AA-1_EE model) with and without a single motor-unit are compared. There is almost no difference, indicating that the motor units cannot be distinguished without some long range ordering, because the intramolecular bond distances are too similar to the backbone of the structure.

9.3.8 NMR Spectra

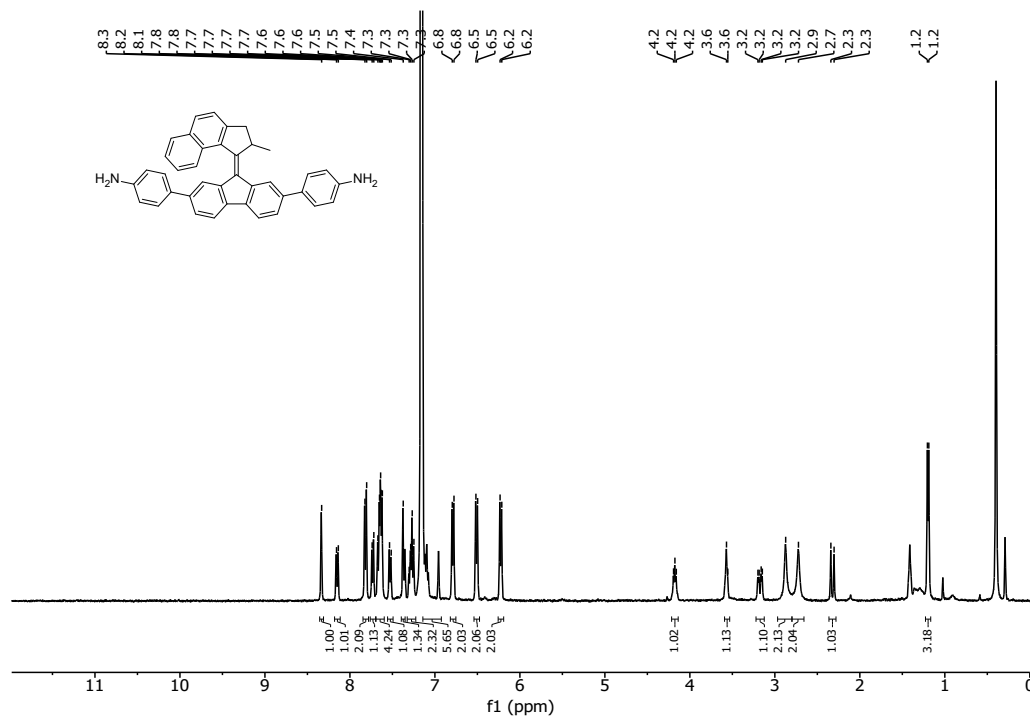


Figure S 9.3-17: ^1H NMR of motor **1** in C_6D_6 .

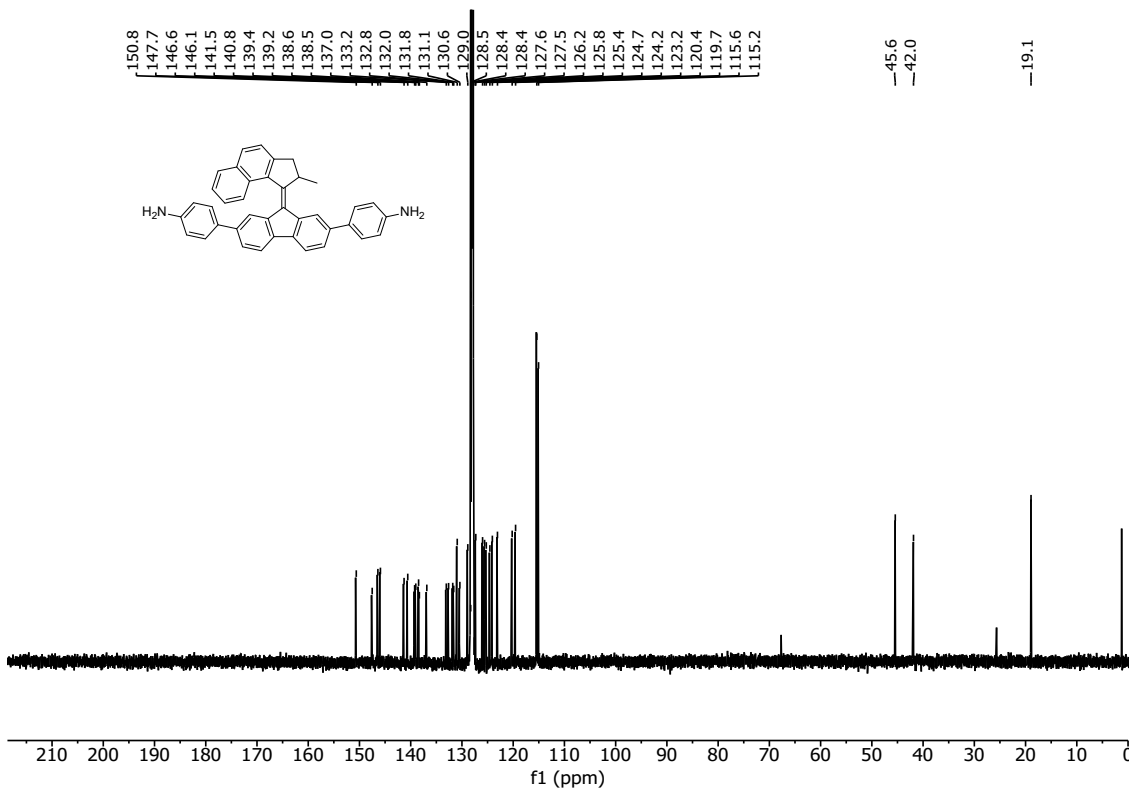
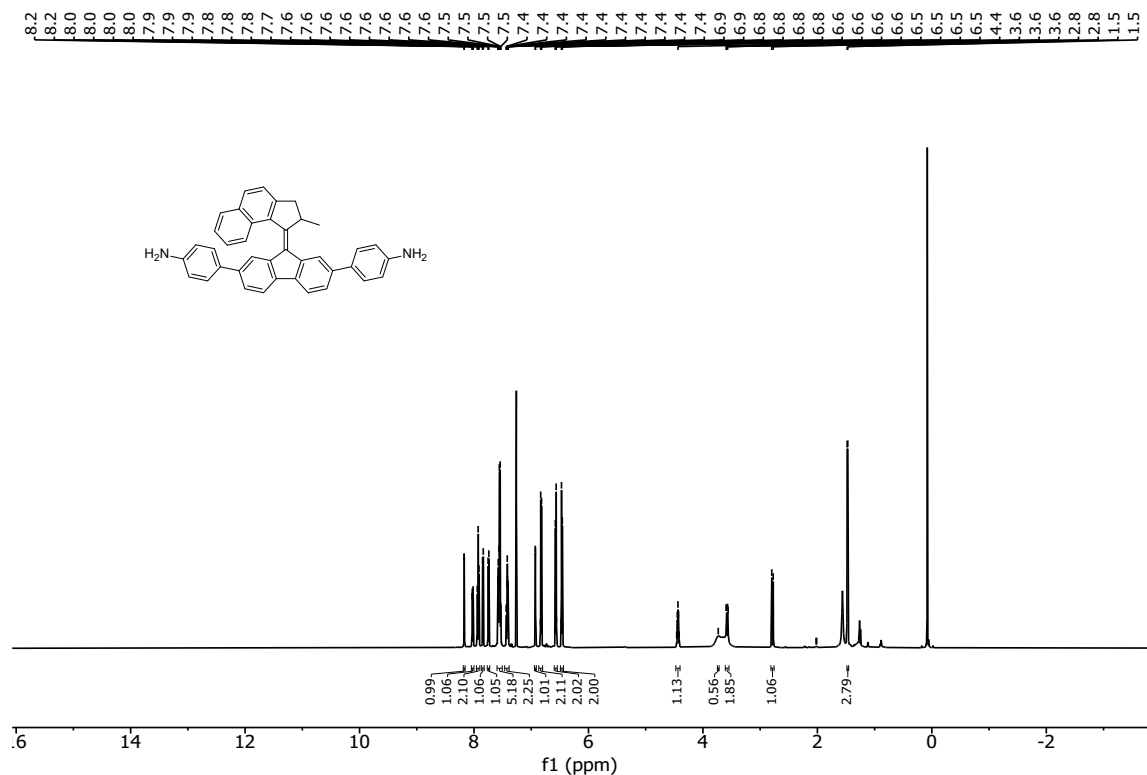
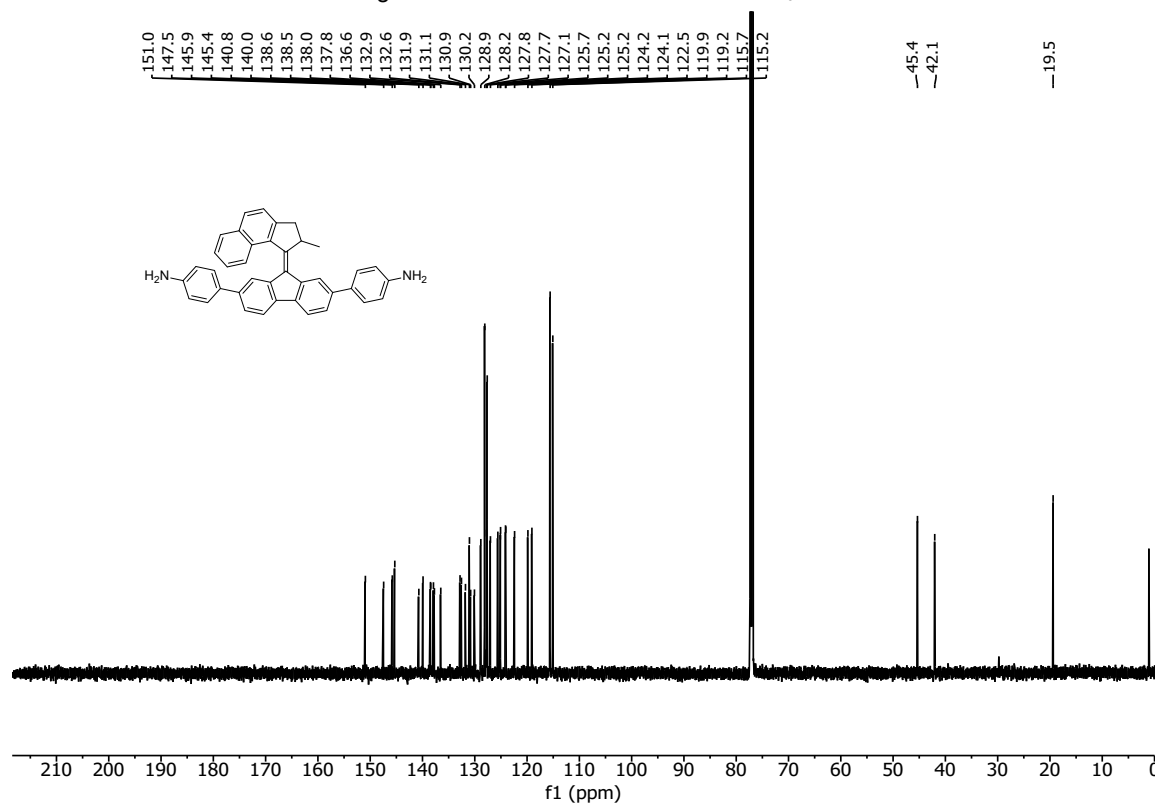


Figure S 9.3-18: ^{13}C NMR of motor **1** in C_6D_6 .

Figure S 21: ^1H NMR of motor **1** in CDCl_3 .Figure S 22: ^{13}C NMR of motor **1** in CDCl_3 .

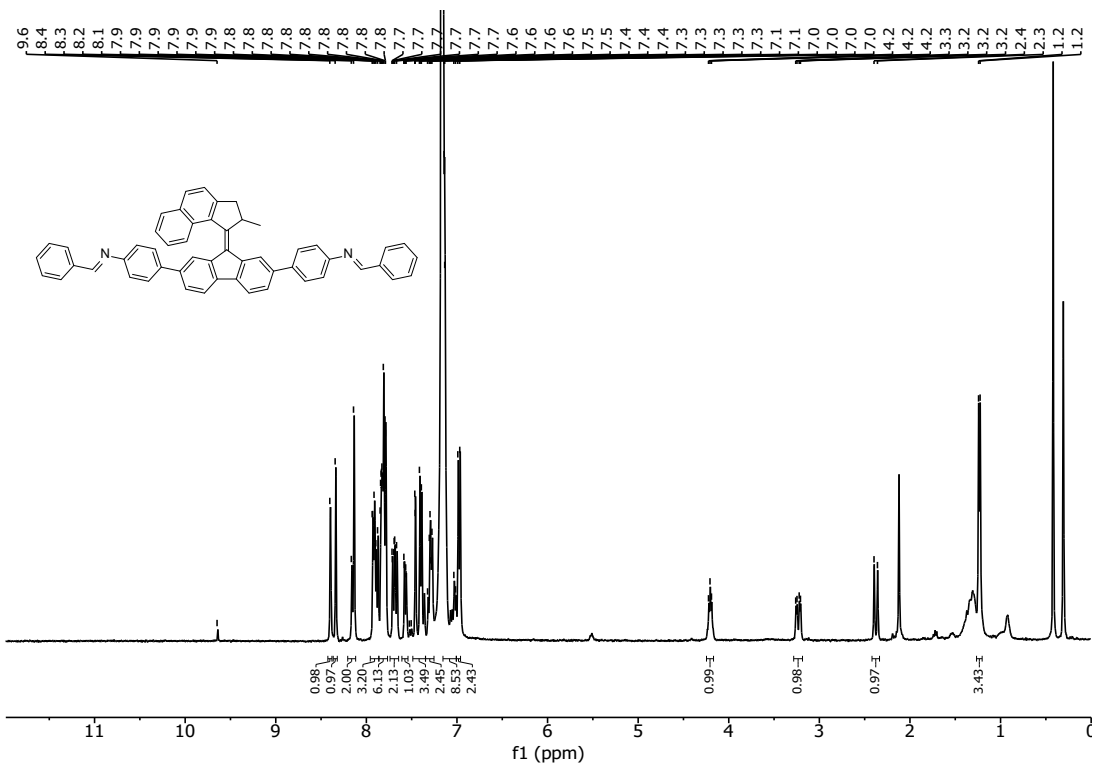


Figure S 9.3-19: ^1H NMR of imine motor **2** in C_6D_6 .

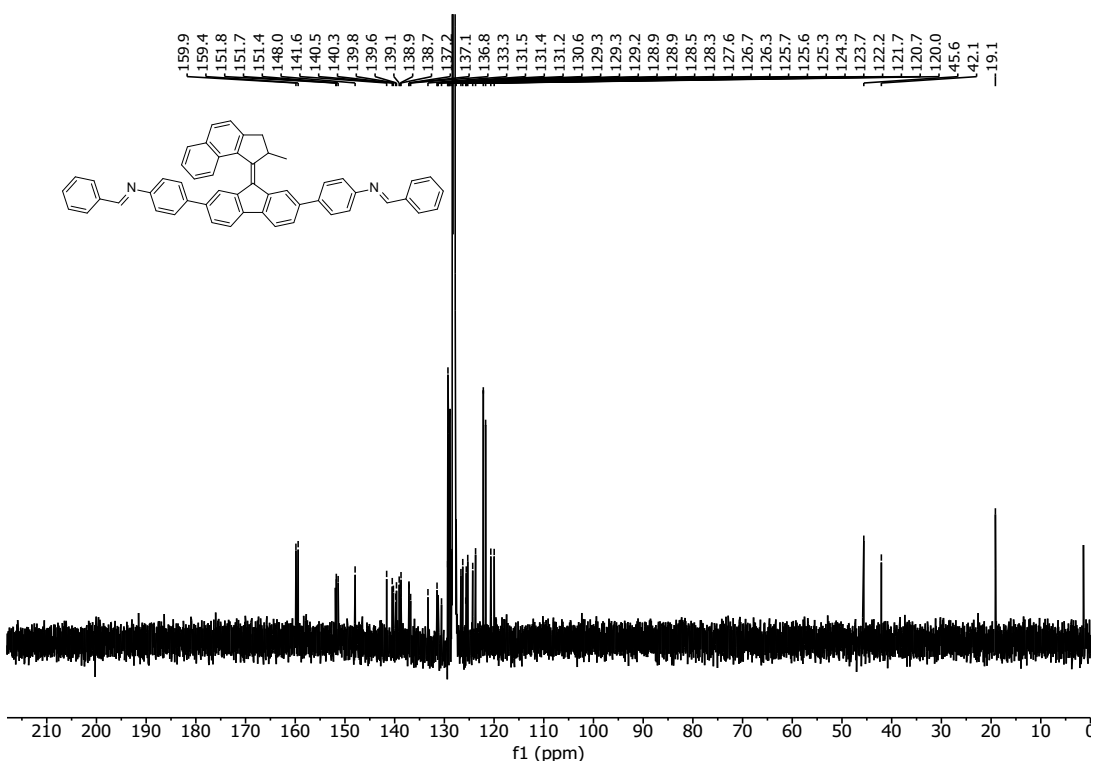
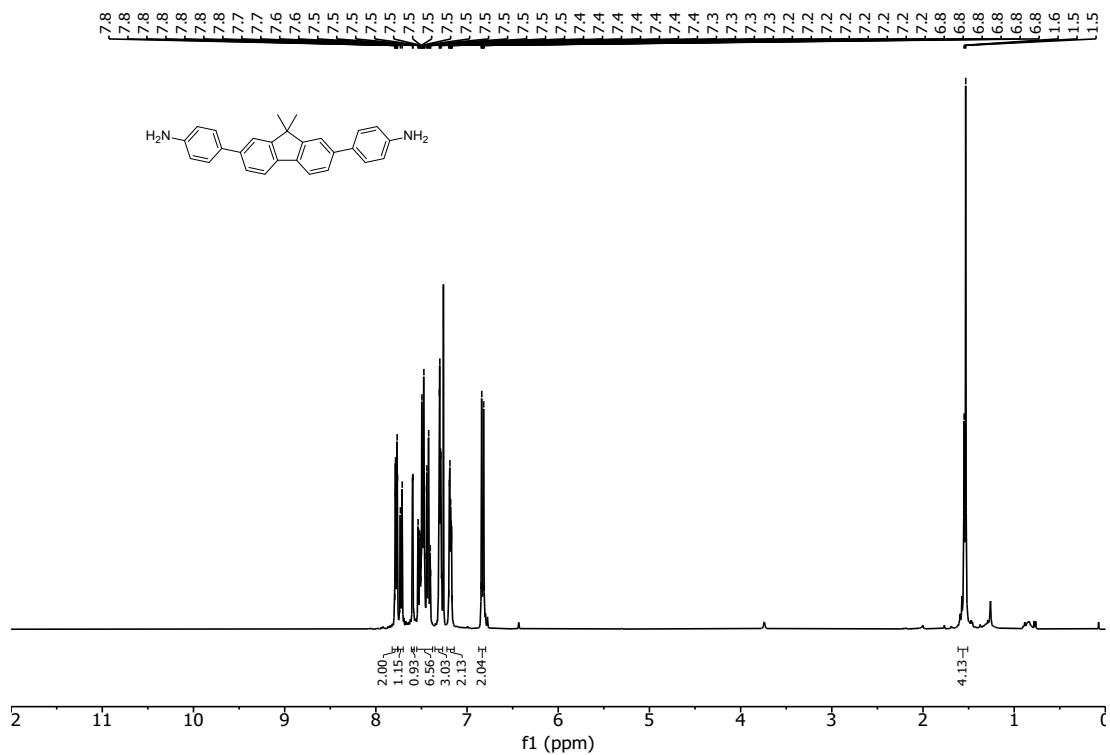
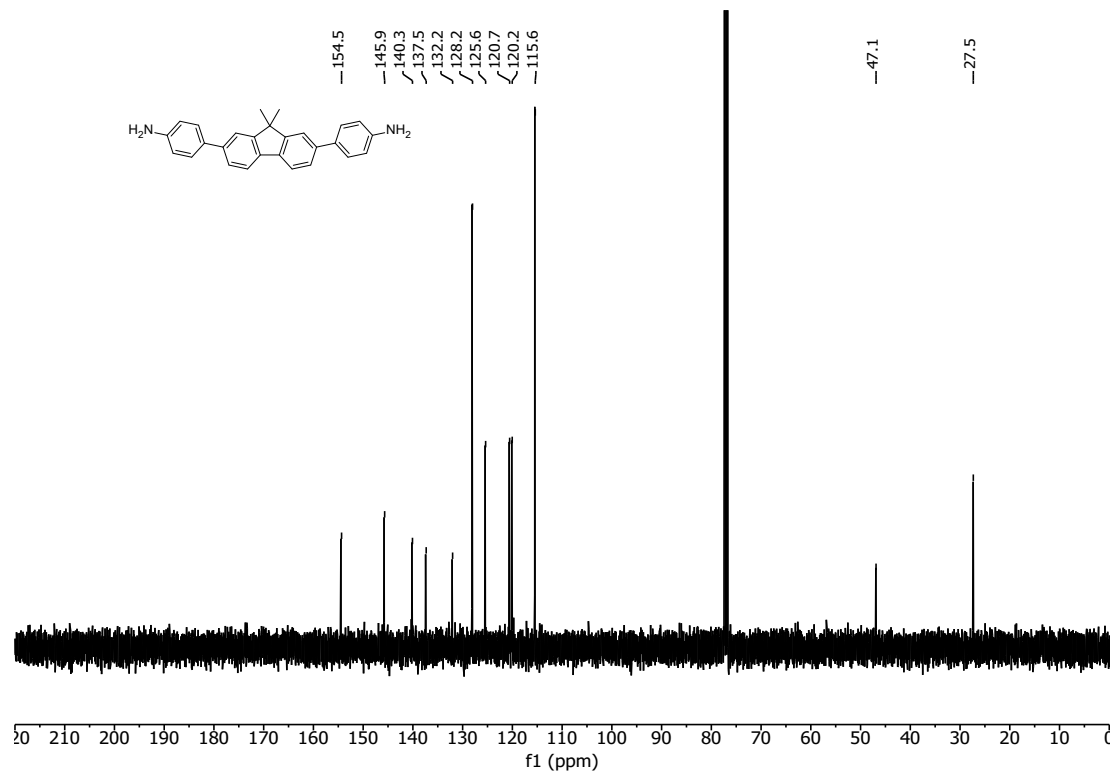


Figure S 9.3-20: ^{13}C NMR of imine motor **2** in C_6D_6 .

Figure S 9.3-21: ^1H NMR of spacer 4 in CDCl_3 .Figure S 9.3-22: ^{13}C NMR of spacer 4 in CDCl_3 .

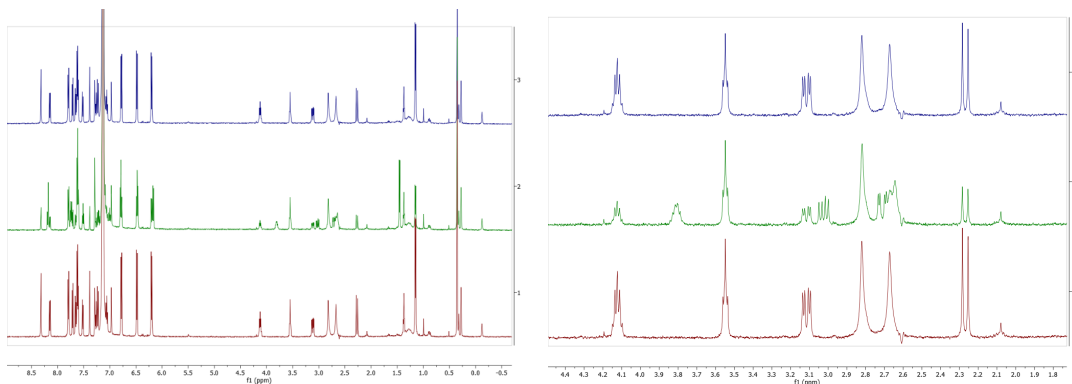


Figure S 9.3-23: ^1H NMR spectra of amine motor **1** in C_6D_6 (4.75 mm) at 10 °C initially (top), after irradiation with 385 nm to the photostationary state of 54:46 (metastable:stable) (middle) and after full thermal relaxation at 10 °C (full spectrum and selected region).

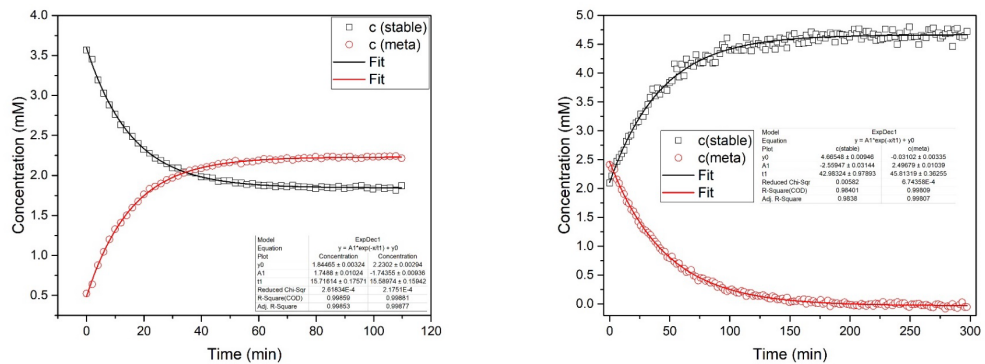


Figure S 9.3-24: Change of concentration of the stable amine motor **1** (black squares) and metastable **1** (red circles) during irradiation with 365 nm at 10 °C (left) and during thermal relaxation at 10 °C (right) in ^1H -NMR (C_6D_6 , 4.75 mm).

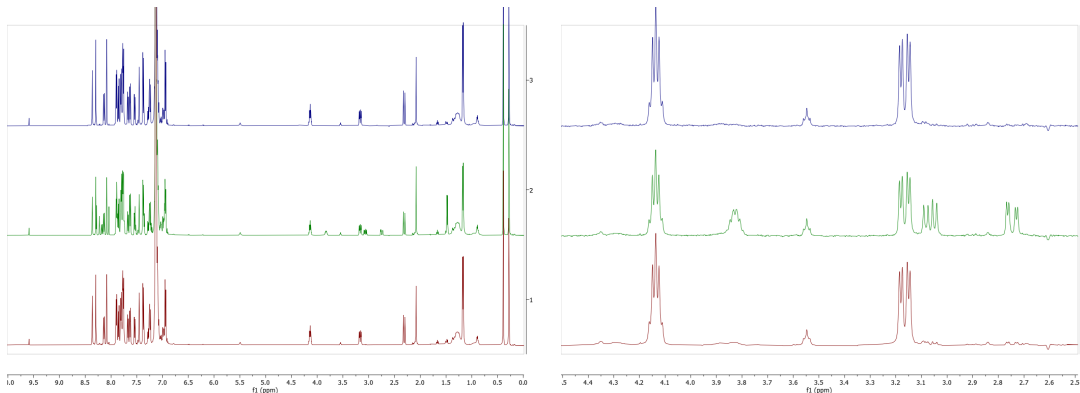


Figure S 9.3-25: ^1H NMR spectra of imine motor **2** in C_6D_6 (9.40 mm) at 10 °C initially (top), after irradiation with 385 nm to the photostationary state of 22:78 (metastable:stable) (middle) and after full thermal relaxation at 10 °C (full spectrum and selected region).

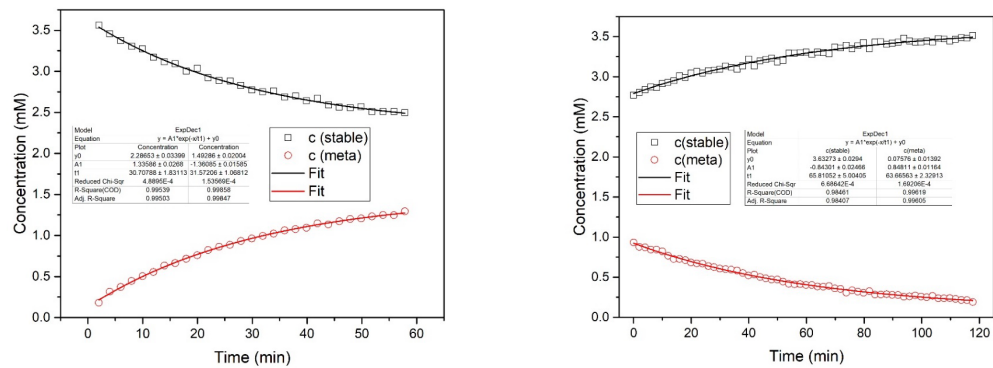


Figure S 9.3-26: Change of concentration of the stable imine motor **2** (black squares) and metastable **2** (red circles) during irradiation with 385 nm at 10 °C (left) and during thermal relaxation at 10 °C (right) in ^1H NMR (C_6D_6 , 4.75 mm).

9.3.9 ssNMR Spectra

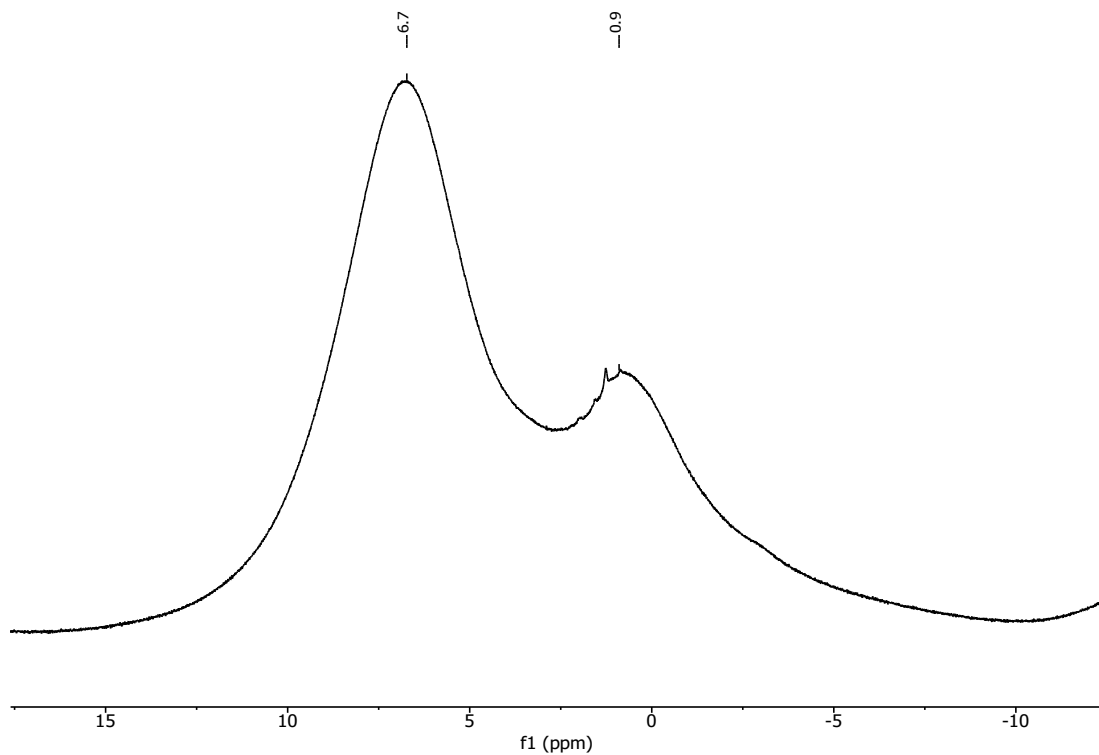


Figure S 9.3-27: ¹H ssNMR MAS spectrum of **m₀-polymer**.

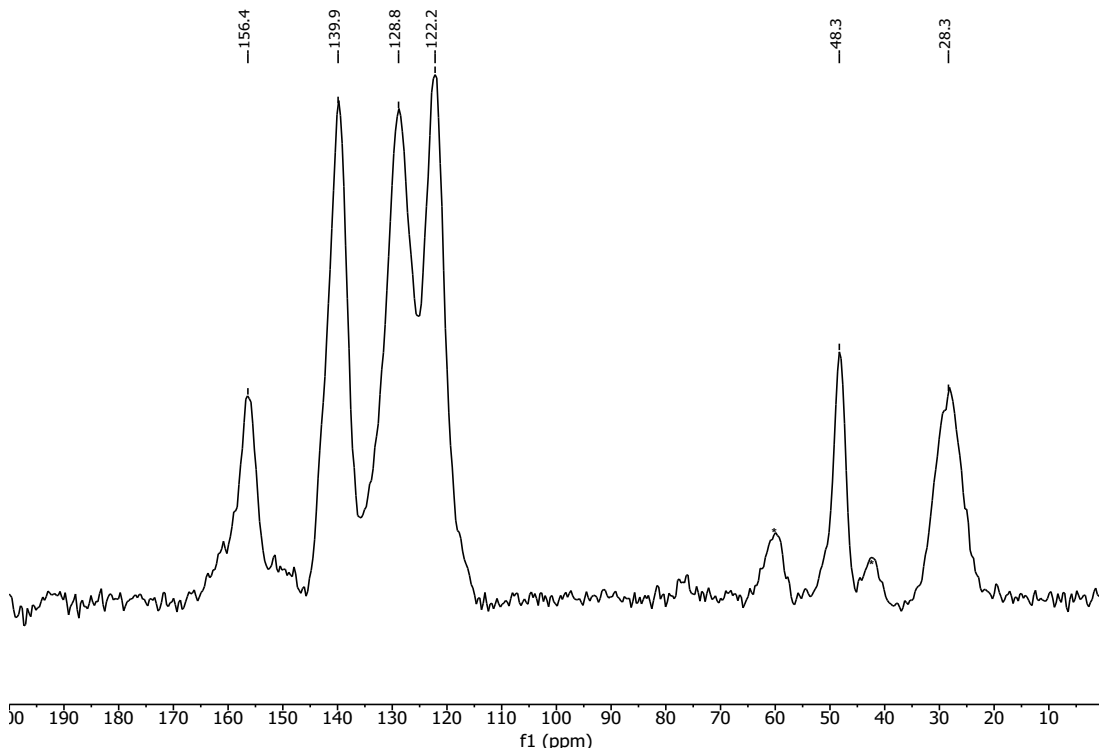


Figure S 9.3-28: ¹³C ssNMR CP-MAS spectrum of **m₀-polymer**. Note that the signals at 60 and 42 ppm are spinning sidebands.

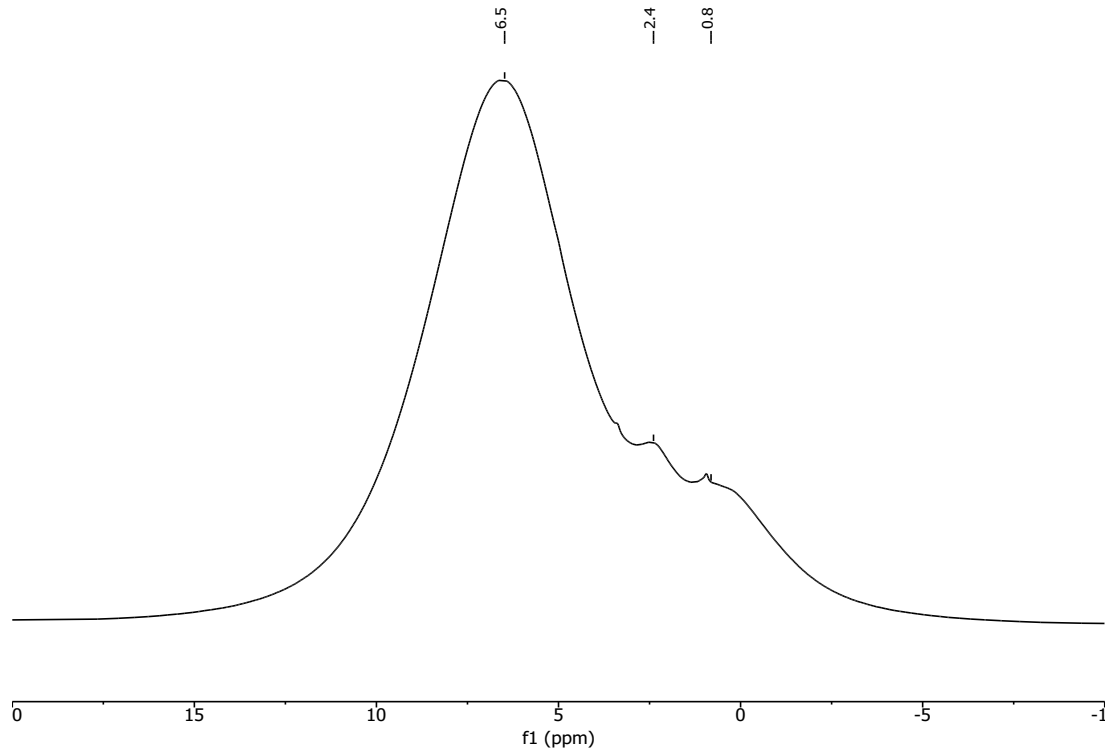


Figure S 9.3-29: ¹H ssNMR MAS spectrum of **m₁₀₀-polymer**.

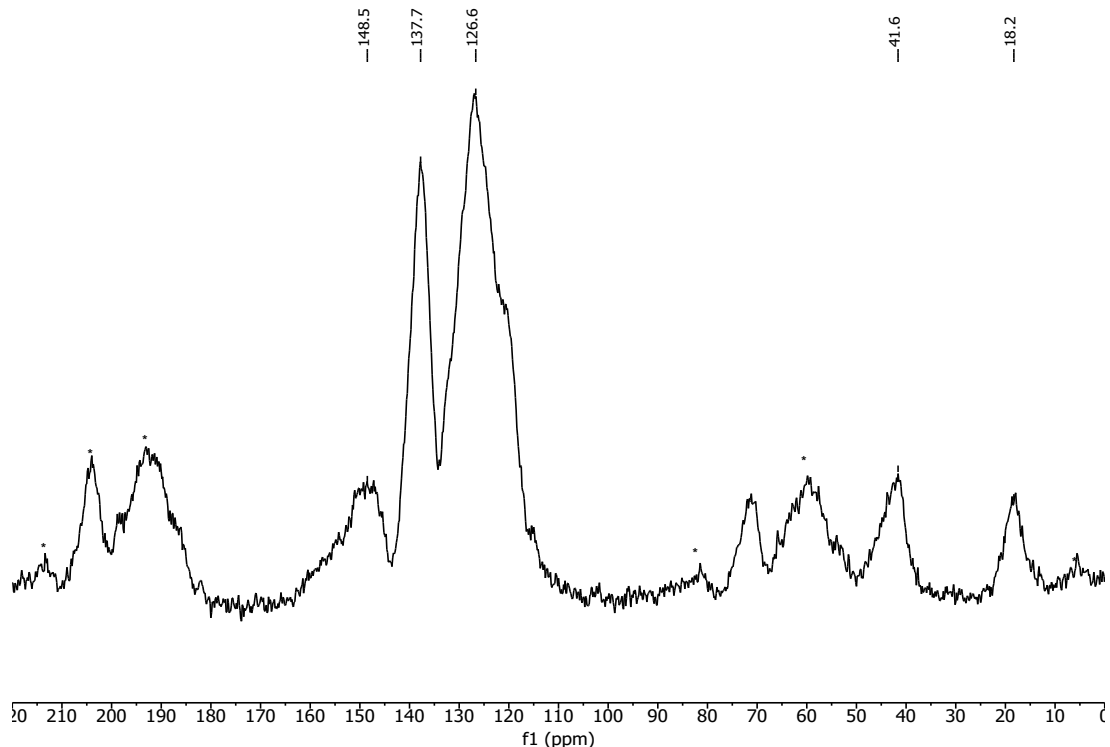


Figure S 9.3-30: ¹³C ssNMR CP-MAS spectrum of **m₁₀₀-polymer**. Asterisks indicate spinning site bands.

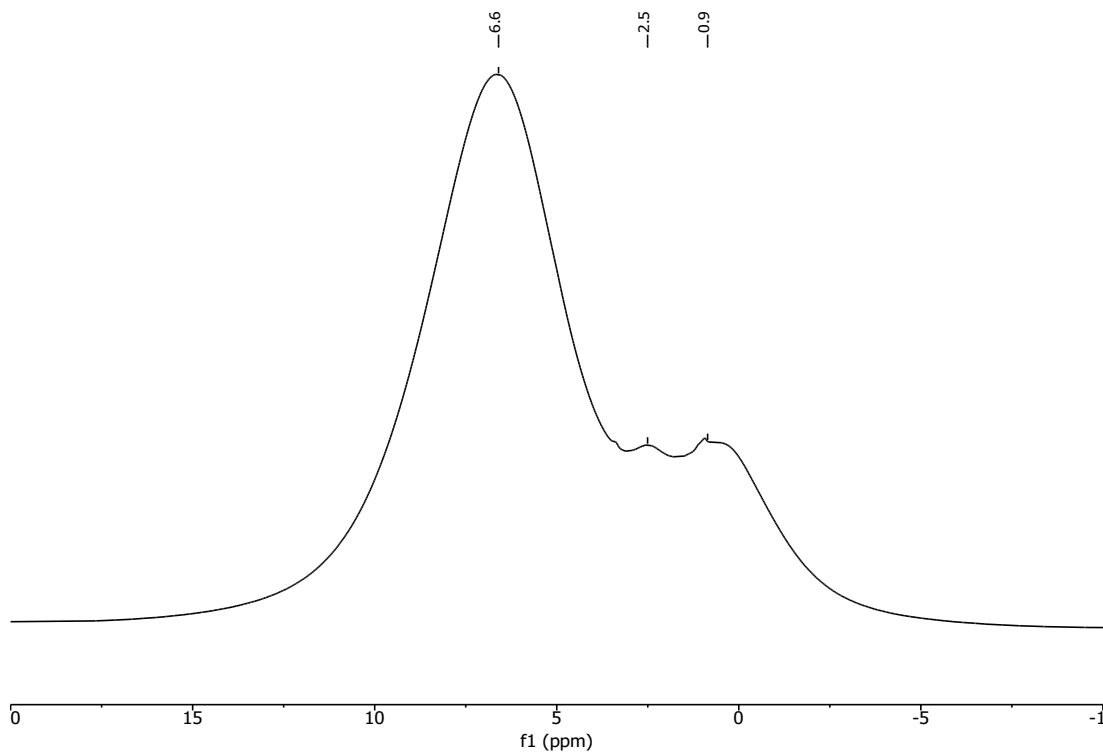


Figure S 9.3-31: ¹H ssNMR MAS spectrum of **m₅₀-polymer**.

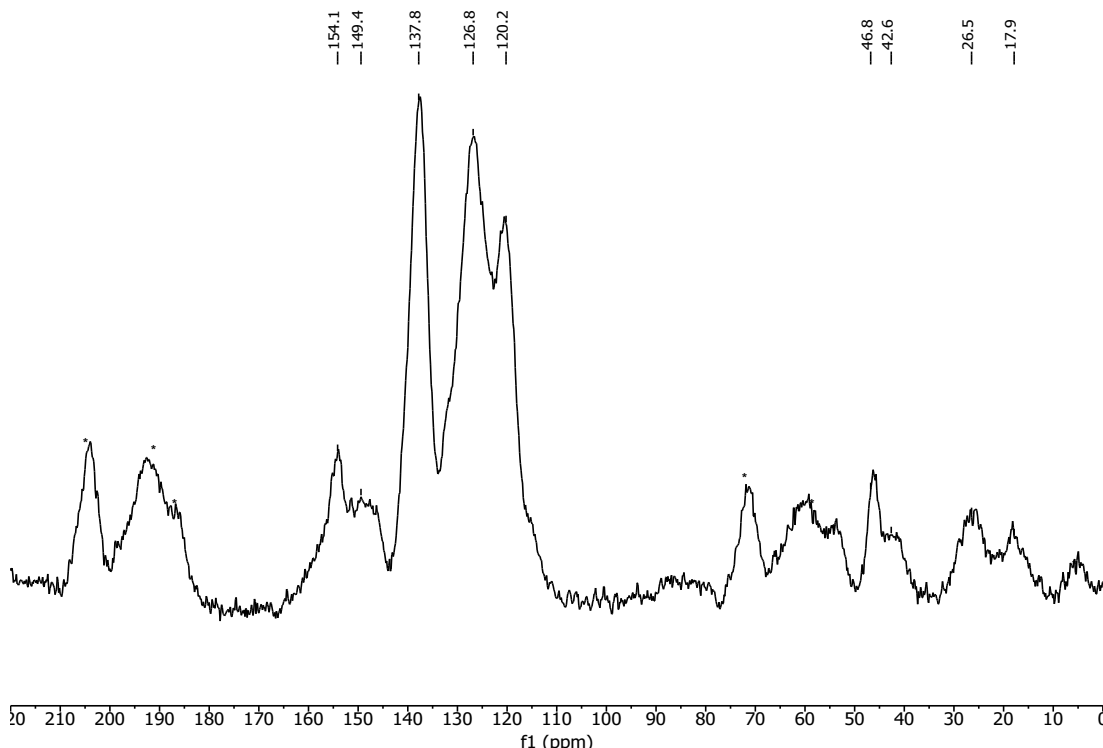


Figure S 9.3-32: ¹³C ssNMR CP-MAS spectrum of **m₅₀-polymer**. Asterisks indicate spinning site bands.

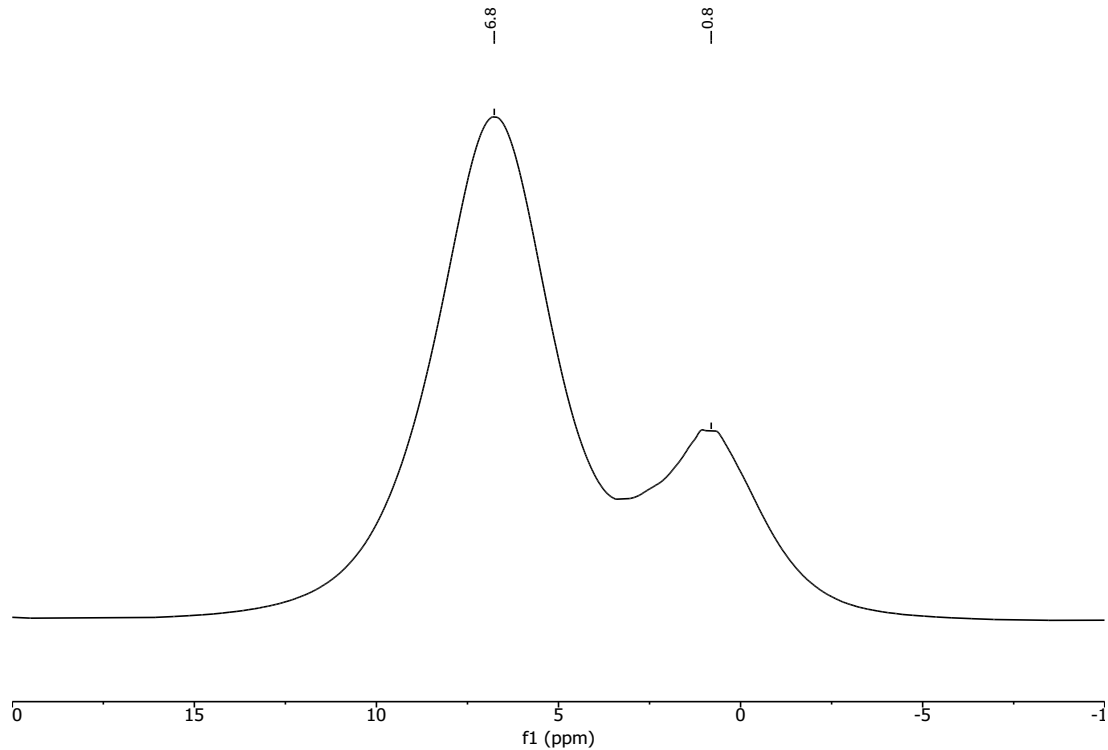


Figure S 9.3-33: ¹H ssNMR MAS spectrum of **m**₀-COF (with 0% amine-motor as building block).

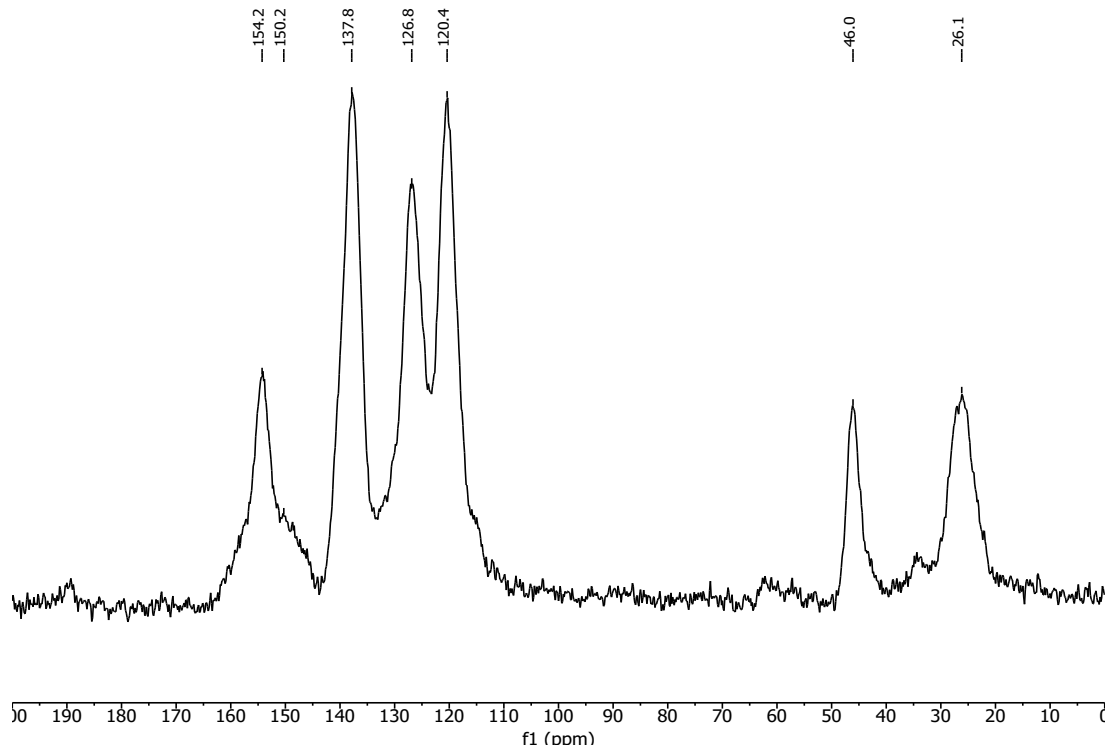


Figure S 9.3-34: ¹³C ssNMR CP-MAS spectrum of **m**₀-COF.

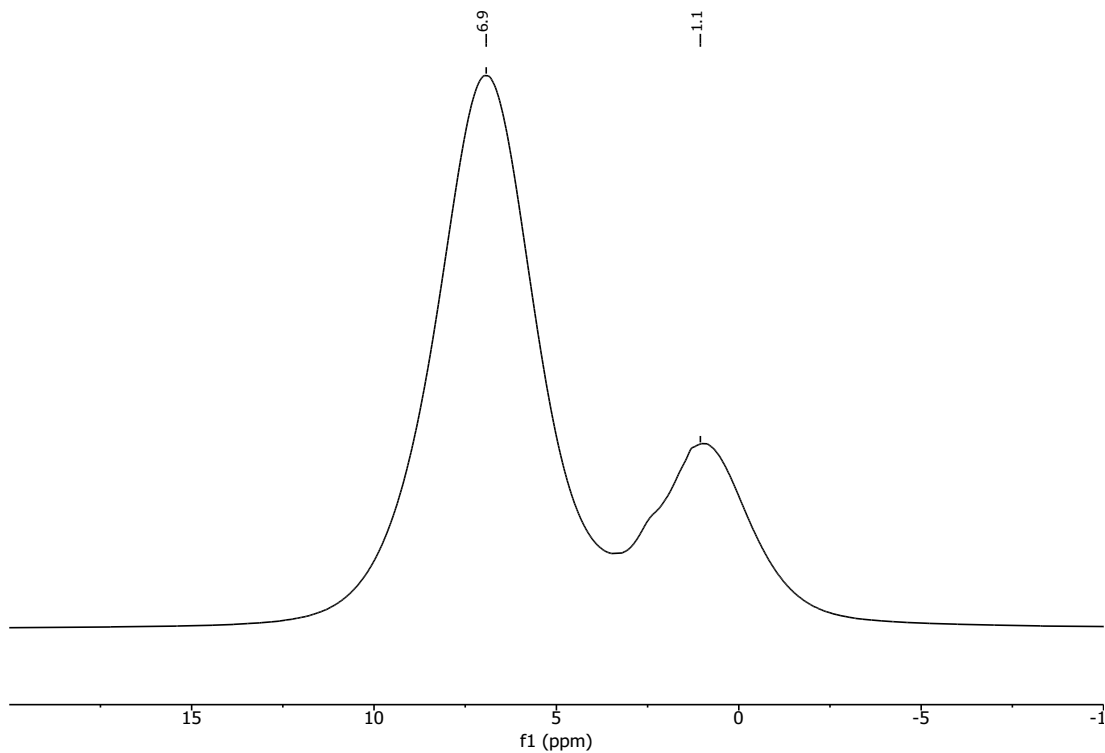


Figure S 9.3-35: ¹H ssNMR MAS spectrum of **m₂₀-COF**.

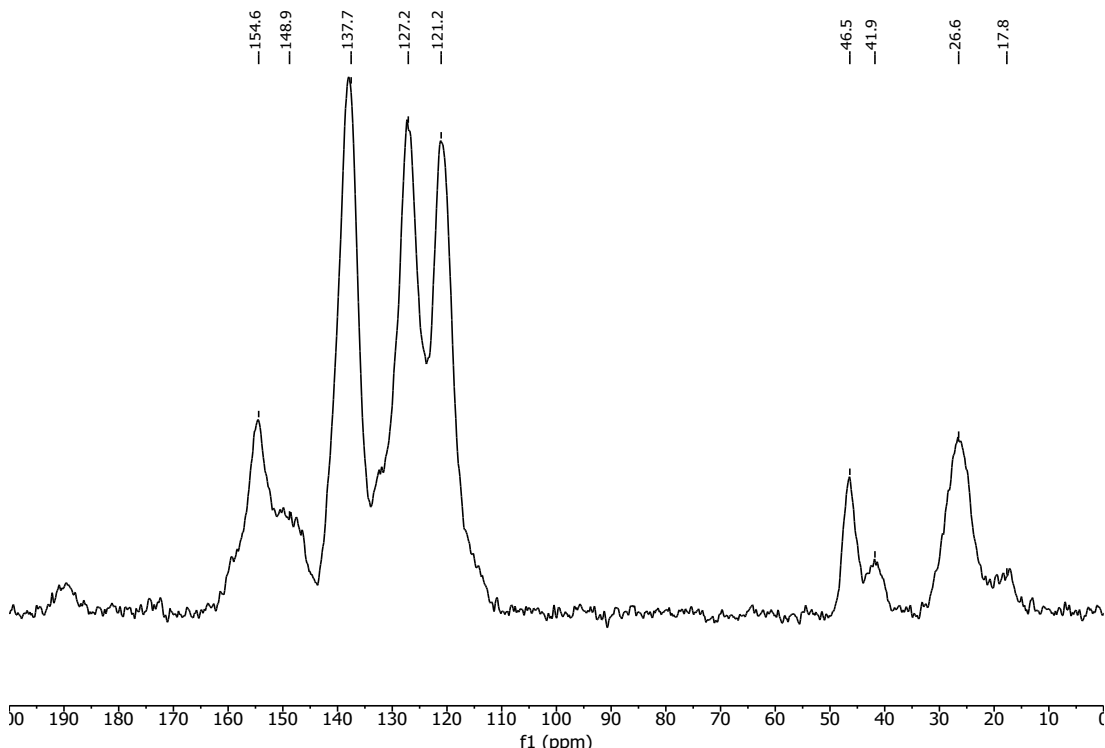


Figure S 9.3-36: ¹³C ssNMR CP-MAS spectrum of **m₂₀-COF**.

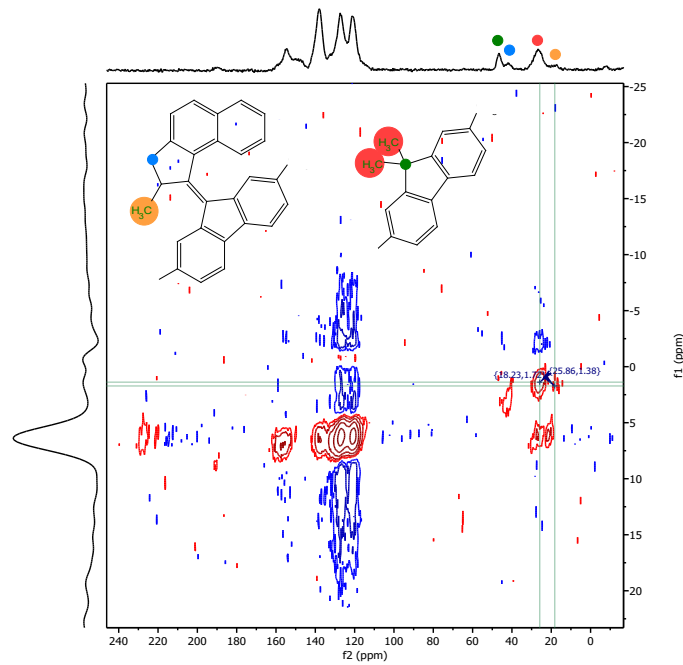


Figure S 9.3-37: $^1\text{H}/^{13}\text{C}$ HETCOR spectrum of **m₂₀-COF** with distinct signals for spacer (green) and motor (blue) moieties. The correlations highlight that the signal at 47 ppm contains intensity for the quaternary carbon of the spacer (green) as well as the allylic carbon of the motor unit. Thus, these peaks cannot be used for the quantitative integration from the direct excitation experiment. Instead, only the methyl groups (orange, red) were used for this analysis.

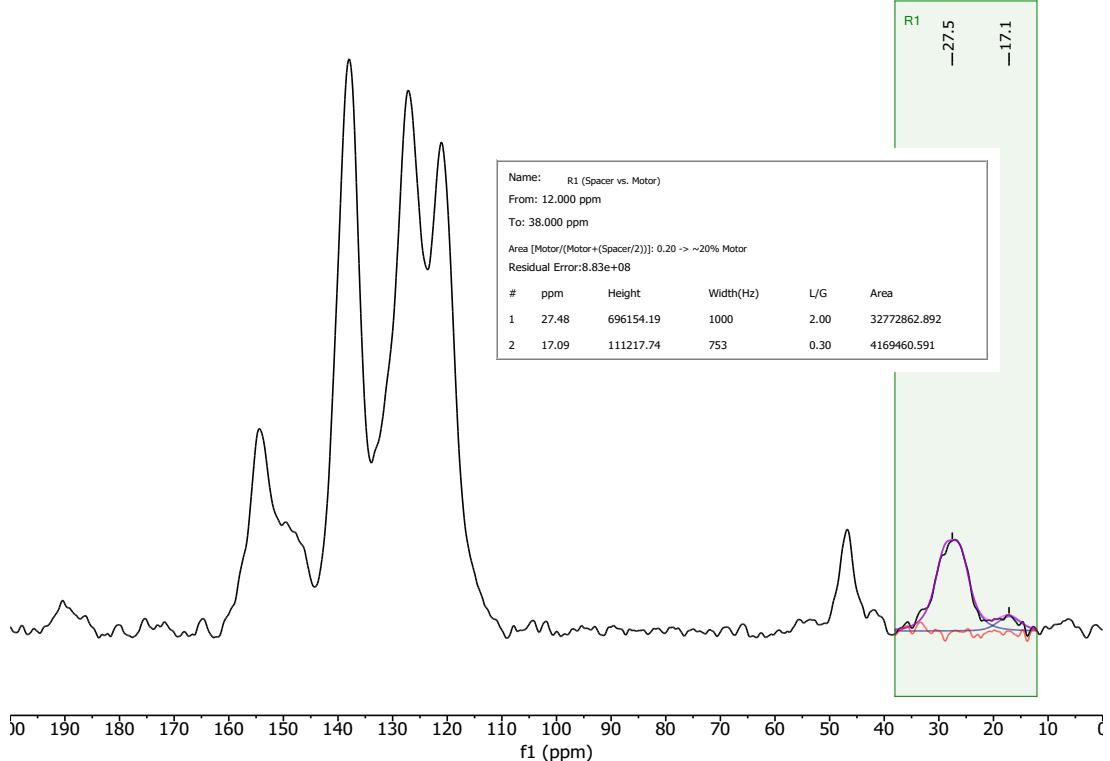


Figure S 9.3-38: ^{13}C ssNMR direct excitation spectrum of **m₂₀-COF**. The signal at 27.5 ppm refers to the two methyl groups of the spacer moiety and the signal at 17.1 ppm to the methyl group of the motor (see Figure S 9.3-37), respectively. The relative area of both signals gives a quantitative indication for the motor content in the material of ~20%.

9.3.10 Nitrogen Gas Sorption Analysis

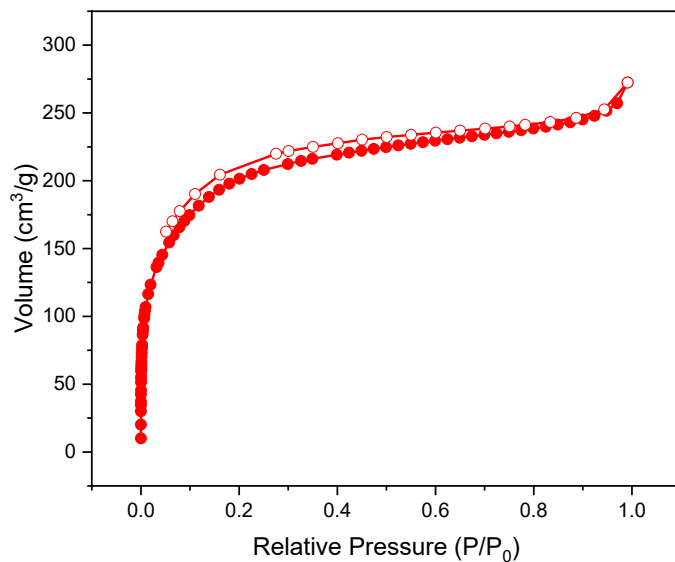


Figure S 9.3-39: N₂ sorption isotherm of **m₀-Polymer**. Filled dots represent data points of the adsorption branch, hollow dots those of the desorption branch, respectively.

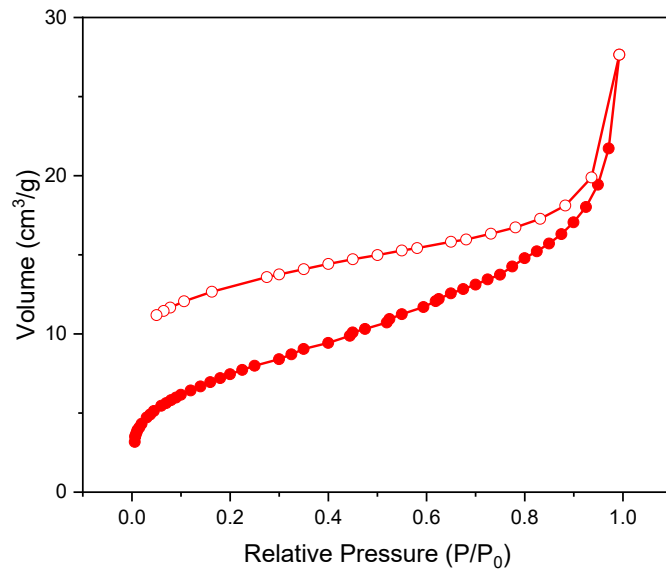


Figure S 9.3-40: N₂ sorption isotherm of **m₁₀₀-Polymer**. Filled dots represent data points of the adsorption branch, hollow dots those of the desorption branch, respectively.

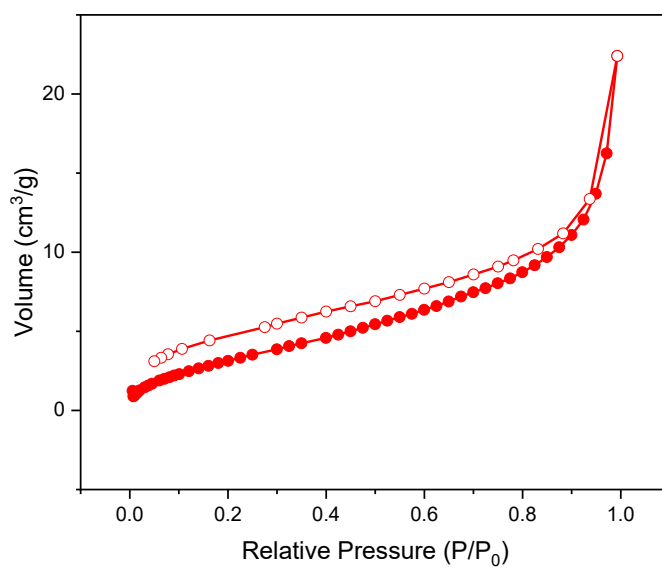


Figure S 9.3-41: N_2 sorption isotherm of **m₅₀-Polymer**. Filled dots represent data points of the adsorption branch, hollow dots those of the desorption branch, respectively.

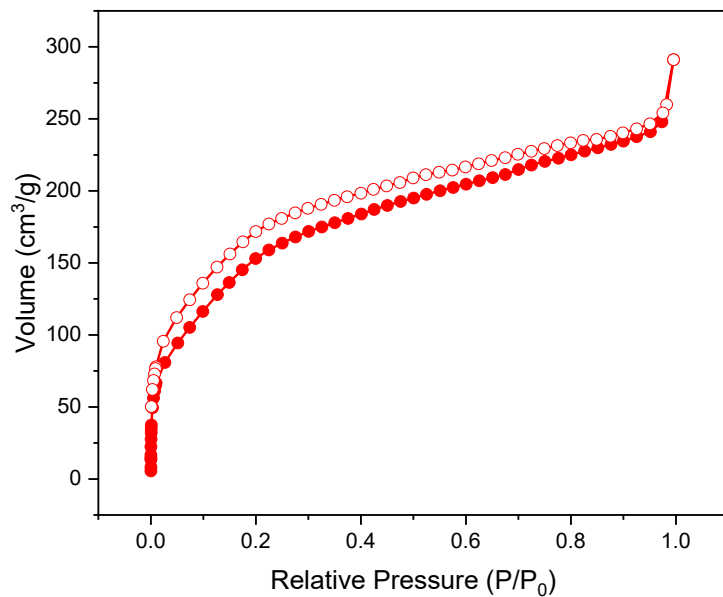


Figure S 9.3-42: N_2 sorption isotherm of **m₂₀-COF**. Filled dots represent data points of the adsorption branch, hollow dots those of the desorption branch, respectively.

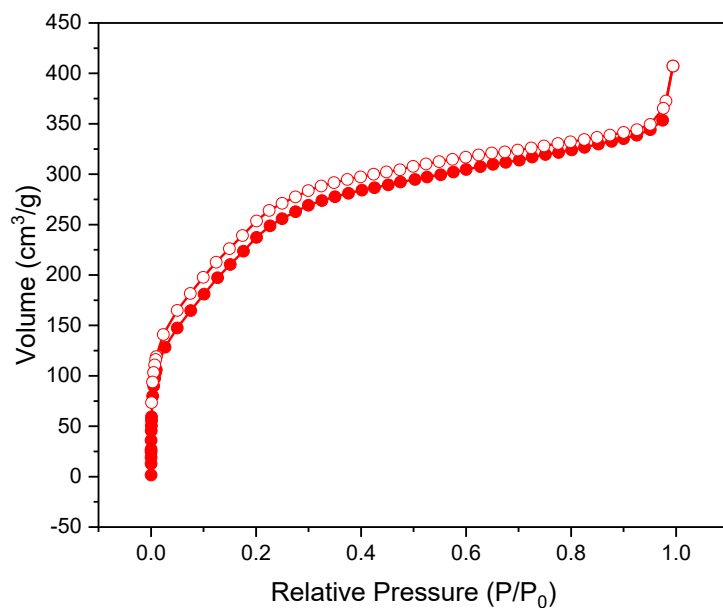


Figure S 9.3-43: N₂ sorption isotherm of **m₀-COF**. Filled dots represent data points of the adsorption branch, hollow dots those of the desorption branch, respectively.

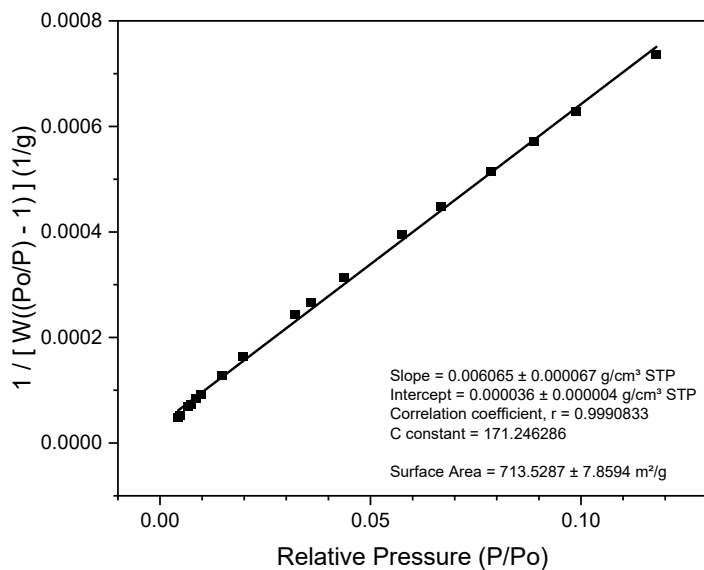


Figure S 9.3-44: BET-Plot of **m₀-Polymer**.

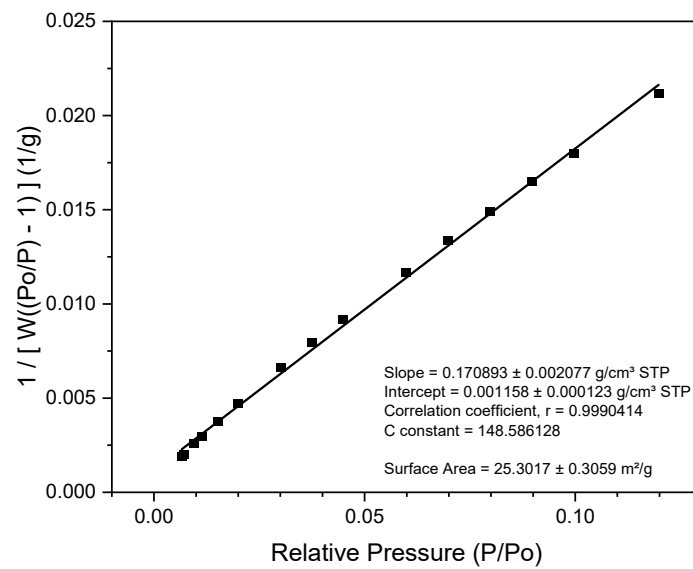


Figure S 9.3-45: BET-Plot of \mathbf{m}_{100} -Polymer.

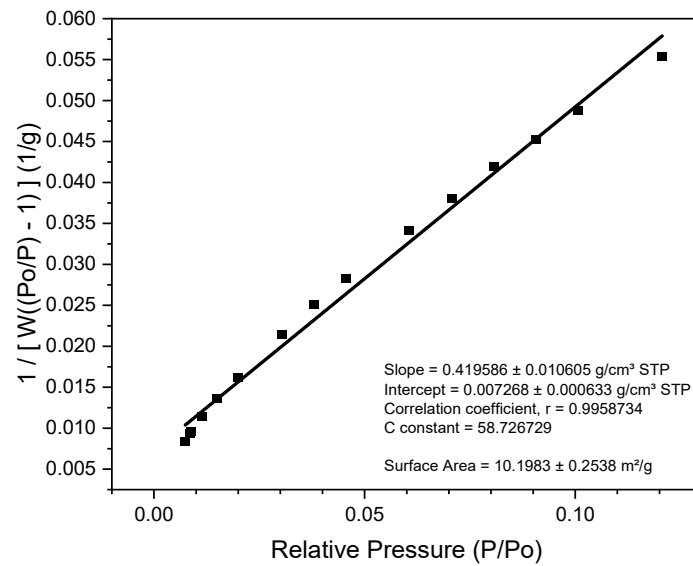
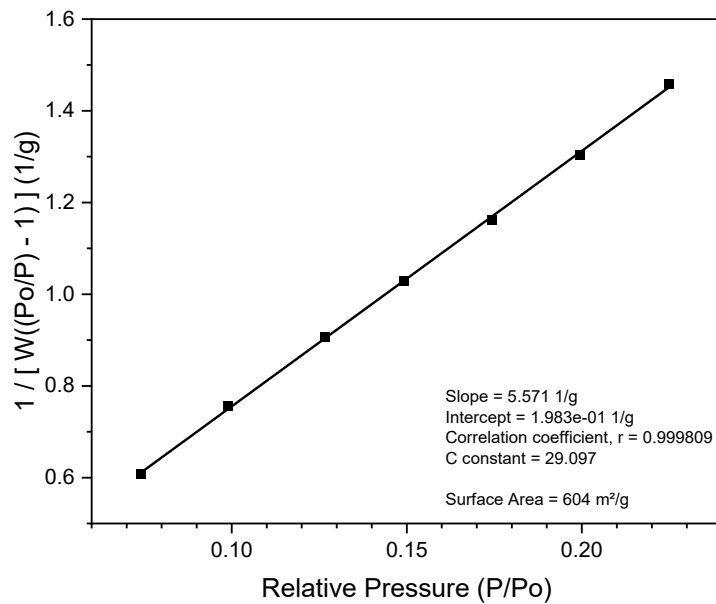
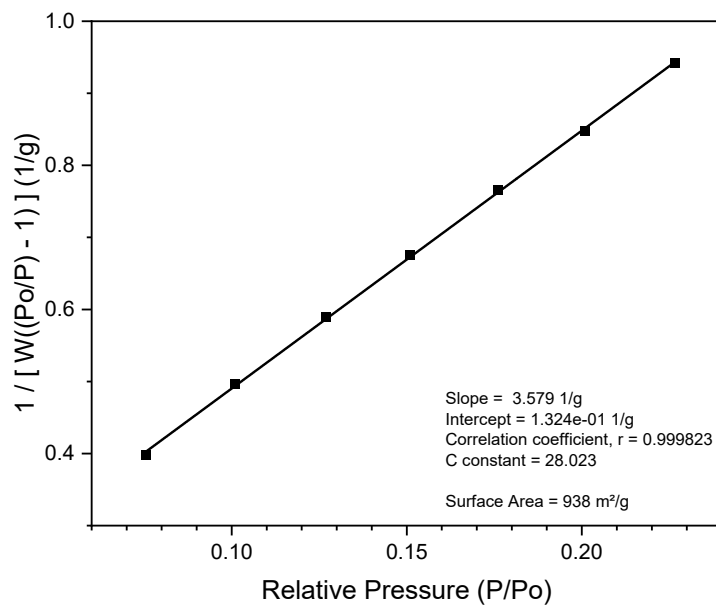


Figure S 9.3-46: BET-Plot of \mathbf{m}_{50} -Polymer.

Figure S 9.3-47: BET-Plot of **m₂₀-COF**.Figure S 9.3-48: BET-Plot of **m₀-COF**.

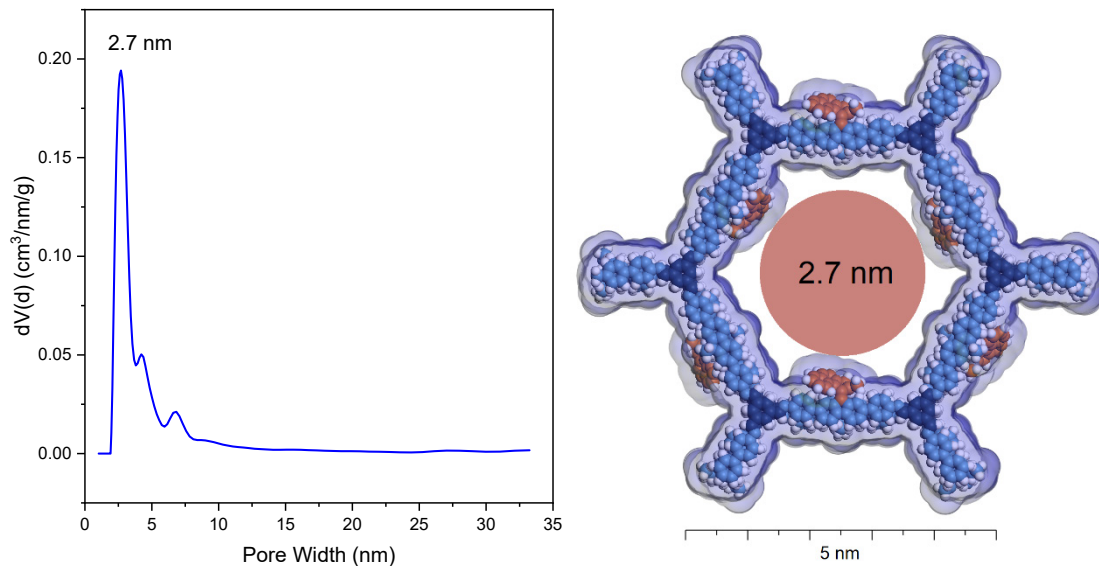


Figure S 9.3-49: Experimental pore size distribution in **m₂₀-COF** (left) and estimated minimal pore diameter (N_2 accessible surface) based on an idealized eclipsed stacked structure model (AA-1_EE; see Fig. S10) with equally distributed motor units (represented by a theoretical **m₁₀₀-COF**) in Material Studio (right). With smaller motor content, e.g. as found in **m₂₀-COF**, the diameter should approach a value closer to **m₀-COF** (see Figure S 9.3-50).

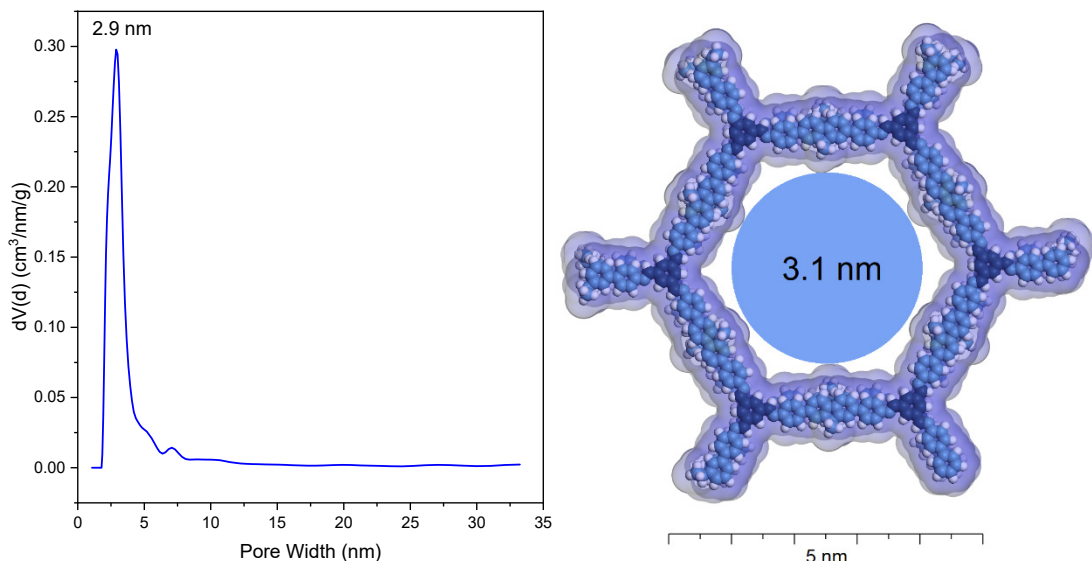


Figure S 9.3-50: Experimental pore size distribution in **m₀-COF** (left) and estimated minimal pore diameter (N_2 accessible surface) based on an idealized eclipsed stacked structure model (AA-1_EE; see Fig. S10) in Material Studio (right).

9.3.11 SEM/TEM Analysis

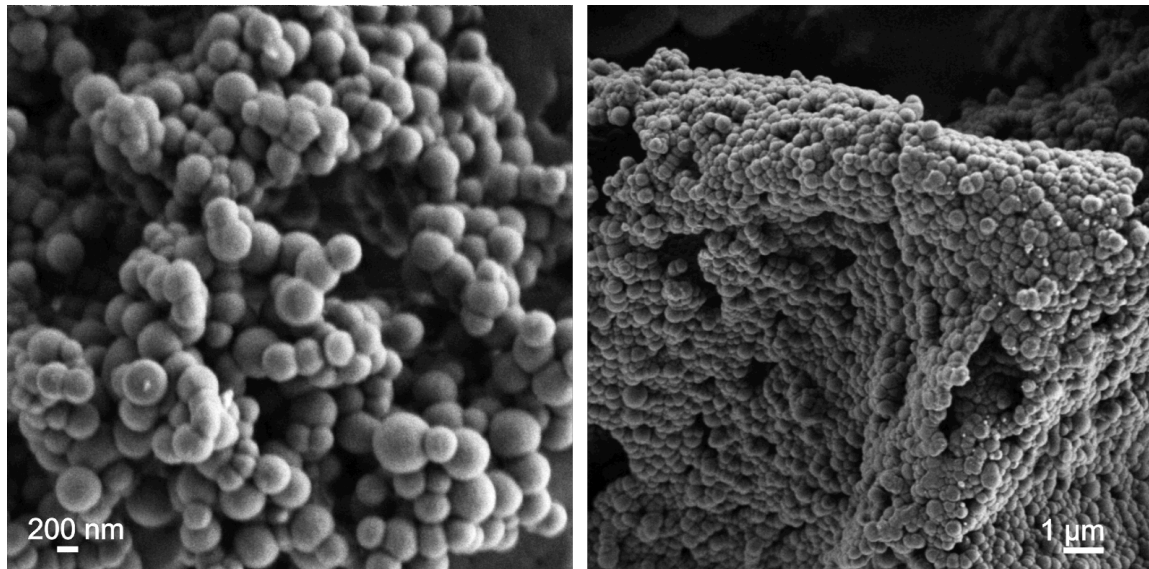


Figure S 9.3-51: SEM images of **m₂₀-COF** showing intergrown spherical particles.

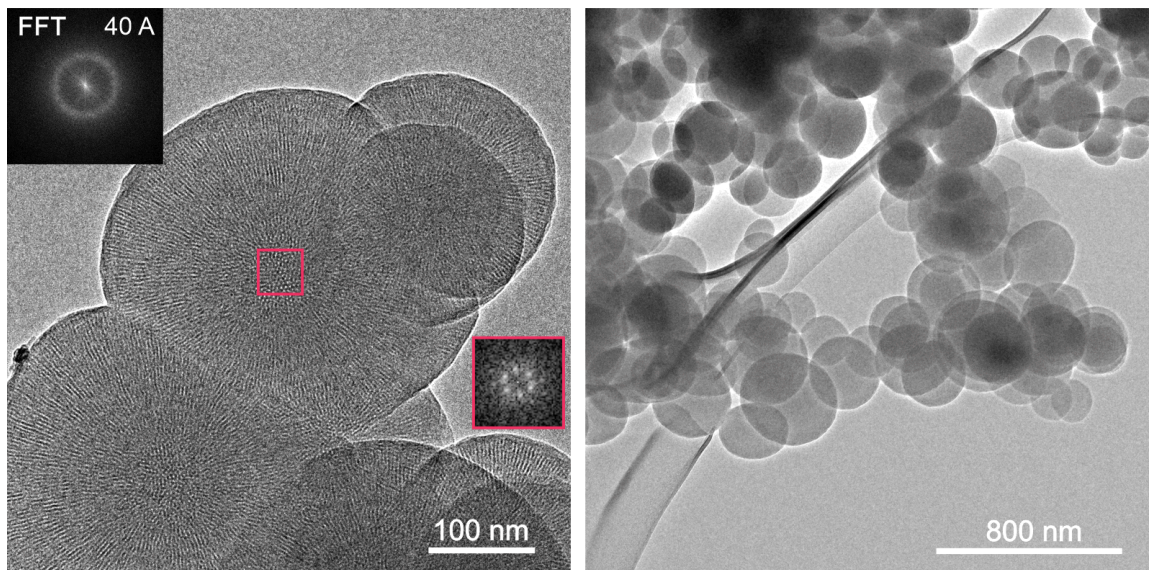


Figure S 9.3-52: TEM images of **m₂₀-COF** showing crystalline, intergrown spherical particles with ~150-350 nm diameter. The FFT (red) shows a hexagonal pattern, proving the structure model.

9.3.12 DFT Calculations

General methods

All the structures subject to the analysis were pre-optimized using the semiempirical GFN2-xTB level, as implemented in the xTB software.^[9] Compounds **1** and **2** were optimized considering the states involved in the thermal step of a molecular motor (stable, **S**; metastable, **MS**; THI transition state, **TS**) and the different orientations of the aryl rings attached to the stator (see Figure S 9.3-53 and Figure S 9.3-54). For each molecule, four conformers were considered, from which the rotational cycle could start:

- 1: left aryl backwards/right aryl front
- 2: both aryls front
- 3: left aryl front/right aryl backwards
- 4: both aryls backwards

The conformers of each compound were enumerated accordingly (e.g. **1-S2** for the second conformer of the stable state of molecule **1**) and their structures reoptimized with DFT at ω B97X-D/def2-SVP level, with the Gaussian 16, Rev B.01 software package. All stationary points were confirmed to be such due to the number of imaginary frequencies obtained after the Hessian calculation (0 for minima, 1 for transition states). The Gibbs free energy correction was applied to all the electronic energies. The energy distribution of the metastable states was used to calculate a Boltzmann distribution to be applied to the simulated THI reaction. The results gave a simulated ΔG^\ddagger of 97.7 kJ/mol for **1** and 99.7 kJ/mol for **2**. The choice of functional and basis set affords an error of ca. 10 kJ/mol compared to the experimental barrier, correctly retrieving the relative order of reactivity (**1** slightly more reactive than **2**). The UV-Vis spectra of stable and unstable states were calculated at the TD- ω B97X-D/def2-TZVP level over the first 15 singlet transitions on the geometries calculated in the gas phase. The SMD implicit solvent method (for MeCN) was applied. The broad absorption band centered around 350 nm of the stable state and the appearance of a more prominent transition around 450 nm were correctly modelled. All xyz coordinates are reported as separate files, while the simulated UV-Vis for stable and unstable compounds are reported below (left, gas phase, right MeCN).

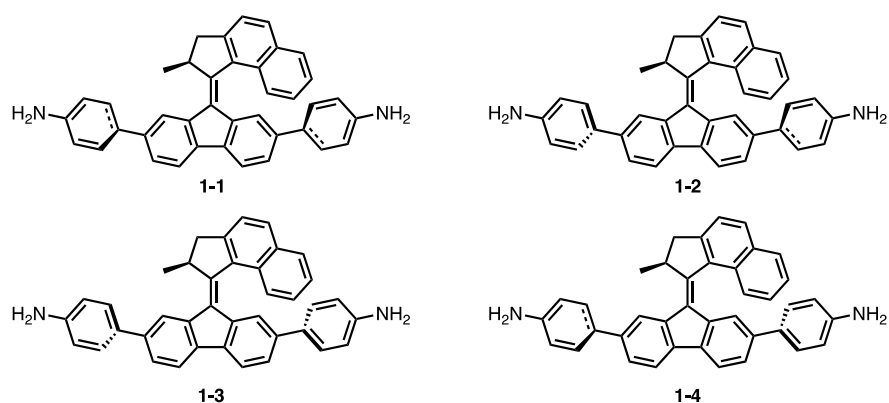
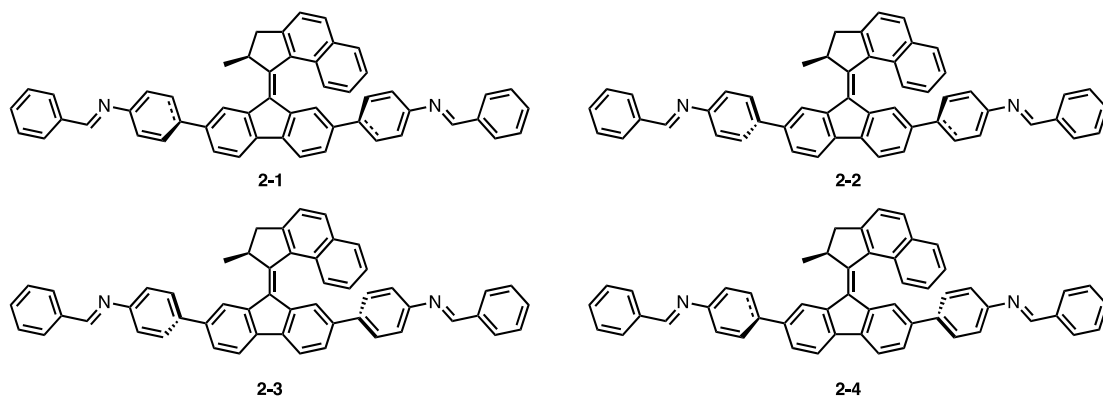


Figure S 9.3-53: Conformers of motor **1** considered in the DFT studies.

Figure S 9.3-54: Conformers of motor **2** considered in the DFT studies.Table S 9.3-2: Energy Barriers and half-lives of conformers of motor **1**.

Conformers	Energy Barrier [kJ/mol]	Energy Barrier [kcal/mol]	k [s-1]	t _{1/2} [s]	t _{1/2} [min]
MS1-TS1	88.21	21.08	2.19E-03	317	5
MS3-TS3	99.04	23.67	2.77E-05	25029	417
MS2-TS2	98.21	23.47	3.87E-05	17910	298
MS4-TS4	91.14	21.78	6.71E-04	1034	17

Table S 9.3-3: Energy Barriers and half-lives of conformers of motor **2**.

Conformers	Energy Barrier [kJ/mol]	Energy Barrier [kcal/mol]	k [s-1]	t _{1/2} [s]	t _{1/2} [min]
MS1-TS1	90.25	21.57	9.60E-04	722	12
MS3-TS3	101.38	24.23	1.08E-05	64310	1072
MS2-TS2	99.54	23.79	2.27E-05	30576	510
MS4-TS4	90.47	21.62	8.79E-04	788	13

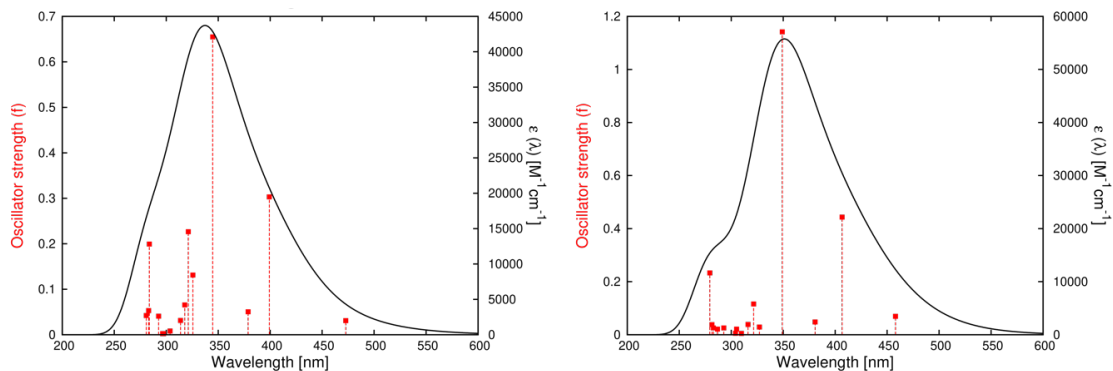


Figure S 9.3-55: Simulated UV-Vis absorption spectra for compound **1-S1** in gas phase (left) and acetonitrile (right).

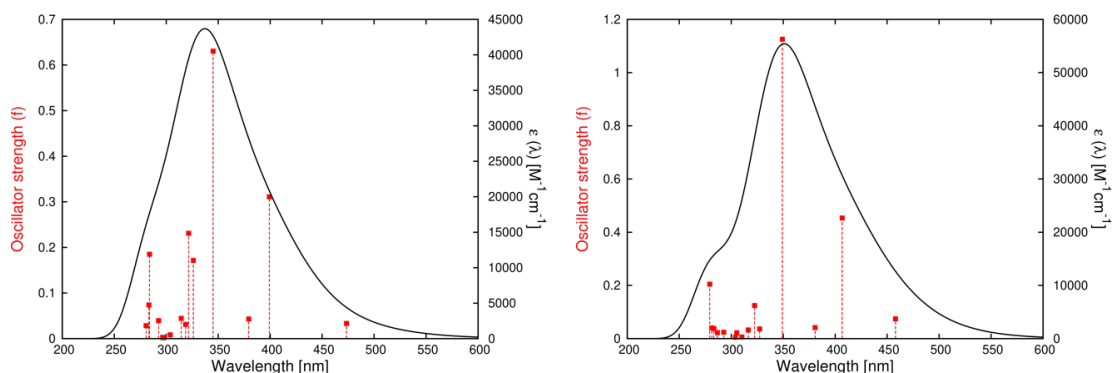


Figure S 9.3-56: Simulated UV-Vis absorption spectra for compound **1-S2** in gas phase (left) and acetonitrile (right).

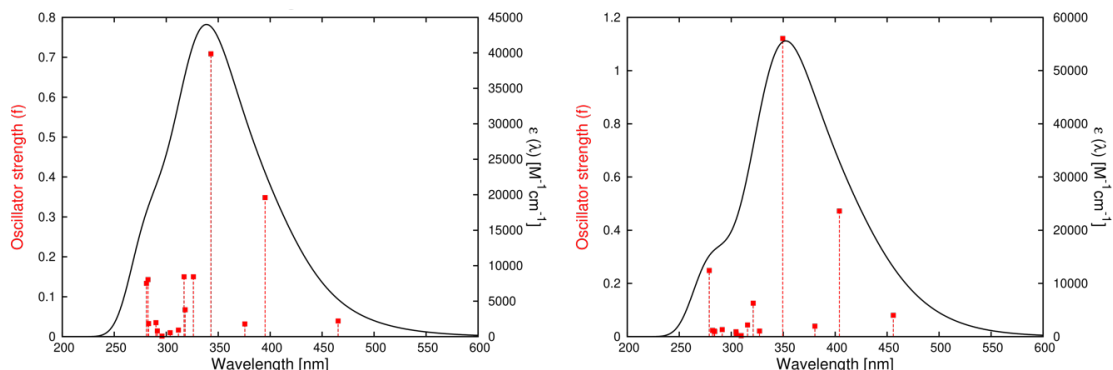


Figure S 9.3-57: Simulated UV-Vis absorption spectra for compound **1-S3** in gas phase (left) and acetonitrile (right).

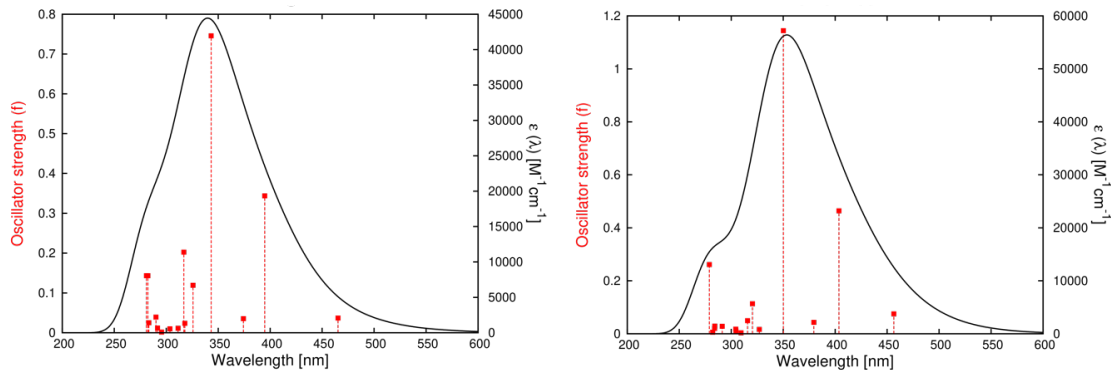


Figure S 9.3-58: Simulated UV-Vis absorption spectra for compound **1-S4** in gas phase (left) and acetonitrile (right).

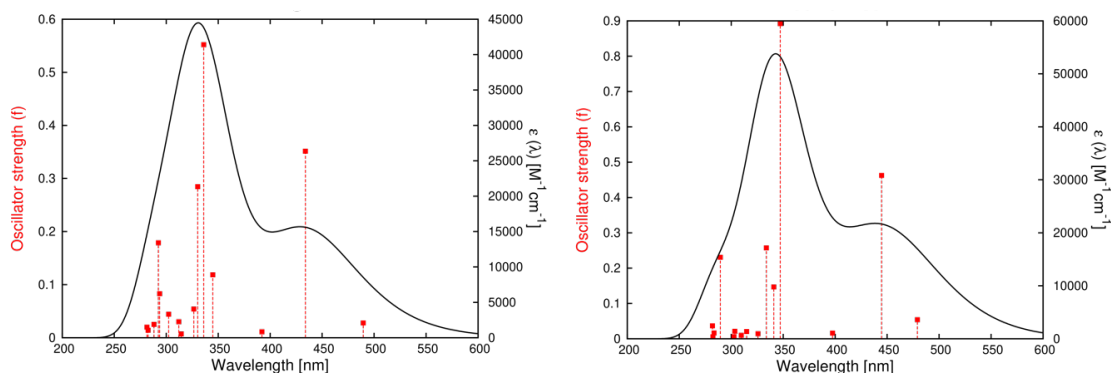


Figure S 9.3-59: Simulated UV-Vis absorption spectra for compound **1-MS1** in gas phase (left) and acetonitrile (right).

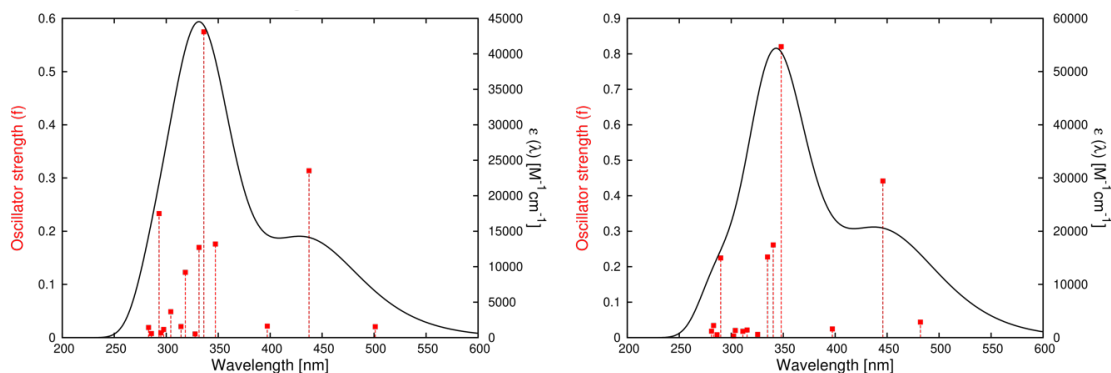


Figure S 9.3-60: Simulated UV-Vis absorption spectra for compound **1-MS2** in gas phase (left) and acetonitrile (right).

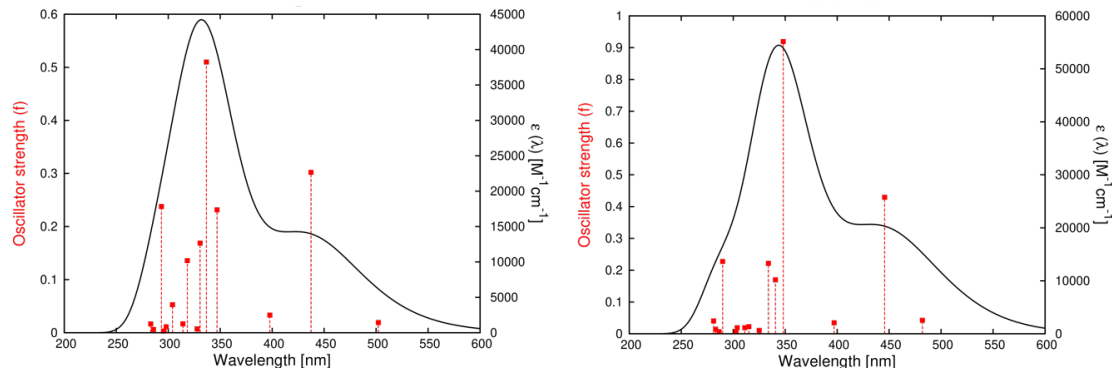


Figure S 9.3-61: Simulated UV-Vis absorption spectra for compound **1-MS3** in gas phase (left) and acetonitrile (right).

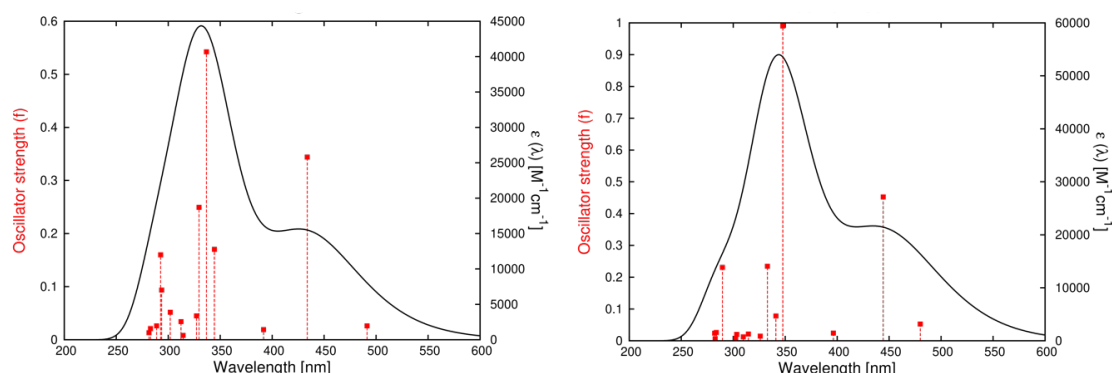


Figure S 9.3-62: Simulated UV-Vis absorption spectra for compound **1-MS4** in gas phase (left) and acetonitrile (right).

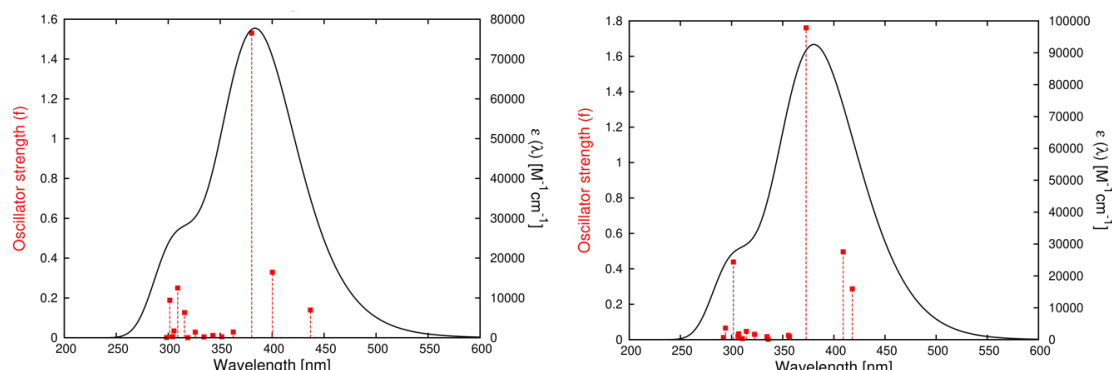


Figure S 9.3-63: Simulated UV-Vis absorption spectra for compound **2-S1** in gas phase (left) and acetonitrile (right).

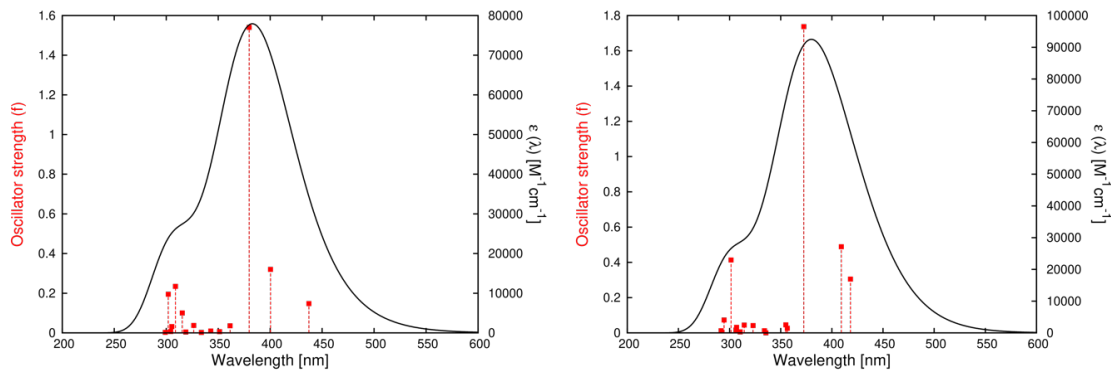


Figure S 9.3-64: Simulated UV-Vis absorption spectra for compound **2-S2** in gas phase (left) and acetonitrile (right).

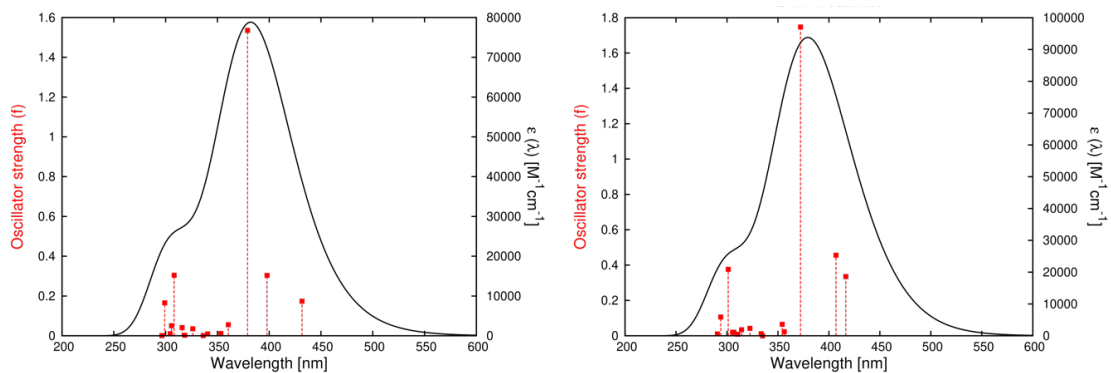


Figure S 9.3-65: Simulated UV-Vis absorption spectra for compound **2-S3** in gas phase (left) and acetonitrile (right).

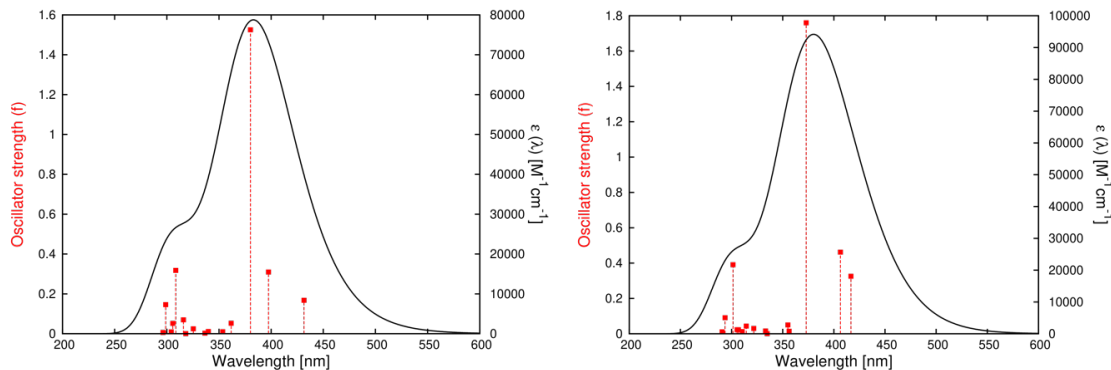


Figure S 9.3-66: Simulated UV-Vis absorption spectra for compound **2-S4** in gas phase (left) and acetonitrile (right).

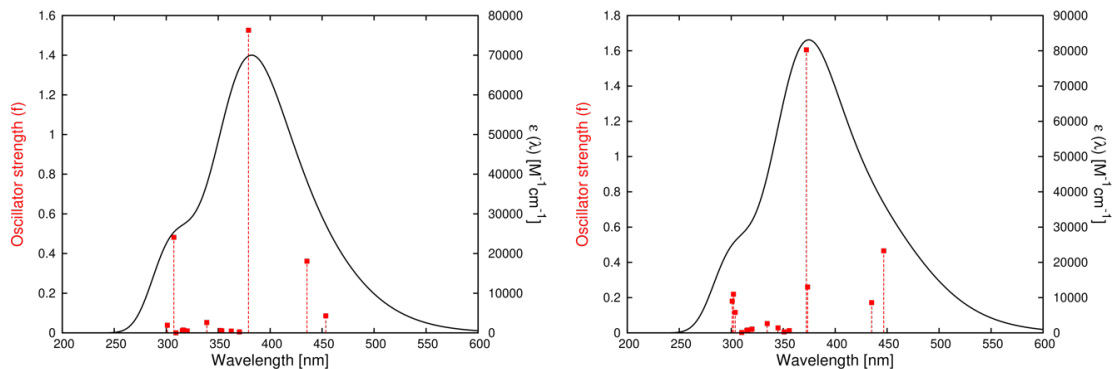


Figure S 9.3-67: Simulated UV-Vis absorption spectra for compound **2-MS1** in gas phase (left) and acetonitrile (right).

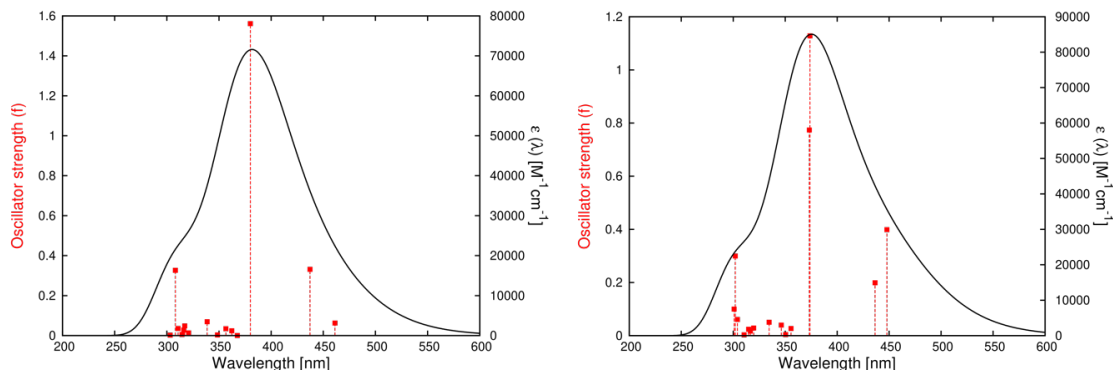


Figure S 9.3-68: Simulated UV-Vis absorption spectra for compound **2-MS2** in gas phase (left) and acetonitrile (right).

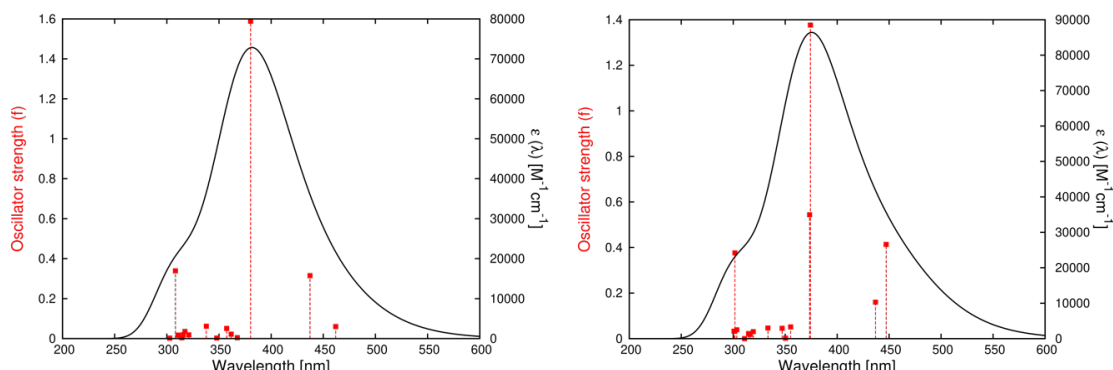


Figure S 9.3-69: Simulated UV-Vis absorption spectra for compound **2-MS3** in gas phase (left) and acetonitrile (right).

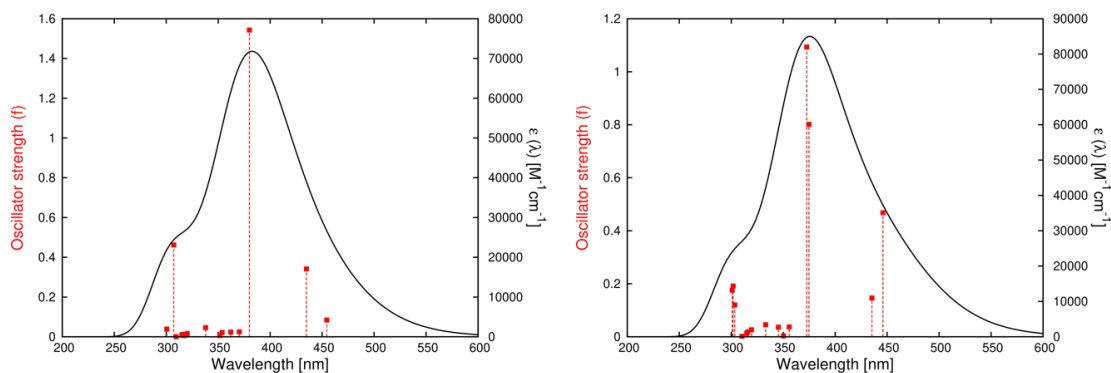


Figure S 9.3-70: Simulated UV-Vis absorption spectra for compound **2-MS4** in gas phase (left) and acetonitrile (right).

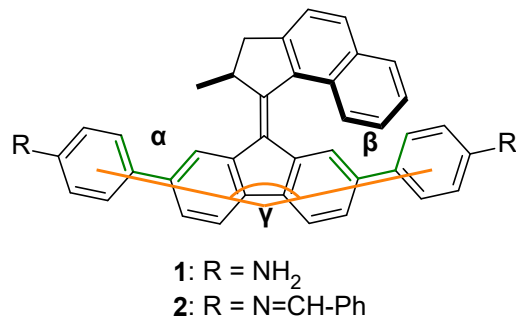


Figure S 9.3-71: Measured angles from optimized structures in DFT of 1 and 2. The dihedral angles marked in green are summarized in Table S 9.3-4. The angle marked in orange indicates the angle in which the molecule is bend out of plane.

Table S 9.3-4: Summary of dihedral angles (as indicated in green in Figure S 9.3-71) for stable, metastable and transition states of motor **1** and **2** and bending angles (marked in orange in Figure S 9.3-71).

Conformer	dihedral α [°]	dihedral β [°]	bending γ [°]	Conformer	dihedral α [°]	dihedral β [°]	bending γ [°]
1-S1	39	35	164	2-S1	39	35	161
1-MS1	38	40	162	2-MS1	38	40	162
1-TS1	40	38	152	2-TS1	41	39	152
1-S3	-39	-36	164	2-S3	-40	-38	159
1-MS3	-36	-39	161	2-MS3	-37	-40	162
1-TS3	-25	-40	150	2-TS3	-27	-41	151
1-S2	-39	35	165	2-S2	-40	35	160
1-MS2	-36	40	162	2-MS2	-37	40	162
1-TS2	-26	38	151	2-TS2	-27	39	149
1-S4	39	-36	167	2-S4	39	-37	164
1-MS4	38	-39	161	2-MS4	38	-40	161
1-TS4	-40	40	149	2-TS4	41	-41	152

9.3.13 DIFFaX Simulations

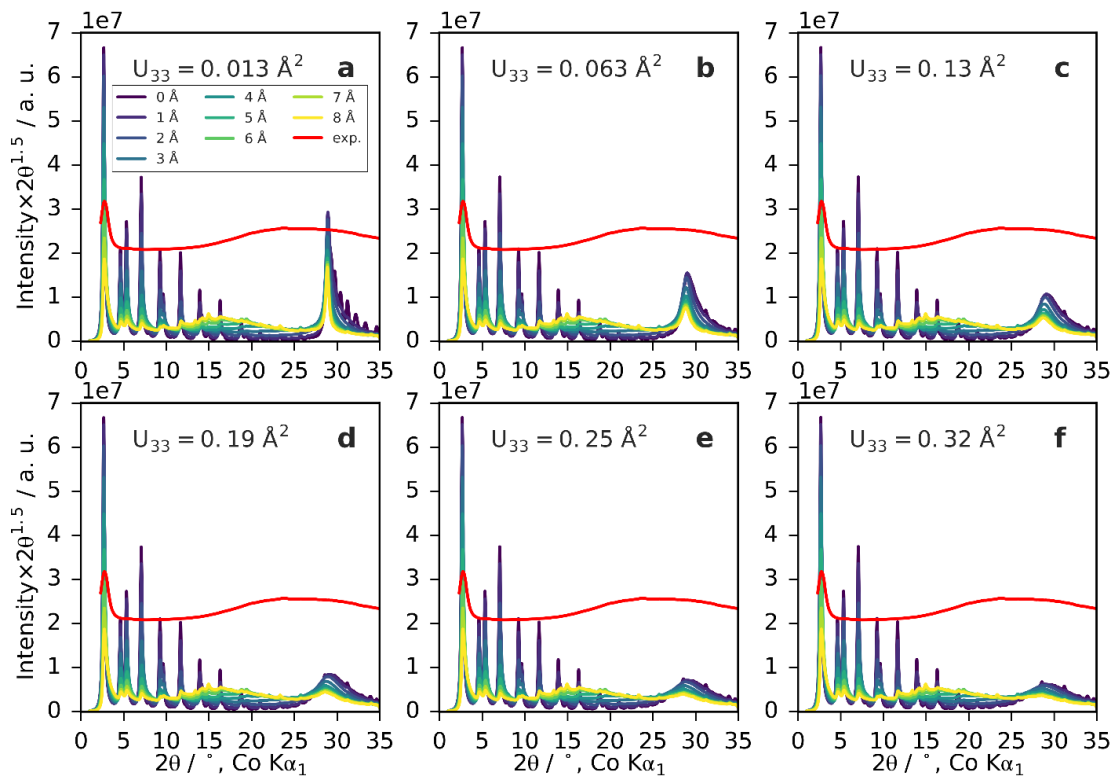


Figure S 9.3-72: Diffraction patterns of turbostratically disordered **m₂₀-COF** were simulated using the program DIFFaX^[10]. Layers were allowed to shift with equal probability in six directions: [100], [110], [010], [-100], [-1-10], [0-10]. Then, the magnitude of the shifts were increased incrementally, and the simulations were repeated with different values for the interlayer atomic displacement parameter U_{33} to simulate decreasing coherence between the layers. To keep the complexity of the simulations manageable, only a single layer orientation was considered (e.g., to properly account for antiparallel stacking would require two alternating orientations), and the motor units were also not considered. We found that a combination of both interlayer offsets and increased U_{33} are required to satisfactorily destroy the interlayer diffraction effects as seen in the experimental data. Increased offsets up to about 8 Å and very high U_{33} values led to substantial broadening and coalescence of diffuse intensities around 15-35° 2θ . Shift magnitudes larger than 8 Å led to the re-emergence of other diffraction peaks that are not observed. It is difficult to quantify the limits of these effects, as other factors such as distributions of stacking magnitude, motor units, conformational disorder, and different relative orientations (i.e., antiparallel versus parallel stacking) can be expected to have further complicating effects, and possibly are also necessary to obtain the “X-ray amorphous”-looking patterns seen experimentally.

9.3.14 References

1. Chupas P. J. et al. Rapid-Acquisition Pair Distribution Function (Ra-Pdf) Analysis. *J. Appl. Crystallogr.* **36**, 1342-1347 (2003).
2. Ashiotis G. et al. The Fast Azimuthal Integration Python Library: Pyfai. *J. Appl. Crystallogr.* **48**, 510-519 (2015).
3. [cited] Available from: <https://xpdacq.github.io/xpdtools/index.html>
4. Juhás P., Davis T., Farrow C. L., Billinge S. J. L. Pdfgetx3: A Rapid and Highly Automatable Program for Processing Powder Diffraction Data into Total Scattering Pair Distribution Functions. *J. Appl. Crystallogr.* **46**, 560-566 (2013).
5. Yang X., Juhas P., Farrow C. L., Billinge S. J. Xpdfsuite: An End-to-End Software Solution for High Throughput Pair Distribution Function Transformation, Visualization and Analysis. Preprint at <https://arxiv.org/abs/1402.3163> (2015).
6. Farrow C. L. et al. Pdfit2 and Pdfgui: Computer Programs for Studying Nanostructure in Crystals. *J. Phys.: Condens. Matter* **19**, 335219 (2007).
7. Danowski W. et al. Unidirectional Rotary Motion in a Metal-Organic Framework. *Nat. Nanotechnol.* **14**, 488-494 (2019).
8. Gobel D., Clamor N., Lork E., Nachtsheim B. J. Aerobic C(Sp(2))-H Hydroxylations of 2-Aryloxazolines: Fast Access to Excited-State Intramolecular Proton Transfer (Esipt)-Based Luminophores. *Org. Lett.* **21**, 5373-5377 (2019).
9. Pracht P., Bohle F., Grimme S. Automated Exploration of the Low-Energy Chemical Space with Fast Quantum Chemical Methods. *Phys. Chem. Chem. Phys.* **22**, 7169-7192 (2020).
10. Treacy M. M. J., Newsam J. M., Deem M. W. A General Recursion Method for Calculating Diffracted Intensities from Crystals Containing Planar Faults. *Proc. R. Soc. Lond. A* **433**, 499-520 (1991).

9.4 Supporting Information to Chapter 7 Self-Diffusion of Acetonitrile in a Covalent Organic Framework: Simulation and Experiment

9.4.1 Materials and Methods

General Methods: All reactions, unless otherwise noted, were performed with magnetic stirring under inert gas (N_2 or Ar) atmosphere using standard Schlenk techniques. Reaction temperatures were electronically monitored as external heating block temperatures. Reagents were purchased from different commercial sources and used without further purification.

Infrared Spectroscopy: IR spectra were recorded on a Perkin Elmer UATR Two FT-IR spectrometer equipped with an attenuated total reflection (ATR) measuring unit. IR data are reported in wavenumbers (cm^{-1}) of normalized absorption. The IR bands are characterized as w (weak), m (medium), s (strong), or br (broad).

Supercritical CO_2 Activation: Activation of the methanol-soaked COF samples with supercritical CO_2 was performed on a Leica EM CPD300 critical point dryer.

Gas Sorption Measurements: Sorption measurements for COFs were performed on a Quantachrome Instruments Autosorb iQ MP with Nitrogen at 77 K. The samples were degassed for 12 h at 120 °C under vacuum prior to the gas adsorption studies. Pore size distribution was determined from nitrogen adsorption isotherms using the QSDFT cylindrical pores in carbon model for nitrogen at 77 K. For multipoint BET surface area calculations, pressure ranges were chosen with the help of the BET assistant in the ASiQwin software, which chooses BET tags in accordance with the ISO recommendations equal or below the maximum in grams per square meter.

Vapor Sorption Measurements: Vapor sorption experiments were performed on a Quantachrome Instruments Autosorb iQ MP with acetonitrile at different temperatures. The samples were degassed for 12 h at 120 °C under vacuum prior adsorption studies. Values of the adsorbed amount V_{STP} [$cm^3 g^{-1}$] were converted to gravimetric adsorbed amount [$g^1 g^{-1}$] = $V_{STP}/22414*41.05$.

X-Ray Powder Diffraction (XRPD): X-ray powder diffraction experiments were performed on a Stoe Stadi P diffractometer (Co- $K\alpha_1$, Ge(111)) in Debye-Scherrer geometry. The samples were measured in sealed glass capillaries (OD = 0.7 mm) and spun for improved particle statistics.

Pawley Refinements: Pawley refinements were performed using TOPAS v6. The background was corrected with Chebychev polynomials (Order 10). Simple axial and zero-error corrections were used together with additional corrections for Lorentzian crystallite size broadening.

Scanning Electron Microscopy (SEM): SEM SE (secondary electron) detector images were obtained on a Zeiss Merlin SEM.

Transmission Electron Microscopy (TEM): TEM analysis was performed with a Philips CM30 ST (300kV, LaB6 cathode). The samples were prepared dry onto a copper lacey carbon grid (Plano).

Computational Methods: To simulate the self-diffusion-coefficient we use the following overall workflow. A COF structure is determined experimentally and then relaxed by Density Functional Theory (DFT) calculations. Adsorption loading is simulated in Grand Canonical Monte Carlo (GCMC) simulations. Molecular Dynamics (MD) simulation are then started with the results from GCMC simulations to obtain self-diffusion coefficients. The individual steps are now described in detail.

GCMC Adsorption: Starting from a COF structure determined by powder diffraction, we refine the framework using DFT calculations. Atomic partial charges of the framework are calculated on basis of a single point DFT calculation of the charge density of the framework applying the DDEC6 method.^[1-4] The obtained structure is kept rigid during GCMC and MD simulations.

Adsorption isotherms were calculated by the GCMC methodology^[5] implemented in RASPA molecular simulation package.^[5] To describe adsorbate-adsorbate interactions we use the TraPPE force field.^[6, 7] Therein acetonitrile is modelled in a united-atom description containing 3 Lennard-Jones beads namely CH₃, C and N with atomic point charges on each. The quadrupole moment of nitrogen is taken into account by placing negative point charges on each nitrogen atom and a neutralizing charge in the center of mass of the molecule. Lennard-Jones parameters of the framework were taken from the DREIDING force field^[8] and unlike interactions are calculated by Lorentz-Berthelot combining rules.^[9, 10] The combination of both force fields has been used extensively.^[6-8]

To compare to experiment we first determine the void fraction of the framework and then calculate excess adsorption. We use a spherical cut-off-radius of 14 Å for Van-der-Waals interactions and electrostatic interactions. Long range electrostatics are considered using Ewald summation.^[11] Sufficient statistics are reached by 100,000 Monte Carlo cycles for

equilibration and productions each. Experimental adsorption isotherms show excess adsorption. Therefore, the void fraction of the framework is obtained computationally. A detailed description is given in our earlier work.^[12]

MD simulations were performed in Gromacs version 2019.6.^[13, 14] The TraPPE force field model of acetonitrile is a linear one with fixed angles of 180° which may lead to problems in the force calculation for the bending potential. To cope with that the model is adjusted using the potential proposed by van der Spoel *et al.*^[15]

We first evaluate the force field's ability to reproduce self-diffusion coefficients in the liquid phase. Good statistics are assured by running 10 independent simulations with starting velocities drawn from a Maxwell-Boltzmann distribution, 3 ns equilibration and 10 ns production with a timestep of 1 fs. Finite size effects are accounted by an extrapolation to an infinite box size. Therefore, we vary the size of the simulation box and the number of molecules accordingly. Temperature is kept constant by applying the Nose-Hoover-Thermostat.^[16, 17] In NpT-simulations pressure is controlled by the Berendsen barostat.^[18] Long range Van-der-Waals corrections and Ewald summation for electrostatics are used in liquid phases and simulation in pores. In bulk, we sample the Mean-squared displacement in xyz-direction from 1 to 5 ns and calculate the self-diffusion coefficient accord to the Einstein Equation

$$D_s = \frac{1}{2dN} \lim_{t \rightarrow \infty} \frac{d}{dt} \left\langle \sum_{i=1}^N |\mathbf{r}_i(t) - \mathbf{r}_i(0)|^2 \right\rangle \quad (\text{Eq. S1})$$

where \mathbf{r} is the position of the center of mass of a molecule, N is the number of molecules and d is the dimension of the system. NpT-simulations and NVT-simulations with densities taken from NpT-simulations yield results within the margin of error.

To simulate the diffusion-coefficient in the COF pore we first insert rigid COF pore into the simulation box. Adsorbate molecules are added until the previously determined average loading by GCMC calculations is reached. Then we follow the procedure described for liquid simulations with following adjustments. In simulation a porous media acts as an external field which results in a change of the degrees of freedom of the simulated system.^[19]

As in a 2D-COF the diffusion process becomes 1 dimensional after short timescales we sample only the mean squared displacement in direction of the pore axis, so the dimension in equation S1 reduces. Sampling the mean squared displacement in less dimensions reduces the quality of statistics. This is mitigated by extending simulation time to 5 ns equilibration

and 20 ns production. We sample the MSD from 1 ns to 8 ns. Gromacs settings are ensured by a comparison to MD simulations in RASPA.

Pulsed Field Gradient Nuclear Magnetic Resonance Spectroscopy (PFG-NMR):

Diffusion measurements were performed in flame-sealed 5 mm NMR tubes on a Bruker Avance III 400 MHz spectrometer (*diff60* probe) between 270 and 300 K with a stimulated-echo sequence^[20] (*diffSte* program, Bruker TopSpin) without sample spinning. A variable temperature control unit ensured constant sample temperature during the experiment. For temperatures below room temperature, a stream of chilled nitrogen was connected to the temperature control unit. To restrict the vapor filled volume to the temperature-controlled region below the sample spinner, a PTFE-silicone stopper was inserted into the NMR tube (see Figure S 9.4-1).



Figure S 9.4-1: NMR sample tube with a PTFE-silicone insert and PI-3-COF sample (yellow). The insert restricts the vapor volume of MeCN to the temperature controlled zone below the spinner.

Data processing was performed with the Bruker TopSpin 3.5 *Dynamics* module using automated peak picking, integration and fitting of the integrated signal *I* vs. gradient *B* according to the Stejskal-Tanner equation (Eq. S2). T_1 relaxation times were determined using a standard inversion-recovery pulse sequence. T_2 relaxation times were obtained by fitting the signal attenuation during a cpmg pulse sequence with a delay time $d1 = 8$ s. For a typical measurement with a COF, a gradient pulse with a duration of $\delta = 0.3$ ms (*opt* shape) and diffusion times $\Delta = 20\text{-}100$ ms were used. The gradient was varied linearly in 32 steps between 0 and 900 Gs/cm. Diffusion experiments with pure, liquid acetonitrile were performed in a tube-in-tube setup to reduce convection effects.^[21] A small diameter NMR tube filled with acetonitrile was immersed in a 5 mm NMR tube with *d*-chloroform. In addition, the double stimulated-echo pulse (*dSte*) sequence was used to reduce convection

effects on the diffusion experiment.^[22] A gradient pulse with a duration of $\delta = 1$ ms (*opt* shape), diffusion times $\Delta = 20\text{-}100$ ms were used. The gradient was varied linearly in 16 steps between 0 and 75 Gs/cm.

$$I = I_0 \exp \left[-D\gamma^2 g^2 \delta^2 \left(\Delta - \frac{\delta}{3} \right) \right] = I_0 e^{[-DB]} \quad (\text{Eq. S2})$$

9.4.2 Experimental Procedures

Synthesis of PI-3-COF: PI-3-COF with low-porosity (-lp) and high-porosity (-hp) were synthesized according to a previously described procedure.^[23] To a mixture of benzene-1,3,5-tricarbaldehyde (22.1 mg, 0.13 mmol, 1.0 eq.) and 4,4',4''-(1,3,5-triazine-2,4,6-triyl)trianiline (46.8 mg, 0.13 mmol, 1.0 eq.) in mesitylene (2.7 mL) and 1,4-dioxane (1.3 mL), aqueous 6 M AcOH (0.5 mL) was added. The suspension was heated at 120°C for 72 h. Suction filtration of the precipitate, washing with DMF (20 mL), THF (20 mL) and DCM (20 mL) and drying under reduced pressure, afforded PI-3-COF-lp (55.5 mg, 91%) as a yellow solid. PI-3-COF-hp (53.9 mg, 88%) was obtained with the same procedure extended by an additional Soxhlet-extraction of the material with MeOH and supercritical CO₂ drying, instead of drying under reduced pressure. **FT-IR (ATR):** $\nu = 1579$ (m), 1511 (vs), 1413 (m), 1369 (s), 1174 (w), 1141 (w), 1013 (w), 968 (w), 864 (w), 813 (m), 679 (w), 530 (w) cm^{-1} .

9.4.3 Supporting Analytical Data

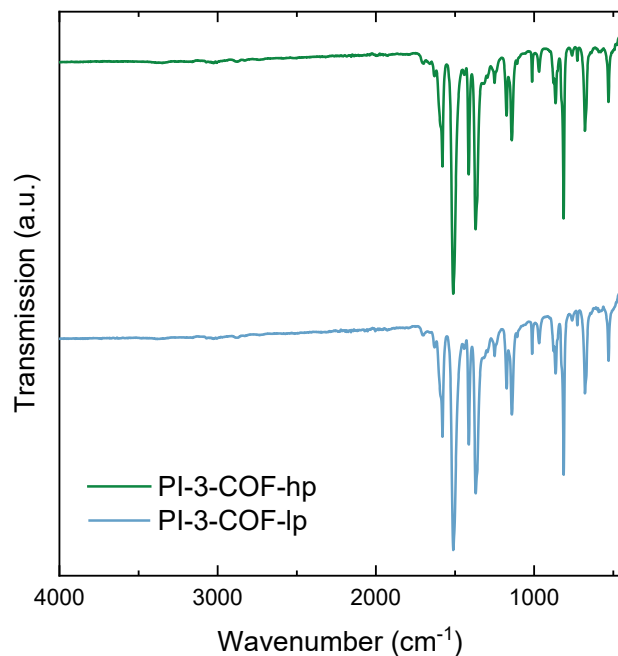


Figure S 9.4-2: FT-IR spectra of PI-3-COF-lp/-hp. Both spectra are essentially identical.

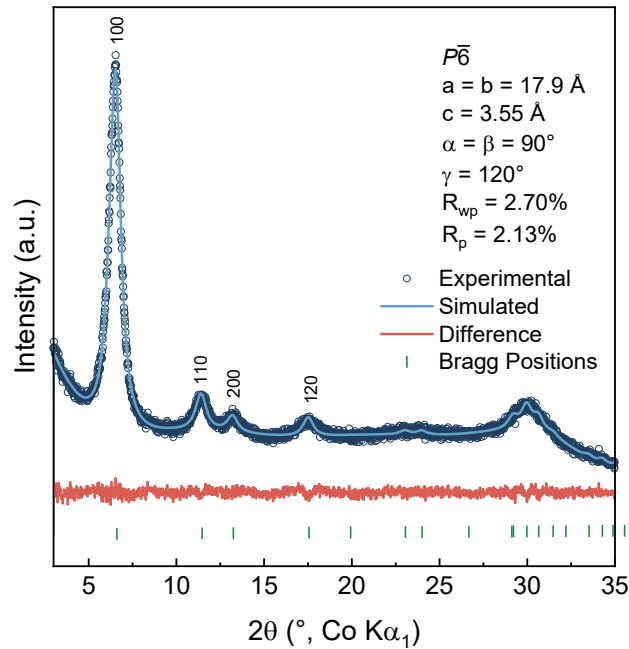


Figure S 9.4-3: Pawley refinement of XRPD data (PI-3-COF-lp). Obtained cell parameters are in agreement with previous reports.

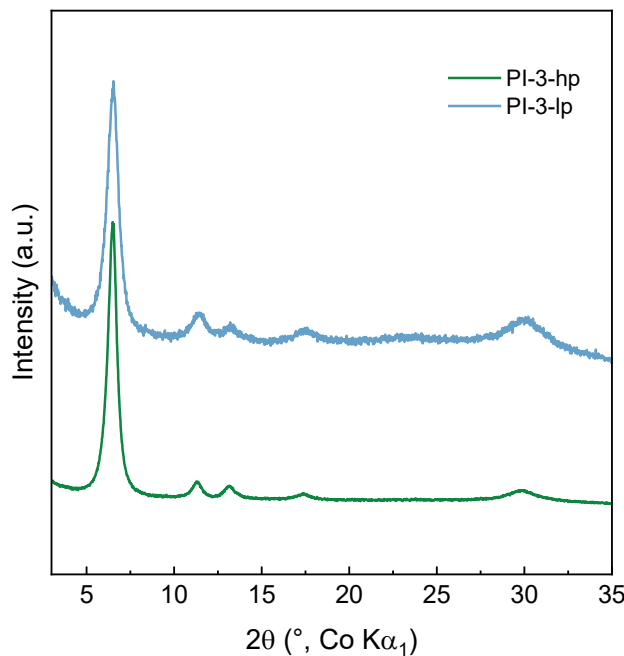


Figure S 9.4-4: XRPD comparison of PI-3-COF-lp/hp. PI-3-COF-hp shows higher crystallinity evident from better defined reflections (smaller FWHM), in agreement with its higher porosity.

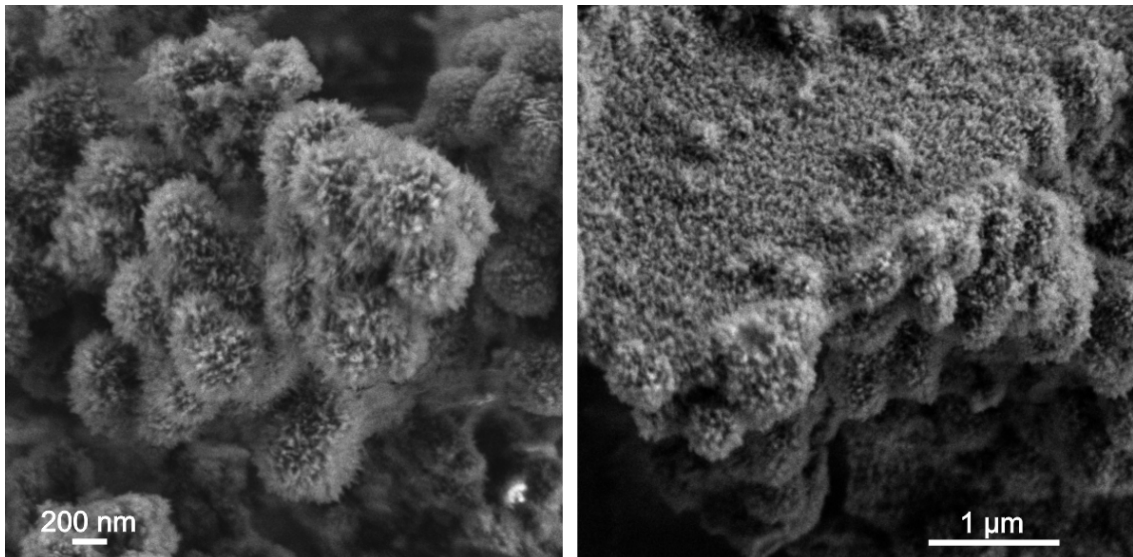


Figure S 9.4-5: SEM images of PI-3-COF-1p showing irregular spherical particles with a rough surface.

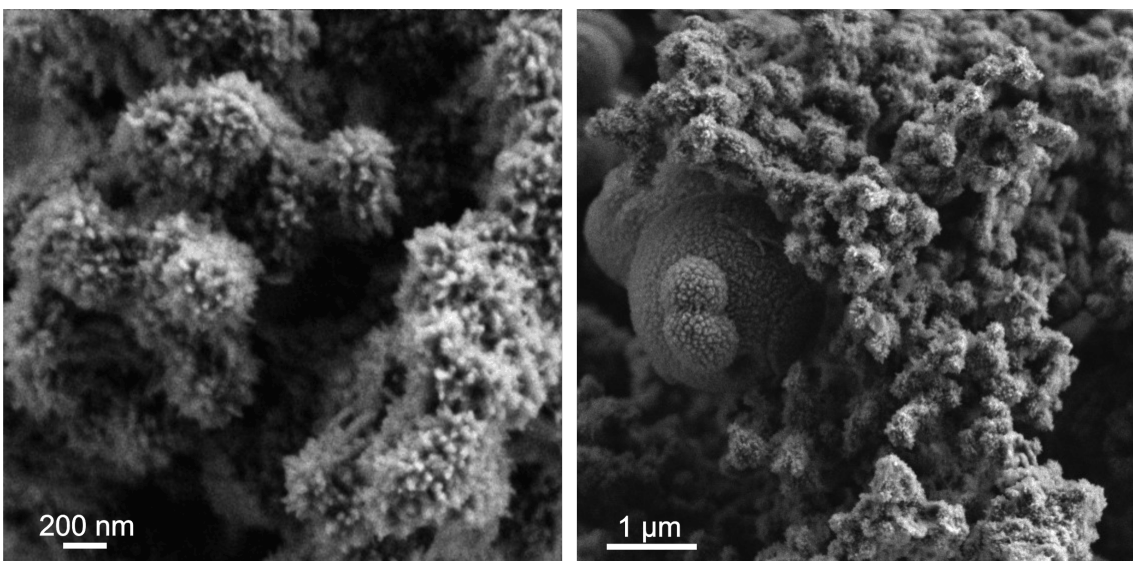


Figure S 9.4-6: SEM images of PI-3-COF-hp show agglomerated and intergrown irregular spherical particles similar to the 1p with a rough surface.

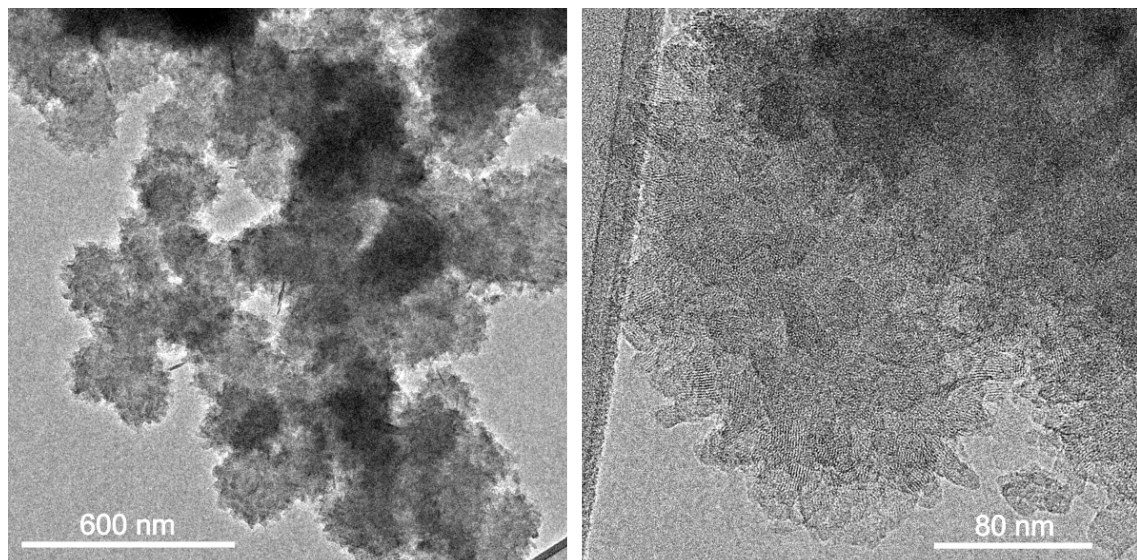


Figure S 9.4-7: TEM images of PI-3-COF-1p showing spherical particles with ~ 200 nm diameter and a rough surface with crystalline stings. The primary crystallite size is in the range of a few tens of nanometers.

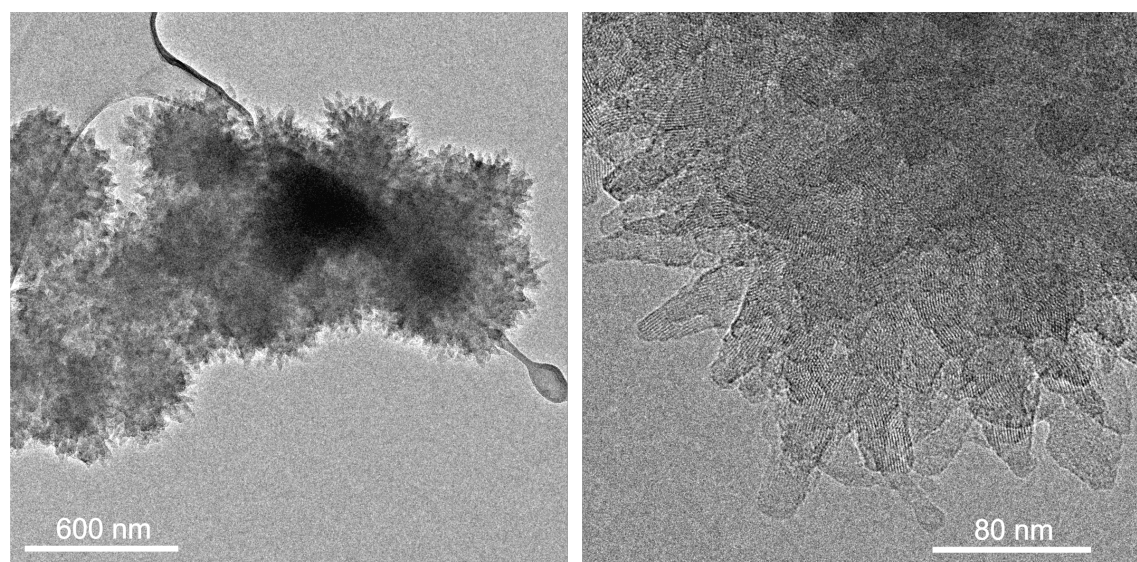


Figure S 9.4-8: TEM images of PI-3-COF-hp show similar morphology to PI-3-COF-1p with slightly larger spherical particles with a rough surface, decorated with crystalline stings.

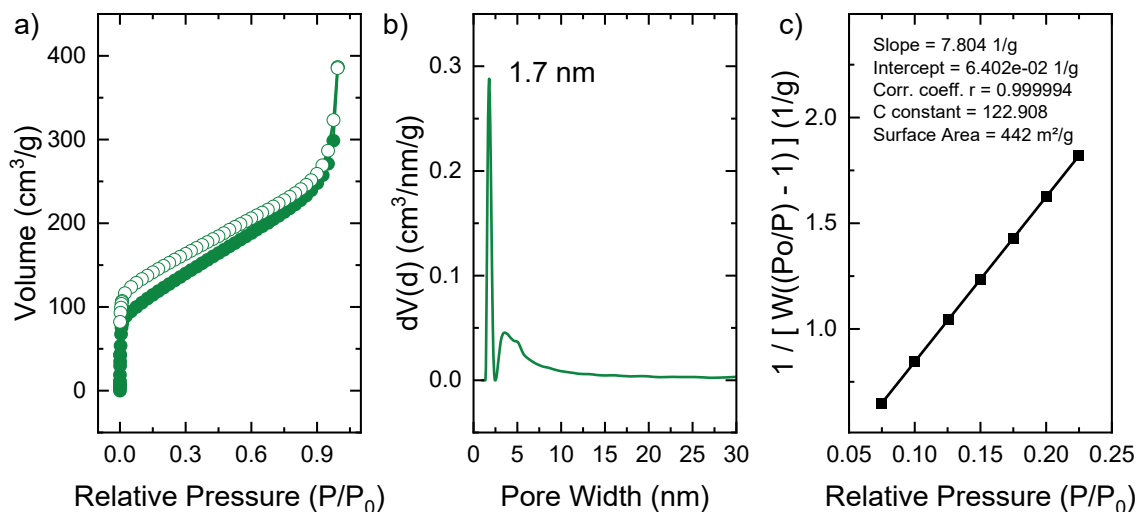


Figure S 9.4-9: N₂ sorption isotherm (a), pore-size distribution (b), and BET plot (c) for PI-3-COF-1p.

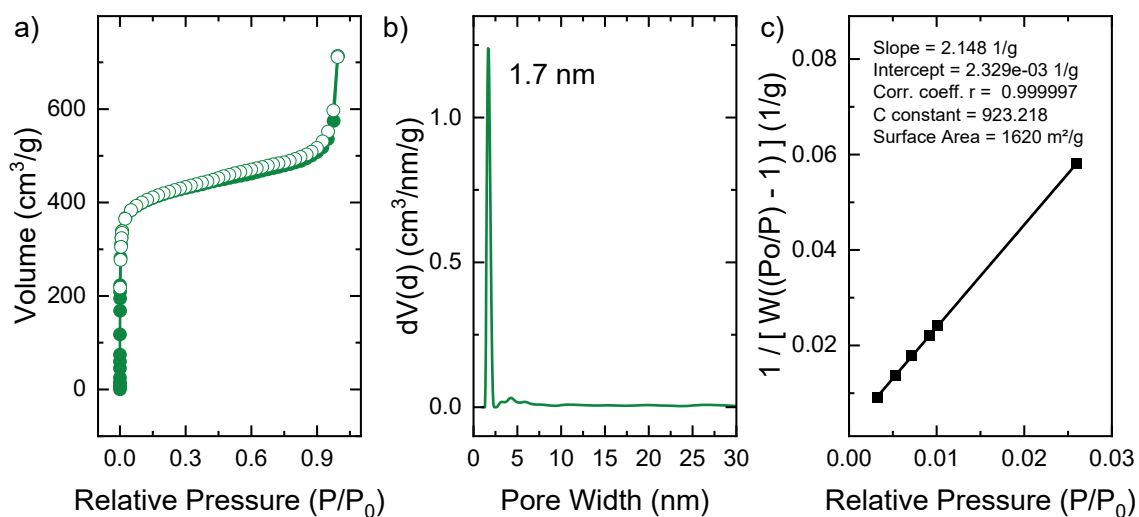


Figure S 9.4-10: N₂ sorption isotherm (a), pore-size distribution (b), and BET plot (c) for PI-3-COF-hp.

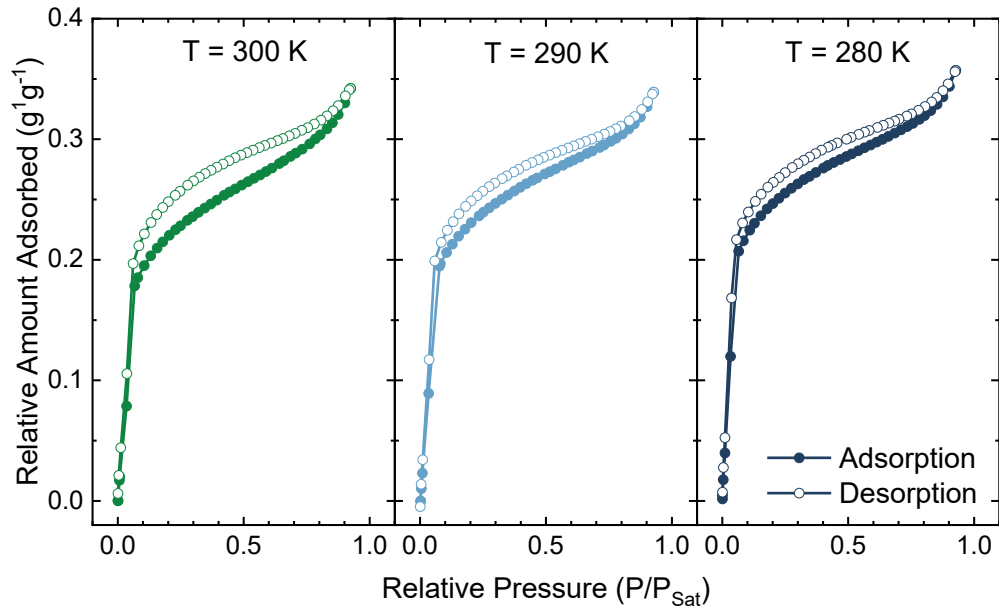


Figure S 9.4-11: MeCN vapor adsorption isotherm of PI-3-COF-lp at different temperatures. Filled dots represent data points of the adsorption branch, hollow dots those of the desorption branch, respectively.

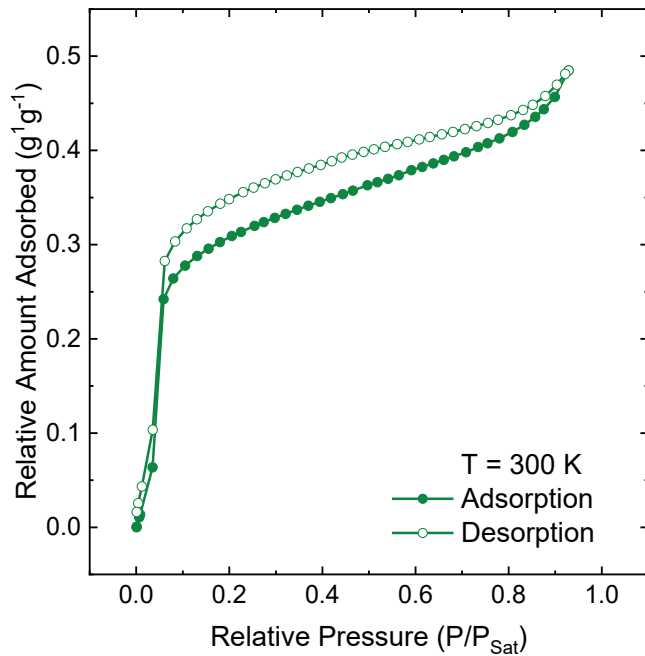


Figure S 9.4-12: MeCN vapor adsorption isotherm of PI-3-COF-hp at 300K. Filled dots represent data points of the adsorption branch, hollow dots those of the desorption branch, respectively.

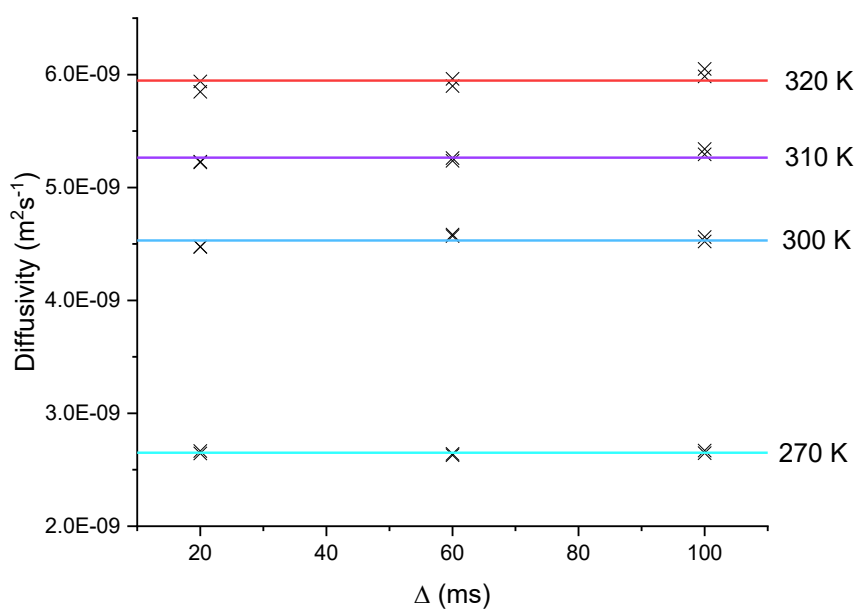


Figure S 9.4-13: Fitted diffusion coefficients from PFG NMR signal attenuations for acetonitrile at different temperatures. The diffusivity is independent of the diffusion time and increases for higher temperatures.

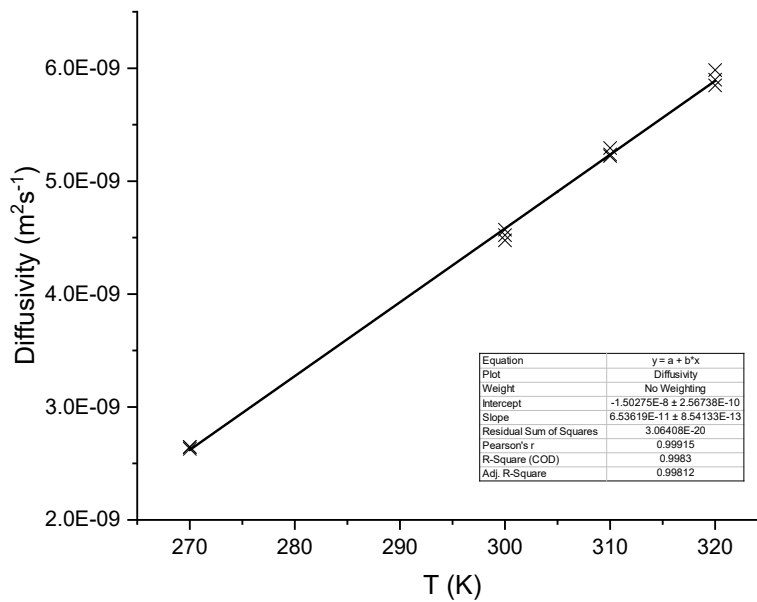


Figure S 9.4-14: Diffusion coefficients of acetonitrile plotted against temperature. As expected for regular, isotropic diffusion, the diffusivity shows a linear correlation to temperature, following the Stokes-Einstein equation. Diffusivities agree well with previous studies.^[24-26] Notably, in this qualitative comparison the influence of viscosity changes is neglected.

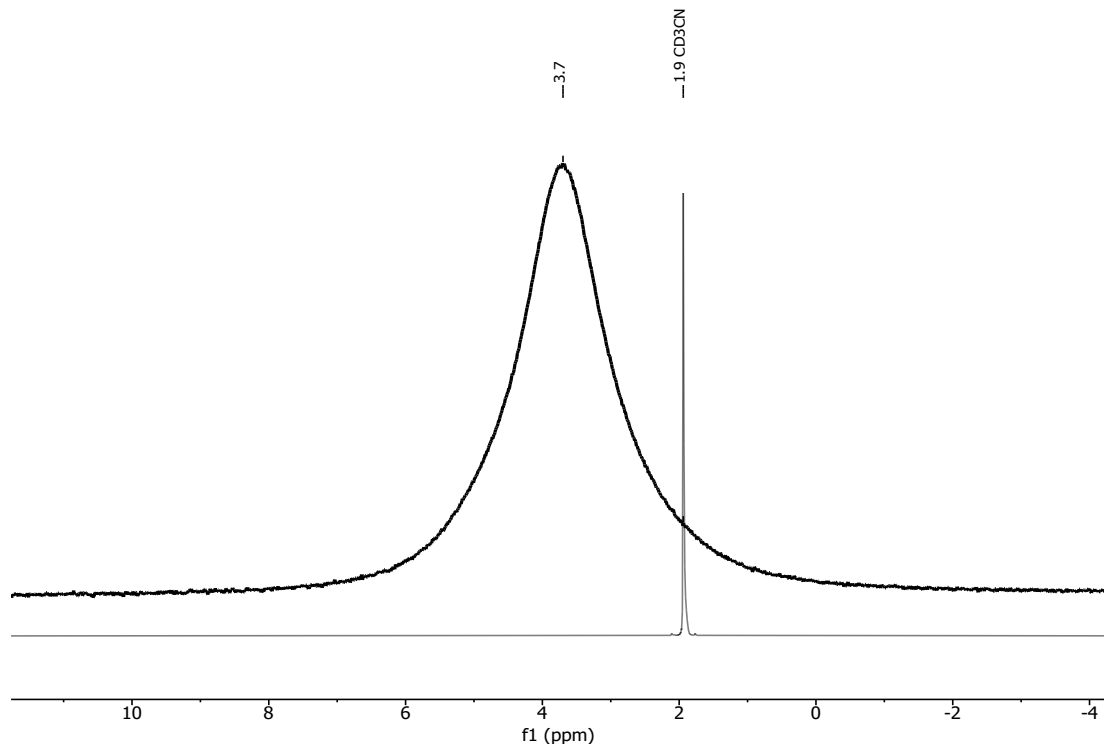


Figure S 9.4-15: ^1H -NMR spectrum of liquid acetonitrile (light grey, bulk) compared to the spectrum of acetonitrile loaded into the pores of PI-3-COF Ip (black). Intensities are adjusted for visibility.

Table S 9.4-1: T_1/T_2 relaxation times of acetonitrile (MeCN) compared to acetonitrile loaded PI-3-COF-Ip/-hp.

	T_1 [s]	T_2 [ms]
MeCN (T=300K)	14.2	850
PI-3 + MeCN (T=300K) -Ip/-hp	1.80/1.94	0.54/0.85
PI-3 + MeCN (T=290K) -Ip/-hp	1.62/1.81	0.49/0.77
PI-3 + MeCN (T=280K) -Ip/-hp	1.41/1.66	0.45/0.70

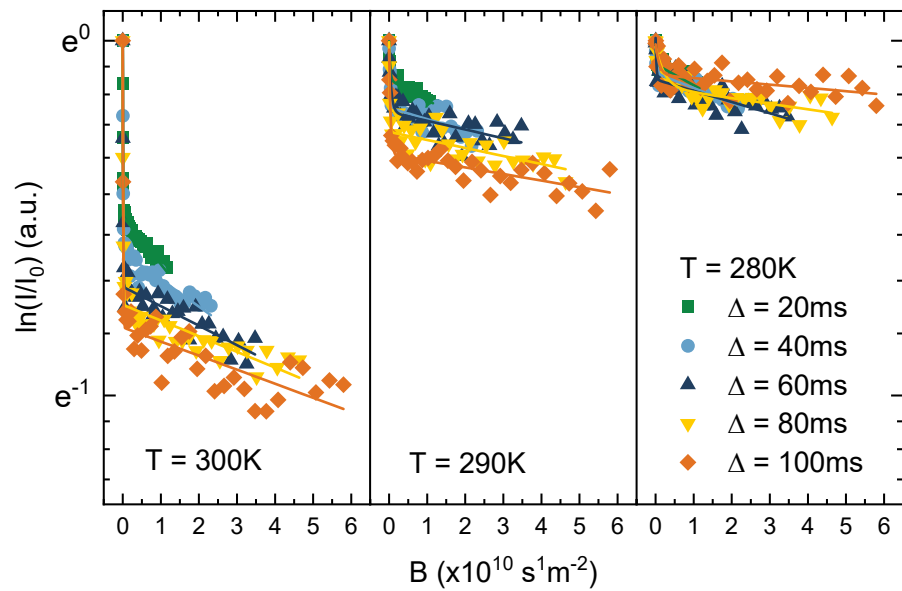


Figure S 9.4-16: PFG-NMR spin-echo attenuation for MeCN loaded PI-3-COF-1p with varying diffusion times (Δ) at different temperatures. Lines represent fits with a simple bi-exponential model.

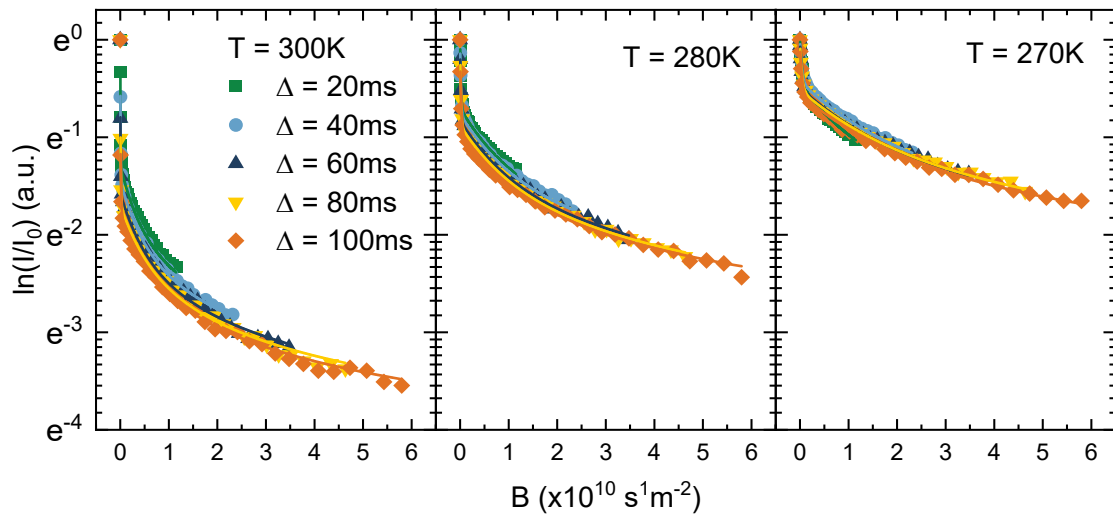


Figure S 9.4-17: PFG-NMR spin-echo attenuation for MeCN loaded PI-3-COF-hp with varying diffusion times (Δ) at different temperatures. Lines represent fits with an anisotropic diffusion model.

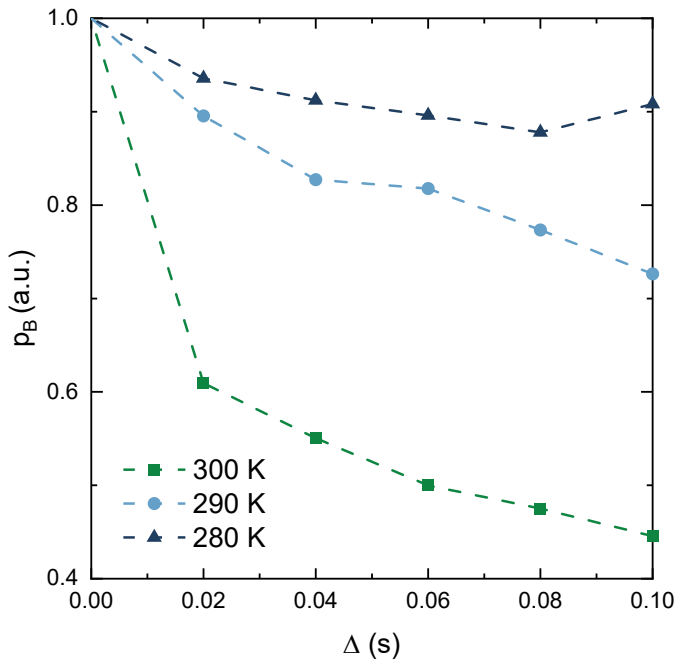


Figure S 9.4-18: Population p_B for PI-3-COF-lp as a function of diffusion time. With lower temperature the fraction of molecules diffusing only within the particle during the diffusion time become larger, corresponding to a larger population p_B .^[27] Dotted lines added to aid visibility.

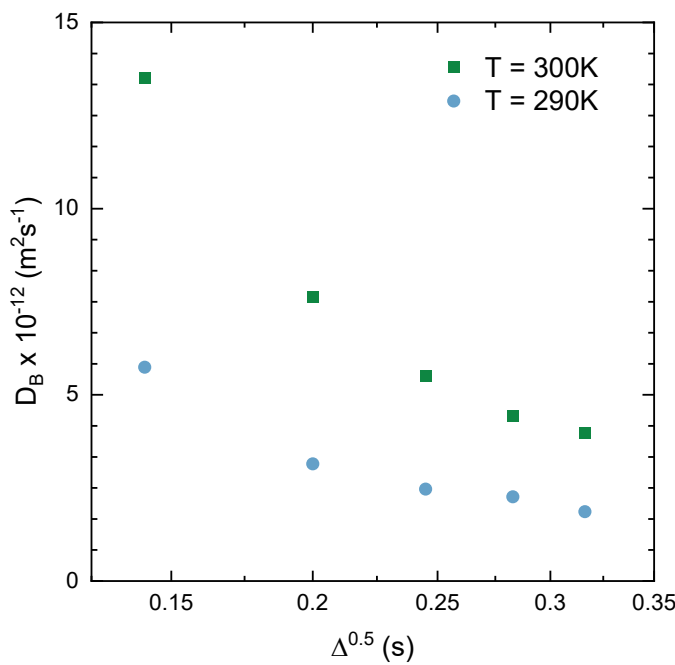


Figure S 9.4-19: Diffusion coefficient D_B (intraparticle) of MeCN-loaded PI-3-COF-lp at different diffusion times. The data was plotted against $\Delta^{0.5}$ according to a restricted diffusion model developed for zeolites.^[28] As visible from the non-linear trend, this model does not fully reflect the experimental data.

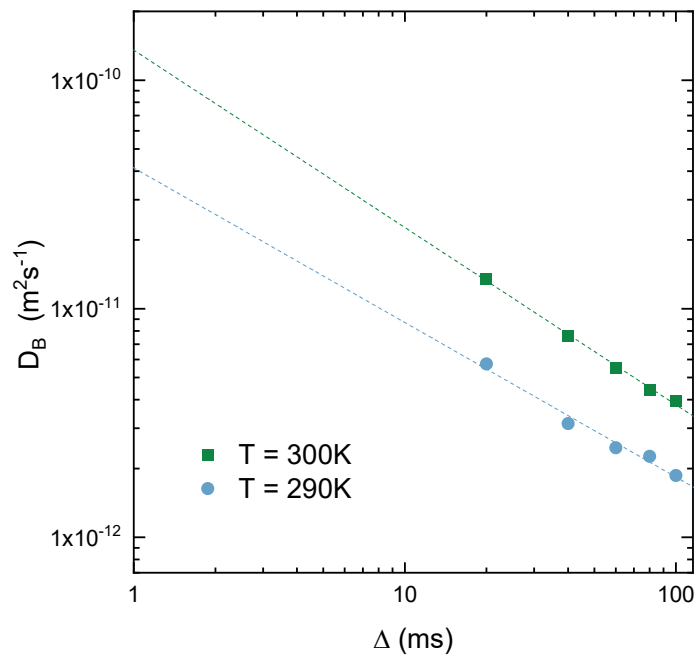


Figure S 9.4-20: Diffusion coefficient D_B of MeCN-loaded PI-3-COF-Ip at different diffusion times, plotted in a phenomenological log-log presentation. Extrapolation to $\Delta = 1\text{ ms}$ suggests a short-range diffusion coefficient in the range of $D_B \approx 10^{-10} \text{ m}^2\text{s}^{-1}$ at $T = 300\text{ K}$.^[29]

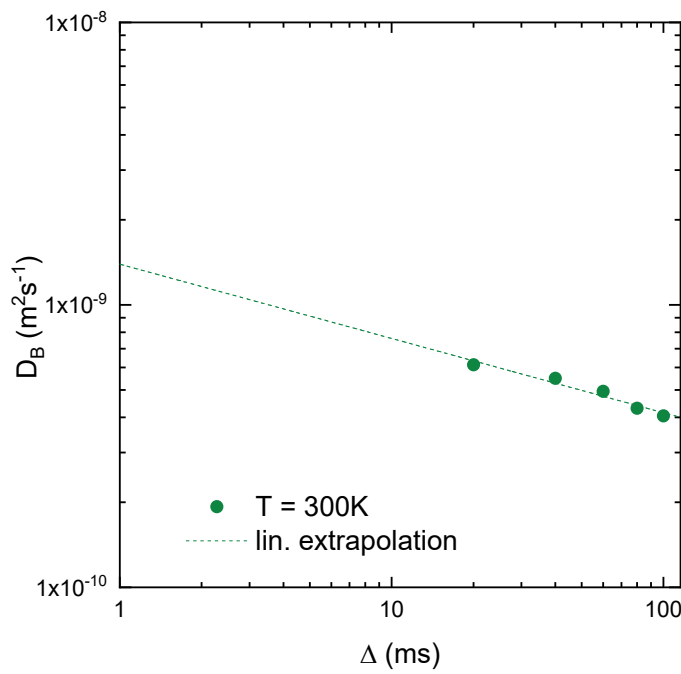


Figure S 9.4-21: Diffusion coefficient D_B of MeCN-loaded PI-3-COF-hp at different diffusion times, plotted in a phenomenological log-log presentation. Extrapolation to $\Delta = 1\text{ ms}$ suggests a short-range diffusion coefficient in the range of $D_B \approx 10^{-9} \text{ m}^2\text{s}^{-1}$ at $T = 300\text{ K}$.^[29]

Table S 9.4-2: Isotropic diffusion radii ($r = (\langle z^2 \rangle)^{0.5}$) for PI-3-COF-lp and hp for different diffusion times at 300 K for D_B . Notably, the calculated radii neglect diffusion anisotropy and molecular exchange between different regions in the materials.

Δ [ms]	r_{LP} [μm]	r_{HP} [μm]
20	0.73	4.95
40	0.78	6.63
60	0.81	7.71
80	0.84	8.29
100	0.89	8.99

9.4.4 References

1. Manz T. A., Limas N. G. Introducing Ddec6 Atomic Population Analysis: Part 1. Charge Partitioning Theory and Methodology. *RSC Adv.* **6**, 47771-47801 (2016).
2. Limas N. G., Manz T. A. Introducing Ddec6 Atomic Population Analysis: Part 2. Computed Results for a Wide Range of Periodic and Nonperiodic Materials. *RSC Adv.* **6**, 45727-45747 (2016).
3. Limas N. G., Manz T. A. Introducing Ddec6 Atomic Population Analysis: Part 4. Efficient Parallel Computation of Net Atomic Charges, Atomic Spin Moments, Bond Orders, and More. *RSC Adv.* **8**, 2678-2707 (2018).
4. Manz T. A. Introducing Ddec6 Atomic Population Analysis: Part 3. Comprehensive Method to Compute Bond Orders. *RSC Adv.* **7**, 45552-45581 (2017).
5. Dubbeldam D., Calero S., Ellis D. E., Snurr R. Q. Raspa: Molecular Simulation Software for Adsorption and Diffusion in Flexible Nanoporous Materials. *Mol. Simul.* **42**, 81-101 (2015).
6. Pott J. J., Siepmann J. I. Vapor-Liquid Equilibria of Mixtures Containing Alkanes, Carbon Dioxide, and Nitrogen. *AIChE J.* **47**, 1676-1682 (2001).
7. Wick C. D., Stubbs J. M., Rai N., Siepmann J. I. Transferable Potentials for Phase Equilibria. 7. Primary, Secondary, and Tertiary Amines, Nitroalkanes and Nitrobenzene, Nitriles, Amides, Pyridine, and Pyrimidine. *J. Phys. Chem. B* **109**, 18974-18982 (2005).
8. Mayo S. L., Olafson B. D., Goddard W. A. Dreiding: A Generic Force Field for Molecular Simulations. *J. Phys. Chem.* **94**, 8897-8909 (2002).
9. Lorentz H. A. Ueber Die Anwendung Des Satzes Vom Virial in Der Kinetischen Theorie Der Gase. *Ann. Phys.* **248**, 127-136 (1881).
10. Berthelot D. Sur Le Mélange Des Gaz. *C. R. Chim.* **126**, 15 (1898).
11. Ewald P. P. Die Berechnung Optischer Und Elektrostatischer Gitterpotentiale. *Ann. Phys.* **369**, 253-287 (1921).

12. Kessler C. et al. Influence of Layer Slipping on Adsorption of Light Gases in Covalent Organic Frameworks: A Combined Experimental and Computational Study. *Microporous Mesoporous Mater.* **336**, 111796 (2022).
13. Hess B., Kutzner C., van der Spoel D., Lindahl E. Gromacs 4: Algorithms for Highly Efficient, Load-Balanced, and Scalable Molecular Simulation. *J. Chem. Theory Comput.* **4**, 435-447 (2008).
14. Abraham M. J. et al. Gromacs: High Performance Molecular Simulations through Multi-Level Parallelism from Laptops to Supercomputers. *SoftwareX* **1-2**, 19-25 (2015).
15. van der Spoel D. et al. A Potential for Molecular Simulation of Compounds with Linear Moieties. *J. Chem. Phys.* **153**, 084503 (2020).
16. Nosé S. A Molecular Dynamics Method for Simulations in the Canonical Ensemble. *Mol. Phys.* **52**, 255-268 (2006).
17. Hoover W. G. Canonical Dynamics: Equilibrium Phase-Space Distributions. *Phys. Rev. A: At. Mol. Opt. Phys.* **31**, 1695-1697 (1985).
18. Berendsen H. J. C. et al. Molecular Dynamics with Coupling to an External Bath. *J. Chem. Phys.* **81**, 3684-3690 (1984).
19. Xu H., Cabriolu R., Smit B. Effects of Degrees of Freedom on Calculating Diffusion Properties in Nanoporous Materials. *J. Chem. Theory Comput.* **18**, 2826-2835 (2022).
20. Tanner J. E. Use of the Stimulated Echo in Nmr Diffusion Studies. *J. Chem. Phys.* **52**, 2523-2526 (1970).
21. Sinnaeve D. The Stejskal-Tanner Equation Generalized for Any Gradient Shape—an Overview of Most Pulse Sequences Measuring Free Diffusion. *Concepts Magn. Reson. A: Bridg. Educ. Res.* **40A**, 39-65 (2012).
22. Jerschow A., Müller N. Suppression of Convection Artifacts in Stimulated-Echo Diffusion Experiments. Double-Stimulated-Echo Experiments. *J. Magn. Reson.* **125**, 372-375 (1997).
23. Grunenberg L. et al. Amine-Linked Covalent Organic Frameworks as a Platform for Postsynthetic Structure Interconversion and Pore-Wall Modification. *J. Am. Chem. Soc.* **143**, 3430-3438 (2021).
24. Keaveney S. T. et al. Nmr Diffusion Measurements as a Simple Method to Examine Solvent-Solvent and Solvent-Solute Interactions in Mixtures of the Ionic Liquid [Bmim][N(So(2) Cf(3))(2)] and Acetonitrile. *ChemPhysChem* **17**, 3853-3862 (2016).
25. Hurle R. L., Woolf L. A. Self-Diffusion in Liquid Acetonitrile under Pressure. *J. Chem. Soc., Faraday Trans.* **78**, 2233 (1982).
26. Marekha B. A. et al. Translational Diffusion in Mixtures of Imidazolium IIs with Polar Aprotic Molecular Solvents. *J. Phys. Chem. B* **118**, 5509-5517 (2014).
27. Kärger J., Pfeifer H. N.M.R. Self-Diffusion Studies in Zeolite Science and Technology. *Zeolites* **7**, 90-107 (1987).
28. Krutyeva M. et al. Surface Barriers on Nanoporous Particles: A New Method of Their Quantitation by Pfg Nmr. *Microporous Mesoporous Mater.* **104**, 89-96 (2007).
29. Hedin N. et al. Intracrystalline Transport Barriers Affecting the Self-Diffusion of Ch(4) in Zeolites |Na(12)|-a and |Na(12-X)K(X)|-A. *Langmuir* **35**, 12971-12978 (2019).

9.5 List of Figures

Figure 1-1: COFs provide a unique combination of properties, such as permanent porosity, chemical and thermal stability on a single crystalline platform, which is highly versatile and tunable by the tools of organic chemistry. Reproduced under the terms of CC-BY-NC 3.0 license. ^[4] Copyright 2021 Royal Society of Chemistry.....	9
Figure 1-2: Different network topologies can be designed by the choice of building blocks.(A) Combinations of planar building blocks, creating two-dimensional COFs. (B) Selected topologies of 3D COFs. Adapted with permission. ^[3] Copyright 2020 Elsevier.	10
Figure 1-3: Reversible bond formation during COF synthesis allows to heal defects in the material. Reproduced under the terms of CC-BY-NC 3.0 license. ^[11] Copyright 2020 Royal Society of Chemistry. ..	11
Figure 1-4: A selection of common condensation reactions to construct linkages in COFs. Reprinted with permission. ^[2] Copyright 2018 John Wiley and Sons.	12
Figure 1-5: Obtaining complex COFs with high crystallinity and high stability remains a challenging task for COF researches, known as the COF trilemma. Adapted under the terms of CC-BY 4.0 license. ^[11] Copyright 2020 Royal Society of Chemistry.....	13
Figure 1-6: Methoxy group substituted building blocks increase interlayer interactions in large pore diameter COFs and stabilize the structure against thermally induced layer displacement. Adapted under the terms of CC-BY 4.0 license. ^[33] Copyright 2021 American Chemical Society.....	14
Figure 1-7: A comparison between a targeted isolated network and the experimentally obtained interpenetrated structure due to extensive π -stacking of building blocks. Adapted with permission. ^[6] Copyright 2021 John Wiley and Sons.	15
Figure 1-8: A steric stabilization strategy combined with guest molecule incorporation during synthesis allowed synthesis of a non-interpenetrated, yet structurally stable 3D COF. Reprinted with permission. ^[37] Copyright 2020 American Chemical Society.	15
Figure 1-9: Trigonal pore channels feature an optimized spatial arrangement of nucleation sites in their pore channels, leading to optimized properties for water vapor adsorption, compared to COFs with different topologies. Adapted under the terms of CC-BY 4.0 license. ^[44] Copyright 2021 Springer Nature.....	16
Figure 1-10: Substoichiometric designs for COFs in 2D (A) and 3D (B) structures. Adapted under the terms of CC-BY 4.0 license, ^[45] and with permission. ^[46] Copyright 2019 Springer Nature, and 2021 American Chemical Society, respectively.	17
Figure 1-11: Redox-active 2,6-diaminoanthraquinone (DAAQ) moieties as building blocks enables energy storage. Reprinted with permission. ^[49] Copyright 2013 American Chemical Society.	18
Figure 1-12: Pore surface engineering presented by post-synthetic linkage modification to fine-tune water vapor adsorption highlights the potential of the linkages as an active site, besides the building block, to modulate framework functions. Reprinted under the terms of CC-BY-NC-ND 4.0 license. ^[54] Copyright 2022 American Chemical Society.....	19
Figure 2-1: Post-synthetic modification of as synthesized COFs can change application-relevant properties of the porous framework, including its stability, among other factors.....	24

Figure 2-2: A comparison of modification strategies for an exemplary imine-linked COF is shown. In contrast to building block engineering, post-synthetic modification strategies make use of the condensed, crystalline, porous structure and circumvent incompatibilities that may occur during the synthesis of the framework.....	24
Figure 2-3: The porous and ordered structure of COFs, which enables the penetration of PSM reagents deep into the material, allows a precise modification of both outer and inner surfaces (pore channels). In contrast to porous polymers, traditional dense polymers only allow (outer) surface modification.....	25
Figure 2-4: Post-synthetic modification reactions can target different sites in the framework, leading to changes at the linkage, the building block, or multiple sites in the material.....	26
Figure 2-5: In contrast to an isolated modification of imine-linkages by oxidation, post-synthetic metallation of coordination sites in a salen-COF leads to a combined modification at linkage- and building block-related sites in the material.....	27
Figure 2-6: Irreversible polymerization reactions do not allow defect healing. Thus, irreversibility in bond-formation reactions leads to less crystalline, usually amorphous polymers. In contrast, reversibility of dynamic covalent reactions allow to obtain well-ordered frameworks, such as crystalline COFs.	28
Figure 2-7: Selected linkage types reported for covalent organic frameworks. A dichotomy between stability and crystallinity occurs, since linkages formed by less reversible reactions suffer from limited error-correction governed by the reversibility of linkage formation. On the other hand, well-ordered materials usually suffer from limited stability.....	28
Figure 2-8: How can imine COFs withstand aqueous conditions, while small molecular imines hydrolyze?	29
Figure 2-9: Imine bonds are reactive toward oxidation and reduction reactions. Due to polarization, the carbon center of the imine bond is susceptible for addition of nucleophiles, especially if promoted by the coordination of Lewis acids to the nitrogen. Likewise, the polarized imine bond can also engage in cycloaddition reactions.	32
Figure 2-10: An overview of reported post-synthetic linkage conversions of imine linkages in COFs. The strategies are categorized by oxidative (light blue segments) and reductive transformations (yellow). Besides simple oxidations or reductions, also reductive additions, or oxidative/reductive cyclizations have been developed.....	33
Figure 2-11: Oxidative linkage conversion of imine- to amide-linked COFs.	33
Figure 2-12: Oxidative cyclizations to benzothiazole (a) and benzoxazole (b) linkages in COFs, with respective benoxazolidine and thioamide intermediates.....	34
Figure 2-13: A comparison of synthetic steps associated with ex-situ PSM protocols and condensed in-situ PSM reactions, where the pristine COF occurs as an intermediate.	35
Figure 2-14: N-oxidation of imine linkages with an electrophilic oxidizing agent led to more polar nitrone linkages.	36
Figure 2-15: Reduction of imine to amine linked COFs with formic acid. The strategy “locks“ the linkage against hydrolysis and can be performed as an in-situ, i.e. one-pot reductive crystallization.	37

Figure 2-16: Besides their enhanced hydrolytic stability, the nucleophilic secondary amine centers in amine-linked COFs can serve as reactive centers for functionalization at the pore wall. This enables access to tailored functional and stable, yet crystalline frameworks.	37
Figure 2-17: Coordination of a Lewis acid on the nitrogen center of the imine polarizes and thus activates the electrophilicity of the carbon center for an addition of a nucleophile, such as cyanide to yield cyano-substituted amine linkages.	38
Figure 2-18: Lewis acid activation activates the imine linkage for cycloaddition reactions, affording tetrahydroquinoline-linked frameworks. Further oxidation leads to quinoline-linked COFs.	39
Figure 2-19: Oxidative cyclization with an alkyne may also occur intramolecularly – combining linkage modification strategies with building block engineering approaches.	39
Figure 2-20: A guide for decision making in reaction optimization of PSM reactions in COFs.	51
Figure 3-1: Overview about the topics addressed in this thesis: synthetic modification of complexity in covalent organic frameworks and dynamic processes in their pore channels.	56
Figure 4-1: (a) Synthesis of amine-linked covalent organic frameworks. (b) FT-IR spectra, (c) ^{13}C CP-MAS ssNMR spectra, and (d) XRPD pattern comparison of PI-3-COF (green) and rPI-3-COF (blue). (e and f) Chemical structure of a single pore of (e) rPI-3, (f) rTTI, and (g) rPy1P-COF. (h–j) Rietveld refinements for (h) rPI-3, (i) rTTI, and (j) rPy1P-COF.	62
Figure 4-2 (a) Energy surface plot for different values of dihedral angles U and Z in the molecular model PI-3 M. The blue crosses highlight the lowest energy conformation for the single-pore model PI-3 SP. (b) Energy surface plot for the molecular model rPI-3 M. The blue crosses highlight the lowest energy conformation for the single-pore model rPI-3 SP. As a comparison, the conformation of a protonated molecular model H+rPI-3 M is shown on the surface (red cross). Notably, in this simple molecular model, the effect of the anion and charge repulsion, occurring in the layered real structure, are neglected. (c) Dihedral angles U and Z shown in a section of PI-3 M. (d) Reduced total scattering patterns and (e) pair distribution functions for crystalline and disordered materials are overlaid. (f and g) Sixteen-layer structure models derived from PDF analysis for disordered rPI-3-COF (left) and rPI-3-COF (right) considering random translational disorder in 1–10 directions are shown.	67
Figure 4-3 (a) Reaction sequence for post-synthetic functionalization of amine-linked covalent organic frameworks. Frameworks entirely connected by secondary amine linkages (rCOF) or hybrid materials with mixed amine/imine bonds (prCOF) and partially formylated amine-linkages (pfrCOF) are accessible in a single step from imine COFs. As experimentally shown with pfrPI-3-COF (middle), <i>N</i> -formyl groups in pfrCOFs can be deprotected under acidic conditions. Released secondary amine linkages may allow two-step functionalization to afford bifunctionalized frameworks. The amine/ <i>N</i> -formyl amine ratio is arbitrary. (b and c) FT-IR spectra of rTTI-COF samples functionalized with (b) benzoyl chloride (BzCl) and (c) toluenediisocyanate (TDI) are shown and compared to rTTI-COF. Gray areas in (b) highlight reduced N—H, emerging C=O, and characteristic C=C vibrations in BzCl-rTTI-COF. For TDI-rTTI-COF, vibrations of dangling -NCO and emerging C=O vibrations are highlighted (gray).	69
Figure 4-4 Pathways leading to a set of amine-linked covalent organic frameworks as demonstrated with the PI-3 COF system.	70
Figure 5-1: (a) Synthesis scheme for the post-synthetic transformation of imine- into nitrone-linked covalent organic frameworks. (b) Chemical structure of a single pore of (b) NO-PI-3-COF and (c) NO-TTI-COF.	78

Figure 5-2: (a) XRPD pattern comparison of PI-3 (green), rPI-3 (blue) and NO-PI-3-COF (dark blue) obtained from multi-step linkage conversion. As indicated by arrows, the position of the stacking reflection shifts depending on the linkage type in the framework. (b) ^{13}C CP-MAS ssNMR spectra of these materials with characteristic signals highlighted by arrows. (c) ^{15}N CP-MAS ssNMR spectra of rPI-3 and NO-PI-3-COF.....	79
Figure 5-3: Rietveld refinements for NO-PI-3-COF (a) and NO-TTI-COF (b).....	80
Figure 5-4: (a) Comparison of water vapor adsorption isotherms of PI-3- and NO-PI-3-COF. (b) Water adsorption-desorption cycles of NO-PI-3-COF. (c) Adsorption isotherms of TTI-, rTTI-, and NO-TTI-COF.	83
Figure 5-5: <i>In situ</i> XRPD measurements of NO-PI-3-COF (a): XRPD patterns in dehydrated (green) and hydrated states (blue) including the background diffraction signal attributed to the sample holder and the humidity chamber (asterisks) and selected reflection indices. (b) Time-dependent intensity of the 100 reflection obtained from <i>in situ</i> XRPD patterns during hydration and dehydration. (c) Modulation of the 100 intensity during multiple hydration and dehydration cycles.....	84
Figure 6-1: (a) Configurational changes upon photoswitching and thermal helix inversion of motors 1 and 2 . (b) UV/Vis absorption spectra upon irradiation of motors 1 and 2 in acetonitrile at 5 °C. The initial absorption spectra are shown in dark blue. The red spectra correspond to the photostationary state (PSS) at 395 nm for motor 1 and 365 nm for motor 2 . The spectra after thermal helix inversion (THI) are shown in light blue. (c) ^1H NMR spectra of motors 1 and 2 in the dark (blue) and after irradiation (red) in deuterated benzene at 10 °C. Spectra of the PSS show an additional set of signals for the metastable states (grey). (d) Raman spectra (785 nm) of motor 2 in toluene in the dark (blue), after irradiation with 365 nm (red) and after thermal helix inversion (light blue).	95
Figure 6-2: (a) Synthesis of m₂₀-COF from mixtures of spacer and motor building blocks with triformylbenzene (3) under solvothermal conditions. (b) Transmission electron microscopy (TEM) image of m₂₀-COF with visible pore channels along [001] pointing towards the surface of the spherical particle (blue inset). Fast Fourier transformed (FFT) insets show a hexagonal pattern (red box, viewing direction [001]). (c) XRPD pattern and unit cell parameters of m₂₀-COF obtained by Pawley refinement with a simplified unit cell proxy model (see Table S 9.3-1) (d) ^{13}C -CPMAS ssNMR spectrum of m₂₀-COF containing signals of the motor and spacer building blocks. (e) N_2 adsorption isotherm of m₂₀-COF	98
Figure 6-3: (a) Schematic illustration of molecular models probing the relative orientation and interlayer distance of the spacer moiety with respect to the imine bond configuration in a condensed framework. The antiparallel EE model combines the least steric repulsion of the methyl groups with best π overlap. (b) Experimental pair distribution function (PDF) for m₂₀-COF and simulated PDFs with different values of the displacement parameter U_{33} , simulating the effects of stacking and conformational disorder, are overlaid. (c) Interlayer density distributions simulated for different layer offset scenarios in 2D honeycomb layered COFs are shown to demonstrate the specific impact of different relative stacking offsets on the PDF profile ($U_{11} = U_{22} = 1.0 \text{ \AA}^2$; $U_{33} = 0.05 \text{ \AA}^2$).....	100
Figure 6-4: Raman spectra of the imine motor 2 as a thin-film (a), m₅₀-P (b), and m₂₀-COF . The thin-film of the molecular imine motor 2 was recorded at 785 nm and irradiated at 365 nm with a UV-LED. Raman spectra of m₅₀-P (b), m₂₀-COF and m₀-COF (c) were recorded with a Raman laser at 355 nm for simultaneous excitation of the motor.....	102
Figure 6-5: FT-IR spectra of a thin film of the imine motor 2 (a) and m₂₀-COF (b) under prolonged irradiation at 365 nm (UV-LED). Grey area highlights appearing C=O vibrations during irradiation of imine motor 2 . Direct reflectance UV/Vis spectra (c) and XRPD patterns of m₂₀-COF before and during irradiation (>1.5h) at 365 nm are shown. The patterns are stacked with an arbitrary offset to aid visibility.	104

Figure 7-1: (a) Chemical structure of a single pore of PI-3-COF. (b) XRPD pattern and (c) N ₂ adsorption isotherm comparison of PI-3-COF-lp (green) and PI-3-COF-hp (blue).	115
Figure 7-2: PFG-NMR spin-echo attenuation for (a) liquid MeCN, (b) MeCN loaded PI-3-COF-lp, (c) MeCN loaded PI-3-COF-hp with varying diffusion times (Δ) at T = 300K. Lines represent fits with a mono- or bi-exponential model for MeCN and MeCN loaded COFs, respectively.....	117
Figure 7-3 Comparison between experimental N ₂ adsorption isotherms at 77K (low porosity in blue, high porosity in green) and simulated ones. The isotherm resulting from the shifted structure is depicted in black squares, the one of the eclipsed stacked structure in red triangles.....	121
Figure 7-4 Visualization of the eclipsed (a) and the shifted structure (b) of PI 3-COF. Violet surfaces depict the N ₂ accessible pore surface based on Van der Waals parameters.	122

9.6 List of Publications

Publications included as chapters in this thesis

1. *Book Chapter: Post-Synthetic Linkage Modification in Covalent Organic Frameworks*
L. Grunenberg, F. Haase and B. V. Lotsch, in *Reticular Chemistry – A Practical Approach for Metal-Organic Frameworks and Covalent Organic Frameworks* (Eds.: M. Kalmutzki, C. Diercks and O. M. Yaghi), *in preparation*.
2. *Amine-Linked Covalent Organic Frameworks as a Platform for Postsynthetic Structure Interconversion and Pore-Wall Modification*
L. Grunenberg, G. Savasci, M. W. Terban, V. Duppel, I. Moudrakovski, M. Etter, R. E. Dinnebier, C. Ochsenfeld, and B. V. Lotsch, *J. Am. Chem. Soc.* **2021**, *143*, 3430–3438. doi: 10.1021/jacs.0c12249
3. *Postsynthetic Transformation of Imine- into Nitrone-Linked Covalent Organic Frameworks for Atmospheric Water Harvesting at Decreased Humidity*
L. Grunenberg, G. Savasci, S. T. Emmerling, F. Heck, S. Bette, A. Cima Bergesch, C. Ochsenfeld and B. V. Lotsch, *J. Am. Chem. Soc.* **2023**, *145*, 13241–13248. doi: 10.1021/jacs.3c02572
4. *Light-Driven Molecular Motors Embedded in Covalent Organic Frameworks*
C. Stähler,[‡] L. Grunenberg,[‡] M. W. Terban, W. R. Browne, D. Doellerer, M. Kathan, M. Etter, B. V. Lotsch, B. L. Feringa and S. Krause, *Chem. Sci.* **2022**, *13*, 8253–8264. doi: 10.1039/d2sc02282f ([‡] equal contribution)
5. *Self-Diffusion of Acetonitrile in a Covalent Organic Framework: Simulation and Experiment*
L. Grunenberg,[‡] C. Keßler,[‡] T. W. Teh, R. Schuldert, F. Heck, J. Kästner, J. Groß, N. Hansen, and B. V. Lotsch, **2023**, *to be submitted*. ([‡] equal contribution)

Publications not included as chapters in this thesis

6. *Downsizing Porphyrin Covalent Organic Framework Particles Using Protected Precursors for Electrocatalytic CO₂ Reduction*
K. Endo, A. Raza, L. Yao, S. Van Gele, A. Rodríguez-Camargo, H. A. Vignolo-González, L. Grunenberg, B. V. Lotsch, **2023**, *submitted*.
7. *The Weyl Semimetals M_{Ir}Te₄ (M = Nb, Ta) as Efficient Catalysts for Dye-Sensitized Hydrogen Evolution*
M. Samanta, H. Tan, S. Laha, H.A. Vignolo-Gonzalez, L. Grunenberg, S. Bette, V. Duppel, P. Schützendübe, A. Gouder, B. Yan, B. V. Lotsch, *Adv. Energy. Mater.* **2023**, 2300503. doi: 10.1002/aenm.202300503
8. *Escaping the Horns of the COF Dilemma*
L. Grunenberg and B. V. Lotsch, *Matter* **2022**, *5*, 2483–2484. doi: 10.1016/j.matt.2022.06.026

9. *Covalent Organic Framework Nanoplates Enable Solution-Processed Crystalline Nanofilms for Photoelectrochemical Hydrogen Evolution*
L. Yao, A. Rodríguez-Camargo, M. Xia, D. Mücke, R. Guntermann, Y. Liu, L. Grunenberg, A. Jiménez-Solano, S. T Emmerling, V. Duppel, K. Sivula, T. Bein, H. Qi, U. Kaiser, M. Grätzel, B. V. Lotsch, *J. Am. Chem. Soc.* **2022**, *144*, 10291-10300. doi: 10.1021/jacs.2c01433

10. *Light-Driven Carbon Nitride Microswimmers with Propulsion in Biological and Ionic Media and Responsive On-Demand Drug Delivery*
V. Sridhar, F. Podjaski, Y. Alapan, J. Kröger, L. Grunenberg, V. Kishore, B. V. Lotsch and M. Sitti, *Sci. Robot.* **2022**, *7*, eabm1421. doi: 10.1126/scirobotics.abm1421

11. *Palladium-Catalyzed C–O Cross-Coupling as a Replacement for a Mitsunobu Reaction in the Development of an Androgen Receptor Antagonist*
A. Hager, N. Guimond, L. Grunenberg, C. Hanisch, S. Steiger and A. Preuss, *Org. Process. Res. Dev.* **2021**, *35*, 654–660. doi: 10.1021/acs.oprd.0c00484

12. *Interfacial Engineering for Improved Photocatalysis in a Charge Storing 2D Carbon Nitride: Melamine Functionalized Poly(Heptazine Imide)*
J. Kröger, A. Jiménez-Solano, G. Savasci, P. Rovó, I. Moudrakovski, K. Küster, H. Schlomberg, H. A. Vignolo-González, V. Duppel, L. Grunenberg, C. B. Dayan, M. Sitti, F. Podjaski, C. Ochsenfeld, B. V. Lotsch, *Adv. Energy Mater.* **2021**, *11*, 2003016. doi: 10.1002/aenm.202003016

13. *A Flavin-Inspired Covalent Organic Framework for Photocatalytic Alcohol Oxidation*
S. Trenker, L. Grunenberg, T. Banerjee, G. Savasci, L. M. Poller, K. I. M. Muggli, F. Haase, C. Ochsenfeld, B. V. Lotsch, *Chem. Sci.* **2021**, *12*, 15143–15150. doi: 10.1039/D1SC04143F

14. *Sustained Solar H₂ Evolution from a Thiazolo[5,4-*d*]thiazole-Bridged Covalent Organic Framework and Nickel-Thiolate Cluster in Water*
B. P. Biswal, H. A. Vignolo-González, T. Banerjee, L. Grunenberg, G. Savasci, K. Gottschling, J. Nuss, C. Ochsenfeld, B. V. Lotsch, *J. Am. Chem. Soc.* **2019**, *141*, 11082–11092. doi: 10.1021/jacs.9b03243

Earlier publications

15. *Organic Photocatalysis for the Radical Couplings of Boronic Acid Derivatives in Batch and Flow*
F. Lima, L. Grunenberg, H. B. A. Rahman, R. Labes, J. Sedelmeier, S. V. Ley, *Chem. Commun.* **2018**, *54*, 5606–5609. doi: 10.1039/C8CC02169D

16. *A Lewis Base Catalysis Approach for the Photoredox Activation of Boronic Acids and Esters*
F. Lima, U. K. Sharma, L. Grunenberg, D. Saha, S. Johannsen, J. Sedelmeier, E. V. Van der Eycken, S. V. Ley, *Angew. Chem. Int. Ed.* **2017**, *56*, 15136–15140. doi: 10.1002/anie.201709690